Gas retention and transport processes in low-permeability rocks

Von der Fakultät für Georessourcen und Materialtechnik
der Rheinisch-Westfälischen Technischen Hochschule Aachen genehmigte

Habilitationsschrift

von Dr. rer. nat. Andreas Busch

Köln

Gutachter: Prof. Dr. H. Stanjek
Prof. Dr. C.J. Spiers
Prof. Dr. D. Elsworth

Tag der Habilitation: 05. Juli 2014

Diese Habilitation ist auf den Internetseiten der Universitätsbibliothek online verfügbar.

Contents

1 INTRODUCTION 6

1.1 ORGANISATION OF THESIS AND INPUT OF AUTHOR TO INDIVIDUAL CHAPTERS 6

1.2 FOCUS AREA: CARBON CAPTURE AND STORAGE AND UNCONVENTIONAL GAS PRODUCTION 8

1.3 HOW DOES THIS THESIS RELATE TO GEOLOGICAL STORAGE OF CARBON DIOXIDE AND GAS PRODUCTION FROM UNCONVENTIONAL RESERVOIRS? 20

2 CBM AND CO_2-ECBM RELATED SORPTION PROCESSES IN COAL: A REVIEW 24

2.1 INTRODUCTION 24

2.2 ADSORPTION METHODS 26

2.3 WATER SORPTION ON COAL 40

2.4 COAL-SPECIFIC FACTORS CONTROLLING WATER SORPTION 42

2.5 DEPENDENCE OF CO_2, CH_4 AND WATER SORPTION ON COAL PROPERTIES 51

2.6 CO_2 AND CH_4 SORPTION KINETICS ON COAL 58

2.7 CONCLUSIONS 67

3 GAS SATURATION AND CO_2 ENHANCEMENT POTENTIAL OF COALBED METHANE RESERVOIRS AS A FUNCTION OF DEPTH 68

3.1 INTRODUCTION 68

3.2 SAMPLES AND SAMPLE PREPARATION 74

3.3 EXPERIMENTAL AND CONCEPTUAL PROCEDURE 75

3.4 RESULTS AND GEOLOGICAL IMPLICATIONS 80

3.5 DISCUSSION 86

3.6 CONCLUSION 88

3.7 APPENDIX 90

4 A PRELIMINARY EVALUATION OF THE CO_2 STORAGE POTENTIAL IN UNMINABLE COAL SEAMS OF THE MÜNSTER CRETACEOUS BASIN, GERMANY 91

4.1 INTRODUCTION 91

4.2 GEOLOGICAL SETTING OF THE MÜNSTER CRETACEOUS BASIN 92

4.3 METHODOLOGY 94

4.4 RESULTS AND DISCUSSION 97

4.5 CONCLUSION 108

5 HIGH-PRESSURE METHANE AND CARBON DIOXIDE SORPTION ON COAL AND SHALE SAMPLES FROM THE PARANÁ BASIN, BRAZIL 109

5.1 INTRODUCTION 109

5.2 GEOLOGICAL SETTING 110

5.3 SAMPLES 113

5.4 METHODS AND EXPERIMENTAL PROCEDURES 114

5.5 Results and Discussion 114
5.6 Conclusions 132

6 LABORATORY EXPERIMENTS ON ENVIRONMENTAL FRIENDLY MEANS TO IMPROVE COALBED METHANE PRODUCTION BY CARBON DIOXIDE/FLUE GAS INJECTION 134

6.1 Introduction 134
6.2 Equipment Design 135
6.3 Sample Description 137
6.4 Preferential Sorption Behaviour 138
6.5 Experimental Procedure and Data Interpretation 139
6.6 Results and Discussions 141
6.7 Conclusions 159
6.8 Appendix 160

7 PREDICTING CAPILLARITY OF MUDROCKS 166

7.1 Introduction 166
7.2 Terminology & Background 167
7.3 Overview of measurement methods to determine capillary pressures in mudrocks 172
7.4 Database content 174
7.5 Results and Discussion 175
7.6 Conclusions 192

8 THE SIGNIFICANCE OF CAPROCK SEALING INTEGRITY FOR CO_2 STORAGE 193

8.1 Introduction 193
8.2 CO_2 diffusion 193
8.3 CO_2 sorption on clay mineral surfaces 195
8.4 Capillary entry pressure and capillary leakage 196
8.5 Fault leakage 200
8.6 CO_2-water-rock interactions affecting caprock sealing capacity 201
8.7 Conclusions 202

9 EXPERIMENTAL INVESTIGATION OF THE CO_2 SEALING EFFICIENCY OF CAPROCKS 204

9.1 Introduction 204
9.2 Samples 206
9.3 Experimental 207
9.4 Results 213
9.5 Discussion 219
9.6 Conclusions 225

10 CARBON DIOXIDE STORAGE POTENTIAL OF SHALES 227

10.1 Introduction 227

10.2 Sample Description 228
10.3 Experimental 230
10.4 Results 232
10.5 Discussion 238
10.6 Conclusion and Outlook 242
10.7 Appendix - Evaluation of effective diffusion coefficients 243

11 INTERACTION OF CARBON DIOXIDE WITH NA-EXCHANGED MONTMORILLONITE AT PRESSURES TO 640 BARS: IMPLICATIONS FOR CO_2 SEQUESTRATION 246

11.1 Introduction 246
11.2 Experimental methods 247
11.3 Data processing 252
11.4 Experimental results 254
11.5 Discussion 259

12 X-RAY DIFFRACTION STUDY OF K- AND CA-EXCHANGED MONTMORILLONITES IN CO_2 ATMOSPHERES 263

12.1 Introduction 263
12.2 Experimental methods 264
12.3 Results and Discussion 268

13 CONCLUSIONS AND SUGGESTIONS FOR FUTURE RESEARCH 275

13.1 Main Conclusions 275
13.2 Implications for future research 281

14 REFERENCES 287

1 Introduction

This thesis discusses gas transport and gas retention in low permeability rocks. These are timely processes in light of potential applications like (a) caprock sealing above hydrocarbon or CO_2 storage reservoirs and (b) gas production from unconventional reservoirs such as shale or coal.

In order to set the scene for the overall applicability of the work summarised here, an overview of the current high-level discussion is given which is followed by the integration of the contents of this thesis into these high-level scenarios.

1.1 Organisation of thesis and input of author to individual chapters

This thesis starts with an introduction, discussing the wider focus area, relating to (enhanced) gas production from unconventional gas reservoirs and mudrocks acting as seals for carbon storage. It is further separated into two parts: **Chapters** 2 **to** 6 focus on natural coal for primary production of coalbed methane (CBM), CO_2 enhanced CBM production (CO_2-ECBM) or geological storage of carbon dioxide. **Chapters** 7 **to 12** relate to mudrocks and shales mainly as barriers for containment of CO_2 in geological stores, in addition providing references to shale and tight gas production and CO_2 enhanced shale gas production in general.

All chapters are based on selected published articles by the author in international journals, either as main author or as co-author. In the following an overview is provided for each chapter with details of the specific contribution by the author:

In the first part of this thesis, **Chapter** 2 is based on a review article focusing on gas adsorption of gases and water on coal (Busch and Gensterblum, 2011). Main measurement techniques are described to record sorption isotherms with reference to error sources. This is followed by a detailed discussion of the interplay between water, gas (CO_2, CH_4) and coal functional groups. Gas sorption properties are discussed as a function of coal maturity for CO_2 and CH_4 with reference to CO_2-ECBM and CBM production. Finally, sorption kinetics is discussed, as well as the modelling approaches and kinetic parameters (like diffusion coefficient). In **Chapter 3** sorption parameters of different maturity coals are used to predict gas saturations of coals with burial history and is basically based on two previous articles (Gensterblum et al., 2013; Gensterblum et al., accepted). Sweet-spotting potential are derived for CBM and CO_2-ECBM and a large dataset for gas adsorption on coal presented. Input of the author was supervision of the underlying laboratory and analytical work by the main author, manuscript drafting and detailed discussion of results. **Chapter 4** contains a detail case study for CBM and CO_2-ECBM in the Münster Cretaceous Basin, Germany (Kronimus et al., 2008), including geological aspects, limitations and detailed capacity appraisal based on laboratory studies. Author's input was in the overall supervision of this study as well as the detailed laboratory work and capacity estimates. **Chapter 5** is focusing on a case study for CBM and CO_2-ECBM in the Paraná Basin, Brazil (Weniger et al., 2010). Based on core samples from a continuous core, intersecting

various coal seams and organic-rich shales, sorption relations as a function of clay and organic matter content was derived showing that inorganic material has a substantial impact on CO_2 sorption capacity of natural rocks, as compared to CH_4, which is limited. Author's input was in drafting of manuscript, discussion of results and part of the laboratory work. **Chapter 6** studies the competitive gas transport of CO_2 and CH_4 and flue gases and CO_2 in coal core samples (Mazumder et al., 2008). Author's input was in the drafting of the manuscript, detailed data evaluation and discussion as well as the determination of flue gas PVT data used in the evaluation.

Within the second part of this thesis, focusing on mudrock and shale material, **Chapter 7** provides a review of transport properties and capillary pressures in mudrocks with the aim to derive global equations to predict capillarity (Busch and Amann-Hildenbrand, 2013). These are relevant parameters to better constrain gas transport in unconventional gas plays but also to better understand sealing lithologies as barriers for CO_2 storage. **Chapter 8** provides an overview on natural leakage pathways for CO_2 from geological CO_2 stores (Busch et al., 2010). Leakage rates and leakage risks by diffusion, capillary-controlled flow and through fault systems are evaluated and discussed. **Chapter 9** discusses a case study in relation to chapter 4, focusing on the sealing lithologies in the Münster Cretaceous Basin (Wollenweber et al., 2010). It discusses capillary entry pressures, diffusion coefficients, sorption capacity and mineral reactions for carbonate-rich tight sediments. Author's input to this chapter was supervision of the overall work, support in laboratory efforts, and evaluation of data and drafting of manuscript. **Chapter 10** discusses shale and clay minerals as storage media for CO_2 by adsorption in addition to gas diffusion (Busch et al., 2008). It is shown how relatively large amounts of CO_2 can be immobilised by adsorption on clays. **Chapters 11 and 12** build on the findings in chapter 10 and investigate clay mineral swelling when exposed to CO_2 under varying pressures and temperatures (Giesting et al., 2012a, b). While **chapter 11** is more concerned with method development and the study of CO_2 intercalation in Na-rich smectite, showing for the first time that smectite is expanding significantly under reservoir CO_2 pressure conditions, **chapter 12** provides a detailed study of CO_2-interaction with K and Ca-rich smectite. Author's input here was on concept and idea development, planning of laboratory program and drafting of manuscript, including relevance for geological storage of CO_2.

1.2 Focus area: Carbon capture and storage and unconventional gas production

1.2.1 Capture and geological storage of carbon dioxide in the light of Global Warming

Although partly still discussed controversially, global warming is one of the primary concerns of the 21st century. The Intergovernmental Panel on Climate Change has shown that atmospheric CO_2 levels have risen from pre-industrial levels of 280 ppm to 387 ppm in 2005 (and even close to 400 ppm in 2013; CO2Now, 2013), with current growth rates of ~1.9 ppm/year (IPCC, 2007). The increase in atmospheric CO_2 levels is attributed to the ongoing and further increasing (~3% increase/year, Le Quere et al., 2012) burning of fossil fuels such as coal, oil and natural gas and is illustrated in Figure 1-1. A recently published report by the International Energy Agency (IEA, 2013) shows an increase in global carbon emissions in 2012 up by 1.4% compared to 2011. This is the highest value ever reported.

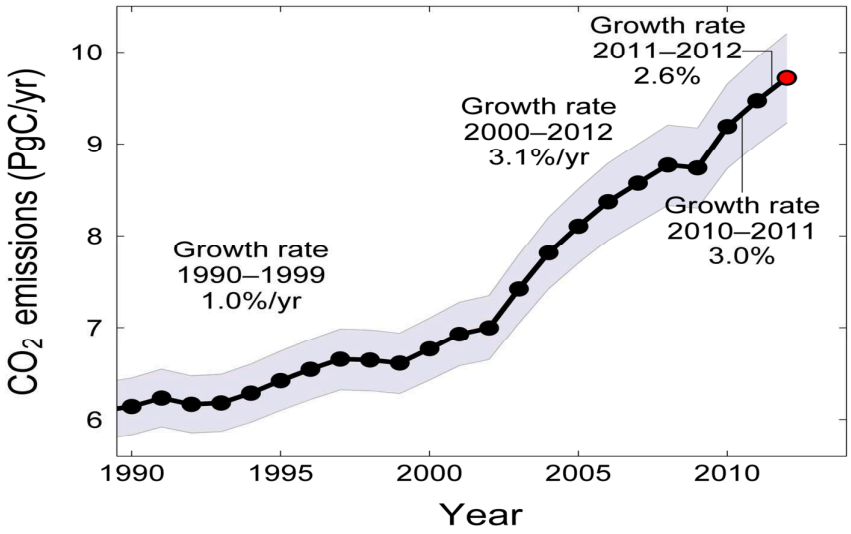


Figure 1-1. Growth rates in annual carbon emissions from 1990 to 2011/2012 (after Le Quere et al., 2012).

This increase in emission is attributed to developing countries (mainly China and India) as illustrated in Table 1-1. While the developed countries reduced emissions in 2011 by 0.7%, compared to the previous year, those in the developing countries have increased by 6.5% compared to 2010. This results in a global growth of 3% as outlined above.

In order to counteract rising global CO_2 emissions many scenarios and future projects have been published, proposed and presented while the common agreement is to keep the global temperature increase to a limit of 2°C compared to pre-industrial values.

Table 1-1. Per capita and total emission as well as emission growth for the year 2011. Data given in PgC (= Pentagram Carbon = billion metric tonne or 10^{15} g). Data from Global Carbon Project, 2012; Peters et al., 2012.

Region/Country	Per capita emissions (tonnes C/p)	Total emissions (PgC*, % of global)	Emissions growth (PgC*/yr, %/yr)
Global	1.4	9.5	0.28 (3.0%)
		Developed Countries (selected)	
Total	3.0	3.6 (40%)	-0.026 (-0.7%)
USA	4.7	1.5 (16%)	-0.028 (-1.8%)
EU27	2.0	1.0 (11%)	-0.029 (-2.8%)
Russian Federation	3.2	0.46 (5.1%)	0.013 (2.9%)
Japan	2.6	0.32 (3.6%)	0.001 (0.4%)
Germany	2.5	0.20 (2.2%)	-0.008 (-3.6%)
		Developing Countries (selected)	
Total	0.9	5.4 (60%)	0.329 (6.5%)
China	1.8	2.5 (28%)	0.226 (9.9%)
India	0.5	0.62 (6.8%)	0.043 (7.5%)
Iran	2.3	0.17 (1.9%)	0.003 (1.9%)
South Korea	3.3	0.16 (1.7%)	0.006 (3.7%)
South Africa	2.8	0.14 (1.6%)	0.002 (1.5%)
* PgC= Pentagram Carbon = billion metric tonne or 10^{15} g			

There are various ways to reduce carbon emissions by increasing:

- renewable energies
- further shift in energy production to natural gas
- biofuels
- nuclear energy
- carbon capture and storage

Or energy conservation and increasing efficiency:

- increase in mass transportation
- more efficient road transportation
- energy efficiency of buildings
- low-energy appliances
- or simply doing things differently

One example of how these technologies can help reducing global carbon missions until 2050 is presented by the International Energy Agency (IEA, 2010, Figure 1-2). The figure projects that by 2050 carbon capture

and storage (CCS) could account for 19% of the emission reduction. In this projection total amounts to be stored would be ~8 Gt annually. Whatever the solution will be in 2050 or 2100, CCS has the potential to play an important role in the short to medium term.

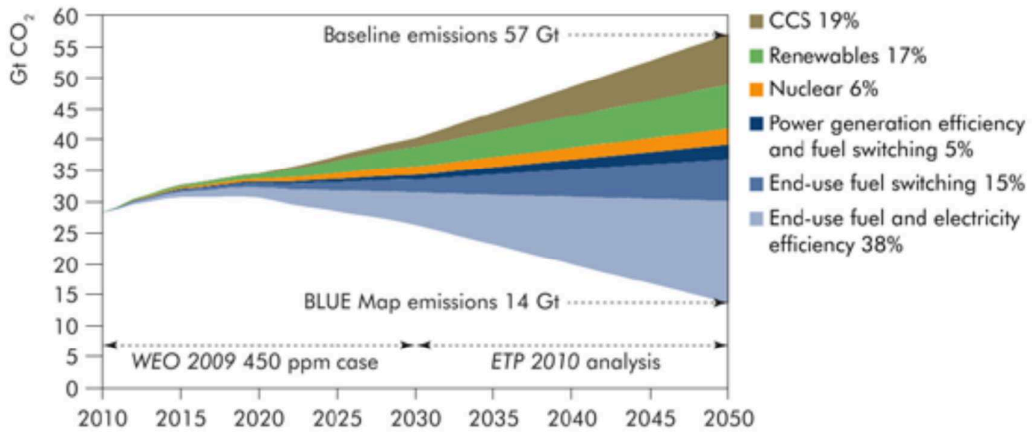


Figure 1-2. Key technologies for reducing CO_2 emissions to arrive at annual emissions of 14 Gt CO_2 in 2050, corresponding to a global 2 degree temperature rise as compared to pre-industrial levels (Source: IEA, 2010).

What is CO_2 capture and storage in some more detail? The key principles of the full chain – carbon capture, transport and storage in deep geological formations – is summarized in the special IPCC report on CCS (IPCC, 2005) and the reader is referred to this literature source especially for more details on capture and transport. An overview on the CCS supply chain is given in Figure 1-3.

For carbon storage several options are considered to move into and industrial stage that are deep saline aquifers, depleted hydrocarbon reservoirs and potentially deep unminable coal seams (Figure 1-4). A comprehensive summary of geological carbon storage is given by Bickle, 2009.

For pore-space storage several trapping mechanisms are considered: hydrodynamic, dissolution, mineral and capillary trapping (Pentland, 2010). **Hydrodynamic (or structural) trapping** is well understood from the oil and gas industry as it is the primary mechanism through which hydrocarbons accumulate in the subsurface. Accumulation occurs below a caprock due to migration caused by density differences (buoyancy) between the hydrocarbons and the host brine (e.g. Bachu et al., 1994). Carbon dioxide dissolved in water can be safely stored in the geological formation and this is known as **solubility trapping**. The CO_2 saturated brine is denser than the surrounding brine resulting in convective mixing (e.g. Lindeberg, 1997). The denser CO_2 saturated brine migrates deeper into the formation and slowly dilutes through contact with unsaturated brine at depth. This process is important as it is typically orders of magnitude faster than pure diffusion. It is estimated to begin anywhere between one year and hundreds of years after CO_2 injection, depending upon formation permeability (pure diffusion may take up to tens of thousands of years, e.g. Ennis-King and Paterson, 2005).

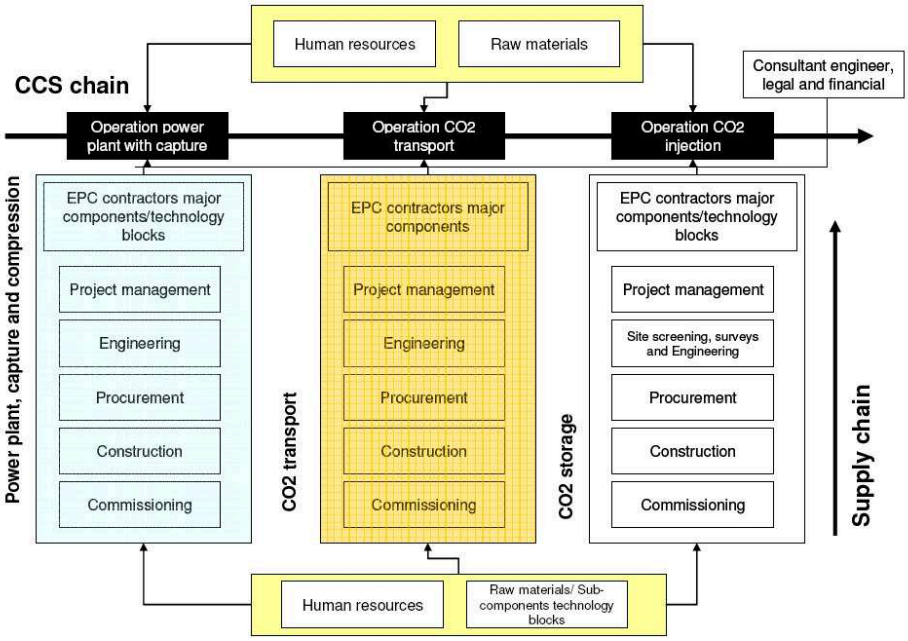


Figure 1-3. Graphical representation of the three parts of the supply chain for CCS (from IEAGHG, 2012).

Mineral trapping is also an important mechanism, although it occurs over longer timescales than other trapping methods. As CO_2 dissolves in formation brine carbonic acid forms (H_2CO_3). This acid is unstable and dissociates. The species formed react with the host rock and brine over long periods of time, generally tens of hundreds of years. If the reactions result in carbonate minerals being precipitated then CO_2 is trapped permanently in the subsurface (e.g. Gunter et al., 1997; Gunter, 1993). The next trapping mechanism involves CO_2 being trapped as immobile pore scale bubbles surrounded by brine. This is known as **capillary trapping** and relies upon displacement hysteresis and the capillary pressure characteristics of the CO_2-brine system. Importantly it can occur over shorter time frames than the other trapping mechanisms and is proven. In oil fields a considerable quantity of the oil originally in place is not produced as it has been trapped and rendered immobile in the pore space through the imbibition process of water flooding. The combination of effective well characterised trapping on a short time scale makes capillary trapping important for CCS (e.g. Pentland, 2010).

When considering coal as a medium to store CO_2, **physical adsorption** is considered as the primary trapping process (e.g. Busch and Gensterblum, 2011). Physical adsorption was also found to be an important process in sandstones where clay minerals are present (Busch et al., 2008). This topic is however still under investigation.

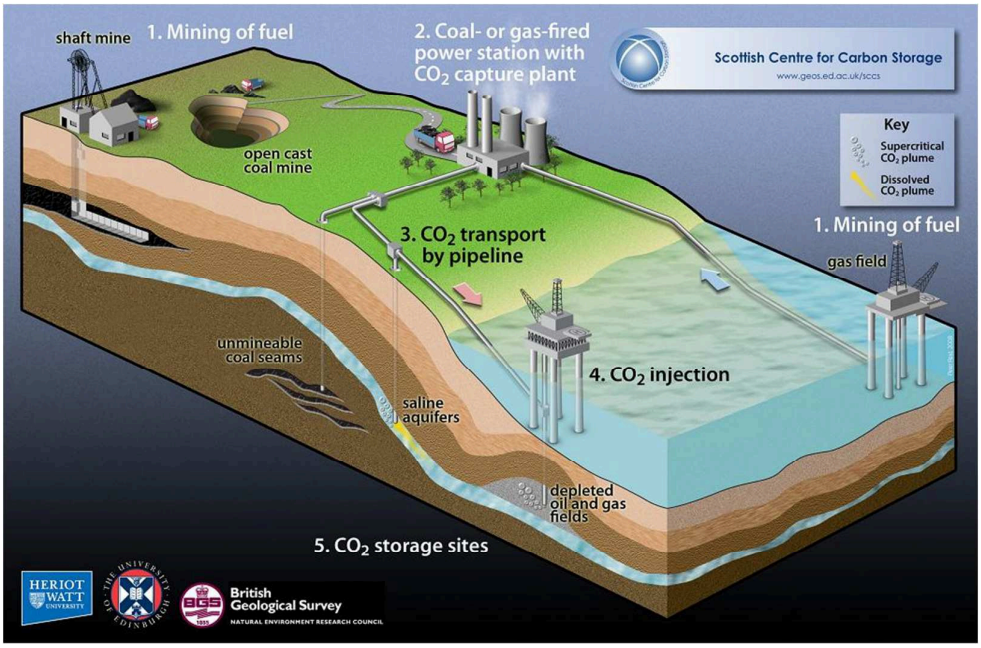


Figure 1-4. The full chain of carbon capture and storage. Storage options with large potentials considered are (i) saline aquifers, (ii) depleted oils and gas fields and (iii) unminable coal seams. Illustration from Scottish Carbon Capture and Storage, 2013.

After having summarized storage mechanisms, we will briefly summarize global capacities in the following. Figure 1-5 and Table 1-2 show these capacities which should be treated as theoretical capacities that need to be matched against operational or realistic capacities following source-sink matching. Global CO_2 storage capacities are estimated in the order of up to 10,000 Gt (Table 1-2, Dooley et al., 2006; IEA; IPCC, 2005) and will allow storage of global carbon emissions for 200-300 years.

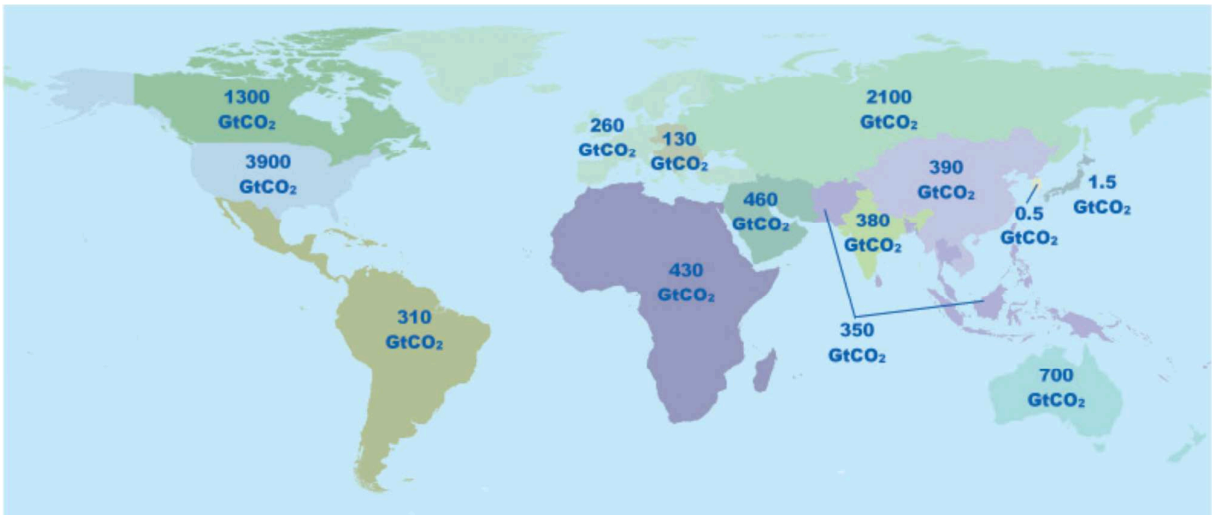


Figure 1-5. CO2 storage capacities by region (Dooley et al., 2006).

Table 1-2. Global CO_2 storage capacities in Gt CO_2.

	Dooley et al., 2006	IPCC, 2005	IEA
deep saline formations	9,500	1,000 - ~10,000	400 - 10,000
depleted oil and gas reservoirs	820	675 - 900	920
unminable coal seams	140	3 - 200	>15

Having discussed theoretical capacities it seems reasonable to document how these relate to the current injection rates and ongoing projects. There is a large discrepancy between these theoretical capacities and current injection rates as can be obtained from the Global CCS Institute (Global CCS Institute, 2013) and which is summarized in Table 1-3. It can be seen that for industrial operations (neglecting smaller scale demonstration or research projects) there are only six projects worldwide (neglecting enhanced oil production operations). Of these six projects only three are in the operate phase and three more in the execute phase, meaning they have passed the phase of final investment decision. In summary these projects will reduce global emissions by about 8 Mt annually as compared to the ~35 Gt emitted each year (factor factor 4400).

Table 1-3. Industrial geological CO_2 storage projects worldwide, either in the operate or execute phase. Data from Global CCS Institute, 2013.

Project	In Salah CO_2 Storage	Sleipner CO_2 Injection	Snøhvit CO_2 Injection	Gorgon CO_2 Injection Project	Illinois Industrial CCS Project	Quest
Region	Africa	Europe	Europe	Australia/New Zealand	United States	Canada
Stage	Operate	Operate	Operate	Execute	Execute	Execute
Status	Active	Active	Active	Active	Active	Active
Capture Type	Pre-Combustion (incl. Gas Processing)	Pre-Combustion (incl. Gas Processing)	Pre-Combustion (incl. Gas Processing)	Pre-Combustion (incl. Gas Processing)	Industrial Separation	Pre-Combustion (incl. Gas Processing)
Transport Type	Pipeline	Direct injection	Pipeline	Pipeline	Pipeline	Pipeline
Transport Details	Onshore to onshore pipeline 14 km	Direct injection	Onshore to offshore pipeline 152 km	7 km Onshore to onshore pipeline	Onshore to onshore pipeline 1.6 km	Onshore to onshore pipeline 84 km
Storage Details	Onshore Saline Aquifer	Offshore Saline Aquifer	Offshore Saline Aquifer	Onshore Saline Aquifer	Onshore Saline Aquifer	Onshore Saline Aquifer
Annual Storage (MM tons)	~1	~1	~0.7	3.4-4	~1	~1,2
Storage Depth (m)	2000	800	2600	2300	2100	2000
Industry	Natural Gas Processing	Natural Gas Processing	Natural Gas Processing	Natural Gas Processing	Chemical Production	Hydrogen Production

1.2.2 (Enhanced) gas production from unconventional reservoirs

Unconventional natural gas is a hydrocarbon type that is stored either in the free or in the adsorbed phase of low-permeability rocks (tight sandstone, shale, coal). In order to produce this gas stimulation techniques usually need to be applied by hydro-fracturing the rock for increased accessibility. This hydro-fracturing (fraccing) has raised many debates all over the world in terms of pollution of drinking water by co-injected chemicals.

In this thesis we solely focus on the rock types where gas is stored primarily by adsorption (gas shale, coal).

1.2.2.1 Gas Shale

Gas shales usually have high total organic carbon (TOC) contents of up to 30% and the mineralogy does not necessarily need to consist of the mineral mix typical for shales: many of these shales can be rich in carbonate or quartz and would be classified as marlstone or silty mudrock (e.g. Littke et al., 2011b). It is a typical feature of gas shales that they act as source rock as well as reservoir rock. Gas shales are of very low permeability (usually in the order of nD to µD, 10^{-21} to 10^{-18} m^2, e.g. Amann-Hildenbrand et al., 2012; Busch and Amann-Hildenbrand, 2013) and gas production from such reservoirs would either require low production rates or high costs by drilling sufficient wells. To overcome this problem and by using more advanced drilling technology, horizontal wells are drilled into the gas shale reservoirs. Once drilled, certain sections of the well get isolated and large quantities of water (including some sand and chemicals) are pumped into these sections at high pressures. This results in the creation of fractures into the shale formation, perpendicular to the well. The co-injected sand (or any other proppant) has the purpose to keep the fractures open after pressure is released; while the chemicals help to reduce bacterial growth, lower fracture pressure and increase fracture propagation, decrease corrosion of equipment, reduce pumping friction, etc.

A schematic of shale gas extraction from deep reservoirs is shown in Figure 1-6. It is assumed that hydro-fractures will not reach vertically from several kilometres depth (where the reservoirs are) to a few hundred meters depth (where the drinking water horizons are) (Davies et al., 2012). As indicated in Figure 1-6, a risk of contaminating drinking water horizons is when the fraccing fluid is back produced and gets in touch with these reservoirs at shallow depth.

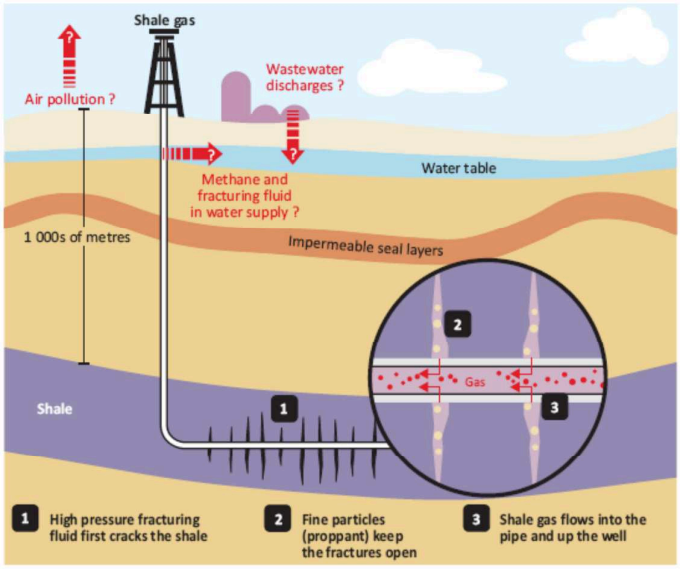


Figure 1-6. Concept of fracturing and producing shale gas and possible environmental hazards(from IEA (International Energy Agency), 2012 after Aldhous, 2012).

Once accessibility to the shale matrix is increased, gas will migrate from the shale matrix through the fractures into the production well upon pressure decrease by pumping. Gas flow to the fractures is driven by diffusion through the water-filled pore space (depending on water-saturation) or permeability and besides gas being stored in the pore system as free gas, large amounts are adsorbed to organic matter in the shale or event to clay mineral surfaces.

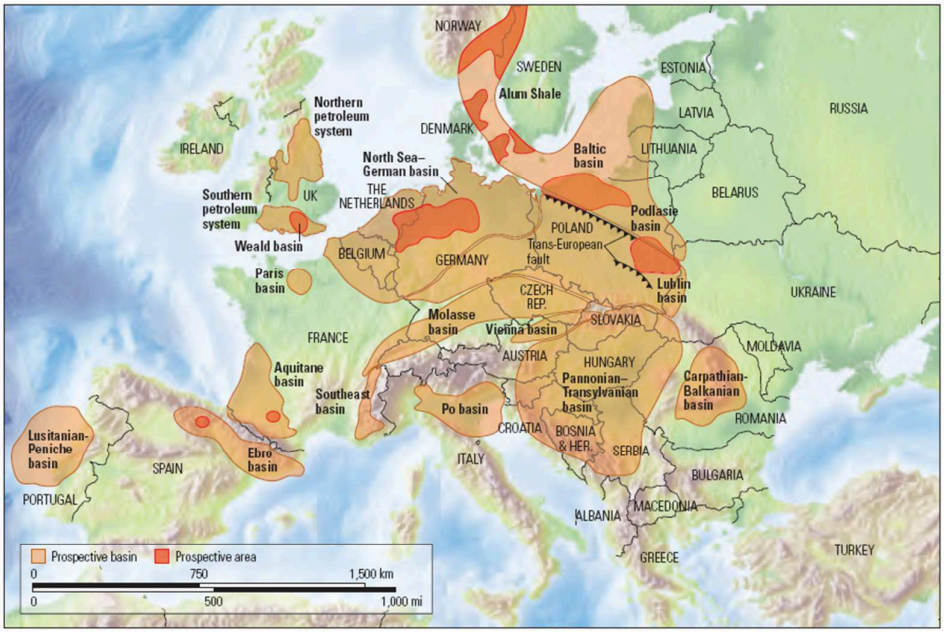


Figure 1-7. Gas shale bearing basins in Europe (from Boyer et al., 2011 after Kuuskraa et al., 2011).

Where can shale gas be found? Figure 1-8 shows assessed worldwide sedimentary basins where resources re partly estimated. This is especially the case for Europe, North and South America, Australia, China, India,

South Africa and some regions in the North of Africa. The most prominent examples are certainly the huge shale gas bearing formation in the USA (e.g. Marcellus, Eagle Ford, and Barnett). An overview of the shale gas bearing basins in Europe is given in Figure 1-7. As a result, Table 1-4 shows worldwide gas consumptions in comparison to natural gas resources and technically recoverable shale gas resources. It becomes clear that in many countries (especially USA, South Africa, Argentina, Mexico, Canada, China, and Australia) the shale gas potential is huge and exceeds the conventional gas resources drastically.

Nevertheless large development costs are expected for these resources that will depend on the global oil and gas price. Strict regulations will be applied to shale gas exploration and production in many parts of the world that will make its production even more complicated (e.g. European Union) and a broad refusal of the public, as can be seen all over Europe at the moment, will certainly not help to develop these resources.

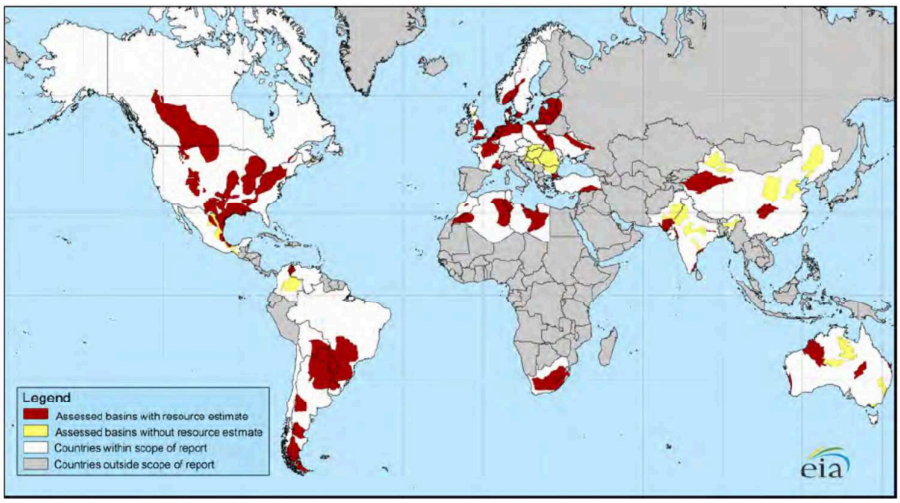


Figure 1-8. Sedimentary basins worldwide with assessed or un-assessed shale gas potential (source: US DOE/EIA, 2011).

Table 1-4. Estimated shale gas resources for select basins that are technically recoverable, compared to existing reported reserves, production and consumption during 2009 (data from US DOE/EIA, 2011).

	2009 Natural Gas Market (billion m^3)			Proved natural gas resources (billion m^3)	Technically recoverable shale gas resources (billion m^3)
	Production	Consumption	Imports (Exports)		
Europe					
France	0.8	49.0	98%	6	5,097
Germany	14.4	92.6	84%	176	227
Netherlands	79.0	48.7	(62%)	1,388	481
Norway	103.4	4.5	(2,166%)	2,039	2,350
U.K.	59.2	88.1	33%	255	566
Denmark	8.5	4.5	(91%)	59	651
Sweden	-	1.1	100%		1,161
Poland	5.9	16.4	64%	164	5,295
Turkey	0.8	35.1	98%	6	425
Ukraine	20.4	44.2	54%	1,104	1,189
Lithuania	-	2.8	100%		113
Others	13.6	26.9	49%	77	538
North America					
USA	583.3	645.6	10%	7,716	24,409
Canada	159.4	645.6	(87%)	1,756	10,987
Mexico	50.1	60.9	18%	340	19,284
Asia					
China	83.0	87.2	5%	3,030	36,104
India	40.5	53.0	24%	1,073	1,784
Pakistan	38.5	38.2	-	841	1444
Australia	*47.3*	*30.9*	*(52%)*	*3,115*	*11,270*
Africa					
South Africa	2.0	5.4	63%	-	13,734
Libya	18.7	5.9	(165%)	1,549	8,212
Tunisia	3.7	4.8	26%	65	510
Algeria	81.6	28.9	(183%)	4,502	6,541
Morocco	0.0	0.6	90%	3	311
Western Sahara	-	-		-	198
Mauretania	-	-		28	0
South America					
Venezuela	18.4	20.1	9%	5,066	311
Colombia	10.5	8.8	(21%)	113	538
Argentina	41.3	45.9	4%	379	21,917
Brazil	10.2	18.7	45%	365	6,400
Chile	1.4	2.8	52%	99	1,812
Uruguay	-	0.0	100%		595
Paraguay	-	-			1,756
Bolivia	12.7	2.8	(346%)	750	1,359
Total above areas	*1,787*	*1,869*	*(3%)*	*36,076*	*183,861*
Total world	*3075*	*3021*	*0%*	*187*	

1.2.2.2 Coalbed Methane and Enhanced Coalbed Methane

Coalbed methane (CBM) production from coal seams is a known technology and operations take place since many years, mainly in the USA but also in Australia and some parts of Europe. An example to the continuous increase in CBM production in the US is shown in Similar to gas shales, coal acts as both, source rock and reservoir where during coalification huge amounts of gas (CO_2, N_2, CH_4) are produced and stored in the coal microporous system by adsorption. Coals usually consist of >50% TOC (e.g. Littke et al., 2011b)

and are found all over the world (Figure 1-10) and through different geological time scales. Different to the gas shales, coalbeds usually provide a well-developed natural cleat (fracture) system (e.g. Laubach, 1998) that allows production of gas at higher rates, assuming permeabilities in the order of mD (10^{-15} m^2) compared to the gas shale permeabilities that can be several orders of magnitude lower than that. A comprehensive review of the major aspects relevant for CBM is provided by Moore, 2012.

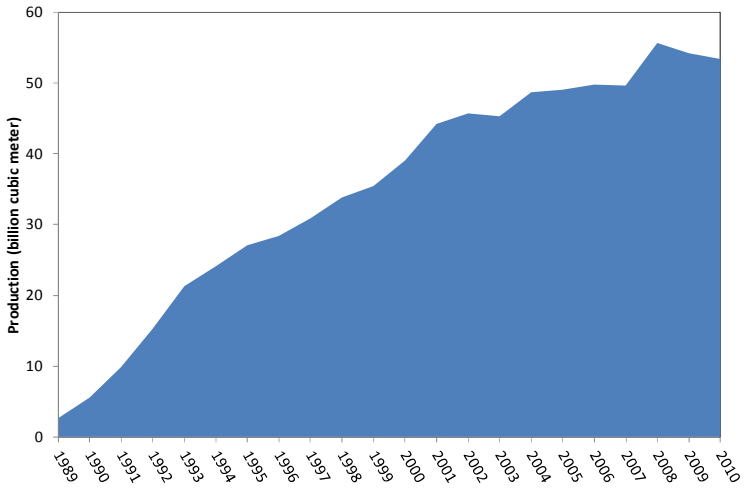


Figure 1-9. CBM production in the US between 1989 and 2010 in billion cubic meters (Gm^3). Data from US Energy Information Administration (EIA, 2013).

Figure 1-11 schematically illustrates CBM production. Here, and especially in shallow CBM reservoirs of few 100 meters only, vertical wells are used for gas production, making use of the natural fracture system of the coals. Maximum depth of CBM production is usually around 1000 m, while it can be debated if this is still economic or only technically feasible. Major production in USA and Australia takes place at depth down to about 500 m.

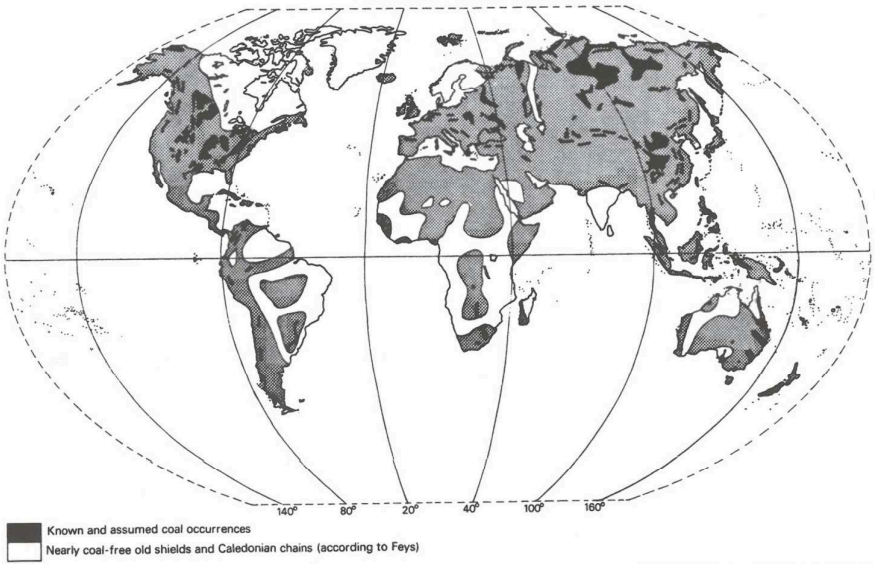


Figure 1-10. Coal basins worldwide (van Krevelen, 1993).

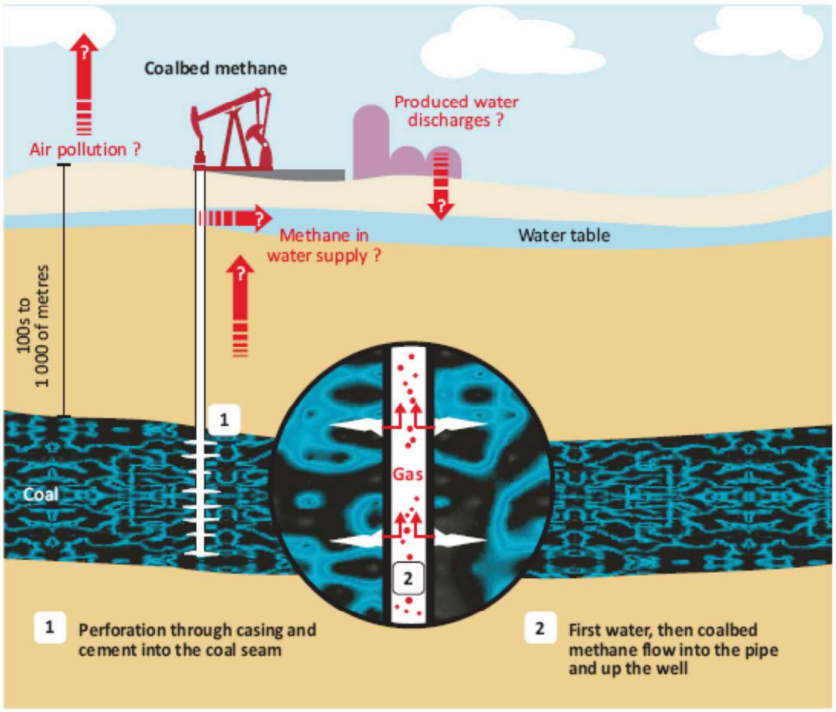


Figure 1-11. Concept of producing coal bed methane (CBM) environmental hazards(from IEA (International Energy Agency), 2012 after Aldhous, 2012).

In the past many research activities were dealing with the option of enhancing CBM production by injecting CO_2 or N_2 (see White et al., 2005 for a review). The promise of combining subsurface storage of CO2 and at the same time increasing natural gas production led to large national research programs in the USA, Australia and Europe with the outcome of a hand full of demonstration projects in the last few years (e.g. Poland, Japan, China, and Canada, s. e.g. Busch and Gensterblum, 2011 for a summary) and only one commercial field operation in the San Juan Basin of the USA (Erickson and Jensen, 2001).

The principle is relatively simple: Methane is bound to the coal microporous surface by weak physical interaction forces (adsorption). Upon an increase in temperature or decrease in pressure, there is an increased tendency for the methane to return to the gas phase. Introducing CO2 to the system, which has a higher affinity to interact with the coal surface, will further increase the ratio of methane in the gas, compared to the adsorbed phase and more methane can be produced. The adsorption ratio between CO_2 and methane can be high for low rank coal with factors up to 10 but is usually around 2 for higher mature coals (Busch and Gensterblum, 2011).

One major problem with this technology is, besides possible dilution of the produced natural gas with CO_2 that carbon dioxide swells the coal and, hence reduces permeability considerably, resulting in limited production rates (e.g. van Bergen et al., 2009b).

1.3 How does this thesis relate to geological storage of carbon dioxide and gas production from unconventional reservoirs?

This thesis combines some of the articles published by the author during the last ~8 years. This combined work mainly addresses gas transport and retention in shale and coal. With application to geological storage of CO_2 the main focus was on sealing integrity of fine-grained, low-permeability rocks above CO_2 storage reservoirs. There are many potential pathways for injected CO_2 to escape from such reservoirs, like along wells, faults or fracture systems or by diffusion or as viscous flow through the pore network of the seal. It is of great importance to locate and quantify these leakage processes for de-risking CO_2 storage and provide input for conceptualising a monitoring system for such storage sites.

An overview of leakage mechanisms through faults and intact caprock is provided (Busch et al., 2010) and the time scales of diffusive and viscous flow of CO_2 through the intact caprock are provided. In addition it is shown from natural analogue systems what potential leakage rates could be. In an earlier study, Busch et al., 2008 and Wollenweber et al., 2010 showed that for a realistic caprock effective diffusion coefficients through the water-saturated pore space ranges in the order 10^{-10} to 10^{-11} m^2/s which is recalculated in the order of centimetres per year of travel distance through the caprock. In the same study it was shown that caprocks containing large quantities of clay minerals can serve as a sink for CO_2 by physically adsorbing the gas on the large surface area of the clay minerals. This was shown on real shale material but also on standard clay minerals like illite, montmorillonite and kaolinite and a rather novel finding with expected implications to the physical adsorption capacity of CO_2 in reservoir rocks. In a follow-up study (Weniger et al., 2010) it was shown that for rocks from the same coal-bearing basin (Parana, Brazil) the methane sorption capacity mainly depends on the organic matter content of the rocks while a significant portion of the CO_2 sorption capacity can be attributed to the inorganic material in these sediments, namely clay minerals.

Wollenweber et al., 2010 studied capillary entry pressures and sorption potential of two potential caprock samples (one carbonate, one clay-rich marlstone) of the Cretaceous Münster Basin in Germany. Results showed that while sorption capacity for the relatively pure carbonate is rather low, it is quite significant for the marlstone with a clay content of ~30%. While CO2 sorption capacity on clay minerals is confirmed, within the work by the author of this thesis but also by other studies (e.g. Rother et al., in press), it was shown in a cooperation with University of Illinois, Chicago that clay minerals swell on contact with CO_2 (Giesting et al., 2012a, b). Swelling strain on clay powders can be up to about 15% under hydrostatic stress conditions, as observed from high temperature/pressure X-ray diffraction. This is verified by investigating clay and shale aggregates in an optical cell (de Jong et al., submitted, not shown here). Finally, swelling pressures of clays in contact with CO_2 in the order of 10 MPa have been observed in a follow-up study by de Jong under uniaxial stress conditions representative to reservoir conditions at 1.5 to 2.5 km depth (de Jong et al., in preparation, not shown here).

A major effort was invested in the understanding of capillary pressures in the system water/CO_2/rock by studying the methods (Busch and Müller, 2011) used for determining capillary entry pressures but also for the magnitude of these pressures and the implications on storage integrity (Amann-Hildenbrand et al., in press; Amann et al., 2011; Wollenweber et al., 2010). Several fundamental and case studies were undertaken on different caprock material (marlstones, carbonates, mudrocks, tight rocks, etc.) to improve the general understanding and to provide datasets for empirical correlations. A review of this data was performed, including more than 200 datasets performed on mainly mudrocks but also higher permeability rocks to cover a broad permeability range. The main focus was on the possible prediction of difficult to determine parameters like capillary pressures on shales from parameters that are easier to obtain, like porosity, permeability or mineralogy (Busch and Amann-Hildenbrand, 2013). This is an important topic since capillary failure is an often occurring process in geological reservoirs (e.g. gas chimneys are considered to evolve from this, Cathles et al., 2010) and will determine storage capacity as well as storage safety.

In order to understand gas storage capacities and mechanisms as well as gas transport from and into unconventional gas reservoirs (specifically coal and shale) in much greater detail, significantly more research effort is needed. This thesis addresses some of these processes, especially related to primary and enhanced (by CO_2 injection) production of coalbed methane.

This study addresses mainly adsorption characteristics and the transfer of those sedimentary basins. Transport processes in coals have intentionally been excluded from this thesis (e.g. Han et al., 2010a; Han et al., 2010b) to keep the focus on adsorption properties.

Gas adsorption (both capacity and kinetics) on coal has been covered within several articles by the author during the PhD thesis (Busch et al., 2003a; Busch et al., 2004a; Busch et al., 2006; Busch et al., 2003b; Busch et al., 2004b; Busch et al., 2003c) which was followed by several more articles after PhD (Busch et al., 2007; Gensterblum et al., submitted; Gensterblum et al., 2010; Gensterblum et al., 2009; Goodman et al., 2007b; Goodman et al., 2004; Han et al., 2013; Hildenbrand et al., 2006; Li et al., 2010; Mazumder et al., 2006; Siemons and Busch, 2007). All these studies have been combined in addition to data published by other authors in a review article (Busch and Gensterblum, 2011) discussing the various methods to determine gas sorption isotherms on coal, the competing interactions between gas (CO_2, CH_4) and water and global correlations with coal maturity. The purpose of this study was to improve the general understanding of gas and water interaction with the coal microporous surface in order to better predict gas adsorption and exchange processes as well as the kinetics involved.

In addition to this attempt several case studies have been performed related to the evolution of CO_2 and CH_4 sorption capacity as a function of burial history (Hildenbrand et al., 2006 for the Campine Basin, Belgium) and a more generic study discussing the effect of coal maturity on the gas sorption evolution through geological time frames (Gensterblum et al., accepted) Both studies aimed at predicting best suited

coalification windows and burial depth to either extract primary methane or to enhance the production by CO_2 co-injection. Also, the conceptual approach is well suitable to be integrated in dynamic basin modelling.

One further case study (Kronimus et al., 2008) is dealing with the specific estimation of CO_2 storage and methane production amounts within the German Cretaceous Münster Basin that was already used as a case study to investigate caprock seal integrity by Wollenweber et al., 2010.

With regard to unconventional gas production from gas shales the systematic of capillarity and permeability have been investigated in order to predict difficult to obtain parameters from more easy ones (Busch and Amann-Hildenbrand, 2013). This study was using a large dataset of mudrocks with typical parameters like permeability, porosity, specific surface area, mineralogy and capillary breakthrough and snap-off pressures.

Gas Adsorption and Fluid Transport in Coalbed Reservoirs

2 CBM and CO_2-ECBM related sorption processes in coal: A review

2.1 Introduction

The technical development of coalbed methane (CBM) and secondary CO_2 enhanced CBM (CO_2-ECBM) production and CO_2 storage in and from coal seams requires detailed and reliable information on fluid transport and gas sorption as well as their inter-dependent interaction. An improved understanding of these processes from the macroscopic to the microscopic scale is important for the accurate prediction of gas and water production rates as well as CO_2 injection rates. The mechanisms of storage and transport of gas and water in coal differ significantly from conventional gas reservoirs. Commonly, gas transport in coal is considered to occur at two scales (Figure 2-1): (I) laminar flow through the cleat system, and (II) diffusion and sorption in the coal matrix. Flow through the cleat system is pressure-driven and may be described using Darcy's law, whereas flow through the matrix is assumed to be concentration-driven and is modelled using Fick's law of diffusion. Gas storage by physical sorption occurs mainly in the coal matrix (e.g. Harpalani and Chen, 1997).

Various articles address laboratory or field research performed in the context of primary coalbed methane (CBM) or secondary CO_2 enhanced CBM (CO_2-ECBM) recovery and reviews are provided by e.g. Moore, submitted; White et al., 2005.

There are many factors that need to be addressed when attempting to understand the complexity of the interaction of CH_4, CO_2 and water with coal in the cleat system and the coal matrix, and research has diversified substantially, especially since CO_2 storage in coal is considered as a potential way of permanently immobilizing CO_2 in the sub-surface.

Coalbed methane recovery projects are currently developed commercially all over the world with a main focus on countries like Australia, China and the United States, and exploration is ongoing in many further regions in e.g. Europe, Ukraine, or Indonesia. One of the first CO_2-ECBM micro-pilot field tests was set up in Alberta, Canada (Gunter et al., 2004) which was similarly performed in China some years later (Wong et al., 2007). One operation with a two-well test setting was carried out in Japan (Ohga et al., 2006; Yamaguchi et al., 2004). The only large-scale ECBM field pilot using CO_2 injection was operated in the San Juan Basin in New Mexico, United States (Erickson and Jensen, 2001; Reeves et al., 2003). Finally a two-well demonstration test was performed in the Upper Silesian Basin, Poland within the RECOPOL[1] and MOVECBM[2] projects funded by the European Union (van Bergen et al., 2006).

[1] http://recopol.nitg.tno.nl/
[2] www.movecbm.eu

To predict a CBM production profiles either during primary or secondary production, aspects like coal permeability and porosity, density, ash and moisture content, initial gas-in-place (GIP) (from canister desorption tests), gas sorption capacity from laboratory isotherms (to obtain gas saturations and desorption pressure), gas diffusivities, coal volumetrics (thickness and areal extent) or thermodynamic properties (e.g. viscosity, equation of state) of the fluids involved need to be understood as a minimum requirement. When dealing with CO_2-ECBM selective adsorption, counter diffusion in the coal matrix, or coal shrinkage and swelling (from CH_4 desorption and CO_2 adsorption, respectively) need to be investigated in addition to the parameters above.

During CO_2-ECBM processes, the areal distribution of the CO_2 injected is accomplished by flow through the cleat network. When CO_2 is entering the coal matrix by a combined sorption/diffusion process it will sorb to the coal inner surface and at the same time replace part of the CH_4. This replacement occurs either by a reduction in the CH_4 partial pressure or by a higher selective sorption of CO_2 over CH_4. Because of a concentration gradient between CH_4 in the matrix compared to the cleat system, CH_4 diffuses from the coal matrix into the cleat system where, by pressure drawdown towards a production well, it can be produced (Figure 2-1).

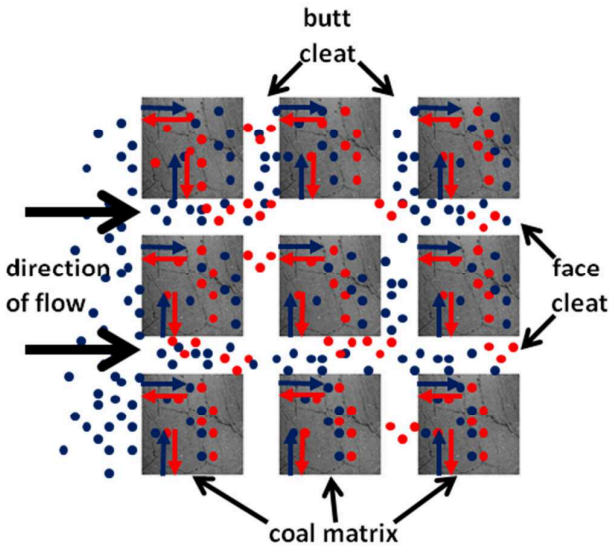


Figure 2-1: Illustration showing coal matrix blocks and cleat system of a coal.

In this context this review summarizes gas (CO_2, CH_4) and water sorption on coal and specifically addresses the following topics:

- The most common experimental setups for determining gas and water sorption on coal (or other microporous materials), its differences and experimental uncertainties. Further the modelling of sorption isotherms and the problems of calculating absolute from excess sorption is addressed.
- CO_2 and CH_4 sorption on natural coals and its dependence on coal specific parameters like coal rank, maceral composition or ash content.

- Water sorption on coal, its dependence on coal properties like rank and coal chemistry and gas sorption in the presence of water.
- Findings related to sorption kinetic data obtained from the pressure decline versus time plots of individual sorption steps. The different model assumptions are introduced, sorption rates are compared for different moisture contents, coal rank and differences between CO_2 and CH_4 sorption rates are defined.
- Concluding remarks and recommendations for future research to better understand gas/water/coal interaction.

In this review we do not cover the following issues due to insufficient data published and because we aim at providing a focused and consistent paper addressing the issues above:

- Sorption of any other gases than CO_2 and CH_4 since (i) we want this paper to specifically address sorption related to CO_2-ECBM or CBM recovery and (ii) only limited datasets are available on the sorption of e.g. N_2 or flue gas mixtures with additional co-contaminants like e.g. H_2, CO, O_2, or SO_2.
- Gas sorption from gas mixtures. Although there are studies available dealing with binary CO_2/CH_4 and CO_2/N_2 or ternary $CO_2/CH_4/N_2$ gas mixtures, data is limited and the experimental techniques still rather pre-mature. Some work has been published however (e.g. Busch et al., 2003a, 2007; Busch et al., 2006; Fitzgerald et al., 2005; Pini et al., 2010).
- A detailed review of the various models available for fitting sorption isotherms. A summary on this can be retrieved from textbooks dealing with gas sorption or from dedicated journals dealing with microporous sorbents in a more general manner.

Although investigated in detail lately we also do not cover coal swelling in this study. Authors are aware that coal swelling is an important mechanism affecting gas sorption on coal and the interpretation of sorption isotherms. There are several studies dealing with experimental (e.g. Battistutta et al., 2010; Day et al., 2008b; Karacan, 2003, 2007; Kelemen, 2006; Mazumder et al., 2005; Mazumder and Wolf, 2008; Reucroft, 1986; van Bergen et al., 2009b) and theoretical (e.g. Palmer and Mansoori, 1998; Pan and Connell, 2007; Vandamme et al., 2010) aspects of this phenomenon.

2.2 Adsorption methods

Sorption processes are subdivided, according to the energies of interaction involved, into chemical (chemisorption) and physical sorption (physisorption). In chemisorption, the sorbate is bound to specific sorption sites on the solid surface by electron transfer or electron sharing which makes this process highly specific compared to physisorption which is nonspecific. Chemisorption typically involves monolayer while physisorption can involve either monolayer or multilayer surface coverage (Karge et al., 2008).

Physisorption occurs via van der Waals forces, i.e. attraction due to permanent and/or induced dipoles between the sorbate molecules and the atoms composing the sorbent surface. The enthalpy of

physisorption is not much larger than the enthalpy of condensation of the sorbate and considered to be 1.0 to 1.5 times the latent heat of evaporation (compared to chemisorption where the enthalpy is >1.5 times the heat of evaporation) (Karge et al., 2008).

Physisorption, in contrast to chemisorption, is distinguished by only minor changes in the sorbate and sorbent. The sorbent remains unaltered until relaxation of the substrate lattice occurs. Further the bondings in the sorbate are changed, which becomes apparent through a modified oscillation frequency (measurable by FTIR- or Raman spectroscopy). Physical adsorption is a reversible process, because there is no covalent bond between the sorbate molecules and the solid surface. It is most likely that adsorption occurs as a monolayer at low pressures and as multilayers at higher pressures, depending on the type of sorbent and the sorbate investigated.

The investigation of sorption and desorption of microporous materials (in this case natural coal) can be subdivided into two main areas: (a) measurements at low pressures that are typically in the range of the vapour pressure of the sorptive gas and (b) measurements at high pressures where the gas species is usually above its supercritical pressure. Low pressure sorption measurements are used for determining structural parameters, like e.g. pore size distribution or specific surface areas and micro- or mesopore volumes. In high-pressure experiments the sorption capacity of gases on natural coals is determined. Low-pressure sorption is not covered in this study; this topic would be subject of an overview article of its own.

2.2.1 Methods to determine gas sorption

For the determination of high-pressure gas sorption isotherms of coals two different techniques are commonly used. The techniques differ in terms of the physical parameters used to determine the isotherms: (1) The manometric/volumetric method requires very accurate determination of cell and void volumes. Here the amount of gas sorbed is recorded by pressure readings (manometric method) or pressure and volume readings (volumetric method). (2) In the gravimetric method, the amount of gas sorbed is measured at constant pressure by means of a very accurate balance, with the sample either suspended mechanically or by magnetic coupling across the wall of a high-pressure vessel.

2.2.1.1 Manometric Method

The manometric method is most widely used for determining gas sorption capacities on coal (e.g. Busch et al., 2003a, 2007; Busch et al., 2004a; Bustin and Clarkson, 1998; Chaback, 1996; DeGance, 1993; Harpalani et al., 2006; Joubert et al., 1973; Krooss et al., 2002; Laxminarayana and Crosdale, 1999b; Li et al., 2010; Mastalerz et al., 2004; Mavor, 1990; Nodzenski, 1998; Prinz et al., 2001; Siemons and Busch, 2007). The setups are either custom made or designed in-house and consist typically of calibrated reference volume and sample cells. Pressure and temperature transducers are either connected to the sample cell only or to both, reference and sample cell. To analyze sorption from gas mixtures (combination of usually N_2, CH_4 and CO_2) the gas composition has to be determined additionally by using a gas chromatograph (GC) equipped,

for instance, with a Thermal Conductivity Detector (TCD). Either sample or reference cell or both are connected to the GC through a sampling valve. A basic schematic of this setup is provided in Figure 2-2.

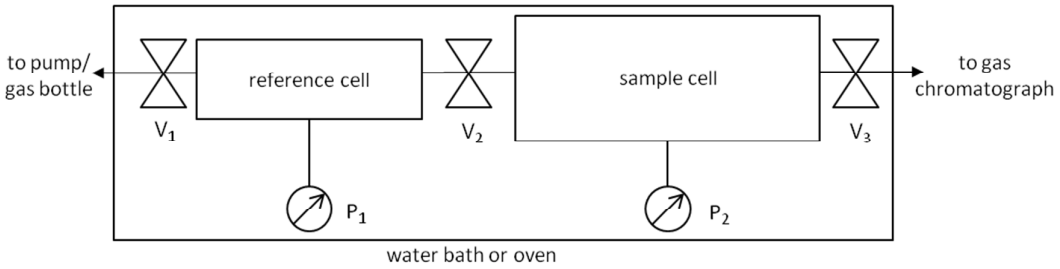


Figure 2-2. Schematic setup for manometric sorption devices. V denotes valves and P denotes pressure transducers.

In the manometric procedure, defined amounts of gas are successively transferred from a calibrated reference volume into the sample cell containing the coal sample. Prior to the sorption experiment the void volume (V^0_{void}) of the sample cell is determined by expansion of a "non-sorbing" gas, which is typically helium. Helium densities are calculated using the equation of state (EOS) by McCarty and Arp, 1990 or using the van der Waals equation with the *a* and *b* parameters reported by Michels and Wouters, 1941. This procedure also provides the skeletal volume (V^0_{sample}) and the skeletal density (ρ^0_{sample}) of the sample.

For gas sorption isotherms, the void volume multiplied by the density of the gas (or supercritical) phase ($V^0_{void} \cdot \rho^{CO_2}(T,p)$), yields the "non-sorption" reference mass, i.e. the amount of gas (supercritical fluid) that would be accommodated in the measuring cell if no sorption takes place. Densities are calculated using the corresponding EOS for CO_2, CH_4, N_2 or their binary and ternary mixtures (Kunz et al., 2007; Peng and Robinson, 1976; Setzmann and Wagner, 1991; Span and Wagner, 1996). The excess sorption mass ($m^{CO_2}_{excess}$) is the difference between the mass of gas that has been transferred into the measuring cell up to a given pressure step and the "non-sorption" reference mass:

$$m^{gas}_{excess} = m^{gas}_{transferred} - V^0_{void} \cdot \rho^{gas}(T,p) \qquad (2\text{-}1)$$

The mass transferred from the reference cell into the measuring cell during *N* successive pressure steps is given by:

$$m^{gas}_{transferred} = \sum_{i=1}^{N} V_{ref} \cdot \left(\rho^{gas}_i(p_i,T) - \rho^{gas}_{i-1}(p_{i-1},T)\right) \qquad (2\text{-}2)$$

Rather than in mass units, the excess amount of sorbed gas is usually expressed in amounts of substance (mol) or volume of sorbed gas under standard temperature and pressure (STP) conditions (m^3; 288 K, 0.1 MPa). The excess sorption is usually normalized to the initial mass of the sorbent.

2.2.1.2 Volumetric Method

The volumetric method (Fitzgerald et al., 2005; Gasem et al., 2002b; Hall et al., 1994; Ozdemir et al., 2003; Ozdemir et al., 2004; Reeves et al., 2005; Sudibandriyo et al., 2002; Sudibandriyo et al., 2003).

A simplified scheme of the experimental apparatus is shown in Figure 2-3. The pump/reference and sample cell sections of the apparatus are maintained in two constant temperature air baths. Similar to the manometric method, the sample is placed in the sample cell, the volume of which is determined using helium as non-sorbing gas. The isotherm is determined by continuously decreasing the volume in the piston pump and thus increasing the gas pressure. The amount of gas injected is determined by an accurate reading of the volume changes in the pump. By adjusting the piston pump volume, sorption quantities can be determined at defined pressures while for the manometric method (with fixed reference and void volumes) the equilibrium pressure depends on the reference to sample cell volume ratio and the pressure charge in the reference cell. The amount of gas injected $m_{gas}^{injected}$ can be determined from the pump position as it moves forward. Therefore:

$$m_{gas}^{adsorbed} = m_{gas}^{injected} - m_{gas}^{unadsorbed} \qquad (2\text{-}3)$$

while

$$m_{gas}^{injected} = \left(\frac{p\Delta VM}{ZRT}\right)_{pump} \qquad (2\text{-}4)$$

and

$$m_{gas}^{unadsorbed} = \left(\frac{pV_{void}M}{ZRT}\right)_{sample\ cell} \qquad (2\text{-}5)$$

Here *m* denotes the mass of gas, *p* is pressure, *T* is temperature, *M* is the molar mass of the gas species, *Z* is the compressibility coefficient of the pure gas species and *R* is the universal gas constant. ΔV is the volume change in the pump and V_{void} is the volume of the free gas in the sample cell.

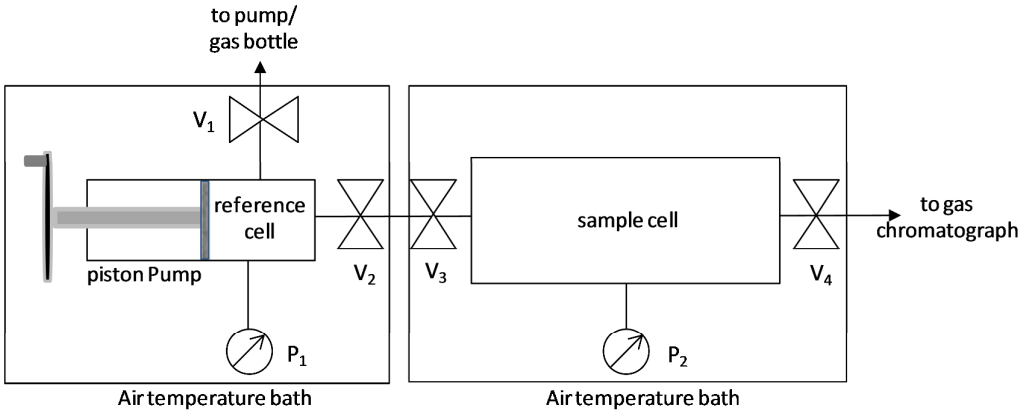


Figure 2-3: Schematic diagram of volumetric gas sorption device. Modified after Sudibandriyo et al., 2003.

2.2.1.3 Gravimetric Method

Most commercial gravimetric sorption devices used for determining gas sorption capacities are commercial (Bae and Bhatia, 2006; Charrière et al., 2010; De Weireld et al., 1999; Ottiger et al., 2006; Pini et al., 2010; Pini et al., 2006a; Pini et al., 2006b), either used as delivered or with in-house modifications. In this instrument the sorbent is placed into the high-pressure compartment of a magnetic suspension balance and exposed to the sorptive at constant temperature (Figure 2-4). The excess sorption is determined from the weight change (apparent mass change) of the sample ($\Delta m = m_{measured}(T,p) - m^0_{sample}$) recorded during individual sorption steps, where m^0_{sample} is the original sample mass. The excess sorption is derived from its apparent weight change by a buoyancy correction based on the skeletal volume (V^0_{sample}) of the sample, corresponding to the same reference state as in the manometric procedure. The determination of the skeletal density or volume is performed with helium. The excess sorbed mass is then given by:

$$m^{gas}_{excess} = \Delta m + V^0_{sample} \cdot \rho_{gas}(T,p) \qquad (2\text{-}6)$$

$$m^{gas}_{excess} = \Delta m + \frac{m^0_{sample}}{\rho^0_{sample}} \cdot \rho_{gas}(T,p) \qquad (2\text{-}7)$$

As in the manometric procedure, the volume and density of the sorbed phase are not known and therefore their effect on the buoyancy term cannot be explicitly taken into account. The excess sorption values are normalized to the original sample mass m^0_{sample}. The magnetic suspension balance is capable of measuring weight changes with an accuracy of ±2 µg. The system consists of an electromagnet linked to the balance and a permanent magnet at the top of the suspension system for the crucible containing the sorbent. More details are given in e.g. De Weireld et al., 1999.

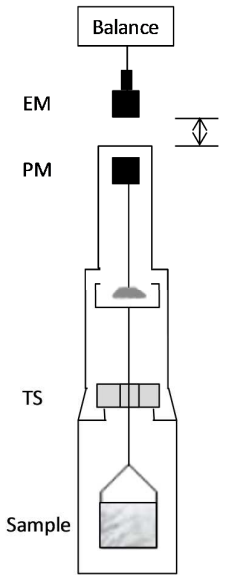


Figure 2-4: Suspension magnetic balance. EM=electro magnet; PM=permanent magnet; TS=titanium sinker. Adapted from Charrière et al., 2010.

Several studies use an in-house built gravimetric device (e.g. Day et al., 2008c; Day et al., 2005; Sakurovs et al., 2009; Sakurovs et al., 2008, Figure 2-5). This set-up measures the weight change of the sample cell upon gas sorption/desorption. The free gas volume in the sample cell is determined by He-pycnometry as in the manometric method. In addition an empty reference cell is used to determine the mass of a defined volume of gas at the same pressure as in the sample cell. Thus, the gas density at each reference pressure can be determined without having to rely on an EOS. Especially for gas mixtures where EOS are unavailable or not sufficiently accurate this method is practical.

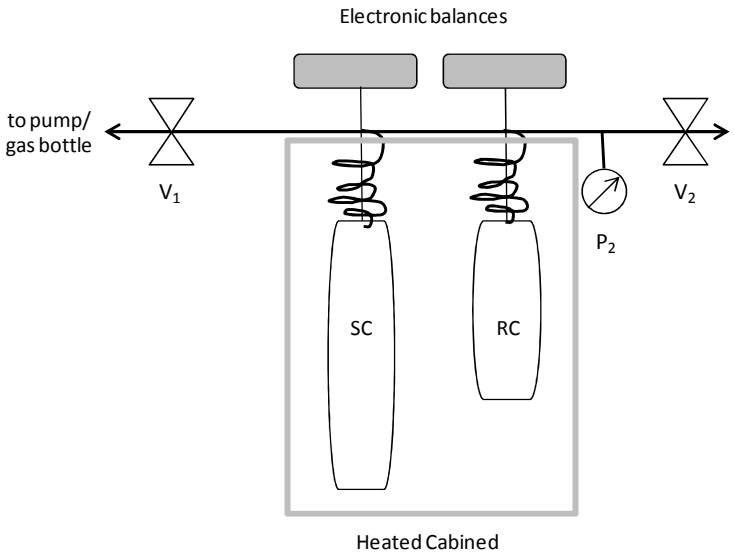


Figure 2-5. Gravimetric sorption device used at CSIRO Energy Technlology, Newcastle, AUS. RC and SC are reference and sample cells respectively. Adapted from Day et al., 2005.

2.2.1.4 Alternative methods for recording gas sorption on coal

Two additional test methods for sorption on coal have been reported recently. There are many more methods used but not applied to coal/gas systems to the knowledge of the authors:

Gas sorption (CO_2, CH_4) under controlled confining stress (6.9-13.8 MPa) on a cylindrical coal sample plug (Pone et al., 2009) using a volumetric method. Results were compared to powdered samples under unconfined conditions and showed a reduction in sorption capacity by up to 91% for methane and up to 69% for CO_2.

Hol et al., 2011 recently reported a new, direct method of determining the uptake of CO_2 by coal (i.e. by adsorption plus pore-filling). A cylindrical coal sample, 4 mm in diameter and 4 mm in length, is jacketed in a tightly fitting, annealed gold capsule and exposed to CO_2 at constant pressure and temperature. Adsorption-induced swelling of the sample is accommodated by ductile deformation of the capsule. Once the coal is saturated, the capsule is sealed by mechanical loading and the external CO_2 pressure removed. This allows the CO_2 to desorb from the coal and flow into an inflatable Al-foil bag attached to the capsule. The volume of the bag, and hence the amount of CO_2 stored in the coal sample, is determined using the

Archimedes method. While the capsule method is time-consuming and not easily executed, the advantage is that it is independent of any Equation of State (EOS), and that no volumetric effects or impurities distort the shape of the isotherm as with the methods below. The method reported by Hol et al., 2010b is currently being tested and compared to the manometric method in collaboration with the present authors. First detailed results are expected in the near future (pers. com. Hol).

2.2.2 Uncertainties in recording sorption isotherms

Potential sources of experimental errors have been discussed in numerous papers, both within the coal research community and in relation to other microporous materials. Here we only refer to those studies dealing with natural coals (e.g. Gensterblum et al., 2010; Mavor et al., 2004; Mohammad et al., 2009; Pini et al., 2006b; Sakurovs et al., 2009; van Hemert et al., 2009; van Hemert et al., 2007; Yu et al., 2008a). Issues related to temperature control, determination of sample cell volume, equations of state, gas impurities, water vapor pressure and gas uptake in water (by dissolution) and mineral matter surfaces are addressed her in some detail.

2.2.2.1 Helium as reference gas

Both, the gravimetric and the manometric/volumetric methods use helium (sometimes argon) as reference gas to determine the buoyancy of the sample (gravimetric) or the void volume of the sample cell (manometric/volumetric). By definition and experimental practice, they represent differential methods with respect to helium.

Helium is commonly considered as ‘‘non-sorbing’’. A small degree of helium sorption (which cannot be excluded but also not quantified) will lead to an underestimation of the sample volume for both methods. Gumma and Talu, 2003 proposed a method to correct sorption data for helium sorption. Helium sorption in turn, would result in an error (underestimation) of the excess sorption capacity. As noted by Sakurovs et al., 2009, helium adsorption, if present, will be in the µmol g^{-1} range as compared to CH_4 or CO_2 sorption capacity on coal which is usually in the mmol g^{-1} range and hence can be neglected.

Another potential problem in using helium as a reference gas is related to the accessibility of the pore space. It is commonly assumed that the same pore volume is accessed by helium as to CO2 or CH4. An overview on the state of discussion is provided by e.g. Sakurovs et al., 2009; Siemons and Busch, 2007; Walker Jr., 1988.

2.2.2.2 Temperature

Inaccuracies in temperature measurements and their effects on sorption measurements have been reported and discussed frequently in the literature. Temperature errors are commonly between 0.1 and 0.3 K for experimental temperatures well above room temperature. This is because it is typically easier to heat a system than to cool it and to keep it at a constant temperature (in time and space). Therefore, experimental temperatures below room temperature are expected to have a larger uncertainty. Figure 2-6

shows CO_2 and CH_4 isotherms measured on dry Carboniferous coal from the Silesia coal mine in Poland using a manometric sorption device. The measurements were performed in the context of the RECOPOL project of the European Union. For both isotherms the error in excess sorption capacity upon an increase in temperature of 0.1 K has been calculated. Evidently this effect is almost negligible for CH_4 (<0.1 %). For CO_2 however it is quite significant and exhibits a maximum around the critical pressure of CO_2 (p_c=7.39 MPa) where small temperature changes cause large changes in CO_2 density.

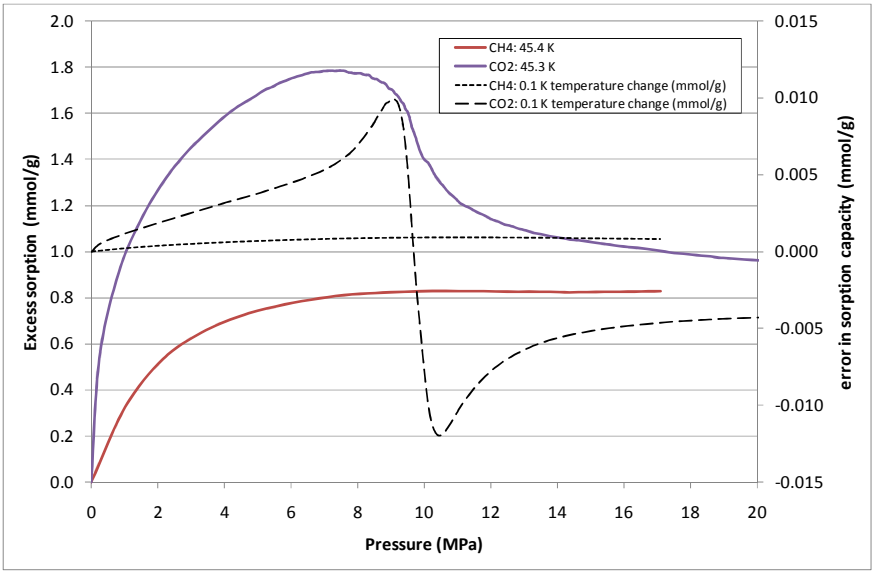


Figure 2-6: Error in calculating CH_4 and CO_2 sorption isotherm for a temperature increase or decrease by 0.1 K. Carboniferrous coal from Silesia mine (seam 315) of the Upper Silesian Basin, Poland, measured in the dry state using a manometric method.

2.2.2.3 Equations of State (EOS)

For mass balance calculations an equation of state (EOS) is required to calculate the density of the gases (CO_2, CH_4) at certain pressures and temperatures. There are numerous different EOS available, however the most commonly used ones are Span and Wagner, 1996 and Setzmann and Wagner, 1991 for CO_2 and CH_4 respectively, and the more universal EOS of Peng-Robinson (PR) and Soave-Redlich-Kwong (SRK). The two latter ones can be used for a large suite of gas species, using different interaction parameters. Mavor et al., 2004 performed a similar comparison of z-factor variations, including further EOS for CH_4. As a consequence, Mavor et al., 2004 pointed out that these differences in EOS can lead to variations of up to 20% in the calculated sorption capacities for methane. The comparison in Figure 2-7 shows for a temperature of 318 K a maximum standard deviation in z-factors of 2 % at 30 MPa. CO_2 shows its highest deviation of ~6.5 % at about 12 MPa. More details on errors related to EOS are provided by van Hemert et al., 2010.

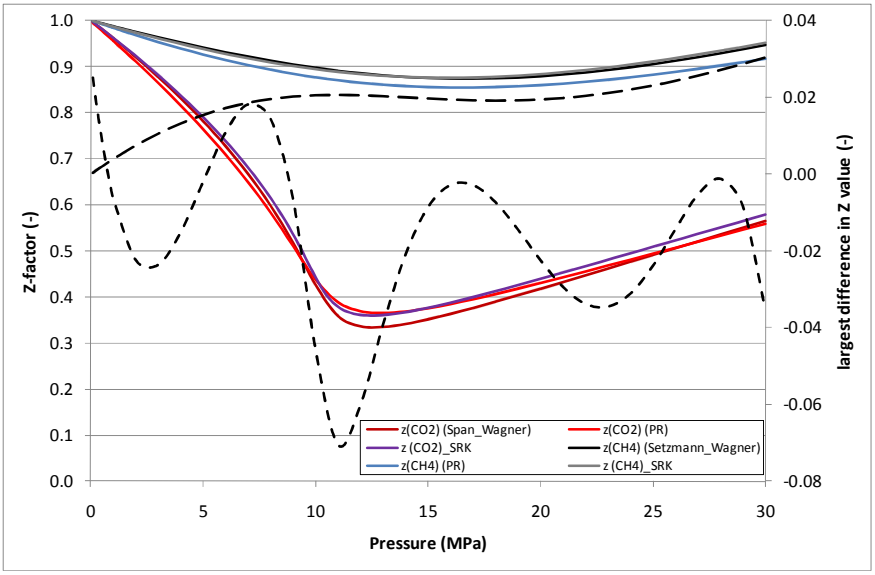


Figure 2-7. Comparison of compressibility factors (Z) for CO_2 and CH_4 at 318 K and pressures up to 30 MPa. calculated with different equations of state (EOS): Soave-Redlich-Kwong (SRK), Peng-Robinson (PR) and Span and Wagner, 1996 (SpW, CO_2) and Setzmann and Wagner, 1991 (SeW, CH_4). Dashed lines indicate the largest difference between the respective EOS for CO_2 (between SpW and SRK; short dashed line) and CH_4 (between SW and PR; long dashed line)

2.2.2.4 Volume calculations

The accurate volume determination of the reference/pump volume and void volume in the sample cell are indispensable for accurate prediction of the sorption capacity in manometric/volumetric setups. Figure 2-8 and Figure 2-9 show potential deviations from the initially calculated sorbed amounts when changing the reference cell volume and void volume in the sample cell by 0.5 %. Since the reference cell volume is constant (independent on sample volume) and impacts directly the calculation of the void volume in the sample cell, the error remains constant over the entire pressure range (0.5 %) for both gases, CO_2 and CH_4. Increasing or decreasing the void volume of the sample cell however leads to an error that is about one order of magnitude larger. For CO_2 this error increases sharply around the critical pressure and temperature and has an error of 12 % for CO_2 (Figure 2-8) while the error for CH_4 increases linearly to 7 % (Figure 2-9) at the respective final experimental pressure. These errors will depend on the volume ratio of sample cell to reference cell (which also depends on the sample volume in the sample cell) and are valid for the given example only.

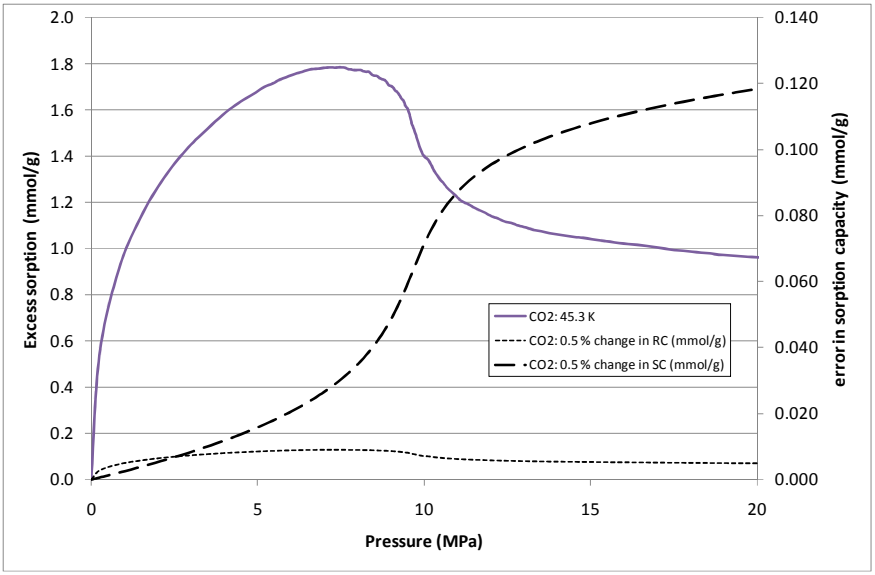


Figure 2-8: Error in calculating CO_2 sorption isotherm for an uncertainty in reference and sample cell volume of 0.5 %. Silesia 315 coal, Upper Silesian Basin, Poland, measured in the dry state.

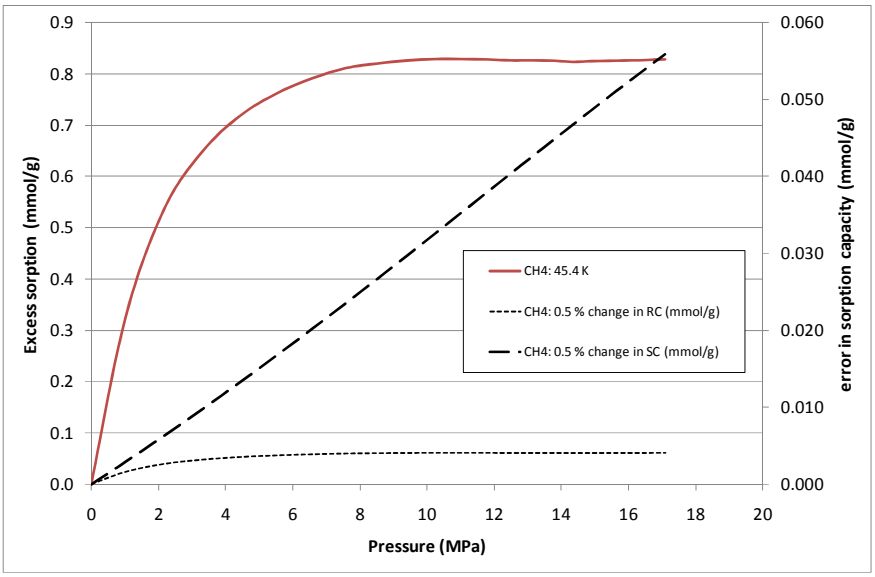


Figure 2-9: Error in calculating CH_4 sorption isotherm for an uncertainty in reference and sample cell volume of 0.5 %. Silesia 315 coal, Upper Silesian Basin, Poland, measured in the dry state.

2.2.2.5 Impurities in the measurement gas

Small gas impurities in the void volume can further lead to inaccuracies in the determination of the true gas density and hence to wrong sorption capacities. Impurities can be introduced by residual gas in the coal when sample cell evacuation or sample degassing was not properly performed, i.e. evacuation was too short or the end pressure not low enough. Further reasons might be helium from void volume determination that remained in the tubing system or impurities in the measurement gas itself.

Gensterblum et al., 2010 showed that by using CO_2 with different purities (0.9999 opposed to 0.999999) the difference in CO_2 density at 10 MPa and 45°C would be 0.1 % using the gas-mixture EOS by Gensterblum et al., 2010; Kunz et al., 2007. The same authors analyzed the case when helium is not accurately evacuated from the system prior to CO_2 or CH_4 measurement and assumed a remaining helium partial pressure of 0.1 MPa. This would lead to much higher errors of 6.1 % under the same p/T conditions as above. Small impurities in the CO_2 stream result in drastic changes in the shape of the isotherm and therefore are easy to detect.

Contamination of the measuring gas can also occur for measurements on samples containing water. To represent sub-surface moisture conditions, coal samples are typically moisture equilibrated using a standard test method (ASTM, D1412-93) which saturates the sample at 30°C and a relative humidity of 96-97 % under vacuum. This will lead to a certain partial water pressure in the free gas phase leading to uncertainties in the gas density but also in sample mass. Figure 2-10 shows the error in CO_2 and CH_4 densities at 45°C when assuming a water vapor partial pressure (in this case 0.009595 MPa). The error is relatively high at pressures <2 MPa but negligible at higher pressure. This uncertainty is not considered to have an impact on the sorption isotherm.

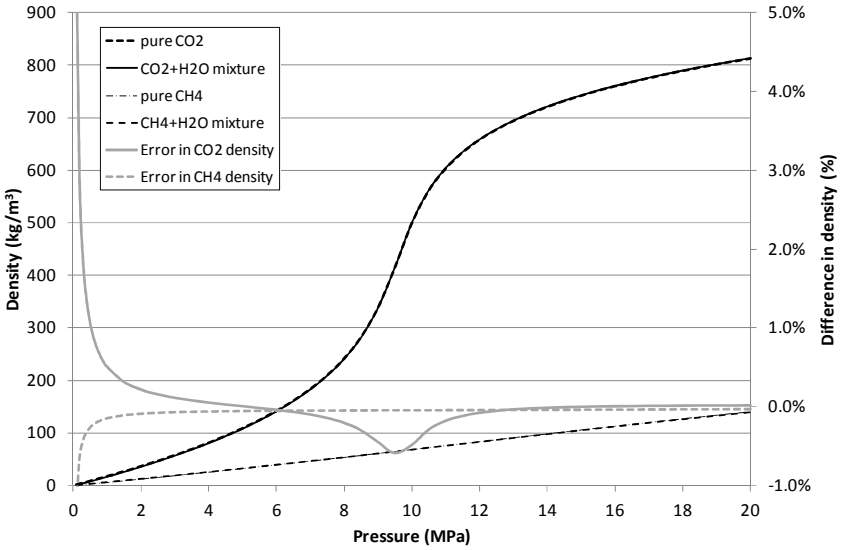


Figure 2-10. Plot of pure CO_2 versus CO_2+H_2O and CH_4+H_2O densities calculated at 45°C and water vapor pressures from Wagner and Pruss, 1993. Density calculations have been performed following the equation of state by Kunz et al., 2007.

2.2.2.6 Gas dissolution in water and gas sorption on mineral matter

Gas sorption capacities are typically reported on a dry, ash-free (daf) basis assuming no gas uptake by dissolution in water or sorption on mineral surfaces. Methane dissolution in water is known to be more or less negligible whereas CO_2 has shown to dissolve in water in relevant amounts depending on the sample moisture content (Busch et al., 2007).

Gas sorption on mineral surfaces (especially clays) has been found to be significant (Busch et al., 2008; Weniger et al., 2010; Wollenweber et al., 2010). Although methane sorbs on clay minerals (RWTH Aachen University, Germany, unpublished data), the total amounts are small. For CO_2 however sorption capacities are in the same order as for coal. Research on this topic is still in progress and mechanisms are not well understood. Therefore it might be misleading to report CO_2 sorption capacities on a daf basis since dissolution in water and adsorption on clay mineral surfaces (depending on the respective contents) is significant and should not be neglected.

2.2.2.7 Minor sources of errors related to gas sorption on coal

A number of minor sources of error have been reported in the literature (van Hemert et al., 2007) which are listed below but will not be discussed in detail:

- Gas leakage: Every setup has a certain leakage rate that cannot be avoided and if this rate is significant compared to the amounts of gas sorbed the mass balance calculation should account for this.
- Thermal and mechanical expansion/contraction of cells in the manometric/volumetric setups. This is mainly relevant if the volume calibrations are performed with large pressure differences between reference cell loading and relaxation into the sample cell or the volume calibrations are performed at a different temperature than the sorption measurement.
- Changes in cell volumes due to changes in pressure
- Measuring gas contamination from the steel typically used for cells leading potentially to changes in gas density.
- Sample mass determination: Weight balances usually have an accuracy of 100 µg. Since sample masses of >1 g are typically used this will pose a negligible error of <0.01 %.
- Further sources of error are attributed to the coal sample itself (moisture content, volumetric effects etc.) and will be addressed at a later stage of this manuscript.

2.2.3 Modeling of adsorption isotherms

Many methods have been discussed to model sorption isotherms on coal or other microporous materials and an overview is provided by Ozdemir et al., 2003 while other methods have been proposed by e.g. Fitzgerald et al., 2006 and Sakurovs et al., 2007.

This paper does not intend to discuss the various isotherm modeling efforts since this would again be an overview paper of its own. In the (E)CBM industry and related reservoir simulations approaches the well-known Langmuir equation is used as a simple method and provides a reasonable fit to most experimental data:

$$n_{ads} = \frac{n_L \cdot p}{k_L + p} \qquad (2\text{-}8)$$

Here n_L is the Langmuir volume, denoting the amount of gas sorbed at infinite pressure p_∞ and k_L is the Langmuir pressure, corresponding to the pressure at which half of the Langmuir volume n_L is reached.

2.2.4 Excess versus absolute sorption

For gases like CO_2 or CH_4, the excess sorption m_{excess} is defined as the amount gas sorbed on the sorbent (coal), however without occupying a certain volume for the sorbed phase ($\varrho^{excess}_{adsorbed\ phase}=\infty$). Sorption of gas molecules takes place in one or more layers on the surface at a higher density than the gas phase ($\varrho^{absolute}_{adsorbed\ phase}\geq\varrho_{gas\ phase}$). (Figure 2-11, Mohammad et al., 2009; Sircar, 1999). However, excess sorption does not consider the potential different pore accessibility between Helium and gases like CH_4 or CO_2 and therefore: $V^{He}_{Void} \overset{\text{def}}{=} V^{CO2,CH4}_{Void}$.

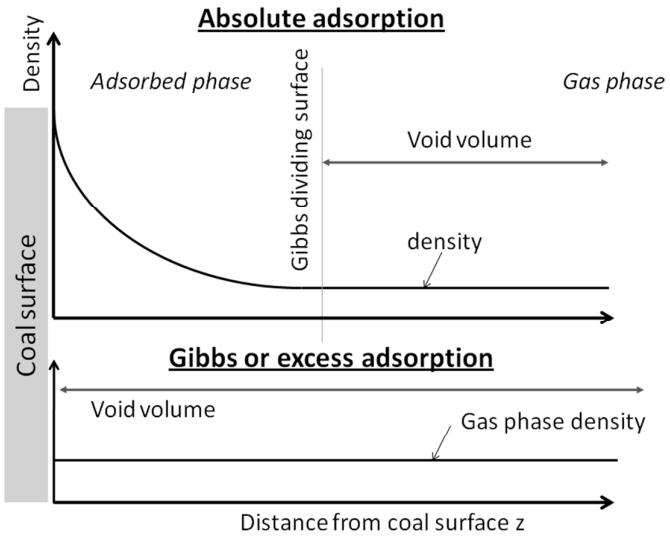


Figure 2-11. Schematic diagram of sorbate density in Gibbsian sorbed phase (simplified and modified after Sircar, 1999). The arrow marked as void volume in excess and absolute sorption denotes the measurement range for the void volume.

Gas molecules sorbed occupy a certain volume V_{ads}, hence increase the solid volume. The density of the sorbed gas ϱ_{ads} can be calculated knowing the sorbed phase volume V_{ads} and its mass m_{abs} referred to as the absolute sorption:

$$m_{ads} = V_{ads} \cdot \varrho_{ads} \qquad (2\text{-}9)$$

Calculating absolute from excess sorption can be done for the manometric (volumetric) and for the gravimetric methods. The different calculation paths are given below:

2.2.4.1 Gravimetric method

For the *non-sorption case* the calculated apparent mass change („weight change“) due to buoyancy of the sample in the gas (sorptive) at pressure *p* and temperature *T* is calculated according to:

$$\Delta m_{grav}^{ns} = m_{sample} - V_{sample} \cdot \rho_{gas}(P,T) = m_{sample} - \frac{m_{sample}}{\rho_{sample}} \cdot \rho_{gas}(P,T) = m_{sample}\left(1 - \frac{\rho_{gas}(P,T)}{\rho_{sample}}\right) \quad (2\text{-}10)$$

(sample mass – (calculated) sample buoyancy in the gas phase (sorptive))

For the *sorption case* the measured apparent mass change („weight change") due to the combined effect of sorption (mass uptake), buoyancy of the sample and buoyancy contribution of the sorbed volume can be calculated according to:

$$\Delta m_{grav}^{s} = m_{sample} + m_{adsorbed} - V_{sample} \cdot \rho_{gas}(P,T) - V_{adsorbed} \cdot \rho_{gas}(P,T) =$$
$$= m_{sample}\left(1 - \frac{\rho_{gas}(P,T)}{\rho_{sample}}\right) + m_{adsorbed}\left(1 - \frac{\rho_{gas}(P,T)}{\rho_{sorbate}}\right) \quad (2\text{-}11)$$

(sample mass + sorbed mass - sample buoyancy – buoyancy of sorbed phase)

Further the excess mass normalized to the initial sample mass is:

$$m_{grav}^{excess} = \Delta m_{grav}^{s} - \Delta m_{grav}^{ns} = m_{adsorbed}\left(1 - \frac{\rho_{gas}(P,T)}{\rho_{sorbate}}\right) \quad (2\text{-}12)$$

2.2.4.2 Manometric method

In the *non-sorption case* (void volume previously determined with He) the calculated amount of (sorptive) gas accommodated in the void volume of the measuring cell at given pressure and temperature (requiring determination of the void volume by He expansion and the equation of state of the sorptive gas) is calculated according to:

$$m_{man}^{ns} = V_{void}^{0} \cdot \rho_{gas}(P,T) \quad (2\text{-}13)$$

In the *sorption case* the measured amount of (sorptive) gas actually transferred into the measuring cell at given pressure and temperature $(V_{void}^{0} - V_{ads})$ is the residual free gas volume:

$$m_{man}^{s} = m_{ads} + (V_{void}^{0} - V_{ads}) \cdot \rho_{gas}(P,T) \quad (2\text{-}14)$$

$$m_{man}^{excess} = m_{man}^{s} - m_{man}^{ns} = m_{adsorbed} - V_{ads} \cdot \rho_{gas}(P,T) \quad (2\text{-}15)$$

$$m_{man}^{excess} = m_{adsorbed}\left(1 - \frac{\rho_{gas}(P,T)}{\rho_{sorbate}}\right) \quad (2\text{-}16)$$

Both procedures (for manometric and gravimetric methods) yield equivalent expressions for the excess sorption.

A major problem in determining absolute sorption is that ϱ_{abs} cannot be determined directly and certain assumptions have to be made. Most authors use the liquid gas density at the boiling point at ambient pressure which is 1278 and 423 kg m^{-3} for CO_2 and CH_4 respectively (Yee et al., 1993; Dreisbach, 1999; Mavor et al., 2004). Murata et al., 2001 provides an overview of additional approaches to determine values for the sorbed density. Absolute sorption can be calculated from excess sorption for manometric (volumetric) and gravimetric methods:

Especially for CO_2 several other attempts have been used to incorporate potential further changes of the volume of the sorbent like coal swelling. A summary of such effects is provided by several authors (Siemons and Busch, 2007; Ozdemir et al., 2003; Sircar, 1999; Sudibandriyo et al., 2003). Ozdemir et al., 2003 used an additional correction factor accounting for the sorbent volume increase caused by the sorbed phase volume. Siemons and Busch, 2007 used a fitting procedure to combine all volumetric effects.

A common procedure to estimate the density of the sorbed phase consists in plotting the sorbed amount against the free gas density. This approach was used for instance by Humayun and Tomasko, 2000. The slope and intercept of the linear portion of this plot (at high free gas densities) yield the density and the volume of the sorbed phase. For a Filtrasorb-400 activated carbon the sorbed phase obtained by this method agrees well with the van der Waals density of 23.45 mmol cm^{-3} (1032 kg m^{-3}). Similar values were obtained by Gensterblum et al., 2009 for the same activated carbon. For CO_2 sorption on natural coals, however, Gensterblum et al., 2010 found higher sorbed phase density values. These might be due to an increase in the solid volume by a poroelastic expansion of the coal (coal swelling), not caused by the volume of the sorbed phase alone.

Significant volumetric effects are not expected for CH_4 and using a sorbed phase density of 423 kg m^{-3} to calculate absolute sorption seems to be a generally accepted number. For CO_2 this is more complex since every coal sample swells to a different amount, has a specific pore system with a more or less unique distribution of functional groups which makes the conversion from excess to absolute sorption non-universal. The use of the graphical method proposed by Humayun and Tomasko, 2000 is only appropriate if the experimental pressure is high enough such that the isotherm shows the typical decline with increasing pressure or gas density. Further fundamental research is needed to obtain more reliable information on the density of the sorbed phase and any additional factors that contribute to an increase in sorbent (coal) volume.

2.3 Water sorption on coal

The interaction of carbon materials like natural coal with water is more complex than with nonpolar gases like helium, argon, nitrogen, methane, or carbon dioxide. This complexity is due to the weak dispersion interaction of water with coal, the tendency of water to form hydrogen bonds with other sorbed water molecules and surface chemical species, and the chemisorptive interaction with the coal mineral matter.

Many studies address the issue of water sorption on coal or gas sorption on moist coal either by describing the principles or by determining sorption capacities of gases (CO_2, CH_4) on moist coal samples (Allardice et al., 2003; Busch et al., 2007; Busch et al., 2003b; Clarkson and Bustin, 1999a; Clarkson and Bustin, 2000; Day et al., 2008c; Fei et al., 2006; Fei et al., 2007; Goodman et al., 2007b; Gutierrez-Rodriguez, 1984; Hartman and Pratt, 2005; Joubert et al., 1973; Joubert et al., 1974; Kelemen and Kwiatek, 2009; Krooss et al., 2002; Lynch and Webster, 1982; Moore and Crosdale, 2006; Nishino, 2001; Ozdemir and Schroeder, 2009; Suuberg, 1993; Unsworth, 1989).

Figure 2-12 shows the difference in the isotherm shapes that is the result of the combined effects of carbon hydrophobicity and the presence of surface functional groups that act as primary sorption sites. It is believed that water molecules are strongly sorbed on the surface sites via hydrogen bonds. This is followed by further sorption that results in the creation of water clusters and eventually pore filling (Brennan et al., 2001).

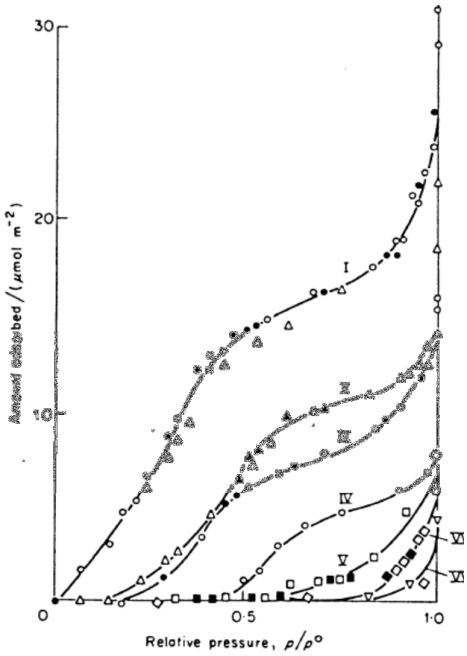


Figure 2-12: Adsorption of water vapor on oxygenated carbons: (I) heated in vacuum at 200°C; (II) in vacuum at 950°C; (III) in vacuum at 1000°C; (IV) at 1100°C in a hydrogen stream; (V) in hydrogen at 1150°C; (VI) in hydrogen at 1700°C; and (VII) at 3200°C (Muller et al., 1996).

Additionally the pore size distribution has an important control on water sorption on coal or carbon materials in general. It plays a significant role in the observed energies of the water sorption process (Salame and Bandosz, 1998). Based on X-ray diffraction of sorbed water molecules in molecular sieving carbons, Hanzawa, 1998 and Iiyama, 1997 concluded that water forms an ordered assembly structure in the hydrophobic nanospace. The estimated size of such a cluster is about 0.6 nm and is likely associated with the microscopic anomalies of water confined in small pores (Brennan et al., 2001; Iiyama, 1997). Alcaniz-Mongue, 2001 found that the process of water sorption is due to both physical sorption and

chemical interaction with surface groups. In accordance with this process, micropore filling is progressive: the narrow micropores are filled first, and subsequently, water is sorbed in the remaining greater range of microporosity. This study confirms that water sorbed in the porosity of carbon has a solid-phase structure throughout the whole range of micropore size.

Several studies investigate the structure of water (clustering) in the sorbate phase (Allardice and Evans, 1971; Salame and Bandosz, 1998, 1999, 2000). Klier and Zettlemoyer (1977) elucidate water cluster stabilities and referred to quantum mechanical calculations performed mainly by Del Bene and Pople, 1969. These calculations describe how water molecules form larger clusters, ranging from dimers to cyclic tetramers. They become energetically more stable with energies per water molecule changing from -12.8 to-43.9 kJ/mol, respectively.

2.4 Coal-specific factors controlling water sorption

2.4.1 Functional groups

The sorption of water vapour and methane on coal surfaces has been studied for some time, and carboxylic and hydroxylic functional groups have been shown to be important for this process. Joubert et al., 1974 determined that methane sorption capacities of high oxygen coals undergo a much greater reduction when saturated with moisture than do their low-oxygen counterparts.

The mechanism of water sorption was originally proposed by Dubinin and co-workers (Dubinin, 1980; Dubinin and Serpinsky, 1981). Their conclusions are based on the results of experiments where the first points on the isotherm were measured at a relative pressure of about 0.1. The authors proposed that water sorbs on primary adsorption centres first (functional groups containing oxygen), followed by sorption on secondary centres (sorbed water molecules) via hydrogen bonding (Given, 1986; Gutierrez-Rodriguez, 1984; Lynch and Webster, 1982; Nishino, 2001).

Direct measurement by FTIR (Mu and Malhotra, 1991) and ionic thermal current (Suárez et al., 1993) confirm the assumption that water vapour is mostly sorbed on carboxyl groups, where strong interactions occur and the amount of water vapour sorption on hydroxyl groups is limited.

2.4.2 Coal rank

Several studies report a correlation between coal rank and the extent of water uptake, particularly at high relative pressures, indicating that water uptake decreases with an increase in rank, showing a minimum at about 1.2 % V_{Rr}. Water uptake then increases towards higher rank coals (Figure 2-13, e.g. Prinz et al., 2004; Bratek et al., 2002). This parabolic behaviour is similar to the rank dependence of the micropore volume. Prinz and Littke, 2005 applied low pressure sorption isotherms to show that water molecules do not seem to be able to penetrate the interlayer spacing of crystallite structures (<0.4 nm). Instead, water is present in the mesopores and larger micropores (~0.4–30 nm). The results of this study are in general agreement with observations by Lu et al., 2001.

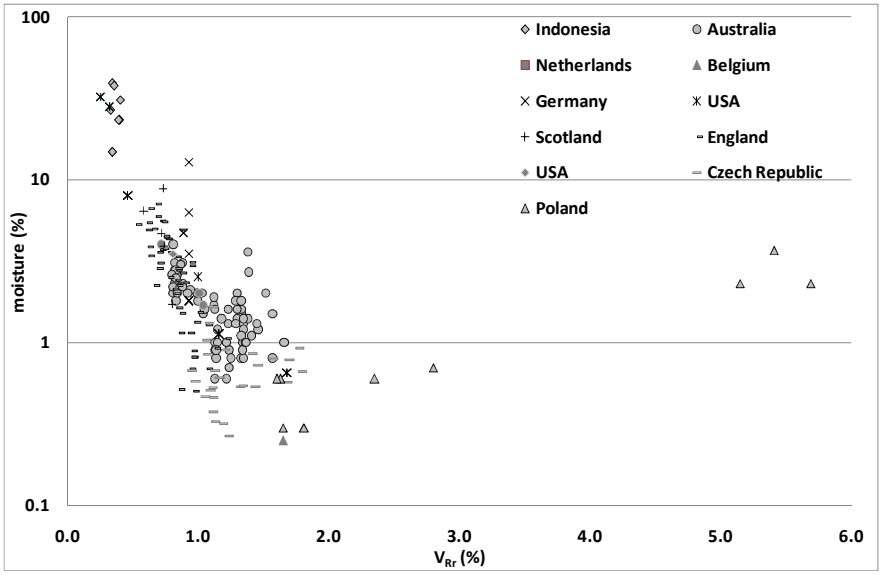


Figure 2-13: Equilibrium moisture content of coals of varying rank (Beamish and Crosdale, 1998; Bratek et al., 2002; Busch et al., 2007; Clarkson and Bustin, 2000; Crosdale et al., 1998b; Day et al., 2008c; Day et al., 2005; Gasem et al., 2002a; Hildenbrand et al., 2006; Laxminarayana and Crosdale, 1999a; Laxminarayana and Crosdale, 2002; Mastalerz et al., 2004; Moore and Crosdale, 2006; Ottiger et al., 2006; Ozdemir and Schroeder, 2009; Pan and Connell, 2007; Prinz et al., 2004; Saghafi et al., 2007).

2.4.3 The isosteric heat of water sorption on coal

Thermodynamically adsorption is an exothermic process and the sorption capacity decreases with increasing temperature because of a higher ordered adsorbed state (Sircar, 1992). The temperature dependence of the sorption capacity is controlled by the isosteric heat of sorption which is a function of surface coverage. In general the isosteric heat of sorption depends on the surface chemistry and the pore structure.

Many published studies show that the isosteric heat of sorption Q_{st} for gases decreases slightly when adding water. This suggests that there are some higher energetic sorption sites within the coal that have a greater affinity for these sorbates, but these sites are preferentially occupied by water molecules (e.g. Day et al., 2008c, Figure 2-14). This is consistent with the classification by Dubinin and co-workers of primary and secondary sorption sites (see 2.4.1). The isosteric heat of water sorption was found to have values very close to the latent heat of bulk water condensation (45 kJ mol^{-1} at a surface coverage up to 10%). It was also found that when pores are too small to accommodate functional groups, the released heat of sorption at very low relative pressure is equal to the heat of condensation. It has even been observed to be a few kJ per mol above the heat of condensation (Salame and Bandosz, 2000). Therefore we can conclude that the isosteric heat of sorption is higher than the heat of condensation when functional groups are present.

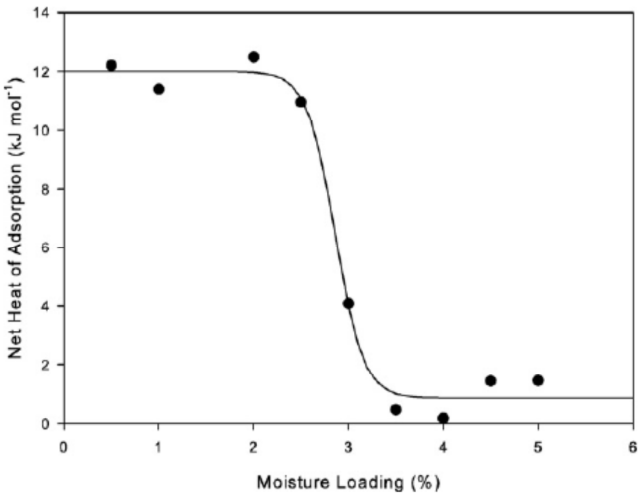


Figure 2-14: Net heat of water sorption on coal as a function of moisture content (Day et al., 2008c). The net heat of sorption Q_{net} is equal to the isosteric heat of sorption Q_{st} and subtracting the heat of condensation. This relationship is only valid for inert sorbents.

The low isosteric heat of sorption Q_{st} at high surface coverage suggests that interaction between the carbon surface and water molecules is weak (Walker Jr. and Mahajan, 1993). It was calculated (Rubes et al., 2010; Rubes et al., 2009) and demonstrated (Avgul and Kiselev, 1970) that the energy of interaction of water molecules and a pure graphite surface is low.

Mahajan (1970) argued that hydrogen bonding should produce higher heats of sorption at low surface coverage (Mahajan, 1970). They referred to Darcey et al., 1958, who reported results for water sorption on Saran charcoals with a heat of sorption of 63 kJ/mol for a surface coverage of only 1%, whereas at about 5% surface coverage the heat of sorption approaches the heat of water condensation (45 kJ mol^{-1}) (Darcey et al., 1958; Mahajan, 1991; Walker Jr. and Mahajan, 1993). Huang et al., 1995 discussed changes in the hydrogen bonding patterns for water molecules bound to high and low densities of oxygen functional groups on the coal surface. For high oxygen content coals the oxygen functional groups are in close proximity to one another, enabling the formation of bridged clusters of water molecules.

Salame and Bandosz (1998) observed a similar trend in the heat of sorption on various activated carbons with different degrees of surface oxidation. Their results showed that the isosteric heats of water sorption are affected by surface chemical heterogeneity only at low surface coverage (Salame and Bandosz, 1998). This conclusion is also supported by Gubbins and co-workers and based on a good agreement between molecular simulations (Maddox et al., 1995; Muller et al., 1996; Ulberg and Gubbins, 1995) and experimental data. It was shown that on the surface of activated carbons with functional groups the creation of water clusters occurs before all primary sorption centres are occupied by water molecules (Salame and Bandosz, 1998, 1999, 2000).

Referring to the competitive sorption of gases, CO_2 and CH_4 are forced to lower energy sites when water is present. Water appears to be sorbed on functional groups, whereas CO_2 and CH_4, although showing some

degree of preferential sorption, are generally able to access all of the sorption sites throughout the coal (Day et al., 2008c).

2.4.4 Water sorption/desorption hysteresis

Puri, 1966 reported sorption-desorption hysteresis for activated carbons with different surface chemistry which is schematically documented in Figure 2-15. With the presence of acidic oxygen surface groups the sorption-desorption isotherm is not completely reversible at zero relative vapour pressure. A certain amount of water cannot be desorbed under vacuum (10^{-4} mbar), only by additionally elevating the temperature. This residual moisture is irreversibly sorbed water and is presumably held tightly within the micropores (Mahajan, 1970). McCutcheon et al., 2001 and Charrière and Behra (2010) found that the extent of hysteresis for sorption/desorption (integrated area difference) correlates linearly with the coal oxygen content. The data of Mahajan, 1970 supports this hypothesis. Contrary, Allardice and Evans (1970) suggest that hysteresis occurs because the swelling is proportional to the water sorbed. However, they suggest that the corresponding shrinkage of the structure during desorption is pressure delayed by water strongly sorbed on primary sorption sites on the internal surface of the coal, and this sorbed water appears to be confined to the monolayer region.

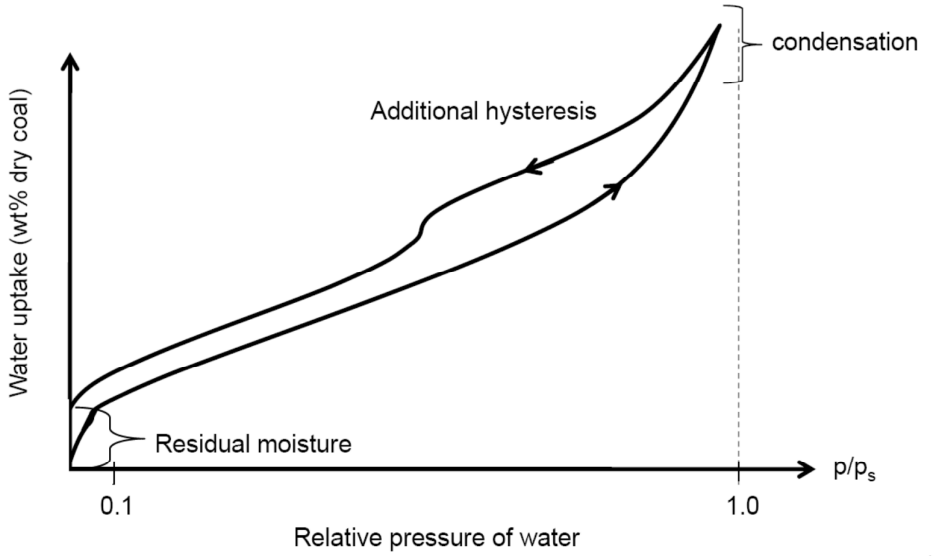


Figure 2-15: Schematic of water uptake on coal.

Figure 2-15 shows schematically a water isotherm. Monolayer sorption occurs in the lower relative pressure range of the isotherm. A sharp increase in the isotherm, where the relative water vapour pressure is still below 0.1 is attributed to water sorption on the primary sorption sites. Multilayer condensation is responsible for the straight line region in the middle section of the isotherm. Capillary condensation is the dominating factor in the upper concave part of the isotherm. The inflection point is the pressure where capillary condensation kicks-in. Allardice and Evans, 1971 showed that this inflection point shifted to higher relative pressures with increasing temperature.

McCutcheon et al., 2001 and Charrierre and Behra (2010) examined two parts of the hysteresis while studying water sorption on coals with different ranks. Low and high relative pressure hystereses have occurred especially for lower rank bituminous coals. McCutcheon et al., 2001; McCutcheon et al., 2003 and Charrière and Behra, 2010 have suggested that the hysteresis at high relative pressure is due to the ink-bottle effect, which would require a condensation (a liquid phase).

Horikawa et al., 2010 observe recently that the water cluster size in mesopores is larger than in micropores, and the hysteresis loop of sorption–desorption in mesopores is greater than in micropores.

Finally, we would like to underline that most of this hypothesis is based on only a few experiments, and in some cases, on indirect observations. To verify this hypothesis, further investigations are needed (Gauden, 2005).

2.4.5 CH_4 and CO_2 sorption of coals in the presence of water

2.4.5.1 Effects on sorption capacity

As early as 1936, Coppens reported the observed decrease in methane sorption capacity due to moisture in several Belgian coals (Coppens, 1936). Polar sites such as hydroxyl groups on the coal surface are preferentially occupied by water and in the process reduce the capacity for CO_2 and CH_4. Therefore moist coals have a significantly lower maximum sorption capacity for either gas compared to dry coal. However, the extent to which the capacity is reduced depends on coal rank. Higher rank coals are less affected by the presence of moisture than low rank coals (Day et al., 2008c).

Sorption capacity decreases with increasing moisture content until the equilibrium moisture content is reached. Above this moisture content the gas sorption capacity remains constant (Day et al., 2008c; Joubert et al., 1973; Joubert et al., 1974). This limiting moisture content depends on the rank of the coal and, for Australian low rank coals, corresponds approximately to the equilibrium moisture content that would be attained by exposing the coal to about 40–80% relative humidity. Allardice and Evans (1970) conclude, based on entropy calculations, that water above this limit has a liquid structure. Therefore they conclude water condensates on the surface and that gas will only dissolve in this water (Allardice and Evans, 1971). The experimental results indicate that the loss of sorption capacity by the coal in the presence of sorbed water can simply be explained by "volumetric displacement of CO_2 and CH_4 by water" (Day et al., 2008c; Levy et al., 1997). An interesting consequence of volumetric displacement would be that estimates of wet coal sorption capacity could be calculated from dry coal isotherms. Dry samples are experimentally easier to handle in comparison to moisturized samples. The assumption behind this hypothesis is that the density of the sorbed phase is constant for comparable coal types. For Australian and Chinese bituminous coals, approximately 0.3 molecules of CO_2 are displaced by each water molecule and each molecule of water displaces 0.2 molecules of CH_4 up to the limiting moisture content (Day et al., 2008c). To verify a general validity of this hypothesis, further investigations are necessary.

The fact that CO_2 and CH_4 continue to be sorbed on moisture-equilibrated coals indicates that water and these two gases compete only for a portion (Figure 2-16, intersection α and β or γ) of the total available sorption sites. Figure 2-16 shows schematically the total set of sorption sites for CO_2, CH_4 and water on coal at constant temperature and pressure. Carbon dioxide has the highest amount of sorption sites, followed by methane and water. The ratio of sorption capacity or sorption sites of CO_2 and CH_4 is in the range of 1 to 9 (s. below) and changes strongly to lower ratios when water content decreases or coal rank increases. The intersection area of water and methane γ is smaller than the intersection area of water and CO_2 (β), as illustrated in Figure 2-16. This intersection area is based on the observation of secondary sorption sites of water. Intersection δ represents the primary sorption sites of water. If there is water present in the system, these sorption sites will be occupied by water molecules, because of the higher heat of sorption for water on the primary sorption sites compared to CO_2 and CH_4. However, the intersection areas and their respective ratios of these will change when temperature and pressure are varied. For example at very low total surface coverage the amount of sorbed water will be high in comparison to CH_4 and CO_2, because of the high energetic primary sorption sites.

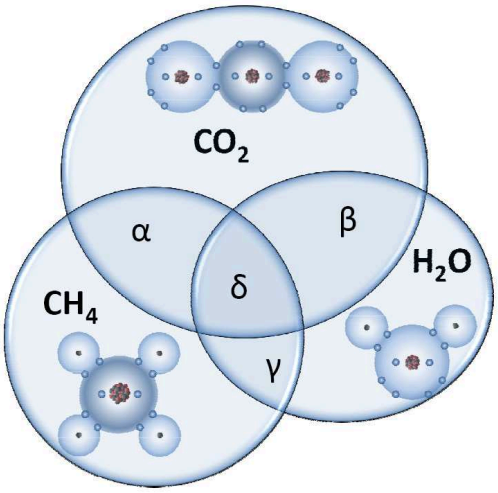


Figure 2-16: Sorption sites of each gas at one given fixed surface coverage (fixed p,T) and the intersection for multi-component sorption isotherms.

The coal surface can be envisaged to consist of sets of more water-prone (hydrophilic) and more gas-prone sorption sites and there is a partial overlap of these sets of sorption sites.

For dried coals, sorption capacity shows a parabolic dependence on rank, whereas as-received coals display a more linear dependence on fixed carbon content (Figure 2-17, Ozdemir and Schroeder, 2009).

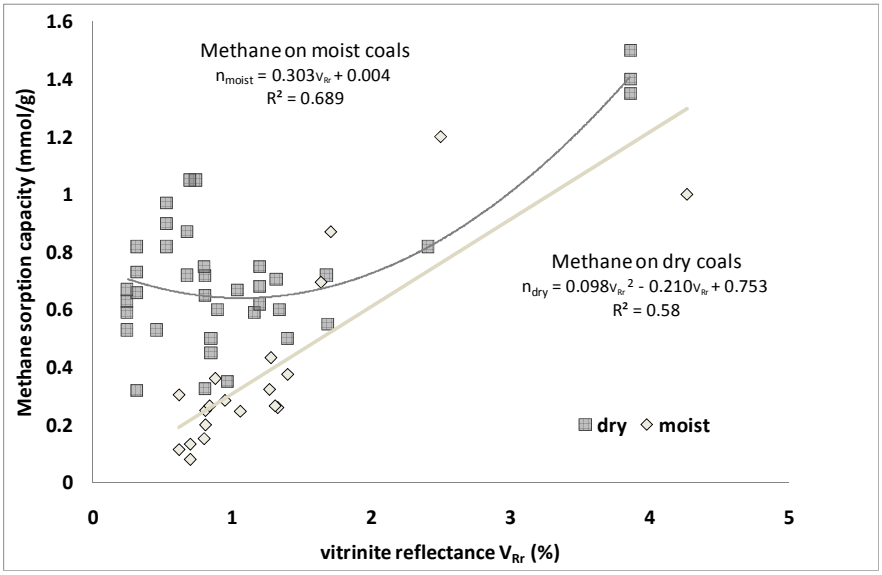


Figure 2-17: Sorption capacity at reference pressure of 5 MPa as a function of coal rank for moist and dry coals (Bae and Bhatia, 2006; Battistutta et al., 2010; Busch et al., 2003a; Bustin, 2004; Chaback, 1996; Day et al., 2008c; Fitzgerald et al., 2005; Harpalani et al., 2006; Kelemen and Kwiatek, 2009; Li et al., 2010; Mastalerz et al., 2004; Pini et al., 2010; Reeves et al., 2005; Ryan and Richardson, 2002; Sakurovs et al., 2007; Weniger et al., 2010; Yu et al., 2008b).

2.4.5.2 CH_4 sorption capacity and the influence of moisture at elevated temperatures

High-pressure methane sorption isotherms are in general less sensitive to changes in temperature than to variations in moisture content (Day et al., 2008c; Joubert et al., 1974; Moore and Crosdale, 2006; Ozdemir and Schroeder, 2009). As discussed in the previous chapter, CH_4 sorption capacity decreases with increasing moisture content until moisture saturation is reached. Above this moisture saturation limit, the gas sorption capacity remains constant (Day et al., 2008c; Joubert et al., 1973; Joubert et al., 1974).

However, an increase in temperature results in a decrease in moisture-saturation. Lower equilibrium moisture contents will increase the gas sorption capacity; higher temperature will decrease the sorption capacity (Day et al., 2008c; Joubert et al., 1974; Moore and Crosdale, 2006; Ozdemir and Schroeder, 2009). This relationship is illustrated in Figure 2-18 and confirmed experimentally by Gaschnitz, 2000 on coals from the Ruhr Basin, Germany.

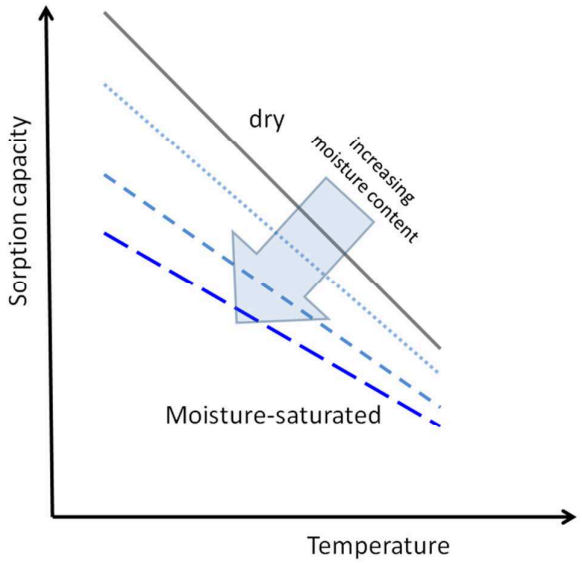


Figure 2-18: Schematic diagram of sorption capacity of coals at different moisture contents and as a function of temperature.

Which of these opposing effects has a larger influence on gas sorption capacity is property specific for each coal and depends on the isosteric heat of sorption and the surface coverage (amount of available sorption sites). Sorption of water on primary sorption sites (intersection area 4 in Figure 2-16) results in higher sorption enthalpies compared to CH_4 or CO_2. Therefore, it is unlikely to observe competition for the primary sorption sites of water. For sorption on the secondary sorption sites, sorption enthalpies for water and each gas type are likely to become more similar, especially when the moisture content of the sample is close to the saturation content. Accordingly we observe a significant competition for this sorption site between methane and water molecules. Up to a sample-specific limit additional water is only present as free water on the surface coal without occupying sorption sites.

Crosdale et al., 2008 investigated the influence of moisture and temperature on the CH_4 sorption capacity of low-rank coals. Their results show no significant temperature dependence for CH_4 sorption capacity at constant moisture content (Figure 2-19, Case 2). The common expectation for sorption isotherms as a function of temperature at different moisture-levels would be that increasing temperature will cause a decreasing sorption capacity (Figure 2-18, Figure 2-19 Case 1). However, due to the high displacement ratios (2.4.5.1) it is possible that the release of water sorption sites could be able to compensate the decrease in CH_4 total sorption sites due to the higher temperature. Nevertheless, further studies are required to elucidate this observation.

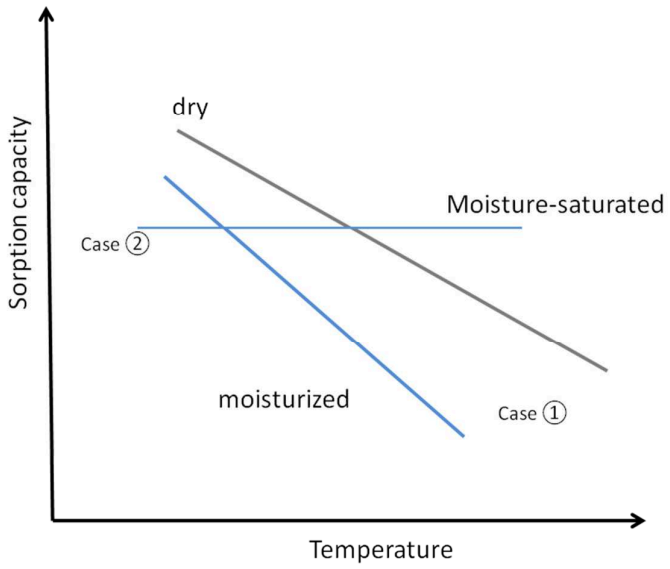


Figure 2-19: Schematic plot of the sorption capacity in the dry and moisturized state as a function of temperature.

2.4.6 Water sorption kinetics on coal

A novel application of an empirical kinetic model was proposed by McCutcheon et al., 2001 to quantify water sorption kinetics in bituminous coals. They introduced a flow rate kinetic parameter to quantify the rate of water transfer from outside the coal particle to the intra-particle pore structure. Most of the bituminous coals investigated by a gravimetric method show similar uptake rates at relative water vapour pressures in the range of 0.2-0.9. However for two semi-anthracites the flow rate was significantly less than for all other bituminous coals investigated. McCutcheon et al., 2001 believe that this difference is caused by differences in the coal structure. Variations between coals in the uptake rate at low relative pressures (0-0.2) appear to be caused by variations in the primary sorption sites. Effective diffusivities for water uptake on coal have been measured by two authors and are summarised in Table 2-1.

Table 2-1: Effective water diffusivities on coal (Charrière and Behra, 2010; McCutcheon et al., 2003).

Coal type	**T [K]**	**relative pressures [/]**	**grain size [mm]**	**model**	**uptake rate [cm^3 min^{-1} g^{-1}]**	**effective diffusivity [s^{-1}]**	**Source**
bituminous	299	0.05<0.9	<0.25	empirical kinetic model	0.07-0.015	10^{-2} - 10^{-3}	McCutcheon
high volatile bituminous, lignite	298	0.1<0.9	0.04-0.25	unipore model	n.E.	10^{-4} - 10^{-5}	Charriere

2.5 Dependence of CO_2, CH_4 and water sorption on coal properties

2.5.1 The influence of coal composition on gas sorption

Most sorption analyses of coal are carried out on dried samples and the sorption capacity is reported to this basis. These results can be modified to expressions having another basis, as illustrated in Figure 2-20.

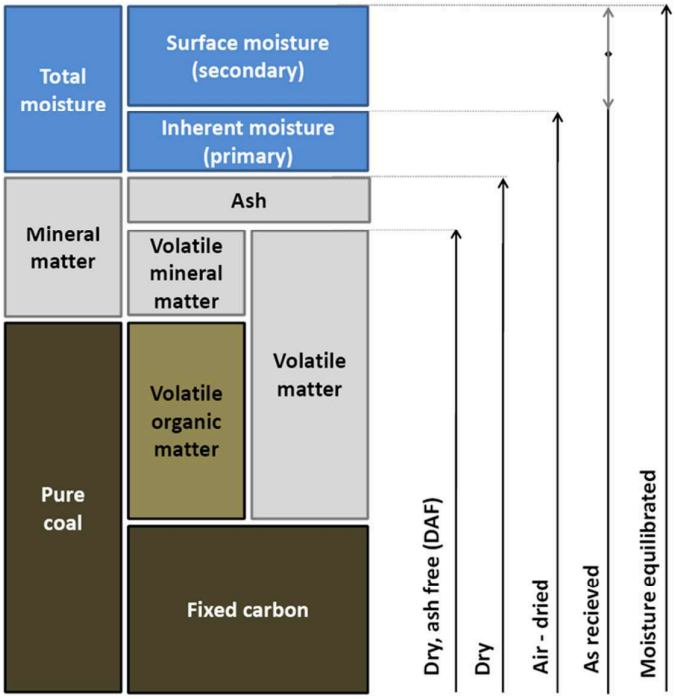


Figure 2-20: Relationship of different analytical bases to various coal components

The moisture content of moisture-equilibrated coals is defined as the maximum water sorption capacity of the specific coal. The “as received” moisture content of coals is not a fixed coal specific value, because the moisture content is in equilibrium with the surrounding or environmental humidity. It depends on the oxygen content of the coal, because the functional groups represent more energetic sorption sites for water molecules. Therefore a coal with a higher oxygen content will have a higher “as received” moisture content. Derived from the thermodynamic equilibrium between the chemical potential of the water partial pressure in the free gas phase and the sorbed phase of water, it is obvious that the amount of occupied sorption sites is higher for a coal with a higher density of functional groups. If the water partial pressure is reduced using only drying agents without elevating the temperature, an “air-dried“ moisture content of the coal is achieved. The “air-dried” moisture content is the coal specific moisture content.

Furthermore, the ash and total organic carbon (TOC) contents are sensitive to sample heterogeneity. Often an increase in minerals matter in sieve fractions (especially at particle diameters less then 100µm) is observed.

2.5.2 Total Organic Carbon (TOC) and ash content

Weniger et al., 2010 confirmed recently that CH_4 and CO_2 sorption capacities on coal can be correlated with the total organic carbon content (TOC) (Figure 2-21). For carbon dioxide the linear regression showed a non-zero intercept, indicating a significant sorption capacity of the mineral matter for this gas species. This was not the case for CH_4 (Weniger et al., 2010). These findings support our conclusion that CH_4, CO_2 and water compete for a part of all sorption sites (Figure 2-16).

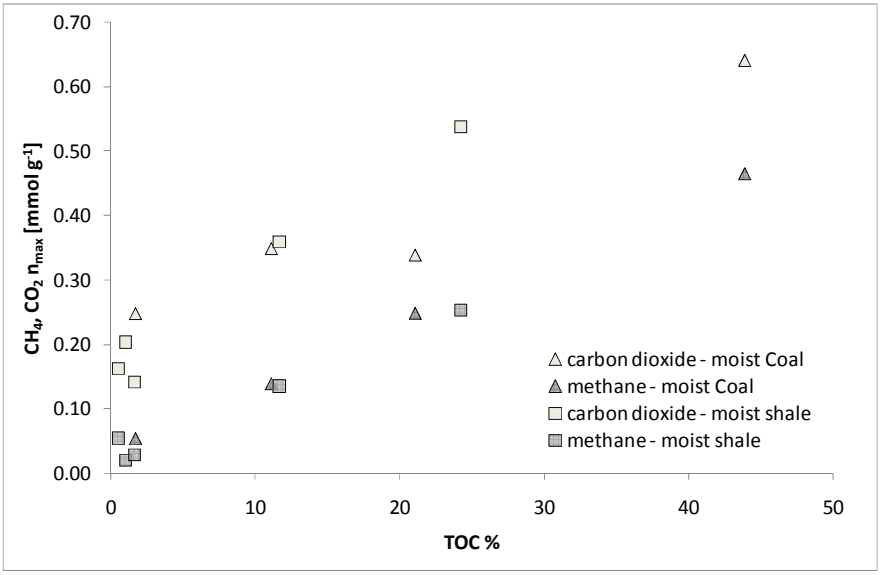


Figure 2-21: Sorption capacity of CH_4 and CO_2 as function of total organic carbon (TOC) (Weniger et al., 2010).

The sorption capacity of coal for CH_4 and CO_2 is negatively correlated with ash content (Bustin and Clarkson, 1998; Faiz et al., 2007; Laxminarayana and Crosdale, 1999a; Laxminarayana and Crosdale, 2002; Yee et al., 1993). From this observation we conclude that organic matter controls the CH_4 and CO_2 storage capacity. However the mineral content accommodates a small additional CO_2 sorption capacity

2.5.3 Coal Rank

Besides the effect of mineral matter or ash content on the sorption capacity, the rank of coals and related coalification processes has an important impact on the CO_2 and CH_4 sorption capacity. In some rank ranges the maceral composition seems to be dominant.

The study by Prinz, 2004 shows a parabolic shape for the CH_4 sorption capacity of dry coals as a function of rank for the Ruhr Basin, Germany. For moisture-equilibrated coals, the CH_4 sorption capacity shows a slightly linear increasing trend with rank.

Laxminarayana and Crosdale, 2002 investigate the CH_4 sorption capacity of Indian coals. Sorption isotherm analysis of dry samples showed that the sorption capacity follows a second-order polynomial trend with rank (0.62% up to 1.46% $R_{0\ max}$). Moisture-equilibrated samples showed a linear increase in sorption capacity with rank and a significantly reduced sorption capacity compared to dry coals. The observed

effective diffusivity ($D_e = \frac{D}{r^2}$) decreased with rank. This was attributed to an increase in micro-porosity during coalification. Bulk coals (i.e. a coal sample with seam specific mixture of dull and bright layers) tested showed 2–3 times larger effective diffusivities than bright coals, while dull coals have intermediate values.

Levy et al., 1997 suggest that the minimum in sorption capacity with rank may correspond to a coalification step, which occurs at around 87% fixed carbon. This step is characterised by a reduction in the oxygen and water content of the coal and an increase in methane release (Stach et al., 1982). More recent investigations Prinz and Littke, 2005; Prinz et al., 2001) have shown a minima in micropore volume of dry coals in the same rank range. This might be due to plugging of the micropore structure by liquid hydrocarbons in high-volatile bituminous coals, thus reducing its micropore volume At higher coal maturity these volatiles will undergo thermal cracking hence liberating surface area which results in an increased sorption capacity Rice, 1993.

Further, Saghafi et al., 2007 considered the effect of rank on CO_2 sorption capacity for the Sydney basin, but only up to pressures of 5 MPa.

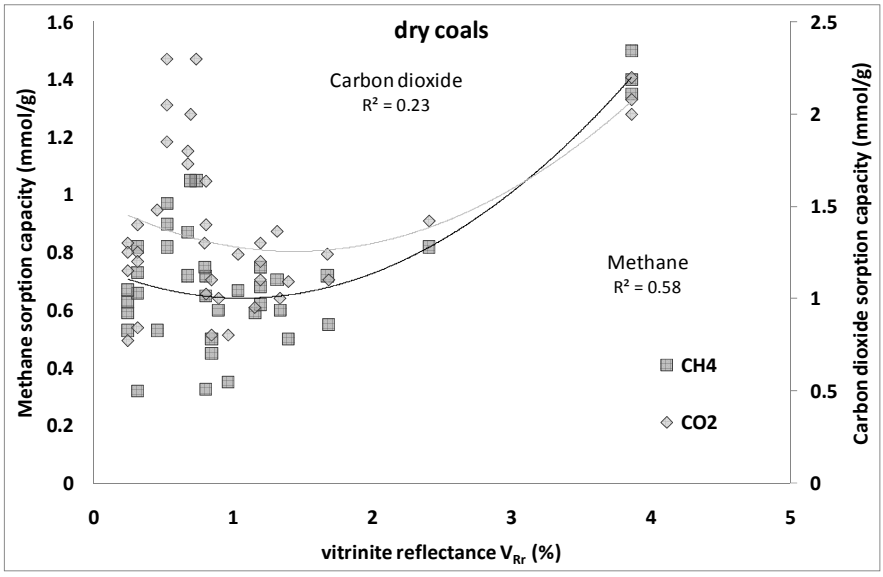


Figure 2-22: CH_4 and CO_2 sorption capacity of dry coals and the influence of rank. The two lines show the second-order polynomial fit for CH_4 and CO_2. The regression factor for methane is in an acceptable range, however for CO_2 it is not.

Because of the lack of sorption data of coals at higher coal rank, the reliability of Figure 2-22 and Figure 2-23 has to be proven. So far, the crossover of the trend lines in these figures has no significant meaning.

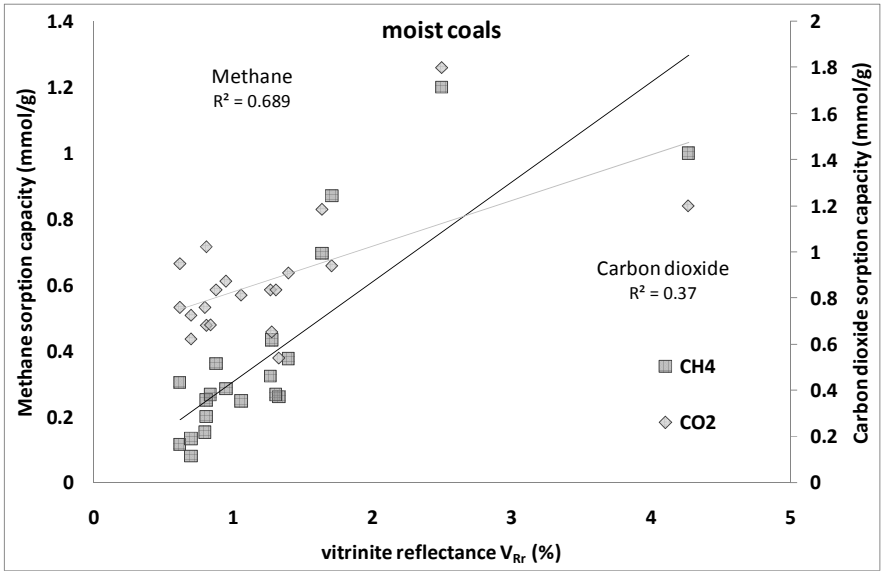


Figure 2-23: CH_4 and CO_2 sorption capacity on moisture-equilibrated and as received coals as a function of rank. The two lines show the linear fit for CH_4 and CO_2. The regression factor for CH_4 is in an acceptable range; however for CO_2 the trend is weaker and dominated by the data point at high vitrinite reflectance.

2.5.4 Dull/bright coals and maceral composition

Besides coalification the primary composition of the coal has a significant influence on the pore structure and therefore on the sorption capacity. Different coal lithotypes have different sorption capacities, because the source material is different. Bright coal is vitrinite-rich and has a lower inertinite content, while the contrary holds for dull coal. This difference in source material results in different porosity, pore structure and therefore, also in different sorption rates (Laxminarayana and Crosdale, 2002). The effect of coal composition, particularly the organic fraction, on gas sorption has been investigated for several worldwide coal basins (Table 2-2).

The gas sorption data from Gamson et al., 1996 suggests that both, dull and bright coals, can be divided into two categories: coals with rapid and coals with slow sorption behaviour. Further research on the effect of petrographic composition on CH_4 sorption capacity showed that bright coals have a higher sorption capacity than dull coals of the same rank (Crosdale and Beamish, 1993; Lamberson and Bustin, 1993; Bustin and Clarkson, 1998; Crosdale et al., 1998a; Clarkson and Bustin, 1999; Laxminarayana and Crosdale, 1999; Mastalerz et al., 2004). Other authors found no correlation between sorption capacity and maceral composition (Carroll and Pashin, 2003; Faiz et al., 2007; Laxminarayana and Crosdale, 2002).

Chalmers and Bustin, 2007 observed that for the CH_4 sorption capacity the maceral composition is more important in high rank coals. It is found that the CH_4 sorption capacity shows a moderate positive trend with microporosity and both increase with rank. Microporosity positively correlates with vitrinite content (in particular the telovitrinite (structured vitrinite) content). Furthermore, the same authors demonstrate that liptinite-rich samples show high CH_4 sorption capacities but low micropore volumes, which might be attributed to the gas being held in solution. Due to a generally low liptinite content in coal, the effect of

liptinite on CH_4 sorption capacity is superseded by the sorption capacity of more dominant macerals and therefore, the effect of liptinite has not been fully examined. For low-rank coals there is no significant difference between bright and dull samples except for one coal with the dull sample having a greater sorption capacity than its bright equivalent. For higher-rank coals, the bright samples have a higher CH_4 sorption capacity than the dull samples and the difference between sample pairs (bright and dull) increases with coal rank (Chalmers and Bustin, 2007).

Table 2-2: World-wide coal basins investigated for gas sorption capacity.

Basin	Country	Reference
Bowen and Sydney	Australia	Laxminarayana and Crosdale, 1999a; Laxminarayana and Crosdale, 1999b; Levy et al., 1997
Hunter Valley and Illawarra coal regions	Australia	Day et al., 2008a
Sydney	Australia	Saghafi et al., 2007
-	India	Laxminarayana and Crosdale, 2002
Raniganj, Jharia, South Karanpura coalfield	India	Dutta et al., 2011
Ruhr Basin	Germany	Prinz et al., 2001; Prinz et al., 2004
Campine Basin	Belgium	Hildenbrand et al., 2006
Upper Silesian Coal Basin		Busch et al., 2004a; Busch et al., 2006; Hemza et al., 2009; Kedzior, 2009; Weishauptová and Sýkorová, 2011
Paraná Basin	Brazil	Weniger et al., 2010
Argonne premium coals	USA	Busch et al., 2003a; Goodman et al., 2007b; Goodman et al., 2004; Kelemen and Kwiatek, 2009; Mastalerz et al., 2004; Ozdemir et al., 2004; Ozdemir and Schroeder, 2009

From investigations of gas sorption uptake of activated carbon, metal organic frameworks and zeolites, it is well known that the specific surface area is inherently linked to the pore size distribution of a sample whereby the specific surface area progressively increases with decreasing pore size for samples with similar porosity. Therefore, vitrinite with high microporosity can store more CH_4 than inertinite (Lamberson and Bustin, 1993; Beamish and Crosdale, 1995) because inertinite contains more macroporosity and less microporosity than their vitrinite equivalents (Unsworth, 1989). Similar studies with CO_2 are not available, it can however be speculated that they will follow a similar trend as with CH_4 because of the higher surface area in microporous vitrinite compared to more meso-/macroporous inertinite.

2.5.5 Temperature

Sorptive surface coverage ϑ at a specific gas pressure decreases with increasing temperature as derived from thermodynamics. At the same time the sorption capacity also decreases with increasing temperature for the pressure range that can be realised in laboratories (up to 50 MPa). This has been observed on sorption isotherms for dry coals (e.g. Lama, 1998; Levy et al., 1997; Sakurovs et al., 2008; Crosdale et al., 2008). However from thermodynamics the sorption capacity of a specific sample is similar for all temperatures at infinite gas pressures, assuming no change of the sample surface area over this temperature range.

The impact of varying temperature on equilibrium constants like the Langmuir pressure K is given by the van 't Hoff equation:

$$\left(\frac{\partial lnK}{\partial \frac{1}{T}}\right)_{\theta} = -\frac{\Delta H}{R} \qquad (2\text{-}17)$$

or

$$\left(\frac{\partial lnK}{\partial T}\right)_{\theta} = -\frac{\Delta H}{RT^2} \qquad (2\text{-}18)$$

The variation of the Langmuir pressure *K* must be isosteric at constant surface coverage ϑ. The enthalpy ΔH is negative, because sorption is an exothermic reaction. *R* is the universal gas constant.

The surface coverage at constant gas pressure decreases with increasing temperature, however the magnitude of this decrease varies for all gases and depends on the sample/gas specific enthalpy of sorption. The gas with the highest sorption enthalpy will have the lowest decrease in sorption capacity.

2.5.6 Isosteric heat of adsorption

Isosteric heats of adsorption can be determined experimentally by measuring sorption isotherms at several temperatures. Here, isosteres are constructed by plotting the pressure as a function of the reciprocal temperature at a constant surface coverage ϑ. From the Clausius–Clapeyron equation, the isosteric heat of adsorption Q_{st} is given by:

$$Q_{st} = -R\left(\frac{\partial lnp}{\partial\left(\frac{1}{T}\right)}\right)_{\theta} \qquad (2\text{-}19)$$

From a plot of *ln p* versus *1/T* the sorption isostere is received, the slope can be used to calculate Q_{st}. If the relative pressure p/p_0 is used instead of *p*, the net heat of sorption is obtained according to:

$$Q_{net} = Q_{st} - Q_{vaporisation} \qquad (2\text{-}20)$$

while $Q_{vaporisation}$ is heat of vaporisation which is a fixed value for each gas. p_0 is the saturation vapour pressure and *R* the universal gas constant.

The heat of adsorption for both CO_2 and CH_4 decreases slightly with increasing moisture content. A fundamental requirement of an equilibrium is that sorption sites are progressively filled (Figure 2-16 α, β and δ). The available higher energy sites for CO_2 and CH_4 on dry coal are already occupied when water is present, gas molecules will compete with water for the same sorption sites, namely the functional groups.

This interpretation or hypothesis is contrary to some previous studies that have indicated no specific adsorption sites for CO_2 (Amarasekera et al., 1995; Goodman et al., 2005). Other evidence supporting the view that CO_2 may be preferentially sorbed at carboxyl functional groups was reported by Nishino, 2001. These sites would be among the first to be occupied by water and would therefore lead to a reduction in the heat of adsorption for both CO_2 and CH_4. Another hypothesis for the observed reduction in heat of adsorption is related to the suggestion that it increases with decreasing pore size (Stoeckli, 1990). In this situation, progressively filling the smallest pores which are highest energy pores by water molecules would reduce the heat of adsorption of CO_2 and CH_4.

2.5.7 CO_2 versus CH_4 sorption

Several studies report CO_2 and CH_4 sorption on the same coal sample under different moisture conditions to obtain information on the selectivity of the coal for either gas species. For all these datasets (Bae and Bhatia, 2006; Battistutta et al., 2010; Busch et al., 2003a; Busch et al., 2004a; Bustin, 2004; Chaback, 1996; Day et al., 2008c; Harpalani et al., 2006; Kelemen and Kwiatek, 2009; Li et al., 2010; Mastalerz et al., 2004; Pini et al., 2010; Reeves et al., 2005; Sakurovs et al., 2007; Weniger et al., 2010; Yu et al., 2008b) higher CO_2 compared to CH_4 sorption was observed while the CO_2/CH_4 sorption ratio varies from 1.1 to 9.1 (Figure 2-24). Interestingly a relative decrease in sorption ratio with coal rank can be observed for moisturized coal samples, having a ratio of ~9 at low coal rank and decreases to 1.2-1.5 for anthracite rank coals. For dry coal such a relationship with coal rank was not observed. Data scatter between ~1 and 3 for different coals maturities.

For single gas measurements higher sorption of CO_2 compared to CH_4 was always observed for the same coal sample under the same pressure and temperature conditions. However a few mixed-gas sorption measurements reported preferential sorption of CH_4 compared to CO_2 specifically at low pressures (e.g. Busch et al., 2006; Busch et al., 2003c; Crosdale, 1999; Majewska et al., 2009). Other authors again report clear preferential sorption of CO_2 from binary gas mixture experiments (e.g. Fitzgerald et al., 2005; Ottiger et al., 2008; Pini et al., 2010). The reason for the different observations is not explained in the literature and further work on gas mixture sorption on coal is recommended.

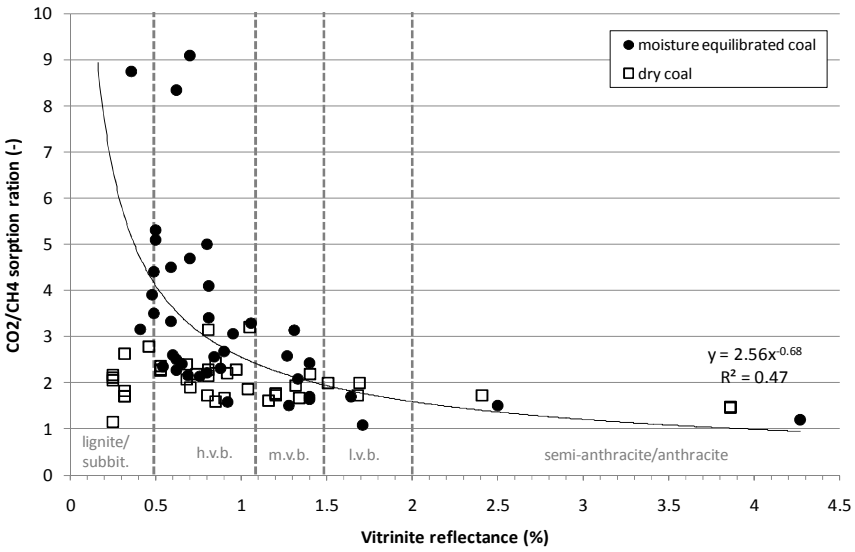


Figure 2-24: CO_2/CH_4 sorption ratio for different moist and dry coal sample at various temperatures as a function of coal rank. Values were picked between 1 and 5 MPa. Data fit for moist samples only (Bae and Bhatia, 2006; Battistutta et al., 2010; Busch et al., 2003a; Bustin, 2004; Chaback, 1996; Day et al., 2008c; Fitzgerald et al., 2005; Harpalani et al., 2006; Kelemen and Kwiatek, 2009; Li et al., 2010; Mastalerz et al., 2004; Pini et al., 2010; Reeves et al., 2005; Ryan and Richardson, 2002; Sakurovs et al., 2007; Weniger et al., 2010; Yu et al., 2008b)

2.6 CO_2 and CH_4 sorption kinetics on coal

Numerical modeling of the processes related to CBM and CO_2-ECBM requires information on the kinetics of the sorption and desorption processes. In principle diffusion determines the rate of CH_4 desorption for primary recovery and the rate of CO_2 sorption for CO_2 storage in coal. For CO_2-ECBM both processes are of importance and the counter-diffusion of CH_4 diffusing out of the coal matrix and CO_2 diffusing into the coal matrix is determined by their respective sorption rates.

In order to better understand sorption rates in coal the pore size distribution should be explained in more detail. Coal is a highly heterogeneous material that develops with burial in sedimentary basins while coal maturity increases with temperature. In coal, four different pore systems are commonly distinguished: cleat-porosity, macro-, meso- and micro-porosity. In each of these porosities different transport processes take place that need to be understood individually. Commonly, gas transport in coal is considered to occur at two different scales: (I) laminar flow through the cleat system, and (II) diffusion through the coal matrix. Flow through the cleat system is pressure-driven and may be described using Darcy's law, whereas flow through the matrix is assumed to be concentration-driven and is modeled using Fick's law of diffusion. Gas storage by physical adsorption occurs mainly in the coal matrix (Harpalani and Chen, 1997; Busch et al., 2004a).

In general, within the coal porous system three distinct diffusion mechanisms can be distinguished: (1) Diffusion described by Fick's law where inter-molecular collisions between gas molecules (Brownian

motion) is the dominant mechanism. This process is significant for large pore sizes and/or high gas pressures; (2) Knudsen diffusion (concentration-driven) by collisions between the gas molecules and pore walls. It is important when the mean free path of the gas molecules is larger than the pore size. This process can be significant for small pore sizes and low gas pressures; (3) surface diffusion where sorbed molecular species move along the pore wall surface. This process is important in micropores with strongly sorbed gas species.

van Krevelen, 1993 defines the matrix pore system as follows:

- Macropores: The pore size is larger than the mean free path of the molecules.
- Mesopores: The pore size is smaller than the mean free path of the molecules.
- Micropores (< 2 nm): Activated diffusion

It should be noted here that the mean free path length depends on temperature and pressure, so this classification cannot be applied to specific pore radii.

This classification is further specified and classified by the International Union of Pure and Applied Chemistry (IUPAC, 2001):

- Macropores: pores with widths exceeding about 0.05 μm (50 nm)
- Micropores: pores with widths not exceeding about 2.0 nm (20 A)
- Mesopores: pores of intermediate size (2.0 nm < width < 50 nm)

In addition some authors proposed ultramicropores, defined as the interlayer spacing of the crystalline carbon structures (d_{002}-spacing) which is <0.4 nm and decreases with rank (Hirsch, 1954; Prinz and Littke, 2005).

Using low pressure sorption techniques applying the BET method (Brunauer et al., 1938), Prinz and Littke, 2005; Prinz et al., 2004 determined surface areas for meso/macropores (using N_2) and for micro/ultramicropores (using CO_2) on a suite of Carboniferous coals from the Ruhr Basin, Germany. This suite ranges in coal rank from high volatile bituminous (h.v.b.) to semi-antracite coals (Figure 2-25). In addition the same authors (Prinz et al., 2004) compared low-pressure N_2 sorption with small angle neutron scattering (SANS) data and found similar results for the specific mesopore surface area of different rank coals from the Ruhr Basin, Germany (Figure 2-25). Further data indicates that significant amounts of closed porosity are only present in low-rank coals of the sample set studied. Further, they found that the microporosity increases with coal rank while at the same time meso/macroporosity decreases. This indicates that coal is dominated by a bimodal pore size distribution up to medium volatile bituminous (m.v.b.) and above this rank coals can rather be classified by a unimodal distribution (Figure 2-26).

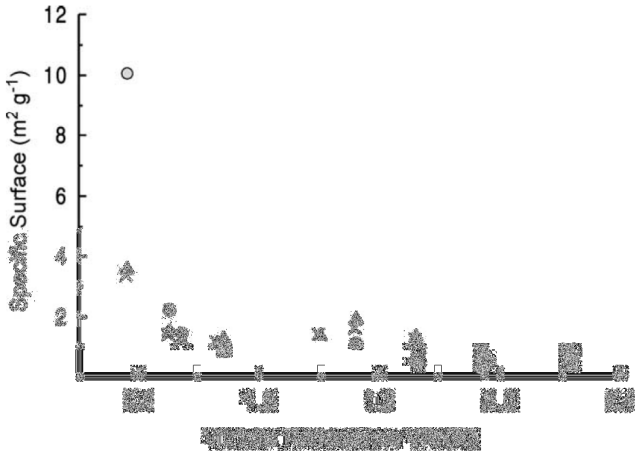


Figure 2-25: Specific surface areas of meso and macropores as obtained from small angle neutron scattering (SANS, circles) and low-pressure N_2 adsorption experiments (triangles and crosses refer to different evaluation methods) (after Prinz et al., 2004).

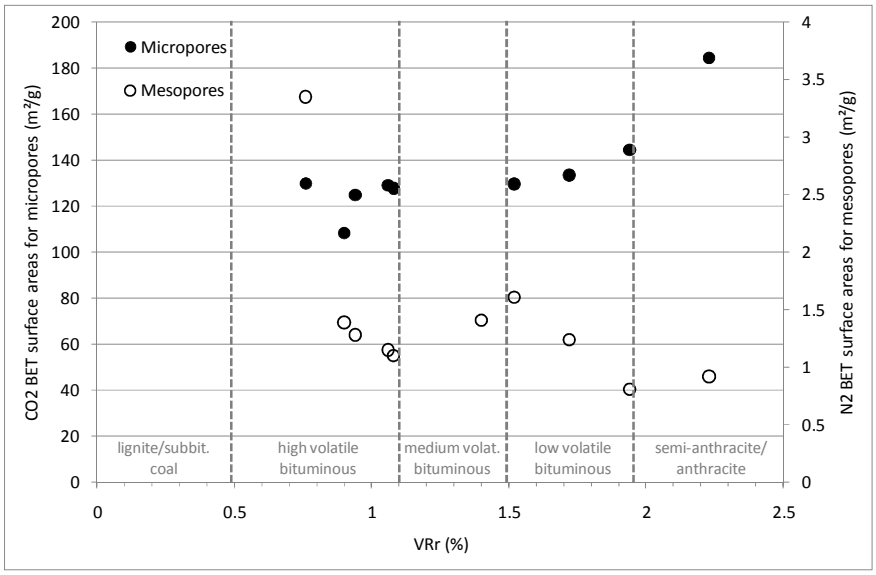


Figure 2-26: Specific surface areas for meso/macropores and micro/ultramicropores determined on a suite of Carboniferous coals from the German Ruhr Basin (Prinz and Littke, 2005; Prinz et al., 2004).

These porosity trends with coal rank should have implications on the sorption rate. It is indicated that a unipore approach is rather suitable for high rank coals while a bidisperse approach is better suited for lower rank coals.

When evaluating the rates of gas sorption by manometric or gravimetric methods it should be kept in mind that the recorded pressure or weight changes only provide a net transfer rate within the closed system from the gas phase to the sorbed phase (gas uptake).

2.6.1 Unipore sorption/diffusion models

The unipore model is based upon the solution to Fick's second law for spherical symmetric flow (Clarkson and Bustin, 1999b):

$$\frac{D}{r^2}\frac{\partial}{\partial r}\left(r^2\frac{\partial C}{\partial r}\right)=\frac{\partial C}{\partial t} \quad (2\text{-}21)$$

with the initial condition:

$$C=0\ at\ t=0 \quad (2\text{-}22)$$

where *r* is the sphere radius (particle radius) and *C* the sorbate concentration within the sphere, *D* the diffusion coefficient and *t* is time. The model assumes isothermal conditions, a homogeneous pore structure and a non-dependence of the diffusion coefficient on concentration and location in the coal particle.

There are several solutions to Fick's Law used in the literature for gas diffusion in coal: For representing gas desorption from coal or gas sorption on coal, Clarkson and Bustin, 1999b and Pan et al., 2010 consider a sphere of radius *r* which is initially at a uniform concentration C_1 while the surface concentration is maintained constant at C_o. Then the total amount of substance entering or leaving the sphere is given by (Crank, 1975):

$$\frac{M_t}{M_\infty}=1-\frac{6}{\pi^2}\sum_{n=1}^{\infty}\frac{1}{n^2}exp\left(-\frac{Dn^2\pi^2t}{r^2}\right) \quad (2\text{-}23)$$

where M_t is the total amount of the diffusing species at time *t* and M_∞ is the total desorbed mass.

It should be noted that the model assumes spherical, homogeneous coal particles of identical radius with smooth surfaces. Although this model is often referred to as "unipore model", a pore system within the spherical particles and surface sorption on the pore walls is not explicitly assumed.

Busch et al., 2004a (and applied in a similar form by Pone et al., 2009) used a diffusion model that assumes a sphere with radius *r*, placed in a fixed volume where the free volume (i.e. not occupied by the particles) is *V*. The concentration of sorptive gas in the free volume is always uniform and is initially C_0. The initial concentration of sorbate within the spheres is zero. The total amount M_t of gas sorbed after time *t* is expressed as a fraction of the corresponding quantity M_∞ after infinite time by the relationship (Crank, 1975):

$$\frac{M_t}{M_\infty}=1-\sum_{n=1}^{\infty}\frac{6\alpha(\alpha+1)}{9+9\alpha+q_n^2\alpha^2}exp\left(-\frac{Dq_n^2t}{r^2}\right) \quad (2\text{-}24)$$

here q_n are the non-zero roots of:

$$tan\ q_n=\frac{3q_n}{3+\alpha q_n^2} \quad (2\text{-}25)$$

and

$$\alpha=\frac{V}{\frac{4}{3}\pi r^3}=\frac{V}{V_{coal}} \quad (2\text{-}26)$$

For small times *t* a simplified model was used by Charrière et al., 2010, based on Carslaw and Jaeger, 1959:

$$\frac{M_t}{M_\infty} = \frac{6}{\sqrt{\pi}}\left(\frac{D}{r^2}t\right)^{1/2} \qquad (2\text{-}27)$$

Here a plot of M_t/M_∞ versus $t^{1/2}$ will have a slope of $6(D/\pi)^{1/2}$. This approach is used by Smith and Williams, 1984b, c to obtain diffusion coefficients for CH_4 desorption from coal seams. However it has limitations for CO_2 rather than for CH_4 as already noted by Charrière et al., 2010: When CO_2 is expanding during a gravimetric or manometric sorption experiment into the measuring cell where the sample is placed (s. above) it will cool due to the Joule-Thompson effect. Especially at small times this cooling may have a large effect on the gas uptake curve, mass balance calculation or buoyancy correction (for gravimetric methods) and might therefore have a significant influence on the calculation of the diffusion coefficient. This effect is lower for CH_4.

2.6.2 Bidisperse sorption/diffusion models

Bidisperse sorption/diffusion models can be used for coals that are characterized by two distinct pore systems (s. above). Ruckenstein et al., 1971 define these as an agglomeration of many microporous spheres that are contained in macropores (Figure 2-27). They developed a model which assumes a linear isotherm in both macro -and microspheres and a step change in the boundary concentration at the start of a sorption step. Model equations are provided in the original publication. A more detailed description of the bidisperse porous coal system was developed by Bhatia, 1987.

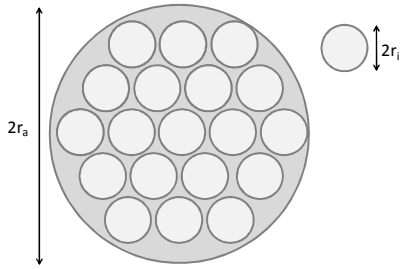


Figure 2-27: Bidisperse pore model as defined by Ruckenstein et al., 1971.

The Ruckenstein model was later extended to model gas flow and transport in fixed beds by Smith and Williams, 1984a to investigate methane desorption rates in coalbeds, and later by Shi and Durucan, 2003a; Shi and Durucan, 2003b to study the mechanisms of CO_2-ECBM.

Clarkson and Bustin, 1999b state that the Ruckenstein model cannot be applied for high-pressure sorption experiments. The reasoning is that the model assumes a step change in external (to sorbent particles) concentration of the diffusing gas at time zero, and that this concentration remains unchanged with time. This assumption is not true for constant volume, variable pressure sorption rate experiments. In addition CO_2 and CH_4 sorption isotherms are typically non-linear for natural coal which further limits the applicability of the Ruckenstein model.

Further bidisperse gas uptake models were used by various authors (Busch et al., 2004a; Clarkson and Bustin, 1999b; Siemons et al., 2007; Yi et al., 2008). The basic principle of all these approaches is similar although the complexity varies largely. Busch et al., 2004a use a linear combination of two first-order reactions and provide, in contrast to the unipore model, a perfect fit of the experimental pressure decay curves for gas uptake for a low-mature coal. They do not speculate on the properties of the two different pore systems for the combined sorption/diffusion but rather classify the transport as "fast" and "slow". For volumetric gas sorption experiments the model proposed by Clarkson and Bustin, 1999b accounts for nonlinear sorption in the micropores, as opposed to the Ruckenstein model (Ruckenstein et al., 1971), and a time-varying gas pressure in the free gas volume in contact with the coal particles. Cui et al., 2004 used a bidisperse model based on previous work by Ruckenstein et al., 1971 and Clarkson and Bustin, 1999b.

2.6.3 Results from CO_2 and CH_4 gas sorption kinetic experiments

Sorption kinetic data are obtained by monitoring the rate of pressure equilibration during individual pressure steps of volumetric sorption tests or the rate of apparent weight changes during gravimetric sorption experiments. These measurements can be readily combined with the determination of sorption isotherms for the assessment of the gas sorption capacity (e.g. Clarkson and Bustin, 1999b).

A summary of the various findings from sorption kinetic measurements are provided in Table 2-3.

Ciembroniewicz and Marecka, 1993 performed CO_2 sorption kinetic experiments on two Polish hard coals at temperatures below 35°C and pressures up to 0.065 MPa. Although the two coals were of similar rank, they exhibited different sorption kinetics. The sorption rate for one coal was significantly faster than for the other one while no significant difference in the rates was observed between sorption and desorption.

Marecka and Mianowski, 1998 studied CO_2 and CH_4 sorption rates on semi-anthracite coal using different grain size fractions. They found decreasing sorption rates with increasing particle size (i.e. lower specific surface area), slightly increasing rates for increasing temperatures and higher rates for CO_2 compared to CH_4 (factor ~10-20). This latter observation is reported by almost all authors under all temperature or pressure conditions and for almost all coal samples and is typically attributed to the smaller kinetic diameter of CO_2 compared to CH_4 and the ability of CO_2 to dissolve in the coal polymer structure (e.g. Charrière et al., 2010).

Clarkson and Bustin, 1999a, b performed CH_4 (dry and moist) and CO_2 (dry) sorption kinetic measurements on different bituminous coals from the Gates formation in Canada. They found that diffusivities are generally higher for CO_2 than for CH_4 (for dry coals). The CH_4 diffusivities on dry coals were faster than on the corresponding moist coals. Authors used a unipore and a bidisperse sorption kinetic model and found that for bright coals (vitrinite rich) with a uniform pore size distribution the unipore model was sufficient. The bidisperse model was found to better represent the observed gas uptake rates of dull or banded coals

(inertinite rich) with a more complicated pore structure. Further, authors found that the applicability of either the unipore or the bidisperse model depends on gas pressure.

Busch et al., 2004a performed CO_2 and CH_4 sorption kinetic experiments on h.v.b. coal from the Upper Silesian Basin, Poland at 32 and 45°C. They reported faster sorption rates for CO_2 than for CH_4 and decreasing sorption rates with increasing grain size (<0.063 mm to 3 mm) while rates did not change significantly at grain sizes >100 µm. This indicates transport limiting grain sizes at a scale of ~100 µm, i.e. above this size small transport pathways in the form of cleats or cracks can trigger fast gas distribtution around the matrix blocks. Further, increasing rates for increasing temperatures and decreasing rates with increasing moisture contents have been reported. These findings are in agreement with a more recent study by Gruszkiewicz et al., 2009. Here similar sorption rates for the 5-10 mm compared to the 1-2 mm grain size fraction have been reported for either gas on h.v.b. coal from the Black Warrior Basin, USA. As in the study by Busch et al., 2004a rates increased with temperature and decreased with moisture.

In another similar study, Li et al., 2010 found for three dry Chinese coals, ranging in rank from subbituminous to anthracite, faster sorption rates for CO_2 compared to CH_4 for measurements on most samples. No distinct differences in rates were observed for the three temperatures chosen (35, 45, 55°C). Rank was concluded to have a larger effect on sorption rates. Authors noted that for both gases, CO_2 and CH_4, rank has a more profound influence on sorption rates than temperature although no clear correlation was found as a function of coal rank (i.e. Li et al., 2010; Seewald and Klein, 1986).

For a moisture-equilibrated h.v.b. coal, Cui et al., 2004 found decreasing sorption rates in the order $CO_2>CH_4>N_2$ at 30°C while the difference between CH_4 and N_2 is small. Authors relate these changes to the differences in kinetic diameter of the gas species ($CO_2<N_2\approx CH_4$; 3.3Å<3.64Å<3.8Å, e.g. Shieh and Chunh, 1999). The determination method of these kinetic diameters however, could not be found in the literature and therefore these values should be used with care.

Pone et al., 2009 studied sorption rates under confined and unconfined conditions using powdered and solid coal for the unconfined measurements and different confining stresses (6.9 and 13.8 MPa) for confined experiments on coal plugs. For both gases, CO_2 and CH_4 they found reduced diffusivities (factor 1.5) when increasing the sample size in the unconfined experiments and an even higher reduction in diffusivity when applying stress on the sample. The latter reduction was found to be proportional to the applied stress.

2.6.4 Summary of sorption kinetic experiments with CO_2 and CH_4

- Unipore and bidisperse gas transport models have been used to interpret and quantify observed gas uptake rates. Some are rather simple and some others more sophisticated. Although not generally confirmed, unipore models seem to better represent the sorption kinetics of high rank

coals (m.v.b. to anthracite) while bidisperse models better apply to low mature coals. This is in line with the observation that micropores increase and mesopores decrease with coal rank.

- Diffusion coefficients for CO_2 range from 10^{-11} to^{-16} m^2 s^{-1} and for CH_4 from 10^{-12} to 10^{-15} m^2 s^{-1} (Table 2-3).
- Gas sorption rates in dry coals are faster than in moist coals under all experimental conditions.
- Gas sorption rates increase with increasing temperature but seem to decrease with increasing surface coverage.
- In general, CO_2 sorption rates are faster than for CH_4 on the same sample. One exception was found for a subbituminous coal (Li et al., 2010).
- CO_2 and CH_4 sorption rates decrease with increasing grain size up to a certain limit. Above this limit, transport through micro-cleats in the coal matrix seem to become dominant.
- Sorption rates under confining stress conditions are slower than under unconfined conditions. Although this was only reported by one author (Pone et al., 2009) it seems to be valid since it is a common finding for all kind of natural rocks that gas transport decreases with increasing effective stress. Experience from coal mining supports these observations: massive degassing of deep, stressed coal seams occurs only when the stress field is strongly disturbed due to mining operations.

Table 2-3. Sorption kinetic experiments performed by various authors (Busch et al., 2004a; Charrière et al., 2010; Ciembroniewicz and Marecka, 1993; Clarkson and Bustin, 1999a, b; Cui et al., 2004; Gruszkiewicz et al., 2009; Kelemen and Kwiatek, 2009; Li et al., 2010; Marecka and Mianowski, 1998; Pan et al., 2010; Pone et al., 2009; Seewald and Klein, 1986; Siemons et al., 2007). h.v.b, m.v.b. and l.v.b are high, medium and low volatile bituminous coals. Diffusion coefficients derived from unipore or bidisperse models in chapters 2.6.1 and 2.6.2.

Author	Gas	Coal Basin	Coal rank	Method	Grain size (mm)	dry/moist	T (°C)	P (MPa)	Model	D (m^2/s)	
										CO_2	CH_4
Gruszkiewicz	CO_2, CH_4, CO_2/CH_4	Black Warrior Basin, USA	h.v.b.	manom.	0.045-0.15; 1-2; 5-10	dry, moist	35, 40	1.4-6.9	graphical (P vs t)	n.a.	n.a.
Busch	CO_2, CH_4	Upper Sil. Basin, Poland	h.v.b.	manom.	<0.063; 0.063-0.177; 0.177-0.354; 0.354-0.707; 0.707-2; ~3	dry, moist	32, 45	CO_2 <6; CH_4<10	unipore, dual matrix porosity	10^{-11}	n.a.
Charriere	CO_2, CH_4	Loraine Basin, France	l.v.b.	gravim.	0.5-1	dry	10-60	<5	unipore	10^{-12} - 10^{-13}	10^{-13}
Li	CO_2, CH_4	Inner Mongolia, Henan, Shanxi, China	subbituminous, m.v.b., anthracite	manom.	0.354-1	dry	35, 45, 55	<5	graphical (P vs t)	n.a.	n.a.
Pone	CO_2, CH_4	Western Kentucky Coalfield, USA	h.v.b.	manom.	<0.25; cylindrical: d 2.5, l 6.2	moist	20	3.1	unipore	n.a.	n.a.
Pan	CO_2, CH_4	Sydney Basin, Aus	m.v.b.	flow exp.	cylindrical: d 25.4; l 82.6	dry, moist	26	<4	unipore	n.a.	
Marecka	CO_2, CH_4	n.a.	semi-anthr.	volum.	<0.032; 0.30–0.10; 0.75–0.49; 1.50–1.00	n.a.	20, 30	n.a.	unipore	n.a.	10^{-12} – 10^{-13}
Ciembroniewicz	CO_2	Polish	anthracite	manom.	0.49-0.75	n.a.	16-35	<0.065	unipore	10^{-12} – 10^{-13}	n.a.
Siemons	CO_2	Great Britain	h.v.b.; semi-anthracite	manom.	0.04-0.06; 0.06-0.18; 0.35-0.71; 0.71-2.0	dry, moist	45	<12	bidisperse	10^{-8} – 10^{-12}	n.a.
Clarkson	CO_2, CH_4	Lower Cret. Gates Fm, Canada	m.v.b.	volum.	<0.25; <4.76	CH_4 dry, moist; CO_2 dry	30	<2	unipore, bidisperse	10^{-11} – 10^{-13}	10^{-12} – 10^{-15}
Cui	CO_2, CH_4, N_2	-	h.v.b.	manom.	<0.25	moist	30	<7	bidisperse	10^{-11} – 10^{-14}	10^{-14} – 10^{-15}
Seewald	CH_4	Ruhr Basin, Germany	h.v.b.; m.v.b.; anthracite	volum.	0.04 to 1 in 9 fractions	dry, moist	0, 15, 50	<0.1	unipore	n.a.	10^{-12} – 10^{-14}
Kelemen	CO_2, CH_4	Argonne Coals, US	h.v.b., l.v.b.	gravim.	~7mm^3	dry	30, 75	1.8	unipore	10^{-13} – 10^{-16}	10^{-14} – 10^{-15}

2.7 Conclusions

This review summarizes the present state of knowledge on the interaction of CO_2, CH_4 and water with the coal matrix in the context of coalbed methane (CBM) and CO_2-ECBM recovery. We aimed at summarizing the various qualitative and quantitative findings related to CO_2, CH_4 and water sorption on coal as well as related sorption kinetic data. Further we provided insights into experimental details of recording sorption isotherms and uncertainties related therewith.

In the following, various aspects that still need to be researched for a better understanding of gas production from coal or gas storage into coal have been defined:

- Gas sorption under reservoir stress conditions. Usually, in conventional sorption experiments no external stress is applied to the coal sample which only represents subsurface conditions in terms of temperature and gas pressure. Experimental effective stress acting on the coal sample changes sorption properties both in terms of sorption amount and in terms of time to reach equilibrium between the sorbate and the sorbent.
- Gas sorption from binary mixtures. Most literature sources report single gas CO_2 and CH_4 on one coal sample while the amount of either gas sorbed at a certain pressure is calculated using the extended Langmuir approach. Indications from few authors exist that gas mixture isotherms may provide different results.
- Matrix CO_2/CH_4 counter diffusion. The timing of gas exchange in the coal matrix for CO_2-ECBM is determined by CO_2 sorption rates and CH_4 desorption rates. These processes happen simultaneously and very limited data is available for recognizing the significance of counter diffusion for CO_2-ECBM.
- Calculation of absolute from excess sorption isotherms. This calculation depends on the sorbed gas density which cannot be determined directly. Therefore literature values like the density at the liquid boiling point, the van der Waals density or a graphical method is used. Although absolute CH_4 sorption does not differ significantly from excess sorption there are large discrepancies when applying this method to CO_2 sorption isotherms using different CO_2 sorbed phase density values especially at elevated pressures (above e.g. 10 MPa).

3 Gas saturation and CO_2 enhancement potential of coalbed methane reservoirs as a function of depth

3.1 Introduction

World gas consumption has steadily increased over the past decades leading to a depletion of conventional gas reserves. The end of nuclear power generation in Germany in 2022 will bring about an increase in gas consumption especially if CO_2 reduction will be part of the European energy strategy. Due to the fact that natural gas has the smallest carbon footprint of the conventional energy sources (like oil, coal, etc.), its importance will increase. In the future gas supply can only be maintained if additional gas resources are utilized. In this context, gas production from unconventional reservoirs has substantially increased in recent years, especially in the USA and Australia. In Europe exploration of these unconventional reservoirs, including tight gas, coalbed methane and gas-shales, has greatly expanded over the last decade Littke et al., 2011a.

Often during exploration campaign coal seam dips have to be considered. The change in saturation due to new p,T conditions can be estimated by using the sorption enthalpy and entropy of the adsorption process. This paper will provide some fundamental considerations and observation which will show how saturation and recovery potential will change with depth.

Hydrocarbons in coal seam gas are derived from either thermal breakdown of kerogen or microbial generation processes (fermentation and/or CO_2 reduction). The gas in place (GIP) content of coal seams is a crucial parameter determining the economics of a gas resource. According to the Gas Research Institute (GRI, 1995#933) CBM gas-in-place estimations take into account: (1) a sorbed phase in which gas molecules have a net attraction to the coal matrix and have a density that approaches that of a liquid n_{sorbed} [mmol g^{-1}]), (2) free gas within the pores and natural fractures ($n_{porosity}$ [mmol g^{-1}]) and (3) gas dissolved in formation water in the coalbed ($n_{formation\ water}$), which is considered negligible for methane:

$$\boldsymbol{GIP} = V_{seam}\ \rho_{bulk\ coal}\left(\boldsymbol{n_{sorbed}} + \boldsymbol{n_{porosity}} + \boldsymbol{n_{formation\ water}}\right) \qquad (3\text{-}1)$$

Another important parameter is the present-day gas saturation, defined as the ratio of the gas content of the coal seam (per unit mass or volume) and the maximum sorption capacity. Gas saturation indicates how much gas can be produced and how big the recovery factor will be.

$$\boldsymbol{S} = \frac{\boldsymbol{n_{total}}}{\boldsymbol{n_{absolute}}} \equiv \frac{\boldsymbol{n_{desorbable}^{predicted}} + \boldsymbol{n_{porosity}} + \boldsymbol{n_{formation\ water}}}{\boldsymbol{n_{total\ uptake}}} \qquad (3\text{-}2)$$

However, the methane saturation is often an error-prone value and difficult to determine since it cannot be derived directly from well logs Diamond and Schatzel, 1998b; Mares et al., 2009; Mavor, 1995. Gas content

is usually determined by canister desorption, while the sorption capacity as a function of pressure and temperature is determined by high-pressure sorption experiments.

The amount of compressed gas $n_{porosity}$ [mmol g^{-1}], which is stored in the open porosity of coal is usually determined during drilling and mainly depends on water saturation. However the laboratory estimation of porosity (using low pressure mercury injection in combination with helium pycnometry) is usually done without external confining stress; porosity values determined by mercury injection on coals tend to be unreliable; therefore, due to pore elasticity, cleat volume compressibility and different penetration properties, porosity values are generally overestimated for coals.

Recent studies indicate, however, that rather than the composition and rank of the organic matter, water content has a dominant or even overriding effect on the gas storage capacity of coals Busch and Gensterblum, 2011. To account for this effect and arrive at more realistic values for sorption capacities, sorption measurements are increasingly performed on moisture-equilibrated samples (Clarkson and Bustin, 2000; Crosdale et al., 2008; Day et al., 2008c; Goodman et al., 2007a) and a summary is provided by Busch and Gensterblum (2011). The dramatic influence of water content on methane storage capacity of coals is illustrated in Gensterblum 2012 (submitted). The methane sorption capacity of moisture-equilibrated coals is only in the order of 40-60% of the sorption capacity of the dry samples Busch and Gensterblum, 2011. Usually the sorption capacity of the "as received" coals varies between these two values.

Figure 3-1 illustrates the theoretical gas content in the accessible porosity (free of water) as a function of depth using the Setzman and Wagner EOS for CH_4. The assumed coal matrix density is 1.4 g cm^{-3}. A thermal gradient of 0.03 K/m and a hydrostatic gradient of 0.01 MPa/m have been assumed. The content of dissolved gas in the formation water ($n_{formation\ water}$, mmol g^{-1}) is very low (Duan et al. 1992; however, for CO_2 it is not Duan and Sun, 2003) and is a function of brine salinity, pressure and temperature. The solubility of CH_4 decreases with increasing salinity of the formation water O'Sullivan and Smith, 1969.

In order to determine the desorbable gas content needed for the GIP determination, the lost gas ($n_{lost\ gas}$, mmol g^{-1}) is the gas desorbed while bringing the core sample to the surface during drilling and sealing it into desorption canisters (lost gas time) Smith and Williams, 1984c. Therefore $n_{lost\ gas}$ is an empirically assumed value. It is commonly determined by backward extrapolating the measured desorbed gas data points collected at reservoir temperature over the lost gas time interval to time zero Metcalfe et al., 1991. Determining the lost gas volume requires a very accurate determination of the desorbed gas ($n_{desorbed}$). The desorbed gas is commonly measured by determining the amount of desorbed gas $n_{desorbed}$ during a canister desorption test. The residual gas content $n_{residual}$ [mmol g^{-1}] remains in the coal sample at the conclusion of canister desorption measurements. It is commonly measured by pulverising the sample and measuring the released gas content. This results in the total desorbable gas [mmol g^{-1}]:

$$n_{desorbable}^{predicted} = n_{lost\ gas} + n_{desorbed} + n_{residual} \qquad (3\text{-}3)$$

It is important to be aware that not all of the desorbed or residual gas has to be methane. Additional gas composition analysis is required. The residual gas content is also crucial for the gas recovery estimation, because due to the strong "trapping" the residual gas content is an indicator for the amount of unproducible gas content. There are several methods to determine the sorbed gas content Diamond and Schatzel, 1998b. By substituting equation 3 into 2 we obtain the predicted in-situ gas saturation.

$$S^{predicted} = \frac{n_{lost\ gas}+n_{desorbed}+n_{residual}+n_{porosity}+n_{formation\ water}}{n_{absolute}} \qquad (3\text{-}4)$$

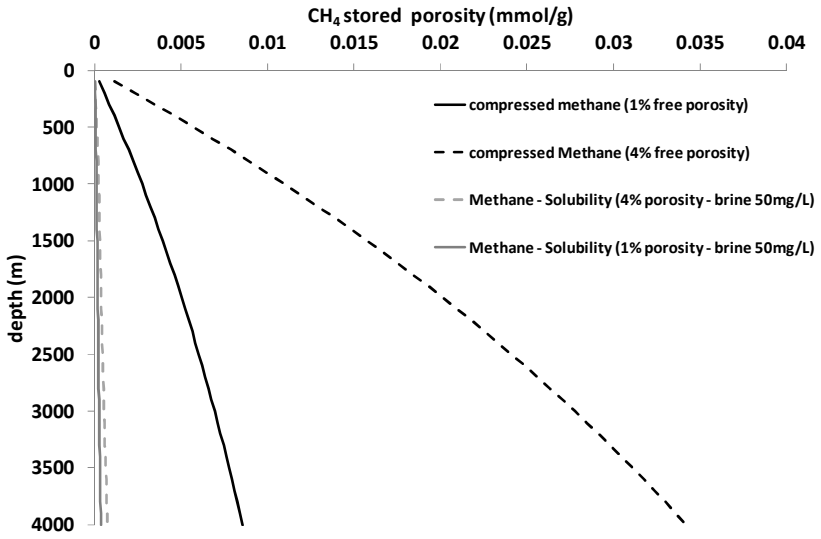


Figure 3-1: Calculated CH_4 storage capacity in the gas-saturated porosity of the coal seam (assumed coal density 1.4 g/cm³) using the EOS for methane Setzmann and Wagner, 1991. Additionally we calculate the dissolved CH_4 content in the formation water (brine) (in grey). A thermal gradient of 0.03K/m and hydrostatic pressure gradient of 0.01MPa/m was used for the calculations (1 mmol/g = 24.5 Std. m³/t). We did not take into account the compaction of the coal or sediment during burial. Therefore we keep the porosity constant with depth.

Sorbed gas is the main storage mechanism for coalbed methane because of the low solubility of CH_4 in water and the generally low porosity of coal seams (Figure 3-1). It has been documented by numerous studies that the sorption properties of coals vary systematically with rank and maceral composition (e.g. Busch and Gensterblum 2011). Due to the observation that the sorption capacity also strongly depends on the moisture content Crosdale et al., 2008; Day et al., 2008c, which ranges between "as received" and (moisture) saturated, determining the sorption capacity on such coals becomes more complicated Goodman et al., 2007a (Figure 3-2).

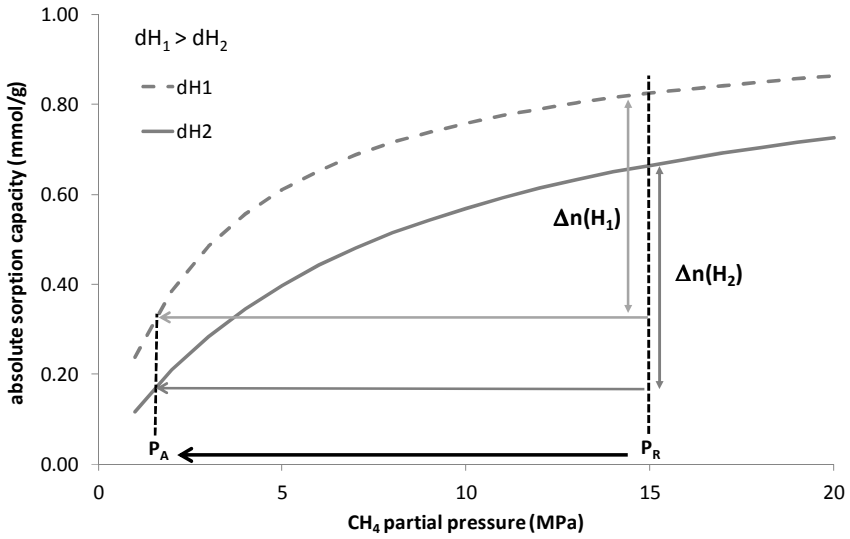


Figure 3-2. Schematic illustration of the CH_4 sorption isotherm, the amount of producible gas and the influence of the CH_4 sorption enthalpy. Different sorption enthalpy could occur for CH_4 sorption on a dry, 'as received or moisture-equilibrated coal sample. The highlighted pressure levels are P_R for initial reservoir pressure prior to production and P_A for abandonment pressure, which is the reservoir pressure at the end of production.

An oversaturated coal seam would be highly beneficial; albeit, they are rather rare (Figure 3-3). Oversaturated coal seams occur when the amount of generated gas is higher than the loss of gas due to a change in the sorption capacity as a result of basin uplift, migration, and diffusion. Therefore, the coal seam has to be low-permeable with low diffusion coefficients for the coal matrix to maintain high CH_4 concentrations over geological time scales and/or should be covered by an efficient caprock. In general the geological reasons for oversaturated seams could be a special geological reservoir situation in combination with very low permeable cap rocks and/or high microbial gas generation, according to the observation by Krooss et al., 1988b and Clayton, 1998 Faiz, 2004. An alternative and more likely experimental reason could be an apparent oversaturation. The adjusted moisture content of the sorption isotherm determined in the laboratory is higher than that within the coal seam Diamond and Schatzel, 1998a; Mares et al., 2009; Zhao et al., , hence lower sorption capacities compared to the in-situ capacities are determined.

The reasons for undersaturated coal seams are simply that less gas from neighbouring or the same coal seam was generated than the coal could adsorb or that a certain amount is lost because of burial and uplift or dissolution of CH_4 in formation brine. Scott, 2002 explains this as an interplay of coalification, gas generation, the hydrogeological situation and burial history. Experimental errors and their impact should also be considered. Experimental gas sorption isotherms are very sensitive to the he moisture content of the coal Goodman et al., 2007a. Due to this fact, moisture content is an important parameter affecting sorption capacity determination. Figure 3-2 illustrates that with increasing Langmuir pressure, productivity improves, because the amount of gas, which will desorb is higher for the same production pressure.

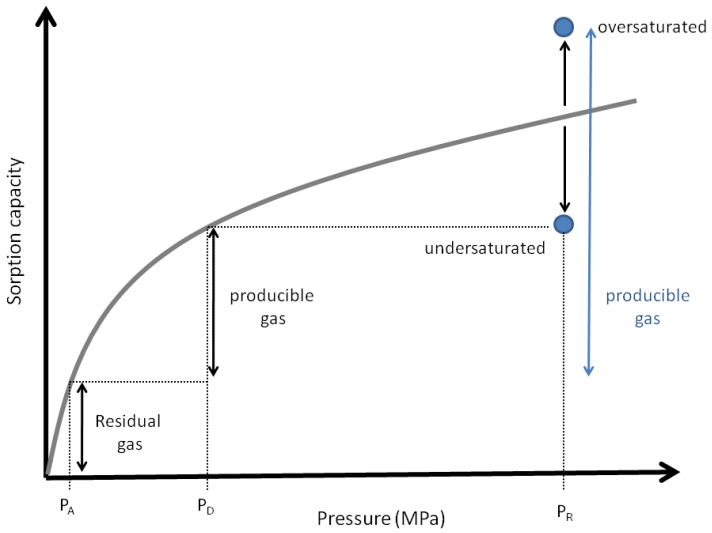


Figure 3-3. Schematic illustration of the methane sorption isotherm, the degree of saturation and the amount of producible gas (modified after Bustin and Bustin, 2008). The two dots mark the amount of gas stored at reservoir pressure. The highlighted pressure levels are the initial reservoir pressure P_R, the initial desorption pressure P_D (also called critical desorption pressure Ayers, 2002), and the abandonment pressure P_A.

The most favoured explanation for undersaturated coal seams is uplift. This argumentation however, mainly depends on the sorption enthalpy and the temperature gradient in the respective basin (Figure 3-4). At maximum burial depth and temperature, T_{max}, 2 - 4 times more gas can be generated than the coal can possibly adsorb (Clayton, 1998; Jüntgen, 1987; Kotarba and Rice, 2001; Rice et al., 1993). It is assumed that the coal at maximum burial depth is either fully or oversaturated. During uplift and exhumation, hydrostatic pressure and temperature decrease. Assuming a closed container, the amount of gas sorbed in the micropores and present in the pore system remains constant. Under certain geological conditions additional gas may be generated by microbial activities. It is commonly assumed that the sorption capacity will increase during uplift, because sorption is an exothermic process (Figure 3-4, solid line). This leads to an undersaturated coal seam. However, it is the consideration between Langmuir pressure and heat of adsorption which have to be made. Therefore, due to the decreasing hydrostatic pore pressure and the presence of water, the sorption capacity as a function of depth is more complex (Figure 3-4, dashed line).

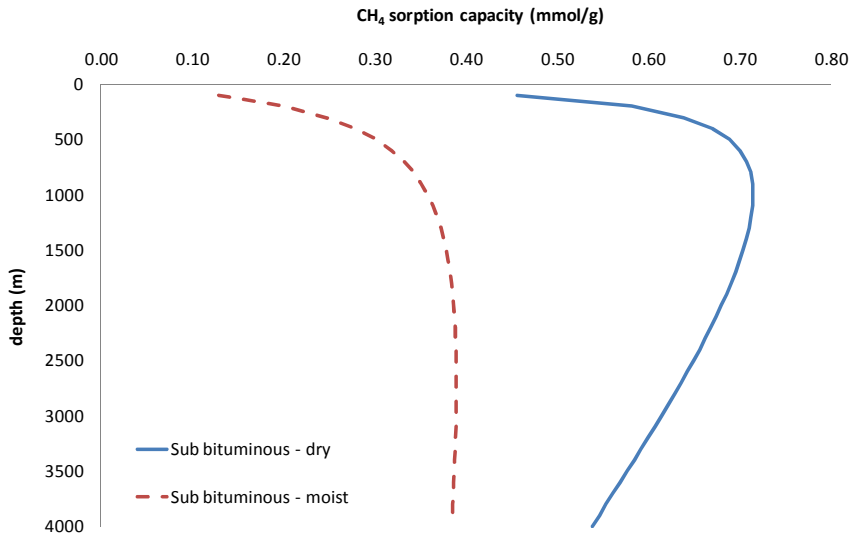


Figure 3-4. Schematic illustration of the CH_4 sorption capacity (same n_∞) with depth and influence of isosteric heat of adsorption on the Langmuir pressure caused by a dry (dH=-28kJ mol^{-1}; ln(K)= 11.5 and n = 0.9mmol g^{-1}) and moisturised sub bituminous coal (dH=-14 kJ mol^{-1}; ln(K)= 7 and n = 0.9 mmol g^{-1}) (Gensterblum et al. 2012) (1 mmol/g = 24.5 Std m³/t).

Beside these considerations for equilibrated geological systems, we need to consider the coalification process as a function of burial history (Equation 5). Obviously, the sorption capacity is a function of coal maturity Busch and Gensterblum, 2011. The coalification during burial will change the maturity or rank R_{max}. The coalification is exclusively a function of temperature *T* and coalification time *t*.

$$\frac{\partial T}{\partial z} = k(t, T(z), T_{max}) \cdot \nabla R_{max} \qquad (3\text{-}5)$$

Nevertheless, the correction factor *k*, which is specific for each basin, must be applied to determine the actual coalification time. This factor is equal to the ratio of the time integral of the burial history and the product of exposure time to gas generated and maximum temperature which is a function of burial depth.

Besides methane, some coal basins contain significant amounts of CO_2, which can even be the dominant gas component like in parts of the Silesia Basin Kotarba and Rice, 2001 or the Sydney Basin (Faiz, 2007; Faiz, 2006). The source of CO_2 in coalbed gases can be attributed to (i) decarboxylation reactions of kerogen and soluble organic matter during burial heating of the coal Boudou et al., 2008, (ii) mineral reactions, like dissolution of carbonates, thermal decomposition or metamorphic reactions, (iii) bacterial oxidation of organic matter Suess and Whiticar, 1989, and (iv) migration from deep-seated sources like magma chambers or from the upper crust Kotarba and Rice, 2001.

This study provides some observations to improve the sweet-spot identification related to coalbed methane and CO_2 enhanced coalbed methane. Furthermore the methane saturation change during uplift will be calculated. Finally, CO_2 storage and CH_4 recovery potential based on the sorption isotherms at three different temperatures will be calculated.

3.2 Samples and sample preparation

To investigate the effect of rank on the sorption enthalpy and entropy, three coal samples of different maturity were used in this study. Two German coals samples of intermediate and high rank from the Ruhr basin and a low rank coal from the Surat basin, Queensland, Australia.

3.2.1 Geological setting

The Prosper Haniel and Ibbenbüren coal samples were obtained from two German coal mines in the Ruhr Basin and are of Upper Carboniferous (Pennsylvanian) age. These coals formed in the paralic foredeep of the Variscan foldbelt Walter, 1992. Because of the complex burial history of the Ruhr basin, the coals show a wide range of rank from high-volatile bituminous (hvb) coal to anthracite. The Westphalian B seams of the Prosper-Haniel mine contain high volatile bituminous coal. Within the Prosper Haniel mine, located near Bottrop, coal seams are mined down to a depth of 1200 m. The sample used in this study was obtained from a depth of 915 m and has a random vitrinite reflectance V_{Rr} of 0.93% (Table 3-1). It is a sub-sample from the one used in the study by Kempka et al., 2011.

The Ibbenbüren deposit is located at the southern edge of the Lower Saxony Basin (LSB) and is also of Upper Carboniferous (Pennsylvanian) age. It represents an isolated uplifted block, which was exposed to an intense secondary coalification by the so-called Bramsche Pluton. The Ibbenbüren coal is of anthracite rank. Details of the complex history of burial and uplift are still under discussion Senglaub et al., 2005a; Senglaub et al., 2005b; Senglaub et al., 2006. Basin modelling studies suggest a maximum burial depth of the coal seams of 4500 to 5000 m during late Carboniferous/early Permian time Senglaub et al., 2005a. Anthracite is mined in Ibbenbüren at a depth down to 1650 m below surface. Gas contents of the anthracite are generally high but vary among seams and also show lateral variations. Mining strategies have been optimized to allow for gas drainage of notoriously gas-rich seams by underground boreholes from over- and underlying workings. The Ibbenbüren anthracite sample was taken from Seam 74 at 1200m depth and has a vitrinite reflectance of 3.3%.

Table 3-1. Samples used in this study

Location	Basin	Lithostratigraphic Units	Age	Seam	Vit.Ref.	Rank
QLD Australia	Surat Basin	Taroom Coal measures	Middle Jurassic	Condamine	0.5	sub-bituminous A
Prosper Haniel mine Germany	Ruhr basin	Westphalia B	Pennsylvanian	K	0.93	high volatile bituminous
Ibbenbüren Germany	Ruhr basin		Pennsylvanian	74	3.3	anthracite

Coalbed methane is produced from the Surat basin in Australia since 2007. The Walloon Subgroup is well developed across the eastern Surat Basin and crops out along the NE margin of the basin Scott et al., 2007. The coals from the Wallon Subgroup are of middle Jurassic age. The sub-bituminous coal sample

investigated (VRr=0.5%) is taken from a cored well and belongs to the Condamine Seam, which is part of the Taroom coal measures.

Sample preparation

For measurements on powdered coal material, crushed samples were divided and aliquots were ground to pass a sieve size of 2 mm. The coal samples were subdivided into four different particle-diameter fractions (0.177–0.354, 0.354–0.5, 0.5–1.0 mm and greater than 1.0 mm). The sieve fraction below 0.177 mm was discarded, because it is considered to be enriched in mineral fragments compared to the larger size fractions. For sorption measurements, the sieve fraction of 0.5 to 1mm was used. The coal samples were moisture-equilibrated in a desiccator over periods of 5 to 14 days at a relative humidity of 97% provided by a potassium sulphate solution (K_2SO_4), ASTM procedure 1412-99. The sample material was then transferred immediately into the adsorption cell. An aliquot was used for determination of the moisture content. A summary, including available data for proximate and ultimate analysis, is provided in Table 3-2.

The equilibrium moisture contents for the high volatile bituminous coals and the anthracite are relatively high compared to data reported by Busch and Gensterblum (2012). However the values are averages of 9 to 11 measurements and the standard deviations indicate their accuracy and reproducibility. Therefore they are considered reliable.

Table 3-2. Ultimate and proximate analysis of coal samples used in this study

	QLD Australia (Sub-bit. A)	Prosper Haniel mine Germany (High volatile bit.)	Ibbenbüren Germany (anthracite)
Volatile mater: [+] (%)	43.5±0.4	31.7±1.2	6.0
Fixed carbon: [+] (%)	49.5±0.1	58.0±1.7	88.2
Ash content: [+] (%)	3.5±0.2	7.3±2.2	5.8
As received (%) moisture content	3.6±0.2	3.0 ±0.2	0.85
Equilibrium moisture* (%)	6.4±0.1	4.0±0.5	4.8 ±0.3
Vitrinite / huminite (%)	61.4	69.3 ±3.2	83
Liptinite (%)	31.4	7.1 ±2.3	0
Inertinite (%)	0.6	14.6±4.0	17
Mineral matter (%)	6.6	8.7±1.4	n.a.
Vit.ref.	0.5	0.93	3.3

* Equilibrium moisture content at 97% humidity
[+] dry basis

3.3 Experimental and conceptual procedure

All experimental sorption data reported here were obtained using the manometric method. The set-up used for sorption isotherm measurements and for determining sorption kinetics is explained in detail by Busch and Gensterblum (2011). Further experimental details on this method were reported by Gensterblum et al. (2009, 2010).

Free phase gas densities of CH_4 and CO_2 as a function of pressure and temperature were calculated using the GERG multi-component equation of state (EOS) Kunz et al., 2007 that provides also mixture densities for CO_2/water and CH_4/water.

For quality reasons and to test consistency of the experimental results, volume calibrations of the experimental set-up were performed with different gases (He, CH_4 and CO_2) by successive expansion steps and using the GERG EOS for the corresponding gas.

3.3.1 Parameterisation of experimental sorption data

The Langmuir equation (Langmuir, 1918) is frequently used as a first approach to describe gas adsorption on solid surfaces as a function of pressure and at constant temperature (sorption isotherms).

$$n(p) = n_{\infty}\left(\frac{p}{P_L+p}\right) \qquad (3\text{-}6)$$

Here *n(p)* [mmol g^{-1}] is the amount of substance adsorbed at pressure *p* [MPa], n_{∞} [mmol g^{-1}] is the amount of substance adsorbed at infinite pressure and P_L [MPa] is the Langmuir pressure (pressure at which half of the sorption sites are occupied). The underlying assumptions (monomolecular coverage, energetically identical sorption sites etc.) are discussed in Langmuir (1918) and textbooks on sorption science.

In the derivation of the Langmuir equation the volume of the adsorbed phase is usually neglected. This is justified in low-pressure sorption experiments where the density of the adsorbed phase is much higher than the density of the free gas phase in equilibrium with it. In high-pressure sorption experiments the density difference between the free gas and the adsorbed phase is much smaller and the volume of the adsorbed phase has measurable effects in the experiments: in the manometric and volumetric methods it reduces the void volume of the measuring cell and in the gravimetric method it generates additional buoyancy. By explicitly taking into account the volume of the adsorbed phase (which is proportional to the absolute amount of substance adsorbed) at a given pressure, the following equation for the experimentally measurable excess sorption can be derived:

$$n_{excess}(p) = n(p) \cdot \left(1 - \frac{\rho_{free}}{\rho_{adsorbed}}\right) \qquad (3\text{-}7)$$

Here ρ_{free} is the density of the free gas phase, which is usually accurately known for given pressure and temperature conditions, and $\rho_{adsorbed}$ is the density of the adsorbed phase. The excess sorption $n_{excess}(p)$ is the parameter that is determined experimentally Sircar, 1999. It constitutes the net effect of removing gas molecules from the free phase and depositing them on the surface of the sorbent (formation of an adsorbed phase) and simultaneously increasing the volume of the "condensed phase" (sorbent + adsorbate) by an unknown amount. In Equation 7, *n(p)* denotes the "absolute sorption". The absolute adsorption has the property of increasing monotonously with increasing gas pressure and approaching a saturation when $p \rightarrow \infty$.

It is evident that for low gas pressures, as ρ_{free} approaches zero, the difference between excess sorption and absolute sorption vanishes.

Taking the Langmuir equation as a model equation for absolute sorption, combination of Equations 6 and 7 yields:

$$n_{excess}(p) = n_{\infty}\left(\frac{\mathrm{p}}{P_L+\mathrm{p}}\right)\cdot\left(1-\frac{\rho_{free}}{\rho_{adsorbed}}\right) \qquad (3\text{-}8)$$

In Equation 8 the Langmuir function may be replaced by any other reasonable "absolute sorption" function.

The absolute sorption cannot be determined directly from sorption experiments because the density of the adsorbed phase ($\rho_{adsorbed}$) is not known, consequently this parameter has to be estimated. It was found experimentally that the adsorbed phase density for methane on silica gel is close to the inverse of the van der Waals volume (b_{vdW} = 0.04286 and 0.04301 L/mol Weast, 1972) of the adsorbate Humayun and Tomasko, 2000. The interaction parameters between CO_2 and silicia are slightly different those for CO_2 and carbon atoms. However many experimental studies use 1027 and 373 kg m^{-3} for CO_2 and CH_4 as reasonably good approximations, respectively (Gensterblum et al., 2010; Gensterblum et al., 2009).

3.3.2 Temperature-dependence of gas sorption isotherms

While the (excess) sorption isotherms describe the pressure-dependence of gas sorption on solids, the temperature dependence has to be accounted for as a relevant parameter in geological systems. In general only the Langmuir pressure (P_L) is considered to be temperature-dependent (Equation 9). For dry coals the amount of sorption sides is constant over wide temperature ranges. However for moisturised coals the situation is more complicated because the sorption sites are partly occupied by water molecules. The amount of sorbed water molecules at a defined partial pressure depends also on the temperature.

$$\begin{aligned} P_L(T) &= P_0 exp\left(\frac{-\Delta H_{KL}}{RT}\right) \\ n_{\infty}(T) &= n_{\infty,T=0} exp\left(\frac{-\Delta H_n}{RT}\right) \end{aligned} \qquad (3\text{-}9)$$

where $n_{\infty}(T)$ and $P_L(T)$ are sorption capacity and Langmuir pressure at temperature T and at a constant moisture content. Due to the fact that water sorption enthalpies on coals are much higher than those of methane (H_{KL} and H_N) the total methane sorption sides (total sorption capacity) n_{∞} are here kept constant (ΔH_N=0) for the temperature range of this study (Equation 10):

$$\begin{aligned} n_{\infty}(T) &= n_{\infty} \\ \rho_{ads}^{\infty}(T) &= \rho_{ads}^{0}(T) \end{aligned} \qquad (3\text{-}10)$$

Therefore we use 7 degrees of freedom (n_{∞},$P_{L,T=303K}$,$P_{L,T=319K}$,$P_{L,T=334K}$, $\rho_{T=303K}$, $\rho_{T=319K}$, $\rho_{T=334K}$) for CH_4 and CO_2 Isotherms at three different temperatures. The quality of the fit by using equation 9 and 10 is shown in the appendix (Figure 3-11 and Figure 3-12).

3.3.3 In-situ gas sorption capacity of coal seams

Gas sorption capacity of coal seams is primarily controlled by the *in-situ* moisture, pressure and temperature conditions. The relationships for the temperature dependence of the parameters of the excess sorption isotherms can be used to compute the sorption capacity of the coal for individual gases as a function of depth.

If a relationship for the change of sorption capacity with coal rank is established and incorporated into the calculation scheme, too, then the dynamic evolution of the sorption characteristics of a coal seam throughout its burial history can be reconstructed Bustin and Bustin, 2008; Gensterblum et al., 2009; Hildenbrand et al., 2006, Weniger et al., 2012).

3.3.3.1 Static case (present-day sorption capacity of a coal seam of known coal rank and depth)

A geothermal gradient of 0.03 K/m with a surface temperature of T_0=288K (15°C), and a hydrostatic pressure gradient of 0.01 MPa/m were chosen to represent temperature and pressure conditions for a hypothetical CBM reservoir as a function of depth. Methane sorption isotherms were measured at 303, 318, 333, and 348 K corresponding to reservoir depths of 500, 1000, 1500, and 2000 m, respectively. Sorption capacities for shallower and deeper depths have been extrapolated.

3.3.3.2 Dynamic case (evolution of sorption capacity with burial history)

The Langmuir parameters and the CH_4 and CO_2 sorption enthalpies determined for moisture-equilibrated coals were taken from Gensterblum et al. 2012 (Table 3-1 to Table 3-3 and

Table 3-5 to Table 3-7). This reference also provides more details about the fitting procedure as well as aspects regarding the evaluation and assumptions that have to be made.

The sorption capacity as a function of depth *n(z)* is also a function of thermal *T(z)* and pressure gradient *p(z)* with depth of each specific basin. For simplicity a time-invariant linear geothermal gradient and a hydrostatic pressure gradient were assumed in this calculation (Equation 11).

$$n(z) = n(p(z), T(z)) = n_\infty(T(z)) \left(\frac{p(z)}{P_L(T(z)) + p(z)} \right)$$

$$T(z) = \vartheta \cdot z + T_0$$

$$p(z) = \gamma \cdot z + p_0 \qquad (3\text{-}11)$$

Where ϑ and γ are temperature and hydrostatic pressure gradients, respectively and T_0 and P_0 are surface temperature and pressure, respectively. Integration of into the Langmuir equation leads to Equation 12.

$$n(z) = n_\infty exp\left(\frac{-\Delta H_n}{R(\vartheta \cdot z + T_0)}\right) \left(\frac{\gamma \cdot z + p_0}{P_0 exp\left(\frac{-\Delta H_K}{R(\vartheta \cdot z + T_0)}\right) + \gamma \cdot z + p_0} \right) \qquad (3\text{-}12)$$

As argued above, the Langmuir volume for methane should be independent of temperature especially for the small temperature range used in this study. Equation 12 has been simplified accordingly. Further, since

the available experimental temperature range is limited (303-349 K) it is important to verify the equation used for extrapolation to higher pressures and temperatures.

$$\mathrm{n(z)} = n_{\infty}\left(\frac{\gamma \cdot z}{P_0 exp\left(\frac{-\Delta H_K}{R(\vartheta \cdot z + T_0)}\right) + \gamma \cdot z}\right) \quad (3\text{-}13)$$

The thermal gradient ϑ was varied between 2 and 4 K per 100 m; the surface temperature T_0 was chosen as 15°C. The hydrostatic gradient was kept constant at 1 MPa per 100 m. Formation fluid density was kept constant at 1 g/cc. It must be considered that at greater depths, water density decreases with increasing temperature but usually increases with increasing salinity. These changes are, however considered to be minor for the purpose of this study and have been disregarded.

Equation 14 is an empirical formula after Barker and Pawlewicz, 1994 describing the correlation (coefficient r^2=0.7 and sample n>600) between vitrinite reflectance V_{Rr} and maximum temperature T_{max} for humic organic matter Schoenherr et al., 2007. Kinetic aspects of the hydrocarbon gas generation during the coalification process are not considered Burnham, 1979a, b; Burnham and Sweeney, 1989; Cramer et al., 1998; Krooss, 1988; Krooss et al., 1995

$$T_{max,peak\ burial} = \frac{\ln V_{Rr} - 1{,}68}{0{,}0124} \quad (3\text{-}14)$$

Consequently, following equation 11 and 14 the maximum temperature was 362K, 403K and 504K for the sub bituminous A, high volatile bituminous and the anthracite coal respectively. Assuming a thermal gradient of 3K/100m, this leads to maximum burial depths of ~2500m, 3900m and 7300m, respectively. Therefore a representative temperature gradient for the specific basin is important and a sensitive parameter for this saturation considerations.

In order to calculate maximum CH_4 saturations as a function of basin uplift starting at maximum burial depth we use the conceptual simplified model shown in Figure 3-5. At maximum burial depth, the generation rate of thermogenic methane reaches its maximum. The total amount of gas generated is 2-4 times the sorption capacity, e.g. Hunt and Steele, 1991; Tang et al., 1996). Recently Heim and co-workers investigated the gas genesis potential for the anthracitic coal sample used in this study Heim et al., 2011. Therefore 100% CH_4 saturation of coal can be expected at maximum depth. The excess of generated gas will lead to an overpressure and/or will migrate into neighbouring formations. Gas saturation during uplift is calculated using the sorption capacity as a function of depth and the amount of methane sorbed at pressure and temperature conditions at maximum burial depth (2500m, 3900m and 7300m). However, the maximum burial depth for the anthracite is not in line with study of Senglaub et al 2005 where due to the Bramsche Pluton a lower maximum burial depth of roughly 5000m. Therefore we choose for the Senglaub model p_{max}=50MPa and T_{max}=505K.

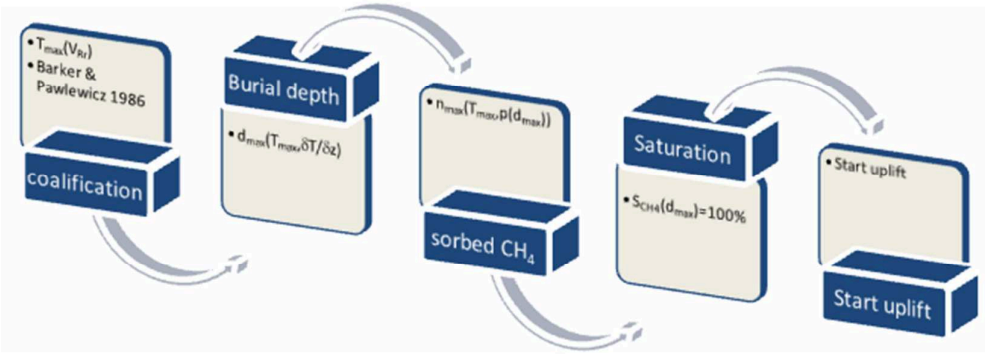


Figure 3-5. Conceptual design of the evolution of the in-situ gas saturation of coal seams as a function of maturity and thermal gradient.

3.3.4 Gas recovery potential of coal seams

Equation 3-15 can be used to calculate the recovery potential as a function of burial depth. By subtracting the residual gas amount at abandonment pressure p_A from the CH_4 sorption capacity at critical desorption pressure p_D, the estimated amount of gas recovered can be obtained (see Figure 3-3). The abandonment pressure p_A is commonly controlled by the installed gas peripheral equipment of the CBM field.

$$n(z) = n_\infty \left[\frac{p_D}{K_0 exp\left(\frac{-\Delta H_K}{R(\vartheta \cdot z + T_0)}\right) + p_D} - \left(\frac{p_A}{K_0 exp\left(\frac{-\Delta H_K}{R(\vartheta \cdot z + T_0)}\right) + p_A} \right) \right] \quad (3\text{-}15)$$

3.4 Results and geological implications

The isotherms of all samples show a clear increase in CH_4 Langmuir sorption capacity n_∞ as a function of rank (Table 3-3 to Table 3-6 for CH_4). Table 3-3 to

Table 3-5 show the fitted Langmuir parameters for CH_4 sorption on three (moisture-equilibrated) coals at three different temperatures 303, 319 and 334K, respectively. We observe that the Langmuir pressure K_L decreases with rank.

Table 3-3. Fitted Langmuir parameters for methane excess sorption isotherms on sub bituminous A coal at three different temperatures (7 degrees of freedom for 3 Isotherms).

Sub-bit. A	P_L (MPa)	n_∞ (mmol/g)	ρ_{ads} (kg/m³)	Δn (mmol/g)
303K	7.10	0.774	600	0.004
319K	10.47	0.774	393	0.005
334K	13.57	0.774	373	0.003

Table 3-4. Fitted Langmuir parameters for methane excess sorption isotherms on high volatile bituminous coal at three different temperatures.

High volatile bit.	P_L (MPa)	n_∞ (mmol/g)	ρ_{ads} (kg/m³)	Δn (mmol/g)
303K	6.04	0.88	293	0.011
319K	7.89	0.88	618	0.004
334K	10.99	0.88	553	0.005

Table 3-5. Fitted Langmuir parameters for methane excess sorption isotherms on anthracite at three different temperatures (see text).

Anthracite	P_L (MPa)	n_∞ (mmol/g)	ρ_{ads} (kg/m³)	Δn (mmol/g)
303K	3.45	1.90	946566*	0.014
319K	4.78	1.90	511	0.014
334K	6.59	1.90	419	0.012

The listed Langmuir pressure P_L, total CH_4 sorption amount n_∞ and the adsorbed phase density ρ_{ads} values are the parameters of Equation 8. The Δn values denote the average deviation between measured data points and the best fit function. We were not able to achieve acceptable fitting results with a constant adsorbed phase density ρ_{ads}. Therefore the experimental data were fitted by adjusting P_L and ρ_{ads} for each of the three isotherms and taking n_∞ as a common temperature-independent parameter for each coal. The 303K isotherm of the anthracite did not reach an equilibrium (plateau) value and therefore the sorbed phase density derived from the fitting procedure is very high.

Table 3-6 lists the isosteric heats of sorption CH_4 for the three different coal samples. The CH_4 isosteric heats of adsorption of this study are in very good agreement with the reported values of previous publications Yang and Saunders, 1985 (18-20 kJ mol^{-1}) Nodzenski, 1998.

Table 3-6. Isosteric heats of CH_4 sorption on moist coals of different rank based on Langmuir pressure (see Appendix, Figure 3-11).

CH_4	dH (kJ/mol)	ln (P_L)
Sub bituminous A coal	-17.9 ± 1.6	9.09 ± 0.6
High volatile bituminous	-16.7 ± 1.5	8.41 ± 0.6
Anthracite	-18.1 ± 0.4	8.39 ± 0.1

Table 3-7 to Table 3-9 list the CO_2 Langmuir parameters used to calculate the temperature-dependence of the CO_2 Langmuir pressure for the three coals. The isosteric heats of adsorption for CO_2 are higher than the respective CH_4 values and in the same range as values reported in previous studies (17-29 kJ mol^{-1}) Nodzenski, 1998 Ozdemir and Schroeder, 2009.

Table 3-7. Fitted Langmuir parameters for CO_2 excess sorption isotherms on sub bituminous A coal at three different temperatures.

Sub-bit. A	P_L (MPa)	n_∞ (mmol/g)	ρ_{ads} (kg/m³)	Δn (mmol/g)
303K	4.62	1.80	878	0.015
318K	8.29	1.80	1260	0.022
333K	12.09	1.80	1500	0.014

Table 3-8. Fitted Langmuir parameters for CO_2 excess sorption isotherms on high volatile bituminous coal at three different temperatures

High volatile bit.	P_L (MPa)	n_∞ (mmol/g)	ρ_{ads} (kg/m³)	Δn (mmol/g)
303K	3.03	1.63	1189	0.018
318K	5.59	1.66	1124	0.017
333K	8.0	1.67	1247	0.013

Table 3-9. Fitted Langmuir parameters for CO_2 excess sorption isotherms on anthracite at three different temperatures.

Anthracite	P_L (MPa)	n_∞ (mmol/g)	ρ (kg/m³)	Δn (mmol/g)
318K	1.39	1.94	1270	0.020
333K	2.09	1.94	1167	0.023
348K	3.21	1.94	1466	0.004

Sorption enthalpies for CH_4 and CO_2 are listed in Table 3-6 and Table 3-10, respectively. They were calculated from the fitted Langmuir pressures K_L for different temperature with a common Langmuir volume n_∞ following equation 9.

Table 3-10. Isosteric heats of CO_2 sorption on moisturized coals based on Langmuir pressure (see Appendix, Figure 3-12).

	dH (kJ/mol)	ln P_L
Sub bit. A	-29.2 ± 2.8	12.59 ± 1.0
High volatile bit.	-27.7 ± 3.0	11.54 ± 1.1
Anthracite	-25.6 ± 1.1	10.02 ± 0.4

Figure 3-6 and Figure 3-7 show the calculated CH_4 and CO_2 sorption capacity as a function of burial depth for the specified geothermal and hydrostatic pressure gradients. For all samples these curves exhibit a maximum followed by a slight decrease with increasing depth (Figure 3-6). This is because the effect of temperature (decrease in sorption capacity with increasing temperature) exceeds the pressure effect (increasing sorption capacity with increasing pressure). This maximum is more pronounced for large geothermal gradients (Figure 3-6). Further the reduction in CH_4 and CO_2 sorption capacity between its maximum value and the sorption capacity at 4 km depth increases with increasing geothermal gradient but also with increasing coal maturity from sub-bituminous to anthracite. The difference in sorption capacity between the different coal rank decreases with increasing depth. In general these trends are much more sensitive to the geothermal gradient than to the hydrostatic pressure gradient.

The maximum of the CH_4 sorption capacity depth trend is located at shallower depth than the maximum of the CO_2 trend (Figure 3-7). It is more pronounced and it shifts to shallower depth as the thermal gradient increases. The maximum in the sorption capacity trend occurs at greatest depth for the high volatile bituminous coal (Figure 3-6). The maxima for the sub-bituminous and anthracite coals occur at similar

depth levels. This can be explained by decreasing sorption enthalpies with increasing rank as summarised in Table 3-6 and Table 3-10.

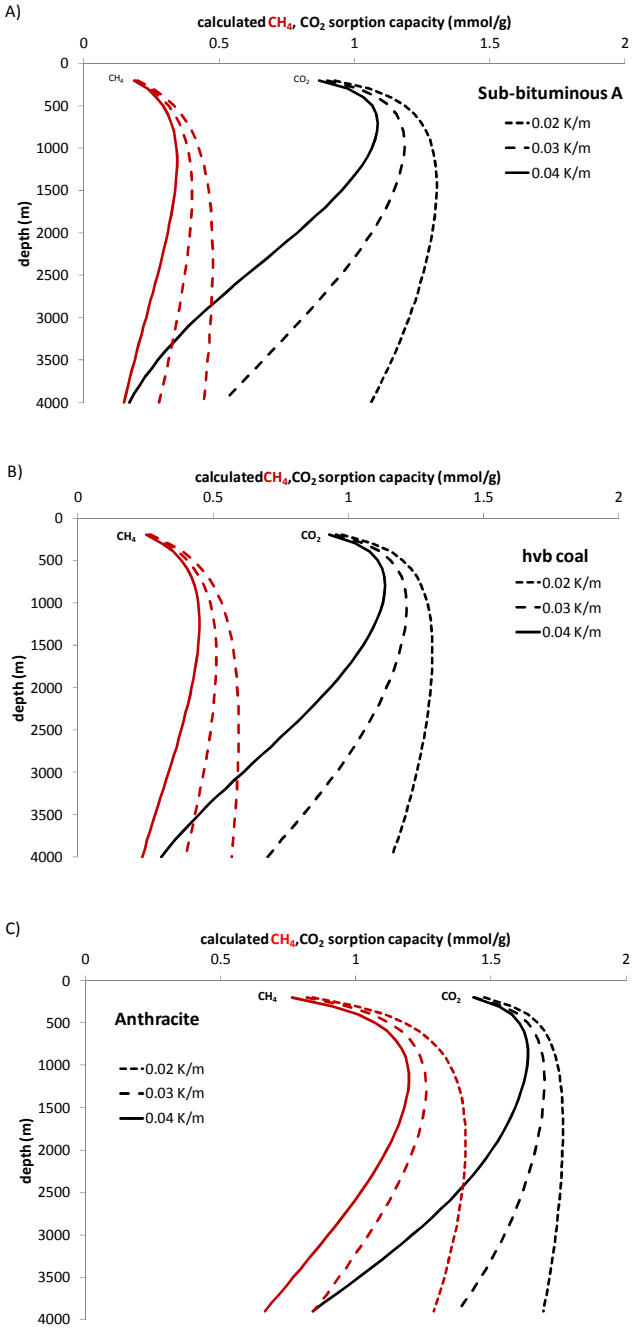


Figure 3-6. CH_4 (red) and CO_2 (black) sorption capacities as function of depth and thermal gradient for the three coal samples investigated here (1mmol/g =24.5 Std. m^3/t).

Table 3-7 to Table 3-9 show the fitted CO_2 Langmuir parameters of the three coal samples at the three temperatures 319, 334 and 349K but a dependence of the Langmuir volume n_∞ on coal rank cannot be observed. The anthracite has the highest CO_2 sorption capacity, followed by the sub-bituminous A and the high volatile bituminous coal.

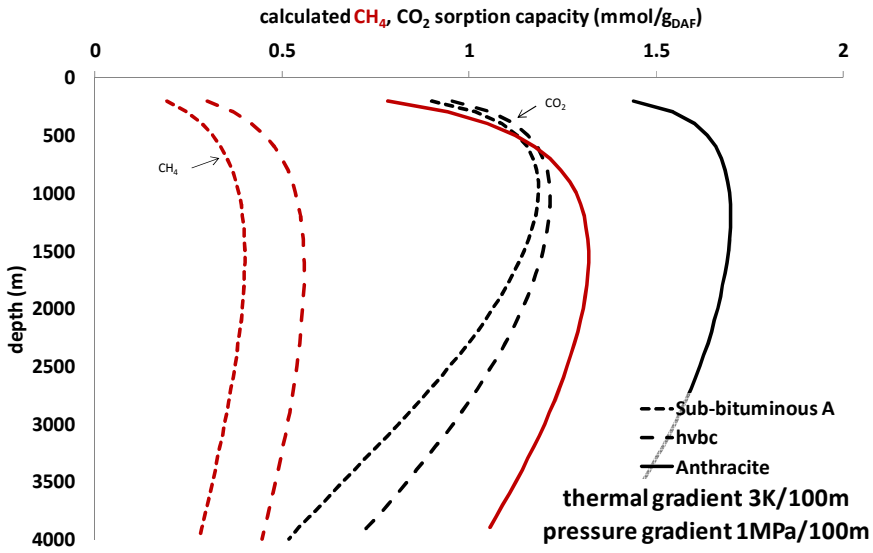


Figure 3-7. CH_4 (red) and CO_2 (black) sorption capacities as function of depth assuming a thermal gradient of 3 K/100m for sub-bituminous A, high volatile bituminous and anthracite coal deposits (1mmol/g =24.5 Std. m³/t).

Using equation 15, the potential recovery capacity for CH_4 and CO_2 has been calculated as a function of depth (Figure 3-8). These calculations show a stronger decrease in CO_2 sorption capacity with depth for moist low rank coals at approximately 1000 m than for high rank coal. However the maximum recovery potential only decreases slightly for moist high rank coals. This implies that CO_2-ECBM will become less effective at depths of more than ~1000m.

All coal samples show lower sorption capacities for CH_4 than for CO_2 and the CO_2/CH_4 sorption ratio varies from 5 at shallow depths to <3.5 for the sub bituminous and high volatile bituminous coal respectively (Figure 3-9). The sorption capacity of the anthracite coal shows a different depth trend: The total change in sorption capacity with depth is smaller and increases with depth. Additionally, Figure 3-8 illustrates that the CO_2 storage capacity decreases at depths > 900m, but is still larger than for CH_4. The sorption capacity ratios illustrated in Figure 3-10 and Figure 3-11 decrease with depth for the sub bituminous and the high volatile bituminous coal, respectively. Minimal to no differences are observed with different thermal gradients for the high volatile bituminous, the sub bituminous and anthracite coal. Only the anthracite coal shows an increasing ratio with increasing depth (Figure 3-12). This trend is more pronounced at higher thermal gradients.

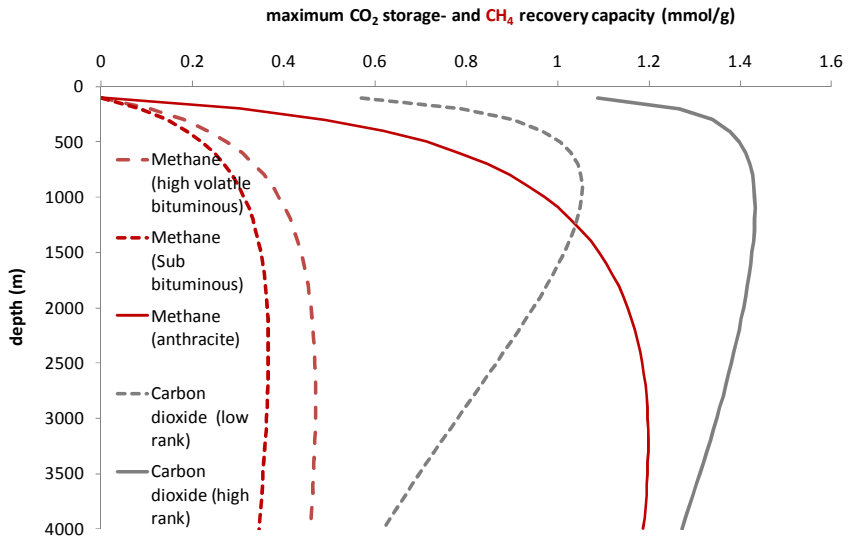


Figure 3-8. CH_4 recovery potential as a function of depth. Sorption enthalpies used from Table 3-6 and Table 3-10, assuming a constant abandonment pressure of 1 MPa, normal hydrostatic pressure gradient and geothermal gradient of 3K/100m.

The enthalpies obtained from the fitted Langmuir pressures (Table 3-10) are in line with the observations by Taraba (2011) Taraba, 2011. However, the CO_2 sorption enthalpies correlate inversely with rank, only.

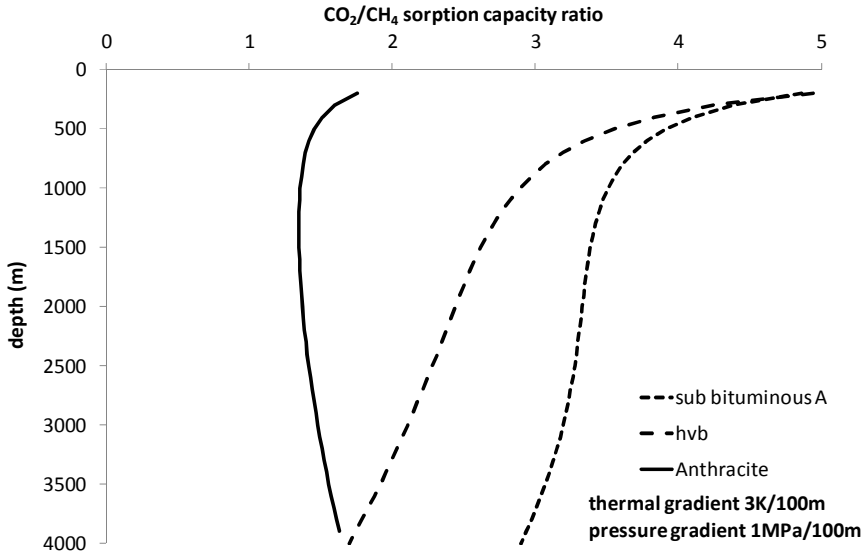


Figure 3-9. CO_2/CH_4 sorption capacity ratio as a function of depth for the three coal samples studied here, assuming a thermal gradient of 3K/100m and a hydrostatic pressure gradient of 1MPa/100m.

The total amount of gas generated from coals is usually considered to amount to 2-4 times the sorption capacity, e.g. Hunt and Steele, 1991; Tang et al., 1996). The excess gas will lead to an overpressure and/or will migrate into adjacent formations. Considering oversaturation or overpressured reservoirs it should be mentioned that in the geological time scales needed for this uplift, diffusion and/or pressure diffusion are a relevant transport mechanisms. For the following considerations, we assume that at the beginning of uplift,

i.e. at maximum burial depth, the coal seam is fully gas saturated and equilibrated (cf. Figure 3-5). This gas content is used as the reference value to calculate the relative gas saturation during uplift. The results of these computations are shown in Figure 3-10 for three different coal ranks. The calculated maximum burial depth of 7300m by Barker et al. 1986 for the anthracite is not in line with a maximum burial depth of 4500 to 5000m from a basin modelling study by Senglaub et al. (2006). Additionally an assumed maximum burial depth of 7300 m requires an extensive extrapolation of the measured sorption data to high pressures and temperatures.

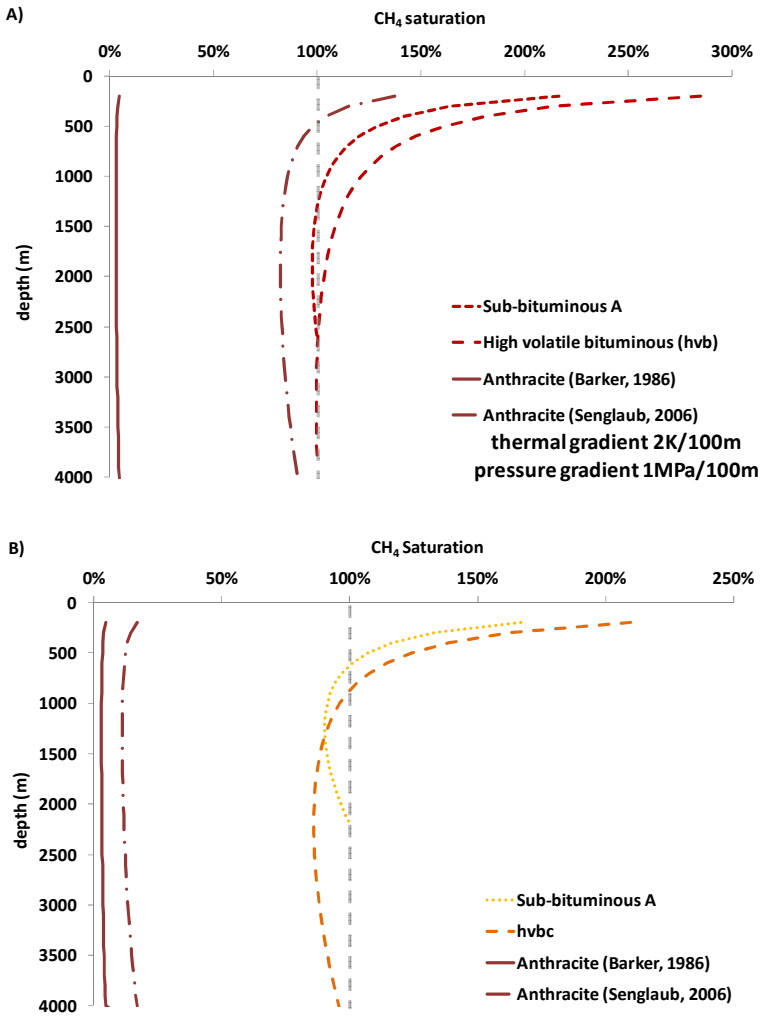


Figure 3-10. Calculated CH_4 saturation trends after uplift from the maximum burial depth (burial history model A: 2500, 3900, 7800m Schoenherr et al., 2007; Senglaub et al., 2005b; Senglaub et al., 2006 and model B: 2200m, 4400m and 9800m Barker and Pawlewicz, 1986 or 5000m (T_{max}=504K,p_{max}=50MPa) Senglaub et al., 2005b; Senglaub et al., 2006) assuming no loss of CH_4, a geothermal gradient of 0.02K/m (model A) and 0.03K/m (model B) and a hydrostatic pressure gradient of 0.01MPa/m.

3.5 Discussion

Since gas sorption is an exothermic process, the initial slope of the isotherms at zero pressure (corresponding to the reciprocal of P_L) decreases with increasing temperature. This means that higher

pressures are necessary to reach the same sorption capacity n(p) at higher temperatures. Based on the assumption that a temperature increase (35°C up to 75°C) will not change the surface, pore or chemical structure of the coal, we assume that the sorption capacity n_{∞} should be independent of temperature, i.e. the total amount of sorption sites (sorption capacity) should remain constant with temperature. However, due to the presence of moisture, a shift in the portion of sorption sites occupied by water can be assumed. The saturation moisture content, or sorption capacity of water, will decrease slightly with increasing temperature, because sorption enthalpy of water is much higher than the sorption enthalpies of carbon dioxide or methane Busch and Gensterblum, 2011. Using this as simplification, the total amount of sorption sites remains constant with temperature, approximately; however, the individual share of sorption sites for CH_4 and CO_2 at a given temperature and pressure will decrease slightly.

Due to the opposing effects of increasing pressure and temperature with depth, it depends on the magnitude of the sorption enthalpy if increasing pressure will lead to higher surface coverage or if the thermal energy will reduce the surface coverage at a given depth. Generally, sorption capacity is reduced to a greater extent with increasing depth at higher temperature gradients. This is in line with previous observations (Bustin and Bustin, 2008; Hildenbrand et al., 2006; Weniger, 2012). For this computation of of sorption capacity n_{sorbed} [mmol g^{-1}] with depth (pressure and temperature), Hildenbrand et al (2006) used methane sorption isotherms measured for dry coals, while Bustin and Bustin (2008) used methane sorption isotherms on moisturised coals with vitrinite reflectance values of 0.4, 0.5 and 1.7%.

The decrease in sorption capacity with depth calculated in the present study is lesser than the trends obtained by Hildenbrand et al. (2006). This is essentially due to the use of isotherms for moisture-equilibrated coals in this work as opposed to data for dry coals used by Hildenbrand et al. (2006).

3.5.1 Influence of water on gas sorption capacity

The sorption of methane or carbon dioxide in moist coal samples is largely controlled by competition with water. In general, the interaction force between coal and water is much stronger than for methane or carbon dioxide, especially for low water surface coverage. It is reasonable to assume that the amount of sorption sites occupied by water molecules will change with temperature. For moisturised coals several publications report a change in the Langmuir amount of sorbed substance with temperature Crosdale et al., 2008; Moore and Crosdale, 2006; Ozdemir, 2009.

Figure 3-10 shows the calculated gas saturations relative to the saturation at maximum burial depth for three uplifted coal seams. Based on the trends illustrated in Figure 3-6, we can expect a high saturation level during uplift for the sub bituminous and high volatile bituminous coals. The highest saturation for any thermal gradient could be expected for high volatile bituminous followed by sub bituminous coal. The calculated maximum burial depth of 7300m by Barker et al. (1986) for the anthracite is not in line with the basin modelling study by Senglaub et al. (2006). Higher CH_4 saturation should be expected if uplift starts from a maximum burial depth of 4000m to 5000m for anthracite deposits Senglaub et al., 2006, due to the

high decrease in sorption capacity with depth. Gas contents in the German anthracite mine in Ibbenbüren and gas outbursts that occurred in the past indicate that current CH_4 saturation levels in the anthracite seams are much higher than 5-10%. Therefore it is believed that the saturation data of Figure 3-10 for the anthracite needs further investigations. A lower thermal gradient would be one possible explanation (Figure 3-10A).

It is likely that coal deposits are undersaturated with respect to CO_2 because of the high solubility in formation brine (Figure 3-1). The results of this study suggest that, due to the rapid decrease of CO_2 sorption capacity with depth, carbon capture and storage (CCS) becomes unattractive with high geothermal gradient and less favourable for depths greater than ~2 km. As illustrated in Figure 3-3 and Figure 3-4, an increase in Langmuir pressure will increase the productivity, because the higher amounts of gas desorbing at the same pressure drop (p_D-p_A). In Table 3-1 to Table 3-3 and

Table 3-5 to Table 3-7, we show that with increasing rank, the Langmuir pressure decreases. Therefore, we can conclude that lower rank coal deposits are more likely to degas than high rank coal deposits (Figure 3-8). Furthermore, Figure 3-8 illustrates that CO_2-ECBM is more feasible for depths shallower than 1000 m, regardless of the coal sorption enthalpies. For depths greater than 1000 m, CO_2-ECBM becomes less efficient for low rank coals. It should be mentioned, that transport processes or effects resulting from coal swelling or changes in permeability - stress relationships, etc. are not considered in these conclusions.

Saturation values determined from dry or as-received coal samples suggest much low saturations after uplift and the sorption capacity will show a more pronounce decrease with increasing depth and thermal gradient. Due to lower Langmuir pressures b_L and higher sorption enthalpies for the CH_4 sorption on dry or as received coals, the maximum recovery potential will be also misleading.

3.6 Conclusion

Among the three possible gas storage mechanisms in coals (compressed gas in the open porosity, dissolved gas in the formation water and sorbed gas), sorption is the dominant mechanisms for CBM reservoirs (Figure 3-1). For example, given a porosity of 15%, the amount of compressed gas is 2.5 to 10 times lower than the sorption capacity for methane and carbon dioxide. The largest difference is observed for the anthracite. The ratio of compressed and sorbed gas shows a decreasing trend with increasing depth. Carbon dioxide solubility in water is higher than for methane (Figure 3-1). Nonetheless, the amount of dissolved gas for either methane or carbon dioxide is still roughly 100 times lower than the carbon dioxide sorption capacity of the moisture-equilibrated coal. Therefore the amount of gas dissolved in water or brine is negligible for methane and in most instances also for CO_2.

The main parameters controlling ultimate gas recovery from coal deposits are the natural cleat permeability and the total gas content. Sorption capacity denotes the maximum amount of gas that can physically be stored in coal seams under given subsurface conditions. Sorption capacity (generally speaking) is influenced by pressure and temperature, the current moisture content, the composition of the organic material, the mineral content, and coal rank. Sorption capacity and sorption enthalpy are strongly

influenced by coal properties, such as macerals composition, total carbon content, coal rank, pore structure, pore size distribution and mineral matter (Busch and Gensterblum 2011). The sorption enthalpy is an important factor when considering gas saturation based on the burial and uplift history of a CBM deposit. Measurements performed on dry coals and at different water contents reveal that even very low water contents lead to a strong reduction of CH_4 sorption capacity. A decrease in sorption capacity by up to 50% has been measured for high volatile bituminous coal.

The evaluation of the measured isotherms reveals that for coals of a sub-bituminous A rank, which is common in many producing CBM reservoirs, and pressure and temperature gradients typical for most sedimentary basins, the sorption capacity of coals decreases only slightly during uplift.

The geothermal gradient is much more important than the hydrostatic pressure gradient for the CH_4 sorption capacity prediction as a function of depth. For CBM as well as CO_2-ECBM activities a low geothermal gradient is more favourable.

We conclude from this study that low rank coal deposits require a lower pressure draw down than high rank coal deposits to desorb an equivalent amount of methane. In high rank coal seams it is more likely to observe undersaturated gas contents than in low rank deposits.

Based on the results of this study, the often observed undersaturation of coal seams in the field is more likely related to loss of methane from the coal seam to other formations than changes in the sorption capacity, especially for the high volatile bituminous coal. Discovering an oversaturated coal seam is not likely; but if so, it can only be explained by the decrease in sorption capacity at shallow depths (below 1000 m), or due to additional gas generation, e.g. by microbial activities.

These findings indicate that reliable information on the *in-situ* moisture content of coal seams is crucial for the estimation of reservoir capacities and resource potential. One shortcoming is the lack of published sorption isotherms on moisture-equilibrated coals.

Considering only the sorption measurements and recovery calculations, the feasibility of CO_2 storage and CH_4 recovery for CO_2-ECBM will increase with increasing rank and will decrease with depth. The feasibility of CO_2-ECBM aiming at carbon storage depends on the thermal gradient of the deposit and will decrease with increasing depth for thermal gradients lower than 0.03K/m. Methane recovery decreases with increasing methane sorption enthalpy because the Langmuir pressure will increase more rapidly with depth than the thermal reduction of the surface coverage for coals with a lower methane sorption enthalpy.

CO_2-ECBM is likely to become less effective with increasing depth because the CO_2/CH_4 ratio decreases with depth, hence CO_2-ECBM is expected to be less effective with increasing maturity due to the observation that the highest selectivity is observed for low mature coals.

3.7 Appendix

Figure 3-11 and Figure 3-12 illustrate the quality of the fitting (according to equation 8 and 9). Furthermore the figures show that it is acceptable to extrapolate sorption capacity values down to temperature of a depth of 4km.

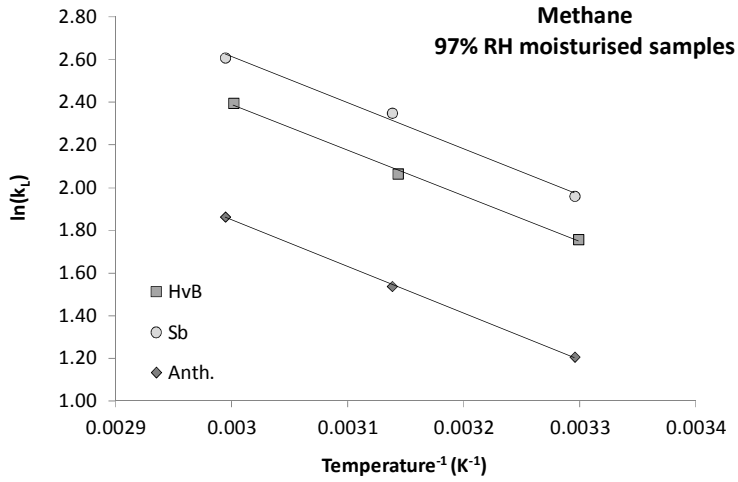


Figure 3-11. The methane Langmuir pressure for moisturised coal sample of different rank as a function of the inverse temperature to calculate the heat of adsorption (adsorption enthalpy) Myers, 2004.

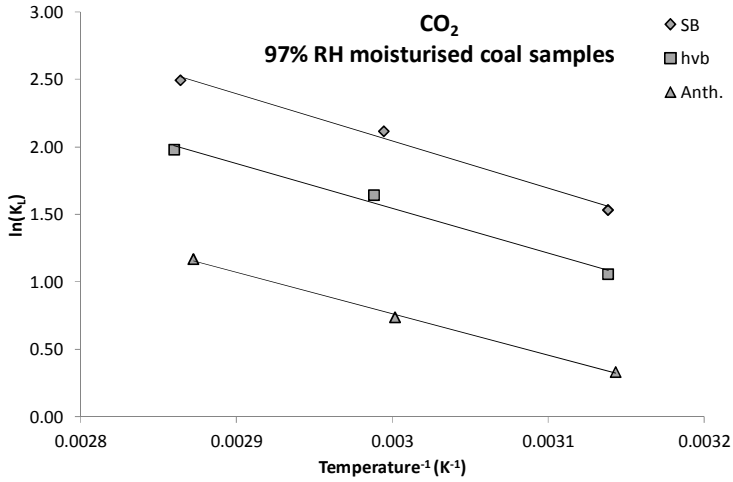


Figure 3-12. The carbon dioxide Langmuir pressure for moisturised coal sample of different rank as a function of the inverse temperature to calculate the heat of adsorption (adsorption enthalpy) Myers, 2004.

4 A preliminary evaluation of the CO_2 storage potential in unminable coal seams of the Münster Cretaceous Basin, Germany

4.1 Introduction

Currently energy production is largely based on the combustion of extensive masses of fossil fuels, resulting in shifts within the global biogeochemical carbon cycle. The consequence is a globally increasing CO_2 content in the atmosphere. Due to the causal interrelation between atmospheric CO_2 contents and global mean surface temperatures, the global warming may originate from anthropogenic CO_2 emissions. In order to diminish such effects, the Kyoto Protocol committed a reduction of the emissions of the three most important greenhouse gases (CO_2, CH_4, N_2O) for developed countries (United Nations, 1998).

Energy saving, the most sensible strategy for a CO_2-emission reduction, is limited due to the global energy demand. Improved combustion efficiencies alone wouldn't be sufficient either. Increased deployment of nuclear power, allowing a CO_2-reduced energy conversion, is accompanied with other disadvantages, e. g. the final storage of nuclear waste. Renewable energy sources are reasonably promising, however the period until such sources will satisfy the energy demand are assumed to last until the second half of this century. One of the greenhouse gas mitigation options during this transition period is carbon capture and storage (CCS), defining the process chain of separating CO_2 before or after combustion in the power plant, followed by compression of the gas and injection into appropriate geological formations in the subsurface.

Generally, CO_2 can be stored in the subsurface as a compressed gaseous or supercritical phase in porous and/or fractured rocks, by physical sorption on the effective surface area of unminable coals or by geochemical trapping as carbonate minerals. In order to achieve a reasonable efficiency, the geological storage of CO_2 at high density in saline aquifers should be performed at depth levels >800 m. Efficient sorptive storage of CO_2 in coal seams may occur at considerably shallower depths (200 – 800 m). The option of sorptive storage of CO_2 in coals would exclusively target unminable coal seams with no long-term production potential in order to prevent conflicts of interests. Future exploitation of coal seams used for CO_2 storage would require "venting" of the CO_2 to the atmosphere. Prior to the deployment of coal seams as a CO_2 storage reservoir, issues of future use under the aspect of changing economical conditions and new production techniques have to be considered carefully. Within the RECOPOL-Project of the European Union, about 760 tons of CO_2 have been injected into coal seams of the Upper Silesian Basin (van Bergen et al., 2006). However, the technology for large-scale CCS in coal seams is not readily available yet (IPCC, 2005). Nevertheless, this strategy may provide a contribution to greenhouse gas mitigation activities in the future, requiring the technological and economic feasibility.

Coal-related CO_2-storage holds two advantages: (i) Coal-fired power plants are often situated close to coal deposits, implying moderate transport distances to the target formations and (ii) CO_2 injection into coal seams can be combined with coal bed methane (CBM) production. Coal Bed Methane represents a hydrogen-rich fuel, practically free of toxic side products. CO_2-injection is considered to enhance CBM production (CO_2 Enhanced Coal Bed Methane, CO_2-ECBM, White et al., 2005).

The Münster Cretaceous Basin is a wide synclinal structure situated in the western part of North Rhine-Westphalia, Germany (Figure 4-1). The Palaeozoic bed rocks contain unminable Carboniferous coal seams. Several fossil fuel-fired power plants are situated within and around the basin. Therefore, the evaluation of the CO_2 storage potential in the coal seams of the basin is of economic interest. The objective of the present study has been the investigation of the existence of the CO_2 storage potential and the assessment of its importance. This has been done in order to define suitable areas for CO_2 storage and to determine the corresponding potential storage capacities considering regional geological and hydrogeological conditions.

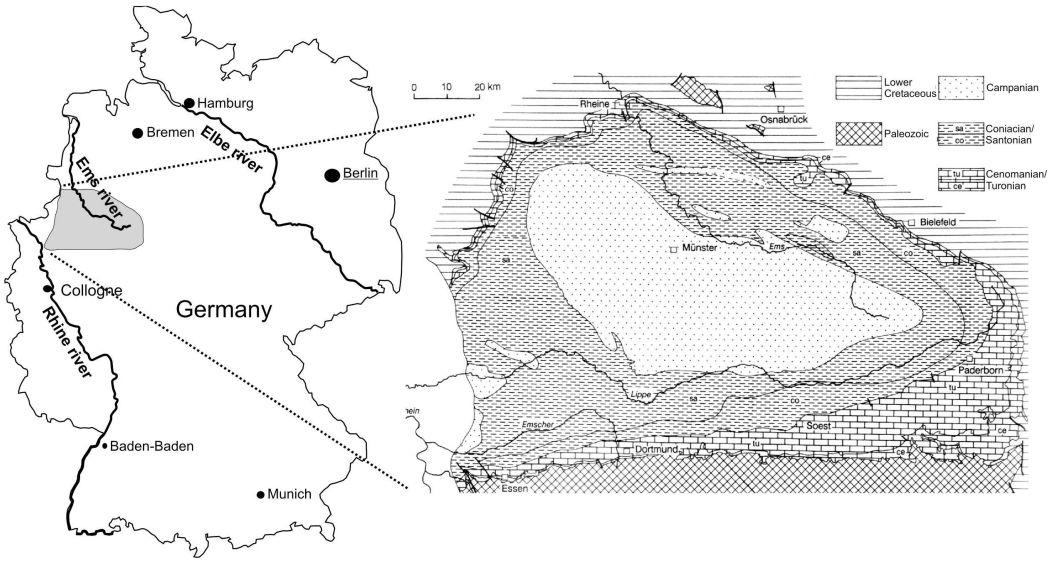


Figure 4-1. Position of the Münster Creataceous Basin in Germany (left) and geological overview without Cenozoic depositions (right, modified from Walter, 1995, after Arnold, 1964)

4.2 Geological setting of the Münster Cretaceous Basin

The geological evolution of the Münster Cretaceous basin has been described in detail by the Geological Survey of North Rhine-Westphalia, Germany (GLA, 1995). An evaluation with respect to CO_2 storage potentials relies on the recent configuration of the basin rather than on its evolution. Therefore, a short description of the recent basin configuration is given in the following.

The distinct geometry of the basin is characterized by a steep northern and a gently north-dipping southern flank (Figure 4-2). The deepest bedrock deposits in the northern part of the basin reach

maximum depths of approximately 2700 m (interpreted from maps in Baldschuhn et al., 2001). The basin can be separated into four units:

The first unit is formed by the basement, consisting of Upper Carboniferous bedrocks. These contain coal-bearing clastic sediments, which have been deposited between the Namurian C and Westphalian D. However, the deposits of the Westphalian D have been eroded almost completely. Distinct tectonical features of the bedrock are broad NE-SW-striking folds which originate from the Hercynian orogeny. The coal content of the coal-bearing Carboniferous is ~ 4% in the southern part of the basin, decreasing to the north (GLA, 1995). South of the Münster Basin the Upper Carboniferous reaches the surface. The coal seams represent the reservoir formation considered for the CO_2 injection strategy presented in this study. The sediments beneath and above the seams, consisting of sand-, silt and claystones are generally of low permeability. The permeability of the coals ranges between 0.02 and 0.5 mD (Gaschnitz, 2001), which is below the minimum permeability needed for CO_2-ECBM (e.g. Gale and Freund, 2001).

The Cenomanian/Turonian-Complex – the second unit – overlies the Carboniferous bedrock discordantly. It largely consists of carbonates and alternating carbonate-marl sequences. The complex represents a saline karst aquifer characterized by a hydraulic gradient driving water flow from north to south (Figure 4-2). The aquifer is confined by the underlying low permeable Upper Carboniferous clastic sediments and the overlying 'Emscher Mergel'. It is meteorically recharged by seepage water in the northern part of the basin where the aquifer crops out at the surface. At the southern outcrop of the Cenomanian-Turonian-Complex, the brine is in hydrodynamical equilibrium with fresh water aquifers. This implies a potential leakage pathway for injected CO_2 escaping the Carboniferous. The hydrogeology of the saline aquifer of the Münster Cretaceous basin has been described in several studies (Baskan, 1970; Fricke, 1961; GLA, 1995; Michel, 1963, 1983; Struckmeier, 1990).

The overlying 'Emscher Mergel' - the third unit - is a clayey marl separating the salt water of the Cenomanian-Turonian-Complex from the shallow fresh water aquifers in the Campanian and Cenozoic sediments, which represent the forth and uppermost unit of the basin. The Emscher Mergel is supposed to act as a cap rock, impending the upward migration of CO_2, entering the Cenomanian-Turonian-Complex. The Emscher formation is of middle Coniacian to lower Campanian age and is fractured by a complex fault system potentially decreasing its sealing efficiency. A detailed description of the formation, including a lithological description is given by Hiss, 2006. The effective permeability for CO_2 is ~1 to 3 nD (Wollenweber et al., 2009). The 'Emscher Mergel' and coeval depositions crop out zone follows the one of the Cenomanian-Turonian-Complex (see Coniacian/Santonian-distribution in Figure 4-1). The sand content of the marl increases in the western part of the basin, implying an increasing permeability.

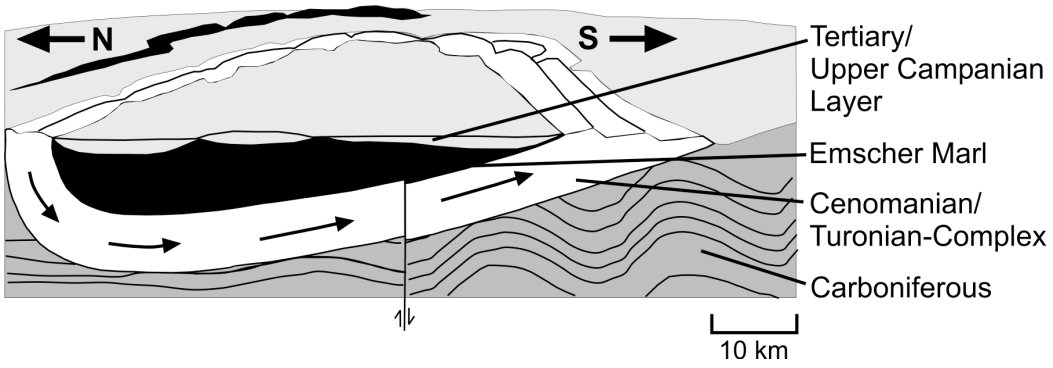


Figure 4-2. Schematic cross section through the Münster Cretaceous Basin. The arrows indicate the hydraulic gradients of the brine aquifer.

4.3 Methodology

4.3.1 Selection of the storage site and general approach

Migration through the 'Emscher Mergel' and transport by the saline aquifer of the Cenomania-Turonian-Complex represents the main potential leakage pathways for injected CO_2. Storage site selection was based on defining an area holding the lowest potential for leakage throughout the Münster Basin. This can be achieved by indications and estimations rather than by precise measurements. For estimating potential leakage risks the following indicators have been chosen:

- Coal bed methane concentration profiles in the Carboniferous
- Main ion-distribution in waters of shallow aquifers above the Emscher Mergel
- Occurrence and stable carbon isotope signatures of methane in waters of the shallow aquifers
- Evaluation of the fault system of the Münster Basin
- Hydraulic properties of the Cenomanian-Turonian-Complex

After defining a potential storage area by the indicators listed above, the coal inventory within this area was calculated by means of a computer-based model described below. Sorption experiments on coal samples enabled an estimation of the CO_2 sorption capacities of the calculated coal inventory within the confined area.

Many studies have been published recently on the potential of CO_2-ECBM. These studies list a series of screening criteria important for CO_2-ECBM site selection and the feasibility of this scenario (Amorino et al., 2005; Bachu et al., 2007; Byrer, 1999; Damen, 2005; Faiz, 2007; Frailey et al., 2006; Gale and Freund, 2001; IPCC, 2005; Mavor, 2004; Nelson et al., 2005; van Bergen et al., 2006). Coal seams suitable for CO_2-storage should:

– Have sufficient capacity for injecting large volumes of CO_2

- Possess adequate permeability of at least 1 to 5 mD. This relates to an adequate injectivity to allow injection of CO_2 into the subsurface at reasonable rates
- Be covered by an effective cap rock in oder to avoid gas movement to the surface or to e.g. adjacent active (coal) mining
- Have high gas saturation (from a methane-production perspective)
- Be unminable, now or in the future. Unminable coals are coals that are too thin, too deep, or too unsafe to mine; they may be too high in sulphur or mineral matter, or be too low in heat value to be economically profitable
- Possess suitable coal geometry with preferentially few, thick (>1 m) rather than multiple, thinner seams. However, this in a way contradicts the argument of unminable since thick coal seams have a higher potential of being mined than multiple thin seams
- Have a favourable structure (minimal faulting and folding) with lateral continuity
- Be located at an adequate depth. Recent studies did not investigate depth intervals deeper than 1500 m. Higher depth than that will mainly depend on permeability and drilling costs
- Possess the ability to dewater the reservoir formation and a low water saturation because coals with low water saturation are easier to dewater prior to CBM production and CO_2 injection

4.3.2 Coal inventory calculations

The coal inventory calculation model (KVB-Model) of the Geological Survey of North Rhine-Westphalia (NRW), Germany has been used to determine coal volumes in the target area of the Münster Cretaceous Basin. The KVB-model is based on digital projections of the coal inventory of all hard coal deposits in NRW derived from drilling data. It contains no opportunity for error estimations. A detailed description of the model is given by Juch et al., 1994 and Juch, 1997. The model subdivides the coal seams into subsections, which are linked to attributes such as 3D coordinates, dipping, thickness, and volumes in a data base. The present coal volumes in the target area have been calculated by linking the data base to a geographic information system (ArcGis Desktop 9.1, ESRI Redlands, CA, USA) and isolating the relevant seam subsections from the generic data.

4.3.3 Samples

4.3.3.1 Coal sample

For gas sorption experiments, one reference coal sample from the German Ruhr District (southern Münster Basin; coal mine Auguste Victoria, Marl), has been used during the course of this study. The maturity of the coal sample is high-volatile bituminous A, it has an ash content of 2.7 and an “as received” moisture content of 1.7 %. The mine is still in operation and sample material has been

obtained as a large block directly from the excavation area. A representative aliquot of the sample was crushed and milled to particle sizes <200 µm.

4.3.3.2 Water samples

For analysis of stable carbon isotope signatures water samples from shallow groundwater aquifers in the Münster Basin were collected in pre-evacuated spherical steel containers of 30 mm diameter equipped with a toggle shut-off valve (Hoke, 1500 Series). Sampling locations have been kept anonymous. Sampling was performed by dipping the shut-off valve completely into the water, opening it and closing it again after approximately 30 seconds.

4.3.4 Sorption experiments

In order to determine the sorptive gas storage capacity as a function of depth (pressure and temperature), CH_4 and CO_2 single-gas sorption experiments were performed on "as received" coal sample material from the coal mine Auguste Victoria (described above) at three different temperatures (40, 50, 60°C). These temperatures were considered relevant for CO_2 injection in the coal seams.

Details on the manometric method for measuring the sorption isotherms is provided in Section 2.2.1.1

4.3.5 Gas chromatography- isotope ratio mass spectrometry (GC-irmMS) measurements

Analyses of stable carbon isotope signatures of dissolved methane in the shallow groundwater samples described above have been conducted by GC-irmMS-measurements, performed on a Delta Plus XL mass spectrometer (ThermoFinnigan, Bremen, Germany) equipped with a GCC III combustion interface and linked to a 6890A gas chromatograph (Agilent, Waldbronn, Germany). Separation of the gas components was carried out on a CARBOXEN 1010 PLOT (Supelco, Bellefonte, PA, USA) fused sillica capillary column (30m x 0.32 mm) with helium carrier gas (flow rate: 5 mL/min) at 100 °C (isothermal).

Calibration of the carbon isotope reference gas used (carbon dioxide) was performed by means of a certified reference standard (Chiron, Trondheim, Norway) containing *n*-undecane (-26.11 ‰ vs PDB), *n*-pentadecane (-30.22 ‰ vs PDB) and *n*-eicosane (-33.06 ‰ vs PDB).

Transfer of the dissolved and free methane from the sample containers onto the GC-column was achieved by connecting the toggle shut-off valve to a stainless steel vacuum system with a 250 µL sample loop and a pressure transducer. After evacuating the system the shut-off valve was opened and the gas from the sample container was expanded into the sample loop. The sample loop was then switched into the carrier gas stream of the capillary column by a VALCO-valve (VICI AG International, Schenkon, Switzerland). Transfer of evaporated water onto the capillary column was prevented by a $CaSO_4$-trap.

4.4 Results and Discussion

4.4.1 ECBM site selection

4.4.1.1 CBM concentration profiles

Concentrations of methane-in-place in the Carboniferous as a function of depth is an indicator for the integrity of the Cretaceous overburden. In the Ruhr Basin (the southern portion of the Münster Cretaceous Basin), two characteristic concentration profiles have been observed: the Lower Rhenish type and the Westphalian type (Kaffanke, 1988). The Lower Rhenish profiles are characterized by almost gas-free zones beneath the overburden which can reach down to about 100 to 400 m below the top of the Carboniferous. In contrast, below the overburden in the Westphalian type profiles concentration maxima with gas contents >4 m^3/t are shown. Two theories have been proposed concerning the evolution of the two gas distribution characteristics. During the late Carboniferous, the deposited peat was coalified. After vast erosion processes at the end of the Carboniferous, the coal-bearing bedrock was not efficiently sealed any more, until the Cretaceous overburden deposited. During this period the gas was released from the coal seams resulting in gas free coals even in considerable depths. A basin simulation study of the bore hole "Münsterland-1" did not support the hypothesis of a post-Carboniferous re-coalification (Littke et al., 1994). Hedemann (1970) established the hypothesis of gas migration from the Cretaceous overburden into the Carboniferous. Although this hypothesis was restated by von Treskow, 1985, the Westphalian profiles are nowadays regarded as indication for the sealing efficiency of the overburden and the present CBM gas-in-place is attributed to a Carboniferous residue (Kaffanke, 1988). Several bore holes in the central part of the basin revealed high gas contents ($\geq$ 10 m^3/t) beneath the overburden (Gaschnitz, 2001), indicating its reasonable integrity in this area.

4.4.1.2 Ion distribution in waters of shallow aquifers

Although not directly involved into the gas play, the geochemical attributes of the shallow aquifers provide important information, appropriate for assessing the sealing efficiency of the 'Emscher Mergel'. Figure 4-3 shows the typical ion distribution patterns occurring in waters of shallow aquifers in the Cretaceous Basin. This distinct feature of shallow aquifers in the Münster Basin was initially observed by Lotze, 1958. Such waters, dominated by Na^+, Cl^- and HCO_3^-, result from mixing of fresh water and brine accompanied by ion exchange (e.g. Appelo and Postma, 2005), and therefore indicate a hydrodynamic equilibrium of the brine and the freshwater aquifer systems by migration pathways through the 'Emscher Mergel'. The present geological framework has remained essentially unchanged (stable) since the Cretaceous/Tertiary-boundary (65 Ma). On the other hand, sealing periods of 5000 years concerning sequestered CO_2 are considered sufficient (Zhou et al., 2004). Consequently, brine migration through the 'Emscher Mergel' does not imply insufficient sealing efficiency of the formation over periods relevant for CO_2 storage.

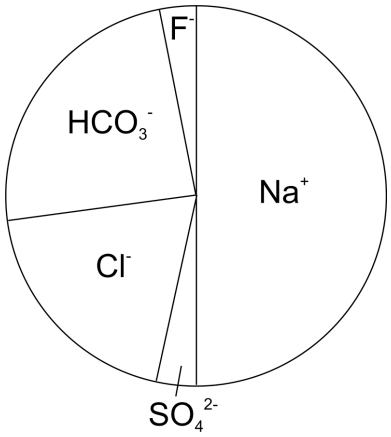


Figure 4-3. Typical ion distribution in shallow aquifer waters of the Münster Cretaceous Basin.

4.4.1.3 Concentrations and stable carbon isotope signatures of dissolved CH_4 and CO_2 in shallow aquifers

Another distinct geochemical feature of shallow aquifers in the Münster Cretaceous Basin is the local occurrence of significant quantities of dissolved methane (Weidmann, 2005) in shallow aquifers (<100 m depth). Such phenomena could result from Carboniferous methane migrating through the 'Emscher Mergel' into the shallow aquifers. The isotopic CH_4 composition was expected to provide further hints on its origin and the sealing efficiency of this formation. For this purpose, 17 water samples have been analysed by compound-specific isotope mass spectrometry (GC-irmMS). Thermogenic methane can be distinguished from microbial methane by its isotopic signature and the contents of higher molecular-weight hydrocarbon gases (Bernard, 1978). While thermogenic methane has stable carbon isotope signatures $\delta^{13}C > -55$ ‰ vs. Vienna PeeDee Belemnite (VPDB), microbial methane derived from methanogenic archaea is strongly depleted in ^{13}C. Gaschnitz (2001) determined the compound specific stable carbon isotope signatures of CH_4 in coal samples of the "Natarp-1" well (Figure 4-4). These ranged between -26 and -43 ‰, indicating clearly a thermogenic origin. In contrast, the CH_4 isotope signatures in the shallow aquifer waters investigated in this study indicate a predominantly microbial origin (Table 4-1). Thus, significant migration of Carboniferous coalbed methane across the 'Emscher Mergel' does not appear to occur. This finding supports that the 'Emscher Mergel' formation has a good sealing efficiency.

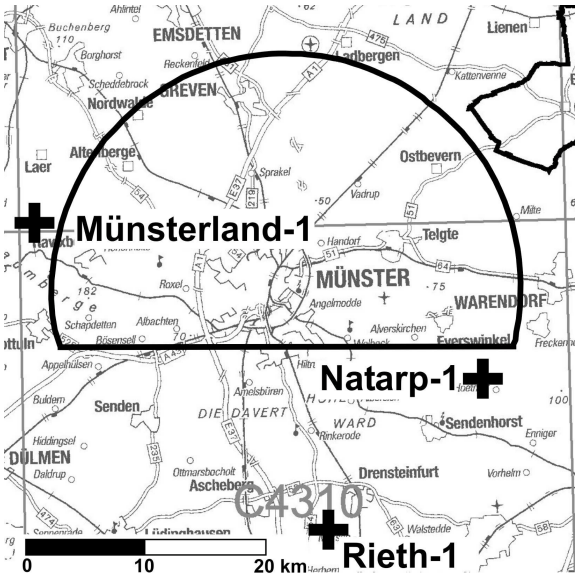


Figure 4-4. Map of the study area with the proposed CO_2 storage option with CBM exploration wells Nartarp-1 and Rieth-1, and the deep Münsterland research well.

Table 4-1. Results of the stable carbon isotope analaysis. The isotope signatures are expressed relative to VPDB. Most measurements have been performed in dublicates.

	$\delta^{13}CH_4$			CH_4 concentration		$\delta^{13}CO_2$		CO_2 concentration		CH_4/CO_2	
sample	anal 1	anal 2	mean	(mol/l)	(mg/l)	anal 1	anal 2	mean	(mol/l)	(mg/l)	(mol/mol)
1	-27,9	-11,3	-19,6	2,08E-06	0,033	-1,3	-4,4	-2,9	1,78E-06	0,078	1,17
2	-72,5	-72,7	-72,6	2,81E-05	0,449	-10,3	-12,5	-11,4	1,02E-05	0,447	2,76
3	-42,4		-42,4	3,53E-07	0,006	-8,1		-8,1	5,46E-07	0,024	0,65
4	-60,4	-61,9	-61,2	1,27E-04	2,028	-12,3	-13,5	-12,9	1,24E-05	0,544	10,26
5	-63,9	-64,3	-64,1	1,87E-04	2,996	-8,5	-10,3	-9,4	6,45E-06	0,284	29,02
6	-58,1	-59,6	-58,9	9,80E-05	1,568	-16,4	-13,8	-15,1	1,23E-06	0,054	79,67
7	-62,3	-62,4	-62,3	1,02E-05	0,163	-16,3	-16,7	-16,5	4,49E-05	1,976	0,23
8	-60,9	-61,1	-61,0	3,30E-04	5,285	-11,2	-10,8	-11,0	8,74E-06	0,385	37,80
9	-74,4		-74,4	1,16E-05	0,186	2,5		2,5	3,41E-07	0,015	34,06
10	-36,0		-36,0	2,37E-05	0,379	-14,5		-14,5	2,61E-05	1,150	0,91
11		-69,6	-69,6	1,34E-06	0,021		-16,0	-16,0	1,09E-05	0,480	0,12
12	-35,0		-35,0	2,53E-07	0,004	-4,5		-4,5	3,47E-07	0,015	0,73
13	-48,3		-48,3	2,39E-04	3,822	-13,6		-13,6	4,38E-06	0,193	54,49
14	-66,6	-66,7	-66,7	3,24E-04	5,183	-12,2	-12,1	-12,1	1,08E-05	0,474	30,09
15	-59,5	-58,7	-59,1	1,87E-06	0,030	-14,5	-15,2	-14,9	3,37E-05	1,483	0,06
16	-74,9	-75,1	-75,0	1,41E-04	2,264	-10,5	-10,7	-10,6	1,49E-05	0,654	9,52
17	-70,7	-71,5	-71,1	1,12E-04	1,790	-9,4	-11,7	-10,5	6,59E-06	0,290	16,97

Stable carbon isotope signatures were also determined for dissolved CO_2 from shallow wells. Most samples had values around -10 ‰ vs. VPDB, indicating a mixed origin due to decarboxylation of organic matter and carbonate-decomposition.

Fault system

The Münster Cretaceous Basin is affected by a complex fault system which has been described in detail by Drodzewski and Wrede (1994). This implies potential leakage pathways for injected CO_2 to the surface. In the Münster Cretaceous Basin, gas eruptions have been observed partly at fault zones

associated with the occurrence of strontianite ($SrCO_3$), indicating migration pathways through the overburden. Due to mining of shallow deposits of this mineral over large areas in the 19th century and based on modern exploration data, the structures of strontianite occurrence have been recognized in detail (Dölling and Juch, 2004). Even if such structures are not connected to the coalbearing strata, strontianite-affected areas have to be avoided with respect to CO_2 storage. To minimize leakage through faults, CO_2 storage is restricted to areas showing high overburden thickness (> 700 m, considered from the base of the 'Emscher Mergel').

4.4.1.4 Cenomanian-Turonian-Complex

The Cenomanian-Turonian-Complex represents a brine aquifer and has been described as low permeable, even virtually stationary in the central part of the basin (Struckmeier, 1990), where the aquifer reveals the highest hydraulic resisitivity due to its largest extension. Therefore, low transport velocities of the aquifer are expected in the basin centre, scaling down the leakage risks through the Cenomanian/Turonian-Complex. The water supply area in the northern part of the basin is elevated at approximately 120 m above sea level. The area of hydrodynamic equilibrium with fresh water aquifers in the southern basin part is elevated at approximately 100 m above sea level. Due to the marginal hydraulic potential generated by this elevation difference over a lateral distance of >50 km, transport velocities below 1 m/a have been estimated.

4.4.2 Estimation of the CO_2 storage potential in Carboniferous intervals of the Münster Cretaceous Basin

4.4.2.1 Criteria for the selection of the storage region

Considering the results presented above, the following criteria have been defined for a suitable CO_2 storage location:

- It should be south of the deepest basin threshold, in order to prevent upward migration of injected CO_2 along the steep northern flank
- It should be located in the central part of the basin, where the Cenomanian/Turonian-Complex provides a maximum hydraulic resisitivity, resulting in low transport rates
- Thickness of the overburden should exceed 700 m, measured from the base of the 'Emscher Mergel'
- The western part of the basin should be avoided due to increasing sand contents of the 'Emscher Mergel'
- The southern part of the basin should be avoided because of the occurrence of strontianite-associated faults

- A minimum distance of 10 km from mining activities in the Ruhr area and to mining concessions in the southern part of the basin, where the Cretaceous overburden is or will be anthropogenically affected

Based on these criteria a CO_2 storage area of 820 km^2 has been defined (Figure 4-4). Table 4-2 shows the thickness of the 'Emscher Mergel' and the overburden from its base at three drilling locations. These data have been adopted from Gaschnitz (2001) and Kelch, 1963.

Table 4-2. Thickness of the Creataceous overburden considered from the base of the 'Emscher Mergel' (OB) and thicknesses of the 'Emscher Mergel' (???), interpreted from the documentation of the drillings indicated in Figure 4-5.

Well	Thickness OB (m)	Thickness EM (m)
Münsterland-1	1400	800
Natarp-1	1000	500
Rieth-1	710	360

4.4.2.2 Gas sorption as a function of depth

Figure 4-5 shows the results of the interpretation of the CH_4 and CO_2 sorption measurements on Auguste Victoria coal at 40, 50 and 60°C. The isotherms are not presented on an ash-free or dry ash-free basis because it is known that (i) CO_2 and CH_4 are able to physically sorb on inorganic materials like clay minerals and that (ii) CO_2 dissolves into water to significant amounts (Busch et al., 2008. Resulting Langmuir parameters are summarised in Table 4-3.

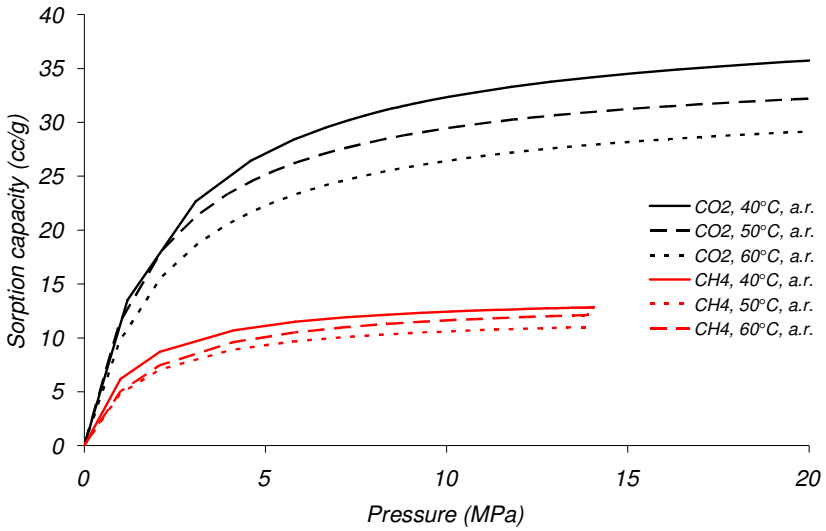


Figure 4-5. Comparison of CH_4 and CO_2 sorption isotherms on as-received Auguste Victoria coal at different temperatures.

In order to consider volumetric effects (e.g. volume of the sorbed phase, uncertainties in void volume calibration) associated with CO_2 sorption on the coal sample a fitting procedure proposed by Siemons

and Busch (2007) has been used in this study to take into account of these effects. This has been done in order to find a way to make this capacity estimation concept comparable to other studies (e.g. Bachu et al., 2007; Wong et al., 2007). However this interpretation potentially neglects useful information that can be gathered from excess sorption isotherms. Absolute (or total) sorption capacities are used throughout the entire literature for CBM potential or CO_2 storage capacity assessment. However, these can only be regarded as an interpretation of excess sorption isotherms and hence, estimates are possibly associated with significant errors, especially for CO_2 (s. below).

Table 4-3. Comparison of CO_2 and CH_4 Langmuir parameters.

T (°C)	n_L (mmol/g)	K_L (MPa)
CH_4		
40	0.62	1.26
50	0.61	1.72
60	0.55	1.52
CO_2		
40	1.78	2.34
50	1.59	2.06
60	1.45	2.30

As already mentioned above, it is shown here that gas sorption capacity decreases with temperature and this decrease is larger for CO_2 than for CH_4 (Figure 4-6). The decrease in sorption capacity with temperature is ~0.26 to 0.30 cc/g/K for CO_2 and ~0.09 cc/g/K for CH_4 and, thus similar for the three different pressures chosen in this study. Regression for all linear fits is excellent with R^2=0.98 to 1.00.

It will be shown later that pressure at reservoir depth in this study partly exceeds the maximum experimental pressure range. Therefore, for pressures higher than 20 MPa, sorption capacities have been extrapolated which may additionally result in an uncertainty factor.

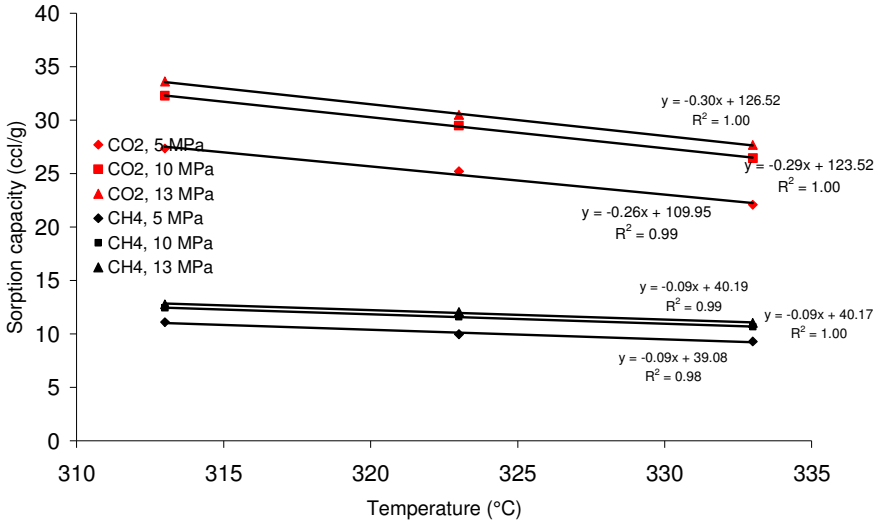


Figure 4-6. CH_4 and CO_2 sorption for Auguste Victoria coal as a function of temperature at different pressures.

4.4.2.3 CO_2 storage and CBM recovery potential

For the estimation of the CO_2 storage potential in unminable coal seams of the Münster Cretaceous Basin the coal inventory model of the Geological Survey of North-Rhine Westphalia (KVB-model) has been used. It is based on a comprehensive assessment of the German hard coal deposits by means of a detailed geometric 3D model (Juch et al., 1994, Juch, 1997). Further parameters (geothermal gradient, CH_4 gas-in-place, etc.) have been obtained from Gaschnitz (2001). Reservoir pressure was calculated assuming a hydrostatic pressure gradient of 0.001 MPa m^{-1}.

For the determination of the coal volumes in the target area the data of the KVB-model has been transferred to an ArcGIS-System. Subsequently coal volumes were determined and subdivided into depth intervals of 50 m. A depth range between 1000 and 3000 m was chosen in order to cover ~90 % of the coal-in-place for this area. This results in a bell-shaped curve for the amount of coal with a maximum at 2100 m, yielding a total cumulative value of ~37.5 Gt (10^9 t) (Figure 4-7).

Figure 4-8 shows the cumulative CO_2 storage potential of the target area. All parameters used for this calculation are listed in Table 4-4. A summary of the results is presented inTable 4-5. Three different approaches have been considered:

- Case A. The coal contains no CBM (after primary CBM recovery). Therefore all sorption sites are accessible to CO_2. The completion factor is 100 %. This results in a cumulative CO_2 storage potential of 1220 Mt.
- Case B: The coal contains an average CH_4 GIP of 10 m^3/t. This results in competitive sorption of CO_2 and CH_4. Recovery and completion factors are 100 %. This results in a cumulative CO_2 storage potential of 490 Mt.

- Case C: Same as case B: recovery and completion factors (80 and 40 % respectively) has been considered (Bachu et al., 2007; van Bergen et al., 2001). This results in a reduction of the CO_2 storage capacities of 68 % and in a cumulative CO_2 storage potential of 160 Mt.

Figure 4-9 presents the variations of the sorbed gas concentrations for CO_2 and CH_4 with depth, considering initial CH_4 GIP contents of 10 m³/t. The decrease in CO_2 sorption capacity is caused by a much stronger temperature effect as compared to CH_4. Therefore, below a certain depth the increase in CO_2 sorption with pressure is compensated by its decrease with temperature. These effects result in increasing CH_4 sorbed gas concentrations with depth. In this example no CH_4 will desorb at depths below ~2900 m.

Table 4-4. Parameters used for determination of CO_2 storage potential in Münster Basin.

Parameter	**Value**	**Unit**
T-gradient	0.04	°C/m
P-gradient	0.01	MPa/m (hydrostatic)
Coal density	1.35	t/m³
CH_4 GIP[1]	10	m³/t
Ash content	10	%

Sorption-parameters[2]

	Langmuir Volume n_L (mmol/g)	Langmuir Pressure P_L (MPa)	T-dependent parameter m (mmol/g)
CH_4	0.62	1.26	-0.004
CO_2	1.78	2.34	-0.013

[1]GIP = CH_4 gas-in-place

[2]Determination of sorption parameters at 40°C; T-dependency determines increase or decrease of sorption capacity with pressure. Moisture and ash contents not considered.

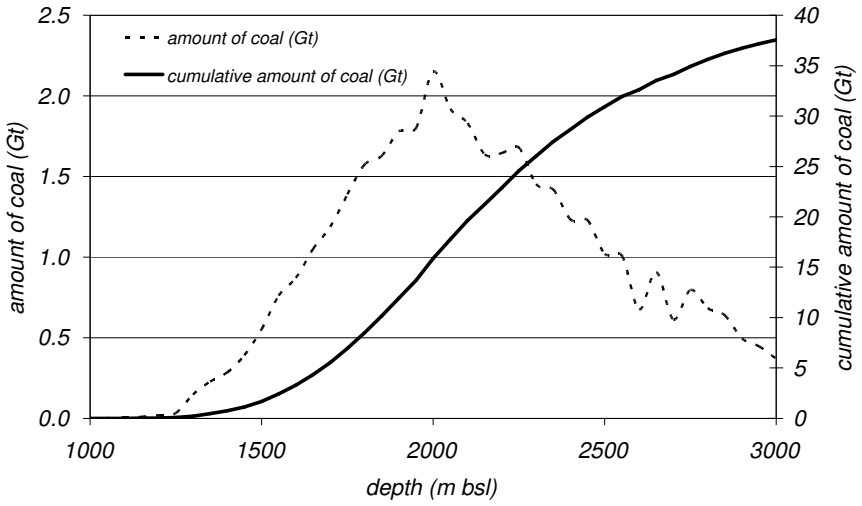


Figure 4-7. Amount of coal for selected area in the target area of the Münster Basin.

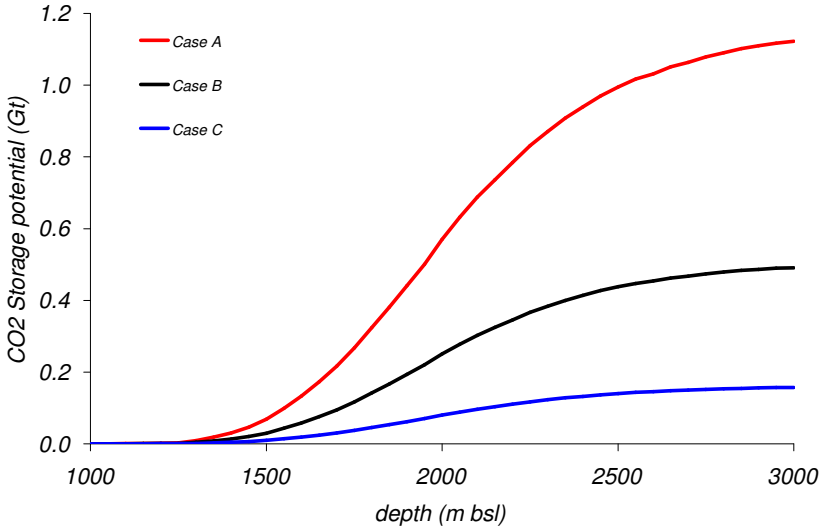


Figure 4-8. CO_2 storage potential in the target area.

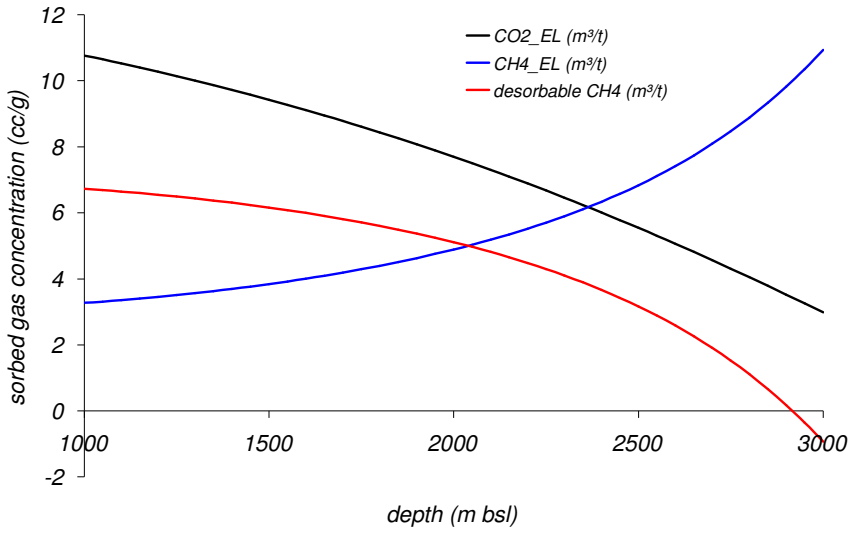


Figure 4-9. CO_2 storage capacity as a function of depth, considering an initial methane gas-in-place of 10 m³/t.

Table 4-5. Summary of cumulative amount of coal in the target area as well as CO_2 storage potentials for the different cases considered.

	target area	**unit**
cumulative mass of coal	37.5	Gt
depth of maximum coal mass	2.1	km
average coal thickness	37	m
target area	820	km²
Case A: maximum cumulative CO_2 storage potential (no CH_4 GIP)	1.28	Gt
Case A: relative maximum CO_2 storage potential (no CH_4 GIP)	1.56	t/m²
Case B: maximum cumulative CO_2 storage potential (CH_4 GIP)	0.56	Gt
Case B: relative maximum CO_2 storage potential (CH_4 GIP)	0.68	t/m²
Case C: maximum cumulative CO_2 storage potential (CH_4 GIP, considering completion and recovery)	0.18	Gt
Case C: relative maximum CO_2 storage potential (CH_4 GIP, considering completion and recovery)	0.22	t/m²

4.4.2.4 Uncertainties in determining the ECBM potential in the Münster Cretaceous Basin

Considering the screening criteria for CO_2-ECBM listed above, the central Münster Cretaceous Basin is not an ideal location for injecting CO_2 into coal seams. Permeabilities are low (<0.5 mD), the coal seam formations are faulted and folded and the depth of maximum coal volumes is around 2000 m (while coal

seams are at 1000 to 3000 m depth), indicating high drilling costs and low injectivities. Low injectivities and low accessibilities can only be compensated by multiple injection wells horizontal and multilateral drilling (fishbone patterns), again increasing drilling costs significantly.

There are many uncertainties associated with the considerations leading to CO_2 storage potential estimations in this study. Only one coal sample has been used in the experimental program that was considered to be representative of the entire coal strata underlying the Cretaceous formations in the Münster Basin. In recent studies Busch et al., 2003a and Siemons and Busch, 2007 have shown that the CO_2 sorption capacity for various coals under the same experimental conditions can vary up to 100 %. Since these differences are usually between very low mature coals (lignites) and hard coals, a potential error in the sorption capacity can be considered as high as 50 %. This value is supported by low pressure/temperature CO_2 sorption isotherms on a suite of coals from the southern Münster Basin, covering maturities from 0.76 to 2.23 % VRr.

Further, as pointed out by e.g. Bachu et al. (2007) and IPCC (2005) permeabilities lower than 1 mD are not suitable for CBM recovery or CO_2 injection and a maximum depth for ECBM operations of 1300-1500 m has been proposed. Since in the present study area permeabilities are <0.5 mD (Gaschnitz, 2001), the CO_2 storage potential would essentially reduce to zero using this constriction. Low permeabilities cause low injectivities and therefore multiple cost-intense injection wells have to be drilled for providing a reasonable injection rate (e.g. CO_2 emissions of an average coal-fired power plant). Directly related to the permeability is the CBM recovery and the CO_2 storage factor, i.e. the part of the coal seam that is accessible to CO_2 or where methane can be produced from. Here, following van Bergen et al. (2001) a value of 80 % has been used for the CO_2 storage estimations (s. above). This value, however was applied for CBM recovery, not for CO_2 storage. Because CO_2 injection in coal seams will cause swelling, leading to even lower permeabilities, the recovery factor has to be reduced to a much more reasonable value of 20 %.

Lastly, the whole CO_2 storage potential estimation is based on a coal inventory calculation model (KVB-model) that is mainly based on extrapolations between exploration wells. Therefore an additional estimated error of 20 % can be assumed.

Considering an uncertainty in the CO_2 and CH_4 sorption isotherms of 50 %, a reduction in the recovery factor from 80 to 20 % and an error in the coal volumes of 20 %, the CO_2 storage potential ("Case 3", s. above) reduces realistically from 160 Mt to a range of 16 to 55 Mt.

A further uncertainty is the CBM content of the target seams. Although an average concentration of 10 m^3/t seems reasonable, lower gas contents towards larger depths can be expected. This will increase CO_2 storage capacities; however will reduce the ECBM potential and, hence economic benefits of this technology.

Nevertheless technologies need to be investigated for the future and this example is certainly rather a possibility for the midterm when e.g. energy prices are high enough to consider high drilling costs or low CO_2 storage and CBM recovery rates. Screening for "sweet spots" with locally high permeabilities and high coal volumes at reasonable depth could be one strategy scenario.

4.5 Conclusion

It is shown in this study that site selection suitable for CO_2 storage and the estimation of its storage capacity is very complex. Among others, geological, hydrogeological, tectonic, petrophysical, and reservoir engineering information need to be considered in the assessment of ECBM potentials.

In the Münster Cretaceous Basin, a storage area of 820 km² has been defined, yielding under the criteria chosen in this study an estimated storage potential of 160 million metric tons of CO_2 within 37.5 Gt of coal. This dimension would provide sufficient capacity for industrial storage applications. Several fossil fuel fired power plants operate in the vicinity of the basin, implying moderate transport distances when deploying CCS. However, several aspects are considered to restrict the suitability of the basin as a CO_2 storage option. First, including possible uncertainties the CO_2 storage potential estimation reduces to a range of 16 to 55 Mt. Second, suitable technologies for CO_2 injection in coals characterized by permeabilities ≤0.5 mD and depth larger than ~1500 m are currently not available. Third, the defined storage option is situated in a densely populated area (e.g. the city of Münster), comprising a high sensitivity of the area concerning risks on health, safety and environment. Furthermore, leakage risks by the complex fault systems of the basin are understood only on a basic level.

5 High-pressure methane and carbon dioxide sorption on coal and shale samples from the Paraná Basin, Brazil

5.1 Introduction

Worldwide coal-bed methane (CBM) resources are estimated to range between 2976- 12649 x 10^{12} scf (84.2 - 358.2 x 10^{12} m^3) (Murray, 1996). Conventional proven gas resources are in the order of 6533 scf (185 x 10^{12} m^3) (BP Statistical Review of World Energy, 2009). Considering this volume of conventional proven gas resources, corresponding CBM gas volumes would be 46% (minimum estimate) or 193% (maximum estimate) (Holz et al., 2010). Presently CBM is being produced or under exploration in the USA, Canada, China, Australia, Germany and other countries.

In Brazil the principal coal resources occur in the southern part of the Paraná Basin, associated with the Permian age Rio Bonito Formation. Earlier studies (Kalkreuth and Holz, 2000; Kalkreuth et al., 2003) have identified the Santa Terezinha coalfield (Figure 5-1), Rio Grande do Sul (RS), as the prime candidate for coal-bed methane exploration in Brazil, based on coal distribution (coal thickness, lateral continuity of coal beds), size and depth of coal beds and coal rank, estimating a CBM gas-in-place (GIP) volume of 672 x 10^9 scf (19 x 10^9 m^3) for this coalfield.

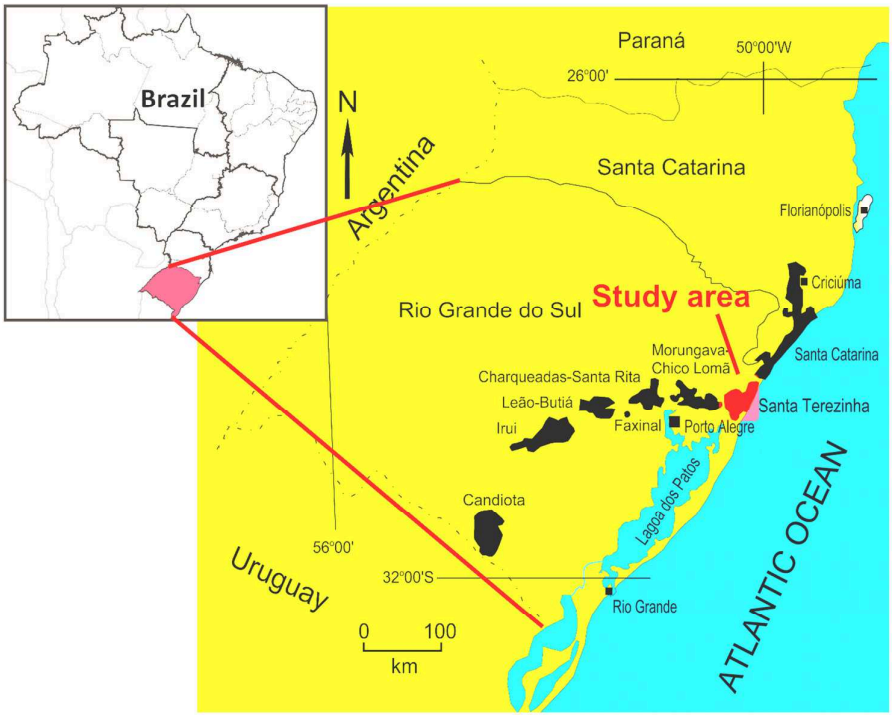


Figure 5-1. Location of the Santa Terezinha coal field, State of Rio Grande do Sul, Brazil (Kalkreuth et al., 2008b).

In 2007 the first Brazilian CBM test well (CBM 001-ST-RS) was drilled in the Santa Terezinha Coalfield (Figure 5-1), where samples from 12 coal seams and carbonaceous shales were collected from an depth interval of 605 to 638 m using wire line core retrieval techniques, followed by canister desorption tests and coal quality analyses of a total of 24 samples (Kalkreuth et al., 2008a; Kalkreuth et al., 2008b). Total gas contents (desorbed gas, lost gas, estimated residual gas) were found to range from 0.34 to 2.18 m^3/t with an average value of 1 m^3/t). Gas composition was determined on nine samples, indicating that methane constitutes > 94 Vol. % in all samples (Kalkreuth et al., 2008b), with minor contributions of hydrocarbon homologues (ethane, propane, butane), CO_2 and N_2. Stable carbon isotope values indicate a mixed (thermal/biogenic) origin of the methane (Kalkreuth et al., 2008b). Based on the averaged total desorbed gas volume, and 3D modeling of the coal volume in an area 20 x 40 km (Kalkreuth et al., 2008b) a total gas in place (GIP) of 194 x 10^9 (5.5 10^9 m^3) CH_4 was estimated to be associated with the coals and carbonaceous shales.

Only few studies have been published on the evaluation of the gas storage capacity of coals from Brazil. Soares, 2007 performed sorption experiments on dry coals from Santa Catarina State at sub-atmospheric pressures (<1 bar) and at a temperature of 30°C. They report CO_2 storage capacities ranging between 0.089 and 0.186 mmol/g.

In the present study on seven samples (coal and carbonaceous shale) from the CBM-001-ST-RS well (Table 5-1), high pressure sorption isotherms were measured for methane (CH_4) and carbon dioxide (CO_2), to evaluate the potential for coalbed methane (CBM) production, enhanced CBM recovery (CO_2-ECBM) and CO_2 sequestration in the Santa Terezinha coalfield.

Earlier studies revealed that the moisture content of coal has a reducing effect on methane (Joubert et al., 1973) and carbon dioxide sorption capacity (Crosdale et al., 2008; Day et al., 2008a; Krooss et al., 2002; Ozdemir and Schroeder, 2009). To evaluate the effect of moisture for Brazilian coals, high pressure sorption isotherms for methane and carbon dioxide have been measured on one coal, first in the as received moisture and then in the moisture equilibrated state. In addition, this study includes five shale samples (Table 5-1) considered to be the principal petroleum source rocks of the Paraná Basin (Ponta Grossa Fm., Devonian; Irati Fm., Permian).

5.2 Geological setting

The Paraná Basin is a huge intracratonic basin, located in southern Brazil, Paraguay, Uruguay and Argentina, covering an area in excess of 1,400,000 km^2. Sediments and volcanic rocks of the basin range in age from Ordovician to Cretaceous (Milani et al., 2007; Zalãn et al., 1991; Zalãn et al., 1990), with a cumulative thickness in excess of 7000 m in the depocentre. The samples analysed in this study come from the Permian age Irati and Rio Bonito formations and from the Devonian age Ponta Grossa Formation.

mple list and results of proximate and petrographic analyses, for stratigraphic position of canister samples see Fig. 2.

rm	Age	Sample Type	Seam interval, (Canister #)	Depth [m]	Total Gas Content [m^3/t coal]*	M.V. [%] (M.V. % daf)	Ash Yield [wt.%]	TOC [wt.%]	VRr [%]	Moisture Content [wt.%, a.r.]	VIT, mmf [Vol%]	LIP, mmf [Vol%]
ti	Permian	shale	n.d.	n.d.	n.d.	n.d.	n.d.	1.62	n.d.	0.92	n.d.	n.d.
ti	Permian	shale	n.d.	n.d.	n.d.	n.d.	n.d.	24.21	n.d.	1.65	n.d.	n.d.
ti	Permian	shale	n.d.	n.d.	n.d.	n.d.	n.d.	11.66	n.d.	1.20	n.d.	n.d.
o Bonito	Permian	carb sh	L1, (2)	609.10	0.38	5.00 (79.37)	93.11	1.73	2.61	1.38	10.0	0.0
o Bonito	Permian	carb sh	L2, (3)	610.30	1.04	9.94 (39.99)	67.21	21.09	1.51	1.33	42.0	0.5
o Bonito	Permian	coal	C, (7)	618.24	1.69	19.73 (37.88)	35.8	n.d.	0.82	0.98	46.0	6.0
o Bonito	Permian	coal	D, (11)	620.80	2.18	21.26 (43.19)	41.99	43.9	0.92	0.93	53.0	9.0
o Bonito	Permian	carb sh	G, (20)	630.35	0.68	15.20 (42.26)	61.1	n.d.	1.62	0.89	20.0	6.0
o Bonito	Permian	coal	H, (22)	636.47	1.03	22.72 (43.17)	44.9	n.d.	0.88	0.59	61.0	0.0
o Bonito	Permian	carb sh	I, (24)	637.86	0.31	10.10 (52.80)	81.69	11.13	1.05	0.82	17.0	4.0
nta ossa	Devonian	shale	n.d.	n.d.	n.d.	n.d.	n.d.	1.29	n.d.	3.26	n.d.	n.d.
nta ossa	Devonian	shale	n.d.	n.d.	n.d.	n.d.	n.d.	0.70	n.d.	1.01	n.d.	n.d.

ed desorbed gas, lost gas and estimated rest gas, from Kalkreuth et al (2008b)
VRr[%]=mean vitrinite reflectance value, determined in random mode; VIT=vitrinite; LIP=liptinite; IN=inertinite;
ter-free basis; carb sh=carbonaceous shale, n.d.= not determined

5.2.1 Irati Formation

According to Milani, 1997 the Permo-Carboniferous sequence of the Paraná Basin was deposited during maximum flooding of the basin. The organic-rich bituminous shales, siltstones, sandstones and carbonates of the Permian Irati Formation occur basinwide from the state of Rio Gande do Sul in the south, to the state of Mato Grosso in the north (a distance of approximately 2500 km). The Irati Formation varies in thickness from 10 - 50 m, with major bituminous shale development in Rio Grande do Sul (Padula, 1969), where cumulative shale thickness reaches up to 13.5 m.

The bituminous shales of the Irati Formation are considered the principal petroleum source rocks of the basin (Milani and Zalán, 1999), with TOC contents between 8-13 wt.%, and TOC peaks in excess of 20 wt.%. Level of preservation of the organic matter (kerogen type I/II) was controlled by variations in the redox potential during deposition (Medeiros de Araújo et al., 2004).

5.2.2 Rio Bonito Formation

Coal deposits occur in the southern part of the Paraná basin in the Permian age Rio Bonito Formation, a fluvial to marine sand- and shale prone lithostratigraphic unit (Holz, 1998), where peat accumulated in coastal mires that formed in a back barrier/strand plain depositional system (Holz and Kalkreuth, 2004; Holz et al., 2000). In the Santa Terezinha coalfield the cumulative coal thickness increases towards the north-east from ca. 4 m to more than 10 m, with individual coal seam thicknesses of up to 3 m (Kalkreuth and Holz, 2000).

Coal rank, based on vitrinite reflectance values, also increases towards the north-east, from sub-bituminous to high volatile A bituminous. Local diabase intrusions have increased locally the thermal maturity of the coals to semi-anthracite and anthracite rank, with vitrinite reflectances of up to 5.46% VRr. (Kalkreuth and Holz, 2000; Kalkreuth et al., 2008a; Kalkreuth et al., 2008b). Petrographic analysis of coal seams from the Santa Terezinha coalfield indicated high inertinite contents, often exceeding 50%, and also high mineral matter contents (Araújo et al., 1995; Kalkreuth et al., 2008a; Kalkreuth et al., 2006; Kalkreuth et al., 2008b) grading coal seams into carbonaceous shale.

Recent sequence stratigraphic analysis (Kalkreuth et al., 2008a; Kalkreuth et al., 2008b) identified five coal bearing sequences (parasequences) in the Santa Terezinha Coalfield, with major coal development in parasequence 2.

5.2.3 Ponta Grossa Formation

Marine shale and sandstones of the Devonian Ponta Grossa Formation are widespread in the Paraná Basin (Zalãn et al., 1991; Zalãn et al., 1990), reaching a maximum thickness of about 600 m (Neto, 1995). Black shales developed in the São Domingo Member of the Ponta Grossa Formation (Candido and Rostirolla, 2007) are considered important source rocks in the Paraná Basin (Milani and Zalán, 1999), with TOC

contents ranging between 1.5 - 2.5 wt.%, occasionally reaching more than 4 wt.%. The organic matter is of kerogen type II and accumulated paleogeographically in an epicontinental sea depositional environment.

5.3 Samples

Seven coal and carbonaceous shale samples (Table 5-1) were obtained from the CBM pilot well CBM-001-ST-RS, drilled in early 2007 in the Santa Terezinha Coalfield, State of Rio Grande do Sul (RS), Brazil. The samples were collected from a depth interval between 605 and 638 m, using a wireline core retrieval technique. A stratigraphic overview of the CBM well as well as locations of sampled seam intervals are shown in (Figure 5-2).

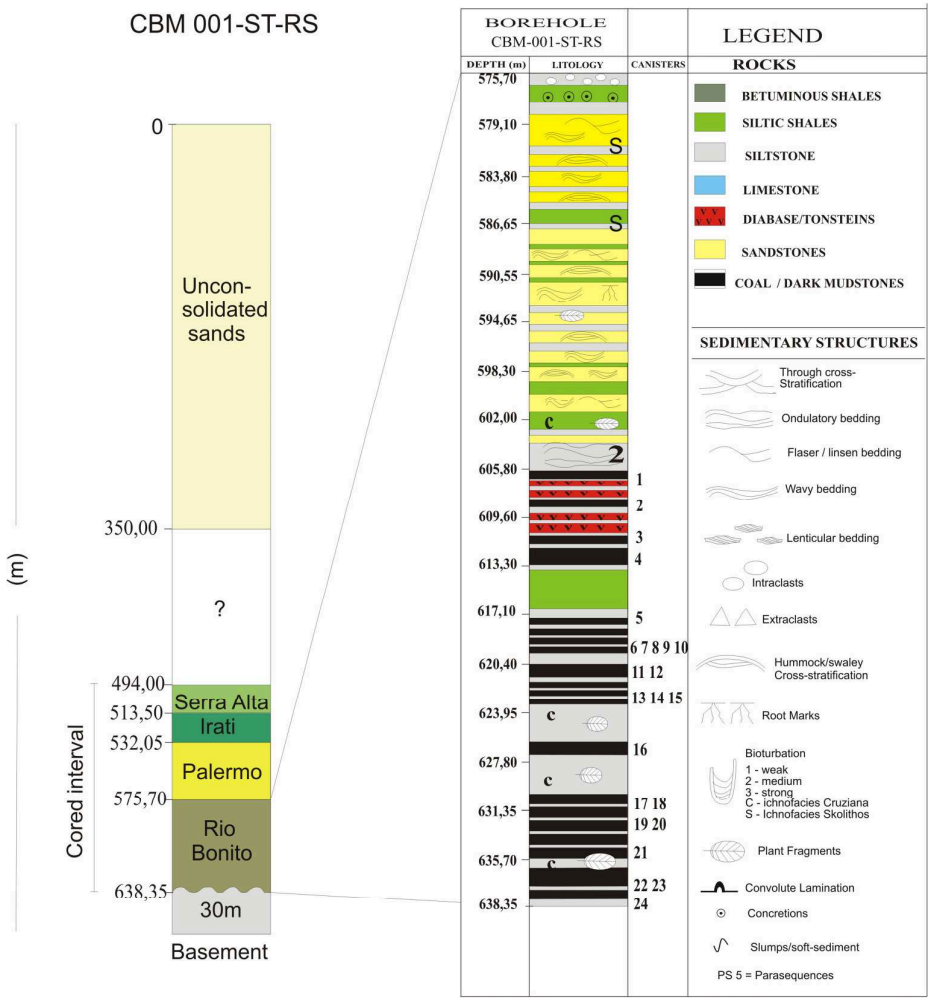


Figure 5-2. Stratigraphic profile of the CBM-001 ST RS well and position of canister samples analysed by Kalkreuth et al. (2008b). Sorption experiments of the present study were carried out on samples from canisters 2, 3, 7, 11, 20, 22, 24.

Additionally, three oil shale samples of the Permian Irati Formation and two Devonian source rock samples of the Ponta Grossa Formation have been investigated in this study.

Excess sorption isotherms for CH_4 and CO_2 were measured in the “as received” moisture state, i.e. without drying. To assess the effect of moisture on sorption isotherms, methane and carbon dioxide sorption

isotherms were measured both in the “as received” state and after moisture equilibration on one coal sample (07_166).

5.4 Methods and Experimental procedures

A detailed description of the sample preparation experimental method for recording sorption isotherms is provided and sample preparation in Section 2.2.1.1 and in Busch et al., 2004a.

5.4.1 Coal characterisation

Proximate analyses of coal samples were carried out according to DIN 51700: “Testing of solid fuels”. The analysis comprised a thermo-gravimetric determination of the “as received” (hygroscopic) moisture content (DIN 51718) and ash yield (DIN 51719). All analyses were performed in triplicate on powdered sub-samples (1 g, <0.2 mm grain size).

Optical petrographic characterization was performed on grain mounts and polished blocks according to common petrographical procedures (e.g. Bustin et al., 1989) at the Instituto de Geociencias Laboratories, Porto Alegre, Brazil. The characterization comprised vitrinite reflectance measurements (VRr %) and maceral group analysis (point counting).

Total organic carbon (TOC) contents were determined in duplicate with a multiphase carbon analyzer RC-412 (LECO, USA). Sample quantities of the carbonaceous shale were in the range of 50 mg, with grain sizes <0.2 mm.

5.5 Results and Discussion

5.5.1 Proximate Analysis

The results of the proximate analyses (“as received” moisture content and ash yield) are summarized in Table 5-1. Moisture contents of coal and carbonaceous shale samples from the CBM well range between 0.6% and 1.4%, and from 0.9% to 3.3% for the shale samples from the Irati and Ponta Grossa formations. Comparison of moisture contents measured in Brazil, shortly after retrieval of samples from the CBM well, with “as received” moisture contents measured ca. 1.5 years later in the RWTH laboratory, Aachen, revealed an average moisture loss of 0.3 wt% (Figure 5-3). Ash yields for the CBM well samples, reported on a dry basis, are generally high, ranging from 36% to more than 90%. This indicates that coal seams are grading into carbonaceous shales. A comparison of ash yields, determined at Universidade Federal do Rio Grande do Sul, (UFRGS) and at RWTH Aachen University, revealed no significant differences.

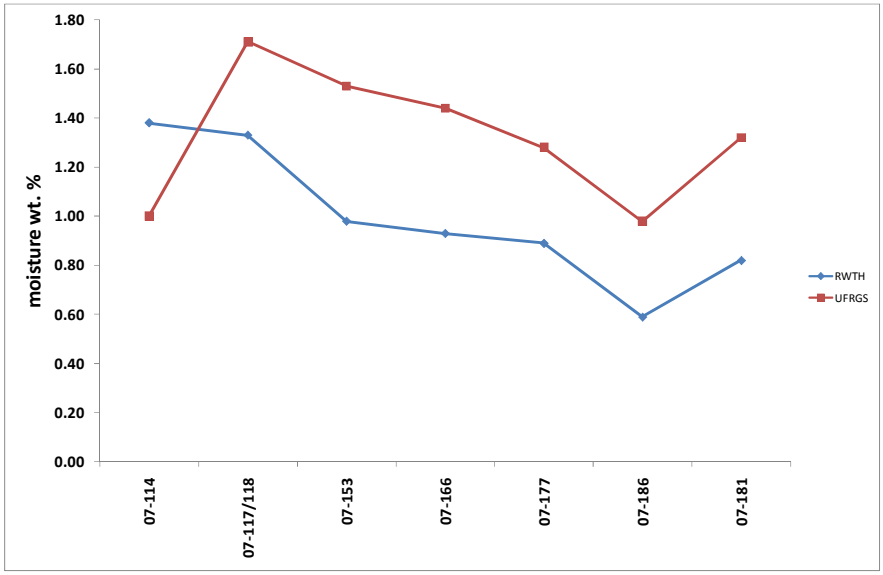


Figure 5-3. Comparison of moisture content determined after sample acquisition in Brazil (UFRGS) and later before sorption tests in Germany (RWTH) indicating drying of powdered coal samples.

5.5.2 TOC contents

TOC values for the two samples from Ponta Grossa Formation were 0.7% and 1.3% while the Irati oil shale had TOC contents extending from 2.3 to 26.3%. The TOC values of the samples from the Rio Bonito Formation ranged from 1.7% to 43.9%.

5.5.3 Coal Petrography

5.5.3.1 Vitrinite Reflectance

Coals from the Rio Bonito formation in the Santa Terezinha Coalfield are of high volatile bituminous rank (Kalkreuth et al., 2003) and have reached anthracite rank locally, where the coal seams were thermally altered by diabase intrusions. The measured vitrinite reflectance values for the coals and carbonaceous shales from the CBM well range between 0.8 and 2.6%, with coals in contact with igneous intrusions (interval L and G) showing the highest vitrinite reflectance.

5.5.3.2 Maceral group analysis

The maceral compositions of the Rio Bonito samples show large variations (Table 5-1). Inertinite contents are generally high and range from 38% to 90% with an average value of 61%. Most coals with high vitrinite reflectance (>1%) also show high inertinite contents (>50%). Liptinite is absent in coal seams from interval L and H and reaches its highest value of 9% in interval D. Vitrinite content varies between 10% in interval L1 and 61% in interval H.

5.5.4 Gas contents

The coalbed gas contents of different intervals of the Rio Bonito CBM well have been reported previously by Kalkreuth et al. (2008b), based on temperature and pressure controlled gas (canister) desorption values.

Gas contents range between 0.3 and 2.1 m³/t coal with the highest values in intervals C and D at a depth of ~ 620 m. Coal samples with less than 1% vitrinite reflectance show the highest gas contents. However, no clear correlation of gas content with maturity is observed. A slight correlation of gas content with increasing sorption capacity was observed for methane. This trend is less expressed for carbon dioxide (Figure 5-4).

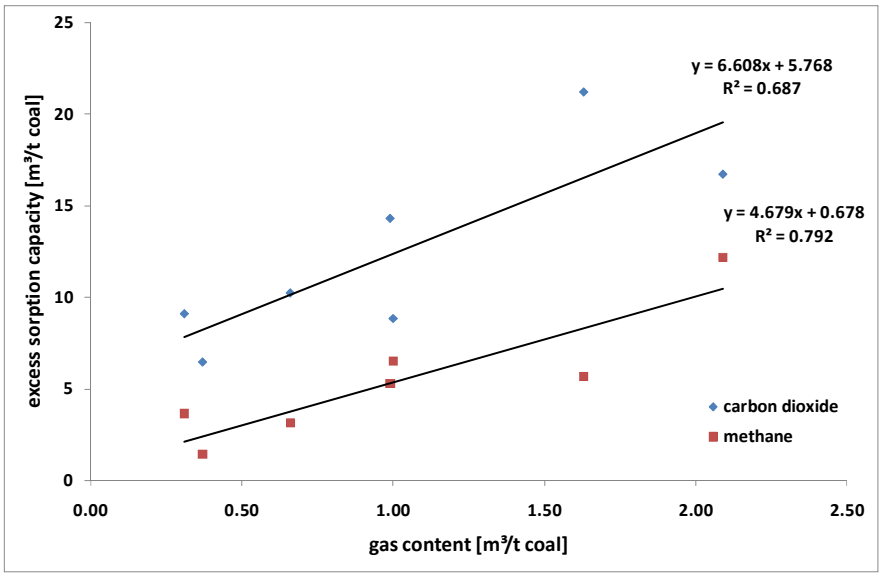


Figure 5-4. Correlation of excess sorption capacity with gas content of coal and carbonaceous shale from CBM 001-ST-RS well.

5.5.5 Results of gas sorption experiments

Most gas sorption isotherms in this study were measured at 45°C and pressures up to 17 MPa for methane and up to 25 MPa for carbon dioxide. Three samples (07_153, 07_177, 07_186) were measured at 35°C. This temperature is only slightly above the critical temperature of CO_2 (31.1°C) where the CO_2 density is very sensitive to temperature variations. Sorption isotherms for CO_2 in this temperature range therefore carry an inherent risk of inaccuracy due to even slight errors in temperature measurements.

Maximum measured excess sorption values and the Langmuir parameters (n_L and P_L for CH_4 and n_L, P_L and ρ_{ads} for CO_2), obtained from approximation of the experimental data are listed in Table 5-2. Results of sorption measurements are reported in units of mmol/g, and in mmol/g dry, ash-free coal (daf). Conversion of the adsorbed amount of substance to gas volumes (Std. m³/t coal, daf) was performed using the standard conditions for gases (IUPAC, 2001).

Table 5-2. Results of high pressure methane and carbon dioxide sorption experiments measured at 45°C.

	CH_4 isotherms			Langmuir parameter				
sample number	n_{max} CH_4 [mmol/g]	n_{max} [mmol/g, daf]	V_{max} [m³/t, daf]	n_L CH_4 [mmol/g]	n_L [mmol/g] daf	P_L [MPa]	V_L [m³/t] at 6.25 MPa	He density [g/cm³]
07_114	0.05	0.79	17.94	0.07	1.02	4.09	0.95	2.32
07_117/118	0.25	0.77	17.49	0.28	0.87	2.31	4.68	2.29
07_153[a]	0.22	0.34	7.72	0.27	0.43	3.73	n.d.	1.84
07_166	0.47	0.81	18.40	0.57	0.99	4.23	7.72	1.66
07_166[b]	0.25	0.44	9.99	0.30	0.53	3.35	4.06	1.70
07_177[a]	0.12	0.31	7.04	0.15	0.38	3.34	n.d.	2.07
07_186[a]	0.20	0.37	8.40	0.25	0.46	3.47	n.d.	1.83
07_181	0.14	0.77	17.49	0.18	1.02	5.79	2.18	2.04
08_100	0.02	1.63[c]	n.d.	0.04	3.37[c]	16.09	n.d.	2.59
08_101	0.05	7.78[c]	n.d.	0.08	11.45[c]	7.09	n.d.	2.46
08_168	0.25	1.02[c]	n.d.	0.37	1.52[c]	8.39	n.d.	1.90
08_170	0.13	1.27[c]	n.d.	0.25	2.36[c]	14.16	n.d.	2.25
08_154	0.03	1.28[c]	n.d.	0.04	1.77[c]	5.65	n.d.	2.72

	CO_2 isotherms				Langmuir parameter					
sample number	n_{max} [mmol/g]	P at n_{max} [MPa]	n_{max} (CO_2 /CH_4	V_{max} [m³/t]	n_L [mmol/g]	P_L [MPa]	$\rho_{sorbate}$ [g/cm³]	V_L [m³/t] at 6.3 MPa	V_{LCO2}/ V_{LCH4} at 6.3 MPa	He dens [g/cm³]
07_114	0.25	8.70	4.58	5.63	0.69	8.43	960	6.66	7.0	2.81
07_117/118	0.34	9.47	1.36	7.69	0.80	6.19	1133	9.14	2.0	2.46
07_153[a]	0.81	6.88	3.40	18.45	1.91	3.40	n.d.	n.d.	n.d.	1.72
07_166	0.64	7.94	1.38	14.56	1.11	3.18	1129	16.63	2.2	1.88
07_166[b]	0.28	7.65	1.12	6.38	0.43	1.87	825	6.47	1.59	1.69
07_177[a]	0.39	7.35	3.30	8.91	1.18	1.14	n.d.	n.d.	n.d.	1.93
07_186[a]	0.55	6.34	2.71	12.45	1.54	3.56	n.d.	n.d.	n.d.	1.66
07_181	0.35	9.08	2.51	7.92	0.90	12.01	862	6.99	3.2	2.02
08_100	0.20	9.083	10.01	4.62	0.78	20.0	882	n.d.	n.d.	2.23
08_101	0.16	8.13	3.00	3.68	0.69	19.03	902	n.d.	n.d.	2.71
08_168	0.54	9.63	2.13	12.21	2.02	15.0	907	n.d.	n.d.	1.88
08_170	0.359	7.32	2.76	8.15	1.25	13.43	823	n.d.	n.d.	2.27
08_154	0.14	8.73	4.93	3.22	0.65	19.9	960	-	-	2.72

[a]= measured at 35°C; [b]= moisture equilibrated; [c]= [mmol/g TOC]; n_L= Langmuir sorption; P_L= Langmuir pressure; n_{max}= maximum excess sorption; n.d.= not determined

5.5.5.1 Methane sorption isotherms

The methane sorption isotherms, measured on the coal and carbonaceous shale samples from the Rio Bonito Formation of the CBM-001-ST-RS well are shown in Figure 5-5 and Figure 5-6. Sorption capacities for these samples range between 0.07 and 0.57 mmol/g (0.38 to 1.02 mmol/g coal, daf). Normalization of sorption isotherms to the dry ash-free basis shows that the first three samples have a significantly lower sorption capacity. This is controversial because these isotherms were measured at a lower temperature (35°C) than the other samples (45°C). The reason for the lower sorption capacity is most likely a difference in moisture content during measurements. As described in chapter 5.1, coal samples lost a significant amount of water before sorption tests. It is very likely that samples measured at 45°C lost additional moisture until measured. However, most sample material was consumed and thus isotherms measured at 35°C could not be re-measured at 45°C and the moisture loss could not be quantified. For better comparison, isotherms measured at 35°C have been excluded in further data interpretation.

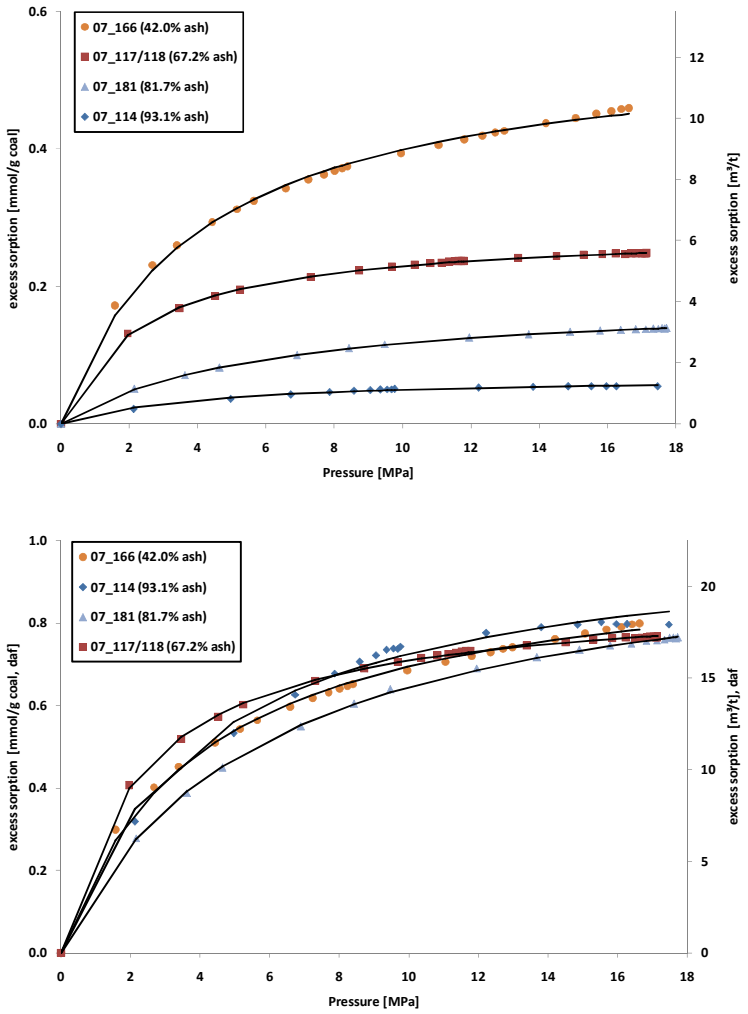


Figure 5-5. Methane sorption isotherms (45°C) with Langmuir approximations (black lines) for coal and carbonaceous shale samples from the Permian Rio Bonito Formation of CBM well 001-ST-RS on a raw basis (top) and dry, ash-free basis (bottom).

The experimental data were fitted by the Langmuir sorption function (1) and the 3-parameter function (2), shown in the diagrams. The Langmuir parameters nL and PL for the individual sorption isotherms are listed in Table 5-2. Methane sorption isotherms, measured on the Permian and Devonian carbonaceous shales are shown in Figure 5-7. As expected, the shale samples show lower methane sorption capacities (between 0.04 and 0.37 mmol/g) than coals. Normalized to TOC content, sorption capacities of the shale samples are, however, significantly higher than capacities of coal samples on a daf basis (1.5 to 11.5 mmol/g, TOC). For shale samples with low TOC contents (<3 %) (e.g. samples 08_100, 08_101 and 08_154), the bulk excess sorption values are also low and bear a relatively large error. The potential analytical error is increased by experimental uncertainties in the assessment of low TOC values. In consequence, the TOC-normalization of the sorption isotherms is likely to overestimate the methane sorption capacity of these samples.

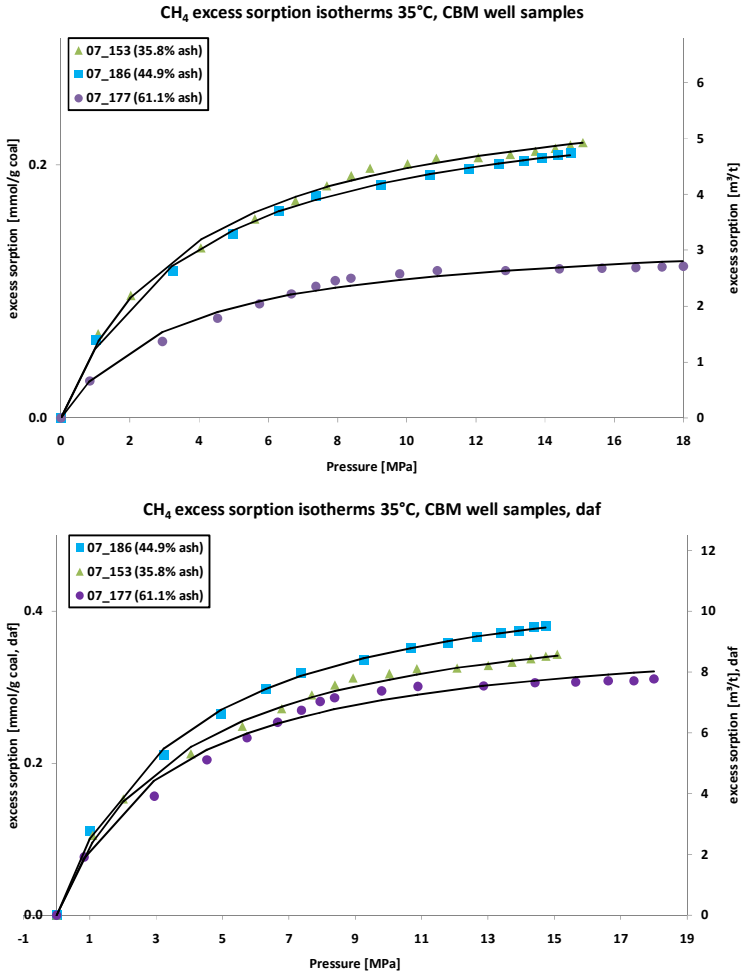


Figure 5-6. Methane sorption isotherms (35°C) with Langmuir approximations (black lines) for coal and carbonaceous shale samples from the Permian Rio Bonito Formation of CBM-001-ST-RS well on a raw basis (top) and dry, ash-free basis (bottom).

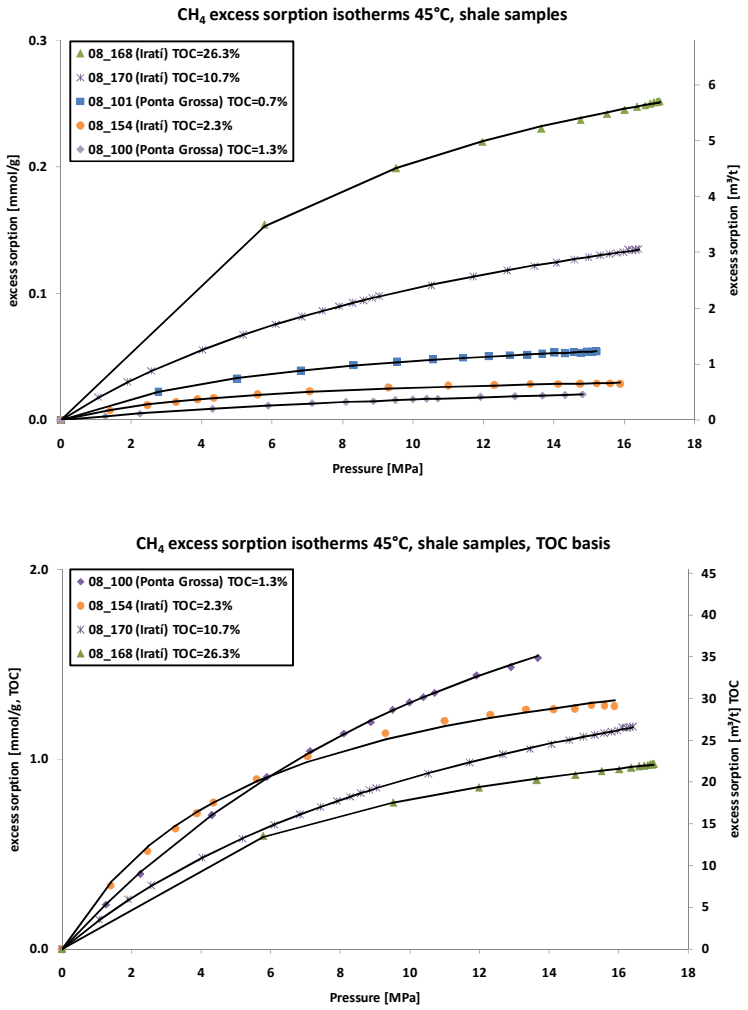


Figure 5-7. Methane sorption isotherms) with Langmuir approximations (black lines) for Permian (Irati) and Devonian (Ponta Grossa) shale samples on a raw basis (top) and TOC basis (bottom, sample 08_101 with TOC < 1 % not included).

The gas contents of coals from the CBM-001-ST-RS well are lower than their CH_4 sorption capacity (excess sorption), i.e. the coals are under-saturated in methane. Assuming a hydrostatic pressure gradient of 10 MPa/km, the reservoir pressure in the depth interval under consideration should range between 6.1 and 6.4 MPa. Sorption capacities for the mean reservoir pressure (6.25 MPa) calculated from the Langmuir fits range between 7.7 and 16.5 m³/t coal. The actual methane contents of the coal seams, determined by canister desorption, thus represent between 13 and 38% of the sorption capacity.

5.5.5.2 Carbon dioxide sorption isotherms

Carbon dioxide excess sorption isotherms measured at 45°C on coal and carbonaceous shales from well CBM-001-ST-RS are shown in Figure 5-8, and another set of isotherms measured at 35 °C in Figure 5-9. While the 45°C isotherms were determined up to pressures of more than 20 MPa, the 35 °C isotherms were recorded only up to a pressure of ~7 MPa. Figure 5-10 shows 45°C CO_2 sorption isotherms measured for the Permian (Irati) and Devonian (Ponta Grossa) shales.

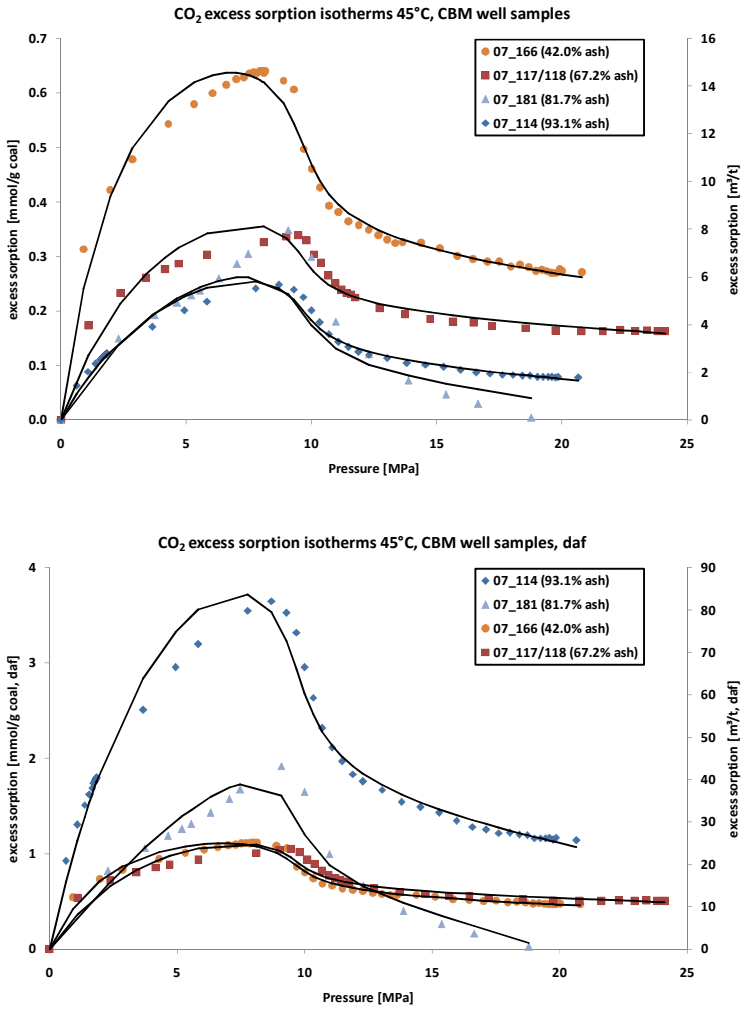


Figure 5-8. Carbon dioxide sorption isotherms for coal and carbonaceous shale samples from well CBM-001-ST-RS on a raw basis (top) and dry, ash-free basis (bottom), measured at 45°C.

The CO_2 isotherms at 45°C typically exhibit a maximum in the 8 to 12 MPa pressure range and then show a continuous decline. The maximum is related to the steep increase in the specific density of supercritical CO_2 in the corresponding pressure range (cf. Gensterblum et al., 2009). Maximum excess sorption capacities for CO_2, measured in this pressure interval, range from 0.25 to 0.81 mmol/g (5.6 to 18.5 m³/t) for coals and carbonaceous shales and from 0.14 to 0.54 mmol/g (3.2 to 12.2 m³/t) for the shales from the Irati and Ponta Grossa formations.

The measured CO_2 isotherms were approximated by the excess sorption function given in equation 2. The three parameters n_L, P_L and $\rho_{adsorbed}$, adjusted by a least-squares optimization procedure, for the individual isotherms are listed in Table 5-2.

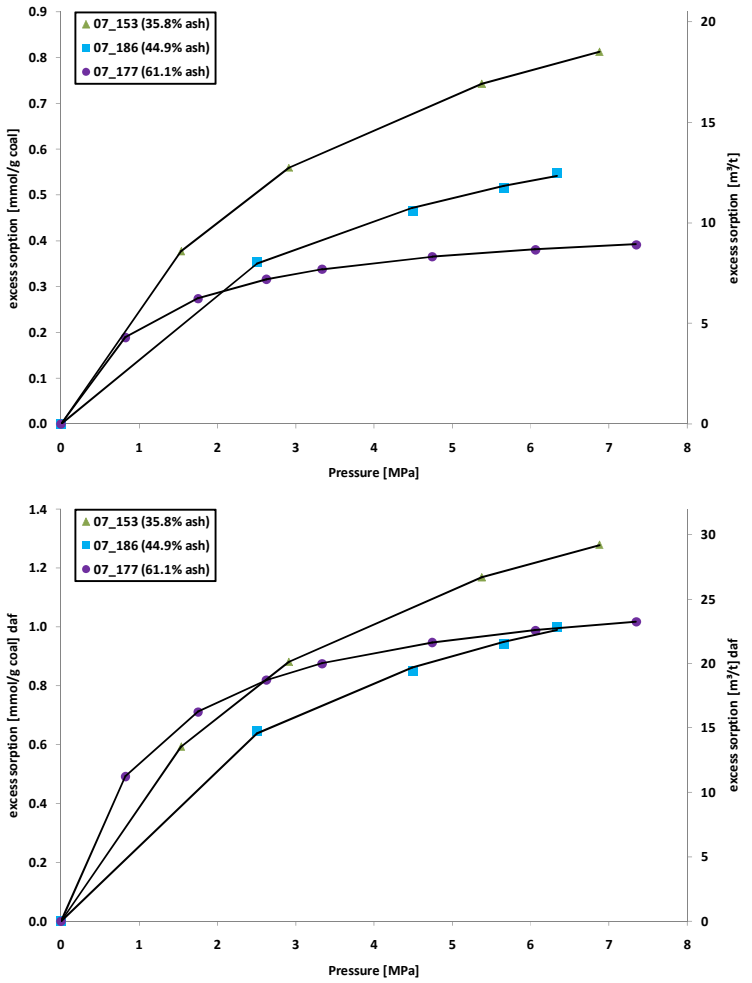


Figure 5-9. Carbon dioxide sorption isotherms for coal and carbonaceous shale samples from CBM well 001-ST-RS on a raw basis (top) and dry, ash-free basis (bottom), measured at 35°C. Solid lines represent Langmuir fit.

Some of the CO_2 isotherms for the shale samples (Figure 5-10) showing pronounced maximum with a steep decline in the pressure range between 9 and 11 MPa. These isotherms could not be satisfactorily approximated by the 3-parameter fitting function. Isotherms with similar shapes were obtained by Busch et al. (2008) for CO_2 sorption on the Australian Muderong shale and on pure clay minerals, such as illite, montmorillionite and kaolinite.

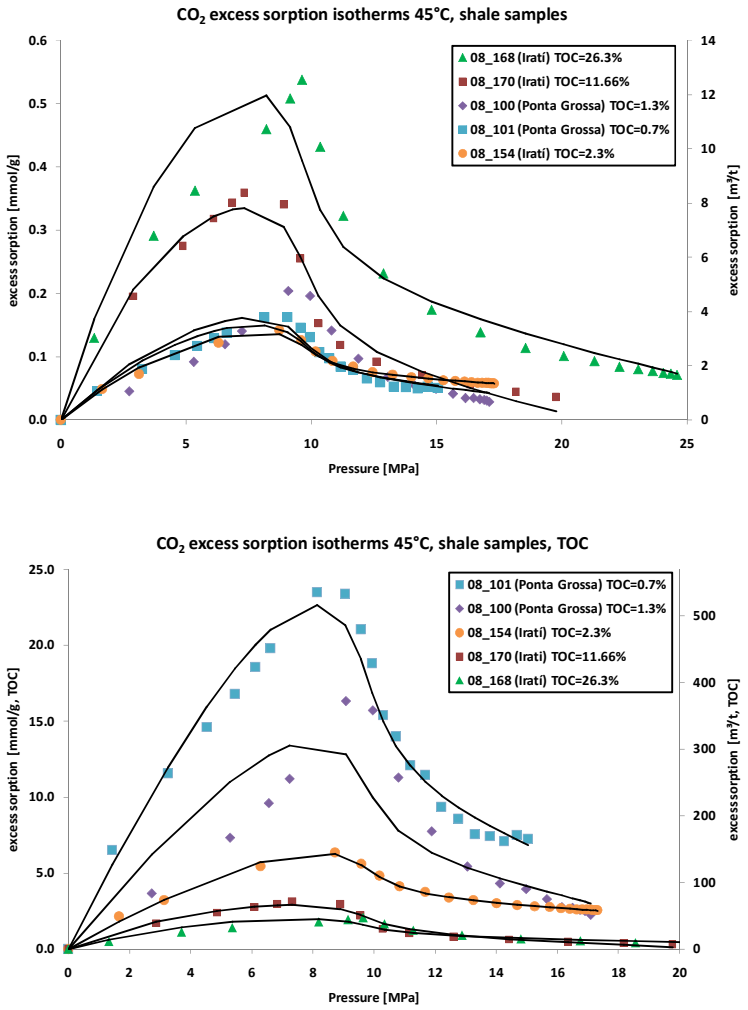


Figure 5-10. Carbon dioxide sorption isotherms for Permian (Iratí) and Devonian (Ponta Grossa) shale samples on a raw basis (top) and TOC basis (bottom), measured at 45 °C.

5.5.6 Effect of mineral matter content (ash yield) on gas sorption

Coal seams from the Santa Terezinha coalfield are known to have high mineral matter and inertinite contents as reported by Araújo et al. (1995) and more recently by Kalkreuth et al. (2006, 2008a,b). It has been suggested that the high ash yields of coals from the Rio Bonito Formation are related to the occurrence of diamictites (Begossi and Della Fávera, 2002). X-ray diffraction analysis on coal samples from the CBM-001-ST-RS well revealed that the mineral matter is mostly composed of quartz, kaolinite and mica, with minor contributions of pyrite, ankerite, calcite, dolomite, albite and alunite (Kalkreuth et al., 2008b).

Using the ash yield as a proxy for the mineral matter content, Figure 5-11 shows an essentially linear decrease of the maximum sorption capacity of methane and carbon dioxide with increasing mineral matter content for the coals and carbonaceous shales from the CBM-001-ST-RS well. The regression line for methane indicates that the sorption capacity is close to zero for ash yields approaching 100%, i.e. an organic matter content of zero. This supports the predominant role of organic matter in methane sorption in coals and carbonaceous sediments and is in agreement with findings reported, for instance, for

Australian Bowen Basin coals (Laxminarayana and Crosdale, 1999) and coals from British Columbia (Clarkson and Bustin, 2000). According to the regression in Figure 5-11, the maximum sorption capacity for methane in the CBM-001-ST-RS well samples decreases by 0.009 mmol/g for each 1% increase in ash yield. This is somewhat lower than the value of 0.38 cm^3/g (0.017 mmol/g) reported by Laxminarayana and Crosdale (1999), which is likely to reflect differences in the type (maceral composition) and maturity of the organic matter.

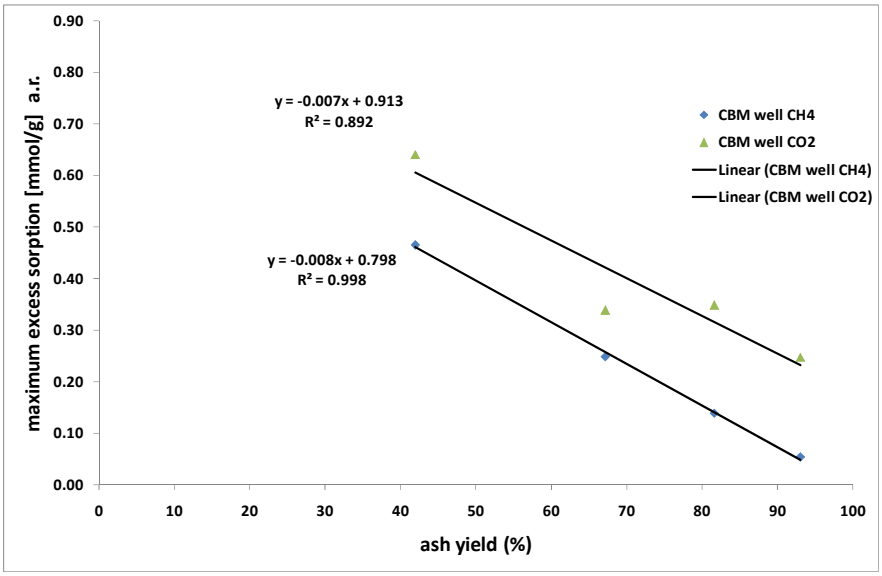


Figure 5-11. Maximum excess sorption capacities (45 °C) of methane and carbon dioxide as a function of ash yield for coals and carbonaceous shales from CBM well 001-ST-RS.

The maximum sorption capacity of carbon dioxide for the CBM-001-ST-RS well samples decreases by 0.008 mmol/g for each 1% increase in ash yield. The regression shows that at ash yields approaching 100%, i.e. organic carbon contents approaching zero, the samples still exhibit a considerable CO_2 sorption capacity (approximately 0.183 mmol/g) which can be attributed to the mineral matter.

Figure 5-12 shows maximum excess sorption capacities of methane and carbon dioxide for coal and shale samples from the CBM-001-ST-RS well and Permian (Irati) and Devonian (Ponta Grossa) formations as a function of organic carbon contents (TOC). The following linear regression functions were obtained:

CH_4 (mmol/g) = 0.009 · TOC (%) + 0.026

CO_2 (mmol/g) = 0.008 · TOC (%) + 0.183

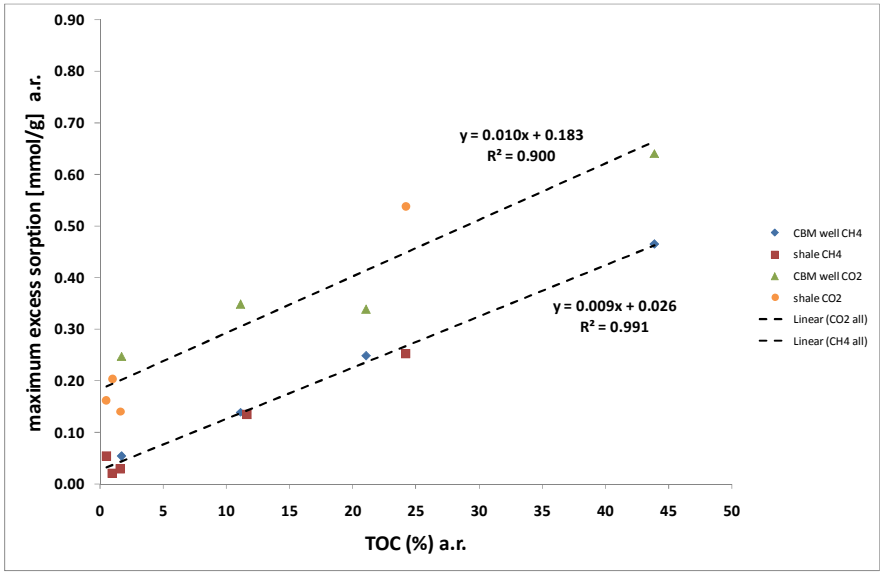


Figure 5-12. Maximum excess sorption capacities for methane and carbon dioxide (8-12 MPa pressure range, 45°C) vs. TOC contents of coal and shale samples from CBM-001-ST-RS well and Permian (Iratí) and Devonian (Ponta Grossa) shale samples.

As stated above, the regression function for CO_2 indicates that the mineral matter exhibits a significant sorption capacity (0.183 mmol/g) for this gas. This finding is in general agreement with results reported by Nuttall et al. (2005), who evaluated the potential for carbon dioxide sequestration and enhanced natural gas production of Devonian black shales in Kentucky. These workers find a linear increase of CO_2 sorption capacity at 400 psia (2.75 MPa) with TOC content described by the regression function:

CO_2 (scf/ton) = 7.9 · TOC (%) + 20.7 (CO_2 pressure = 400 psia)

Expressed in metric units and amounts of substance this yields:

CO_2 (mmol/g) = 0.009 · TOC (%) + 0.025 (CO_2 pressure = 2.75 MPa)

According to these results, the mineral matter in the Devonian black shales of Kentucky would have a significantly lower CO_2 sorption capacity than the sample sequences from the Paraná Basin investigated in the present study.

Table 5-3 shows a comparison of X-ray diffraction mineralogy for Santa Terezinha coal samples reported by Kalkreuth et al. (2006) and for Ohio shale samples (Huron Formation) reported by Nuttall et al. (2005). Evidently, shales and some pure clay minerals exhibit a significant sorption capacity for CO_2. Busch et al. (2008) reported CO_2 sorption capacities for the Muderong shale and pure clay minerals (kaolinite, montmorillonite and illite), ranging from 0.1 mmol/g to 1.2 mmol/g for “as received” samples. The higher kaolinite and carbonate (calcite, ankerite and siderite) content of coal samples explain the larger CO_2 sorption capacity of Brazilian coal samples. The Ohio shale has larger contents of illite and mica, as well as higher amounts of chlorite, plagioclase pyrite and quartz. Illite is reported to have a higher CO_2 sorption capacity compared to kaolinite (Busch et al., 2008). However, the sum of kaolinite and illite content is

higher for the coal samples compared to the Ohio shale. The higher carbonate content of the coals could also contribute to higher CO_2 sorption capacities through carbonate dissolution. However, this comparison is based on few literature data of coal samples. To better understand the variation of CO_2 sorption capacity of mineral matter, a more thorough mineralogical characterization of Santa Terezinha coal samples and shale samples in combination with isotherm measurements is required.

Particularly for high-ash coals and carbonaceous shales carbon dioxide adsorption on the mineral matter cannot be neglected and therefore normalization to a dry, ash-free basis is not appropriate.

5.5.7 Effect of moisture on sorption isotherms

It is well known that the moisture content of a coal significantly influences its methane sorption capacity (Crosdale, 1999; Day et al., 2008c; Joubert et al., 1973; Yalcin and Durucan, 1991). To investigate the effect of moisture, in addition to the measurements on the "as received" sample, methane and CO_2 sorption isotherms were measured on one coal (07_166) in the moisture-equilibrated state (Figure 5-13 and Figure 5-14). The equilibrium moisture content of this sample was 2.44 wt.%, while the hygroscopic (as received) moisture content was 0.98 wt.%. The methane sorption capacity of the moisture-equilibrated coal sample is significantly lower (0.30 mmol/g; 0.53 mmol/g, daf) than the sorption capacity of the "as received" sample (0.57 mmol/g; 0.99 mmol/g, daf). This corresponds to a reduction by 45%.

For carbon dioxide the maximum excess sorption of the moisture-equilibrated sample was 0.28 mmol/g, which is 56% lower than for the "as received" coal (0.64 mmol/g). This indicates a stronger competition for sorption sites (e.g. with functional oxygen groups) between water and CO_2 than for methane, which is in contrast to observations by Day et al. (2008a), who found that water saturation caused a stronger reduction of sorption capacity for methane than for carbon dioxide for a high volatile bituminous Australian coal (Hunter Valley, Australia, R_{max} = 0.8%). According to this study, clusters of water molecules attach to pores with polar sites, which then can become inaccessible for other adsorbates. CO_2 can adsorb on top of the polar water clusters, whereas CH_4 is limited to hydrophonic sorption sites and thus the reduction of methane sorption capacity would be greater than the reduction of CO_2 sorption capacity. This effect diminished for a high rank coal (Illawara, Australia, R_{max} = 1.4%) whith fewer polar sorption sites. Day et al. (2008a) also argue that the smaller kinetic diameter of CO_2, compared to CH4 would allow carbon dioxide to enter some of the blocked pores, whch methane could not access. The observation in the present study, that moisture equilibration results in higher reduction of CO_2 sorption capacity compared to methane sorption capacity, is based only on one sample, further investigation is needed to examine this effect in more detail.

Table 5-3. Semi quantitative and quantitative X-ray mineralogy

Santa Terezinha Coal (Kalkreuth et al., 2006)			
seam	I	D	G
Quartz	40%	45%	30%

Kaolinite	30%	T	60%
Siderite	15%	R	R
Calcite	T	15%	n.d.
Ankerite	n.d.	15%	n.d.
Illite	M	M	10%
Pyrite	n.d.	M	n.d.
Feldspar	T	T	T
Dolomite	n.d.	T	n.d.
Sphalerite	T	R	R
Bassanite	n.d.	T	T
Apatite	T	R	T
Rutile	R	n.d.	T
Hematite	T	R	n.d.

Ohio Shale Nuttall et al., (2005)

formation	Lower Huron	Middle Huron	Upper Huron
Quartz	48%	47%	51%
Kaolinite	1.3%	2.5%	2.3%
Barite	1.1%	0.6%	0.7%
Calcite	0.3%	1.1%	0.3%
Gypsum	0.3%	0.3%	0.5%
Illite+Mica	25%	29%	25%
Pyrite	8.6%	6.2%	5.4%
Feldspar (Plagioclase)	5.4%	7.0%	7.5%
Fe-Dolomite	5.4%	1.3%	4.4%
Chlorite	4.1%	5.0%	3.1%

T=trace amount ≤ 5%, M=minor amount >5 ≤10 %, R=rejected, n.d.=not detected

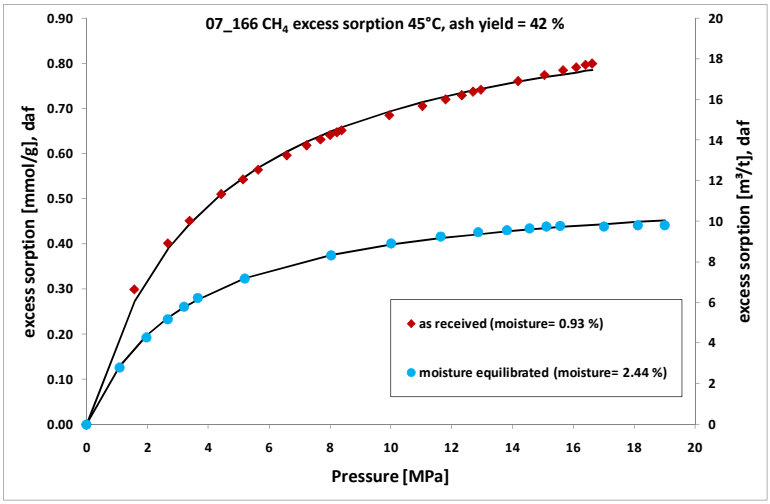


Figure 5-13. Effect of moisture on methane sorption for coal sample 07_166. At equilibrium moisture (2.44%) the sorption capacity is 45% lower as compared to the "as received" coal (moisture content: 0.93%). Solid lines represent Langmuir fit.

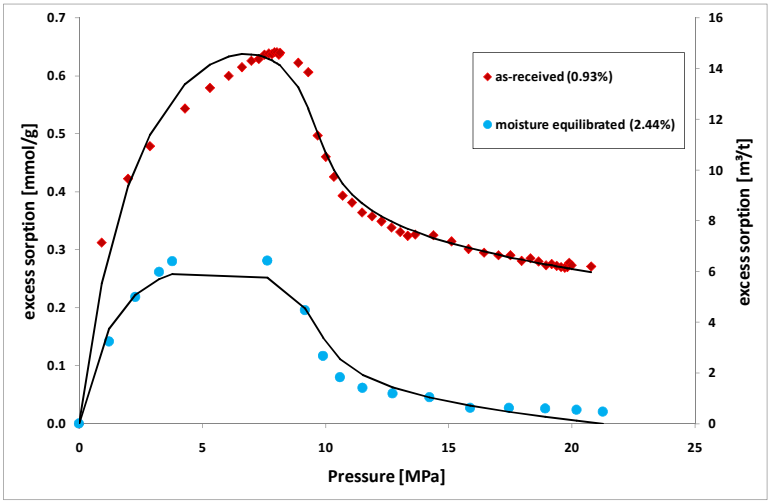


Figure 5-14. Effect of moisture on carbon dioxide sorption for coal sample 07_166 from CBM well ST-RS-001. At equilibrium moisture (2.44%) the sorption capacity is 56% lower as compared to the "as received" coal (moisture content: 0.93%). Solid lines represent 3-parameter fit.

5.5.8 Effect of coal maceral composition on sorption isotherms

The effect of maceral composition on methane and carbon dioxide sorption on coals is related to differences in microporosity of the macerals. Vitrinite is predominantly microporous, whereas inertinite is rather meso- to macroporous (Lamberson and Bustin, 1993). Some authors report a significant influence of maceral composition on sorption capacities (e.g. Chalmers and Bustin, 2007; Lamberson and Bustin, 1993; Mastalerz et al., 2004), whereas others could not observe such a relationship (e.g. Day et al., 2008a; Faiz, 2007; Krooss et al., 2002). To compare the effect of coal composition on sorption, isotherms have to be normalized to a dry ash-free basis. Lamberson and Bustin (1993) report increasing methane sorption with increasing vitrinite content on medium-volatile coals from British Columbia. Chalmers and Bustin (2007) report higher methane sorption capacity for liptinite-rich coals with low microporosity, where methane is held as solution gas. Mastalerz et al. (2004) observed a relationship between maceral composition of coals from Indiana (high volatile bituminous C) and CO_2 sorption capacity, measured at 2.8 MPa (400 psi) and 17°C (62°F). They found increasing CO_2 sorption capacities for coals with higher vitrinite content and suggest that telocollinite content may be of greatest influence on CO_2 sorption capacity of all macerals. Coals with higher liptinite content showed lower CO_2 sorption capacities. No correlation between methane or carbon dioxide sorption capacity and petrographic composition of coal was observed for coals and carbonaceous shale samples analyzed in this study (Figure 5-15). As mentioned in section 5.6, the normalization of carbon dioxide sorption isotherms, measured on high ash coals, to the dry, ash free basis is prone to overestimation of sorption capacity, which could mask a correlation of CO_2 sorption capacity with maceral composition. Laxminarayana and Crosdale, 1999b found that the influence of maceral composition on gas adsorption decreases with increasing rank. The high rank of some coals analyzed in this study (high volatile bituminous A – anthracite) might explain why no correlation with maceral composition was observed.

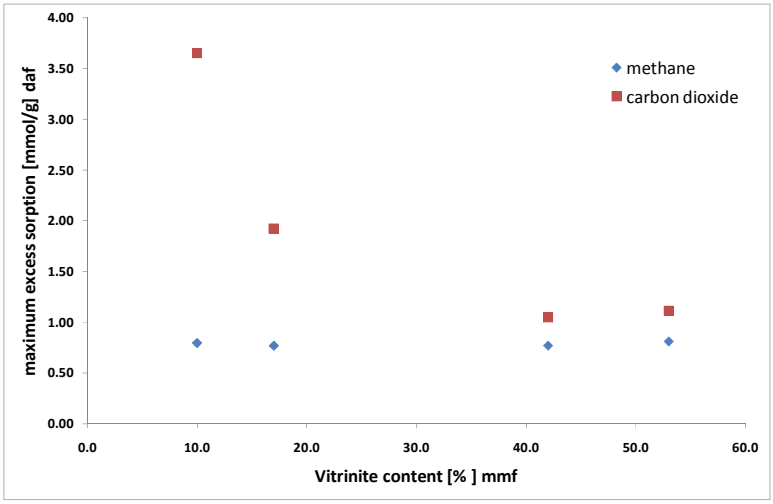


Figure 5-15. Maximum excess sorption of capacity of methane and carbon dioxide vs. vitrinite content for coal samples from well CBM-001-ST-RS.

5.5.9 Effect of maturity on sorption isotherms

Previous studies report that methane sorption capacity decreases with increasing rank to a minimum in the medium volatile bituminous range, followed by an increase with increasing rank (Yalcin and Durucan, 1991, Faiz et al., 2007). This effect has also been observed for carbon dioxide sorption capacity (Busch et al., 2003, Day et al., 2008). With increasing thermal maturity the microporosity of coal increases (Bustin and Clarkson, 1998; Chalmers and Bustin, 2007; Prinz and Littke, 2005). Since most of the physical adsorption takes place in the micropore structure of coal (Yalcin and Durucan, 1991), the increase in microporosity with increasing rank is also considered to cause an increase in sorption capacity from medium volatile bituminous coal to anthracite. In the present study no correlation was found between methane or carbon dioxide sorption and maturity (Figure 5-16).

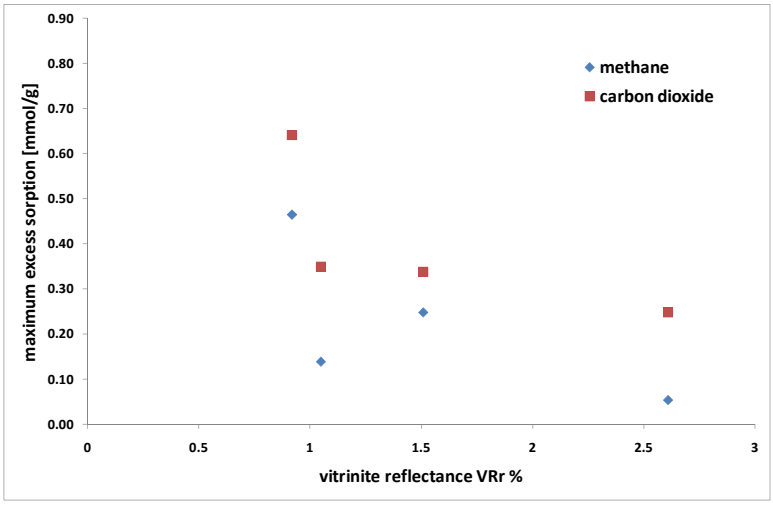


Figure 5-16. Maximum excess sorption of capacity of methane and carbon dioxide vs. vitrinite reflectance for coals from well CBM-001-ST-RS.

5.5.10 Evaluation of potential for carbon dioxide sequestration and enhanced coalbed methane (CO2-ECBM) and shale gas recovery (CO2-ESG).

Sorption capacities for CO_2 on coals and shales are generally higher than for CH_4. Sorption capacities of samples from the CBM-001-ST-RS well ([3]n_L) for an average reservoir pressure of 6.25 MPa, range between 0.29 and 0.73 mmol/g (6.66 – 16.63 m³/t) for carbon dioxide and between 0.04 and 0.34 mmol/g (0.95 – 7.72 m³/t) for methane. The sorption capacity ratios (V_LCO_2/V_LCH_4 at 6.25 MPa) range between 2.0 and 7.0 (average 3.6). Ratios of maximum excess sorption amounts ($n_{max}CO_2/n_{max}CH_4$) range between 1.4 and 4.6 for the coal and carbonaceous shale samples from the CBM well. For the Permian (Irati) and Devonian (Ponta Grossa) shales these ratios range between 2.1 and 10.

Results from the present study suggest that coal seams in the Santa Terezinha coalfield are generally under-saturated in methane, which means that the current gas content is lower than the measured sorption capacity. The free sorption capacity could possibly be used for storage of carbon dioxide. Depending on the economical and market situation the methane present in the coals could be produced prior to CO_2 injection. Simultaneous injection of CO_2 for ECBM is considered less reasonable because the produced gas would have a low calorific value due to co-production of injected CO_2 (cf. van Bergen et al., 2009a). In a first approach to estimate the effective CO_2 storage capacity of a CBM reservoir, a calculation similar to the reduction of initial gas in place (IGIP) to producible gas in place (PGIP) (eq. 3) can be applied (van Bergen et al., 2001).

$$PGIP = RF \cdot C \cdot IGIP \qquad (5\text{-}1)$$

Here the producible part of the gas in place is estimated using a recovery factor (RF) and estimating a completion factor (C). The recovery factor represents the amount of gas that can technically be produced by reducing the reservoir pressure through water production. The completion factor (C) represents an estimation of the part of coal seams that can be accessed through drilling operations.

Hendriks et al., 2004 estimated the global carbon dioxide storage potential in various underground reservoirs. For the CO_2 storage capacity (S_{CO2}) in coal basins during ECBM operations they used the following equation:

$$S_{CO2} = PGIP \cdot ER \cdot \rho_{CO2} \qquad (5\text{-}2)$$

PGIP = producible gas in place (standard conditions) [m³]

ER = exchange ratio [-]

ρ_{CO2} = CO_2 density at standard conditions [1.977 kg/m³].

[3] In mmol/g rock; not daf-normalized

The amount of producible gas in place (PGIP) is estimated according to:

$$PGIP = \cdot A \cdot TH \cdot \rho_{coal} \cdot GC \cdot RF \cdot CF \quad (5\text{-}3)$$

A = area of the coal basin [m²]

TH = cumulative thickness of coal seams [m]

ρ_{coal} = coal density [t/m³]

GC = gas content [m³/t]

RF = recovery factor [-]

CF = completion factor [-]

In equation (5) the initial gas in palace is calculated by multiplying the total mass of coal ($A \cdot TH \cdot \rho_{coal}$) with the average gas content (GC).

Hendricks et al. (2004) conservatively assumed that only 10% of the total area of a coal basin can be used for CO_2 storage and thus they used a completion factor of 0.1. The recovery factor usually ranges between 20% and 60% (van Bergen et al., 2001). For the case of CO_2 sequestration, the recovery factor represents the storage efficiency. It was conservatively assumed to be 40% by Hendricks et al., (2004).

To estimate the CO_2 storage capacity of the study area in the Santa Terezinha Coalfield, we used equation (5), assuming the same recovery factor and completion factor Hendricks et al. (2004) used. Based upon 3D geological modelling for a study area of approx. 20x40 km in the Santa Terezinha Coalfield, Kalkreuth et al. (2008b) calculated the total mass of coal in the coal-bearing sequence to be in the order of $5.46 \cdot 10^9$ t. The aaverage gas content of this area is 1 m³/t (Kalkreuth et al., 2008b). From sorption isotherm measurements for CO_2 and CH_4, an average exchange ratio of 3.6 was calculated.

The CO_2 storage capacity for a 20x40 km area in the Santa Terezinha coalfield has been estimated using Equation (5) (Table 5-4). For the case of replacing sorbed methane by CO_2 injection, the storage potential of the study area would then amount to 1.55 Gt.

For a mean reservoir pressure of 6.25 MPa, the average sorptive storage capacity for CO_2 is 0.43 mmol/g (9.86 m³/t). Considering carbon dioxide sequestration only, e.g. keeping the gas currently stored in the coal (1 m³/t) in place, the remaining "free" CO_2 sorption capacity of 8.86 m³/t could be used for CO_2 storage. Assuming a recovery factor of 40%, the above calculation then yields a total CO_2 storage capacity of 13.8 Gt in the coals of the study area. In a combined ECBM production and CO_2 storage operation, a mass of 15.4 Gt CO_2 could theoretical be stored in the study area of the Santa Terezinha coalfield as defined by Kalkreuth et al. (2008b).

To refine this very simplistic calculation of the CO_2 storage potential of the Santa Terezinha coalfield, additional factors affecting CBM production (e.g. water saturation), injection (e.g. permeability) and

storage (presence and integrity of sealing formations) as well as potential environmental safety and health problems associated with CO2-ECBM need to be considered (Bachu, 2007; White et al., 2005).

Table 5-4. Estimation of the CO_2 storage capacity in a 20x40 km area of the Santa Terezinha coalfield

Sequestration scenario	1 CH_4 in reservoir replaced by CO_2	2 Free CO_2 sorption capacity filled with CO_2	3 CH_4 repalced by CO_2 + CO2 sorption capacity filled with CO_2
CO2 storage capacity	1.55 Gt	13.8 Gt	15.4 Gt

5.6 Conclusions

To evaluate the sorptive storage capacity of the Paraná Basin in Brazil, methane and carbon dioxide sorption experiments were performed on coal and carbonaceous shale samples from a CBM test well, drilled in 2007 in the Santa Terezinha coalfield. Additionally, storage capacities were determined on samples of the two major petroleum source rocks of the basin: the Devonian Ponta Grossa Formation and the Permian Irati Formation. Experiments were performed on powdered samples at pressures up to 25 MPa and temperatures of 35°C and 45°C.

The present study reports the first comprehensive set of high pressure sorption data for methane and carbon dioxide for coals, carbonaceous shales and petroleum source rocks of the Paraná Basin, Brazil.

On a raw mass basis (not dry, ash-free normalized), the Langmuir sorption capacities of methane on coal and carbonaceous shale from the CBM well ranged between 0.05 and 0.47 mmol/g. For the shale source rocks they were lower, ranging between 0.04 and 0.37 mmol/g. For carbon dioxide the maximum excess sorption, reached in the 8-12 MPa interval, ranged between 0.25 and 0.81 mmol/g for coal and carbonaceous shale samples, and between 0.14 and 0.54 mmol/g for shale source rocks. Normalized to dry, ash-free mass, methane sorption capacities of shales exceeded those of coal and carbonaceous shale.

Methane and carbon dioxide sorption capacities of coal and shales correlated with the organic carbon content (TOC). For carbon dioxide the linear regression showed a non-zero intercept, indicating a significant sorption capacity of the mineral matter. This was not the case for methane.

The present-day gas content of coals analysed from the first CBM well in the Santa Terezinha coalfield, as determined from canister desorption, amounts to 13 – 38% of the methane sorption capacity measured on as-received samples.

Moisture-equilibration of one coal sample from seam D (collected from a depth of 620.8 m), followed by sorption experiments, showed that its sorption capacity was reduced by 46% for methane and by 56% for CO_2, compared to the as-received state.

No correlation between sorption capacity and coal composition or thermal maturity was observed.

Carbon dioxide sorption capacity was higher than methane sorption for all samples. The CO_2/CH_4 sorption capacity ratio was larger for coal and carbonaceous shales (1.9 - 6.9) than for source rock shale samples (1.4 – 4.5).

Sorption capacities calculated for reservoir conditions indicated that theoretically an amount of 15.3 Gt carbon dioxide can be stored in coal seams of the study area. This amount would increase, if all methane were produced from coal seams prior to carbon dioxide injection.

In a further step, geological factors such as permeability, presence and integrity of sealing formations and economic factors such as depth and number of wells, costs for transport and injection of CO_2, that influence carbon dioxide storage, need to be evaluated to provide a more realistic view on the feasibility of carbon dioxide storage in the Santa Terezinha Coalfield.

6 Laboratory Experiments on Environmental Friendly Means to Improve Coalbed Methane Production by Carbon Dioxide/Flue Gas Injection

6.1 Introduction

The injection of carbon dioxide (CO_2), in coalbeds is one of the more attractive options of all underground CO_2 storage possibilities: the CO_2 is stored combined with simultaneous recovery of coalbed methane (CBM). Among all the fossil fuels, when combusted, methane emits the least amount of CO_2 per unit of energy released. Therefore, the zero option of CO_2 sequestration and production of methane lead to greater utilization of coalbed resources for both their sequestration ability and energy content. The revenue of methane (CH_4) production can offset the expenditures of the storage operations (Wolf et al., 1999; Wolf et al., 2000).

In the context of the geological storage of CO_2 a few projects consider the direct injection of flue gases from power plants or other flue gas emitting industries. Part of this research is also to investigate how to use industrial flue gas as an alternative to pure CO_2 as an injectant and how it influences the sequestrable amount of CO_2 in dry and water saturated coal. The use of flue gas instead of CO_2 in the ECBM projects may improve the cost-effectiveness of the ECBM projects considerably due to the elimination of the separation process. Flue gas being primarily N_2, the effect of pure N_2 as an injectant is also to be investigated. N_2 is known to act as a stripper. It is interesting to note that on a field scale, post production CH_4/N_2 separation is more expensive than CO_2/CH_4 separation.

Coal is characterized by its dual porosity: it contains both primary (micro pores and meso pores) and secondary (macro pores and natural fractures) porosity systems. The primary porosity system contains the vast majority of the gas-in-place, while the secondary porosity system provides the conduit for mass transfer to the wellbore. Primary porosity gas storage is dominated by adsorption. Primary porosity is relatively impermeable due to its small pore size. Mass transfer for each gas molecular species is dominated by diffusion that is driven by the concentration gradient. Flow through the secondary porosity system is dominated by Darcy flow that relates flow rate to permeability and pressure gradient.

The conventional primary CBM recovery process begins with a production well that is often stimulated by hydraulic fracturing to connect the well bore to the coal natural fracture system via an induced fracture (Mazumder et al., 2003). When the pressure in the well is reduced by pumping water by using artificial lift, the pressure in the induced fracture is reduced. This in turn, reduces the pressure in the natural coal fracture system. Initially, when the operation is started, water begins to move in the direction of the pressure gradient. When the pressure of natural fracture system drops below the critical desorption pressure, methane starts to desorb from the primary porosity and is released into the secondary porosity system. As a result, the adsorbed gas concentration in the primary porosity system near the natural

fractures is reduced. This reduction creates a concentration gradient that results in mass transfer by diffusion through the micro and meso porosity. Adsorbed gas continues to be released as the pressure is reduced (Reznik et al., 1984).

Enhanced recovery of coalbed methane (ECBM) by injecting a second gas maintains overall reservoir pressure, while lowering the partial pressure of the CBM in the free gas. CO2 which is more strongly adsorbable than methane is injected into the coal natural fracture system during the ECBM recovery process; it is preferentially adsorbed into the primary porosity system (Busch et al., 2004a). Upon adsorption the CO_2 drives the CH_4 from the primary porosity into the secondary porosity system. The secondary porosity pressure is increased due to CO_2 injection and the CH_4 flows to the injection wells (Shi and Durucan, 2003b).

The objectives to do the core flood experiments using varied injectants from pure CO_2 and N_2 to multi-component flue gas are as follows: experiments were conducted to analyze the influence of injection pressure and injection rate on the methane recovery, evaluate the influence of water on the CH_4–CO_2 exchange process in coal by conducting experiments under relatively dry and wet conditions, to differentiate the effects of an alternate injection of a strong (CO_2) and weak (N_2) adsorbing gas, to compare the breakthrough time of CO_2 from different CO_2 core flood experiments and to compare the results of pure CO_2 against flue gas flooding experiments.

6.2 Equipment Design

The uniqueness of these experiments, using large cores (800–1,000 cc), makes the design of the setup complex. The reasons to use large core samples are: (i) heterogeneity of the coal matrix is sufficiently guaranteed and (ii) the dual porosity nature of coal is retained. Taking this into consideration a high pressure core flooding setup was constructed. The schematic of the setup is shown in Figure 6-1. The pressure cell of 1 m in length has a maximum confining pressure of 20 MPa and a maximum temperature of 150°C. The confining pressure was applied on the coal core, inside a rubber sleeve. In order to prevent the gas from diffusing through the rubber sleeve, 0.2 mm lead foil was wrapped around the coal core. The rubber sleeve is able to transfer the annular pressure onto the sample. In order to simulate down hole conditions the temperature in the pressure cell was maintained at around 45°C. The pressure cell can handle samples up to a diameter of 120 mm and a core length of 500 mm. The length of the core varied from sample to sample. In order to avoid mechanical end effects on the core permeability, two sieperm plates are fixed at both ends of the core. These sieperm plates have a porosity of 33% and a permeability of 10^{-13} m^2. The injection and production tubings are attached to the end plates. The end plates also serve for maximal distribution of gas at the injection side.

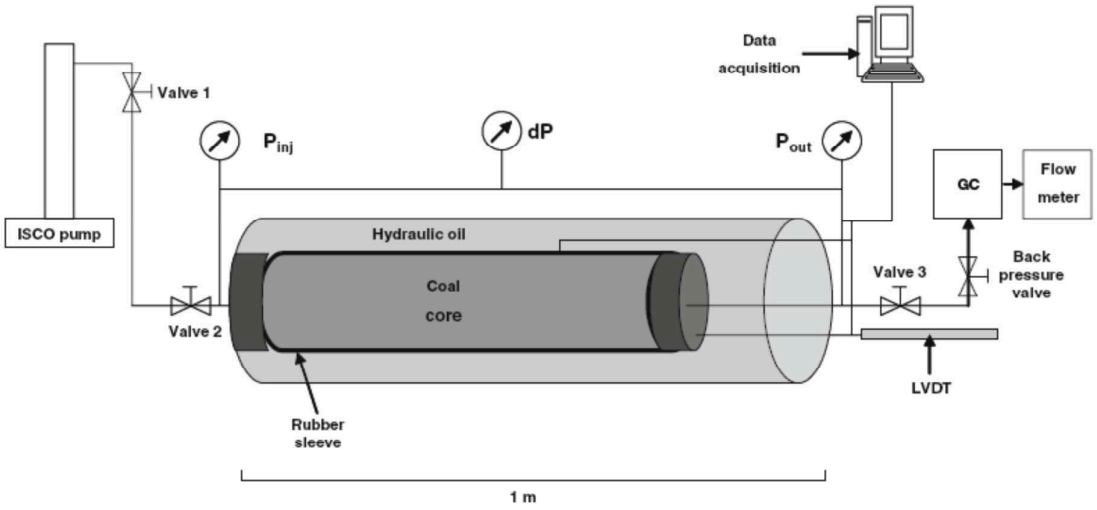


Figure 6-1. Schematic of the high pressure flow cell. The volume of the ISCO pump, including the tubing to valve 1 is 283.02ml, of which 266.50ml can be displaced. The tubing volume between valve 1 and 2 is 44.04ml. The tubing volume between valve 2 and 3 is 74.62 ml (excluding coal volume). The volume of the tubing between valve 3 and the back pressure valve is 46.725 ml. All volumes reported are at STP.

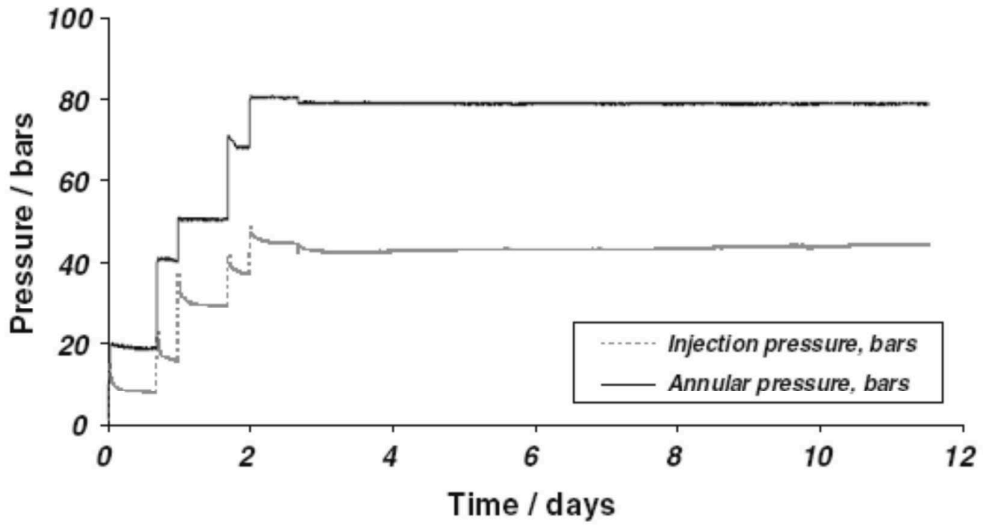


Figure 6-2. Measured system pressure during Experiment I (Beringen 770, dry, CO_2 injection at 6 ml/h). The average effective stress applied was 40 bars.

Following the direction of flow, the high pressure cell consists of the following peripheral devices:

- An ISCO TM plunger pump connected to a bottle of the required gas to be injected. The ISCO plunger pump injects CO_2, CH_4, N_2 and flue gas into the coal core at a constant injection rate. The average of the injection and production pressure was taken as the pressure over the core and used for the calculation of the Darcy permeability. At the production end, a back pressure valve controlled the flow out. A constant effective stress was maintained during the experiment.

- A linear variable displacement transformer (LVDT) measured the axial displacement of thecoredimension (μ-strains), throughout the experiment. The cores were drilled parallel to the bedding plane, thus ensuring that the axial strain measured was parallel to bedding.
- Gas analyzer. The gas chromatograph (GC) used for analyzing the product gas was an Agilent™ 3000 micro GC with a Thermal Conductivity Detector (TCD).
- Flow analyzer. At the end of the line an analog flow analyzer, i.e. an Acataris™ water clock measured the remaining gases leaving the system. This type of analog flow analyzers runs at an accuracy of 0.1 ml/h. The flow rate was camera recorded and afterward used for mass balance calculations and permeability measurements.
- Operational panel, safety device and data acquisition system. The operation panel, the data-acquisition system and safety devices were installed in the control room. During the test, two thermocouples were used to measure temperatures above and below the core inside the pressure cell. In addition, the (differential) pressure, tube/sample expansion and flows were registered every 30 s.

6.3 Sample Description

The unique properties of coal put constraints on preparation and preservation of coal samples. When exposed to air, the effect of drying and weathering results in the alteration of the coal structure and develops new fractures. The permeability and porosity values of such samples may be significantly different from the samples that are well preserved. The cores were drilled from big blocks of coal (>0.25 m^3). Coal samples used for these experiments were kept in water to avoid contact with air and drying. Once drilled the cores were put in sealed polyethylene bags and cooled to prevent oxidation or loss of moisture. All the coal cores were drilled parallel to the bedding plane except for Experiment VII, where a vertical drill core was used. The samples used for these experiments were from the Beringen coal mines (Beringen 770) in Belgium, the Silesia and the Brzeszcze coal mine in Poland and a vertical drill core from the CO_2 injection well (seam 401; Well MS3) in Poland. The details of the samples are shown in Table 6-1. Nine different flooding experiments were conducted on coal cores drilled from the samples mentioned above. The details of the coal cores and their experimental conditions are in Table 6-2. The Silesia and the Brzeszcze samples were in terms of their maceral composition similar in rank. The Silesia coal was vitrinite rich and the Brzeszcze coal was inertinite rich. The micro-pore volume and specific surface are listed in Table 6-1.

Table 6-1. Sample properties.

Sample	Rank (% R_{max})	Maceral composition (%)		Specific surface (m^2/g)	Micropore volume (cm^3/g coal)
Beringen 770 (Belgium)	0.78	Vitrinite	37.8	151.53	0.055
		Liptinite	18.0		
		Inertinite	44.0		
		Mineral matter	0.2		
Silezia 315 II (Poland)	0.68	Vitrinite	71.6	190.00	0.064
		Liptinite	6.8		
		Inertinite	15.0		
		Mineral matter	6.8		
Brzeszcze 501; LW 405 (Poland)	0.75	Vitrinite	38.8	171.00	0.058
		Liptinite	8.0		
		Inertinite	52.8		
		Mineral matter	0.4		
Seam 401 vertical drill core from well MS3 (Poland)	0.85	Vitrinite	53.8	–	–
		Liptinite	6.3		
		Inertinite	21.2		
		Mineral matter	18.7		

6.4 Preferential Sorption Behaviour

Volumetric sorption experiments for pure CH_4 and CO_2 were conducted for all the samples used for the flooding experiments. This data is reported in Appendix D. Only few measurements have been reported for mixtures of two or more gas components under the conditions of competitive sorption. Very few data showed preferential adsorption of CO_2 and preferential desorption of CH_4, as commonly expected. Busch et al., 2006 reported distinct variations in the competitive adsorption and desorption behaviour of the different dry and moist samples, ranging from preferential adsorption of CH_4 in the low pressure range to preferential desorption of CO_2 over the entire pressure range. The preferential sorption behaviour of the Silesia and Brzeszcze samples has been reported by Busch et al., 2006.

Table 6-2. Coal core details and experimental conditions (all core samples were 69.50mm in diameter).

Experiment	Length (mm)	Sweep (%)	P_{mean} (MPa)	P_{eff} (MPa)	Injection rate (moles/min)	Injection rate (ml/h) at 45°C, P_{mean}	Pore volume at STP (ml)	Free CH_4 (moles)	Adsorbed CH_4 (moles)
I (Beringen 770; Dry; CO_2)	334.00	69.1	4.3	3.61	1.6E-4	6.0	63.35	0.43	0.61
II (Beringen 770; Dry; CO_2)	178.30	60.90	8.12	2.01	4.12E-5	0.7	33.82	0.402	0.83
III (Silezia 315 II; Wet; CO_2)	200.50	34.00	8.325	2.25	1.19E-4	1.0	60.86	0.1337	0.2913
IV (Silezia 315 II; Dry; CO_2)	200.50	78.94	9.08	1.59	1.88E-4	1.0	60.86	0.5176	0.409
V (Brzeszcze 501; Wet, CO_2)	208.00	30.18	8.78	1.77	6.25E-5	0.5	63.13	0.4397	0.5784
VI (Brzeszcze 501; Dry, CO_2)	208.00	72.74	8.74	1.72	5.68E-5	0.5	63.13	0.5604	0.45243
VII (Seam 401; Wet; CO_2/N_2)	229.3	37.97	8.67	1.87	Phase 1, CO_2: 6.45E-5 Phase 2, N_2: 2.68E-5 Phase 3, CO_2: 6.55E-5	0.5	52.18	0.5673	0.3467
VIII (Silezia 315 II; Dry; Flue gas)	200.50	35.1	8.42	2.06	4.56E-5	1.0	60.86	0.7222	0.7033
IX (Silezia 315 II; Wet; Flue gas)	200.50	58.00	8.55	1.99	5.1E-5	1.0	60.86	0.4095	0.6312

The free CH_4 is a product of the total gas volume (i.e. coal porosity plus dead volume) and CH_4 density at STP

Differences in the sorption behaviour were observed between the coals as well as between measurements performed on dry and moist samples. The most conspicuous difference in the preferential adsorption with respect to moisture content was found for the coal sample from the Silesia mine: the moist Silesia 315 sample exhibits significant preferential adsorption of CH4 up to about 6 MPa and then switches to preferential CO_2 adsorption (Busch et al., 2006). In contrast, the dry sample shows no fractionation for the first measured data point at about 1 MPa, followed by preferential adsorption of CO_2 with increasing pressure (Busch et al., 2006). This observation could be due to competition of water and CO_2 for specific sorption sites in the moist sample or due wettability reversal (water wet to CO_2 wet). The desorption trends of both experiments are similar and indicate only slight tendency for preferential desorption of CO_2 in the low-pressure range. For the Brzeszcze coal sample, preferential desorption of CO_2 is evident over the complete pressure range for the dry, and even more clearly so for the moist sample. For the adsorption trend there is a clear preferential adsorption of CO_2 over the entire pressure range for the dry sample. The moist Brzeszcze adsorbs CH_4 preferentially up to about 5.5 MPa with an opposite trend for the high pressure range (Busch et al., 2006), the dry sample shows preferential adsorption of CO_2 over the entire pressure range. When comparing the results for the samples it is difficult to detect any distinct relationship between the preferential sorption behaviour and maceral composition or rank. Although all the samples are high volatile bituminous coals, they show distinct differences in their sorption behaviour, which, therefore, cannot be attributed to rank. However, there appears to be regularity in the selective sorption behaviour with respect to moisture content. Although the preferential adsorption trend is not uniform throughout the sample set, moist coals exhibit a reduced tendency towards preferential CO_2 adsorption as compared to dry coals (Busch et al., 2006). The maceral composition might be an influencing factor, because the sample with the highest inertinite content (Brzeszcze) shows the highest degree of preferential CO_2 desorption within the sample set.

6.5 Experimental Procedure and Data Interpretation

The experiments start with a complex procedure of mounting the lead foil wrapped coal core in a rubber sleeve and building it leak free in the high-pressure cell. A detailed procedure for volume measurement was then followed. The volume measurements were conducted with and without the sample built in the pressure cell. The details of the void volume measurements are discussed in Appendix A. The tubing volume in the whole setup is quite considerable. The effect of this dead volume is seen in the results and has been discussed later in this section. All mass balance calculations for CH_4 and CO_2 do take care of the free and the adsorbed volumes separately. At the end of the volume measurement the sample cell was, for at least a week connected to a vacuum pump, to eliminate any form of residual gas or free moisture. During this process temperature was kept constant. Experiment IV (Silesia 315 II; Dry; CO_2) is used as an example to describe the test procedure. The flooding test, which lasted a total of 45 days, consisted of three consecutive stages (Figure 6-14): (i) CH_4 loading, (ii) CO_2 loading, and (iii) continued CO_2 injection with

production under a constant pressure. In a typical wet experiment, the CO_2 loading stage is replaced by a water loading phase (Figure 6-34). In the first stage (7 days), 20.76 l of CH_4 was injected into the system in increasing pressure cycles, till the required saturation was reached. The system pore pressure rose to 6 MPa during two days of injection. After each injection cycle the methane was allowed to sorb onto the coal matrix until equilibrium was reached. In order to meet sub-surface conditions, the difference between the annular pressure and the pore pressure was usually kept at ratios of 2:1 to 5:3. The volume of injected methane was measured with a mass flow meter. The free methane is the product of the total gas volume (i.e. coal porosity plus dead volume) multiplied by the methane density at a particular P,T condition. The sorbed methane is the difference between the total amounts of methane injected in the system minus the free methane. The typical pressure profile during methane loading is shown in Figure 6-14 and Figure 6-34. During the second stage (21 days), the system was further pressurized to 9.0 MPa, with the injection of 32.2 l of CO_2

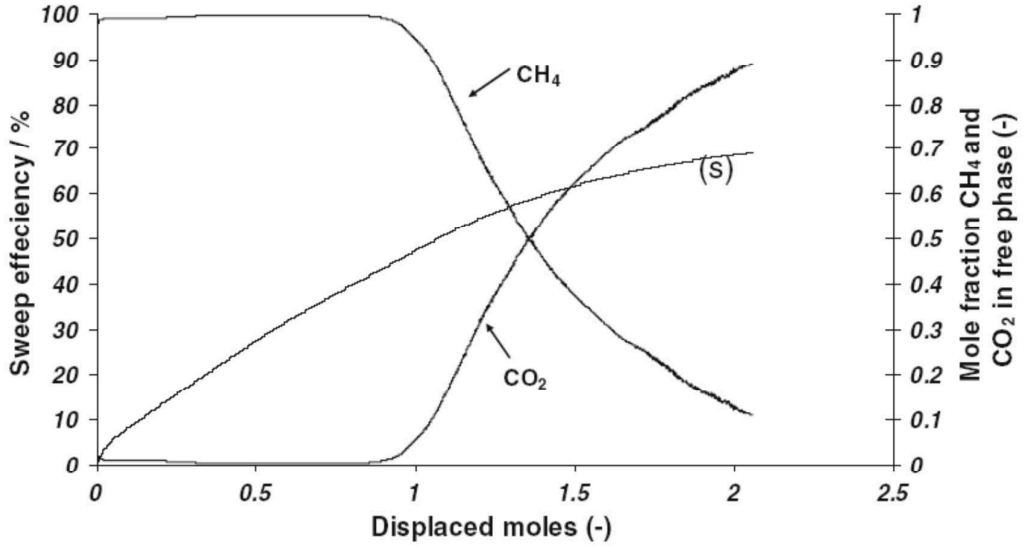


Figure 6-3. Sweep efficiency (s) and molar concentrations of the produced gas against displaced moles from Experiment I (Beringen 770, dry, CO_2 injection at 6 ml/h). The migration data have been plotted against displaced volume to make time dimensionless.

The gas analyzer determined the relative amount of CH_4, CO_2 and N_2 alongside other gases in the product (Figure 6-3). The GC measurements were assumed to be representative of the change in molar concentrations of each component in the free phase. For the CO_2 flooding experiments, the experiment was stopped when the relative amount of carbon dioxide in the product gas reached 98%. The moisture, if present was separated using a silica gel bottle connected to a balance. Hence, for wet experiments the amount of water flowing out was measured. During the tests the recorded data serve as an iterative feedback to control injection volumes for mass balance calculations afterwards.

6.6 Results and Discussions

6.6.1 CO2 Core Flood Experiments

The seven different CO_2 core flood experiments (Table 6-2) range from sub-critical to supercritical CO_2 conditions. In order to compare the effect of varying injection rate and injection pressure on the methane recovery, the results of Experiments I and II have been listed in Table 3. The experimental conditions prior to the start of CO_2 injection are in Table 6-2. Figure 6-3 and Figure 6-7 show migration history of CH_4 and CO_2 Both the experiments were conducted at a temperature of 45°C. While the injection rate for Experiment I was 6 ml/h, that of Experiment II was set as low as 0.7 ml/h. Pressure and temperature conditions were sub-critical for Experiment I, but were super-critical for Experiment II. As can be seen from the migration data (Figure 6-3 and Figure 6-7) the injection pressure does not have a big influence on the methane recovery. Diffusion is much faster under sub-critical conditions as compared to super-critical conditions. CO_2 is five times more dense than CH_4 under super-critical conditions.

CO_2 flooding (Beringen 770)	$CO_2 = 1\%$		$CO_2 = 50\%$		$CO_2 = 90\%$	
	Dry (6 ml/h)	Dry (0.7 ml/h)	Dry (6 ml/h)	Dry (0.7 ml/h)	Dry (6 ml/h)	Dry (0.7 ml/h)
Sweep efficiency (%)	43.6	22.9	58.8	46.7	69.1	58.7
Displaced moles (mole/mole)	0.91	1.77	1.36	5.1	2.06	10.63
Time after production (s)	3.36×10^5	6.6×10^5	5.0×10^5	19.0×10^5	7.7×10^5	39.6×10^5

Table 6-3. Sweep efficiency, displaced moles and time of Experiments I and II.

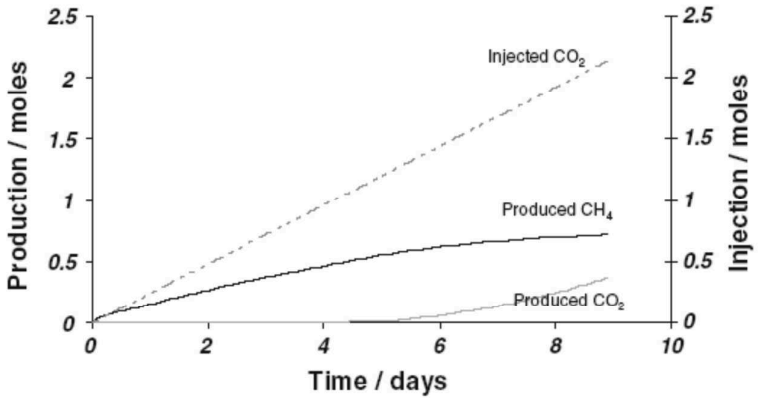


Figure 6-4. Cumulative production of all gases, and injection of CO_2 from Experiment I (Beringen 770, dry, CO_2 injection at 6.0ml/h).

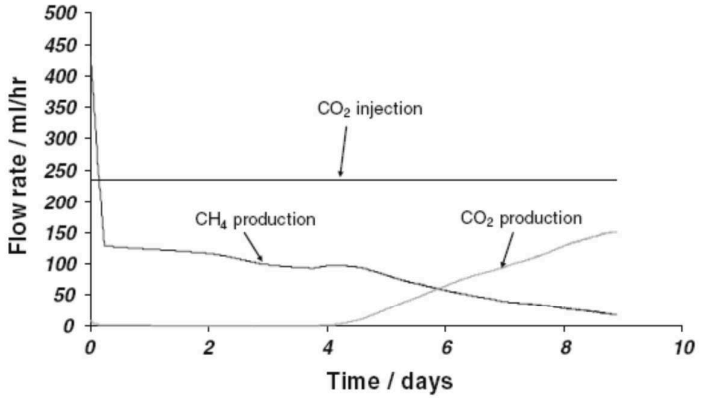


Figure 6-5. Injection and production flow rate of gases for Experiment I at STP. The breakthrough of CO2 took place 4 days after the initiation of simultaneous injection and production.

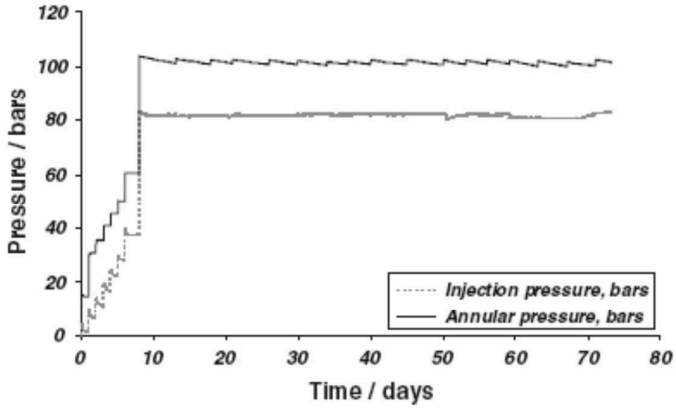


Figure 6-6. Measured system pressure during Experiment II (Beringen 770, dry, CO_2 injection at 0.7 ml/h). The average effective stress applied was 20 bar. The initial phase of CH_4 loading is followed by the stable injection pressures during which simultaneous injection and production was carried out.

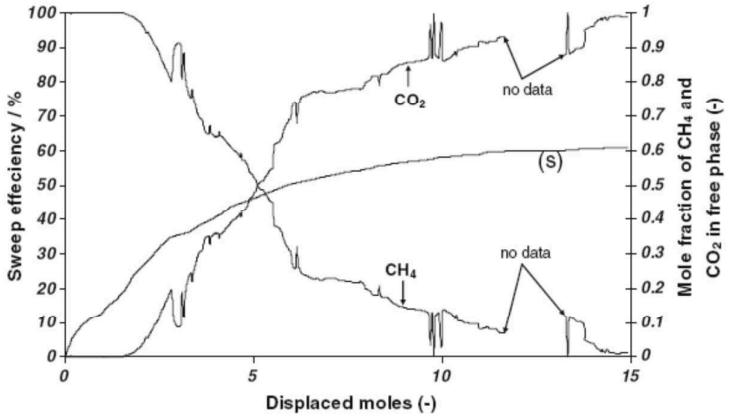


Figure 6-7. Sweep efficiency (s) and molar concentrations of the produced gas against displaced moles from Experiment II (Beringen 770, dry, CO2 injection at 0.7 ml/h). The GC response is dependent on the opening and the closure of the back pressure valve. This brings about fluctuations on the migration data. Some of the sharp events on the plot shown above are due to events like pump filling, heating failure, pressure fluctuations etc.

Sweep efficiency and displaced moles are defined as follows (Bertheux, 2000):

$$sweep\ efficiency\ (\%) = \frac{moles\ of\ CH4\ produced}{moles\ of\ CH4\ initially\ in\ place} \times 100 \qquad (6\text{-}1)$$

$$displaced\ moles = \frac{moles\ of\ injected\ displacing\ gas}{moles\ of\ CH4\ initially\ in\ place} \qquad (6\text{-}2)$$

6.6.1.1 Binary Displacement for Beringen Coal

Figure 6-2 to Figure 6-9 shows the pressure history, molar concentration change, cumulative production and injection of all gases and the injection/production flow rate at STP for the two experiments conducted on the Beringen coal. As can be seen from Figure 6-2 and Figure 6-6, Experiment I was conducted at almost half the injection pressure as compared to Experiment II. On the other hand, the effective stress for Experiment I was almost twice as high as that of Experiment II. The molar rate of injection for Experiment I is almost four times higher than that of Experiment II (Table 6-2). The coal core used in Experiment I is twice as long as that of Experiment II (Table 6-2). As can be seen from Table 6-3, the breakthrough time for Experiment I is almost two times faster than Experiment II. Also at breakthrough (1% CO_2), almost all the free methane in the system has been produced, whereas only half the free volume of methane was produced for the second case. From the displaced moles data, it is evident that in terms of simple methane recovery, at 90% of product CO_2 concentration, Experiment I might look more efficient as it takes almost five times less time to remove almost equal concentration of CH_4 from the system. It can be seen that for better exchange and storage of CO_2, the residence time for CO_2 in the coal has to be longer. Diffusion is more pronounced in Experiment II than in Experiment I where the injected CO_2 moves fast through the core.

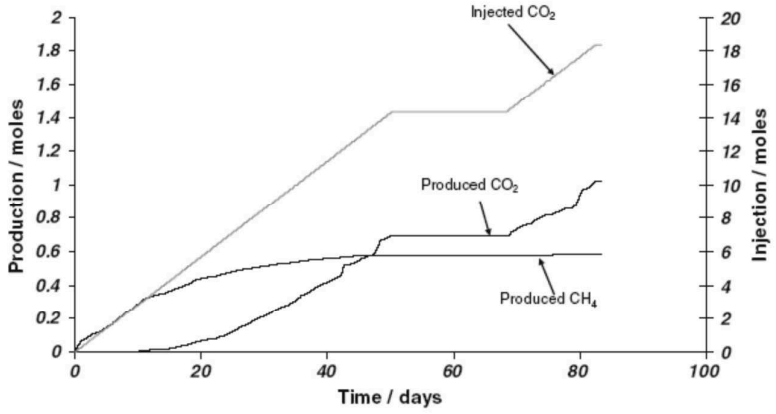


Figure 6-8. Cumulative production of all gases, and injection of CO_2 from Experiment II (Beringen 770, dry, CO_2 injection at 0.7 ml/h). Considerable difference between the injected and produced volumes of CO_2 can be observed.

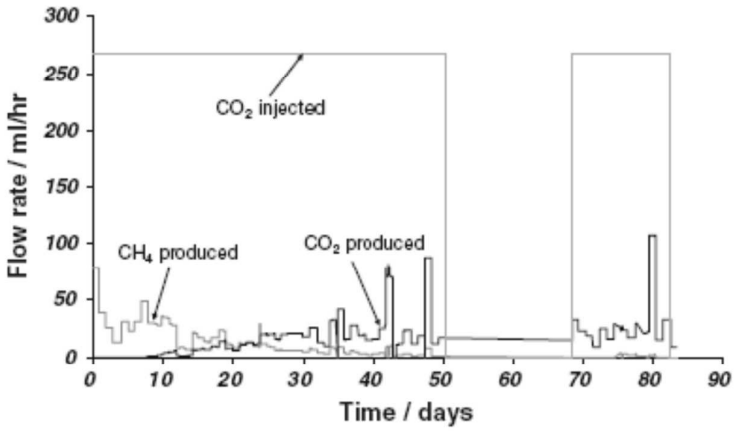


Figure 6-9. Injection and production flow rate of gases for Experiment II at STP.

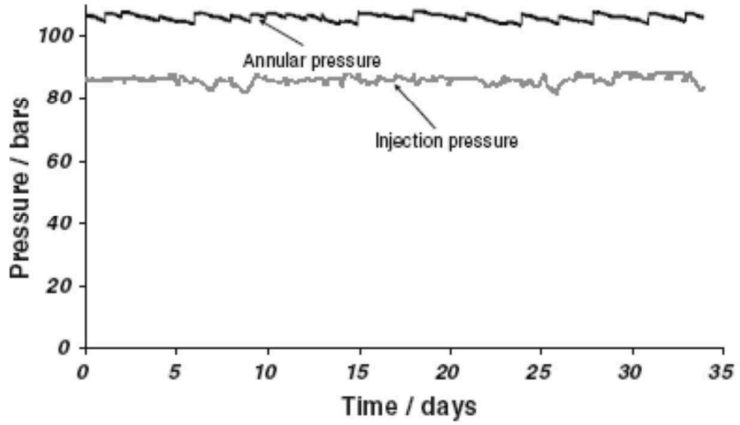


Figure 6-10. Measured system pressure during Experiment III (Silesia 315 II, wet, CO_2 injection at1.0 ml/h). The average effective stress applied was 20 bars. Only the pressure history during the production phase is shown here.

6.6.1.2 Binary Displacement for Silesia Coal

Figure 6-10 to Figure 6-17 shows the pressure history, molar concentration change, cumulative production and injection of all gases and the injection/production flow rate at STP for the two experiments conducted on the Silesia coal. The coal sample of Experiment III and IV have a higher vitrinite content (71.6%) than the inertinite content (15%). Experiments III and IV were conducted to compare the influence of water on the CO_2–CH_4 exchange process in the coal. Considerable influence of water in methane recovery have been predicted by Mazumder et al. (2003)by means of numerical simulation. The experimental conditions for these experiments have been shown in Table 6-2. Both the experiments were conducted on the same coal sample. Experiment II was conducted on a wet coal core with excess water in the fracture system of the coal. No free water was present in the relatively dry Experiment IV. The comparative results of the experiments have been summarized in Table 6-4 and Table 6-5. The duration of the wet experiment was much longer than the dry one. As can be seen from Table 6-2, only 34% of the CH_4 in place was produced at

the end of the wet experiment, whereas almost 79% of the CH_4 in place was produced from the dry experiment. An estimate from the above figures show that, apart from the free methane that was produced, only 3% of the adsorbed methane was produced from the wet experiment as compared to 50% from the dry experiment. Table 6-5 shows that there is no considerable difference in the breakthrough time for both experiments. For the wet experiment the slightly faster breakthrough is due to the solution of CO_2 in the produced water from the fracture spacings. The wet displacement experiment was conducted for a period of 57 days compared to the dry displacement experiment, which was conducted for 38 days. There is no possible explanation for the excess CO_2 being sorbed in the wet experiment. Solution effect of CO_2 in water might be a possible effect. Repeat experiments needs to be conducted to understand the effect. From the sweep efficiencies at different times from Table 6-5, the methane recovery for the relatively dry experiments are much higher as compared to the wet experiment. The CO_2 storage capacity remains constant. This also indicate that CO_2 occupies different sorption sites than CH_4 (Clarkson and Bustin, 1999b). The presence of CO_2 does not affect the sorption capacity of CH_4.The CO_2 and CH_4 migration data for both the experiments are presented in Figure 6-11 and Figure 6-15. Figure 6-12 is a plot of the injection and the production details of Experiment III, which shows two distinct phases of the water production. One, with most of the free water in the fractures, produced in a short span of time, and second from the macro pores, produced much slower.

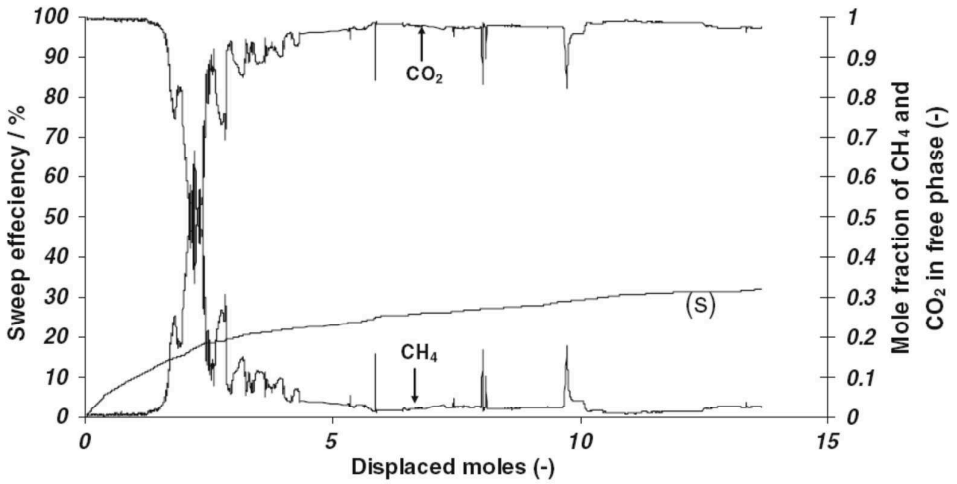


Figure 6-11. Sweep efficiency and molar concentration of the produced gas against displaced moles from Experiment III (Silesia 315 II, wet, CO_2 injection at1.0 ml/h) of all gases, water and injection of CO_2 from Experiment III (Silesia 315 II, wet, CO_2 injection at 1.0 ml/h).

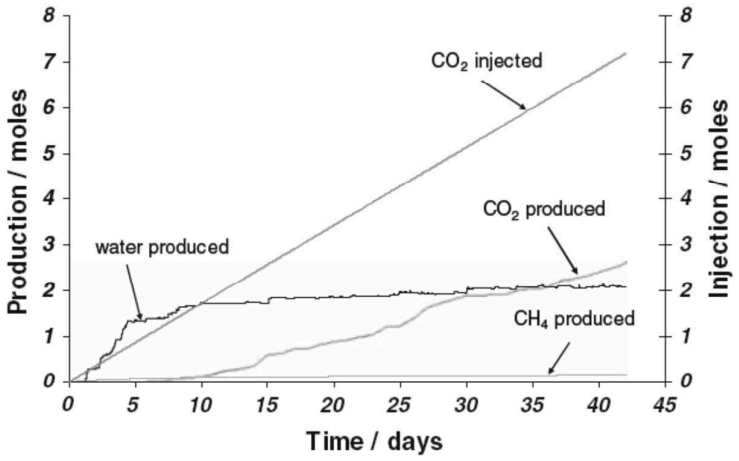


Figure 6-12. Cumulative production of all gases, water and injection of CO_2 from Experiment III (Silesia 315 II, wet, CO_2 injection at 1.0 ml/h).

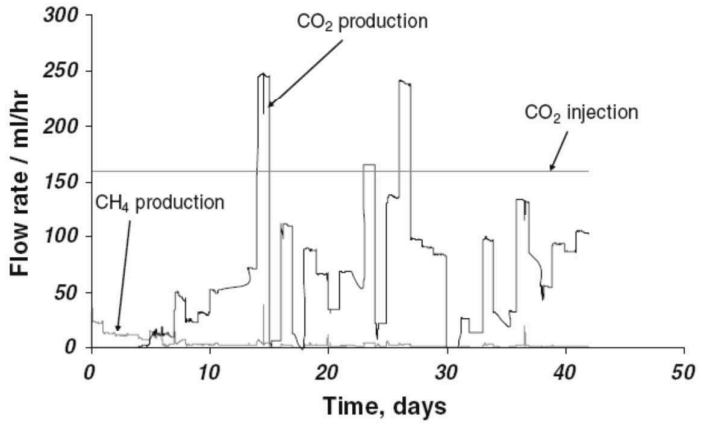


Figure 6-13. Injection and production flow rate of gases for Experiment III at STP.

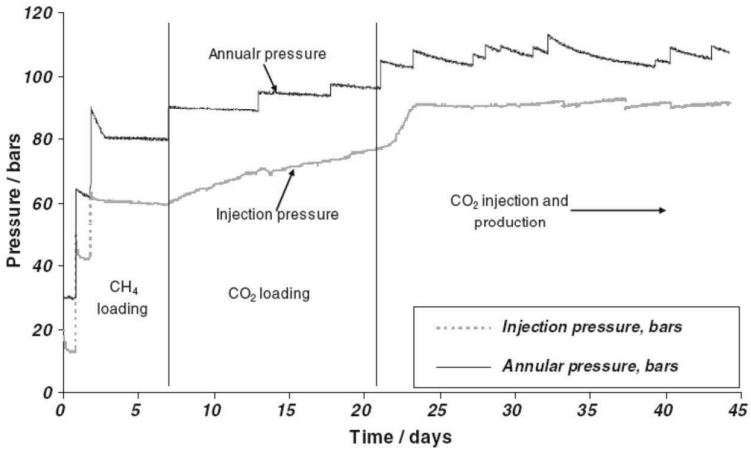


Figure 6-14. Measured system pressure and cumulative CO_2 injection during the test. The purpose of the CO_2 loading phase was to bring up the injection pressure to super-critical conditions and to provide more residence time for CO_2 in the pressure cell.

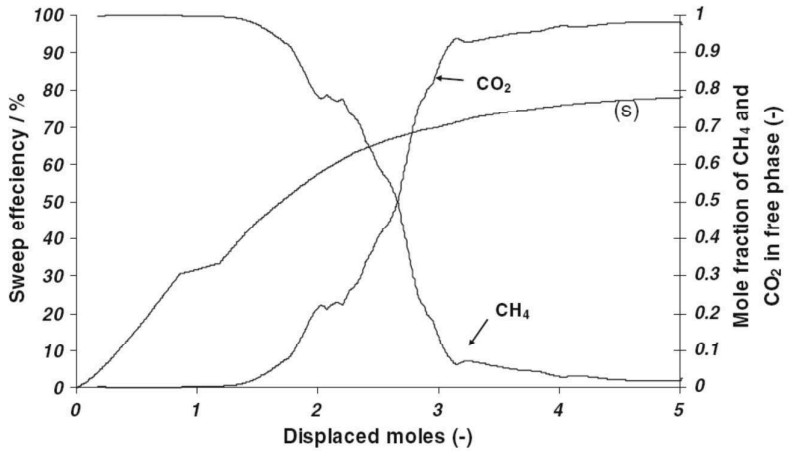


Figure 6-15. Sweep efficiency and molar concentrations of the produced gas against displaced moles from Experiment IV (Silesia 315 II, dry, CO_2 injection at 1.0ml/h).

6.6.1.3 Binary Displacement for Brzeszcze Coal

Figure 6-18 to Figure 6-25 shows the pressure history, molar concentration change, cumulative production and injection of all gases and the injection/production flow rate at STP for the two experiments conducted on the Brzeszcze coal. Experiments V and VI were conducted on a coal sample which had a higher inertinite content (52.8%) than vitrinite content (38.8%). These experiments were conducted to see the effect of water on methane recovery. The results of experiments V and VI are listed in Table 6-6 and Table 6-7. The migration history of these experiments are in Figure 6-19 and Figure 6-23. The injection and production data for Experiment V are listed in Figure 6-20. These two experiments showed different results as compared to Experiments III and IV. Significant differences in the methane recovery was noted between the wet (Experiment V) and dry (Experiment VI) experiments. It could not be explained if the early breakthrough was caused by inherent characteristic for an inertinite rich coal or due to an easy pathway through which the CO_2 moved directly to the production side (preferential flow). Field experiments in Poland also suggest very early breakthrough of CO_2 from these coals in the production well. Note that the injection rate for Experiment V and VI is half of that for Experiments III and IV. It is also true that the maceral composition of these coals, have big influence in the CO_2–CH_4 exchange process.

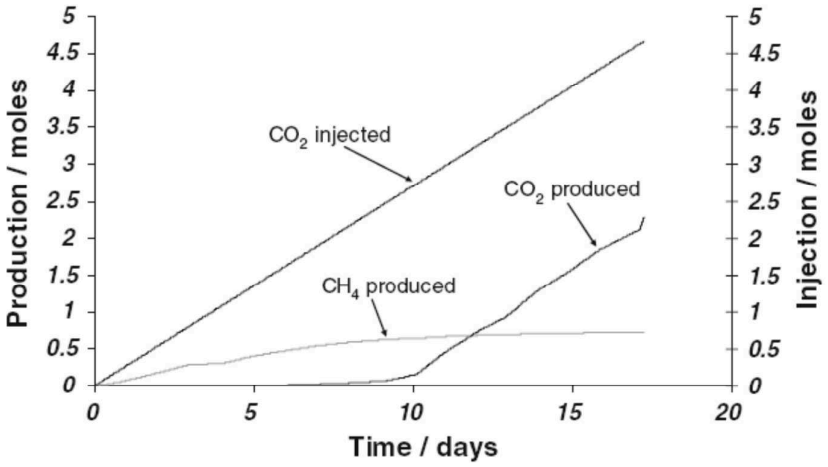


Figure 6-16. Cumulative production of all gases, and injection of CO_2 from Experiment IV (Silesia 315 II, dry, CO_2 injection at 1.0 ml/h).

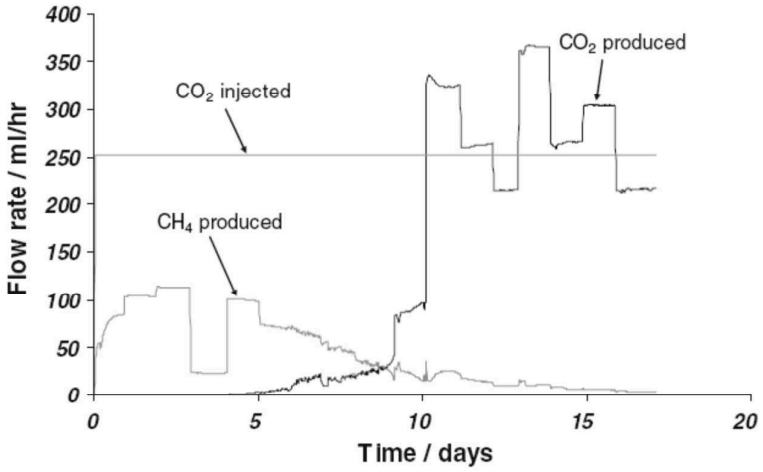


Figure 6-17. Injection and production flow rate of gases for Experiment IV at STP.

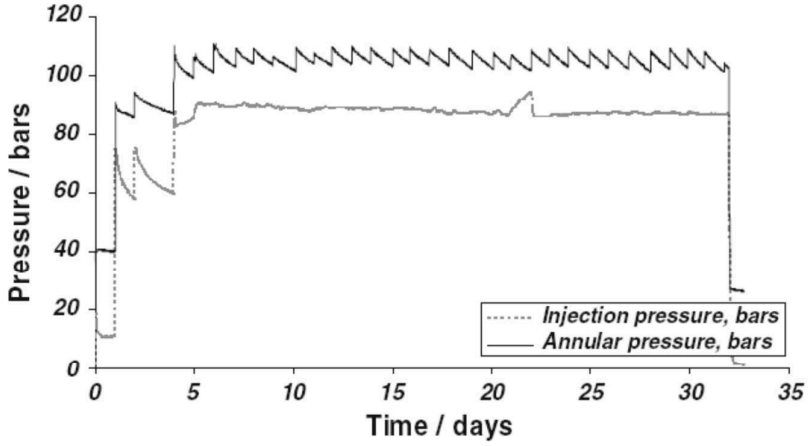


Figure 6-18. Measured system pressure during Experiment V (Brzeszcze, wet, CO_2 injection at 0.5ml/h). The average effective stress applied was 20 bars.

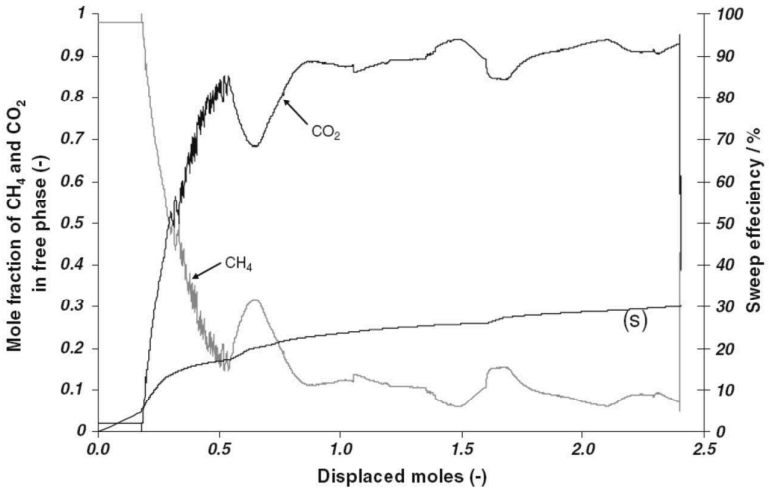


Figure 6-19. Sweep efficiency and molar concentrations of the produced gas against displaced moles from Experiment V (Brzeszcze, wet, CO_2 injection at 0.5 ml/h).

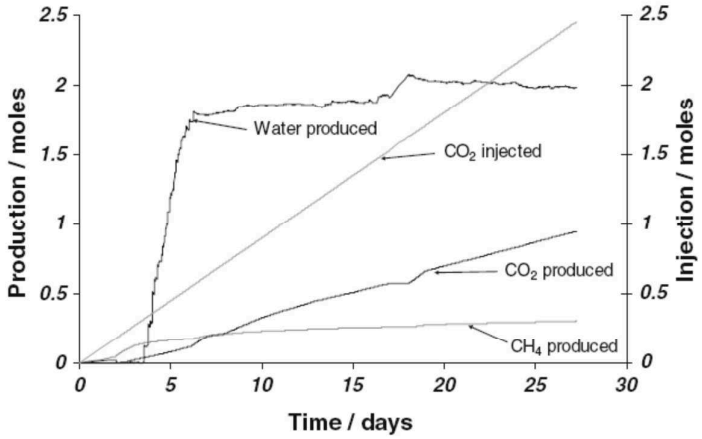


Figure 6-20. Cumulative production of all gases, water and injection of CO_2 from Experiment V (Brzeszcze, wet, CO_2 injection at 0.5ml/h.)

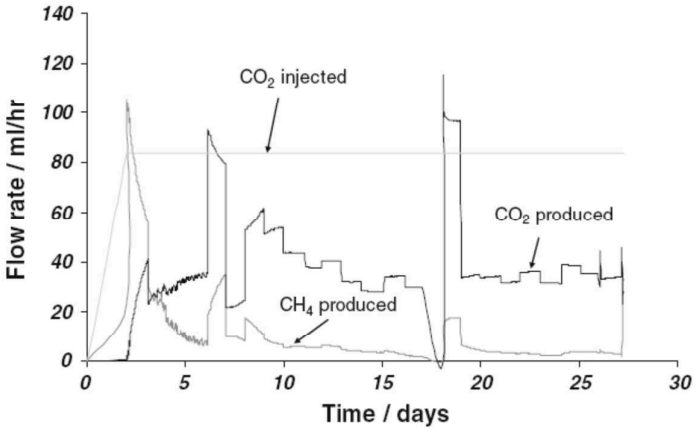


Figure 6-21. Injection and production flow rate of gases for Experiment V at STP.

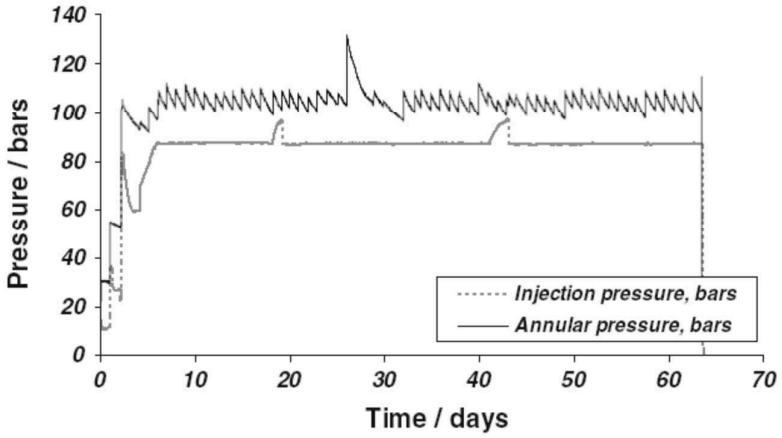


Figure 6-22. Measured system pressure during Experiment VI (Brzeszcze, dry, CO_2 injection at 0.5ml/h). The average effective stress applied was 20 bars.

CO_2 flooding (Silesia 315 II)	Dry	Wet
Total amount of CO_2 injected (moles)	4.665	7.18
Amount of adsorbed CO_2 (moles)	1.604 (max)	3.83
Amount of free CO_2 (moles)	0.7823	0.7394
Total amount of CO_2 produced (moles)	2.279	2.62

Table 6-4. The total, free, adsorbed and produced amount of carbon dioxide in the dry and wet Silesia 315 II flooding experiment.

CO_2 flooding (Silesia 315 II)	CO_2 = 1%		CO_2 = 50%		CO_2 = 90%	
	Dry	Wet	Dry	Wet	Dry	Wet
Sweep efficiency (%)	37.2	11.6	66.25	16.5	69.8	19.5
Displaced moles (mole/mole)	1.28	1.26	2.56	2.09	2.96	2.86
Time after production (s)	3.8×10^5	2.7×10^5	7.6×10^5	4.5×10^5	8.8×10^5	6.1×10^5

Table 6-5. Sweep efficiency, displaced moles and time of Experiment III and IV.

6.6.1.4 Ternary Displacement for Coal Seam 401

Figure 6-26 to Figure 6-29 show the pressure history, molar concentration change, cumulative production and injection of all gases and the injection/production flow rate at STP for Experiment VII conducted on the coal seam 401 Experiment VII was conducted on a vertical drill core from Poland and was intended to compare the effects of an alternate injection of a strong (CO_2) and weak (N_2) adsorbing gas. N_2 has stripping

properties when injected in coal seams. In order to avoid this effect the experiment was so planned that the N_2 injection was done after one pump volume of CO_2 injection. This was also meant to remove all the free methane from the system before nitrogen injection was initiated. The results of this experiment are summarized in Table 6-8 and Table 6-9. Figure 6-27 shows the migration of CH_4, CO_2 and N_2 through the core. As seen from other wet experiments the methane recovery of this experiment too is quite low (38%) and the breakthrough is early too. The experiment started with the injection of one pump volume of CO_2 (Figure 6-27). At a displaced mole of 2.23, N_2 injection started and after one pump volume, the CO_2 injection was resumed at the corresponding displaced mole of 3.14. A sharp increase in CH_4 production was observed alongside N_2 breakthrough. This incremental CH_4 production was quite consistent throughout the N_2 production. With the injection of CO_2 in a CH_4 saturated coal, the partial pressures of CH_4 in the free phase is reduced. This initiates the CH_4 to sorb out of the coal and go into the free phase. Also at near critical conditions of CO_2, the pressure, temperature and density behaviour, is very difficult. The possible cause of this effect is still unknown.

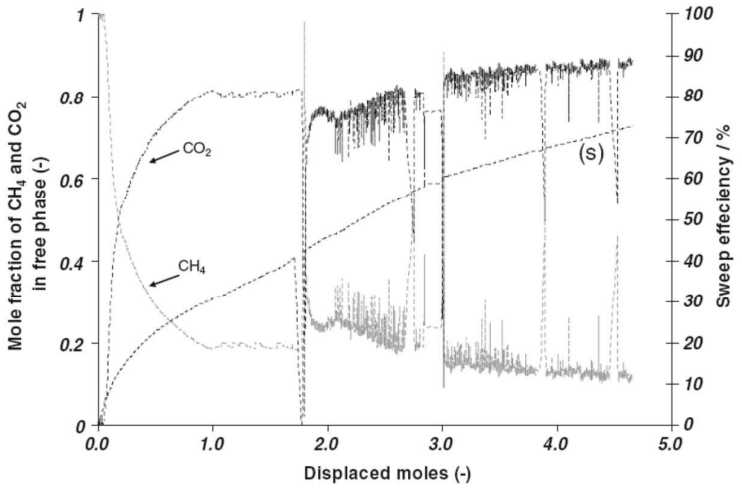


Figure 6-23. Sweep efficiency (s) and molar concentrations of the produced gas against displaced moles from Experiment VI (Brzeszcze, dry, CO_2 injection at 0.5 ml/h). The fluctuations on the migration data are because of the fact that the GC columns were not clean.

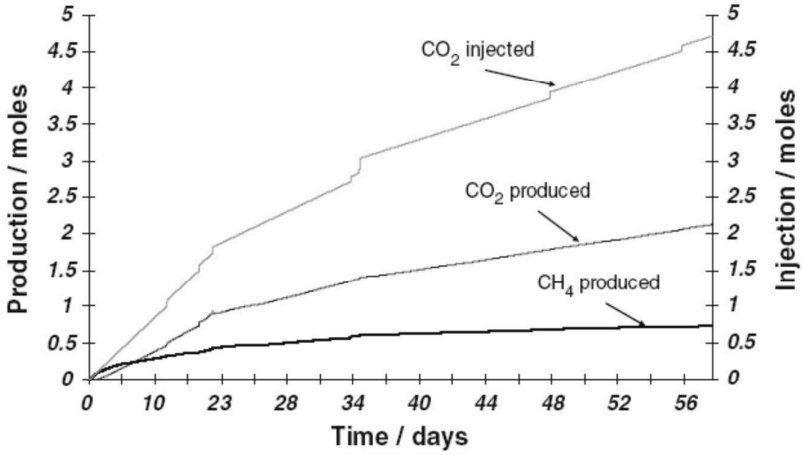


Figure 6-24. Cumulative production of all gases, and injection of CO_2 from Experiment VI (Brzeszcze, dry, CO_2 injection at 0.5 ml/h).

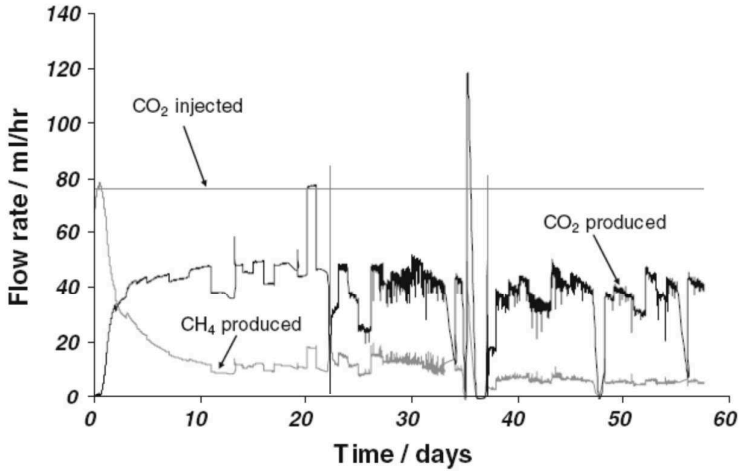


Figure 6-25. Injection and production flow rate of gases for Experiment VI at STP.

Table 6-6. The total, free, adsorbed and produced amount of carbon dioxide in the dry and wet Brzeszcze 501 flooding experiment.

CO_2 flooding (Brzeszcze 501)	Dry	Wet
Total amount of CO_2 injected (moles)	4.7125	2.45
Amount of adsorbed CO_2 (moles)	1.033 (max)	0.423 (max)
Amount of free CO_2 (moles)	1.555	1.08
Total amount of CO_2 produced (moles)	2.1245	0.947

Table 6-7. Sweep efficiency, displaced moles and time of Experiment V and VI.

CO_2 flooding (Brzeszcze 501)	$CO_2 = 25\%$		$CO_2 = 50\%$		$CO_2 = 90\%$	
	Dry	Wet	Dry	Wet	Dry	Wet
Sweep efficiency (%)	8.83	9.2	12.97	13.5	72.62	25.4
Displaced moles (mole/mole)	0.1	0.22	0.18	0.29	4.63	1.36
Time after production (s)	1.08×10^5	2.1618×10^5	1.92×10^5	2.86×10^5	4.959×10^6	1.33×10^6

6.6.2 Flue Gas Core Flood Experiments

Figure 6-30 to Figure 6-37 shows the pressure history, molar concentration change, cumulative production and injection of all gases and the injection/production flow rate at STP for the two experiments conducted on the Silesia coal with flue gas as the injectant. .An alternate injectant to enhance the production of methane is needed because of the higher separation costs of liquid CO_2. Therefore, flooding experiments were performed with commercially available flue gas. The specifications of the flue gas is provided in Table 6-10. The absence of an equation of state for the flue gas makes data processing complex. Hence, an equation of state (EOS) for flue gas have been developed. This EOS calculates densities for the injected flue gas. The algorithm developed by National Institute of Standards and Technology (NIST) predicts the volumetric behaviour of a multi-component gas mixture in a single-phase region. The algorithm works in line with the Peng–Robinson EOS. It performs better than the Redlich–Kwong–Soave equation in all cases and shows greatest advantage in the prediction of liquid phase densities.

Results from the wet and dry flue gas experiments are summed in Table 6-11 to Table 6-13. The core details and the experimental conditions are provided in Table 6-2. Even though the pressures are same in both the dry and the wet experiments, the dry experiment has more amount of methane in there as compared to the wet. This is because of the fact, that in the wet experiment the coal core is made wet by injecting 100.1 g of water after saturating the core with CH_4.

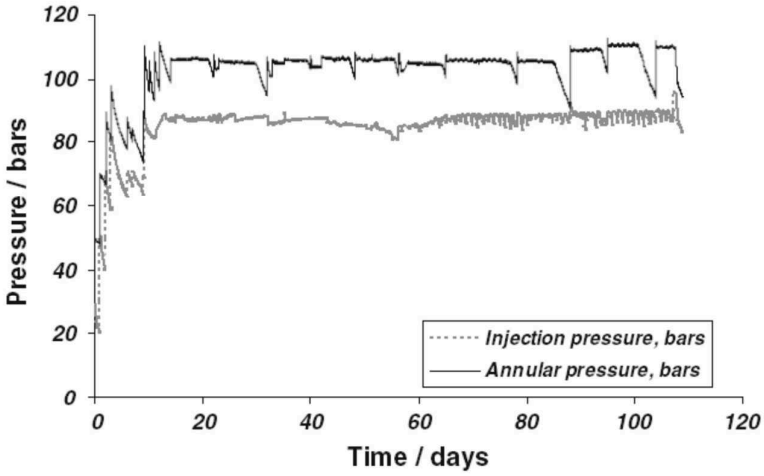


Figure 6-26. Measured system pressure during Experiment VII (Seam 401, wet, CO_2/N_2 injection at 0.5 ml/h). The average effective stress applied was 20 bars.

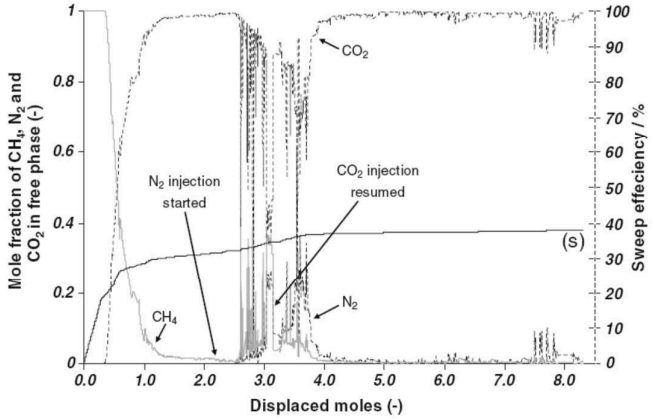


Figure 6-27. Sweep efficiency (s) and molar concentrations of the produced gas against displaced moles from Experiment VII (Seam 401, wet, CO_2/N_2 injection at 0.5ml/h). The alternate injection of a strong (CO_2) and weak (N_2) adsorbing gas result in the fluctuations of the concentration data between a displaced volume of.2.5 and 4.

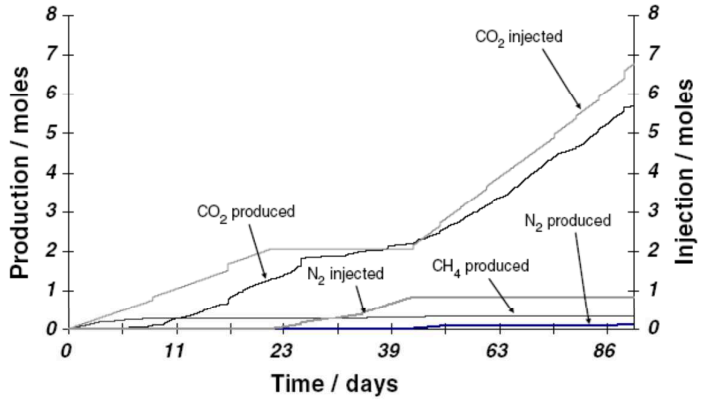


Figure 6-28. Cumulative production of all gases, and injection of CO_2, N_2 from Experiment VII (Seam 401, wet, CO_2/N_2 injection at 0.5 ml/h).

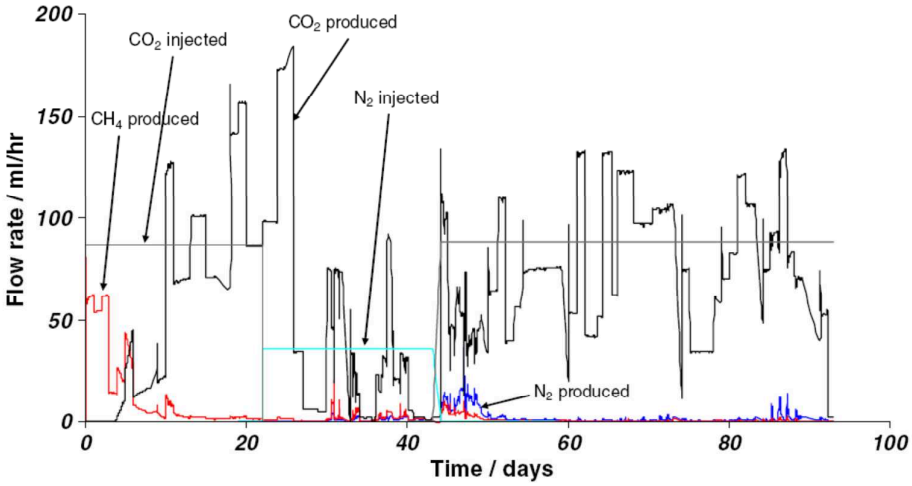


Figure 6-29. Injection and production flow rate of gases for Experiment VII at STP.

Table 6-8. The total, free, adsorbed and produced amount of carbon dioxide and nitrogen in sample Seam 401 (Vertical drill core from well MS3).

Total amount of CO_2 injected (moles)	6.758
Total amount of CO_2 produced (moles)	5.68
Total amount of N_2 injected (moles)	0.8247
Total amount of N_2 produced (moles)	0.0974

Table 6-9. Sweep efficiency, displaced moles and time of Experiment VII.

CO_2/N_2 flooding (Seam 401)	$CO_2 = 1\%$	$CO_2 = 50\%$	$CO_2 = 90\%$
Sweep efficiency (%)	19.59	24.93	28.4
Displaced moles (mole/mole)	0.364	0.553	0.956
Time after production (s)	3.09×10^5	4.698×10^5	8.12×10^6

The migration data of the dry experiment is in Figure 6-32. In the dry flooding experiment the amount of free methane is 0.7222 mol, which is much more than the net amount of CH_4 produced (0.5003 mol). In the dry experiment, with an injection rate of 1ml/h, hardly any adsorbed methane is produced. As compared to the wet experiment the dry one has more free methane. The free methane resides in the tubing system and the fracture porosity of the coal. The recovery factor of the dry experiment is 35.1%. This recovery factor shows that with flue gas as an injectant, there is hardly no enhancement in recovery. The flue gas which is primarily N_2, races through the tubing system and is produced. When the thermo physical properties of N_2 are compared with those of CO_2, the CO_2 has higher density and higher internal energy under reservoir conditions. The viscosity of CO_2 and N_2 does not differ much. The CO_2 in the flue gas does get adsorbed on the surface of the coal but is unable to enhance the production of methane. Thus, as reported (Cui et al., 2004) CO_2 has separate adsorption sites beside CH_4.

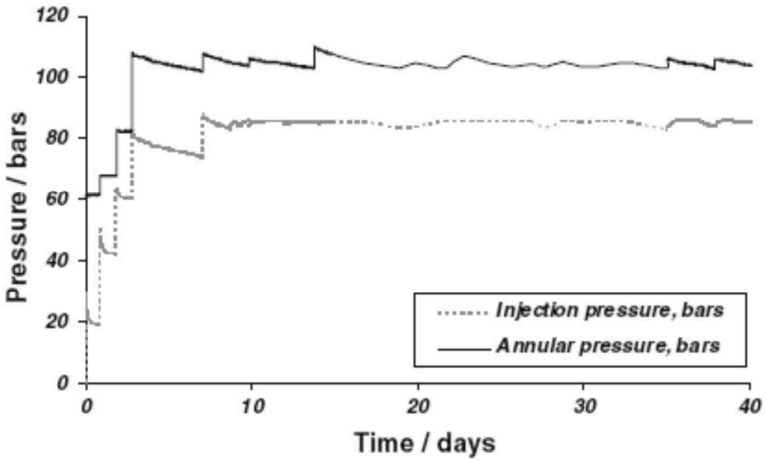


Figure 6-30. Measured system pressure during Experiment VIII (Silesia, dry, flue gas injection at 1.0ml/h). The average effective stress applied was 20 bars.

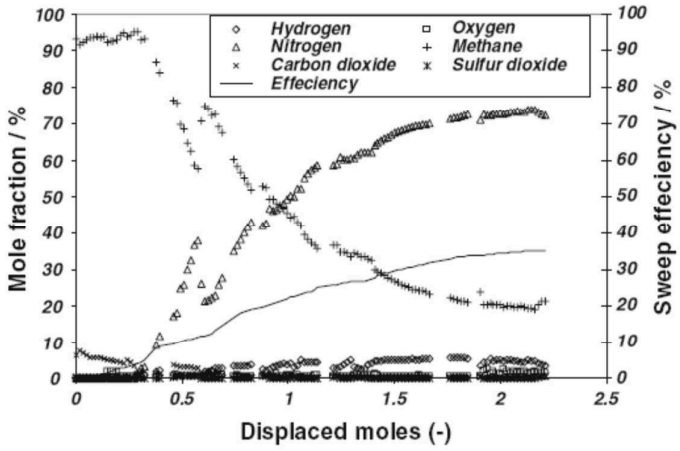


Figure 6-31. Sweep efficiency and molar concentrations of the produced gas against displaced moles from Experiment VIII (Silesia, dry, flue gas injection at 1.0 ml/h).

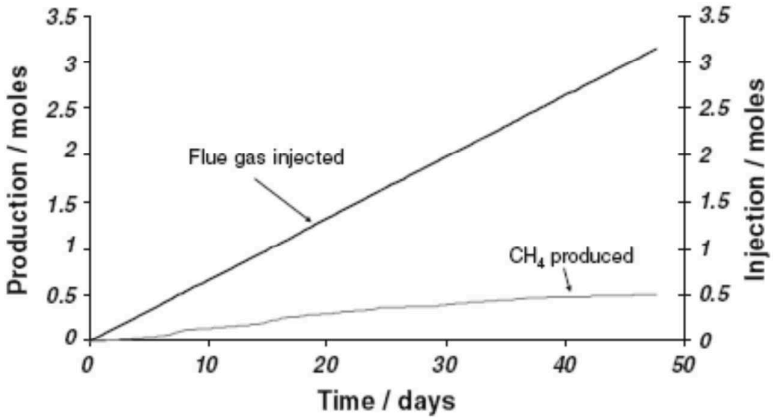


Figure 6-32. Cumulative production of all gases, and injection of flue gas from Experiment VIII (Silesia, dry, flue gas injection at 1.0 ml/h).

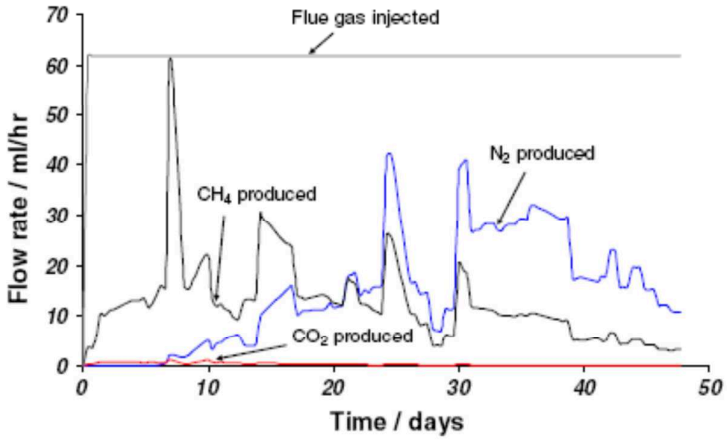


Figure 6-33. Injection and production flow rate of gases for Experiment VIII at STP.

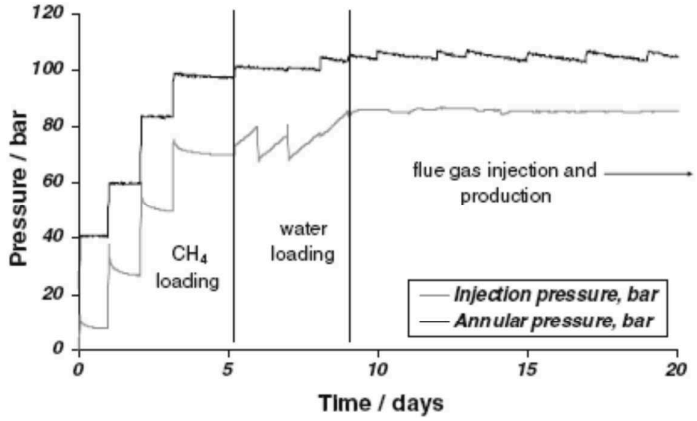


Figure 6-34. Measured system pressure during Experiment IX (Silesia, wet, flue gas injection at 1.0ml/h). The average effective stress applied was 20 bars.

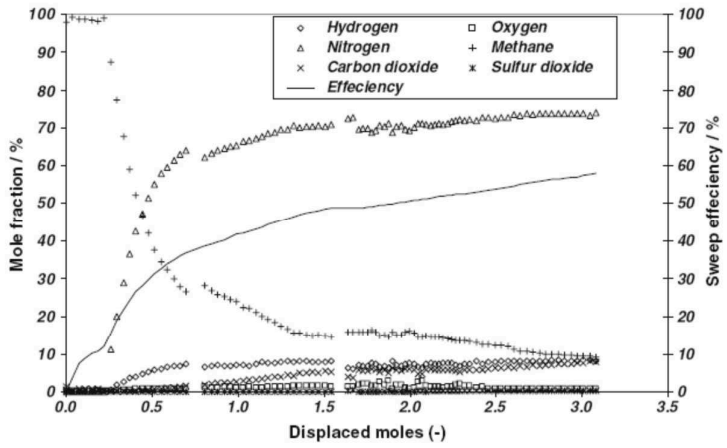


Figure 6-35 Sweep efficiency and molar concentrations of the produced gas against displaced moles from Experiment IX (Silesia, wet, flue gas injection at 1.0 ml/h).

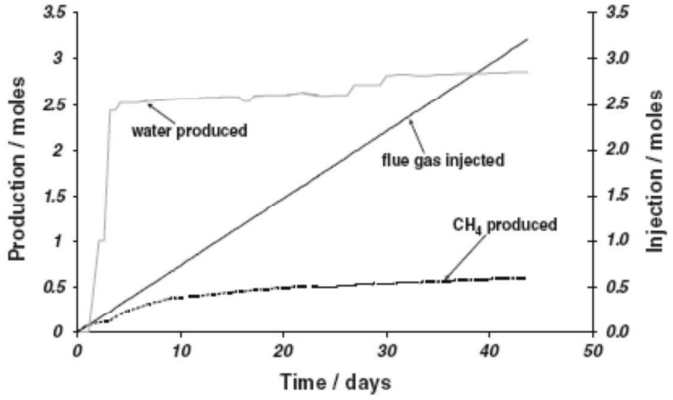


Figure 6-36. Cumulative production of CH_4, water and injection of flue gas from Experiment IX (Silesia, wet, flue gas injection at 1.0ml/h).

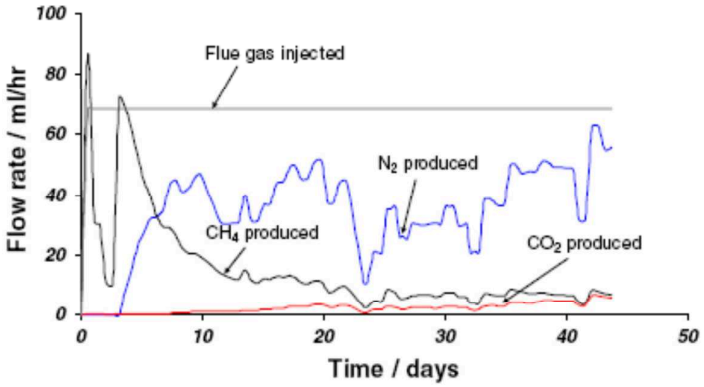


Figure 6-37. Injection and production flow rate of gases for Experiment IX at STP.

Table 6-10. Flue gas specification and used columns/carrier gas for chromatographic analysis and density determination.

Component name	Gravimetric conc. (mole%)	Used column	Carrier gas
CO_2	10.9	Porapack Q	He
CO	0.01	–	–
H_2	9.0	Mole-sieve	Ar
CH_4	3.01	Mole-sieve/porapack Q	Ar/He
O_2	3.00	Mole-sieve	Ar
SO_2	0.106	–	–
N_2	73.974	Mole-sieve	Ar

Table 6-11. The total, free, adsorbed and produced amount of flue gas in sample Silesia 315 II.

Flue flooding (Silesia 315 II)	Dry	Wet
Total amount of flue gas injected (moles)	3.15	3.24
Amount of free flue gas (moles)	0.7273	0.570
Total amount of flue gas produced (moles)	0.8684	1.9801

Table 6-12. Cumulative amount of each component injected and produced during the dry and wet flue flooding experiments.

	H_2		O_2		N_2		CO_2		SO_2	
	Dry	Wet	Dry	Wet	Dry	Wet	Dry	Wet	Dry	Wet
Moles injected	0.29	0.30	0.095	0.10	2.34	2.44	0.35	0.36	0.003	0.004
Moles produced	0.05	0.17	0.012	0.03	0.70	1.57	0.012	0.105	0.001	0.003
% Produced	18.20	57.11	12.14	26.44	29.72	64.56	3.5	29.15	43.00	79.22

Table 6-13. Sweep efficiency, displaced moles and time of the dry and wet flue flooding experiment.

Flue flooding (Silesia 315 II)	$N_2 = 1\%$		$N_2 = 50\%$		$N_2 = 73.9\%$	
	Dry	Wet	Dry	Wet	Dry	Wet
Sweep efficiency (%)	4.175	14.35	22.33	29.12	35.01	57.93
Displaced moles (mole/mole)	0.288	0.245	1.00	0.460	2.17	3.09
Time after production (s)	5.37×10^5	2.99×10^5	1.87×10^6	5.63×10^5	4.04×10^6	3.78×10^6

In the wet experiment the methane saturation is done at a lower pressure (69.8 bar) compared to a dry experiment (84.35 bar). After methane saturation the cell is filled up with 100.1 g of water which in turn brings the pressure up to 85.84 bar. Thereafter, the flue gas was injected at a rate of 1ml/h. The loading process is shown in Figure 6-34. The migration data of the wet experiment is shown in Figure 6-35. Water occupied a part of the free volume in the cell which was in the dry experiment completely occupied by the free methane. Consequently, the free methane volume in the wet experiment (0.4095 mol) is less than the free methane volume in the dry experiment (0.7222 mol). Based on this volume difference we may assume that since most of the water through the cleat system follow Darcy flow, it acts like a plug between the methane and carbon dioxide (Figure 6-36). There is no possible physical reasoning behind this process. Modeling efforts might be able to answer this.

The discussion above implies that the experimental procedure used to inject water is not suitable. The injected water forms a water plug in the cleat system, instead of being uniformly distributed throughout the coal cleats and matrix. An example of water acting as a plug is shown in Figure 6-36. As an alternative the coal core can be soaked with water, shortly evacuated and then saturated with methane.

6.7 Conclusions

With the injection of CO_2, the partial pressure of CH_4 in the free phase decreased, inducing the production of methane. Whether or not CO_2 is preferentially replacing CH_4 was not

clear. The CO_2 mass balance shows that the solubility of CO_2 in coal is more pronounced than that for CH4. The term solubility is used, considering that coal has a highly cross linked macromolecular network. Moreover, the dry experiments indicate that the amount of desorbed CH_4 is marginally greater than the desorption resulting from the reduction in partial pressures of methane. This was not observed in wet experiment. Consequently, under dry conditions, the incremental methane produced is likely due to the preferential desorption of methane in the presence of CO_2. Thus moisture reduces CO_2 selectivity drastically since it appears to block CO_2 sorption sites.

The sweep efficiency of the two experiments (VIII and IX) with flue gas are less compared to the CO_2 flooding experiments under similar conditions. There is hardly any production of adsorbed methane from the coal. The flue gas experiments, with N_2 as the main constituent can be considered as a N_2 stripping experiment. In comparison to the six different components in flue gas, CO_2 was the most adsorbed species. Significant reduction in the CO_2 concentration was measured in the product gas. A process of CO_2 filtration seems promising. From the experiments it is clear, that on a pore scale CO_2 is better adsorbed compared to CH_4.

Comparison of the results for the Silesian Basin coal samples shows that moisture tends to reduce the preferential sorption of CO_2. These effects are attributed to the affinity of both water and CO_2 towards hydrophilic (e.g. hydroxylic, carbonylic, carboxylic) functional groups on the coal surface. These groups are more abundant in inertinite-rich coals (Brzeszcze coal) than in vitrinite-rich coals (Silesia coal) of similar rank. This gives rise to the assumption that inertinite and moisture content are the two controlling factors influencing the preferential adsorption behaviour of CO_2/CH_4 gas mixtures in coal of similar maturity.

Due to the lack of exact duplicate experiments and since it is a first hand investigation on coal cores/gas/liquid systems, experiments have been compared qualitatively. All these experiments should be used to understand processes under those specific experimental condition. The stage for comparison can only be set when there is ample data available by repeating these experiments, so as to get a consistency in the parameters reported.

Pure component and mixed gas sorption isotherms should only be used for qualitative purposes as it is noted that variation in grain sizes has profound effect on the magnitude of any preferential sorption behaviour. The degree of preference for CO_2 sorption evidently increases with increasing inertinite and ash content, both of which increase with decreasing grain size and vice versa.

6.8 Appendix

6.8.1 Appendix A—Void Volume Measurements

For better understanding and comparison of the results, a schematic of the set-up is shown in Figure 6-1. The whole set-up is divided into four parts. These volumes are mostly inherent in the set-up, enclosed by

two valves. Volume measurements have been conducted by helium expansion. All volumes reported below are at standard temperature and pressure (STP).

Starting from left to right (Figure 6-1), the first part of the volume includes the volume of the pump plus a small portion of the tubing leading out of the pump to the injection side. This volume terminates at valve 1. Valve 1 is an air actuated valve which is opened only when the pump is injecting. The volume of this portion is 283.02 ml, out of which the syringe pump itself has a volume of 266.50 ml. Out of the total 283.02 ml, only 266.50 ml can be displaced during the course of the experiment. Thus, the volume enclosed within part 1 does not have any contribution towards the absolute free volume of the set-up.

Second part is the part of the tubing enclosed between valve 1 and valve 2. This part has a volume of 44.04 ml. This volume does contribute towards the absolute free volume of the set-up.

The third part is the volume between valve 2 and valve 3. This comprise of the volume of the tubing in and out of the pressure cell, volume of the tubing leading to the pressure difference measurement over the core and the porous volume of the coal core itself. This part measures different volumes with different coal samples. For experiment I it is 137.97 ml. Out of this, the porous volume of the core is 63.35 ml. As can be seen from the schematic, the volume of the tubing leading to the pressure difference measurement is static. The tubing diameter (OD) of this part is 3.14 mm. This total tubing volume was approximately calculated to be 5 ml. The only way this static volume interacts with the flow stream is by the process of diffusion. The diffusion rates being very low, this volume is neglected. Apart from the porous coal the two end plates attached to the core itself contribute the most towards the volume of this part. The end plates and the tubing volume cannot be eliminated as they are vital in the construction of the set up. Subtracting the porous volume of the coal (63.35 ml) from the total free volume, gives us the tubing volume (74.62 ml). Likewise for Experiments II and VII, the total volume for this part is 108.44 ml and 142.28 ml, respectively. For experiments III, IV, VIII and IX this volume is 135.48 ml and for experiments V and VI the volume is 132.01 ml. The fourth part is the volume between valve 3 and the back pressure valve. This part has a volume of 46.725 ml and does contribute to the free volume of the set up.

When the core is set on production alongside injection, the tubing volume that is on the production side core is set to be displaced first by the injected fluid. This volume is 84.03 ml in total. For example, when CO_2/flue gas is injected at a rate of 1ml/h and assuming that equilibrium was attained, it would take around 3.5 days to flush out 84.03 ml. Since the pressure in the cell remained constant, it is a fair assumption that the core produced at the same rate as that of the injection. Thus the first 3 to 4 days of production data will have the information related to the void volume preceding the coal core.

6.8.2 Appendix B—Single Component Sorption Isotherms

In view of the core flooding experiments, the CO_2 and CH_4 sorption isotherms on the Belgian and Polish coal samples used in the aforesaid study were measured. These experiments also demonstrate the influence of

moisture on high temperature CO_2 and CH_4 sorption isotherms for natural coals. The three Carboniferous coal samples studied, originated from coal mining areas in Belgium and Poland. The sorption experiments in the dry and moisture equilibrated state reported here were performed on two coals (Silesia and Brzeszcze) from the Silesian basin, Poland. These samples were provided by the Polish Central Mining Institute, Katowice, in the context of the EU RECOPOL project. The Beringen coal sample was obtained from a mine in Belgium and only dry absolute sorption isotherms were generated for both CO_2 and CH_4 at 45°C. The petrographic properties of the coal samples used in this study are listed in Table 6-1.

For the determination of CO_2 and CH_4 excess sorption isotherms, the same volumetric method was used as described by Krooss et al., 2002 . Several modifications in the experimental set-up and the procedure have resulted in a significant improvement of the quality of the sorption isotherms: (i) While in the previous set-up the reference cell (including the pressure transducer) and the measuring cell were kept in separate compartments at different temperatures the entire system was now placed into one thermostatic chamber. This modification ensured the reduction of temperature-related effects on the measurements. (ii) Even minor admixtures of other gases result in significant effects on the Equation of State of CO_2. It became evident that small amounts of helium (He) from the preceding assessment of void volume may have remained in the tubing system in some instances. Therefore, specific attention was given to the thorough removal of helium from the system prior to each sorption experiment. (iii) The volumetric method involves two compression/expansion steps: (a) charging a calibrated reference volume with gas and (b) expanding the gas from the reference volume to the measuring cell. Both steps are associated with considerable temperature effects. Sufficient time was always allowed for temperature/pressure equilibration, and the pressure equilibration carefully monitored for all the experiments.

Excess sorption isotherms are expressed in mass (g or kg) or amount of substance (mol, mmol) sorbate per unit mass (g or kg) of sorbent. In the classical Langmuir approach for low-pressure sorption the volume of the sorbed phase is neglected. For high-pressure sorption of the volume of the adsorbed phase is not negligible. For a sorptive/sorbent system consisting of two fluid phases (gas or super critical phase and sorbed phase) and a solid sorbent, the excess sorption is defined as follows:

$$m_{excess} = V_{sorbed} \cdot \rho_{sorbed} + \left(V_{gas} - V_{void}\right) \cdot \rho_{gas} \qquad (6\text{-}3)$$

Here ρ denotes the density of the fluid phases and V_{void} denotes the total volume occupied by the sorbed phase (V_{sorbed}) and the free gas (V_{gas}):

$$V_{void} = V_{sorbed} + V_{gas} \qquad (6\text{-}4)$$

All volumes (V) and masses (m) are normalized to the mass of sorbent and the sorbent is assumed as volume-invariant (non-swelling). Combining yields:

$$m_{excess} = V_{sorbed} \cdot \left(\rho_{sorbed} - \rho_{gas}\right) \Leftrightarrow m_{excess} = m_{sorbed} \cdot \left(1 - \frac{\rho_{gas}}{\rho_{sorbed}}\right) \qquad (6\text{-}5)$$

In the aforesaid equation the excess sorbed mass (i.e. the mass accommodated in the system in excess of the hypothetical non-sorption case) is a function of the ratio of gas phase and sorbed phase density and of the mass of the sorbed phase. The density of gaseous and super critical CO_2 is well known as a function of pressure and temperature. In this study the EOS by Span and Wagner, 1996 was used. The density of the sorbed phase is less well known but can be estimated with some reasonable assumptions. The density of liquid CO_2 ranges between 1,000 and 1,150 kg/m^3. For simplicity a fixed value for the sorbed phase density (ρsorbed) of 1.028kg/m^3 was assumed.

While Figure 6-38 shows the absolute sorption isotherms for dry Beringen 770 coal, Figure 6-39 and Figure 6-40 show the CO_2 and CH_4 excess sorption isotherms measured on the dry and wet Silesia 315 and Brzeszcze coal samples at 45° C. While the absolute sorption isotherms (Figure 6-38) are presented in units of Scf/ton, the excess sorption isotherms (Figure 6-39 and Figure 6-40) are presented in mmol/g coal (1 Std. m^3 CO_2 (1 atm, 15° C) = 42.29 mol).

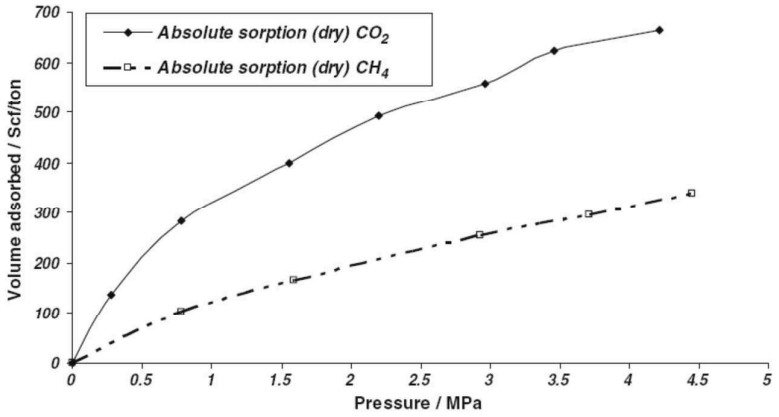


Figure 6-38. Comparison of 45°C CO_2 and CH_4 absolute sorption isotherms on dry Beringen 770 coal.

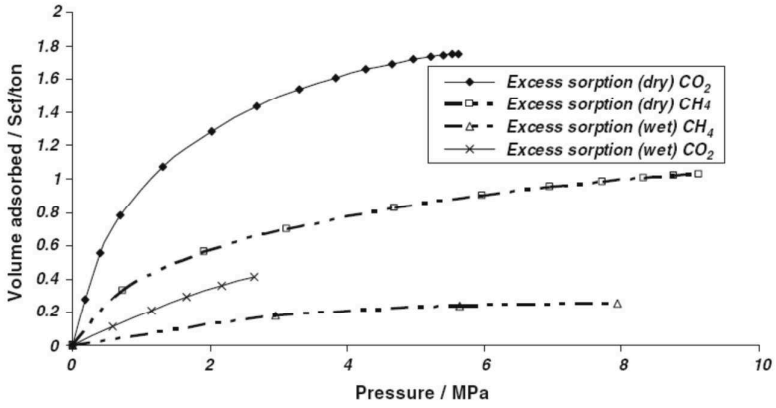


Figure 6-39. Comparison of 45°C CO_2 and CH_4 excess sorption isotherms on wet and dry Silesia 315 coal (size fraction >2mm).

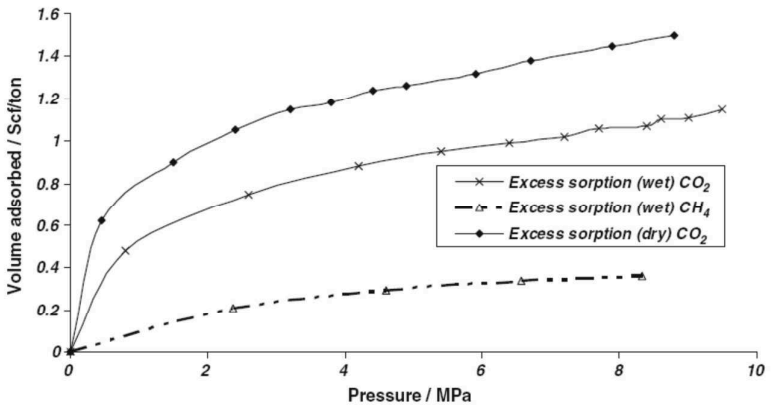


Figure 6-40. Comparison of 45C CO_2 and CH_4 excess sorption isotherms on wet and dry Brzeszcze coal (size fraction <0.2mm). The dry sorption experiment with CH_4 was not conducted.

The CO_2 isotherms for the Belgian and Polish coals measured in this study, show that an optimum pressure exists beyond which storage becomes less effective. The repeatedly confirmed shape of the CO_2 excess sorption isotherms show a decline in excess sorption with increasing pressure. It can be shown, however, that this effect is related to the increase in sorbed-phase volume with pressure and is essentially controlled by the variation of the ratio of the density of free (super critical) and adsorbed CO_2. In many instances the increase in sorbed phase volume cannot account completely for the observed effects so that swelling of the coal matrix must be considered as another contributing factor. This issue is under investigation and thus the data beyond the point of initiation of this effect has not been presented. Additional single component isotherms for the same Polish samples (dry and moist) were conducted by Siemons and Busch, 2007.

Gas Adsorption and Fluid Transport in Mudrocks

7 Predicting capillarity of mudrocks

7.1 Introduction

Low-permeable rocks (mudrocks, evaporites, carbonates, etc.) form part of every natural gas accumulation or CO_2 storage scenario in the sub-surface and special attention should be paid to the characterisation of these rocks. Historically, knowledge and expertise on reservoir rocks was seen to be of priority for oil and gas exploration. Core material of reservoir rocks is regularly made available for proper petrophysical investigations, whereas caprock material (as less important for production) is mostly available in the form of cuttings only which limits potential laboratory measurements to small sample sizes.

Regarding research of hydrocarbon entrapment over geological time scales, methane (and higher carbon number hydrocarbon gases) migration and dissipation is of interest, i.e. the infill of gas reservoirs but also hydrocarbon leakage by diffusion or capillary leakage. Several conceptual, experimental or numerical modelling studies created a thorough understanding of gas transport through low-permeable rocks (e.g. Amann-Hildenbrand et al., 2012; Berg, 1975; Schlömer and Krooss, 1997; Schowalter, 1979b). Similar processes apply for shale gas reservoirs where capillary pressure, diffusion coefficient, adsorption capacity, pore network characterisation and other parameters need to be determined for a better prediction of gas production.

In carbon capture and storage (CCS) discussions, there is sometimes the general opinion that seals that have trapped hydrocarbons for millions of years will do the same for CO_2. This neglects the differences in thermodynamic and geochemical behaviour (CO_2/brine/rock-interactions) of CO_2 compared to hydrocarbon gases. Various comparative studies performed during the last decade have shown that the critical capillary breakthrough pressure is lower for CO_2 than for N_2 and CH_4 (e.g. Hildenbrand et al., 2004a; Li et al., 2005). Although mineralogical and petrophysical characterisation (e.g. porosity, permeability, rock density, mercury porosimetry, specific surface area) is essentially the same for research on CO_2 storage, shale gas reservoirs or nuclear waste storage, gas permeability and wettability might be different.

For CO_2 storage, seal characterisation requires a similar research focus, however for much smaller time scales compared to hydrocarbon plays or radioactive waste storage facilities. Instead of considering millions of years the focus is on <10,000 years. Another difference between these research fields is the gas type itself. Carbon dioxide forms a weak acid when dissolved in brine, reacts with the reservoir and the sealing rocks in time scales of 100's to 1000's of years. It may however influence surface properties of minerals and this again can be considered different to hydrocarbon gases or hydrogen, which is more or less inert when in contact with such minerals. This results in changes in contact angles, which raises the possibility of different wettability states, i.e. CO_2 wetting versus CO_2 non-wetting. It can further be assumed that the wetting behaviour changes with time (or with progressive reaction of CO_2 with brine and minerals). Recent data that support this observation (e.g. Bikkina, 2011; Chiquet et al., 2007a; Espinoza and Santamarina,

2010; Jung and Wan, 2012; Yang et al., 2007) and future research will have to pay more attention to this aspect, especially to understand wettability states of different rock types.

This study mainly addresses published petrophysical and mineralogical parameters of low-permeable mudrocks. For comparison, higher permeable carbonate or sandstone sample are included. The entire dataset cumulates data from nuclear waste storage, hydrocarbon sealing and CO_2 storage research.

7.2 Terminology & Background

7.2.1 Mudrocks

In this study we use the term mudrock to represent clay and silt rich rocks, independent on their diagenetic or metamorphic history. According to Folk, 1980, a mudrock has 50% or more silt and/or clay content and is further sub-classified according to Table 7-1.

Table 7-1. Classification of mudrocks

Grain size of mud fraction	indurated, non-fissile	indurated, fissile
>2/3 silt	siltstone	silt-shale
silt≅clay	mudstone	mud-shale
>2/3 clay	claystone	clay-shale

7.2.2 Capillary breakthrough pressure

7.2.2.1 In-situ measurements on core plugs

Various terms are used in the literature relating to capillary pressures in mudrocks. In this manuscript we define different terms for the critical pressures on the drainage (increasing pressure difference, $\Delta P = p_{gas} - p_{brine}$) and on the imbibition path (decreasing ΔP).

Let us first consider a laboratory experiment on a completely brine saturated core plug. During the experiment the gas pressure will first be increased, thereafter decreased again. Different processes can be distinguished (Figure 7-1). Overcoming the drainage pore entry pressure (P_{c_entry}) the non-wetting fluid starts to displace the wetting fluid from the pore space, reducing water saturation. Reaching the breakthrough pressure (P_{c_brthr}) or threshold pressure ($P_{c\_threshold}$), viscous gas flow is detected at the outflow side of the rock specimen. Further gas pressure increase successively drains the system, resulting in increasing effective gas permeabilities until the irreducible water saturation is reached (IRWS). We have to note, that for the small scales considered in laboratory (mm-/cm-scale) and for very homogeneous samples a clear differentiation between the pore entry and breakthrough pressure may become difficult to impossible. Decreasing the gas pressure leads to the imbibition of water, shutting of successively more pores until the last interconnected pore throat is blocked and gas flow stops. The remaining pressure

difference is defined as the snap-off pressure ($P_{c\_snap\text{-}off}$) or "choke-off" pressure (Jerauld and Salter, 1990; Yu and Wardlaw, 1986). Thereafter, only diffusional transport can be observed.

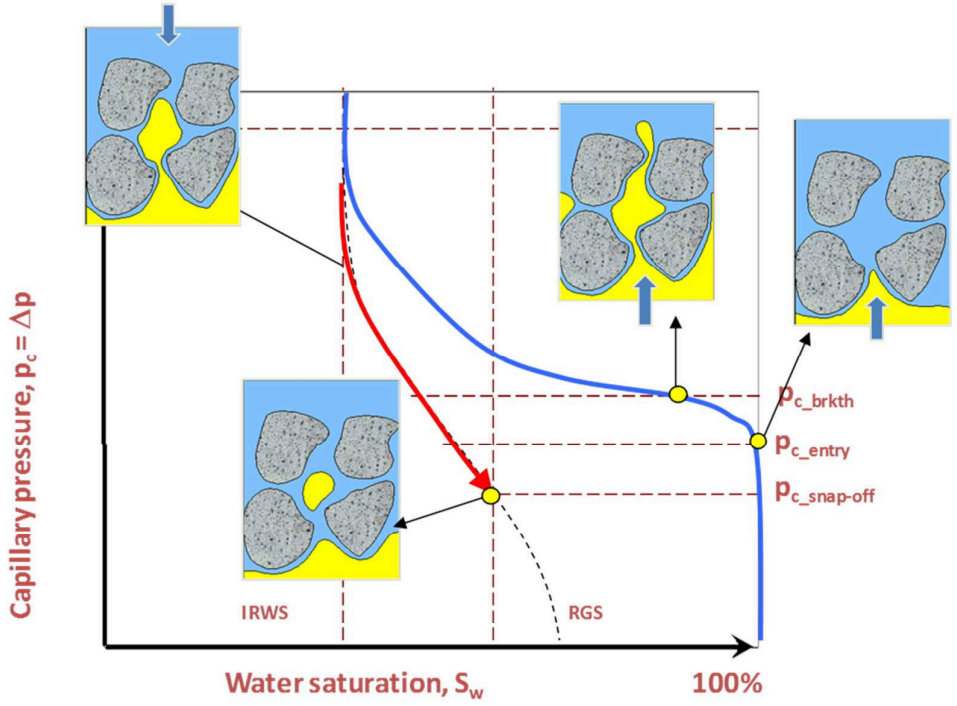


Figure 7-1. Concept of capillary processes in mudrocks.

The imbibition process may be described by a piston-like (connected) advance of the wetting phase and is therefore just the opposite of the drainage process by which the advancing (drainage) contact angle differs from the receding (imbibition) contact angle. Several authors (e.g. Blunt and Scher, 1995; Lenormand and Zarcone, 1984; Lenormand et al., 1983; Pentland, 2010) describe this process following Figure 7-2 where it is schematically shown how a pore may be filled when one or more of its surrounding throats are filled with wetting fluid. When pressure is reduced, the radius of curvature of the fluid interface increases, and the layer of wetting fluid occupying the pore throats will thicken This thickening continues until the wetting layers merge and the throat spontaneously fills with water ("snap-off").

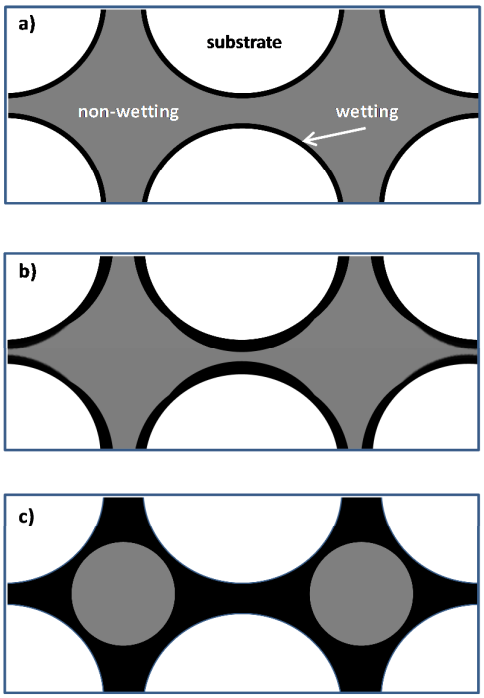


Figure 7-2. Non-wetting phase (e.g. gas) trapping (grey) by a wetting phase (e.g. brine, black) by "snap-off" within a porous medium (white). (a) The wetting phase is connected through wetting layers across the solid surface. (b) The wetting layers thicken as the capillary pressure drops during imbibition. (c) The wetting layers within the throat thicken until the throat spontaneously fills with the wetting phase, isolating and trapping the non-wetting phase in the preceding pore. Modified after Pentland, 2010.

7.2.3 Indirect method - mercury porosimetry

The capillary breakthrough pressure is often determined from mercury injection porosimetry experiments (MIP), which provides information on the mercury excess pressure required to displace air at successively decreasing pore throats. Using maximum injection pressures of 400 MPa, pore radii of approx. 2 nm are invaded (wetting angle of 140°, interfacial tension 485 mN/m). The resulting Hg-curves may be interpreted in different ways, yielding values for porosity, grain and matrix density, critical capillary pressure and, by applying empirical correlations or models, permeability.

However, for a proper interpretation of the Hg-intrusion curve a surface roughness correction first needs to be made, which is often difficult and depends on personal judgements. For low permeable media often a "non-invasion" zone is observed after the occurrence of a "first injection phase" in the low pressure regime. As large pores in the µm-range are not typical for sealing rocks, this first intrusion is seen to correspond to the filling of sample surface irregularities and preparation artefacts (fissures). The corresponding volume has to be subtracted from the entire intrusion volume.

The "second" injection phase, right after the plateau, corresponds to the **pore entry pressure** at which mercury first enters the largest pores of the porous material. Thereafter, successively more pores are filled with mercury until, at a critical pressure, a continuous filament of mercury extends through the sample (Dullien, 1992). As demonstrated by electrical resistance measurements (Katz and Thompson, 1986, 1987),

electrical continuity is established at the inflection point of the cumulative intrusion curve, or the pressure at which a maximum exists on the first derivative (pore radius distribution curve). The critical pressure required to form such a continuous, non-wetting phase filled pore network is somewhat lower and is defined as the **displacement pressure**, which is routinely used for the estimation of capillary sealing efficiency of rocks (Schowalter, 1979a). However, terminology and methods are different in literature. Dewhurst et al., 2002a use the term threshold pressure for the pressure at which the development of this continuous pore network is initiated – "the large gradient increase on the first derivative". Others use the so called tangent-method, for which a tangent is fitted to the inflection point of the cumulative intrusion curve and extrapolated to the logarithmic pressure axis; displacement pressure (ΔP, Schlömer and Krooss, 1997).

Often the pressure at 10% Hg-saturation is taken as valid equivalent of the displacement pressure. This is an average value published by Schowalter (1979a), who compared the results from several unidirectional nitrogen breakthrough experiments and mercury injection porosimetry measurements. For a sample set consisting of sandstones, chalks and silty shales critical saturations of 4.5 to 17.0% non-wetting phase were determined. However, this approach strongly depends on the accuracy of surface roughness correction.

Before the **capillary sealing efficiency** of natural systems can be estimated, the critical entry pressure has to be converted from the system Hg-air to the gas-brine system following

$$P_{c(gas,brine)} = P_{c(Hg,air)} = \frac{\gamma_{gas,brine} \cdot cos(\theta_{gas,brine})}{\gamma_{Hg,air} \cdot cos(\theta_{Hg,air})} \qquad (7\text{-}1)$$

with γ being the interfacial tension and θ the contact angle within the two different multi-phase fluid systems.

7.2.4 Permeability

In general, we have to distinguish between single- and multi-phase flow properties. In a single-phase flow system, where complete saturation is given for one fluid phase only, the term intrinsic or absolute permeability accounts to the conductivity characteristics of a rock specimen. Strictly, the intrinsic permeability is a rock property, and assuming Darcy's law to be valid, it is linearly correlated to the applied pressure gradient and independent of the fluid type. In a multi-phase flow system one has to consider that the conductivity for each fluid phase depends on saturation. In this case, the term effective permeability to the gas/oil/water phase is used. In this study we will focus on the saturated flow only, i.e. the intrinsic permeability.

7.2.4.1 Permeability measurements on core plugs

Single-phase permeability experiments on core plugs and under enhanced pressures and temperatures may either be conducted with a compressible or incompressible fluid. For experiments with water or brine, the absolute permeability is calculated according to Darcy's law for incompressible media

$$\frac{Q}{A} = \frac{dV}{A \cdot dt} = -\frac{k_{abs}}{\eta}\frac{dp}{dx} \qquad (7\text{-}2)$$

with Q being the fluid flux (m s^{-1}), η the dynamic viscosity of the fluid (Pa·s), dp/dx the pressure gradient (Pa m^{-1}), and A (m^2) the cross section area. When gas is used, the permeability is calculated using Darcy's law for compressible media:

$$\frac{dn}{dt} = \frac{p_2}{R \cdot T}\frac{dV_2}{dt} = \frac{V_2}{R \cdot T}\frac{dp_2}{dt} = -\frac{k_{gas} \cdot A}{\eta \cdot R \cdot T}\frac{(p_2^2 - p_1^2)}{2 \cdot dx} \qquad (7\text{-}3)$$

The amount of mass dn (kg) moving through the sample is either calculated from the out-streaming gas volume on the low pressure side V_2/dt with p_2 (Pa) the corresponding pressure (open system), or the pressure increase dp_2/dt in a calibrated downstream compartment V_2 (m^3, closed system). The gas permeabilities calculated from the recorded flux are known to decrease with increasing mean pressure, which is attributed to the slip-flow effect, i.e. the pressure and temperature dependent mean free path length of the gas molecules. This effect is accounted for by the Klinkenberg correction, where an extrapolation to infinite high mean gas pressure yields the intrinsic permeability (Klinkenberg, 1941).

7.2.4.2 Modelling permeability

There are many ways to correlate permeability to parameters like porosity, mineralogy, average grain size etc. An overview is provided by Nelson (1994). For most of these correlations insufficient data are available here or simply too many assumptions have to be made. For this study, we have decided to focus on two approaches, namely the Kozeny-Carman equation, which proved to be useful for the prediction of sandstone and soil permeabilities (e.g. Chapuis and Aubertin, 2003), and the Young and Aplin model (Yang and Aplin, 1998), taking into account clay content and pore shape anisotropy, typical characteristics of compacted mudstones.

The **Kozeny-Carman equation** (Carman, 1956) was successfully used in the past in its original form, or in adapted versions, to predict permeability of (mainly) high permeable rocks from other, easier measurable, petrophysical parameters and is usually presented in the form:

$$k = \frac{1}{KS^2}\frac{\emptyset^3}{\emptyset^2} = \frac{d^2}{36K}\frac{\emptyset^3}{(1-\emptyset)^2} \qquad (7\text{-}4)$$

Where k is permeability (m^2), $\emptyset$ is porosity (-), S specific surface area per bulk volume of rock (S = SSA·ρ_{sample}, (m^{-1})), d (d=6/S) is the mean grain diameter (m) and K is the Kozeny-Carman constant (KC):

$$K = c\tau \qquad (7\text{-}5)$$

While c is the dimensionless Kozeny constant (basically a shape factor), τ the sample tortuosity and ρ_{sample} (kg m^{-3}) the grain density. The KC-constant can vary according to different authors but is usually considered to be approximately 5 for porous media with mainly spherical particles, as typically found in well-sorted sandstone reservoirs.

Yang and Aplin (1998) introduced a permeability formulation, which explicitly considers the nature of an anisotropic, clay-rich rock. Their model includes various parameters: pore size and geometry, pore alignment in dependence of effective stress, porosity and clay content. Both, horizontal and vertical permeability can be predicted using this approach.

Basic mineralogical and petrophysical input parameters are used in the model that are relatively easy to obtain: clay content (fractional clay content (mass of grains less than 2 µm or $2x10^{-6}$ m in diameter), porosity Ø (fraction) and average pore radius r_{mean} (nm or 10^{-9} m) to calculate vertical (k_v) and horizontal (k_h) permeabilities (m^2). The basic equations proposed by Yang and Aplin are:

$$k_v = 10^{-19.21} {J_v}^{1.118} {r_{mean}}^{1.074} \quad (7\text{-}6)$$

$$k_h = [c\ tan(\alpha)]^{2.236} k_v \quad (7\text{-}7)$$

where

$$J_v = \frac{9}{8}\Phi\left(sin(\alpha)\right)^2 \frac{J_1^3}{\left(1+J_1+J_1^2\right)^2} \quad (7\text{-}8)$$

$$J_1 = 2.371 - 1.626clay^2 + 153.8\Phi^4 \quad (7\text{-}9)$$

$$\alpha = 45° - 10.24°(e_{100} - e) \qquad for\ \sigma' > 100kPa \quad (7\text{-}10)$$

$$\alpha = 45° \qquad for\ \sigma' < 100kPa \quad (7\text{-}11)$$

$$e_{100} = 0.3024 + 1.687clay + 1.951clay^2 \quad (7\text{-}12)$$

e is the void ratio and e_{100} is the void ratio at 0.1 MPa effective stress σ':

$$e = \frac{\Phi}{(1-\Phi)} \quad (7\text{-}13)$$

J_1 is the ratio of the largest ratio radius of a pore to its throat radius or the largest pore aspect ratio (assumed to be the same for all pores for a given sample), and α is the average pore alignment angle relative to bedding direction (degree). Further details, discussion and fitting attempts to experimental data was published earlier (Yang and Aplin, 1998, 2004, 2007, 2010; Armitage et al., 2011).

7.3 Overview of measurement methods to determine capillary pressures in mudrocks

7.3.1 Experimental Methods

All methods to determine capillary threshold pressures (P_c) are similar in the experimental setup. It consists of a triaxial arrangement with axial and confining stress options. The cylindrical sample plug is situated in a core holder with porous disks at the bottom and the topic of the sample (Figure 7-3). The disk ensures

uniform distribution of the gas phase on the sample surface. The triaxial setup is usually in a temperature controlled air cabinet, in a water bath or the cell is surrounded by a heating jacket to ensure constant temperature conditions. Pressure and/or fluid flow rates are controlled by a syringe pump and determined by high-accuracy pressure transducers at the top and bottom of the sample. Before applying gas pressure on the high pressure side of the sample water saturation is assured and brine permeability is determined.

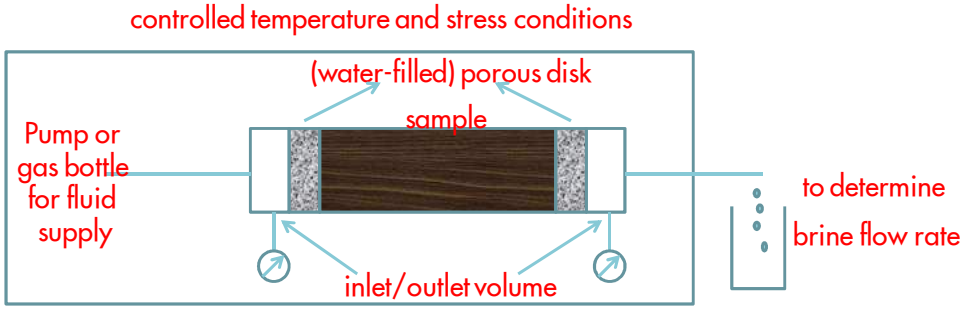


Figure 7-3. Simplified experimental setup to determine capillary threshold pressure on caprocks.

7.3.2 Step-by-step approach

The standard approach for measuring P_c values (e.g. Al-Bazali et al., 2005; Li et al., 2005) consists of a step-by-step increase of the non-wetting phase (e.g. CO_2) pressure at the inlet or high pressure side of the core plug. This approach can be conducted under in-situ conditions and is also very simple to interpret since it relies on the definition of the capillary threshold pressure. Once the gas phase enters the water-filled capillary network, CO_2 pressure decreases along with the flow rate. The inlet pressure is increased step-by-step until gas threshold is observed. The flow is controlled by using a pump in regulated pressure mode and connected at the outlet.

7.3.3 The Continuous Injection Approach

In this approach (Rudd and Pandey, 1973) the non-wetting fluid is injected in small and continuous quantities. This leads to a continuous pressure increase at the inlet until P_c is exceeded and two-phase flow is initiated by CO_2 entering the sample. If the sample material is heterogeneous, the pressure evolution with time may fluctuate that relate to variations of the P_c values throughout the length scale of the sample. A further limitation is the assumption that the viscous gradient in the water phase is negligible when a very small rate is used and can significantly overestimate the threshold pressure (Egermann et al., 2006).

7.3.4 The Residual Capillary Pressure Approach

One advantage of this method (e.g. Hildenbrand et al., 2004a; Wollenweber et al., 2010) is related to experiment duration. Here the inlet pressure is chosen higher than the expected threshold pressure. A transient flow is established over the water-saturated sample and pressure changes in the inlet (P_1) and outlet (P_2) pressure vessels are recorded over time. After flow is established, P_1 decreases while at the same time P_2 increases. When the pressure difference between P_1 and P_2 is close to the threshold pressure

P_c (residual capillary pressure or "snap-off pressure") of the largest interconnecting capillary, water re-imbibes back into the sample, disabling gas transport through the sample.

7.3.5 The dynamic threshold Pc approach

In this approach (e.g. Egermann et al., 2006) CO_2 is injected into the water saturated sample with a constant ΔP that is higher than the expected threshold P_c value. Initially, water is displaced from the inlet part and the flux can be detected at the outlet. As soon as the non-wetting fluid arrives at the inlet face of the core, a significant decrease of the slope (brine flow rate) is recorded due to the capillary pressure jump at the non-wetting phase front. This jump is related to the onset of two-phase flow.

Table 7-2. Ad-/disadvantages of different methods to measure threshold pressures (based and modified after Egermann et al. Egermann et al., 2006).

Mercury porosimetry	pro	available, cheap, commonly used
	contra	CO_2/water IFT and contact angle data needed to convert from Hg/air; sample drying may damage shale structure
Standard	pro	good accuracy of threshold pressure (primary drainage); standard approach with certain availability
	contra	long durations involving small pressure steps; risk of over-estimating threshold pressure
Continuous injection	pro	fast procedure, can be accurate for homogeneous samples
	contra	provide several threshold pressures for heterogeneous samples; might lead to over-estimation of threshold pressures
Residual	pro	fast procedure that requires one pressure fall-off test to determine threshold pressure
	contra	threshold pressures recorded on the imbibition path that provide an underestimation of threshold pressures
Dynamic	pro	good accuracy, heterogeneities can be accounted for
	contra	values can be overestimated since pressures applied are higher than threshold pressure, relatively long time scales

7.4 Database content

A total of 214 datasets were collected, providing mineralogical and petrophysical information of various rock types, e.g. porosity, permeability, capillary breakthrough pressure, mercury porosimetry data, and specific surface area. The main focus, however, was on mudrocks. An overview of the most relevant parameters used in this study and their original sources is provided in Table 7-3.

Table 7-3. Overview of most relevant rock specific parameters used in this study.

Method	Gas	#	rock type	Authors
Drainage capillary breakthrough pressure (P_{c_brkth})				
	N_2	45	mudrocks, evaporites, carbonates, sandstones	Al-Bazali et al. 2005, 2009; Carles et al., 2010; Ibrahim et al., 1970; Ito et al., 2010; Li et al., 2005; Purcell, 1949; Schowalter, 1979b; Thomas et al., 1968; Tonnet et al., 2010
	CO_2	3	evaporites	Li et al., 2005
	CH_4	1	evaporite	Li et al., 2005
	He	24	mudrocks	Harrington and Horseman, 1999; Horseman et al., 1999; Marschall et al., 2005
Total		73		
Imbibition capillary snap-off pressure ($P_{c\_snap\text{-}off}$)				
	CO_2	19	mudrocks, carbonates, sandstones	Hildenbrand et al. 2002, 2004; Amann-Hildenbrand et al., submitted; Wollenweber et al., 2010
	CH_4	12	mudrocks, sandstones	Hildenbrand et al. 2002, 2004
	N_2	29	mudrocks, sandstones	Hildenbrand et al. 2002, 2004; Ito et al., 2010
	He	5	carbonates	Amann-Hildenbrand et al., submitted; Wollenweber et al., 2010
Total		65		
Mercury porosimetry capillary entry pressures				
	Hg	88	mudrocks, carbonates, sandstones	Hildenbrand et al. 2002, 2004; Amann-Hildenbrand et al., accepted; Carles et al., 2010; Ito et al., 2010; Purcell, 1949; Thomas et al., 1968
Permeability data				
	brine/tap water	196	mudrocks, carbonates, sandstone, evaporites	Al-Bazali et al., 2009; Al-Bazali et al., 2005; Alles, 2008; Ibrahim et al., 1970; Ito et al., 2010; Li et al., 2005; Marschall et al., 2005; Schlömer, 1998; Schlömer and Krooss, 1997; Schowalter, 1979b; Tonnet et al., 2010; Wollenweber et al., 2010; Yang and Aplin, 1998, 2007

7.5 Results and Discussion

7.5.1 Correlations for permeability

Permeability and porosity can be considered as the minimum requirement to characterise flow properties of mudrocks. There are different ways to determine the intrinsic or absolute permeability of a rock, which is a rock property. Depending on the type of measurement values may differ from each other (steady state vs. non-steady state, use of water/brine vs. gas). However, it is not the purpose of this report to provide a best practice for permeability tests on low permeable rocks. Shale permeability measurements are different when compared to experiments on high permeable rocks, as a very tight and well calibrated

system is required to detect the small fluid fluxes at the outflow side of the sample plug. Experiments on plugs can take up to days or weeks, especially when using brine as test fluid. The difficulty is in re-establishing water saturation of these rocks, especially for those that contain considerable amounts of swelling clays like montmorillonite.

7.5.1.1 Brine versus tap water permeability

Hildenbrand et al., 2004a provide several datasets for brine and tap water permeability for the same low-permeable argillaceous rock, determined under reservoir effective stress conditions. Although different permeabilities could be expected since different salt solutions and concentrations may swell or shrink swellable clays (e.g. montmorillonite), this was not the case as shown in Figure 7-4. Unfortunately in the work of Hildenbrand et al., 2004a no information on montmorillonite content is provided. Different salt solutions will affect hydration states of montmorillonite which is considered to influence permeability. Nevertheless, in the further course of this study brine and tap water permeabilities are treated equally.

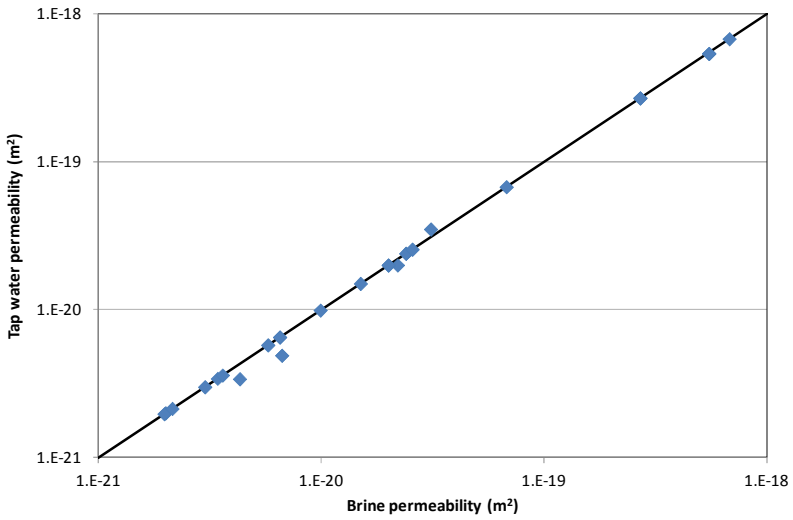


Figure 7-4. Brine versus tap water permeability on various low-permeable rocks (data from Hildenbrand et al., 2004a).

7.5.1.2 Brine versus air permeability

Some studies report air, while others report brine permeabilities, making it useful to find a correlation to obtain additional permeability values if only one value is provided. Figure 7-5 shows three data series; two of which have been reported earlier in the literature with fitted correlations (Macary, 1999; Pugh et al., 1991) and the third is based on data published by Carles et al., 2010 and Thomas et al., 1968. All datasets and their respective correlations are similar and show that air permeabilities are 1-2 orders of magnitude higher than their respective brine permeabilities. Similar observations are reported by Ghanizadeh et al. (submitted), where lower water permeability values are attributed to the reduction of the effective pore throats by thin, non-mobile water films on the pore walls and/or an enhanced supplementary compaction upon wetting.

The correlation determined here will be used in the further course of this study:

$$log(k_{brine}) = log(k_{air}) - 1.03 \; (n = 22, R^2 = 0.92) \qquad (7\text{-}14)$$

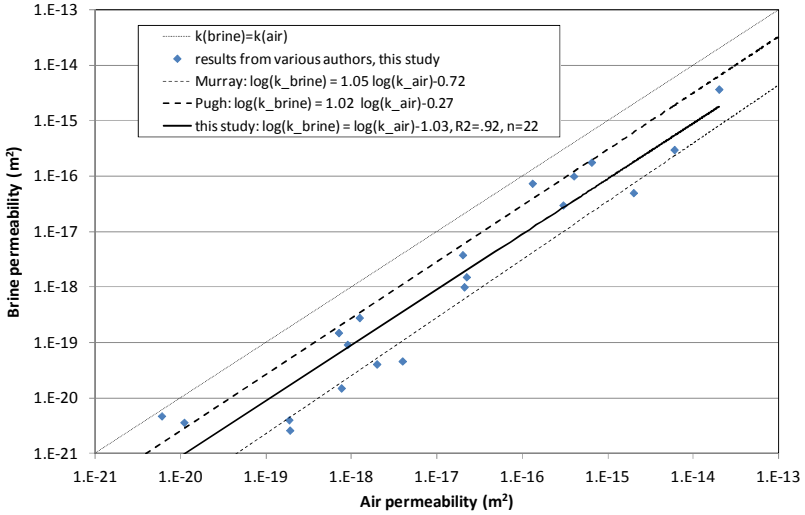


Figure 7-5. Correlation of brine with Klinkenberg corrected air permeabilities for various rock types. Published correlations Macary, 1999; Pugh et al., 1991; additional data forming base of correlation in this study Amann-Hildenbrand et al., submitted; Carles et al., 2010; Thomas et al., 1968.

7.5.1.3 Comparison between measured and modelled permeabilities

Comparing modelled with measured intrinsic permeabilities shows that a good prediction is obtained by the Yang and Aplin model (Figure 7-6, Yang and Aplin, 1998). The approach considered by Yang and Aplin gives fairly accurate predictions for samples with permeabilities higher than 10^{-20} m².

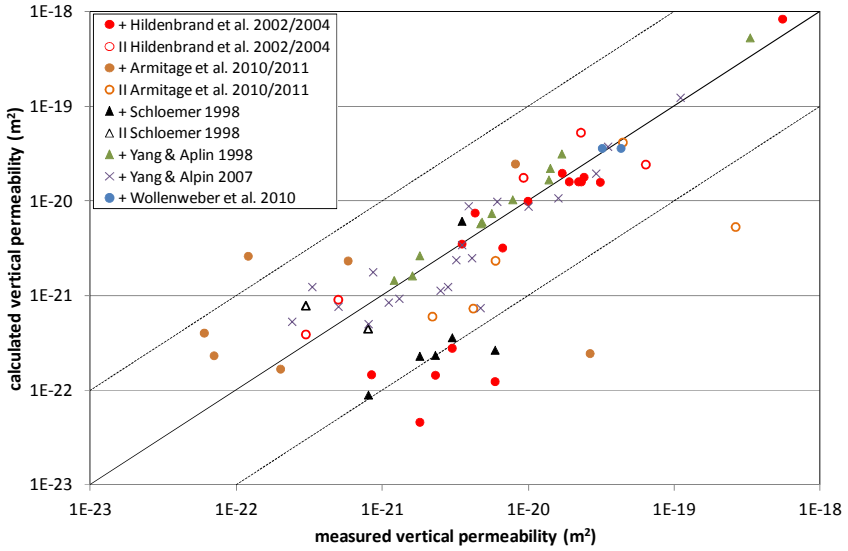


Figure 7-6: Yang and Aplin, 1998 permeability model applied to experimental datasets from various authors Armitage et al., 2011; Armitage et al., 2010; Hildenbrand et al., 2004a; Hildenbrand et al., 2002; Schlömer, 1998; Wollenweber et al., 2010; Yang and Aplin, 1998, 2007.

Equation 5 was applied to the current dataset using the Kozeny-Carman (KC) constant with different tortuosity τ values (providing the best fit to the data). For sandstones KC is usually considered to be 5, representative of spherical grains with low tortuosity. Surface area *S* and porosity Ø values are taken from the database used here. The Kozeny-Carman equation used for sandstones largely overestimates mudrock (and carbonate rich rock) permeability when assuming a standard KC-constant of 5. A better fit to the measured data is obtained by using a KC-constant of 250-500 for perpendicular to parallel permeabilities respectively (Figure 7-7). It is obvious from Figure 7-7 that for most of the mudrock samples there is still a large scatter between measured and calculated permeabilities. The KC values however are in line with Yang and Aplin, 2007 who report a Kozeny-Carman constant of 200 for vertical and 1000 for horizontal permeabilities. The reason for these large KC-values is attributed to much higher tortuosity values for mudrocks. It should be noted that tortuosities can vary from sample to sample. In general mudrocks have a complex pore connectivity and even though porosity can be high (e.g. >10%), not all pores effectively contribute to flow (the same holds for surface area). Another aspect is the method used for determining porosity. Often authors do not report their porosity method, there is a certain risk of comparing different basic values. For example, He-pycnometry and Archimedes based methods may provide higher porosity-values than mercury porosimetry. This is due to diverging accessibility to the pore space for different fluids at given pressures conditions, hence resulting in different porosities. An in-depth discussion is however outside the scope of this report.

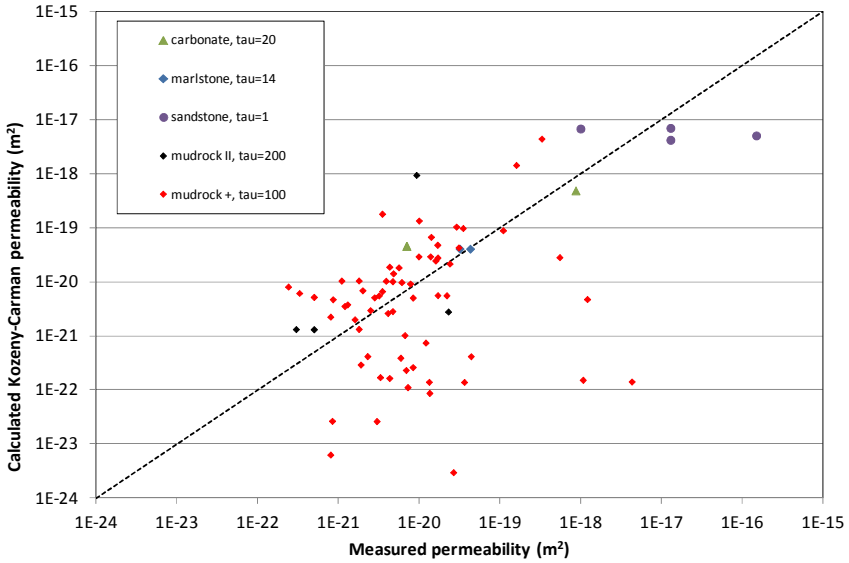


Figure 7-7. Comparison between measured brine permeability and calculated permeability following the Kozeny-Carman relation.

We can conclude that clay-rich, low-permeable rocks are probably too complex in pore and grain-size distribution to successfully apply Kozeny-Carman's approach for determining permeabilities, which is confirmed by e.g. Schlömer and Krooss, 1997).

7.5.2 Capillary pressure correlations

7.5.2.1 Correlations for interfacial tension

Since the comparison of capillary pressure data relies on a common denominator, meaning the thermodynamic and wetting properties of the respective two-phase system, a conversion may easily be done between the different systems. In our case we used CO_2/brine as the reference case because of its importance for the capillary sealing efficiency for geological CO_2 storage. The same conversion could be done for the system CH_4/brine. Although several experimental studies are available showing that CO_2 contact angles can range between ~0 and 90˚ we used perfect water-wet conditions with θ = 0° (cos(θ)=1) which is also assumed for gases like CH_4 or N_2. This simplifies Equation 1 to:

$$P_{c\_brkth} = \frac{2\gamma}{r} \qquad (7\text{-}15)$$

Hence, capillary pressure data available for non-CO_2 gases can be re-calculated to CO_2 capillary pressures following:

$$P_{C\_brkth\_CO2} = P_{c\_x} \cdot \frac{\gamma_{CO2-brine}}{\gamma_{x-brine}} \qquad (7\text{-}16)$$

While *x* denotes the non-CO_2 gas (e.g. N_2, CH_4, He).

In addition, re-calculating mercury porosimetry data to any gas species requires constants for contact angle and interfacial tension (Equation 5):

$$P_{C\_brkth\_x} = P_{c\_entry\_Hg} \cdot \frac{\gamma_{x-brine} \cdot cos(\theta_x)}{480\frac{mN}{m} \cdot cos(141°)} \qquad (7\text{-}17)$$

Although it is generally accepted that the mercury interfacial tension is constant and therefore pressure independent, Hills and Høiland, 1984 measured that the mercury/nitrogen interfacial tension decreases from ~480 mN/m at atmospheric pressures to ~420 mN/m at 75 MPa. For the mercury/air system, the largest Hg/air entry pressure found in the database used in this study is 75 MPa. No data were found for the pressure dependence of the Hg/air contact angle.

Correlation attempts for interfacial tension (IFT) of CH_4 (Figure 7-8a, data from Ren et al., 2000), N_2 (Figure 7-8b, data from Yan et al., 2001), CO_2 (Figure 7-8c, data from Bachu and Bennion, 2009) and He (Figure 7-8d, data from Wiegand and Franck, 1994) are based on best estimate fits as a function of temperature and pressure. In general there are many more studies reporting pressure, temperature and salinity-dependent IFT and it is not the aim of this paper to make a judgement on the suitability of each dataset. Here, those studies with a broad pressure and temperature range have been used to represent reservoir conditions down to a depth of at least 3 km. For CO_2, IFT is considered to depend on brine salinity, suggesting that IFT increases with increasing salinity (Bachu and Bennion, 2009; Li et al., 2012a; Li et al., 2012b). However, the effect of salinity on IFT will not be considered here, as the reported measurements

have generally been performed using either tap water or low salinity brine (e.g. solubility <10,000 ppm). For the different gases, IFT correlations as a function of pressure and temperature are as follows:

$$\gamma_{CH4} = 67.26 - 0.926 \cdot p + 0.011 \cdot p^2 - 0.119 \cdot (T - T_{ref}) \quad (7\text{-}18)$$

$$\gamma_{N2} = 66.03 - 0.353 \cdot p + 0.001 \cdot p^2 - 0.169 \cdot (T - T_{ref}) \quad (7\text{-}19)$$

$$\gamma_{CO2} = 49.08 - 1.582 \cdot p + 0.032 \cdot p^2 + 0.100 \cdot (T - T_{ref}) \quad (7\text{-}20)$$

$$\gamma_{H2} = 72.00 - 0.028 \cdot p - 0.165 \cdot (T - T_{ref}) \quad (7\text{-}21)$$

Where p is pressure (MPa), T is temperature (K) and T_{ref} is the reference temperature (333 K for CH_4 and N_2; 298 K for He; 348 K for CO_2).

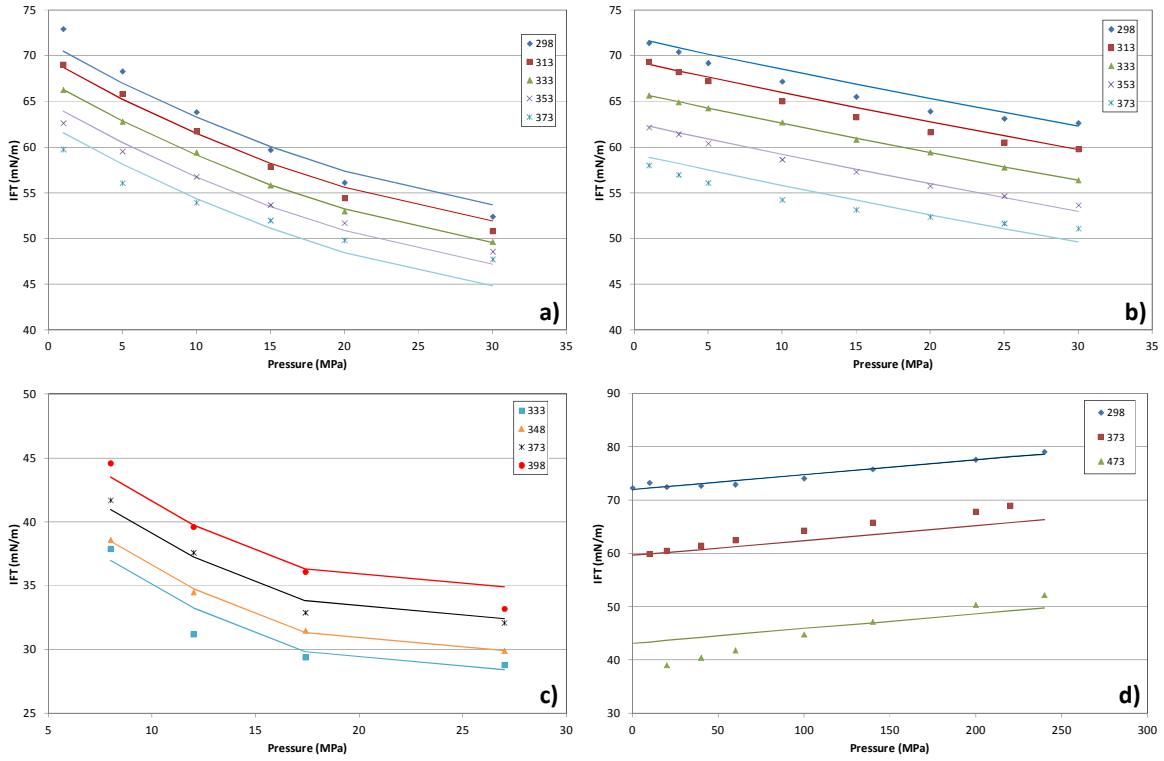


Figure 7-8. Interfacial tension data (symbols) and fits (lines) at various temperatures. Experimental data for CH_4 (a) from Ren et al., 2000, N_2 (b) from Yan et al., 2001, CO_2 (c) from Bachu and Bennion, 2009 and He (d) from Wiegand and Franck, 1994. Note that the correlation for CO_2 is only valid for pressures and temperatures for supercritical conditions (T>~323 K; P>8 MPa).

7.5.2.2 Mercury injection capillary pressure data on cuttings

Figure 7-9 shows MIP versus brine permeability with data from this study compared to other experimental studies and fitted trends from other authors (Harper and Lundin, 1997; Sperrevik et al., 2002). In general there is a large scatter in data with a poor regression. Sperrevik et al., 2002 investigated fault rocks, showing a regression R^2 between MIP and permeability of 0.84, and an even better value for host rocks (R^2= 0.90). However, these regressions cannot be verified through comparison with other datasets.

The fitted equations for the datasets are given below. Note that Hg capillary entry pressure P_{c_entry} is in MPa and permeability k in m^2.

$$this\ study: log(P_{c\_entry}) = -0.11\, log(k) - 1.85\ (n = 88, R^2 = 0.08) \quad (7\text{-}22)$$

$$Harper\ \&\ Lundin: log(P_{c\_entry}) = -0.29\, log(k) - 4.98 \quad (7\text{-}23)$$

$$Sperrevik\ et\ al\ (fault\ rocks): log\left(P_{c_{entry}}\right) = -0.38\, log(k) - 6.37 \quad (R2{=}0.84) \quad (7\text{-}24)$$

$$Sperrevik\ et\ al\ (host\ rocks): log\left(P_{c_{entry}}\right) = -0.40\, log(k) - 6.72 \quad (R2{=}0.90) \quad (7\text{-}25)$$

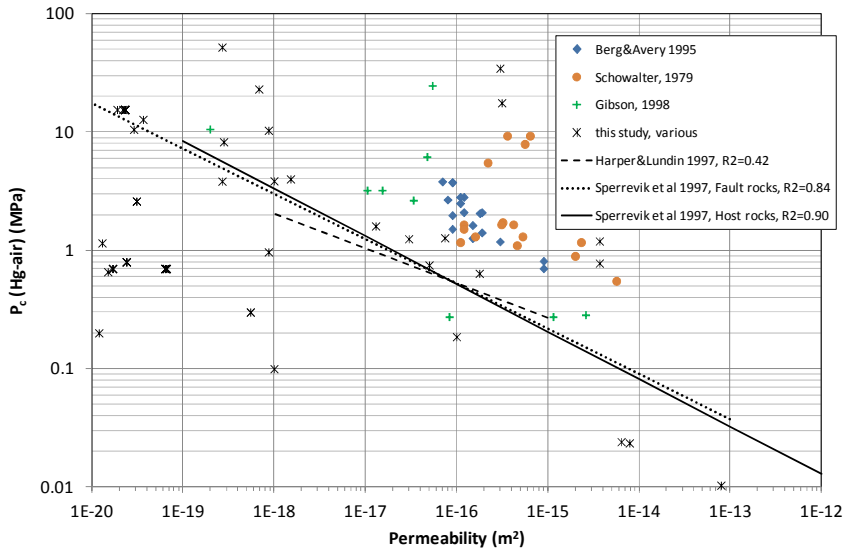


Figure 7-9. Log-log plot of mercury capillary entry pressure vs. brine permeability with data compilations from different authors (Berg and Avery, 1995; Gibson, 1998; Schowalter, 1979b), a compilation from this study and various correlations by other authors (Harper and Lundin, 1997; Sperrevik et al., 2002). Note that trend lines are only given for the permeability range provided in the original study.

Given the poor correlation between P_{c_enrty} and permeability, it seems that Hg/air capillary pressures cannot be predicted from permeability (or vice versa) for the data used in this study. It should also be noted that no further significant relationship was found between Hg capillary entry pressure and other petrophysical or mineralogical parameters. Unfortunately not every study describes the methodology in detail, so no inferences can be made.

7.5.2.3 Capillary pressures from plugs

7.5.2.3.1 Drainage capillary breakthrough pressure

Although this report is concerned with capillary breakthrough pressures in relation to caprock integrity for CO_2 storage there are only three datasets that use CO_2 for P_{c_brkth} measurements (Li et al., 2005) and most datasets were determined using N_2 (typical analogue fluid), He and CH_4 as test gases.

Figure 7-10 shows a plot of N_2 and He drainage capillary pressures as a function of permeability. With good approximation N_2 and He can be treated equally due to similar IFT and wettability data. A good correlation (R^2=0.74) was found for permeabilities ranging from 10^{-13} to 10^{-21} m^2 (0.1 D to 1 nD) for the different rock types. This trend would even be more distinct by excluding the mudrock samples (R^2=0.82).

Accordingly, the P_{c_brkth} versus *k* correlation function for all capillary breakthrough pressure data used in this study:

$$log(P_{c\_brkth}) = -0.348\, log(k_{abs}) - 6.2 \; (n = 59, R^2 = 0.74) \qquad (7\text{-}26)$$

Considering the mudrock samples only (Figure 7-10), a slightly different regression function with, however, poor regression is found:

$$Mudrock: log(P_{c\_brkth}) = -0.25\, log(k_{abs}) - 4.337 \; (n = 27, R^2 = 0.29) \qquad (7\text{-}27)$$

Several other $P_{c\_brkth\_N2}$ measurements on plug samples have been correlated by Davies, 1991 for various rock types based on different studies (Ibrahim et al., 1970; Rose and Bruce, 1949; Thomas et al., 1968; Wyllie and Rose, 1950):

$$Carbonate: log(P_{c\_brkth}) = -0.336\, log(k_{abs}) - 6.060 \; (n = 49, R^2 = 0.80)$$
Ibrahim et al., 1970; Thomas et al., 1968 (7-28)

$$Anhydrite: log(P_{c\_brkth}) = -0.348\, log(k_{abs}) - 6.585 \; (n = 7, R^2 = 0.90)$$
Ibrahim et al., 1970 (7-29)

$$Mudrock: log(P_{c\_brkth}) = -0.344\, log(k_{abs}) - 6.120 \; (n = 22, R^2 = 0.74)$$
Ibrahim et al., 1970 (7-30)

$$Sandstone: log(P_{c\_brkth}) = -0.369\, log(k_{abs}) - 6.602 \; (n = 22, R^2 = 0.97)$$
Rose and Bruce, 1949; Thomas et al., 1968; Wyllie and Rose, 1950 (7-31)

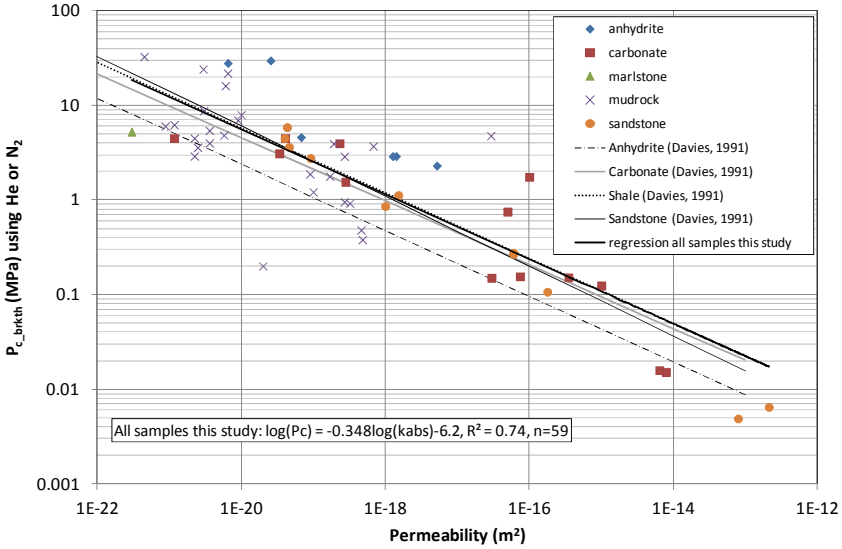


Figure 7-10. Drainage capillary breakthrough pressure (P_{c_brkth}) versus brine permeability on sample plugs using N_2 and Helium on a log-log scale.

The regressions for carbonates, mudrocks and sandstones are similar to those found in this study and basically confirm the general trend given in Equation 23. Only the trend for anhydrite determined by Davies, 1991 is different and shows consistently lower breakthrough pressures compared to siliciclastic rocks and carbonates which is different for the anhydrite samples shown here (Figure 7-10).

In contrast to the trends obtained for permeability versus MIP (Figure 7-9), a much better agreement has been found for plug-derived capillary breakthrough pressures, especially considering the various rock types included.

Figure 7-11 shows a plot of measured N_2 drainage capillary pressure versus corresponding mercury capillary entry pressures. Mercury derived entry pressures typically have higher values than their corresponding N_2 pressures because of higher interfacial tension (~factor 7) of mercury compared to nitrogen. A regression through the data gives the following relationship:

$$log\left(P_{c\_brkth\_N2}\right) = 0.74\ log(P_{c_{entry\_Hg}}) - 0.53\ (n = 17, R^2 = 0.81) \qquad (7\text{-}32)$$

The same figure shows N_2 capillary breakthrough pressures calculated from the MIP data using IFT correlations from Equation 8 and a contact angle with cos(θ)=1. Ideally, these values plot on a linear curve with a slope of 1 assuming that Hg/air capillary pressures can readily be converted to gas/brine data. Figure 7-11 shows that this is not the case, however that the calculated values are not too far off from the expected values. The reason for this deviation might be some uncertainty in IFT values, slight deviations in contact angle from perfectly water-wet conditions (cos(θ)=1) and/or inconsistencies in picking the right capillary entry pressure from mercury porosimetry data as discussed earlier.

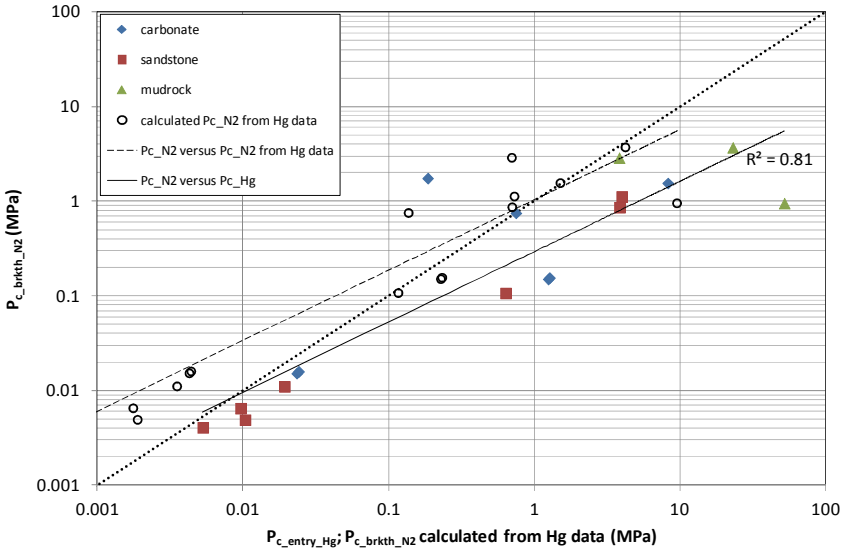


Figure 7-11. Log-log plot of measured drainage N_2 capillary breakthrough pressures on sample plugs versus corresponding MIP from cuttings of the same rock for different rock types (colored symbols). Black circles correspond to re-calculated N_2 breakthrough pressures from MIP data using IFT from correlation in Equation 8 and assuming water-wet conditions. Solid line: trendline for $P_{c\_brkth\_N2}$ versus $P_{c\_entry\_Hg}$; dashed line:

trendline for P_{c_entry} determined from mercury porosimetry and re-calculated to N_2 versus $P_{c\_brkth\_N2}$; dotted line: linear curve with slope of one.

Figure 7-12 shows $P_{c\_brkth\_N2}$ versus porosity relations for a variety of rocks (sandstone, carbonate, anhydrite) for which a reasonable regression was found. Generally $P_{c\_brkth\_N2}$ increases with decreasing porosity following the trend:

$$P_{c\_brkth\_N2} = 0.14e^{-0.84\,\emptyset}\ (n = 23, R^2 = 0.59) \qquad (7\text{-}33)$$

This correlation only applies by excluding the three data points obtained for shales (Ito et al., 2010), which have unusually high porosities for the breakthrough pressures reported. It is assumed that this correlation will not apply for mudrocks because of the highly variable porosity at a given permeability. Due to their texture mudstones exhibit a high percentage of pores, whereas flow is strongly restricted by the alignment of clay particles. However, also the type of porosity method is of importance, resulting in strongly deviating values.

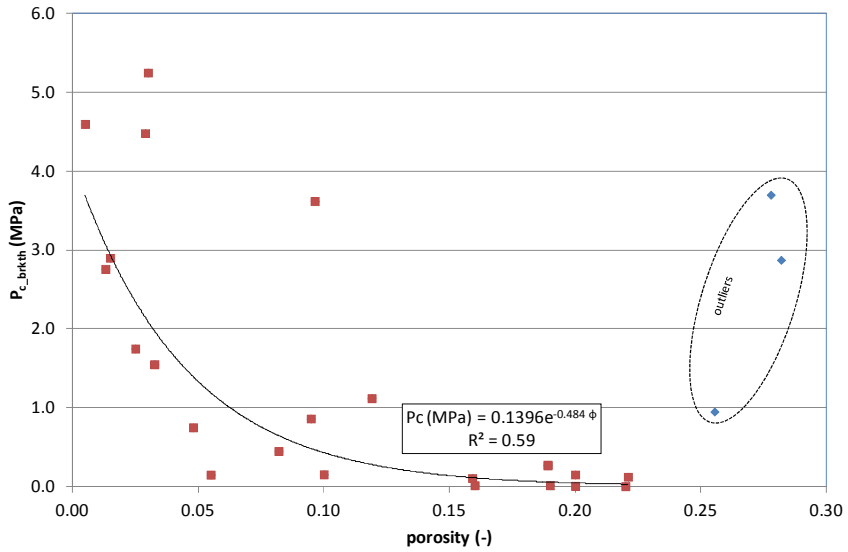


Figure 7-12. N_2 P_{c_brkth} versus porosity plots for various carbonate, anhydrite and sandstones.

7.5.2.3.2 Imbibition capillary entry pressure ("snap-off" pressure)

Figure 7-13 and Figure 7-14 show correlations of imbibition capillary (snap-off) pressures as a function of brine permeability for different rock types independent of gas species (Figure 7-13) and in dependence of the gas species for which sufficient data was available (CO_2, CH_4, N_2, Figure 7-14). In general, data correlate poorly, especially for the low permeability range (<10^{-18} m^2), which is dominated by mudrocks. An exception is the correlation for CH_4 which covers a broader permeability range compared to the other gases and has the following trend (Figure 7-14):

$$CH_4\text{: } log\left(P_{c\_snap-off}\right) = -0.24\ log(k_{abs}) - 4.62;\ R^2 = 0.80, n = 14 \qquad (7\text{-}34)$$

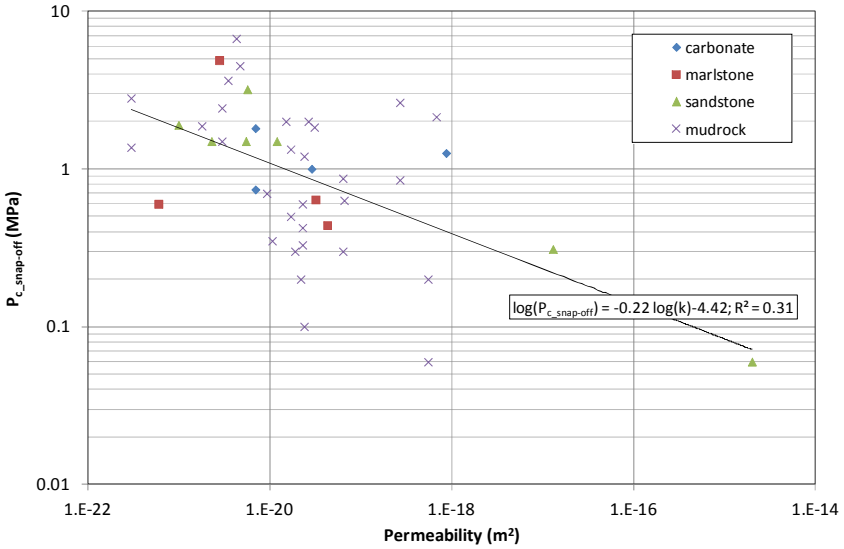


Figure 7-13. Log-log plot of snap-off capillary pressure versus brine permeability on sample plugs using different gases (N_2, CH_4, CO_2, He). Data from Hildenbrand et al., 2004a; Hildenbrand et al., 2002; Ito et al., 2010; Wollenweber et al., 2010.

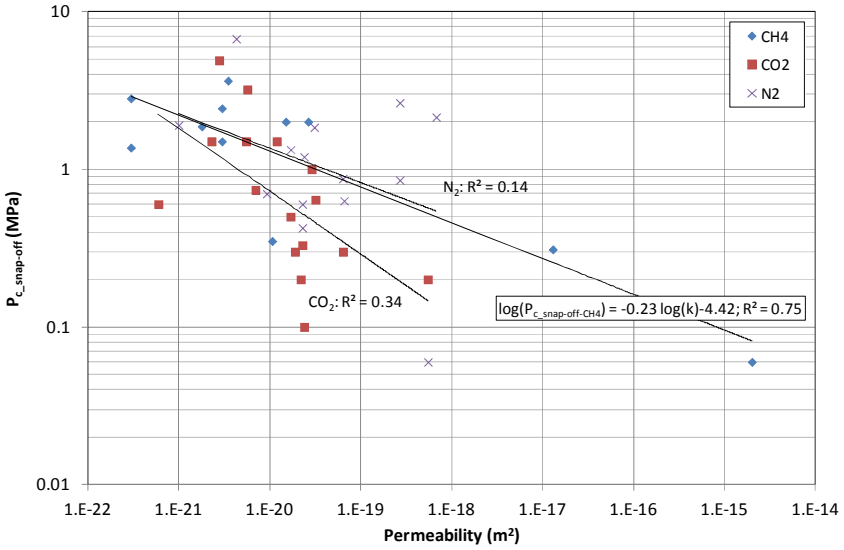


Figure 7-14. Log-log plot of imbibition capillary pressure data for individual gas species (N_2, CO_2, CH_4) as a function of brine permeability. Data from Hildenbrand et al., 2004a; Hildenbrand et al., 2002; Ito et al., 2010; Wollenweber et al., 2010.

Figure 7-15 shows correlations of the effective permeability (k_{eff}) to gas that is measured after drainage capillary breakthrough pressure has been overcome. This data can also be treated as relative permeabilities when normalising to respective brine permeabilities. In these experiments water saturations remain unknown. Data was retrieved from measurements by Hildenbrand et al. (2002, 2004) and details on the experimental procedures are provided therein. Generally it is shown that k_{eff} is up to two orders of

magnitude lower than the corresponding brine values. There are reasonable correlations for the sandstone and mudrock datasets:

$$\textit{Sandstone: } log(k_{eff}) = 0.9\, log(k_{abs}) - 3.33;\ R^2 = 0.83, n = 10 \qquad \textit{(7-35)}$$

$$\textit{Mudrock: } log(k_{eff}) = 1.35\, log(k_{abs}) + 6.1;\ R^2 = 0.69, n = 37 \qquad \textit{(7-36)}$$

Unfortunately, the number of carbonate and marlstone measurements is insufficient for a statistically relevant evaluation.

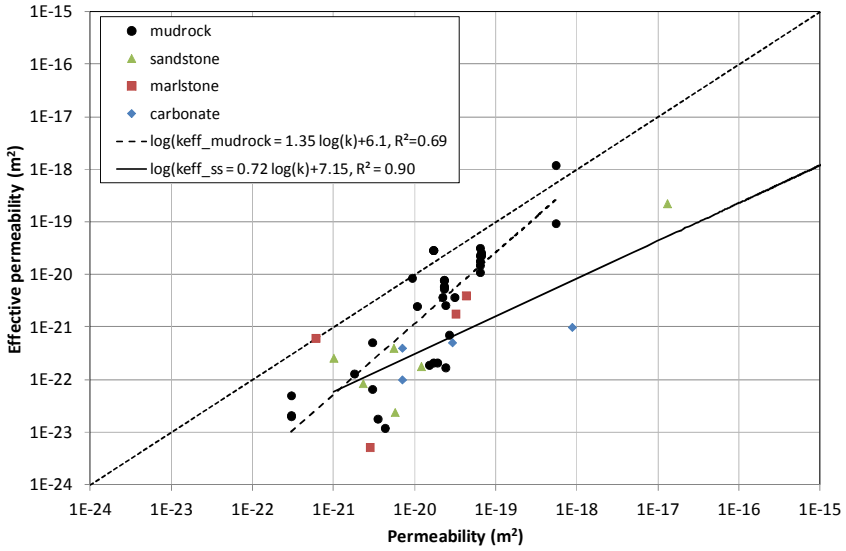


Figure 7-15. Log-log plot of brine permeability versus effective gas permeability after capillary breakthrough pressure is exceeded for different rock types. Data from Hildenbrand et al., 2004a; Hildenbrand et al., 2002; Wollenweber et al., 2010.

When plotting snap-off pressures versus k_{eff} for the different gas species, an expected negative correlation as shown in Figure 7-16 is found. These general trends, while most experimental data presented here are already shown by Hildenbrand et al., 2004a, were added for completeness. It should be noted that for Helium only three datasets were available.

$$CH_4\textit{: } log(P_{c\_snap-off}) = -0.32\, log(k_{eff}) - 6.86;\ R^2 = 0.86, n = 12 \qquad \textit{(7-37)}$$

$$CO_2\textit{: } log(P_{c\_snap-off}) = -0.33\, log(k_{eff}) - 7.15;\ R^2 = 0.73, n = 16 \qquad \textit{(7-38)}$$

$$N_2\textit{: } log(P_{c\_snap-off}) = -0.34\, log(k_{eff}) - 6.96;\ R^2 = 0.74, n = 15 \qquad \textit{(7-39)}$$

$$He\textit{: } log(P_{c\_snap-off}) = -0.36\, log(k_{eff}) - 7.62;\ R^2 = 0.84, n = 3 \qquad \textit{(7-40)}$$

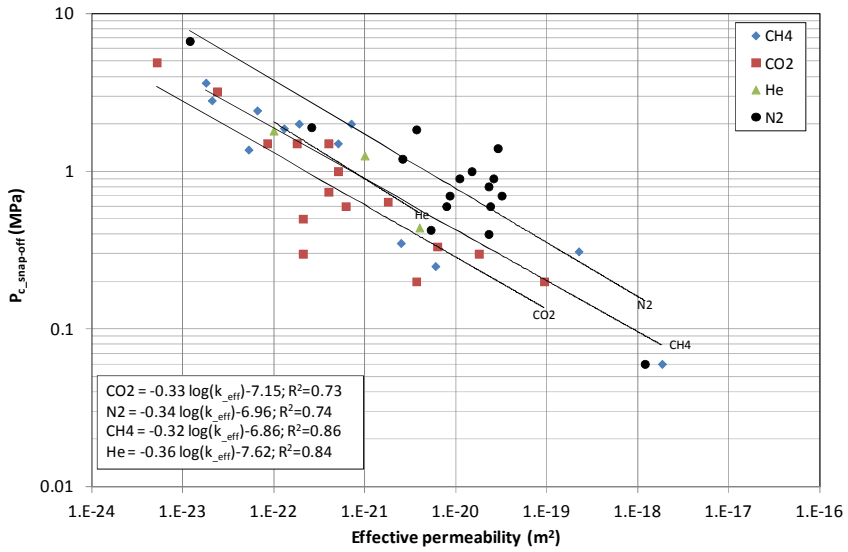


Figure 7-16. Effective permeability (k_{eff}) after capillary breakthrough pressure is exceeded on a log-log scale for different gas species, CH_4, CO_2, N_2 and He. Data from Hildenbrand et al., 2004a; Hildenbrand et al., 2002; Wollenweber et al., 2010.

7.5.2.3.3 Comparison of breakthrough and snap-off capillary pressure

Drainage (breakthrough) and imbibition (snap-off) P_c values differ when plotted against permeability. The reasons are described above and attributed to e.g. advancing (drainage) versus receding (imbibition) contact angles. It can generally be expected that breakthrough pressures are higher than snap-off pressures on the same sample. In the following correlations for sandstones and mudrocks were established. For other rock types the data set was too small and could therefore not be considered.

Figure 7-17 shows drainage and imbibition P_c values for sandstones with a good to excellent regression for a large permeability range (between ~1 D to 1 nD). Original data have been measured using different gases and were all recalculated to CO_2 capillary pressures using IFT values from above and fully water-wet conditions:

$$log\left(P_{c\_snap-off}\right) = -0.30\ log(k_{abs}) - 5.92;\ R^2 = 0.88, n = 8 \qquad (7\text{-}41)$$

$$log\left(P_{c\_brkthh}\right) = -0.44\ log(k_{abs}) - 8.19;\ R^2 = 0.99, n = 10 \qquad (7\text{-}42)$$

Here, P_c values were all re-calculated for CO_2/brine using IFT data from above and assuming fully water-wet conditions, i.e. cos(θ)=1. It can be seen that for permeabilities lower than 10^{-15} m^2 (mD) the imbibition is lower than the drainage capillary breakthrough pressure, while the two lines cross at a permeability of ~1 mD. This shows that the generally considered ratio of drainage to imbibition capillary pressure of two (e.g. Zweigel et al., 2004) is not a constant but rather permeability (or pore throat size) dependent.

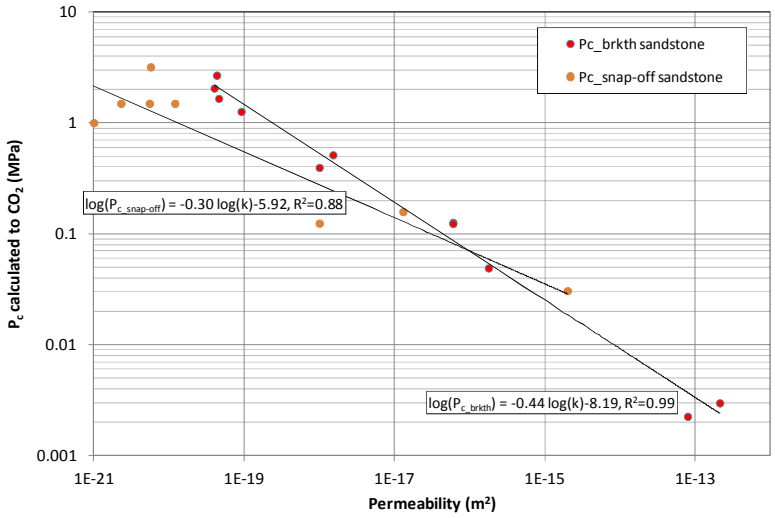


Figure 7-17. Plug-derived drainage (breakthrough) and imbibition (snap-off) P_c (MPa) versus k (m^2) curves for sandstones on a log-log scale. All P_c values have been calculated for CO_2 according to Chapter 7.5.2.1. Note that these are global correlations and snap-off and breakthrough pressures were not determined on the same plug. Breakthrough pressure data from Ibrahim et al., 1970; Purcell, 1949; Schowalter, 1979b; Thomas et al., 1968; snap-off pressure data from Hildenbrand et al., 2004a; Hildenbrand et al., 2002.

A similar approach was followed for mudrock samples as shown in Figure 7-18. It is evident that imbibition values are in general lower than drainage values. However, the scatter is large resulting in poor regression coefficients of R^2<0.5.

$$log\left(P_{c\_snap-off}\right) = -0.29\ log(k_{abs}) - 5.01;\ R^2 = 0.26, n = 30 \quad (7\text{-}43)$$

$$log\left(P_{c\_brkthh}\right) = -0.41\ log(k_{abs}) - 7.81;\ R^2 = 0.46, n = 35 \quad (7\text{-}44)$$

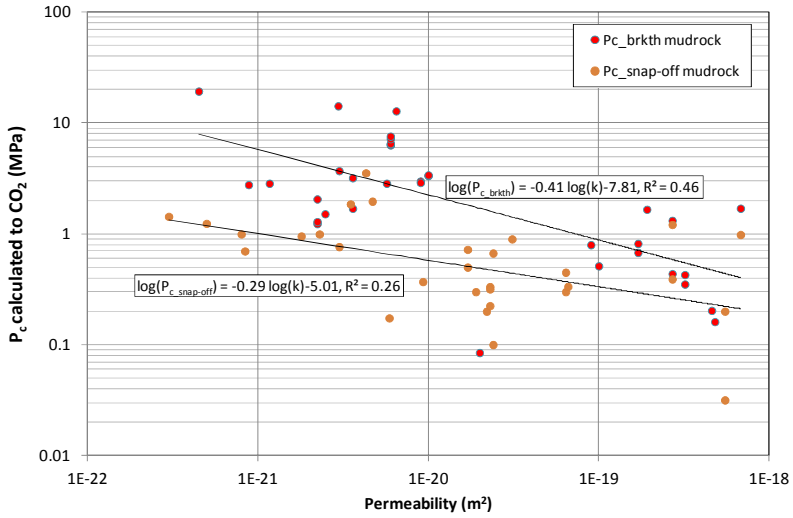


Figure 7-18. Drainage and imbibition P_c (MPa) versus k (m^2) for mudrocks on a log-log scale. All P_c values have been re-calculated for CO_2/brine system according to Chapter 7.5.2.1. Note that these are global correlations and snap-off and breakthrough pressures were not determined on the same plug. Breakthrough pressures from Al-Bazali et al., 2009; Harrington and Horseman, 1999; Ibrahim et al., 1970; Ito et al., 2010; Marschall et al., 2005; snap-off pressure data from Alles, 2008; Hildenbrand et al., 2004a; Hildenbrand et al., 2002; Ito et al., 2010.

Figure 7-19 compares the plug-derived drainage/imbibition ratios for both datasets (sandstone and mudrocks) against permeability. It is shown that both curves follow a similar trend with permeability. The drainage/imbibition ratios are generally higher than 1. For comparison, two data points (Amann-Hildenbrand et al., submitted; Boulin et al., 2011) where imbibition and drainage capillary pressures were determined on the same sample, are included. Both values plot close to the calculated trend lines. Reasons for the clear trend with permeability are only speculative. The aspect ratio, which is the ratio of pore body to pore throat radius has been assumed to play a role and Pentland (2010) has demonstrated that this ratio increases with decreasing permeability for a permeability range of 10 to 0.1 Darcy. Further research should focus on this aspect since no information was found reporting aspect ratios of lower permeable rocks in the literature. High resolution imaging in addition to mercury porosimetry are considered adequate for studying pore throat sizes even in the <100 nm range, which is common in mudrocks.

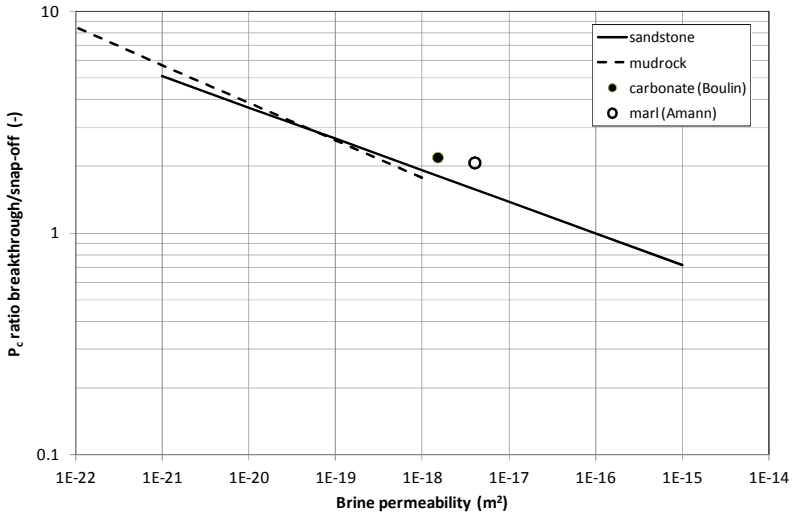


Figure 7-19. Log-log plot of CO_2 drainage/imbibition P_c ratio versus brine permeability. Only the permeability range is shown where data is available. Note that these are global correlations and snap-off and breakthrough pressures were not determined on the same plug. For comparison two data points on two different carbonate-rich rocks are shown where breakthrough and snap-off pressures were determined on the same sample Amann-Hildenbrand et al., submitted; Boulin et al., 2011.

In practical terms, for CO_2 storage operations or hydrocarbon entrapment, the observed difference between drainage and imbibition P_c means that a reservoir that once started to leak, will only be re-sealed by a large pressure reduction, i.e. until water re-imbibition stops fluid flow. This means that already significant amounts of gas may have been dismigrated from the storage site.

Assuming a simple hypothetical case of a shale formation with 1 nD permeability (~10^{-21} m^2), a drainage/imbibition P_c ratio of ~6 and CO_2 drainage capillary breakthrough pressure of 6 MPa; caprock/reservoir interface depth at 2000 m (corresponding to hydrostatic pressure of 20 MPa and temperature of 70°C) and brine density ρ_{brine} 1000 kg/m^3.

Following the relationship:

$$h = \frac{P_{c\_brkth}}{(\rho_{brine} - \rho_{CO2}) \cdot g} \qquad (7\text{-}45)$$

The maximum CO_2 column height *h* would be (with a calculated CO_2 density ρ_{CO2} of ~660 kg/m^3, Span and Wagner, 1996) about 1800 m. If gas percolation through the mudrock is established the gas column needs to be lowered to ~300 m to stop gas flow ($P_{c\_snap\text{-}off}$ of 1 MPa). In terms of lost amount of gas, this would correspond to ~6 Mt/km^2 when assuming an effective porosity of 10% and a residual CO_2 saturation of 30%.

Performing the same calculation for a natural gas reservoir, assumed to be filled with pure CH_4, with a gas density of 123 kg/m^3 (Setzmann and Wagner, 1991), the gas column height to initiate capillary leakage would be ~700 m and ~115 m to stop leakage following water re-imbibition.

7.5.3 Comparability of data

There are many factors impacting the accuracy and/or comparability of the data sets used here. For instance experimental protocols to determine e.g. capillary breakthrough pressures on sample plugs will certainly differ from laboratory to laboratory. A large portion of studies do not even report the method used for porosity determination, like H_2 pycnometry or Hg-porosimetry. As porosities vary significantly from method to method, comparability to other parameters is strongly restricted.

Other uncertainties are the quality of sample plugs used within the various studies (e.g. alteration and desiccation in core sheds for many years) or sample sizes. Plug diameters usually vary between 1 and 1.5 inches and sample length between a few mm up to a few inches. The choice of sample size is important, i.e. during in-situ measurements on plug sample dehydration, plug drilling or other mechanical damage may favour the risk of small artificial fissures leading to a strong underestimation of sealing capacity (too low capillary pressure values).

7.5.3.1 Influence of effective stress

For the datasets used in this study, the confining pressures varied roughly between 15 MPa (Tonnet et al., 2010) and 40 MPa (Wollenweber et al., 2010). This has consequences for the comparability of the data, especially on permeability and capillary pressures since those are directly coupled to effective stress. Katsube and co-workers (Katsube, 2000; Katsube et al., 1991; Katsube and Williamson, 1994) have shown that by increasing the effective stress from zero to 50 MPa, permeability can decrease by 1-2 orders of magnitude for shales. This has consequences on pore radii and therefore on capillary pressure.

Varying effective stress will certainly have an impact on the porosity-permeability relationship since porosity is usually determined under ambient conditions and will remain constant.

7.5.3.2 Wettability

For gas/brine usually a strongly water-wet system is considered with contact angles equal to or close to zero. This reduces Equation 2-1 to:

$$P_{c\_entry} = \frac{2\gamma}{r} \qquad (7\text{-}46)$$

with γ being the interfacial tension and *r* the pore throat radius.

While no contact angle data for the non-CO_2 gases considered in this study have been found in the literature, Table 7-4 summarizes published contact angle data for CO_2. It is shown that most values range between 0 and 60 degree. Some authors measured much higher angles and even values higher than 90 degree (Bikkina, 2011; Yang et al., 2007) for quartz and limestone have been reported. These are mixed-wet values, indicating partial gas imbibition. There are several limitations to basically all datasets which are

Table 7-4: Summary of measured CO_2 contact angles on different substrates. Only single mineral systems have been found in the literature. In brackets cos(ϑ) which directly corrects P_{c_entry} in Equ. 1.

	quartz	calcite	muscovite	limestone	silica surface	advancing/ receding
Espinoza and Santamarina, 2010	20-40 (0.94-0.77)	30-40 (0.87-0.77)				a
Shah et al., 2008			28-38 (0.88-0.79)	27-32 (0.89-0.85)		a
			62-80 (0.5-0.17)	33 (0.84)		r
Bikkina, 2011	46-91 (0.69--0.02)	42-60 (0.74-0.5)				a
Yang et al., 2007				46-130 (0.69--0.64)		r
Tonnet et al., 2010				30 (0.87)		a/r
Chiquet et al., 2007a	11-37 (0.98-0.80)	11-70 (0.98-0.34)				a
Kim et al., 2012					0-80 (1-0.17)	a

(1) The short time scales of up to hours for the interaction between CO_2, brine and the mineral surface. It is therefore not proven if the system was in chemical and thermodynamic equilibrium since mineral surfaces will start reacting with the fluid on time scales depending on the mineral itself (e.g. quartz much slower than limestone). This leads us to the second shortcoming where

(2) Mainly single mineral systems have been considered which do not represent natural systems. The natural system in contact with carbonic acid and bulk CO_2 is dynamic where mineral phases will dissolve and others will precipitate. There is no information on the impact on wettability. Related to this, another shortcoming appears where

(3) Usually clean, idealized systems are considered with perfect surfaces (no fractals), no impurities etc. This is also not representative for the subsurface and should be considered.

Looking at this data and its implications for e.g. calculating CO_2/brine contact angles from mercury/air it can be stated that potentially large errors can be involved when considering perfectly water-wet conditions. While the CO_2 contact angles of >90 degree need to be confirmed a contact angle of 60 degree does not seem to be unusual, correcting calculated CO_2 capillary entry pressures with a value of $\cos(\theta)=0.5$ in Equ. 1. Consequently this may reduce the maximum CO_2 column height that can be contained by a caprock by a factor 2.

7.6 Conclusions

The critical capillary breakthrough pressure and permeability are the most important parameters in order to predict the effective sealing capacity of a lithology. In this study we compared 214 datasets containing the following parameters: permeability, porosity, mineralogy, capillary snap-off pressure, capillary breakthrough pressure and specific surface area. Measured permeabilities and capillary pressures were correlated to other petrophysical parameters. The validity of formulations to derive permeability were tested (Kozeny-Carman vs. Young and Aplin model) and MIP derived critical capillary pressures were compared to those determined under in-situ conditions on core plugs.

In summary we can draw the following conclusions:

- A fair correlation between MIP and comparable plug measurements was observed for entry/breakthrough pressures, however not for snap-off pressures on the imbibition path.
- CH_4 capillary snap-off pressure correlates well with permeability
- The plug-derived capillary breakthrough pressure correlates well with brine permeability and mercury porosimetry capillary entry pressure
- A trend was obtained for the ratio drainage/imbibition pressure vs. permeability, indicating that with decreasing permeability drainage versus imbibition Pc ratios increase. As a result, when capillary entry pressures occurs and two-phase flow is created over a low permeability formation, reservoir pressure (gas column height) needs to be reduced significantly to prevent this flow.
- The conventionally used Kozeny-Carman equation cannot be applied for mudrocks, probably because the pore system, pore alignment, pore network connectivity and mineralogy are too complex.
- Using the Yang-Aplin model to predict mudrock permeabilities from porosity and surface area data we find a fairly good correlation with deviations of up to one order of magnitude only.

8 The Significance of Caprock Sealing Integrity for CO_2 Storage

8.1 Introduction

Geological storage of CO_2 from fossil-fired power plants is intensely examined as an option for reducing anthropogenic emissions of greenhouse gases. Deep saline aquifers, depleted oil and gas fields and unminable coal seams are the primary targets for the underground disposal of supercritical CO_2. One major concern of all CO_2 storage options is the sealing efficiency of low-permeable sequences overlying potential storage reservoirs. The long-term integrity of these sealing layers (caprocks) is one prerequisite to keep the CO_2 in place and avoid dissipative loss towards the atmosphere. The assessment of leakage risks and leakage rates, considering different potential mechanisms, is therefore an important issue for site approval and public acceptance (Pruess, 2008).

Subsurface storage of CO_2 is always associated with an excess pressure resulting from buoyancy forces and injection-related overpressure which constitutes the driving force for different transport processes. Pressure-driven volume flow (Darcy flow) through the caprock is commonly considered as the main risk scenario and can be envisaged to range in intensity over several orders of magnitude:

rapid leakage by seal-breaching (mechanical failure) or damage of wells (corrosion of pipes and cements),

seepage along existing open fault systems and fracture networks,

leakage through the pore-space controlled by capillary forces and permeability (after capillary breakthrough pressure is exceeded).

Another important topic that is still to be investigated thoroughly is the effect of CO_2 and its reactivity on the mechanical stability of caprocks. Up to now only a few experimental results have been published (Angeli et al., 2009; Hangx et al., 2010b).

This paper addresses aspects related to fluid transport through caprocks; capillary threshold pressure, effective permeability after threshold pressure is exceeded as well as diffusion through the water-filled pore space and adsorption. Since CO_2 in aqueous solution reacts with the mineral phases it is important to consider rock/pore network alterations, especially for the sealing lithologies.

8.2 CO_2 diffusion

Carbon dioxide leakage into and through caprocks may occur by molecular transport (diffusion) through the water-saturated pore system. Diffusion controls the rate of certain geochemical reactions that, in turn, may affect the petrophysical and mechanical properties of the sealing layers. Diffusion is considered of little relevance in terms of gas losses as discussed by (Busch et al., 2008). However this conclusion is based solely on the limited number of available data sets on CO_2 diffusion through caprocks. More detailed research was done on molecular gas transport through caprocks focusing on hydrocarbon or nitrogen loss from

natural gas reservoirs (e.g. Krooss and Leythaeuser, 1988; Krooss and Leythaeuser, 1996; Krooss et al., 1992a; Leythaeuser et al., 1980; Nelson and Simmons, 1995). It was concluded that, although diffusive leakage is a perpetual and ubiquitous process at the reservoir/caprock boundary significant losses of reservoir gas can only be expected on geological time scales of tens of millions of years.

In one of the first studies related to CCS, Krooss et al., 2003 reported CO_2 diffusion parameters of samples from different lithotypes (coal, cemented sandstones, shales). The results of this study indicated that shales are able to store significant amounts of CO_2, dissolved either in formation waters, trapped by mineral reactions or sorbed to organic compounds or mineral surfaces. These findings triggered more detailed investigations of the CO_2 sorption and diffusion behaviour of selected shale samples (Busch et al., 2008; Wollenweber et al., 2010). Effective diffusion coefficients of gases in the aqueous phase are in the order of 10^{-8} to 10^{-9} m^2/s. Diffusion in organic matter can be approximated from coal/gas research where diffusion coefficients of 10^{-10} to 10^{-13} m^2/s have been reported. The studies noted above yielded effective diffusion coefficients in the order 10^{-10} to 10^{-12} m^2/s for low permeable argillaceous rocks. A few studies have suggested that effective CO_2 diffusion coefficients may change due to water/rock interactions (Busch et al., 2008; Wollenweber et al., 2010). These changes are rather small within experimental time frames. Upscaling to CO_2 storage times of hundreds to thousands of years is currently not possible.

Disregarding alterations of the caprock due to diffusion-controlled reactions (reactive transport), the rate of propagation of a diffusion front of gas through the caprock can be estimated for different effective diffusion coefficients and the corresponding transport/leakage efficiency can be assessed based on bulk volume concentrations (amount of gas dissolved in pore water, sorbed to organic matter or mineral surfaces, or involved in mineral carbonation reactions) as discussed by Krooss et al Krooss et al., 1992a, b. Steady-state diffusive flux can be calculated by Fick's first law of diffusion:

$$J = -D_{eff} \frac{\Delta C_{bulk}}{\Delta x} \qquad (8\text{-}1)$$

For a caprock of thickness *l* (m), a porosity , a CO_2 concentration of C_{aqu} in the pore water at the caprock-reservoir boundary and assuming a concentration of zero at the top of the caprock the steady-state diffusive flux can be estimated by:

$$J = D_{eff} \frac{\phi \cdot C_{aqu}}{l} \qquad (8\text{-}2)$$

Thus, assuming an effective diffusion coefficient of 10^{-10} m^2, the steady-state diffusive fluxes of CO_2 through caprock layers (porosity 0.1) of 10, 100 and 1000 m with a base depth at 2000 m would be 1640, 164 and 16.4 $kg/m^2/Ma$, respectively.

If the reservoir is initially free of CO_2, the lag-time until steady-state diffusive flux is reached must also be taken into account.

Figure 8-1, adapted from (Krooss and Leythaeuser, 1996), shows the times required to reach 90% of the steady-state diffusive flux as a function of caprock thickness for different effective diffusion coefficients. For the worst-case scenario considered here (effective diffusion coefficient of 10^{-10} m^2/s, caprock thickness of 10 m) this lag-time is 0.1 Ma (Figure 8-1) indicating that diffusive losses through even thin caprock layers are negligible for CO_2 storage operations.

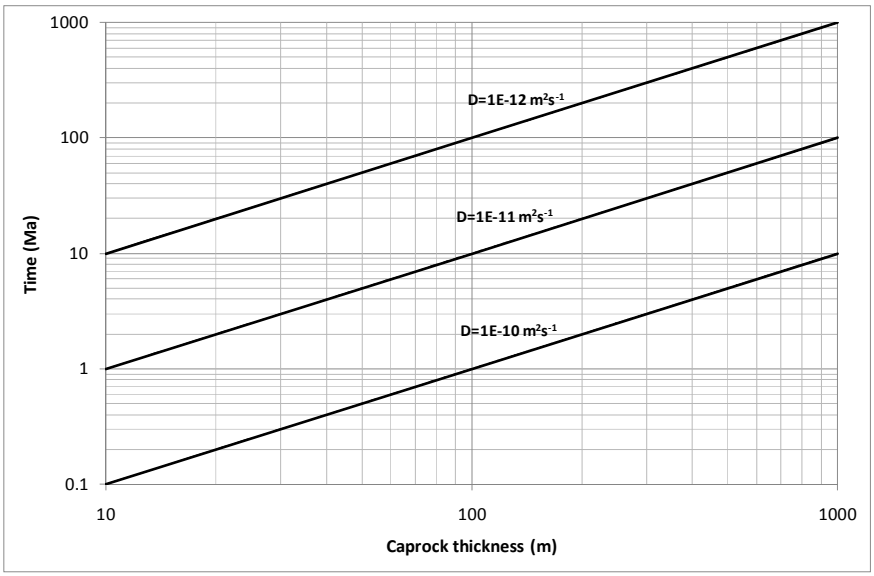


Figure 8-1. Time required to reach 90% of the steady-state value of diffusive gas flux across caprocks as a function of caprock thickness for effective diffusion coefficients from 10^{-12} to 10^{-10} m^2/s. Diagram adapted from Krooss & Leythaeuser Krooss and Leythaeuser, 1996.

8.3 CO_2 sorption on clay mineral surfaces

Gas adsorption on microporous material is a well-known phenomenon and a key factor for coalbed methane or shale gas production. Many studies have correlated methane sorption capacities with organic matter content (total organic carbon, TOC) and usually a good fit can be found that extrapolates to zero (i.e. no organic matter, no methane sorption capacity). This means that for methane only insignificant adsorption on clay mineral surfaces can be expected. Recent studies have shown that this may be different for CO_2. CO_2 adsorption capacities on single clay minerals and shale samples have been found (Busch et al., 2008; Weniger et al., 2010; Wollenweber et al., 2010) to be of the same order as those measured on coals.

Still unknown are the exact mechanisms of CO_2 sorption on clay minerals and the potential implications for CO_2 storage safety. First, this may reduce the risk of CO_2 leakage given the large measured sorption potential of up to 1 mmol/g sample (44 mg/g; Muderong shale, Busch et al., 2008). It is well known from coal gas research that CO_2 sorption on coal causes swelling leading to reduced permeabilities. However this swelling might cause micro-cracking of the coal or, in this case, of the caprock formation. These effects (sorption mechanisms, possibility of clay mineral swelling, potential implications of swelling on sealing integrity) should be the focus of future research. Furthermore, the relation between chemical

clay/CO_2/brine interactions (e.g. dissolution) and sorption should be studied. It is expected that both mechanisms should compete with each other.

Second, it can be stated that CO_2 sorption on clays might immobilize injected CO_2 in the reservoir, particularly in "dirty" reservoirs with high clay contents. The extent of this is however not quantifiable at this stage of research. From the knowledge gained so far, adsorption kinetics are relatively fast for dispersed clays (i.e. where gas diffusion through shale is not the ratedetermining factor for CO_2 sorption), which might provide a sink for CO_2 in the short term, especially compared to long-term effects like mineral carbonation reactions.

8.4 Capillary entry pressure and capillary leakage

Generally, migration through the water-saturated porous network of a caprock may occur when the CO_2 fluid pressure in the reservoir exceeds the capillary entry pressure (Hildenbrand et al., 2004a). This holds for the inter-granular pore space but also for water-filled (micro–) fracture systems. At pressures above the so-called breakthrough (threshold) pressure, at which a continuous flow of the non-wetting fluid forms across the pore system, CO_2 can escape from the upper boundary of the sealing formation (Hildenbrand et al., 2004a; Hildenbrand et al., 2002; Li et al., 2005).

The capillary entry or threshold pressure P_c (pressure difference ΔP needed to displace water in the pore system) of caprocks depends on capillary forces in the rock matrix, i.e. on the pore throat radius r, the water/brine interfacial tension γ and the brine /mineral/CO_2wetting (contact) angle θ:

$$P_c = \Delta P = \frac{2\gamma \cos\theta}{r} \qquad (8\text{-}3)$$

Measurements of the capillary breakthrough pressure of low permeable rocks have initially been performed for the characterisation of hydrocarbon reservoirs or (nuclear) waste disposals (Gallé, 2000; Pusch, 1985; Schlömer and Krooss, 1997). In recent years research focus shifted more to the characterisation of CO_2 storage reservoirs and their sealing lithologies (Al-Bazali et al., 2005; Angeli et al., 2009; Hildenbrand et al., 2004a; Hildenbrand et al., 2002; Li et al., 2006).

In this context a crucial parameter for the characterisation of the sealing efficiency is the CO_2/brine interfacial tension (IFT). Correlations of pressure and temperature with IFT and wetting angle and their effect on CO_2 storage capacities have been investigated by various authors (Bachu and Bennion, 2009; Chalbaud et al., 2007; Chalbaud et al., 2009; Chiquet et al., 2007a; Chiquet et al., 2007b; Yang et al., 2005. Shah et al., 2008 demonstrated that the water-wettability of caprocks can vary depending on the non-wetting gas (CO_2 or H_2S) and the mineral substance of the solid phase.

It is generally assumed that gas is the non-wetting phase where *cos* equals 1. However, a recent study (Chiquet et al., 2007a) has shown that this value decreases with an increase in fluid pressure and values as low as 0.5 for mica and 0.9 for quartz have been reported. These findings have not been verified by other

authors and additional studies on this topic might be required since low $cos\theta$ values directly reduce threshold pressures.

8.4.1 Capillary threshold pressure from mercury porosimetry data

Generally the simplest and fastest approach to estimate *in-situ* threshold pressure (P_c) values is achieved by mercury injection porosimetry (MIP), and combining the results with appropriate values of the IFT and the contact angle for the fluid/rock system under investigation (Egermann et al., 2006). In the oil industry P_c and related gas column heights are usually calculated assuming a completely water-wet system where contact angles are 0 degrees. Also, interfacial tensions are assumed to be constant (e.g. 25 mN m^{-1}, e.g. Dula and Younes, 2004) and independent of fluid type, fluid PVT and reservoir depth. Primary drainage capillary pressures are usually determined by mercury porosimetry measurements and re-calculated from Hg/air to hydrocarbon/brine (or in this case CO_2/brine) systems using contact angle and interfacial data according to the following equation:

$$P_{c\_CO2/brine} = P_{c\_Hg/air} \cdot \frac{\gamma_{CO2/brine} \cdot \cos\theta_{CO2/brine}}{\gamma_{Hg/air} \cdot \cos\theta_{Hg/air}} \qquad (8\text{-}4)$$

Accordingly, maximum hydrocarbon column heights (h_{max}) can be calculated accounting for the buoyancy due to the density difference between brine and hydrocarbon phase:

$$h_{\max} = \frac{P_{c\_Hg/air}}{(\rho_{brine} - \rho_{CO2})} \cdot \frac{\gamma_{CO2/brine} \cdot \cos\theta_{CO2/brine}}{\gamma_{Hg/air} \cdot \cos\theta_{Hg/air}} \qquad (8\text{-}5)$$

Here, ρ_{brine} and ρ_{CO2} are the average fluid densities at the given reservoir conditions.

Egermann et al., 2006 point out that the preparation procedure for drying the caprock material will alter the pore structure. In this context Dewhurst et al., 2002a compared several preparation procedures:

- air drying under laboratory temperature conditions (20-25ºC), removing the pore fluids though not all of the interlayer water
- freeze drying in liquid nitrogen followed by a transfer to vacuum freeze drying in order to sublimate the solid ice without rock fabric alteration
- vacuum drying of wet shale in a vacuum desiccator.

It could be demonstrated that P_c is not significantly affected by the drying method when well-hardened caprocks are studied. For lesser mature shales, especially for smectite-rich mudstones with large interlayer water volumes, accuracy and data consistency are improved significantly by the freeze-drying method because it preserves the pore structure (Dewhurst et al., 2002a). In a similar study, Matenaar, 2002 concluded that only fresh sample material having in-situ water content should be used for MIP. Freeze-drying effectively preserves the pore space and fabric of soft clays and that oven-drying in comparison to freeze-drying will result in a significant reduction of the pore space and, hence in a significant decrease in

mean entrance pore radii. Another disadvantage of the mercury porosimetry approach is that measurements are usually performed under unconfined pressure conditions. It is well known that petrophysical properties of mudstones strongly depend on applied stress. Furthermore, due to the omnidirectional intrusion of mercury into rock fragments during MIP, no information is obtained on the anisotropy of the transport pore system.

In conclusion "all these limitations make mercury porosimetry a rather inaccurate approach and only adequate as a screening method when no other data under in-situ conditions are available" (Egermann et al., 2006). Besides the experimental limitations, mercury porosimetry data should be used for carbon dioxide with great caution, because CO_2 interfacial tensions and contact angles change with pressure, temperature and brine salinity. IFT and contact angle should not be taken as a constant to re-calculate threshold pressures and hence gas column heights from mercury porosimetry data.

As indicated in the literature, different IFT values for the CO_2/brine system vary depending on pressure, temperature and brine salinity (Bennion and Bachu, 2006; Chiquet et al., 2007b; Li et al., 2005). Studies by Chiquet et al. (Chiquet, 2005; Chiquet et al., 2007b) have shown that the CO_2 contact angle is not a universal value and that it diverges from 180 degree for different brine salinities and pressures, as opposed to the general assumption that θ=0, i.e. $cos\theta$=1.

Figure 8-2 shows a comparison of maximum CO_2 column heights using different IFT values from the literature. Calculated column heights vary between 202 and 264 m, corresponding to a difference of 23 % in free gas CO_2 storage volumes. Taking into account the range of *cos* values reported in the literature (0.5 to 1) an additional uncertainty of 50 % arises in maximum capillary threshold pressure (or CO_2 column height) and, in consequence, maximum free gas CO_2 storage potential. The latter uncertainty could even be higher assuming an anticlinal structure where reservoir area increases with depth. Therefore, it is important to have consistent and reliable wetting data for CO_2 storage safety and storage potential in naturally pressured reservoirs, such as saline aquifers.

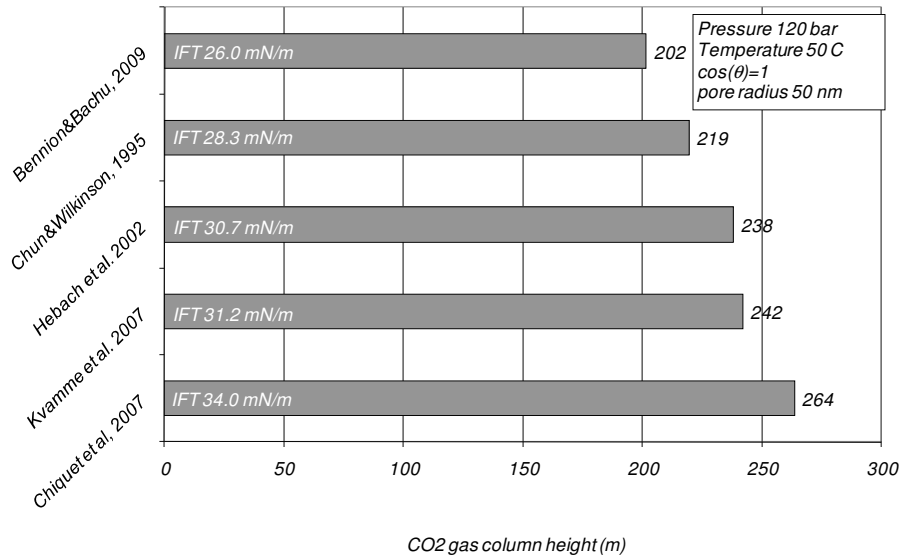


Figure 8-2: Calculated maximum CO_2 column heights using different IFT values and constant cos and pore radius values for a CO_2 storage reservoir at 1200 m depth corresponding to about 12 MPa hydrostatic pressure and 50 °C. The various literature values (partly from interpolation between different measured data points) were taken from Bachu and Bennion, 2009; Chiquet et al., 2007b; Chun and Wilkinson, 1995; Hebach et al., 2002; Kvamme et al., 2007.

8.4.2 Direct methods to determine capillary threshold pressures

Various methods are available to directly determine capillary threshold pressures on caprocks under *in-situ* stress and temperature conditions. A comprehensive overview of the various methods is given by Egermann et al., 2006. A comprehensive set of experimental data has been published by Hildenbrand et al., 2004a. It provides more than 50 data sets for rock-specific parameters, capillary threshold pressures and effective permeabilities to gas after capillary breakthrough occurred. In general, they found that threshold pressures increase in the order $CO_2 < CH_4 < N_2$ and are negatively correlated with effective permeabilities to gas for all three gas species. The reported values for threshold pressures vary between 0.1 and 10 MPa, with maximum effective permeabilities to gas ranging between ~10^{-18} and 10^{-24} m^2 (1000 to 0.001 nD).

To exemplify the effects of these permeability values in terms of leakage rates an attempt has been made to calculate the timing of CO_2 breakthrough after capillary threshold pressure is exceeded. For this calculation Darcy's law for compressible media has been used according to Hildenbrand et al., 2004a:

$$k_{eff} = -\frac{V_2 \cdot \mu \cdot 2\Delta x \cdot dP_2}{A \cdot (P_2^2 - P_1^2) \cdot dt} \qquad (8\text{-}6)$$

In the calculations we assume a reservoir/caprock interface at 2000 m depth with overlying caprock sequences of 10, 100 and 1000 m thickness. Gas viscosities were calculated for mean pressures and temperatures between top and bottom of the caprock. The temperature at the bottom of the caprock was assumed to be 70 °C and pressures were assumed to be overpressured by 2 MPa (a total of 22 MPa at the interface) to initiated capillary entry. Transport porosity in the caprock was taken as 1 %. For the range of

effective permeabilities defined above, the following diagram was created in analogy to the one for diffusive leakage, showing the time of gas breakthrough at the top boundary of the caprock formation (Figure 8-3). It is shown that for relatively high-permeable and thin caprocks CO_2 breakthrough occurs within weeks while hundreds to thousands of years are required for medium to low-permeability caprocks and more realistic thicknesses of 100 m. This is in accordance with an earlier study using a similar attempt for pressure seals (Deming, 1994).

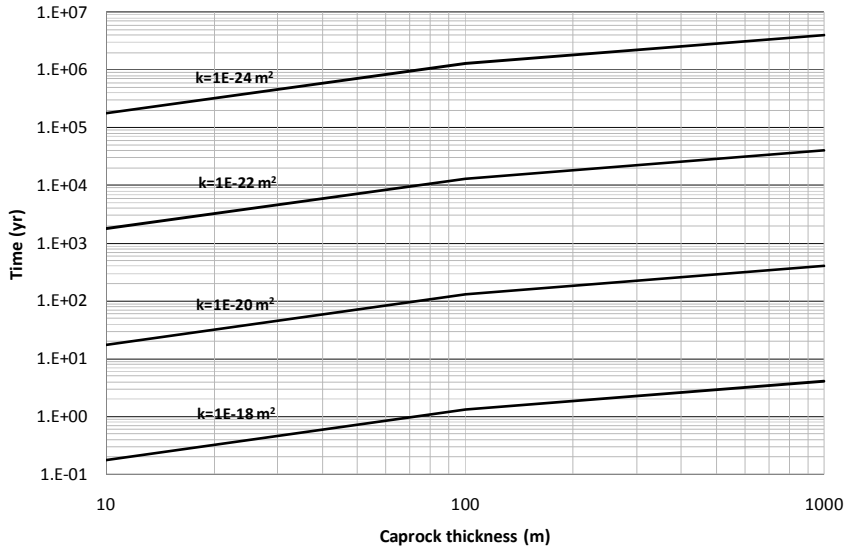


Figure 8-3: Plot showing timing of gas breakthrough after CO_2 threshold pressure is exceeded for varying caprock thickness and effective permeability coefficients.

8.5 Fault leakage

Faults and joints are commonly considered as potential leakage pathways with high CO_2 flux rates out of the reservoir, thus compromising storage integrity. Such rates are impossible or at least very difficult to determine in laboratory tests. Values obtained from natural CO_2 analogues can be used to obtain order-of-magnitude estimates for such leakage. These numbers have been determined for a variety of natural CO_2 fields in the world and are summarized in Table 8-1. Rates are given in tons per year per square meter. In general, they cover a range from 10^{-4} to 10^{2} t/yr/m^2 and should be used with caution when applying them to potential fault leakage in CO_2 storage operations, as these numbers represent the flux measured at the surface, disregarding potential losses between the reservoir and the surface. Such losses could be via carbonation reactions, dissolution in aquifer brines and/or partial transport via fault conduits to a location not covered in the surface flux measurements. In summary, these values are most likely at the low end and therefore (for determining CO_2 leakage) optimistic.

As pointed out by Streit and Watson, 2004, rates determined for shallow geothermal sources (Latera, Maria Laach in Germany) are not representative for CO_2 storage since they do not represent deep storage sites with realistic seals. Also the Matraderesce area, Hungary is not considered as a good example because CO_2

leakage occurs through a highly weathered, highly fractured andesite. For the remaining areas a range of 0.0003 and 0.04 t/yr/m^2 for permeable zones and 0.006 and 0.3 t/yr/m^2 for fault leakage seem to be realistic numbers. It should be noted that leakage to the surface is likely to occur with a delay due to the length of the migration path for deep reservoirs (Streit and Watson, 2004).

Table 8-1: Fault leakage rates from worldwide natural CO_2 analogues (Streit and Watson, 2004). For better comparison leakage rates reported by different authors were converted to the same units. The following conversions were used: 1 ton CO_2 = 556.2 Std.m^3; 1 L CO_2 = 1.861 g at normal conditions (1 atmosphere, 0°C).

Analogue site	CO_2 leakage rate (t/yr/m^2)	Leakage mechanism
Matraderesce, Hungary	6.4	fault
Matraderesce, Hungary	0.2	average flow in area
Little Grand Wash Fault, Colorado	0.3	fault
Little Grand Wash Fault, Colorado	0.04	average flow in area
Crystal Geyser, Colorado	0.4	fault
Latera, Italy	80	fault
Pine Lodge, Otway Basin, AUS	0.02	fault
Pine Lodge, Otway Basin, AUS	0.01	permeable zone
Penola, Otway Basin, AUS	0.006	fault
Maria Laach, volcanic crater, GER	0.2	fault
Maria Laach, volcanic crater, GER	0.0003	permeable zone

8.6 CO_2-water-rock interactions affecting caprock sealing capacity

CO_2-water-rock interaction can affect the sealing efficiency of caprocks in various ways. The most obvious of these is the effect of dissolution/precipitation processes on matrix permeability. Data from experimental research show that such alterations are very slow. Their effects are therefore hard to quantify, within the time span of typical lab experiments (Busch et al., 2008; Wollenweber et al., 2010). Studies of natural analogues confirmed the slow kinetics and generally low impact on seal matrix transport properties (Lu et al., 2009). This is mainly due to the low Darcy flow and diffusion rates in such lithologies, which limit the mass transport required for substantial alteration.

Experimental data on the effect of CO_2-water-rock interactions on fault leakage are scarce to non-existent at present. Studies from analogues exist but could not yet establish whether the effects of the interactions on leakage rates are in general beneficial or rather disadvantageous.

The impact of water-rock interactions on mineral surface properties is an almost virginal field of research. This is nonetheless highly relevant for the assessment of sealing capacity. Surface properties are, besides the pore radius distribution, the main rock property determining capillary entry. Some authors report contact angles between mineral surfaces and CO_2 lower than 180°, and decreasing with time (Chiquet et al., 2007a). Also direct measurements on sample plugs suggest that capillary entry pressure might change with time as the sample is exposed to CO_2 (Wollenweber et al., 2010). Besides this effect on capillary entry pressure, also sorption is to a major extent determined by mineral surface properties.

Alteration of the surface properties of minerals in caprocks is considered more likely than alteration of conventional transport properties, because minor mineral dissolution reactions can have a major impact on the former while they have no significant effect on the latter. Such alterations therefore deserve a lot more attention by the research community.

8.7 Conclusions

The main CO_2 leakage mechanisms have been addressed in this paper, focusing on loss of caprock integrity. Leakage by diffusion is not considered of concern and rather can be envisioned to be the rate-determining mechanism for mineral reactions. However, laboratory data available so far indicate increasing effective CO_2 diffusion coefficients with increasing time of interaction with the caprock.

Capillary leakage can be significant in terms of flow rate after capillary entry pressure is exceeded. This might not be significant for depleted oil and gas reservoirs where reservoir pressurization after CO_2 injection should be below the original reservoir pressure. However for saline aquifers this might become an important factor and direct determination of the capillary threshold pressure on caprock samples under stress is the preferred measurement rather than mercury porosimetry with subsequent conversion from Hg/air to CO_2/brine system.

CO_2 sorption on clay mineral surfaces and its implication for caprock sealing efficiency has been reported recently and further investigation is needed to better understand mechanisms and implications on seal integrity. Potential clay mineral swelling, if proven to occur, may either increase or impair the seal capacity.

Information on fault leakage can only be obtained to a limited extent from lab measurements and should be derived from natural CO_2 analogues. It should however be stressed that many data are not representative for a real-case CO_2 storage scenario and that fluxes measured at the surface represent only the lower limits of CO_2 amounts escaped from the reservoir.

Many aspects still need to be addressed in more detail in order to better estimate leakage risks for CO_2 storage:

- alteration of wetting behavior at the caprock/reservoir interface by geochemical reactions or changing interfacial tension or wetting angles
- consistency of available datasets on CO_2 interfacial tension and wetting angle

- increase of effective permeability to gas due to CO_2/brine/rock interactions after capillary threshold pressure is exceeded
- drying-out (desiccation) of caprocks (removal of pore water and clay interlayer water) at the caprock interface that might lead to decreasing capillary threshold pressures
- CO_2 sorption on clay minerals, potential swelling and its implications as well as sorption versus reactivity of the clay minerals
- fault leakage: escape from the reservoir and potential loss of CO_2 in the overburden between the reservoir and the surface.

9 Experimental investigation of the CO_2 sealing efficiency of caprocks

9.1 Introduction

Presently, the geological storage of CO_2 from fossil-fired power plants is intensely examined as an option for reducing anthropogenic emissions of greenhouse gases. Deep saline aquifers, depleted oil and gas fields and unminable coal seams are the primary targets for the underground disposal of supercritical CO_2 (IPCC, 2005). One major concern of all CO_2 storage options is the investigation of the sealing efficiency of low-permeable sequences overlying potential storage reservoirs. The long-term integrity of these seal layers (caprocks) is one prerequisite to keep the CO_2 in place and avoid dissipative loss towards the atmosphere. The assessment of leakage risks and leakage rates, under the consideration of different potential mechanisms, is therefore an important issue for site approval and public acceptance (e.g. Pruess, 2008).

Subsurface storage of CO_2 is always associated with an excess pressure resulting from buoyancy forces and injection-related overpressure which constitutes the driving force for different transport processes. Pressure-driven volume flow (Darcy flow) through the caprock is commonly considered as the main risk scenario and can be envisaged to range in intensity over several orders of magnitude:

rapid ("catastrophic") leakage by seal-breaching (mechanical failure) or damage of well casing (corrosion of pipes and cements),

seepage along existing open fault systems and fracture networks,

leakage through the pore-space controlled by capillary forces and permeability (after capillary breakthrough pressure is exceeded).

Generally, migration through the water-saturated pore network of a caprock may occur when the CO_2 fluid pressure in the reservoir exceeds the capillary entry pressure (e.g. Hildenbrand et al., 2002). This holds for the inter-granular pore space but also for water-filled (micro-)fracture systems. At pressures above the so called breakthrough (threshold) pressure, at which a continuous flow path of the non-wetting fluid forms across the pore system, CO_2 can escape from the upper top of the caprock sequence (e.g. Al-Bazali et al., 2005; Hildenbrand et al., 2002; Li et al., 2005).

The capillary sealing capacity of caprocks depends on capillary forces in the rock matrix, i.e. on the pore throat radius *r*, the interfacial tension between the caprock surface and the fluid γ (water/brine) and the wetting (contact) angle θ (equation 1).

$$\Delta P = \frac{-2\gamma\cos\theta}{r} \qquad (9\text{-}1)$$

Measurements of the capillary breakthrough pressure of low permeable rocks have initially been performed for the characterisation of hydrocarbon reservoirs or (nuclear) waste disposals (e.g. Berg, 1975;

Gallé, 2000; Pusch, 1985; Schlömer and Krooss, 1997; Schowalter, 1979b). In recent years the focus of research shifted more to the characterisation of CO_2 storage reservoirs and their sealing lithologies (e.g. Al-Bazali et al., 2005; Angeli et al., 2009; Bachu and Bennion, 2008; Hildenbrand et al., 2004a; Hildenbrand et al., 2002; Li et al., 2005).

An additional crucial parameter for the characterisation of the sealing quality is the interfacial tension (IFT) between the rock and the fluid. Chiquet et al., 2007a state that the maximum allowable CO_2 storage pressure may be only a fraction of the initial reservoir pressure. Correlations of pressure and temperature with interfacial tension and wetting angle and their effect on CO_2 storage capacities have been investigated by Yang et al., 2005, Chalbaud et al., 2010; Chalbaud et al., 2009 Chiquet et al., 2007a; Chiquet et al., 2007b. In addition Shah et al., 2008 demonstrated that the water-wettability of caprocks can vary depending on the non-wetting gas (CO_2 or H_2S) and the mineral substance of the solid phase.

Bennion and Bachu, 2008 were the first who provide relative permeability values for CO_2/brine- (and H_2S/brine-) systems for both, the drainage and the imbibition path for the same caprock samples investigated in their earlier works (e.g. Bachu and Bennion, 2008).

Carbon dioxide leakage into and through caprocks may also occur by molecular transport (diffusion) through the water-saturated pore system. This mechanism is considered of little relevance in terms of gas losses as discussed by Busch et al., 2008. It may, however, control the rate of geochemical reactions that, in turn, may affect the petrophysical and mechanical properties of the seal layers. Therefore, the characterisation of caprock alterations caused by chemical reactions and mineral transformations has recently encountered increasing interest. Some fundamental laboratory investigations on mineral transformations in CO_2 storage reservoirs (e.g. Bertier et al., 2006; Hangx and Spiers, 2009; Kaszuba, 2003; Kaszuba, 2005; Kharaka et al., 2006; Wigand et al., 2008) have shown that mineral alterations (e.g. formation/dissolution of carbonates) are caused by the formation of bicarbonate and a pH drop during CO_2 injection. The impact of these changes on porosity and permeability in reservoirs and seals has been addressed in a few studies (e.g.; Busch et al., 2008; Hangx and Spiers, 2009) but still remains to be explored in more detail.

Another important topic what is still to be investigated intensively is the effect of CO_2 and its reactivity on the mechanical stability of caprocks. Up to now only a few experimental results has been published (e.g. Angeli et al., 2009).

Numerical modeling studies on CO_2 underground storage are not addressed in this contribution, but an excellent review on the history and current state of reactive transport modeling is presented in Steefel et al., 2005. Gaus et al., 2008 recently published a comprehensive review of reactive transport modeling applied to the sequestration of CO_2.

In this contribution we report results of the experimental investigation of the seal properties of two regional caprock samples from the Münster Cretaceous Basin, NW-Germany using a combination of i) capillary breakthrough tests, ii) diffusion experiments, iii) sorption measurements iv) mineralogical characterisation. The main purpose, besides characterising the CO_2 sealing efficiency of these rocks was to test for changes in fluid flow properties (effective diffusion coefficient, capillary breakthrough pressure, absolute/effective permeability) due to multiple interactions with CO_2 on the same sample. These measurements were combined with additional investigations on the mineral alteration and the CO_2 sorption capacity of the rock matrix.

The Münsterland Basin is an expanded synclinal basin structure in western Germany containing thick sedimentary sequences including potential storage formations for underground CO_2 storage showing an east-west expansion of 150 km and a north-south expansion of 80 km. With a thickness up to 2000 m the Upper Cretaceous strata form the top seal in the synclinal structure. It can be divided into a Cenomanian-Turonian-Complex accommodating brine aquifers and an upper Coniacian-Santonian-Complex (Emscher Marl Formation). Deeply buried Carboniferous strata with interbedded hard coal seams represent the bottom sequence of the basin. For further details see e.g. Kronimus et al., 2008.

9.2 Samples

In order to compare the CO_2 sealing efficiency of near-surface and deeply buried sequences of the Upper Cretaceous caprock sequence of the Münsterland Basin, two samples from different depths have been selected for this study. The petrophysical and mineralogical properties of the samples are summarised in

Table 9-1. The first sample (05-960; 128 m depth) is of Upper Coniacian age and represents the clay-rich Emscher Marl formation. The sample is a grey marlstone. Quantitative X-ray diffraction analysis (Rietveld method) revealed a calcite content of ~40 % with some additional anorthite, smectite and quartz. Mercury porosity measurements yielded a porosity of 15 % and a grain density of 2.5 g/cm³ (bulk density ~2.1 g/cm³).

The second sample (06-565) originates from a depth of 813 m and represents the top sequence of the Cenomanian lithology. The blue coloured limestone is dominated by calcite (~90 %) with some smaller amounts of quartz and anhydrite. This sample has a porosity of 6 %, a grain density of 2.7 and a bulk density of 2.6 g/cm³.

Hg injection porosimetry indicated very low median pore diameters of 66 and 30 nm (10^{-9} m), while BET measurements yielded SSA values of 21.1 and 3.8 m^2/g for the 05-960 and 05-565 sample, respectively.

Table 9-1. Properties and mineralogy of marl and calcite samples determined by mercury porosimetry, BET, TOC and XRD analysis

Property	05-960			06-565	
Grain Density (g/cm³)	2.5			2.7	
Bulk Density (g/cm³)	2.1			2.6	
Porosity (-)	0.15			0.06	
Average Pore Diameter (nm)	66			30	
Specific Surface Area (m²/g)	21.1			3.8	
Total Organic Carbon (%)	0.38			0.20	
Mineral composition	Content (g/g)				
	initial	after CO_2 breakthr.	after CO_2 diffusion test	initial	after CO_2 breakthr.
Calcite	0.40	0.44	0.56	0.91	0.93
Mica/Illite	0.06	0.05	0.03	-	
Kaolinite	0.01	-	-	-	
Quartz	0.14	0.17	0.18	0.08	0.07
Anorthite	0.14	0.12	0.01	-	
Orthoclase	0.03	0.02	0.02	-	
Anhydrite	-	-	-	0.01	<0.01
Smectite	0.22	0.18	0.20	-	

9.3 Experimental

Fluid flow experiments performed in this study comprise single-phase (water) permeability measurements, gas breakthrough tests with CO_2 and Helium (He) as well as CO_2 diffusion tests. They were conducted in triaxial flow cells constructed for confining pressures and axial loads of up to 50 MPa (e.g. Hildenbrand et al., 2002; Schlömer and Krooss, 2004). The measuring temperature was 21- 45°C. Figure 9-1 shows the constituents of the flow cell and the sample arrangement. Cylindrical rock sample plugs with a diameter of 28.5 mm and a length of ~10 mm were used. The plugs were positioned between two porous stainless steel disks and two stainless steel pistons equipped with conduits for fluid introduction and removal. A double-layered sleeve ensures a diffusion-tight seal around the sample plug (Figure 9-1). The inner coating consists of lead (Pb) foil (0.25 mm) and the outer layer of a thin-walled copper (Cu) tube. In order to guarantee absolute sealing of the sample cell a confining pressure of 40 MPa is applied to the sleeve for several hours prior starting the experiment. Generally, the confining pressure was chosen at least 10 MPa higher than the pore fluid pressure. The efficiency of the sealing system has been established in several studies, performing gas diffusion (Schlömer and Krooss, 1997) and gas breakthrough tests (Hildenbrand et al., 2004a; Hildenbrand et al., 2002).

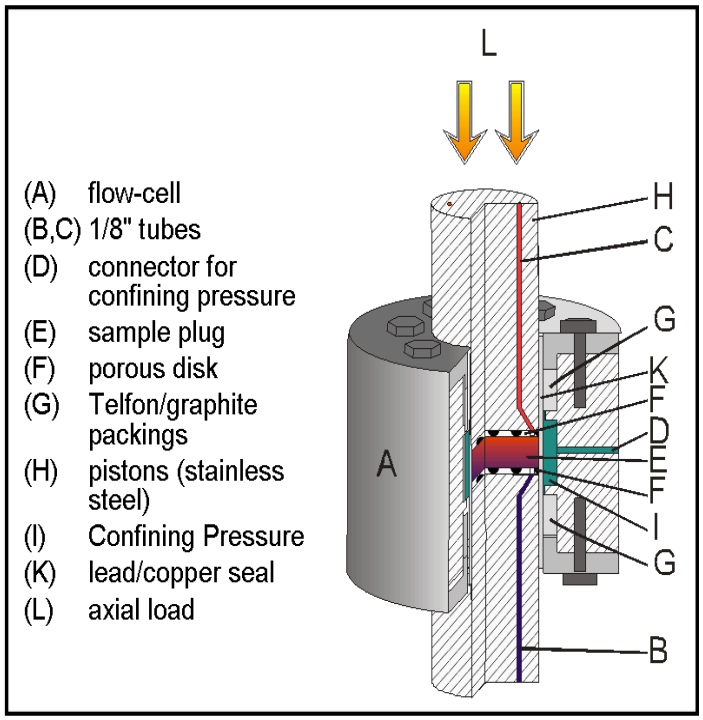


Figure 9-1. Schematic diagram of the triaxial flow cell used for gas breakthrough and diffusion experiments.

9.3.1 Single phase flow experiments

Prior to each gas breakthrough and diffusion experiment single-phase flow tests with water were performed to determine absolute permeabilities using a steady-state approach. Experiments were conducted by applying a constant fluid pressure (3-6 MPa) at the upstream (high-pressure) side and measuring the outflow volume on the downstream (low-pressure) side in a micro pipette (against atmosphere) as a function of time (Figure 9-2b). With the exact diameter and length of the sample plug, the pressure gradient over the sample and the viscosity of the fluid known, absolute permeability coefficients (k_{abs}) of the rock sample were calculated according to Darcy`s law:

$$k_{abs} = -Q \cdot \eta \cdot \frac{\Delta x}{\Delta P} \qquad (9\text{-}2)$$

where Q [m³/m²/s] denotes the volume flux, η [Pa · s] is the dynamic viscosity of the pore fluid and dx/dp is the pore pressure gradient.

Normal tap water was used as fluid phase. Complete water saturation of the conducting pore system was assumed when the fluid flow on the downstream side became constant.

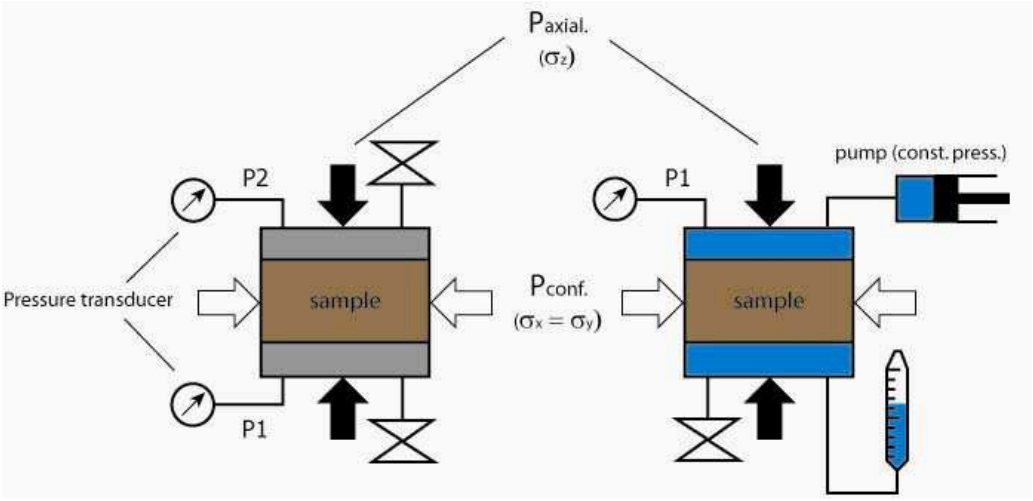


Figure 9-2. Experimental set-up for gas breakthrough (a) and single phase permeability tests (b).

9.3.2 Gas breakthrough experiments

9.3.2.1 Minimum capillary entry pressure

Gas breakthrough tests in this study were performed according to the procedure described by Hildenbrand et al. (2002, 2004) on totally water-saturated samples (Figure 9-2a). The upstream volume of the flow cell is charged with CO_2 at a pressure that is higher than the expected capillary entry pressure of the sample. The pressures in the two compartments and the temperature of the cell are monitored continuously throughout the experiment. The gas fluxes out of the upstream compartment and into the downstream compartment can be determined from the pressure changes over time. For the evaluation of the experimental data the volumes of both compartments have to be known precisely. They are determined by a gas expansion test using Boyle's law prior to each experiment. Length and cross section area of the rock sample are determined before assembling the measuring cell.

Generally the experiments can be divided into three phases:

(i) During the initial phase of the gas breakthrough experiments a significant pressure decline occurs in the high-pressure compartment while the pressure in the low-pressure compartment increases only insignificantly (Figure 9-3).

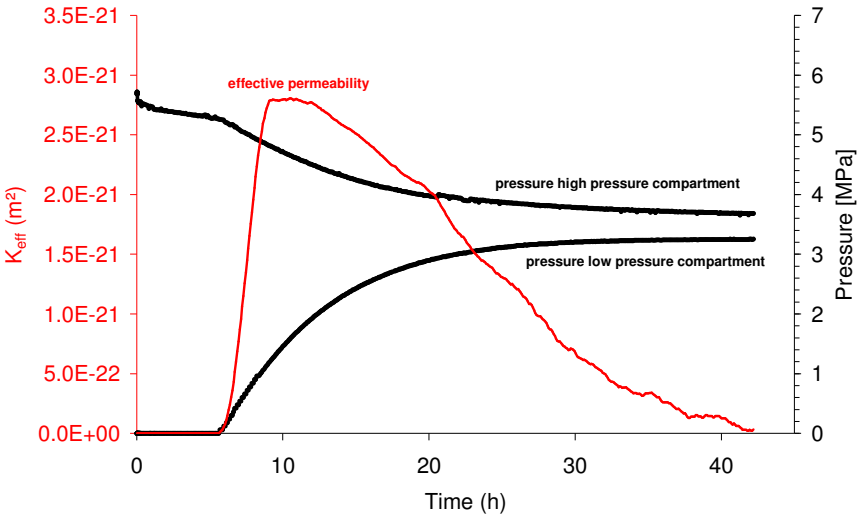


Figure 9-3. Results of a gas breakthrough test (3rd CO_2 breakthrough, sample 05-960)

This phenomenon can be explained by the displacement of residual water from the porous stainless steel disc through the shale plugs as shown schematically in Figure 9-1. The concomitant increase in gas phase volume in the high pressure compartment results in a (comparatively strong) pressure decline in the upstream reservoir. The water volume, which was displaced from the upstream reservoir, enters the downstream reservoir where it reduces the free gas volume. Because the downstream reservoir is at a lower pressure level, the decrease of free gas-volume will result in a relatively small pressure increase in this compartment during this initial phase of the experiment as observed in e.g. Figure 9-8.

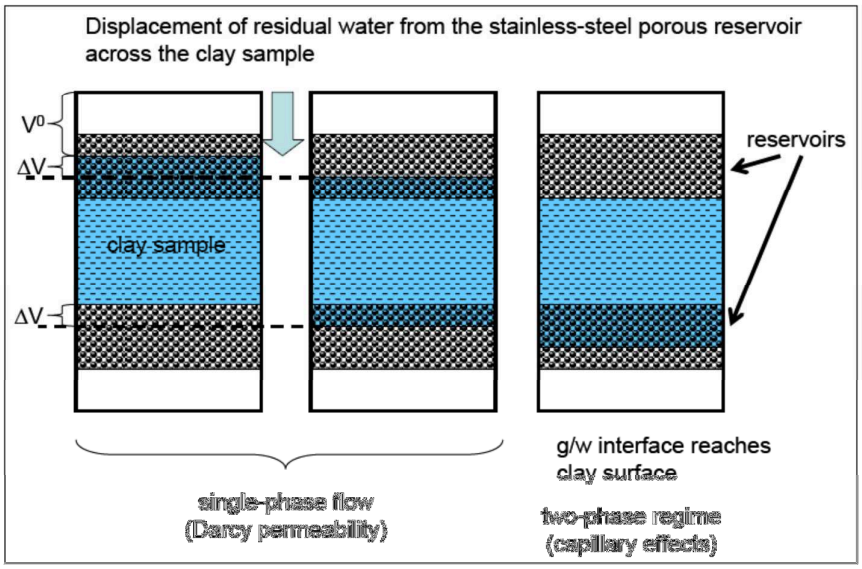


Figure 9-4. Illustration showing the water displacement across the sample during the initial phase of gas breakthrough experiments.

The pressure data recorded during this displacement process can be used to estimate the single phase water permeability of the clay sample.

(ii) When the gas/water interface reaches the face of the fine-grained clay sample plug gas may enter the sample. This obviously changes the slope of the pressure decline curve recorded in the upstream reservoir. Here two different scenarios are conceivable:

1. If the capillary entry pressure is not exceeded, the slope of the pressure decline curve will decrease to nearly zero (no further pressure decrease), because capillary forces prevent pressure-driven fluid transport across the clay sample. This does not hold for diffusive transport (third phase of the experiment) which will continue due to the gas concentration gradient across the sample.

2. If the gas pressure is higher than the capillary entry pressure, gas breakthrough will occur and result in a further pressure decrease in the upstream compartment and a simultaneous rapid increase in gas pressure in the downstream compartment (e.g. Figure 9-5). Pressure equilibration (decline in capillary pressure, re-imbibition of water) between the upstream and the downstream compartment will continue until water shuts off the interconnected pore system and the final capillary pressure difference (Δp) is reached.

(iii) After all gas saturated pathways are disconnected by the imbibing water again or gas breakthrough pressure has not been reached, because initial pressure was chosen too low in phase two, only diffusive transport across the sample occurs.

Evaluation functions were derived for Helium breakthrough tests to analyse the experimental pressure decline curves in the upstream compartment during the initial water-displacement phase (single-phase Darcy flow). The evaluation explicitly takes into account the decrease in downstream volume and predicts the concomitant downstream pressure increase.

In order to investigate rock alterations caused by multiple CO_2 treatments repetitive gas breakthrough experiments were conducted in this study. Before the first experiment and between successive experiments, complete water-saturation of the samples was established by single-phase water (intrinsic or absolute) permeability tests until steady-state flow was reached.

9.3.2.2 Effective Permeability

In general, the effective permeability to each fluid is a function of its saturation in the pore system. At 100% single phase fluid (gas or water) saturation the effective permeability equals the absolute permeability. The ratio of effective and absolute permeability is denoted as the relative permeability.

In this study only the effective permeability to the non-wetting fluid (gas) is calculated as a function of capillary pressure. During gas breakthrough experiments the gas penetrates the previously water-saturated rock sample and, a continuous gas flux will emerge from the high pressure side towards the low pressure side until a constant residual pressure is reached. During the experiment the effective gas permeability (k_{eff})

of the sample decreases because water is re-imbibed into the pore system and continuously reduces the flow-paths of the gas until the last interconnected pore channel is blocked and the pressure gradient remains constant. The effective permeability (k_{eff}) is calculated from the pressure change in the downstream compartment using Darcy's law for compressible media:

$$k_{eff} = -\frac{V_2 \cdot \eta \cdot 2\Delta x}{A(P_2^2 - P_1^2)} \frac{dP_2}{dt} \qquad (9\text{-}3)$$

where V_2 [m³] is the volume of the downstream compartment, A [m²] is the cross section area, η [Pa s] is the dynamic viscosity of the gas, and Δx [m] is the length of the sample. P_1 denotes the pressure at the upstream, P_2 the pressure at the downstream side.

9.3.3 Diffusion experiments

For CO_2 diffusion measurements the same sample cell as for the permeability and the gas breakthrough tests is used (Figure 9-1). An additional setup is connected to the flow cells for fluid sampling and on-line analysis of the gas. The diffusion experiment is initiated by injecting CO_2 into the bottom chamber of the flow cell. A communicating tubing system ensures the absence of a pressure gradient between both compartments. The CO_2 that has diffused through the water-saturated sample plug is collected in the top compartment of the cell in time intervals of 1-2 hours and is then transferred to the sampling system. The CO_2 is stripped from the water phase in a purge vessel by a helium stream and is captured in a molecular sieve trap. An additional step mobilises the trapped carbon dioxide thermally which is then transferred to the gas chromatograph (GC) for quantification with a thermal conductivity detector (TCD). The gas quantities are recorded as a function of time and used to calculate diffusion coefficients and the equilibrium bulk CO_2 rock concentrations within the sample plug. This has been done at 28°C and an effective fluid pressure of ~5 MPa.

The experimental data represent the cumulative amount of CO_2 (Q, mmol/m²) diffused through the unit cross section area of the cylindrical sample plug as a function of elapsed time t (in hours) (Figure 9-9). The slopes of the tangents to the curves represent the steady state diffusion flux. Using the lag time t_0 and Q_0 the effective diffusion coefficient D_{eff} (m²/s) and the CO_2 concentration C_1 (mmol CO_2/m³ rock) can be calculated according to the procedure described by Krooss and Schaefer, 1987a. Here, the C_1-value denotes the bulk volume concentration of CO_2 remaining in the rock after steady-state flux across the sample has been reached.

Detailed information of the diffusion experiments and their evaluation are provided in Schlömer and Krooss, 2004.

9.3.4 Sorption Experiments

High-pressure (up to 20 MPa) sorption experiments are used to determine gas sorption capacities (sorption isotherms) of powdered caprock sample material as a function of pressure by a manometric method.

The experimental device is placed in an air bath ensuring a constant temperature (±0.1°C) throughout the experiments. Single-gas sorption experiments in this study were performed at 50°C. At this temperature CO_2 is either in the gaseous or, at pressures above the critical pressure, in the supercritical state (T_c: 30.95 °C; P_c 7.38 MPa).

A detailed description of the procedure has been given previously (Busch et al., 2003a, 2007; Busch et al., 2004a; Krooss et al., 2002; Siemons and Busch, 2007). The evaluation of the experimental data yields excess sorption (Gibbs sorption) isotherms. Here the observed reduction in gas pressure resulting from gas sorption is compared to the theoretical "non-sorption" case. The volume changes due to the increasing amount of adsorbed phase with pressure are not considered in this evaluation.

9.3.5 Mineralogical and petrophysical characterisation

The mineral phase composition of the powdered samples was analysed by X-ray diffraction using a Huber 423 diffractometer. The instrument was equipped with a graphite monochromator in the diffracted beam and run with Co K-alpha radiation. Powdered samples were filled into a sidefill holder for minimizing particle orientation. Quantitative phase analysis was done with the Rietveld program BGMN (Ufer et al., 2004).

Specific surface areas (SSA) were determined by low-pressure nitrogen sorption on the dry material with a Micromeritics GEMINI 2360 instrument using the BET method (Brunauer et al., 1938).

Mercury injection porosimetry (MIP) was performed using a Micromeritics Autopore II 9220 porosimeter. Cuttings of 5-10 mm were dried at 105°C for 24h. For data evaluation an interfacial tension for mercury- air system of $\gamma = 0.485$ Nm^{-1} (Vavra et al., 1992) and a wetting angle of $\Phi_{Hg} = 141.3°$ was used.

9.4 Results

9.4.1 Single-phase (water) permeability coefficients

Initial absolute permeability coefficients (measured with tap water at room temperature (21-28°C) and fluid pressures of 3-6 MPa) were 32-34 nD (nano-Darcy; 10^{-21} m^2) for sample 05-960 and 5-7 nD for sample 06-565, respectively (Table 9-2).

After three successive CO_2-breakthrough tests the permeability coefficients of the first sample (05-960) increased from 32-34 to 40-43 nD. A similar trend was observed for sample 06-565. Here water permeability increased from 7 to 12 nD after three successive CO_2 gas breakthrough tests.

An increase in absolute permeability values was also observed after successive CO_2 diffusion experiments. Here the increase was more distinct with 35 to 56 nD for sample 05-960 while an increase from 5 to 12 nD was observed for sample 06-565.

Additionally, single-phase permeability values were calculated from the initial phase of the helium breakthrough tests on sample 05-960. The evaluation revealed a water-permeability of 31 nD while the

water in porous steel disc is pressed through the pore space of the sample.. This value is in accordance with the values obtained from single-phase permeability test prior the first CO_2 application on the 05-960 ("Emscher marl") sample.

Table 9-2. Single and two-phase flow parameters obtained from gas breakthrough experiments.

05-960						06-565				
Experiment (in chrono order)	abs. perm (nD)	Helium breakthrough		CO_2 breakthrough		abs. perm (nD)	Helium breakthrough.		CO_2 breakthrough	
		P_{res} (MPa)	$K_{eff(max)}$ (nD)	P_{res} (MPa)	$k_{eff(max)}$ (nD)		P_{res} (MPa)	$k_{eff(max)}$ (nD)	P_{res} (MPa)	$k_{eff(max)}$ (nD)
1	34					7				
2		Failed	failed				1.81	0.1		
3	33					7				
4		Failed	failed						0.74	0.4
5	32					10				
6				0.64	1.0				failed	failed
7	43					10				
8		0.44	4.0						0.41	0.6
9	41					12				
10				0.49	2.6		0.62	0.8		
11	40					12				
12				0.43	2.9					

9.4.2 Capillary Entry Pressure

Residual pressure differences (P_d) observed in the final stages of the various CO_2 and Helium gas breakthrough experiments (i.e. minimum capillary breakthrough pressure, P_d) of the rocks vary from 0.43 to 0.64 MPa for sample 05-960 and from 0.41 to 1.81 MPa for sample 06-565, respectively (Table 9-2). An example of the pressure curves recorded during gas breakthrough tests is shown in Figure 9-3.

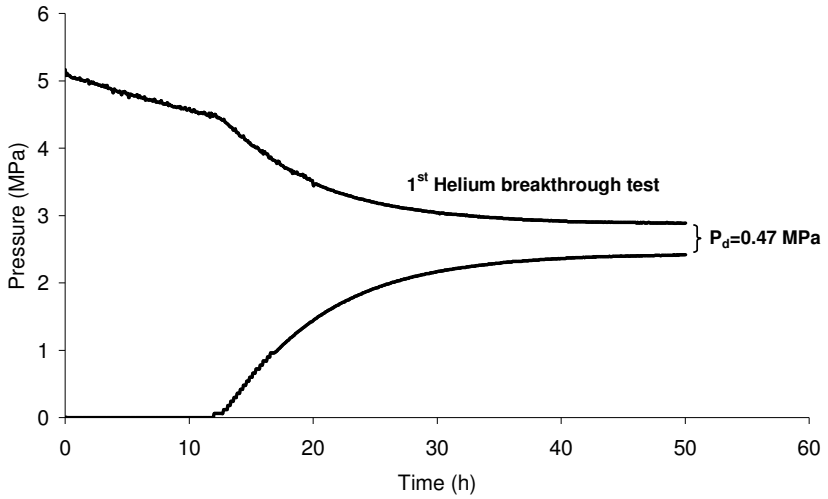


Figure 9-5. Initial helium breakthrough test for sample 05-960 at 28°C.

Sample 05-960: The first helium breakthrough experiment was performed with an initial upstream pressure of 5.1 MPa and atmospheric pressure on the downstream side (Figure 9-5). During the experiment the upstream and downstream pressures converged and stabilized at a residual pressure difference of 0.44 MPa. This is in the same order of magnitude as the residual capillary pressure differences ("capillary entry pressures") for the three repetitive CO_2 breakthrough tests conducted on this sample plug (Table 9-2, Figure 9-6). Generally, repetitive CO_2 breakthrough tests showed a decreasing trend in capillary entry pressures from 0.64 to 0.43 MPa (Table 9-2). The first CO_2 test was characterized by a rapid decrease of the high pressure curve and lower absolute pressures in both compartments at the end of the experiment (Figure 9-6). However, the residual capillary pressure difference was similar to those measured in the other CO_2 tests performed on this sample.

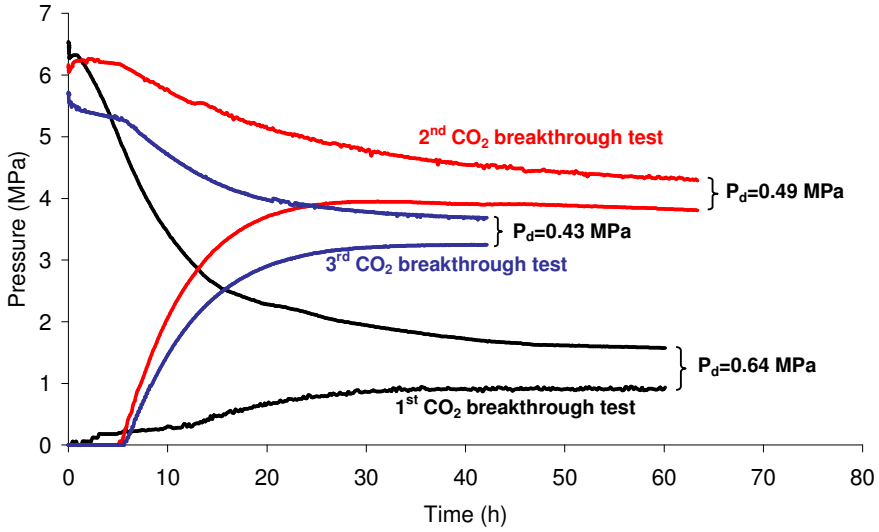


Figure 9-6. Repetitive CO_2 breakthrough tests for sample 05-960 at 28°C.

Sample 06-565: The first and fourth gas breakthrough test was performed with helium (Figure 9-7) and resulted in residual pressures of 1.81 and 0.62 MPa, respectively. The second and third gas breakthrough test was performed with CO_2 (Figure 9-8) and a declining residual pressure from 0.71 to 0.41 MPa was observed. Generally, all follow up gas breakthrough test cycles performed in this study revealed constantly decreasing capillary pressures for both gases (Table 9-2).

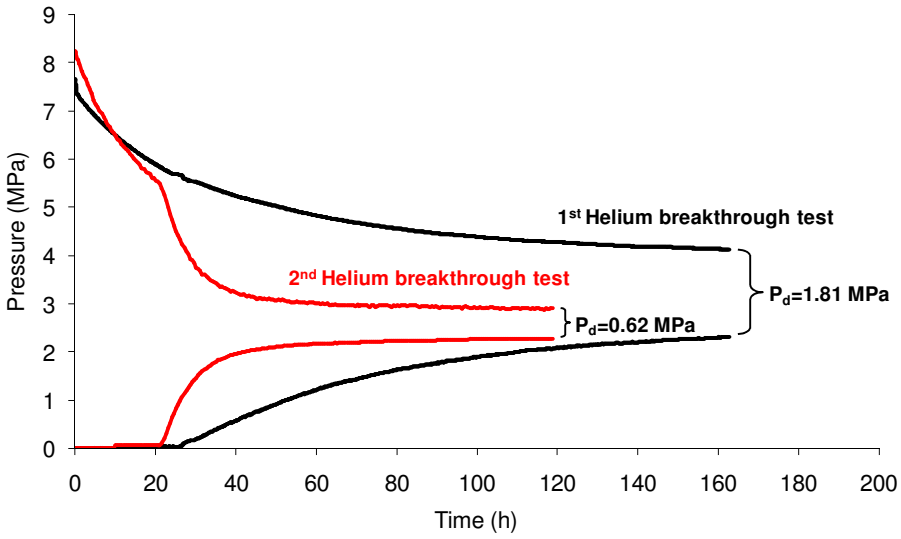


Figure 9-7. Helium breakthrough tests for sample 06-565 at 21°C.

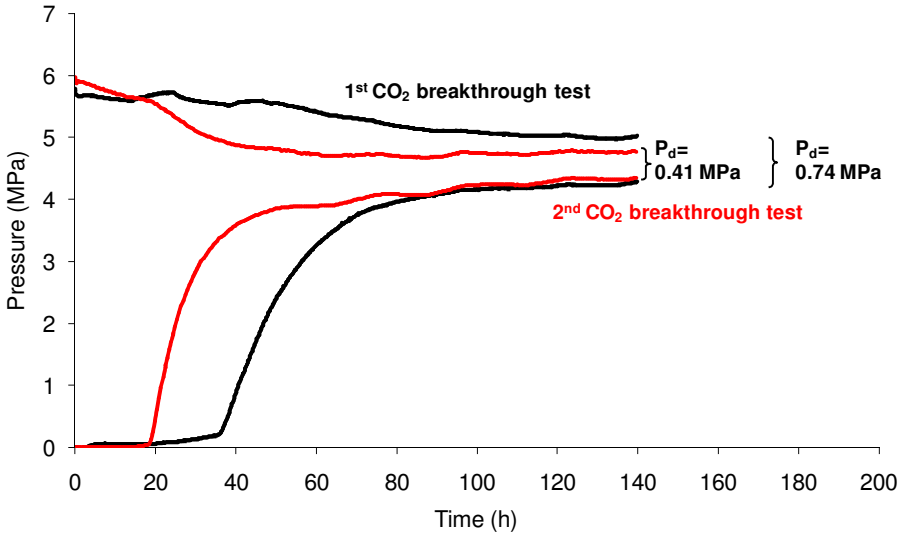


Figure 9-8. Repetitive CO_2 breakthrough tests for sample 06-565 at 21°C.

9.4.3 Maximum effective permeability coefficients ($k_{eff(max)}$)

The total range of maximum effective permeabilities of non-wetting fluids (CO_2, He) vary between 0.1 and 4.0 nD ($10^{-21}m^2$) for helium and from 0.4 to 2.9 nD for CO_2 (Table 9-2). Generally, maximum gas phase permeabilities are much lower than the corresponding absolute permeability values (Table 9-2) as stated in

Hildenbrand et al., 2002. Repetitive CO_2 measurements on both samples yielded increasing $k_{eff(max)}$ values. For sample 05-960 increasing values from 1.0 to 2.9 nD have been obtained; whereas $k_{eff(max)}$ values for sample 05-565 increase from 0.4 to 0.8 nD. For the later sample an increase in helium $k_{eff(max)}$ values measured before (0.1 nD) and after (to 0.8 nD) the third follow-up CO_2 tests was observed (Figure 9-7).

9.4.4 Diffusion experiments

Several repetitive CO_2 diffusion experiments were conducted on both samples, but useful results were only obtained for the clay-rich Emscher Marl sample 05-960 (Figure 9-9 and 10). For the "limestone" sample 06-565 a CO_2 transport across the sample plug was detected, but no characteristic diffusion curve has been recorded and evaluated.

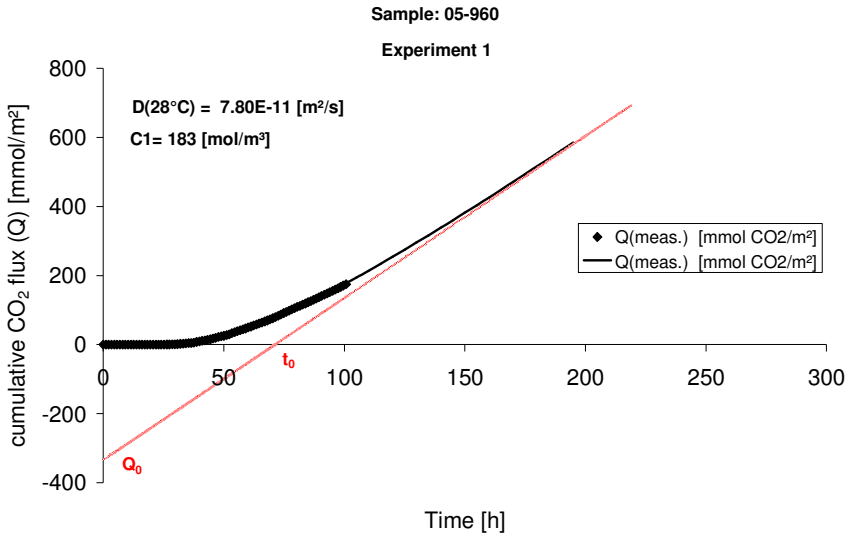


Figure 9-9. First CO_2 diffusion tests on sample 05-960

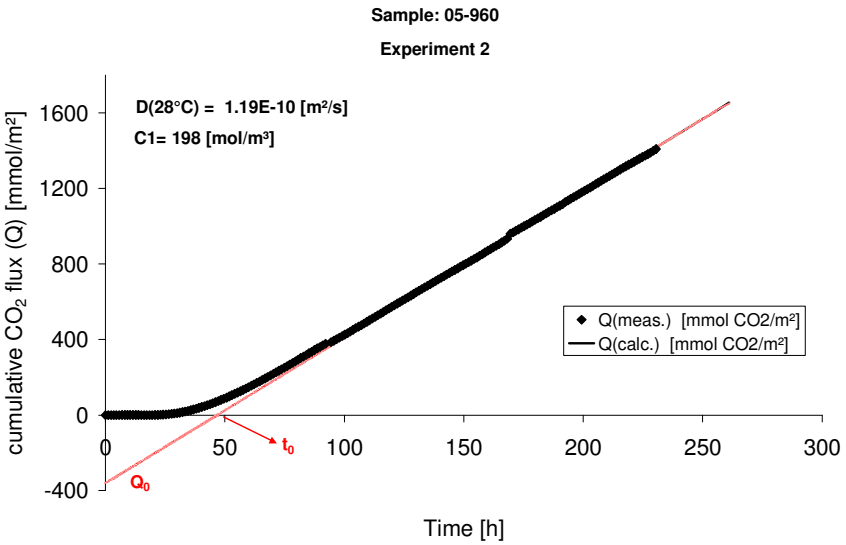


Figure 9-10. Second CO_2 diffusion tests on sample 05-960

The first experiment on sample 05-960 yielded an effective diffusion coefficient of $7.8 \cdot 10^{-11} m^2$ and a C_1-value of 183 mmol/m³ (0.078 mmol/g). A higher effective diffusion coefficient of $1.2 \cdot 10^{-10}$ m² and a similar C_1-value of 198 mmol/m³ (0.084 mmol/g) was obtained from the second diffusion experiment on the identical sample plug (Table 9-3).

Table 9-3. Results of diffusion experiments performed on sample 05-960.

No. Experiment	D(28°C) [m/s²]	C_1 [mol/m³]	Steady state flux [mol/m²/h]	T_0 [h]	Q_0 [mmol/g]
CO_2 Diffusion test	7,80 x 10^{-11}	183	4.69	71.3	-334
CO_2 Diffusion test	1.19 x 10^{-10}	198	7.71	46.8	-361

9.4.5 Sorption experiments

Figure 9-11 shows the results of the high-pressure CO_2 sorption experiments performed on the carbonate (06-565) and the marl (05-960) samples at 45°C with an as received water content. Both excess sorption isotherms show a more or less steep increase up to ~8 MPa followed by a strong decrease, even down to negative values as in the case of the 05-960 sample. Maximum sorption values are 0.27 and 0.14 mmol/g for the 05-960 and 06-565 samples, respectively.

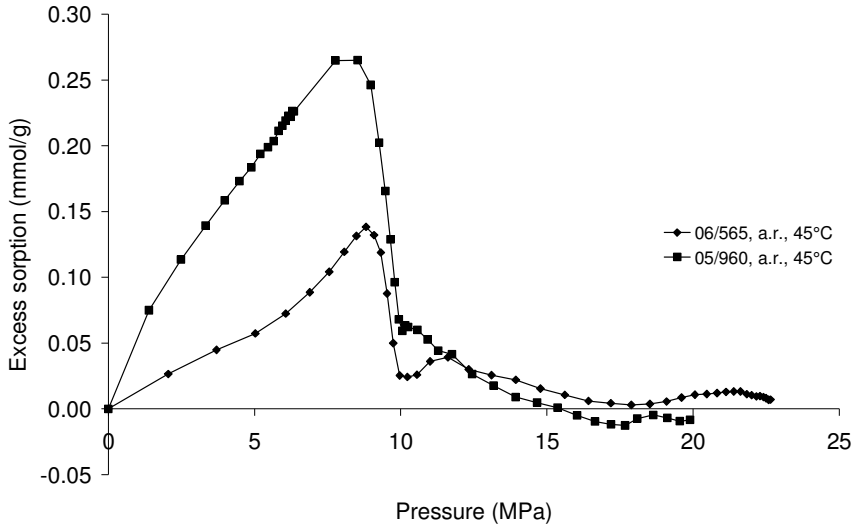


Figure 9-11. High-pressure CO_2 excess sorption measurements on 05/960 and 06/565 samples at 45°C and with the as received water content.

9.4.6 Mineralogical and petrophysical investigations

To test for mineral alterations as a result of CO_2/water/rock interactions (CO_2WRI), X-ray diffraction measurements have been conducted on both, untreated and CO_2-treated samples (i.e. after gas breakthrough and diffusion test cycles). The results of the evaluations using the quantitative Rietveld

method are shown in Figure 2 and 3. The "Emscher Marl" sample 05-960 showed a rather heterogeneous composition, consisting of 8 mineral phases, whereas sample 05-565 consisted predominantly of calcite (~ 90 wt. %) with minor amounts of quartz and anhydrite (Table 9-1).

The XRD analysis of the "limestone" sample 06-565 did not indicate any significant changes in mineral composition upon exposure to CO_2. The "marl" sample plug (05-960) used in the repetitive gas breakthrough tests also showed a slight change in mineral composition pointing towards a possible reaction from anorthite to calcite (Table 9-1). This variation did not significantly exceed the range of experimental error and the natural heterogeneity of the material and needs to be verified.

Mercury- porosimetry and BET measurements prior to and after CO_2 treatment of the samples did not reveal any significant changes in the pore geometry and surface properties.

9.5 Discussion

9.5.1 Sealing efficiency of caprocks

In this study capillary breakthrough tests using the imbibition method according to the procedure described by Hildenbrand et al. (2002) have been performed. Compared to gas breakthrough experiments reported by Al Bazali et al. (2005) or Li et al. (2005), who follow the drainage path by incrementally increasing the gas pressure, the risk for overestimation of the capillary displacement pressure is avoided. Additionally, the dynamics of gas breakthrough processes (i.e. first water displacement, then gas penetration followed by breakthrough; repetitive drainage/imbibition scenario) has been taken into account.

To test for reproducibility and petrophysical changes due to the interaction of the samples with CO_2, repetitive runs were conducted on the same sample plug. Prior to each gas breakthrough experiment complete water saturation was established.

Generally, the samples showed sealing efficiencies with permeability values (single- and two-phase) in the nD-range and moderate threshold pressures.

The CO_2 capillary breakthrough pressures published in this work (0.41-0.74 MPa) are in line with the results of Hildenbrand et al. (2004) and Bachu and Bennion (2006) presenting relative small breakthrough pressures (< 1MPa) for shaly lithotypes. Hildenbrand (2004), Li et al. (2005, 2006), Bachu and Bennion (2006) and Angeli et al. (2009) also revealed higher breakthrough pressures (up to 30 MPa) investigating deeper buried and evaporitic sequences. This demonstrates the large range of breakthrough pressures for different caprock lithologies.

Additionally absolute and gas permeabilities presented in this study match perfectly with the findings of the mentioned authors. Compared to the results of Li et al. (2006) who proposed permeability data for evaporatic caprock sequences in the Weyburn Field, the permeability values of the samples investigated in this study are approximately two orders lower.

However, a continuous reduction of the minimum capillary displacement pressure during the test cycles has been observed for both samples investigated (Table 9-2). The CO_2 capillary breakthrough pressures decrease by ~33 % and 46 % for sample 05-960 and 06-565, respectively. For helium tests on sample 06-565 (first and last experiment in the test cycle) this trend is even more distinct, showing a decrease of ~66 %.

The reduction in capillary breakthrough pressures is associated with a significant increase in $k_{eff(max)}$ values about a factor of ~3 for sample 05-960 and factor of ~8 for sample 06-565 (Table 9-2). This is in line with Longeron (2003) who observed an increase in permeability values for a carbonate core after a percolation test with a mixture of CO_2 and water.

Successive diffusion experiments on the marl sample (05-960) revealed increasing. Effective diffusion coefficients during the test sequence increase from initially $7.8E^{-11}$ to $1.19E^{-10}$ m²/s (Figure 9-9 and Figure 9-10). The C_1-values remained constant within the experimental error in both experiments (183 and 198 mol/m³).

Similar results were obtained by Busch et al. (2008). Repetitive diffusion experiments on the Muderong Shale yielded slightly increased effective diffusion coefficients (D_{eff} = $3.08E^{-11}$ and $4.81E^{-11}$ m^2/s) and a decrease in the concentration of the bulk CO_2 volume from 389 to 222 mol/m^3 in the sample. This was interpreted to result from chemical alteration of the conducting pore system during the first CO_2 experiment, possibly related to mineral reaction/adsorption. Additionally, partly irreversible sorption of CO_2 may have retarded the diffusion front during the first run (resulting in a lower diffusion coefficient), while the interaction of the shale with CO_2 was probably lower in the second experiments (lower C_1-value).

Additionally, absolute permeability values determined from single-phase experiments showed a slight increase, which indicates changes in the pore system rather than experimental errors (~10%). These alterations are more distinct in the diffusion test cycles, probably as a result of the longer exposure of the samples to CO_2 (~240 to ~150h for a single gas breakthrough test).

The findings of this experimental study indicate systematic and significant changes in the fluid transport properties of both samples upon successive treatment with CO_2. These changes are likely to be due to mineral alterations and/or changes in the mineral texture due to dissolution and precipitation of minerals (carbonates). Both processes may lead to changes in porosity and pore geometry. Repetitive CO_2 treatment resulted in a reduction of the capillary sealing efficiency and, in consequence, in an easier and faster propagation of the non-wetting fluid into/across caprocks. Similar observations were made by Chiquet et al. (2007a) and Shah et al. (2008) who found changes of surface properties of mineral phases upon exposure to CO_2.

Further high pressure sorption tests performed on both samples indicate that caprocks have an additional CO_2 retention potential (see section below). Caprocks are able to physically adsorb significant amounts of

CO_2, contributing to the sealing efficiency of the rocks and can also act as an additional CO_2 sink, however on longer time scales (Busch et al., 2008).

9.5.2 Mineral alterations

Follow-up carbon dioxide breakthrough and diffusion tests revealed significant changes in the fluid flow behaviour and sealing efficiency of the samples investigated. To test for mineral alteration occurring during CO_2WRI, X-ray diffraction measurements using the quantitative Rietveld method have been conducted on the initial and the CO_2-treated samples. Preliminary measurements showed that the accuracy of XRD measurements is better than 1% and the heterogeneity of shale samples accounts for up to 5 wt.%. Results are summarised in Table 9-1. XRD analyses were performed on both samples after gas breakthrough and diffusion test cycles (Table 9-1) and compared to analyses of the original sample. The analyses of the "limestone" sample (06-565) did not indicate any significant mineral alteration after CO_2 treatment (Table 9-1). This sample was composed predominantly of calcite (~90 %) and contained practically no other reactive minerals (anorthite or clay minerals). The observed changes in transport properties could be due to a redistribution of calcite (dissolution, re-precipitation) within the sample, which would not be detected by XRD. The changes in mineral composition observed for the "marl" sample 05-960 after CO_2 breakthrough tests are small and could be within the range of rock heterogeneities (Table 9-1). The low alteration might be due to very low transport porosities in capillary breakthrough tests as stated in Hildenbrand et al. (2002). The minor accessibilities lead to a diminished contact between the CO_2 and the rock resulting in reduced mineral reactions. Additionally, the longer duration and higher temperature of the diffusion experiments should be considered here (cf. Sealing efficiency of caprocks). Significant alterations were observed for this sample after the diffusion test cycle, probably due to a longer CO_2 exposure at higher temperatures. The anorthite content decreased from 13.9 % to a negligible amount, whilst at the same time the calcite content increased from 40.4 % to 56 % (Table 9-1). The reaction of anorthite to calcite and quartz in the presence of CO_2 has been investigated in previous studies. Gaus et al., 2005 point out the poor knowledge of kinetic rate constants for feldspar reactions with CO_2. For the reaction of anorthite according to equation 1 they estimate a completion time of 5000 years.

$$CaAl_2Si_2O_8 + CO_{2(g)} + 2H_2O_{(l)} \Leftrightarrow CaCO_{3(s)} + Al_2Si_2O_5(OH)_{4(s)} \qquad (9\text{-}4)$$

anorthite + carbon dioxide + water ⇔ calcite + kaolinite

The results of our study indicate, however, that the decomposition of anorthite takes place at the laboratory time scale (several weeks). These observations are in line with other recent experimental work showing significant corrosion of feldspar (e.g. Bertier et al., 2006) and alteration of clay minerals (e.g., Wigand et al, 2008) within weeks to months. Recently Hangx and Spiers (2009) proposed reactivity of

calcium feldspar on CO_2 treatment at high pressures (6-18 MPa) and temperatures of 200- 300°C at a similar time scale (1-3 weeks). They found a series of secondary minerals (e.g. hydrotalcite, kaolinite, phyllosilicate phases, possibliy aragonite), but no indication of calcite precipitation. They assume that reaction (4) might occur to a limited extent and other reaction might take place.

In this study no significant amounts of kaolinite or secondary minerals like in Hangx and Spiers (2009) were detected in the CO_2-treated plugs of the "marl" sample, but distinct calcite precipitation occurred, maybe promoted by accelerated carbonate nucleation and precipitation by the existing calcite carbonate, also assumed by these authors.

On the other hand the absence of kaolinite is difficult to explain. It might have been precipitated as a microcrystalline (silicate?) phase since a slight increase in quarz content was noted or undergone another unknown transformation reaction. Further investigations are required here.

Stoichiometrically 1 mol of calcite can be produced by reaction of 1 mol anorthite with 1 mol of CO_2. This reaction could account for the decrease in anorthite as well as the increase in calcite. For the observed mineral alterations in this work the ratio anorthite to calcite was found to be ~1:3, which is not in accordance with the stoichiometry of equation 1. Thus, a further Ca^{2+}-source is required to obtain the observed mineralogical changes. One potential source is the smectite acting as a cation exchanger. Although not proven, its occupation by Ca^{2+} is likely, considering the overall constitution of the sample. The steady-state CO_2 diffusion flux through the "Emscher Marl"-sample has been determined to be 7.7 mol/(m²h) which guarantees a sufficient CO_2 supply during the experiment.

Although the input of calcium can be reasonably explained, it cannot be excluded that the observed variations are, to a certain extent, an effect of mineralogical heterogeneities. Thus XRD analysis can so far only be regarded as a qualitative assessment of mineral changes due to CO_2 treatment. The observed changes in the transport properties result from minimal changes in the pore system which cannot be resolved by standard petrophysical methods such as BET and mercury porosimetry.

9.5.3 CO_2 storage capacity of caprock samples

Similar sorption curves as shown in Figure 9-11 have already been reported by Busch et al. (2008) for a clay-rich Australian shale and various clay minerals (kaolinite, illite, smectite).

High pressure sorption tests performed in this study obtained higher maximum excess sorption capacities for the more clay-rich sample 05-960 than for the carbonate 06-565 (0.27 and 0.14 mmol/g, respectively). This can be expected by higher contents of reactive minerals, such as clay minerals and anorthite in the first sample, known as being reactive in the water/CO_2/rock system (e.g. Busch et al., 2008; Bertier et al, 2006; Gaus et al. 2005; Wigand et al., 2008; Hangx and Spiers, 2009). These findings confirm the enhanced CO_2-storage potential for shales and clay minerals reported by Busch et al. (2008).

Compared to the sorption capacity of the Muderong shale from Western Australia Busch et al. (2008) with ~1.0 mmol/g the storage potential of the samples investigated here is in the same order of magnitude, but slightly lower.

However, the statement of Busch et al. (2008) that CO_2 migrating into the pore network of caprocks, can be partly immobilized by the additional storage potential of shales contributing to a higher sealing efficiency of caprocks can be confirmed within this study.

CO_2 sorption on organic matter plays a minor role due to the small TOC contents of the samples investigated (~0.2-0.4 %, Table 9-1) and has found to be negligible in the presence of clay minerals (Busch et al., 2008).

In order to demonstrate the potential CO_2 storage capacity of caprocks, all CO_2 storage mechanisms for the marlstone sample (05-960) are summarized in the following:

Carbon dioxide diffusion experiments on the marl sample (05-960) revealed an estimate for the CO_2 storage potential of ~180-200 mol/m³ (~0.08 mmol/g), providing a first estimate.

Following this result the different possibilities for CO_2 trapping have been evaluated (Table 9-4):

(I) Assuming complete accessibility of the pore space, complete water saturation and a CO_2 solubility in water (at 28°C and pressures up to 5 MPa, Figure 9-12), 0.07 mmol CO_2/g shale are dissolved in water (Duan and Sun, 2003).

(II) CO_2 sorption experiments (Figure 9-11) showed storage potentials of 0.20 mmol/g at 45°C at the pressure conditions used in the diffusion tests. These values might be slightly underestimated: Diffusion tests were performed at lower temperatures here higher sorption capacities can be expected.

(III) Mineral alterations following pre- and post CO_2 diffusion experiments of the clayey marl sample showed a shift from anorthite (14 to 1 wt.%) to calcite (40 to 56 wt.%, Table 9-1). This shift and taking into account the mass of the plug accounts for a mineral carbonation of ~0.68 mmol/g sample during the different CO_2 diffusion tests performed here.

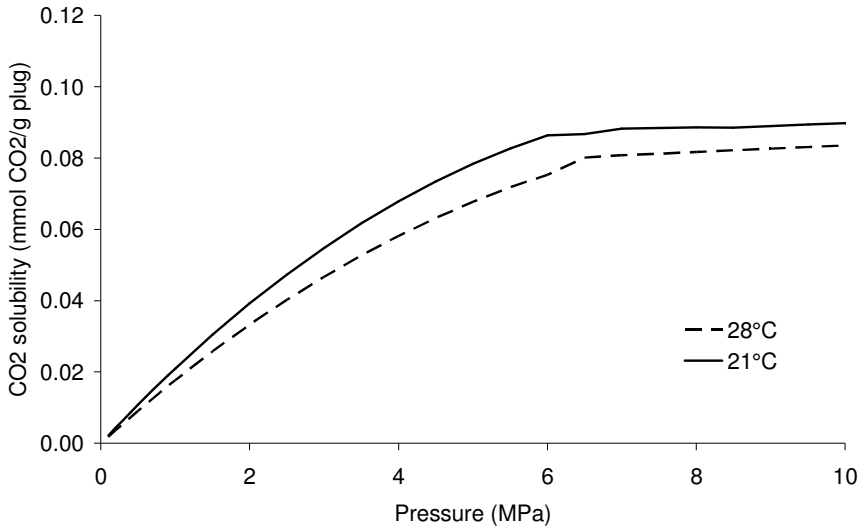


Figure 9-12. CO_2 solubility in water at 21 and 28°C, related to plug mass of sample 05-960 (after Duan and Sun, 2003).

Table 9-4. Evaluation of the CO_2 storage potential during diffusion tests on the marlstone sample (05-960)

Storage mechanism	Storage capacity (mmol/g)	
C_1- value	0.08	estimate from CO_2 diffusion experiment
CO_2 solubility in water	0.07	after Duan and Sun (2003)
CO_2 sorption	0.20	determined from sorption isotherms using experimental pressures
mineral alterations	0.69	calculated by increase in $CaCO_3$ content after experiment series

These three CO_2 storage processes result in a total of 0.95 mmol/g (~40 kg CO_2/t sample) that have been consumed during the two successive diffusion tests. Thereby, mineral trapping accounts for 2/3 of the total potential.

One important aspect that emerged from the almost complete consumption of anorthite is that CO_2 diffuses into the entire pore space and mineral reactions take place on the experimental time scale (several weeks).

In order to reveal further information on the processes involved in these storage phenomena, a desorption test after the 3rd CO_2 breakthrough test on this sample has been conducted to elucidate whether the storage potential is the result of irreversible processes (total conversion of the accessible mineral surface) or irreversible sorption during the first contact between the reactive gas and the rock matrix

After the third gas breakthrough experiment the two volumes at the top and bottom side of the sample plug have been depressurized and a pressure build-up over time has been recorded (Figure 9-13). This desorption experiment underlines the assumption of reversible processes, showing a higher amount of desorbed CO_2 as the amount of CO_2 dissolved in the pore water (considering low transport porosities). Figure 9-13 shows that the desorption on the former upstream side is faster and higher than on the downstream side which should be the result of the pressure gradient over the sample but could also be interpreted as pronounced mineral alteration on the high pressure side, due to higher capillary pressure of the CO_2 at this side.

Carbon dioxide immobilization within the calcite sample is rather unexpected. No mineral alterations have been observed after CO_2 treatment (at 21°C), porosity is rather small (6 %) providing a reduced amount of dissolved CO_2 in the sample and CO_2 sorption is also limited (Figure 9-11). Further, no Ca^{2+}, Fe^{2+} or Mg^{2+}-source (like e.g. anorthite or clay minerals) and hence no alkalinity is available that are required for the precipitation of calcite.

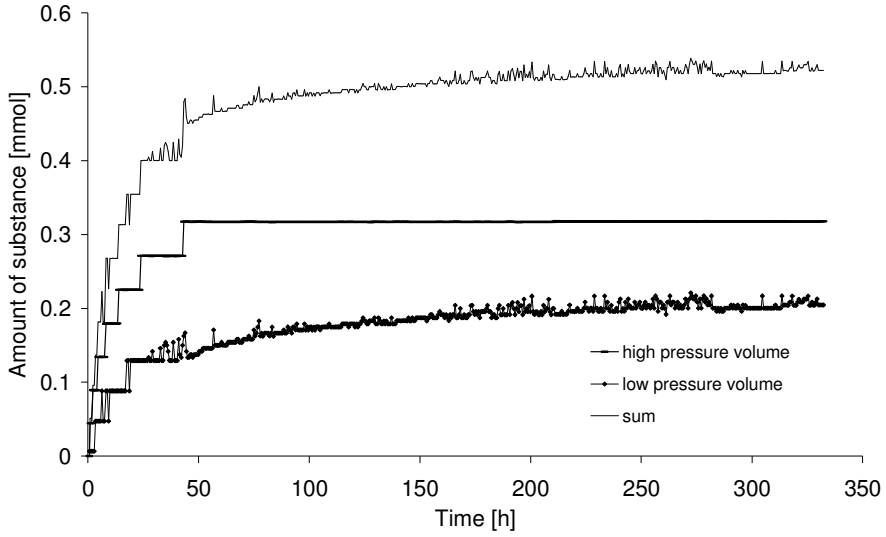


Figure 9-13. Desorption tests on sample 05-960 after 3rd CO2 breakthrough test.

9.6 Conclusions

Potential changes in sealing properties of caprocks exposed to high CO_2 partial pressures are considered one of the key factors in geologic storage of carbon dioxide. Our experimental and analytical study on two caprock samples, a clay-rich marlstone and a calcite-rich limestone from western Germany provided a comprehensive overview of CO_2-related petrophysical and mineralogical alterations of fine-grained lithotypes on the laboratory time-scale of several weeks up to several months. The results of repetitive CO_2 gas breakthrough and diffusion experiments revealed a small but measurable alteration of fluid transport properties for both samples as evidenced by a lowering of gas breakthrough (capillary entry) pressures and a slight increase in permeability coefficients. No significant changes could be detected in other

petrophysical parameters such as specific surface area and pore-size distribution. The overall sealing properties of both lithotypes were not seriously deteriorated. Due to their different mineralogical composition the two samples exhibited differences in their chemical reactivity. While XRD measurements of the limestone before and after exposure to CO_2 did not reveal any distinct changes in mineral composition, a significant decrease in the reactive feldspar component anorthite was observed for the clay-rich marl sample with a simultaneous increase in calcite after CO_2 exposure. These findings are in line with irreversible CO_2 uptake inferred from high-pressure "sorption" experiments also conducted in this study. The chemical CO_2 fixation potential of pelitic rock sequences containing reactive feldspar and clay minerals thus emerges as a new and additional aspect in seal appraisal. Caprocks do not react merely as a flow barrier but may also constitute a permanent sink for significant quantities of CO2. The results of the present study indicate that these mineral reactions occur rapidly, i.e. on the laboratory time-scale. Their impact on the sealing efficiency and fluid flow properties appears to be marginal. In consequence, the presence of "immature" pelitic rocks with significant percentages of unweathered feldspars would constitute an additional criterion for the selection of suitable geological storage sites for CO_2.

The combination of laboratory flow-tests under in-situ conditions with detailed mineralogical and petrophysical analyses constitutes a very promising approach to study the complex physico-chemical processes in the CO_2/water/rock system. The effects of the initial mineral composition on the type and the kinetics of mineral reactions and the CO_2 fixation potential are one focus of ongoing studies. Microscopical methods (e.g. SEM) are being used to exhibit more profound insight into the behaviour of feldspar and clay minerals in the presence of CO_2. The long-term impact of CO_2-triggered mineral reactions on the rock mechanical properties of caprocks is another perspective closely related to the issues addressed here. It is presently under investigation in several seal/caprock-related research projects such as the CO2SEALS Project (http://www.co2seals.de/).

10 Carbon Dioxide Storage Potential of Shales

10.1 Introduction

In recent years, research into subsurface CO_2 storage in geological formations has increased rapidly. The main focus of this research is to seek options for lowering anthropogenic CO_2 emissions which are believed to be a major factor contributing to global warming. Some of the most favoured storage options are saline aquifers, depleted gas and oil reservoirs or unminable coal seams (Bachu, 2000; Bachu et al., 1994; Freund and Ormerod, 1997; Hitchon et al., 1999; Holloway, 1997).

Investigations on this topic cover a wide range of issues such as gas-water-rock interactions, multiphase flow, reservoir engineering and modelling as well as monitoring and verification. One common aspect of all CO_2 capture and storage (CCS) options is the sealing efficiency of cap rocks above potential CO_2 storage reservoirs. The quantitative assessment of leakage risks and leakage rates is a primary prerequisite for site approval, public acceptance and the awarding of credits for stored CO_2 quantities.

Leakage through caprocks may occur in three different ways: (i) rapid ("catastrophic") leakage by seal-breaching (mechanical failure) or damage of well casing (corrosion of pipes and cements), resulting in gas flow through a (micro-) fracture network, (ii) long-term leakage controlled by the apillary sealing efficiency (e.g. Al-Bazali et al., 2005; Chiquet, 2005; Hildenbrand et al., 2004a) and permeability (after capillary breakthrough pressure is exceeded) and (iii) diffusive loss of dissolved gas through the water-saturated pore space.

Molecular diffusion of CO_2 is characterized by a low transport capacity, but it is a permanent and ubiquitous process. Rather than causing substantial gas losses, it must be considered as the rate-controlling step of mineral reactions, seal alteration and sorption processes. However, few data are available on the diffusive transport of CO_2 in geological seals.

Research on molecular gas transport through cap rocks was mainly focused on hydrocarbon loss from natural gas reservoirs (e.g. Krooss and Leythaeuser, 1996; Krooss and Leythaeuser, 1997; Krooss et al., 1988a; Krooss et al., 1992a, b; Krooss and Schaefer, 1987b; Leythaeuser et al., 1980; Montel, 1993; Nelson and Simmons, 1995; Nelson et al., 1992). In one of the first studies related to CCS, Krooss et al. (2003) reported CO_2 diffusion parameters of samples from different lithotypes (coal, cemented sandstones, shales). The results of this study indicated that shales are able to store significant amounts of CO_2 either dissolved in formation waters, trapped by mineral reactions or sorbed to organic compounds or mineral surfaces. These findings triggered more detailed investigations of the CO_2 sorption and diffusion behaviour of selected shale samples and individual clay mineral standards (Ca-Montmorillonite, Na- Montmorillonite, Kaolinite, Repidolithe, Illite). This experimental work was accompanied by geochemical modelling to obtain improved insight into likely dissolution and precipitation of minerals. Currently, extensive and fundamental

experimental and modelling research is performed related to CO_2-water-rock interactions in geological storage formations (e.g. Bertier et al., 2006; Brosse, 2005a, b; Emberley, 2004; Gaus et al., 2005; Gunter, 2000; Gunter, 1993; Kaszuba, 2003; Kaszuba, 2005; Kharaka et al., 2006; Knauss et al., 2005; Rosenbauer et al., 2005; Shiraki and Dunn, 2000).

10.2 Sample Description

The Muderong Shale is the regional top seal in the Carnarvon Basin on the Northwest Shelf of Australia of Cretaceous age. The sample analysed in this study was recovered from a depth of 1454 metres below seafloor (mbsf). The shale was partially dried out when recovered and was preserved under a light process oil from the recovery point onwards to prevent further desiccation. XRD analyses show that this shale dominantly comprises mixed layer illite-smectite, kaolinite and quartz (Table 10-1). It has a porosity of ~20 % and bulk density (calculated from weighing and drying), moderately high specific surface area (by nitrogen adsorption/desorption) and cation exchange capacity (by x-ray fluourescence) in line with its clay-rich nature (Table 10-1). Pore size distributions (by mercury porosimetry) indicate capillary threshold pressures of ~48 MPa (Kovack, 2004). SEM examination shows that the Muderong Shale is a relatively uniform (non-laminated), fissile shale, with clay matrix support (Figure 10-1a,b). Preferential particle orientation of both rigid grains and clay matrix is observed, although the clay matrix orientation can be affected locally by the presence of more rigid particles (Figure 10-1c). Pyritisation of foraminifers is also noted along with precipitation of early diagenetic kaolinite (Figure 10-1b,c) and siderite (Figure 10-1d). Further details on the analytical methods and the composition, physical and mechanical properties of the Muderong Shale have been reported by Dewhurst and Hennig, 2003; Dewhurst et al., 2002a; Dewhurst et al., 2002b.

Table 10-1: Petrophysical properties and composition of Muderong Shale.

Grain Density	(g/cm³)	2.70
Bulk Density (g/cm³)	(g/cm³)	2.33
Porosity	-	0.20
Specific Surface Area	(m²/g)	25.0
Cation Exchange Capacity	(meq)	0.24
Capillary Entry Pressure (Air-Hg)	(MPa)	48.3
Total Organic Carbon	%	<0.5
Clay fraction	-	0.45
Clay content	-	0.66
Mineral composition		Content (%)
Illite-smectite		27
Smectite in I-S		20
Mica/Illite		8
Kaolinite		26
Chlorite		5
Quartz		27
Siderite		2
Orthoclase		3
Pyrite		2

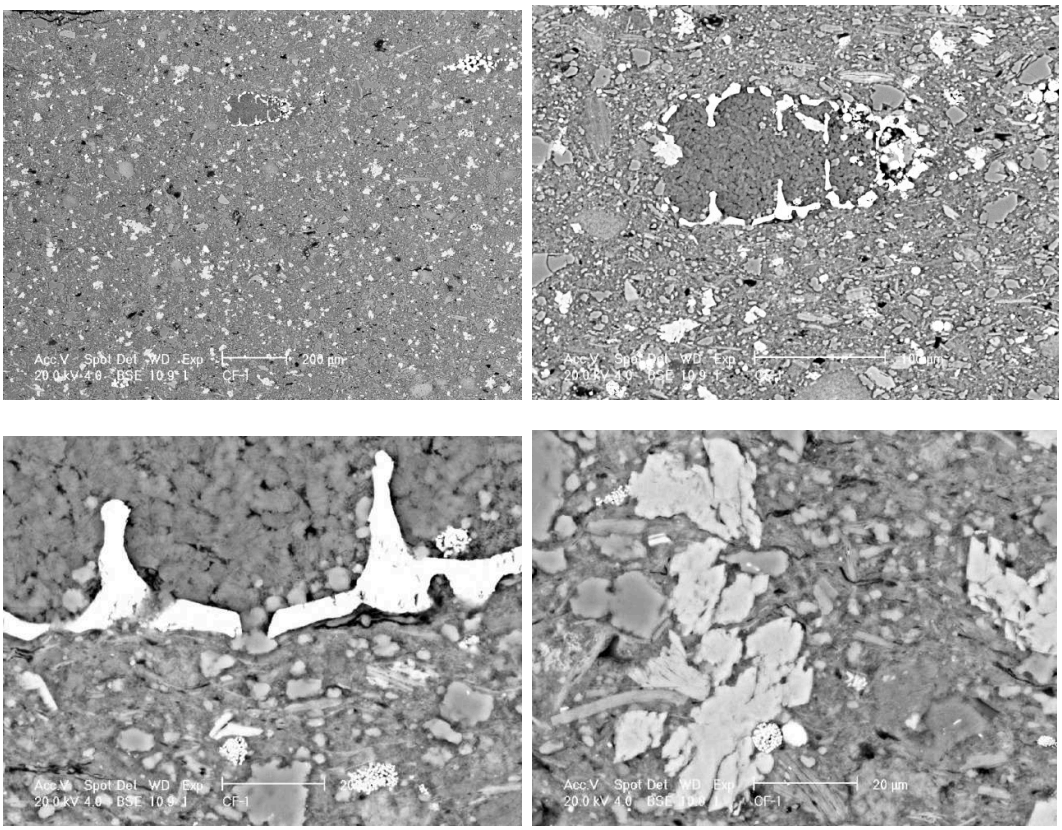


Figure 10-1: Backscattered scanning electron microscope images of the Muderong Shale sample used in these tests; (a) General low magnification image showing the fine grained nature of Muderong Shale (most particles < 50 μm diameter); (b) magnified from (a), showing a pyritised foraminifera infilled with clays; (c) close up of (b) reveals the foram test is infilled with vermicular kaolinite that has been protected from compaction, enhanced compaction of clays around the foram and small pyrite framboids (bright); (d) high magnification image showing siderite (bright), a small pyrite framboid, tightly compacted clay fabric and fine grained quartz particles (larger, grey grains).

Ca-montmorillonite, Na-montmorillonite, illite and kaolinite used in this study (Table 10-2) were obtained from the The Clay Minerals Society's (http://www.clays.org/) Source Clays Repository (Purdue University, Indiana, USA). These represent reference samples that have been analysed in several baseline studies the results of which were published in Clays and Clay Minerals (Vol. 49,5, 2001).

Table 10-2: Source Clay minerals used in this study.

Clay mineral	Code	Origin
Ca-montmorillonite	STx-1b	Gonzales County, Texas, USA
Na-montmorillonite	SWy-2	Crook County, Wyoming, USA
Kaolinite	KGa-1b	County of Washington, State of Georgia, USA
Illite	Imt-1	Silver Hill, Montana, USA

(http://www.clays.org/sourceclays/SourceClays.html)

10.3 Experimental

10.3.1 Diffusion experiments

CO_2 diffusion experiments were conducted in triaxial flow cells constructed for confining pressures and axial loads up to 50 MPa, with temperatures up to 350°C. The cells accommodate cylindrical sample plugs with a diameter of 28.5 mm. The plug length can range from 5 to 20 mm and is usually chosen to keep the experimental time frame reasonable. The plug is placed between two porous stainless steel disks (Figure 10-2) which is then mounted between two stainless steel pistons equipped with boreholes for fluid introduction and removal. To ensure leak and diffusion tightness, the outer surface of the sample/piston arrangement is sealed with a double-layered sleeve. The inner sleeve consists of lead (Pb) foil (0.25 mm thickness); for the outer layer, a thin-walled copper (Cu) tube is used.

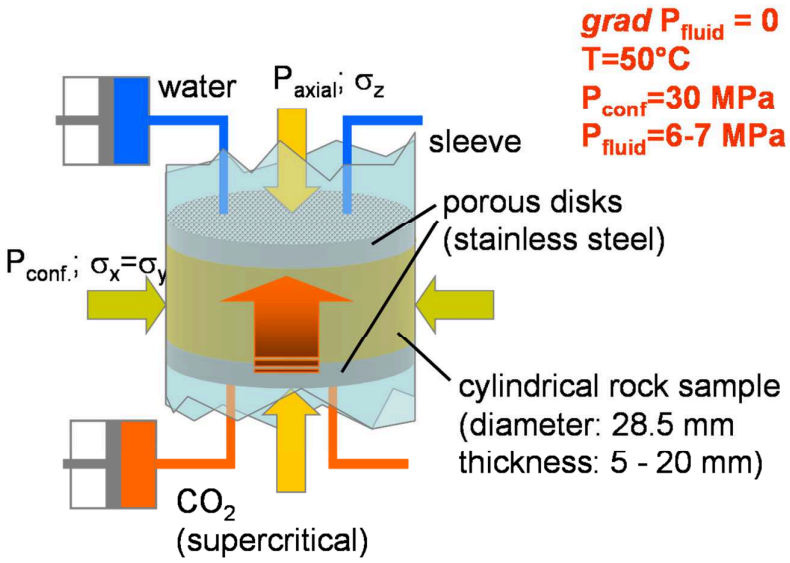


Figure 10-2: Schematic diagram of the CO_2 diffusion experiment under controlled effective stress conditions.

Prior to the diffusion experiments, the conductive pore system of the samples is water-saturated by applying pressures in the range of up to 8 MPa on one side. The resulting water flow at the downstream side is monitored and when it is gas-free the flow-rate is measured to determine the permeability coefficient. Subsequently both chambers of the flow cell are pressurised with water up to the pressure level chosen for the diffusion experiment. The diffusion experiment is started by displacing the water in the bottom chamber (stainless steel porous disk) of the flow cell by CO_2. A communicating tubing system ensures that there is no pressure gradient between top and bottom chamber of the measuring cell.

The flow scheme of the experimental set-up with the peripheral valve and tubing system has been described elsewhere (Schlömer and Krooss, 2004). The gas diffusing through the rock plug is collected in the top chamber of the flow cell for 1–2 hours and then transferred to a purge and trap system. Here CO_2 is

stripped from the water by a helium current and adsorbed on a molecular sieve trap. In a subsequent step the trapped CO_2 is mobilised thermally and transferred to the GC/TCD for quantification.

The diffusion experiments are conducted as non-steady state measurements, i.e. the diffusive breakthrough of the gas is monitored and evaluated to yield the effective diffusion coefficient and the equilibrium bulk rock volume CO_2 concentration at the gas/rock interface in the bottom chamber. A detailed description of the evaluation of effective diffusion coefficients and the derivation of diffusion equations was given by Schlömer and Krooss, 2004. A short outline is provided in the Appendix.

10.3.2 Sorption experiments

10.3.2.1 High-pressure sorption experiments

In the high-pressure sorption experiments (> atmospheric pressure, up to 25 MPa) the gas sorption capacity (sorption isotherms) of powdered sample material is determined as a function of pressure by the manometric method. Figure 10-3 shows a schematic image of the experimental set-up, consisting of a stainless-steel sample cell, a set of actuator-driven valves and a high-precision pressure transducer (max. pressure 16 MPa), with a precision of 0.05 % of the full-scale value. The volume between valve 1 and valve 2, including the void volume of the pressure transducer, is used as reference volume and determined by helium (He) pycnometry in a calibration run. The shale sample plugs are kept in a stainless-steel sample cell. A 2-µm filter-disc is used to prevent mineral particles from entering the valves.

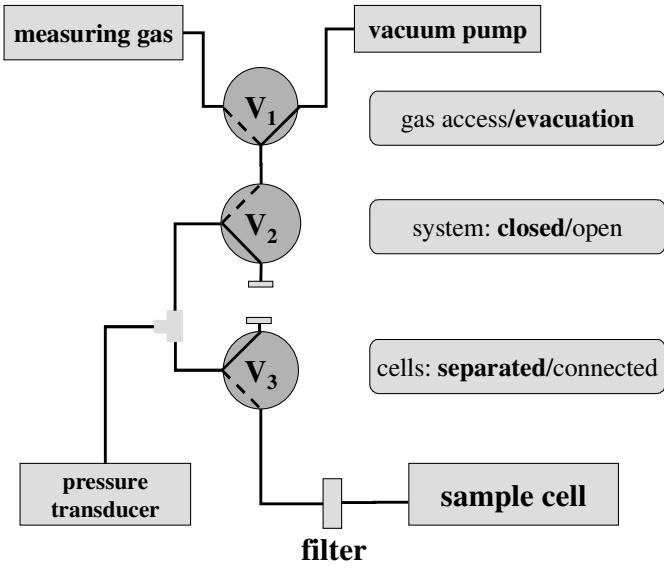


Figure 10-3: Schematic diagram of the experimental set-up for single component gas adsorption on coals. The volume between V_2 and V_3, including dead volume of the pressure transducer, is used as reference volume.

The experimental device is placed in an air bath ensuring a constant temperature (±0.1°C) throughout the experiments. Single-gas sorption experiments in this study were performed at 45°C and 50°C. At this

temperature CO_2 is either in the gaseous or, at pressures above P_c, in the supercritical state (T_c: 30.95 °C; P_c 7.38 MPa).

A detailed description of the procedure has been given previously (Busch et al., 2003a, 2007; Busch et al., 2004a; Krooss et al., 2002; Siemons and Busch, 2007). The evaluation of the experimental data yields excess sorption (Gibbs sorption) isotherms. Here the observed reduction in gas pressure resulting from gas sorption is compared to the theoretical "non-sorption" case. The volume changes due to the increasing amount of adsorbed phase with pressure are not considered in this evaluation.

10.3.2.2 Low-pressure nitrogen sorption experiments

In order to detect any structural changes in the pore system of the clay minerals, specific surface area measurements were performed on the as received Ca-montmorillonite, Na-montmorillonite and kaolinite samples before and after high-pressure sorption experiments with supercritical CO_2. Specific surface areas were determined by low-pressure nitrogen sorption on the dry material with a Micromeritics GEMINI 2360 instrument using the BET method (Brunauer et al., 1938). The measurements were performed at liquid nitrogen temperature (-196°C) up to a final pressure of 0.126 MPa. Because of the low-pressures no correction for non-ideality of the gas was made.

Clay samples were evacuated and kept in a vacuum (<1 Pa) at 105°C for at least 6 hours. The vacuum oven was then vented with helium and the sample cells (quartz) were closed while the samples were still under a helium atmosphere. Until used, the dry samples were stored in a desiccator under helium.

10.4 Results

The permeability tests conducted with the Muderong Shale prior to the first diffusion experiments yielded permeability coefficients between 0.8 and $0.9 \cdot 10^{-21}$ m² (0.8 – 0.9 nDarcy) (Figure 10-4). These values are on the lower end of permeability coefficients typically observed for moderately compacted shales.

10.4.1 Diffusion experiments

The experimental diffusion curves (data points and best fits) obtained from the two diffusion measurements on the Muderong Shale sample plug are shown in Figure 10-5 and Figure 10-6. Here the cumulative amounts (Q) of CO_2 diffused axially through the cylindrical sample plug per unit cross-section area (units of Q: mmol/m²) are plotted as a function of time (t in hours) elapsed since the start of the experiment. The slopes of the tangents to the curves represent the steady-state flux (mmol/m²/h). Indicated in the diagrams are the lag-times (t_0), defined as the intersection of the tangent to the diffusion curve with the x-axis, and the Q_0-values, the intercept of the tangent with the y-axis. These two characteristic parameters of the diffusion curve can be used to derive the effective diffusion coefficient (D) and the gas storage capacity (C_1) of the samples (cf. Krooss and Schaefer, 1987b). The first diffusion experiment was stopped before steady-state flow was reached. However a fit of the diffusion function to the experimental data provided a reasonable estimate of the diffusion parameters.

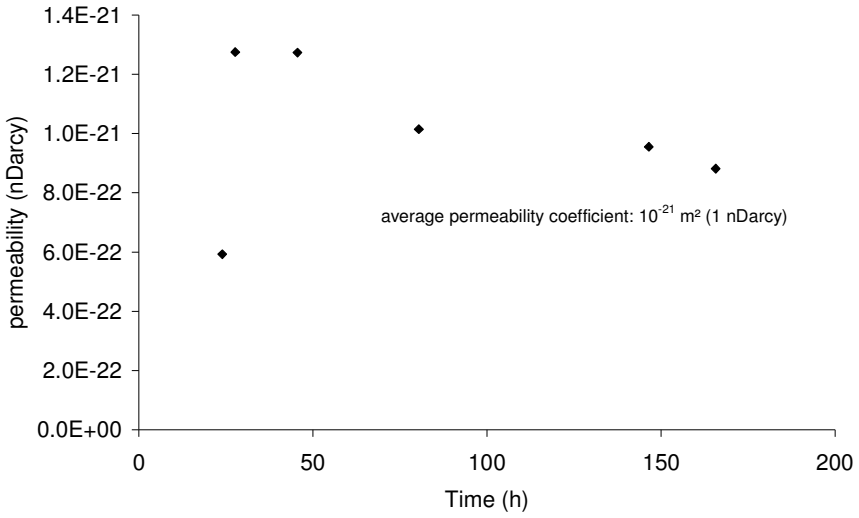


Figure 10-4. Water permeability measurement on Muderong Shale plug prior to first CO_2 diffusion experiment.

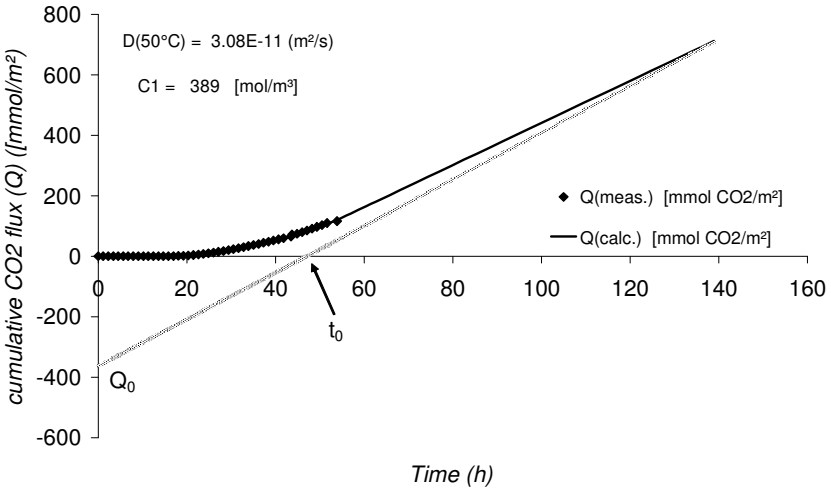


Figure 10-5. Cumulative CO_2 diffusion curve from Experiment 1 on Muderong Shale plug at 50°C.

Table 10-3 summarizes the results of these two experiments in terms of the effective diffusion coefficients and C_1-values. Effective diffusion coefficients of $3.08 \cdot 10^{-11}$ and $4.81 \cdot 10^{-11}$ $m^2 s^{-1}$ were obtained for the first and the second experiment, respectively. The C_1 values denote the bulk volume concentration (mol/m³ shale) of CO_2 within the rock sample at the gas/shale interface. For the first and second diffusion experiment they are as high as 389 and 222 mol/m³ (0.17 and 0.10 mmol/g), respectively.

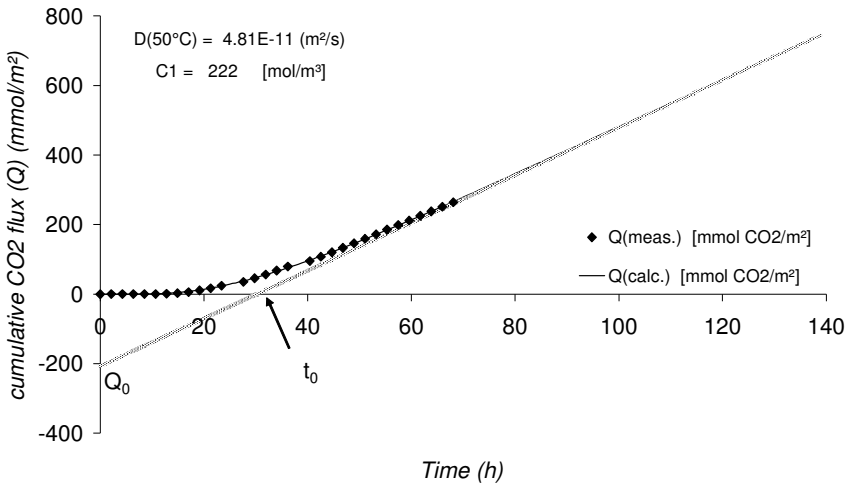


Figure 10-6. CO_2 diffusion experiment on Muderong Shale plug at 50°C (Experiment 2).

Table 10-3: Effective diffusion parameters:

	t_0 (s)	Q_0 (mmol m^{-2})	D_{eff} (m^2 s^{-1})	C_1 (mol m^{-3})
Experiment 1	$1.69 \cdot 10^5$	-363	$3.08 \cdot 10^{-11}$	389
Experiment 2	$1.09 \cdot 10^5$	-207	$4.81 \cdot 10^{-11}$	222

10.4.2 Sorption experiments

10.4.2.1 High-pressure CO_2 experiments

Figure 10-7 shows the excess sorption isotherms for the Muderong Shale measured at 50°C with an "as received" (a.r.) water content of 3.34 % and in the dry state (drying of the sample under vacuum at 105°C for >90 min). The "a.r." sample has a lower water content than might be expected for the Muderong Shale as a result of poor sample preservation before retrieval and as such is not fully saturated in its initial state. On the "a.r." sample, two measurements were performed to investigate reproducibility on the identical sample. The shape of the isotherm differs significantly from "normal" gas sorption isotherms and can be separated into three parts:

Pressure range from 0 to ~7 MPa: Excess sorption shows an almost linear behaviour for all isotherms. This part is almost identical for all measurements indicating no effect of the water content.

Pressure range from 7 to ~12 MPa: Excess sorption shows a steep increase in excess sorption for the untreated sample (1st run "a.r.") and an initial decrease for the other two measurements (2nd run "a.r." and dry), followed by a similar peak as for the untreated sample. The maximum sorption capacity varies for all three samples and decreases from the untreated (1st run "a.r.") to the dry sample from ~1.0 to ~0.4 mmol/g.

Above 12 MPa, all isotherms show a parallel and continuous decrease in sorption capacity with pressure.

The CO_2 sorption isotherms of the pure clay minerals, measured at 45°C, generally differ from those of the shale. Five different samples were tested either with "a.r." moisture content or in the dry state (Figure 10-8). The chlorite sample measured exhibited no measurable sorption capacity beyond the experimental error and is therefore not represented in Figure 10-8. For all samples, the dry measurements yielded higher excess sorption values than the corresponding "a.r." samples. The highest sorption capacities were obtained for Ca-montmorillonite with maximum values of ~1.65 and ~1.3 mmol/g for the dry and the "a.r." sample respectively. The lowest sorption values, however, were found for kaolinite and illite with maximum values < 0.4 mmol/g.

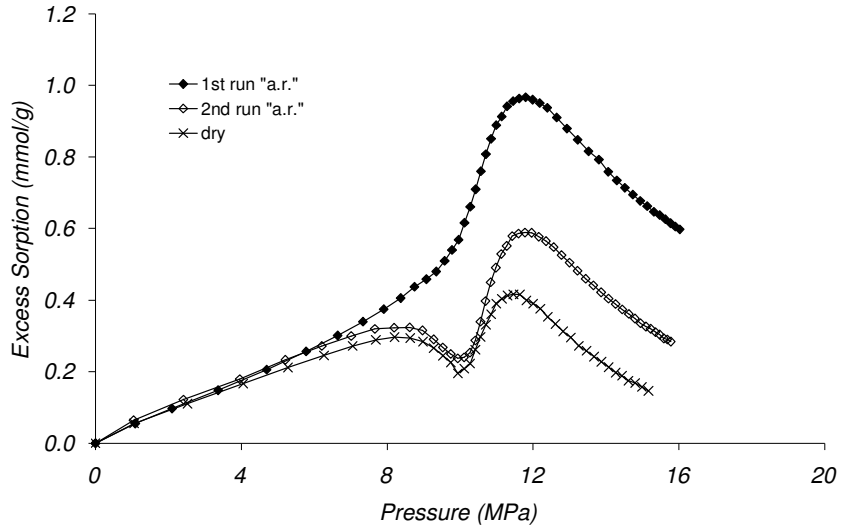


Figure 10-7. CO_2 excess sorption experiment on powdered Muderong Shale at 45°C.

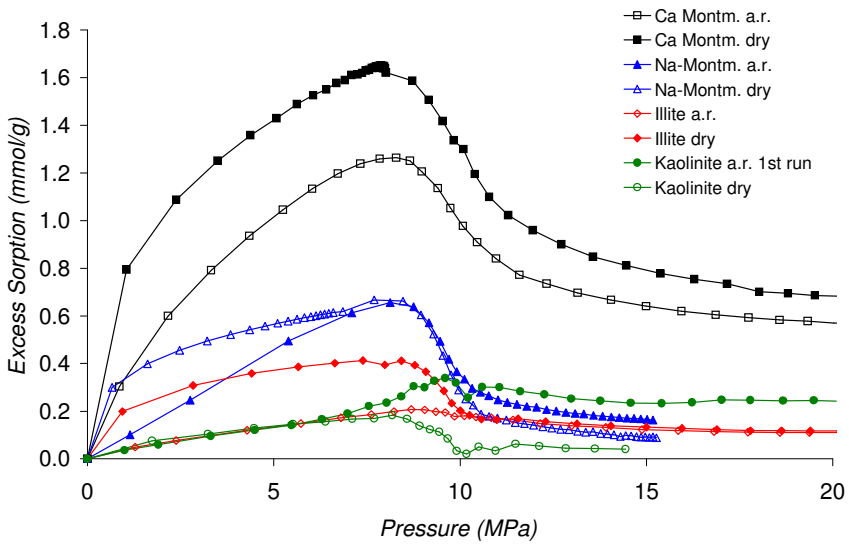


Figure 10-8. CO_2 excess sorption experiments on various powdered clay minerals (Ca-montmorillonite, Na-montmorillonite, illite, kaolinite) in the dry and "as received" moisture state.

The shape of the CO_2 sorption isotherms on kaolinite also differed substantially from those of the other clay minerals (Figure 10-9). The isotherms show fluctuations at pressures above 8-10 MPa. Furthermore, the isotherm of the kaolinite sample measured in the "a.r." moisture state (1st run, Figure 10-9) shows a sorption peak similar to the one observed for the Muderong Shale. A re-run with CO_2 was performed on the same sample to test for reproducibility (2nd run, Figure 10-9). It is obvious that the two isotherms are very similar up to ~8 MPa. At higher pressures, however, the second isotherm shows significantly lower sorption capacities. The same phenomenon was observed for the Muderong Shale (Figure 10-7). It is further interesting to note that the dry measurement shows a very similar behaviour to the re-run of the "a.r." sample (Figure 10-7).

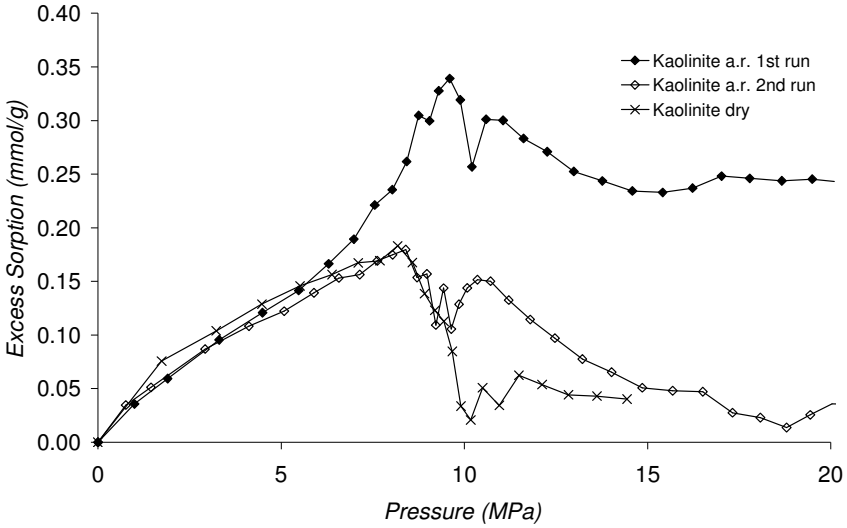


Figure 10-9. CO_2 excess sorption experiments on powdered kaolinite.

10.4.2.2 Low-pressure N_2 sorption experiments

Low-pressure N_2 sorption experiments have been performed on the Muderong Shale in the as received and in the dry state (Figure 10-11) as well as on three different pure clay minerals (Ca-montmorillonite, Na-montmorillonite, kaolinite, Figure 10-10) in the as received moisture state. No differences in N_2 sorption isotherms or specific surface areas (SSA, Table 10-4) have been observed for the clay minerals. The Muderong Shale however showed a decrease in SSA from 14.6 to 13.1 m^2/g for the measurement on the "a.r." sample compared to to the initial sample and no change in SSA for the dry measurement (Table 10-4).

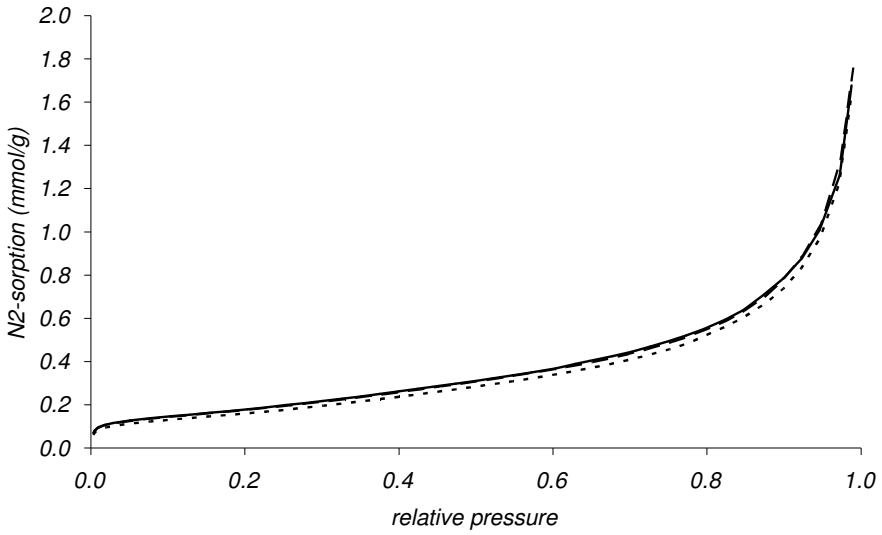


Figure 10-10. Nitrogen sorption isotherms for untreated and treated Muderong Shale sample (untreated: solid line; after treated of dry sample: long dashed line, after treatment of moist sample: short dashed line).

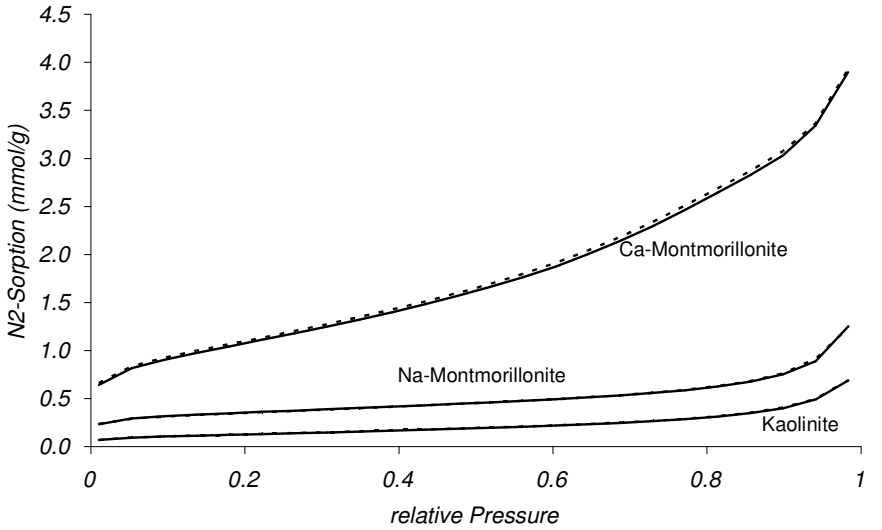


Figure 10-11. Nitrogen sorption isotherms (BET) for untreated and treated clay minerals (untreated: solid line; treated: dashed line)

Table 10-4: Comparison of BET specific surface areas of different clay minerals and Muderong Shale before and after CO_2 treatment

Sample	SSA before treatment (m^2/g)	SSA after CO_2 treatment of moist sample (m^2/g)	SSA after CO_2 treatment of dry sample (m^2/g)
Muderong Shale	14.6	14.5	13.1
Ca-montmorillonite	92.3	94.1	n.a.
Na-montmorillonite	28.0	28.3	n.a.
Kaolinite	11.3	11.1	n.a.

10.5 Discussion

10.5.1 CO_2 diffusion in the Muderong Shale

The CO_2 diffusion coefficients measured on the Muderong Shale in successive tests are of the same magnitude, the second value being slightly higher than the first (Figure 10-5 and Figure 10-6). This could be the result of a chemical modification of the conducting pore network during the first experiment, possibly due to mineral reactions. Effective diffusion coefficients of gases in water-saturated rocks are also affected by sorption processes as evidenced for the diffusion of methane in shales with different contents of organic matter (Zhang and Krooss, 2001). Thus, the elevated and partly irreversible sorption of CO_2 may have retarded the diffusion front in the first Muderong Shale diffusion experiment while the interaction of the shale with CO_2 was probably lesser in the second one, as evident from the lower C_1 value.

Further systematic tests are under way to provide more insight into the natural variability of diffusion coefficients and changes due to CO_2-water-rock interactions.

Diffusion coefficients of CO_2 in water as reported by Gertz and Loeschcke, 1956 and Vivian and King, 1964 range between $2 \cdot 10^{-9}$ and $3 \cdot 10^{-9}$ $cm^2 s^{-1}$ (at 37°C). As discussed by Krooss et al., 1992a, the relationship

$$D_{eff.} = D_{aq} / \tau, \qquad (10\text{-}1)$$

where D_{eff} denotes the effective diffusion coefficient and D_{aq} the diffusion coefficient in the pore water, may be used to estimate the nominal tortuosity (τ) of the shale pore system. For the Muderong Shale this tortuosity value is in the range of 40 to 70.

The C_1 values obtained from the diffusion experiments are a measure of the specific CO_2 storage capacity of the shale at the pressure/temperature conditions of the experiment. Evidently, the C_1 value decreased from 389 mol/m³ in the first experiment to 222 mol/m³ in the second test (cf. Figure 10-5 and Figure 10-6). For comparison, Table 10-5 lists the CO_2 diffusion parameters of the Muderong Shale together with those measured on a Carboniferous coal and a cemented sandstone.

Table 10-5: Comparison of effective CO_2 diffusion parameters measured on a coal, a cemented sandstone and the Muderong shale

Sample	coal BRZ 405		cemented sandstone		Muderong shale	
Exp. (Temp.)	coal 1 (45°C)	coal 2 (45°C)	ss 1 (50°C)	ss 2 (50°C)	sh 1 (50°C)	sh 2 (50°C)
D_{eff} (m^2 s^{-1})	$1.43 \cdot 10^{-9}$	$1.18 \cdot 10^{-9}$	$2.61 \cdot 10^{-10}$	$1.89 \cdot 10^{-10}$	$3.08 \cdot 10^{-11}$	$4.81 \cdot 10^{-11}$
C_1 (mol/m³)	3.30	4.14	9.8	8.3	389	222
steady-state flux [mmol/m²/h]	0.93	1.0	0.73	0.45	7.62	6.9

It is evident that the Muderong Shale exhibits the lowest diffusion coefficients but by far the highest CO_2 storage capacity (C_1 values). The steady-state diffusive flux, which is controlled both by the effective diffusion coefficient and the "solubility" or storage capacity of the gas in the water-saturated rock is also much higher for the Muderong Shale than for the other two samples. The significant decrease in CO_2 storage capacity in the second diffusion experiment is attributed to irreversible storage of CO_2 in the first experiment e.g. by mineral reactions.

10.5.2 CO_2 sorption on shales and clay minerals

In the high-pressure sorption experiments the moist ("as received") Muderong Shale showed higher CO_2 sorption capacities than the dry shale (Figure 10-6). This behaviour was unexpected since water and CO_2 were considered to compete for sorption sites which should result in lower CO_2 sorption capacities. For the pure montmorillonite and Illite samples investigated here, indeed substantially higher sorption capacities were observed with the dry samples while the "a.r." kaolinite exhibited higher CO_2 sorption capacities than the dry one at pressures > 7 MPa (Figure 10-9). It could be speculated that drying of the Muderong Shale and kaolinite might have changed their structural parameters leading to lower sorption capacities. However, the drying procedure was the same in all cases and therefore similar effects would be expected for the pure clays and the shale. Furthermore, any structural rearrangements should be expected to result in deviations over the entire pressure range of the sorption isotherms. This is not the case, since for all measurements performed on the Muderong Shale, the sorption behaviour is quite similar at pressures up to ~7 MPa.

Repetitive sorption runs on the "a.r." Muderong Shale and kaolinite samples, respectively showed a decrease in sorption capacities, especially at elevated pressures. These repetitive measurements however demonstrated sorption behaviour similar to the corresponding dry measurements.

While numerous CO_2 sorption measurements on coals under various conditions have been published in the literature, sorption isotherms on shales at high pressures are rarely reported so far. Nuttall et al., 2005 investigated carbonaceous Devonian black gas shales from Kentucky, USA on their CO_2 storage and methane recovery potential. Experimental conditions were 30°C (sub-critical CO_2 conditions) and pressures up to ~5.5 MPa and 10 MPa for CO_2 and CH_4, respectively. They found a direct positive correlation between CO_2 storage capacity and total organic carbon (TOC) of the shales while no correlation with the clay mineral content was observed. Some of the sorption isotherms presented by Nuttall et al., 2005 indicated a similar peak in excess sorption capacity as found in this study. Unfortunately pressures and temperatures were comparably low (<~5.5 MPa), leaving this similarity rather questionable. Nevertheless, in the study by Nuttall et al., 2005, excess sorption isotherms were represented by a Langmuir isotherm (monomolecular loading) which seems to be inappropriate to represent this peak.

Volzone and co-authors investigated the sorption behaviour of montmorillonite, smectite and kaolinite for various gases such as CO_2, CO, N_2, CH_4 and SO_2 (Melnitchenko et al., 2000; Venaruzzo et al., 2002; Volzone

and Ortiga, 2000, 2005; Volzone et al., 2006). These measurements have usually been performed at 0.1 MPa and 25°C, thus not representing reservoir conditions for CO_2 storage. However, under these low P/T experimental conditions, significant sorption capacities for different clay minerals have been observed with maximum values for $SO_2>CO_2>CH_4\geq N_2$: 0.66>0.24>0.08≥0.07 mmol/g. The mechanisms leading to gas sorption on clay minerals have not been well studied so far. Some correlations are given by e.g. Venaruzzo et al., 2002 who found a reasonable trend with BET surface areas and a very good correlation with the micropore volume of the minerals. The same phenomenon was observed in this study: BET surface areas, as measured with N_2, decrease in the order Montmorillonite>Illite>Kaolinite (e.g. Chlou, 1993, Table 10-4) which is the same trend as observed for the sorption capacity These observations seem to support physical surface sorption as reported for various other porous materials like, for example, activated carbons, coals or polymers.

10.5.3 CO_2 storage potential of shales

The C_1 values obtained from the diffusion experiments provide additional information on the sorptive storage capacity of shales at the experimental pressure/temperature conditions. At the interface of the water-saturated shale and the free CO_2 phase, an equilibrium concentration of CO_2 will be established in the pore water. If no adsorption occurs (i.e. CO_2 resides exclusively in the pore water of the sample), then C_1 should correspond to the product of the aqueous solubility of CO_2 under experimental conditions and porosity:

$$C_1 = C_{aq.} \cdot \phi \qquad (10\text{-}2)$$

Any higher observed C_1 values will be due to sorption or mineral reaction effects. The aqueous solubility of CO_2 in fresh water at the experimental conditions can be estimated by the relationship of Duan and Sun, 2003. At 50°C and pressures between 6 and 7 MPa the solubility of CO_2 in (salt-free) water ranges between ~870 and 960 mol/m³ H_2O (cf. Figure 10-12). Taking the porosity of 20 % for the Muderong Shale (Table 10-1), the bulk volume CO_2 concentration should amount to ~170-190 mol/m³ in the case of non-sorption and assuming complete accessibility of CO_2 to the pore water. Thus, the significantly higher C_1 values (222-389 mol/m³ Figure 10-5 and Figure 10-6) derived from the diffusion experiment indicate a considerable degree of CO_2 sorption (on organic matter and minerals) or mineral reactions in the shale sample. This value for the combined sorption/mineral reaction potential, at the first contact of CO_2 with the shale, could amount to as much as 200 mol/m³ (0.086 mmol/g). Evidently the C_1 value in the second experiment (222 mol/m³, Figure 10-6) is lower than the one in the first experiment (389 mol/m³, Figure 10-5). This indicates that some degree of irreversible sorption/reaction of CO_2 occurred during the first experiment. During the diffusion experiments no complete mineral reaction should be expected, rather changes to the surface sites. If these reactions occurred during the first diffusion experiment they would leave behind less reactive minerals. This could explain the lower CO_2 storage value observed in the second experiment. The verification of this conclusion is shown qualitatively for the Muderong Shale sorption experiments on the

shale (Figure 10-7) and the kaolinite (Figure 10-8). Follow-up measurements on identical samples revealed lower excess sorption capacities, indicating some degree of permanent fixation of CO_2 in the first run.

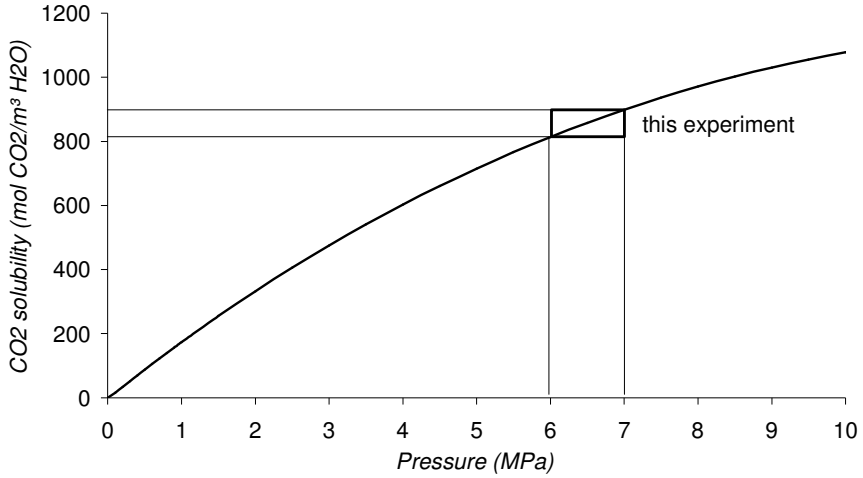


Figure 10-12. CO_2 solubility in water at 50°C assuming zero NaCl concentration calculated after Duan & Sun (2003).

The comparatively high CO_2 storage potential of the Muderong Shale has been verified by sorption experiments on powdered sample material (Figure 10-7). It can be assumed that in the shale plug used for the diffusion test, only surfaces of reactive minerals were accessible to CO_2 at the experimental time scale. This would explain the lower sorption capacities as compared to the sorption experiment on the shale powder under equilibrium conditions. Maximum sorption values for the partially saturated shale sample were ~0.25 to 0.3 mmol/g at pressure conditions identical to the diffusion experiment (6-7 MPa). This is assumed to be realistic, considering equilibration pressures and smaller particle sizes. The sorption measurements on the clay minerals demonstrated that the CO_2 sorption capacity of the Muderong Shale can be attributed entirely to the clay minerals and that sorption on the organic matter probably plays a minor role, especially given the low TOC of the Muderong (<0.5%). Considering the huge abundance of clay minerals in thick cap rock formations, there is a possibility for large CO_2 storage potential in shale sequences of sedimentary basins which is, however, limited by the poor accessibility of these low-permeability lithotypes. Under the aspect of storage safety, this buffering or retention capacity would be considered as an additional beneficial feature of shale caprocks overlying potential underground CO_2 storage sites.

10.5.4 Diffusive loss through a cap rock

In order to demonstrate the low risk of diffusive CO_2 loss through a cap rock formation a diffusive model presented by Krooss et al., 1992a, b has been used in this study. For this evaluation D_{eff} and C1 values for the first diffusion experiment (Table 10-3) have been used. Further a cap rock thickness of 100 m at a reservoir depth of 1000 m (corresponding to temperatures of 45-50°C and pressures of 10 MPa) and an infinite pure CO_2 source has been assumed. The governing equations are given in the Appendix (A5, A12)

and the resulting amounts of CO_2 that has entered the cap rock at the cap rock/reservoir interface and escaped the cap rock respectively are provided in Figure 10-13. This model demonstrates that for the parameters considered, diffusive gas breakthrough at the top boundary of the cap rock occurs after ~ 0.3 Ma. This time frame can be considered as reasonable for geological storage of CO_2, taking into consideration the relatively low thickness of 100 m. However, as geochemical alteration might occur due to CO_2/water/rock interactions, the sealing integrity could be lowered, leading to shorter diffusive breakthrough times.

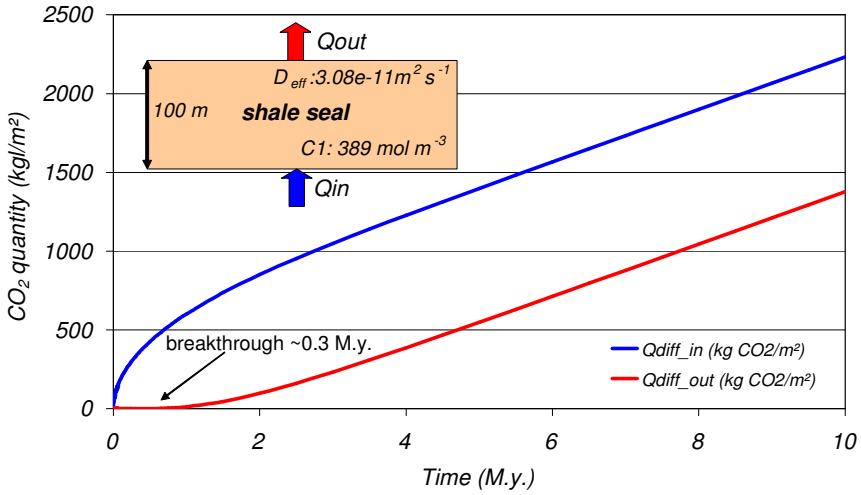


Figure 10-13. Diffusive loss through Muderong Shale, assuming cap rock thickness of 100 m and porosity of 20 %.

10.6 Conclusion and Outlook

The present study is, to our knowledge, the first comprehensive investigation of the CO_2 sorption capacity of a natural shale and individual clay minerals under conditions relevant for CO_2 subsurface storage (45-50°C and pressures up to 20 MPa). A combination of diffusion experiments and conventional gas sorption tests on the Muderong Shale from Western Australia has provided evidence for significant CO_2 storage capacity in shale sequences. The observed CO_2 fixation is attributed to a combination of aqueous solubility, geochemical reactions and physical sorption mainly on clay minerals. Sorption capacities, specifically for montmorillonite are high and of the same order of magnitude as natural coals. These findings have important consequences for the appraisal of CO_2 subsurface storage capacities. They imply higher overall CO_2 storage potentials in sedimentary basins on the one hand and lower leakage rates from reservoirs on the other hand.

The results of this study also indicate that geochemical alterations such as dissolution of silicates and precipitation of carbonates may have measurable effects on the poro-perm and diffusion properties of shales with a tendency to enhance the transport properties. But even these enhanced transport properties

are not likely to create substantial leakage problems through the undisturbed matrix of massive shale sequences. Indeed, by favouring the access to larger volumes of shale, they could positively contribute to mineral trapping of larger amounts of CO_2.

More detailed future studies are considered to be important for a more profound understanding of cap rock alteration resulting from interaction with carbon dioxide. These investigations could include additional diffusion experiments on the same sample plug to detect long term alterations caused by repetitive CO_2 interaction. Further, more detailed experimental studies on mineral alterations are suggested in order to obtain information on additional mineral CO_2 trapping as well as on possible alterations of porosity and permeability.

10.7 Appendix - Evaluation of effective diffusion coefficients

Fick's first law of diffusion describes the diffusive flux rate J_D [mass/area/time] as a function of the concentration gradient (*grad c*; units: [mass/length^4]:

$$J_D = -D \cdot grad\, c \qquad (10\text{-}3)$$

where *D* denotes the diffusion coefficient [length^2/time].

Fick's second law of diffusion is the mass balance equation:

$$\frac{\partial c}{\partial \mathrm{t}} = D \cdot \frac{\partial^2 c}{\partial x^2} \qquad (10\text{-}4)$$

The definition of effective diffusion coefficients has been discussed previously in the literature (Krooss and Leythaeuser, 1997). In this work the effective diffusion coefficient is defined as:

$$J_D = -D_{eff} \cdot grad\, c_{bulk} \qquad (10\text{-}5)$$

Here D_{eff} denotes the effective diffusion coefficient [length^2/time] and c_{bulk} is the bulk concentration of the species under consideration in the (water-saturated) porous medium (mass per volume of bulk rock).

Gas diffusion through the rock samples under the experimental conditions can be described as non-stationary diffusion through a plane sheet. The concentration of the diffusing gas in the plane sheet as a function of distance (*x*) and time (*t*) is given by Crank, 1975

$$c = c_1 + (c_2 - c_1) \cdot \frac{x}{l} + \frac{2}{\pi} \cdot \sum_{n=1}^{\infty} \frac{c_2 \cdot \cos(n \cdot \pi) - c_1}{n} \cdot \sin\left(\frac{n \cdot \pi \cdot x}{l}\right) \cdot e^{-\frac{D \cdot n^2 \cdot \pi^2 \cdot t}{l^2}} + \frac{4 \cdot c_0}{\pi} \cdot \sum_{m=1}^{\infty} \frac{1}{2 \cdot m + 1} \cdot \sin\left(\frac{(2 \cdot m + 1) \cdot \pi \cdot x}{l}\right) \cdot e^{-\frac{D \cdot (2 \cdot m + 1)^2 \cdot \pi^2 \cdot t}{l^2}} \qquad (10\text{-}6)$$

c_1 = concentration within the plane sheet at the boundary x=0 (plane sheet / gas phase interface)
c_2 = concentration within the plane sheet at the boundary x=l (top of plane sheet with length l)
c_0 = initial concentration throughout the plane sheet

Inserting equation (5-6) into equation (5-4) and integrating over time yields the cumulative amount Q_{out} of gas that has passed through the plane sheet at time *t*:

$$Q_{out} = D \cdot (c_1 - c_2) \cdot \frac{t}{l} + \frac{2 \cdot l}{\pi^2} \cdot \sum_{n=1}^{\infty} \frac{c_1 \cdot \cos(n \cdot \pi) - c_2}{n^2} \cdot \left[1 - e^{-\frac{D \cdot n^2 \cdot \pi^2 \cdot t}{l^2}} \right] + \frac{4 \cdot c_0 \cdot l}{\pi^2} \cdot \sum_{m=0}^{\infty} \frac{1}{(2 \cdot m + 1)^2} \cdot \left[1 - e^{-\frac{D \cdot (2 \cdot m + 1)^2 \cdot \pi^2 \cdot t}{l^2}} \right] \quad (10\text{-}7)$$

With the boundary conditions $c_0 = 0$, c_1 = constant ($x = 0$ and $t \geq 0$) and $c_2 = 0$ ($x = l$ and $t \geq 0$) equation (A5) simplifies to

$$\frac{Q_{out}}{l \cdot c_1} = \frac{D \cdot t}{l^2} - \frac{1}{6} - \frac{2}{\pi^2} \cdot \sum_{n=1}^{\infty} \frac{(-1)^n}{n^2} \cdot e^{-\frac{D \cdot n^2 \cdot \pi^2 \cdot t}{l^2}} \quad (10\text{-}8)$$

and for $t \rightarrow \infty$:

$$\frac{Q(t)}{l \cdot c_1} = \frac{D \cdot t}{l^2} - \frac{1}{6} \quad (10\text{-}9)$$

Rearranging equation (A7) gives

$$Q(t) = \frac{c_1 \cdot D \cdot t}{l} + Q_0 \quad (10\text{-}10)$$

with

$$Q_0 = -\frac{l \cdot c_1}{6} \qquad [\mu mol\ m^{-2}] \quad (10\text{-}11)$$

and

$$t_0 = -\frac{Q_0 \cdot l}{c_1 \cdot D} = \frac{l^2}{6 \cdot D} \quad (10\text{-}12)$$

where t_0 is denoted as lag time (Krooss and Schaefer, 1987).

For the evaluation of the diffusion experiments equation (5-9) is fitted to the experimental *Q(t)* values by means of a least-squares procedure and variation of the parameters Q_0 and t_0:

$$Q(t) = Q_0 \cdot \left(1 - \frac{t}{L} + \frac{12}{\pi^2} \sum_{n=1}^{\infty} \frac{(-1)^n}{n^2} \cdot e^{\frac{-n^2 \cdot \pi^2 \cdot t}{6t_0}} \right) \qquad \textit{(10-13)}$$

The corresponding expression for equation A6 the amount of diffusing substance that has entered the cap rock from the reservoir is given as follows:

$$\frac{Q_{in}}{l \cdot c_1} = \frac{D \cdot t}{l^2} + \frac{2}{\pi^2} \cdot \sum_{n=1}^{\infty} \frac{1}{n^2} \cdot \left(1 - e^{\frac{-D \cdot n^2 \cdot \pi^2 \cdot t}{l^2}} \right) \qquad \textit{(10-14)}$$

11 Interaction of Carbon Dioxide with Na-exchanged Montmorillonite at Pressures to 640 Bars: Implications for CO_2 Sequestration

11.1 Introduction

Sequestration of anthropogenic CO_2 in deep sedimentary strata is a widely considered option for reducing greenhouse gas emissions. The challenge of injecting CO_2 into sedimentary rocks is to reliably predict the long-term behavior of the CO_2; this knowledge is essential for both the commercial and political viability of this carbon storage methodology. In particular, the long-term efficacy of the impermeable cap rock in sealing the reservoir requires evaluation. Because this cap rock is generally a shale or mudstone rich in clay minerals, possibly including swelling clays (Abdou and Ahmaed, 2010), we examined the reaction of the swelling clay, montmorillonite (a common smectite), with CO_2.

Krooss et al., 2003 considered CO_2 adsorption and diffusion for coal, sandstone, and shale and found that shales can retain CO_2, although the mechanisms involved are not clear. Nuttall et al., 2005 and Nuttall et al., 2009 evaluated CH_4 and CO_2 sorption by black shales in Kentucky and nearby regions. They associated the gas sorption capacity with shale organic matter content, although their defined trend showed significant outliers for CO_2. This suggests that other factors need to be considered in evaluating CO_2 sorption capacity, such as clay mineralogy. This is confirmed by Fripiat et al., 1974 who studied smectite exchanged with different interlayer cations. These smectites were charged with CO_2 at pressures <1 bar and temperatures of 25 and -70°C. It was concluded that in addition to sorption in inter-lamellar space CO_2 also intercalates the interlayer space and causes swelling. This was found rather for the low than for the high temperature measurement.

Using triaxial flow and manometric sorption setups, Busch et al. (2008) examined sorption and diffusion of CO_2 in samples from the Muderong Shale, Australia, and in other selected clay samples to determine the sealing performance and storage potential for CO_2 of this media at temperatures of 45-50°C and elevated pressures (< 20 MPa), thus at conditions of pressure (*P*) and temperature (*T*) common for deep sedimentary strata. They found that CO_2 sorption on clay surfaces is variable (< 1 mmol/g for Muderong Shale, < 1.6 mmol/g for smectite, but lower for illite and kaolinite). Busch et al. (2008) suggested that the CO_2 retention in these samples is related to CO_2 dissolution in water and sorption onto clay and that alteration reactions at high pressures affect the specific surface area of the constituent particles, which would change over time with repeated exposure to CO_2. Wollenweber (2010) found similar results for carbonate rocks, with sorption capacities up to 0.3 mmol/g for marlstone and less than 0.2 mmol/g for relatively pure limestone.

Primarily by using computer modeling and diffuse-reflectance infrared spectroscopy, Romanov et al., 2010 tentatively concluded that CO_2 may intercalate in the interlayer of smectite. Botan et al., 2010 performed molecular simulation studies of CO_2 intercalation into Na-exchanged montmorillonite and found that CO_2

was stable in the interlayer space, but they did not find either expansion or contraction of the interlayer space as a result of CO_2 intercalation.

Atomic-scale structural studies involving smectite tend to be experimentally demanding. Intercalation reactions at non-ambient conditions often reverse when the experimental charges are returned to room temperature and pressure. Thus, structure-related experimental data using diffraction (or spectroscopic) techniques are more informative when the experiments are done at the *PT* conditions of interest. To obtain reliable structure information, a high-pressure environmental chamber was developed to study mineral interactions with gases at elevated pressure, using X-ray diffraction (XRD) as the analytical tool (Koster van Groos and Guggenheim, 2009; Koster van Groos et al., 2003). The focus of the study presented here was to investigate the reaction of smectite containing varying amounts of interlayer H_2O with CO_2 gas and supercritical fluid to evaluate whether CO_2 can intercalate within swelling clays under subsurface conditions likely to exist in carbon sequestration reservoirs.

11.2 Experimental methods

11.2.1 High-pressure environmental chambers (HPECs)

Two distinct HPEC designs have been constructed and used in our laboratory. A reflection-mode chamber (RHPEC; Koster van Groos et al., 2003) is mounted on a Siemens D5000 θ-θ powder diffractometer. This chamber can be used to 100 bars and to 100°C. Owing to the long X-ray path length within the RHPEC (nearly 2 cm), the X-ray intensity exiting the chamber drops rapidly with pressure. The attenuation depends on the density of the gas/fluid used to pressurize the chamber; for CO_2, the RHPEC cannot be effectively used at pressures above about 40-50 bars.

A second chamber was developed to study the interaction of minerals with a variety of fluids, including gases, supercritical fluids, and liquids, *e.g.*, brines; it can also analyze bulk solid samples. This chamber may be used to 1000 bars and 200°C. The chamber has a transmission-mode X-ray geometry (THPEC). The THPEC mounts on a Bruker D8 three-circle diffractometer, with X-rays transmitted through 1-mm thick diamond windows with O-ring pressure seals. Both entry and exit windows are adjustable to alter the irradiated volume of the sample. In the present experiments, 10 to 12 mg samples of smectite were placed between the diamond windows, which were then adjusted to hold the sample at the center of the chamber with window-to-window distances of 0.25 - 0.5 mm.

11.2.2 Starting material

A Na-rich montmorillonite (Clay Minerals Society Source Clay SWy-2, Costanzo and Guggenheim, 2001 and papers therein) was used as starting material. To remove soluble salts that affect grain-size separation, aliquots of SWy-2 were sonified in distilled water and centrifuged to recover the clay. This washing was repeated until the addition of $AgNO_3$ to the supernatant showed no precipitation of AgCl. Next, the aliquots were grain-size separated to the < 2 μm fraction following Moore and Reynolds, 1997 (pp. 211-213), which

removes all or most of the non-clay material. Next, this fraction was cation exchanged by adding 1 M NaCl solution to the clay aliquots, agitating the mixture with a sonicator, centrifuging the resulting suspension to recover the clay, pouring off the supernatant, then repeating the process two additional times. After the final cation exchange, the aliquots were washed until addition of $AgNO_3$ to the supernatant showed no precipitation of AgCl. The samples, hereafter referred to as NaSWy2, were combined and stored in sealed glass bottles.

All experiments used "bone dry" grade CO_2 from Airgas, which was either used at tank pressure or pressurized using an external pump before being introduced into the respective HPEC.

11.2.3 Sample preparation - THPEC

A 2 g batch of NaSWy2 was dried at 200°C in a muffle furnace in air for 2 days. (This temperature was used for comparison with a sorption study at RWTH Aachen University, Germany.) After drying, the NaSWy2 formed aggregates and thick films adhering to the sides of the crucible. Some material was scraped immediately into an agate mortar, then the crucible was placed in a container of Drierite (anhydrite) desiccant. The clay in the mortar cooled to room temperature in air and was broken into mm-size aggregates. A 10 mg sample of this air-cooled clay (sample TAc) was analyzed in the THPEC. A sample of the clay that had cooled in the desiccator was also analyzed (sample TDc).

The dried NaSWy2 was crushed to pass a 75 µm sieve. A sample of this crushed material was analyzed immediately (sample TGc), while the remaining material was stored in the desiccator; later, a sample was taken from the desiccator and placed in a separate container with a saturated solution of $MgCl_2$ (~33% relative humidity, RH) for 9 days.

11.2.4 Sample preparation - RHPEC

Thin, oriented aggregate mounts of NaSWy2 on small glass slides (~13x18 mm) were prepared using the Method 2 procedure in Koster van Groos and Guggenheim, 2009. One mount was prepared using the method of Moore and Reynolds, 1997 (pp. 214-5), which produces a thicker sample. The samples were either placed directly in a container at a controlled humidity above a saturated salt solution ($MgCl_2$, 33%RH; or NaCl, 75%RH) or dried in an oven for several days at 115°C. One of the oven-dried slides was later placed in an 11%RH atmosphere (over a saturated solution of LiCl), whereas the other was placed in a desiccator. The samples were removed from the controlled humidity atmospheres and loaded quickly in the RHPEC. The preparation methods for the THPEC and RHPEC samples are summarized in Table 11-1.

Table 11-1. Sample preparation summaries. Asterisks denote samples exposed to He instead of CO_2.

Sample	Preparation
TAc	Oven dried at 200°C, allowed to cool at room conditions, loaded as large (mm) aggregates
TDc	Oven dried at 200°C, cooled in desiccator, loaded as large (mm) aggregates
TGc	As TDc, then crushed to powder in mortar at room atmosphere
THe*	Same preparation as TGc, in desiccator for 5 months, then at 33%RH for 9 days
T33	Same sample as THe, vented to 1 bar He before adding CO_2
Rov	Oven dried at 115°C
R11	Oven dried at 115°C, held at 11%RH for 12 days
RHe*	Oven dried at 115°C, held at 11%RH for 17 days
R33	Held at 33%RH for at least 4 days
R75	Held at 75%RH for several days
R75th	Thick (Moore and Reynolds, 1997) mount, held at 75% RH for several days

11.2.5 Experimental methods - THPEC

The THPEC is equipped with a jacket through which heated silicone oil from a NESLAB heater/circulator may flow to control temperature (see schematic, Figure 11-1). Temperature was measured with a type-K thermocouple located ~1 mm from the sample. The THPEC experiments were run at or near 45°C, although data collection was started at a lower temperature for some experiments. Pressure was monitored using an external Bourdon-tube style Heise gauge (range 0-1000 bar, believed accurate to ±0.1%). The THPEC was not evacuated of air or flushed before experiments to avoid dehydrating the sample. CO_2 pressures to ~60 bars were obtained using bottle gas pressure and higher pressures were obtained using a SC Hydraulic Engineering Corporation pump. Samples were allowed to equilibrate with the CO_2 (gas or supercritical fluid, depending on pressure) for varying lengths of time (hold time) before analysis. The hold time listed is the interval between the adjustment of pressure and the start of an X-ray data-collection frame (two-dimensional XRD photograph) or between the start of two sequential frames. For comparison, several series of experiments were made using He. The temperature, pressure, and hold time for each THPEC experiment are summarized in Table 11-2.

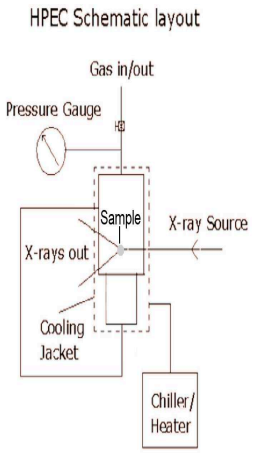


Figure 11-1. Simplified schematic of the THPEC.

The THPEC was mounted on the Bruker D8 diffractometer with a Mo X-ray tube, which was operated at 45 kV and 25 mA. The diffractometer was equipped with a graphite monochromator, MonoCap (0.3° divergence) collimator, and APEX CCD area detector (1024 x 1024 pixels) at a distance of 120 mm from the sample center. All THPEC data frames were collected with the APEX detector centered on 2θ = 0°, which produced a range in data of 2θ = 1.5 to 13.6° (*d* = 27.1 to 3.00 Å). The THPEC frames were collected for times varying from 600 s (10 min) to 2400 s (40 min), with most frames collected for 1200s (20 min). Data collection used the Bruker application SMART (v. 5.6.635, 2010). A typical THPEC data frame is presented in Figure 11-2.

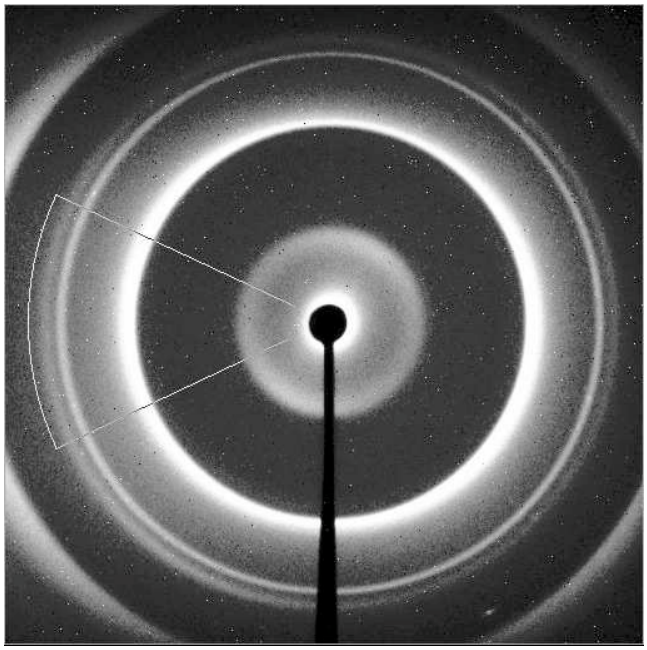


Figure 11-2. Raw data from the THPEC (frame TAc0) showing the integration area (the wedge left of the beam-stop shadow). Integration of this frame resulted in the plot shown in Figure 11-3.

Table 11-2. Experimental conditions for THPEC data collection and resulting (001) peak center positions and spacings. Most THPEC frames were collected for a 1200 s exposure time, with exceptions noted. Pressures in italics denote P(He) instead of P(CO_2).

Frame	T (°C)	P(CO_2 or *He*)	Hold time	Peak center (°)	*d*(001) (Å)
TAc0[1]	32[3]	0 bars	-	3.93	10.37
TAc1[2]	36[3]	52 bars	0 hr	3.64	11.20
TAc2[2]	46	44 bars	11 hr 20 min	3.64	11.20
TAc3[2]	46	36 bars	11 hr 20 min	3.66	11.14
TAc4[2]	46	29 bars	11 hr 20 min	3.68	11.08
TAc5[2]	46	21 bars	11 hr 20 min	3.71	10.99
TDc1	25[3]	0 bar	-	4.03	10.12
TDc3	45	5 bars	2 hr	4.01	10.17
TDc4	45	13 bars	18 hr	4.02	10.14
TDc5	45	21 bars	30 min	4.01	10.17
TDc6	46	41 bars	30 min	3.98	10.24
TDc7	46	36 bars	22 hr	4.01	10.17
THe0	42[3]	*0 bar*	0 hr	3.70	11.02
THe60	46	*59 bars*	1 hr	3.70	11.02
THe60a	46	*59 bars*	3 hr 40 min	3.68	11.08
THe60b	46	*59 bars*	3 hr 40 min	3.66	11.14
THe60c	46	*59 bars*	3 hr 40 min	3.63	11.24
T33-0	45	*1 bar*	< 30 min	3.62	11.27
T33-60	46	57 bar + *1 bar*	1 hr	3.32	12.29
T33-60a	46	57 bar + *1 bar*	4 hr	3.34	12.21
TGc1	24[3]	0 bar	-	3.58	11.39
TGc7[2]	46	48 bars	14 hr	3.35	12.18
TGc11	46	60 bars	1 hr	3.34	12.21
TGc80a	46	80 bars	0 hr	3.38	12.07
TGc80c	46	65 bars	1 hr	3.38	12.07
TGc100b	46	105 bars	30 min	3.38	12.07
TGc200c[2]	46	204 bars	6 hr 40 min	3.38	12.07
TGc400b	46	414 bars	30 min	3.32	12.29
TGc14	47	640 bars	1 hr	3.36	12.14
TGc50D	45	53 bars	0 hr	3.28	12.44
TGc40D	45	41 bars	0 hr	3.31	12.33
TGc30D	46	32 bars	0 hr	3.36	12.14
TGc20D	46	21 bars	0 hr	3.40	12.00
TGc15	46	16 bars	0 hr	3.44	11.86
TGc16	46	11 bars	20 min	3.48	11.72
TGc17	45	6 bars	20 min	3.52	11.59
TGc18	45	3.5 bars	20 min	3.62	11.27
TGc19	45	1 bar	30 min	3.93	10.38

[1] - Frame collected over 600 s

[2] - Frame collected over 2400 s

[3] - Frames started at temperatures significantly below the set point (45°C). Temperature increased toward the set point over the course of data collection.

11.2.6 Experimental methods - RHPEC

The RHPEC samples were run at 25 ± 3°C. Pressure conditions were obtained from a digital Heise gauge. The RHPEC was not evacuated or flushed before experiments to avoid changing the water content of the sample. After each pressure change, samples were equilibrated for a minimum of 10 min before analysis. Gas pressure and results for RHPEC experiments are summarized in Table 11-3.

The RHPEC was mounted on the Siemens D5000 diffractometer with a Cu X-ray tube, which was operated at 40 kV and 25 mA. Each RHPEC scan used a 0.02 degree step size and 1.25 s dwell time. Data collection used the DataScan application (MDI, v. 4.3.355, 2005).

11.3 Data processing

The THPEC data were corrected for air scattering and other background. An empirical correction was applied using a frame collected from the THPEC packed with fluorite (CaF_2) with 0.5 mm spacing. Fluorite has no low-angle diffraction peaks, so the low-angle intensity in the fluorite frame was essentially from background scattering. Fluorite has a higher X-ray attenuation factor than montmorillonite; the resulting background intensity of the fluorite frame was lower than the data frame intensity for all experiments. This background frame was subtracted from the experimental data frame.

Background-corrected THPEC data were integrated over arcs of constant 2θ by the Bruker application GADDS (v. 4.1.14, 2003), using a bin size of 0.1° and an arc length of 50°, to generate intensity vs. 2θ datasets. Given the geometry of the experiment and the pixel density of the area detector, the statistical advantage of using smaller bin sizes was negligible.

Typical integrated THPEC and RHPEC data are presented in Figure 11-3. The THPEC diffraction patterns are similar to random mount patterns for turbostratic smectite (Moore and Reynolds, 1997, p. 338). The RHPEC samples show only (00*l*) peaks owing to preferred orientation; the higher order (002), (003), and (004) peaks are apparent for scans with a sharp (001) peak. No impurity phases were detected in the THPEC or RHPEC samples.

The (001) peak centers at half maximum for both THPEC and RHPEC data are listed in Table 11-2 and Table 11-3, respectively. Peak centers determined from half maximum peak heights are a more reliable determination than using the peak summit. The (001) peak center (which is measured directly as an angle) corresponds to a specific (001) spacing or *d*(001) value, which is a distance calculated from the Bragg equation (e.g., see Moore and Reynolds, 1997, p. 69). This value represents an average interlayer spacing or repeat distance ("*d*" in Figure 11-4) over all diffracting particles in the sample.

Table 11-3. Experimental conditions for RHPEC data collection and peak center results. Most RHPEC scans were collected after a 10 min hold time at pressure (20 min for sample R75th; exceptions noted). Experiments were conducted at ambient temperature (~25°C). Pressures in italics denote P*(He) instead of* P*(CO_2).*

Scan	P(CO_2 or *He*)	Center (°)	d(001) (Å)	Scan	P(CO_2 or *He*)	Center (°)	d(001) (Å)
Rov1	0 bar	8.94	9.89	R75-1	0 bar	6.88	12.87
Rov2	1 bar	8.92	9.92	R75-2	0 bar	6.88	12.87
Rov3	2 bar	8.88	9.96	R75-3	1 bar	7.12	12.43
Rov4	5 bar	8.94	9.89	R75-4	2 bar	7.12	12.43
Rov5	10 bar	8.88	9.96	R75-5	3 bar	7.06	12.54
Rov6	21 bar	8.78	10.07	R75-6	4 bar	7.10	12.47
Rov7[1]	31 bar	8.62	10.26	R75-7[1]	5 bar	7.06	12.54
Rov8	2 bar	8.78	10.07	R75-8	6 bar	6.98	12.68
RHe1	*0 bar*	7.74	11.43	R75-9	7 bar	6.98	12.68
RHe2	*1 bar*	7.62	11.61	R75-10	8 bar	6.94	12.76
RHe3	*2 bar*	7.70	11.49	R75-11	9 bar	6.96	12.72
RHe4	*3 bar*	7.66	11.55	R75-12[1]	10 bar	6.96	12.72
RHe5	*4 bar*	7.60	11.64	R75-13	11 bar	6.96	12.72
RHe6	*5 bar*	7.66	11.55	R75-14	12 bar	6.94	12.76
RHe7	*10 bar*	7.50	11.80	R75-15	13 bar	6.98	12.68
RHe8	*21 bar*	7.60	11.64	R75-16	14 bar	6.98	12.68
RHe9	*31 bar*	7.58	11.67	R75-17	15 bar	6.92	12.79
RHe10	*41 bar*	7.58	11.67	R75-18	16 bar	6.94	12.76
RHe11	*52 bar*	7.52	11.77	R75-19	17 bar	6.96	12.72
R11-1	0 bar	8.88	9.96	R75-20	18 bar	6.92	12.79
R11-2	1 bar	8.86	9.98	R75-21	20 bar	6.86	12.90
R11-3	2 bar	8.88	9.96	R75-22	21 bar	6.88	12.87
R11-4	3 bar	8.80	10.05	R75-23	22 bar	6.88	12.87
R11-5	8 bar	8.80	10.05	R75-24	23 bar	6.92	12.79
R11-6	10 bar	8.78	10.07	R75-25	24 bar	6.90	12.83
R11-7	16 bar	8.58	10.31	R75-26	25 bar	6.88	12.87
R11-8	21 bar	8.50	10.41	R75-27	26 bar	6.90	12.83
R11-9[1]	31 bar	8.40	10.53	R75-28	29 bar	6.82	12.98
R11-10	14 bar	8.32	10.63	R75-29	31 bar	6.80	13.02
R11-11	11 bar	8.24	10.74	R75th1	0 bar	7.04	12.57
R11-12	8 bar	8.28	10.68	R75th2	0 bar	7.04	12.57
R11-13	6 bar	8.24	10.74	R75th3	1 bar	7.06	12.54
R11-14	4 bar	8.26	10.71	R75th4	1 bar	7.04	12.57
R11-15	3 bar	8.36	10.58	R75th5	2 bar	7.04	12.57
R11-16	2 bar	8.36	10.58	R75th6[1]	2 bar	7.06	12.54
R11-17	1 bar	8.48	10.43	R75th7	2 bar	7.06	12.54
R33-1	0 bar	7.06	12.54	R75th8	3 bar	7.06	12.54
R33-2	1 bar	7.06	12.54	R75th9	3 bar	7.04	12.57
R33-3	2 bar	7.06	12.54	R75th10	4 bar	7.06	12.54
R33-4	6 bar	7.04	12.57	R75th11	6 bar	7.06	12.54
R33-5	10 bar	7.06	12.54	R75th12	10 bar	7.04	12.57
R33-6	22 bar	7.04	12.57	R75th13	26 bar	7.02	12.61
R33-7[1]	33 bar	7.04	12.57	R75th14	31 bar	7.06	12.54
R33-8	14 bar	7.06	12.54	R75th15[1]	41 bar	7.02	12.61
R33-9	11 bar	7.08	12.50	R75th16	19 bar	7.08	12.50
R33-10	6 bar	7.08	12.50	R75th17	11 bar	7.06	12.54
R33-11	3 bar	7.08	12.50	R75th18	7 bar	7.06	12.54
R33-12	2 bar	7.08	12.50	R75th19	5 bar	7.06	12.54
R33-13	1 bar	7.10	12.47	R75th20	3 bar	7.08	12.50
R33-14	1 bar	7.10	12.47	R75th21	2 bar	7.06	12.54
				R75th22	1 bar	7.08	12.50
				R75th23	1 bar	7.06	12.54

[1] – Sample was held ~16 h between this scan and the next scan.

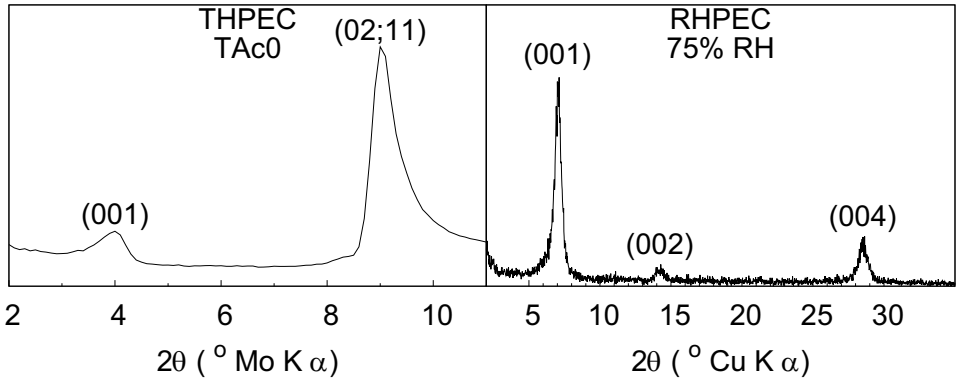


Figure 11-3. Diffraction patterns of typical starting material (samples TAc and R75th). The THPEC data have been integrated, but no background correction has been applied. THPEC samples are random mounts and show the prominent, asymmetric (02;11) turbostratic band as well as the (001) interlayer peak. RHPEC samples are oriented aggregates on glass slides and show only (00l) series peaks. No impurity peaks are visible.

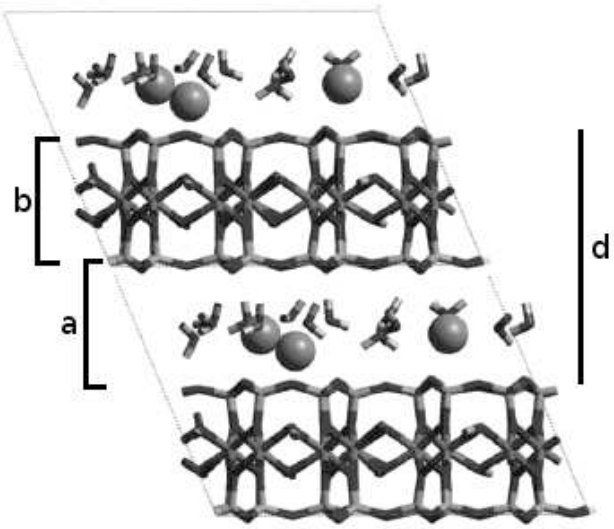


Figure 11-4. Structure of Na-exchanged montmorillonite (after Cygan et al. 2004). Area "a" is the interlayer, including interlayer Na^+ (spheres) and H_2O groups, whereas "b" shows the silicate sheet. Region "a" is expandable, whereas region "b" is essentially rigid. "d" shows the d*(001) layer repeat distance, which is about 12.1 Å in this figure.*

11.4 Experimental results

11.4.1 THPEC results

Sample TAc. At 0 bars, the sample has a (001) spacing of 10.37 Å, increasing $P(CO_2)$ to 52 bars results in an increase in the (001) spacing to 11.20 Å. When $P(CO_2)$ was gradually reduced to 21 bars the (001) spacing decreased to 10.99 Å (Figure 11-5a).

Sample TDc. In this sequence, the sample was taken from the desiccator without apparent change by ambient humidity. Increasing $P(CO_2)$ to 52 bars did not result in an increase in the (001) spacing (Figure 11-5b).

Sample THe/T33. In this sequence (Figure 11-5c), sample *THe* was stored at RH = 33%. After exposure to P(He) = 59 bars, the (001) spacing changed little between scans over 12.5 h (Frame *THe0* - *THe60c*, Table 11-2). Next, He was released and the chamber was pressurized with 57 of CO_2 resulting in an increase in (001) spacing to 12.21 Å (Frame T33-0 – T33-60a, Table 11-2).

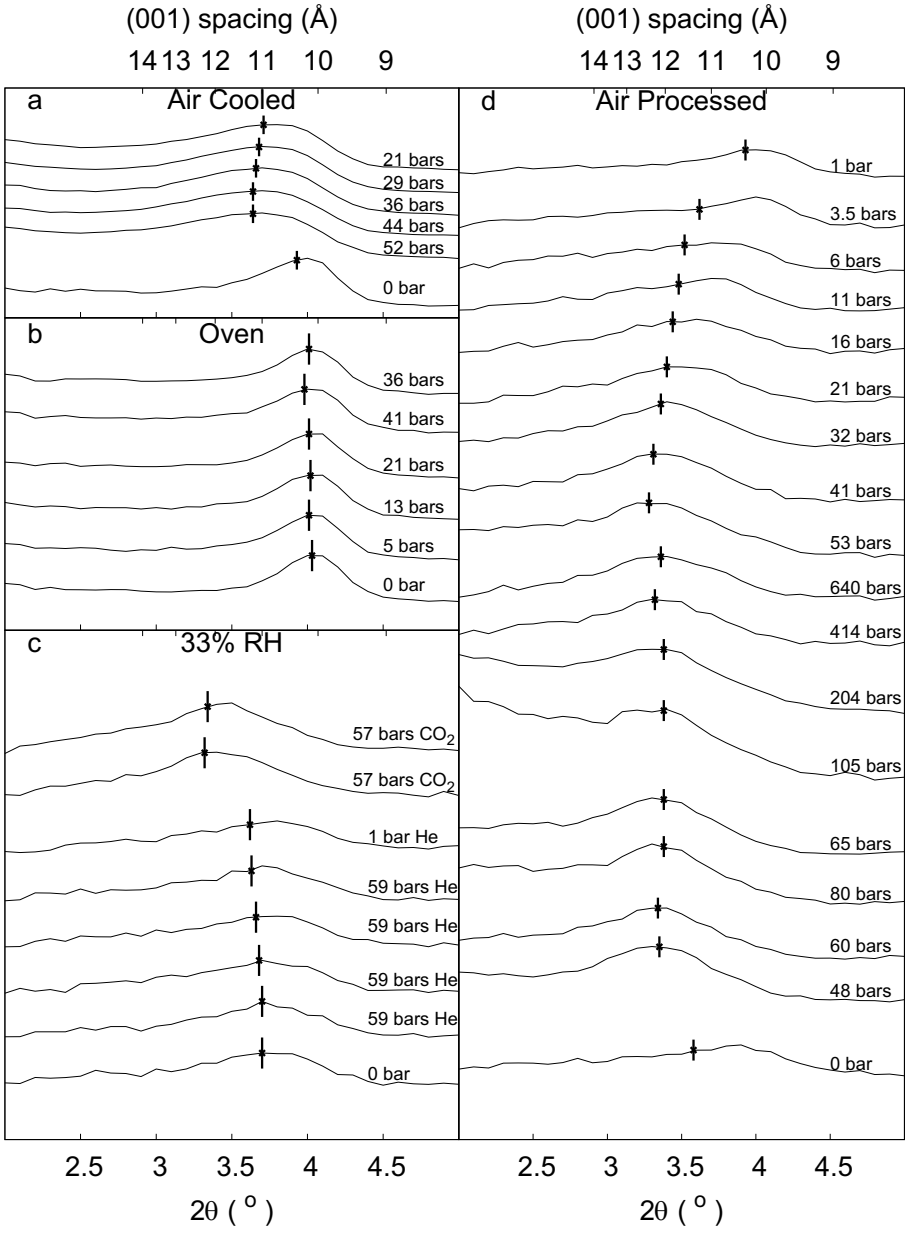


Figure 11-5. Data, collected using Mo radiation, integrated and background corrected, showing the migration of the (001) peak as a function of CO_2 (or He) partial pressure. Intensities are normalized by exposure time. Data are shown in chronological order from bottom to top. See Table 11-1 for sample preparation details. ***(a)*** *Sample TAc.* ***(b)*** *Sample TDc.* ***(c)*** *Sample THe/T33.* ***(d)*** *Sample TGc.*

Sample TGc. Pressurizing the chamber to 48 bars of CO_2 resulted in a sharpening of the peak and a shift to a higher (001) spacing from 11.39 to 12.18 Å. Further increase in pressure to 640 bars resulted in little change of the (001) spacing (Frame TGc7 – TGc14, Table 11-2). A decrease to $P(CO_2)$ to 53 bars increased the (001) spacing to 12.44 Å. Finally, a gradual reduction of pressure from 53 bars to 1 bar resulted in a considerable decrease in *d*(001) to 10.38 Å (Figure 11-5d), which is significantly lower than the original spacing at 11.39 Å. This hysteresis effect is shown in Figure 11-6, as well as the general relation between $P(CO_2)$ and layer spacing for this sample and sample R11 (see below).

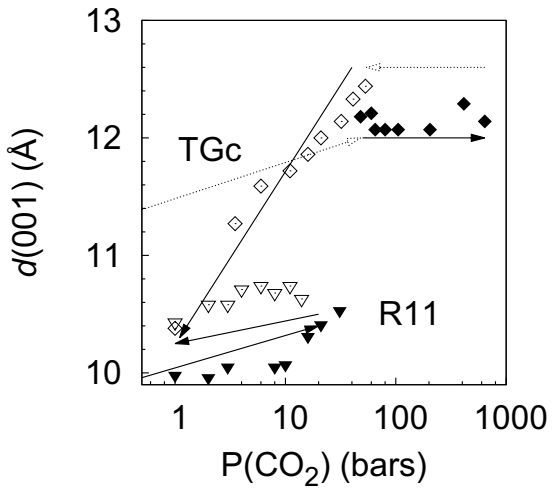


Figure 11-6. Center of the (001) peak plotted against partial pressure of CO_2 for samples TGc (diamonds) and R11 (triangles). Solid symbols indicate that data were collected while the pressure was being increased, and open symbols indicate that data were collected as the pressure was lowered. Arrows indicate the chronological progress of the experiment; dashed arrows indicate a pressure range that was passed over with no data frames collected.

In contrast to the (001) peak, the (02;11) peak (Figure 11-3), a diffraction band representing turbostratic layers, retains its position and shape, as is expected because diffraction bands originate from within the layers and they are not related to layer spacing.

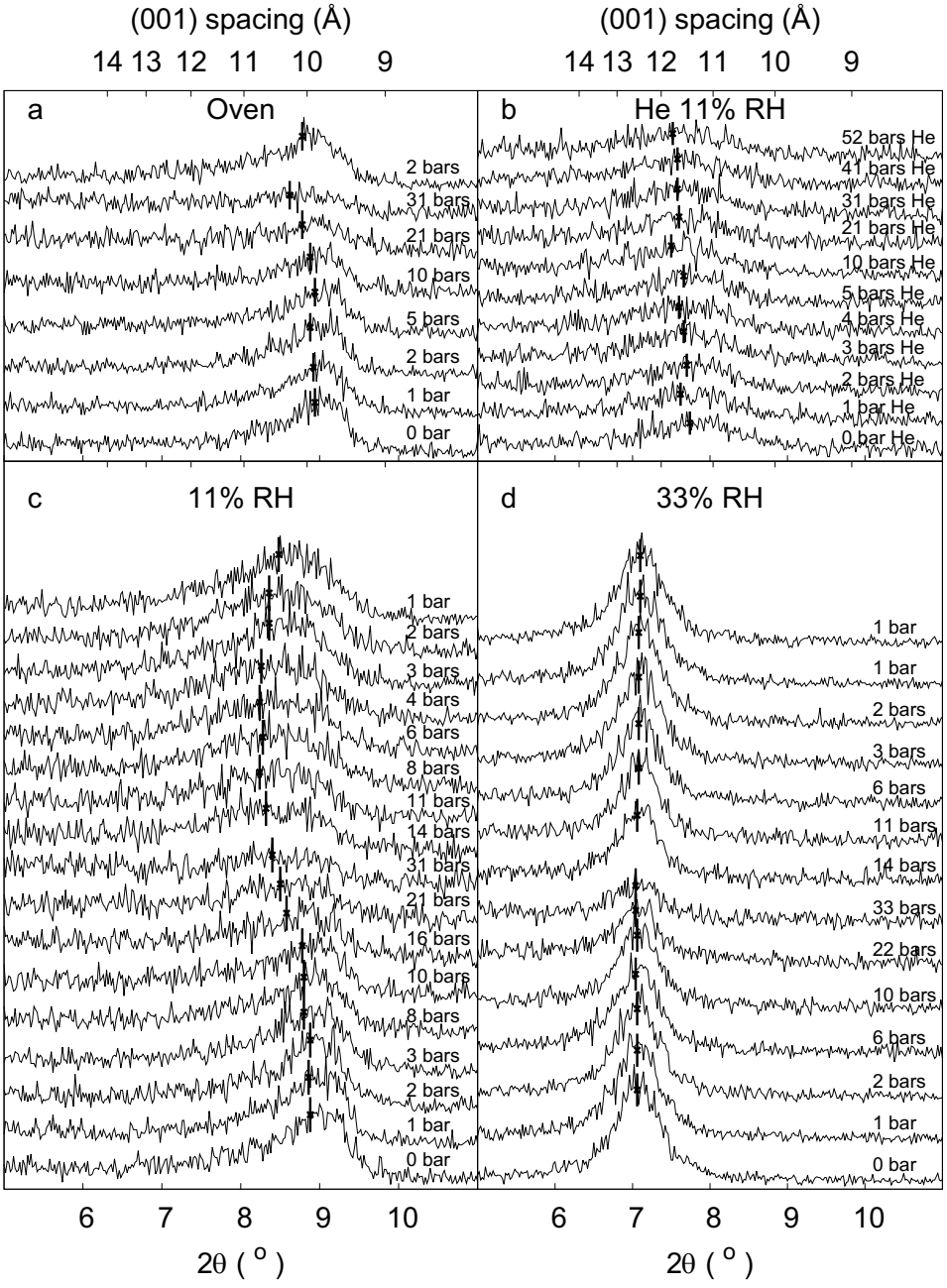
11.4.2 RHPEC results

Sample Rov. The diffraction patterns for this sample (Figure 11-7a) do not change or change slightly between 0 and 10 bars. At higher pressures (21 - 31 bars), the intensity of the (001) peak diminishes and the peak occurs at slightly higher (001) spacings, although the precise location is uncertain owing to the reduction of peak size. The final scan, at 2 bars, is similar to the earlier scan at 2 bars.

Sample RHe. In this sequence of scans with He pressure, the peaks are not well developed. There is a small and irregular increase in (001) spacing with pressure (Figure 11-7b).

Sample R11. From 0 – 10 bars, the (001) spacing (9.98 – 10.07 Å) does not change in position. At higher CO_2 pressures (16 – 31 bars), the (001) spacing increases with pressure (to 10.53 Å), and they show a further

increase (to 10.74 Å) at 6 bars. As pressure is released further the spacing is reduced until the pressure reaches 1 bar (10.43 Å) (Figure 11-7c). Note in Figure 11-6 that the *d* values do not return to the original spacing, indicating hysteresis.



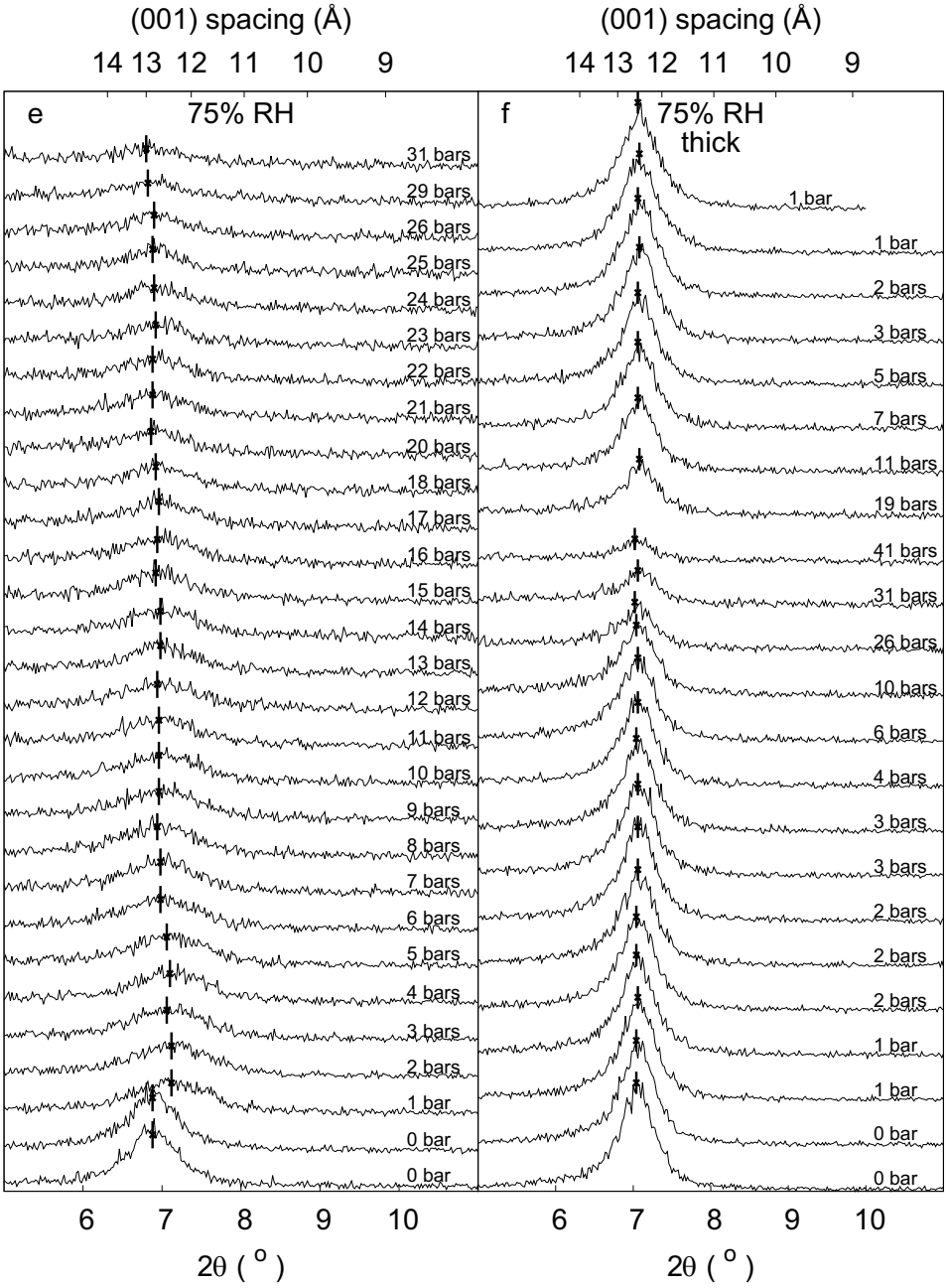


Figure 11-7. RHPEC data, collected using Cu X-rays, showing the migration of the (001) peak as a function of CO_2 (or He) partial pressure. Data are shown in chronological order from bottom to top. See Table 11-1 for sample preparation details. ***(a)*** *Sample Rov.* ***(b)*** *Sample RHe.* ***(c)*** *Sample R11.* ***(d)*** *Sample R33.* ***(e)*** *Sample R75.* ***(f)*** *Sample R75th.*

Sample R33. No significant change in the (001) spacing (~12.54 Å) was observed for this sample over the pressure range of $P(CO_2)$ = 0 - 33 bars (Figure 11-7d).

Sample R75. This sample (Figure 11-7e) showed an initial decrease in (001) spacing (12.87 Å) at $P(CO_2)$ = 0 to 12.45 Å at 1 bar. This decrease in the (001) spacing of the R75 sample from 12.8 Å in air to 12.5 Å with the addition of 1 bar CO_2 suggests a change in relative humidity upon loading in the environmental

chamber. At higher pressures, the (001) spacing is not well defined but appears to gradually increase to *d*(001) of ~13.0 Å at 31 bars, larger than its original starting value.

Sample R75th. As in sample R33, a ≤ 0.11 Å change in (001) spacing was observed for this sample between $P(CO_2)$ = 0 – 41 bars (Figure 11-7f). Repeated experiments with longer hold times (up to 16 h) did not produce significantly different results.

11.5 Discussion

Figure 11-8 shows the maximum *d*(001) for each sample as a function of the initial *d*(001). The initial H_2O content of the interlayer is measured by the *d*(001) value and ranges from little to no H_2O [*d*(001) = ~9.89 Å] to one H_2O plane [*d*(001) = ~12.5 Å]. The straight line represents no interlayer expansion. Significant expansion in the presence of CO_2 occurs when the initial *d*(001) values are between 10 and 11.5 Å; no expansion is observed with initial *d*(001) values above 12.5 Å. Thus, the intercalation of CO_2 in NaSWy2 is a function of the H_2O content of the interlayer. It is assumed that CO_2 is able to intercalate the interlayer space in collapsed smectites (*d*(001)~10 Å) which, however does not cause swelling. This is based on measurements by Busch et al. (2008) who showed significant CO_2 sorption for illite and smectite clays dehydrated at 200°C for several hours. Contrary to our finding, Fripiat et al. (1973) report interlayer expansion for collapsed smectite up to 12.3 Å at low (-70°C) temperature. The reasons are unclear and might be related to the larger sorption amounts that can be expected at the low temperature used in the Fripiat study.

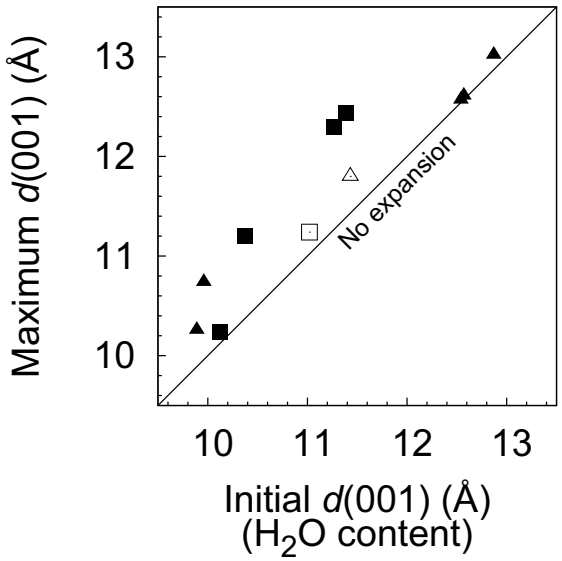


Figure 11-8. Maximum value of the (001) spacing under CO_2 or He pressure as a function of the initial (001) spacing (affected by H_2O content). Boxes signify THPEC samples and triangles signify RHPEC samples. Filled symbols show the results of CO_2 experiments and open symbols signify He experiments.

This study suggests that at low H_2O concentrations in the interlayer, interlayer swelling caused by sorbing CO_2 is dependent on the presence of a small number of H_2O molecules. Similarly, if the interlayer contains about one H_2O layer, possibly further CO_2 intercalates into the structure but causes no fuether interlayer expansion. At intermediate interlayer H_2O content, e.g., *d*(001) = 11.4 Å, CO_2 enters the interlayer, but does not exceed one layer of H_2O + CO_2 [*d*(001) ≈ 12.5 Å].

Montmorillonite forms aqueous complexes that are well understood. The hydration of montmorillonite interlayers involves discrete numbers of H_2O groups. These cause the individual interlayers to assume one of a series of characteristic spacings (MacEwan and Wilson, 1984). The silicate (2:1) layer is rigid or semi-rigid and is little affected by H_2O sorption (Figure 11-4); the different (001) spacings are caused by the presence of different numbers of H_2O planes within the interlayer. A montmorillonite interlayer with no H_2O has a layer-to-layer spacing of about 9.6 Å (with a designation of 0W in the notation of Ferrage et al., 2005, whereas an interlayer with one plane of H_2O groups (1W) has a spacing near 12.5 Å. The series continues, with ~15.5 Å (2W); larger spacings occur also. Bulk montmorillonite often shows broad, low intensity diffraction peaks centered at intermediate positions owing to the presence of interlayers with different spacings in random sequence in the individual crystallites. Other conditions could result in the presence of multiple distinct peaks, but is not observed in the diffraction data presented here.

Our initial diffraction data (before exposure to CO_2) for each sample fit this paradigm (Figure 11-5 and Figure 11-7). Sample TDc, which was thoroughly dried, had dominantly 0W interlayers, resulting in a relatively sharp and intense (001) peak centered near the 0W value (~ 9.9 Å). Sample Rov, also dried in an oven, presumably adsorbed a small number of H_2O during handling, resulting in a diffraction peak near 10 Å but showing some intensities representing higher *d*(001). Other THPEC samples (TAc, THe/T33, and TGc) and sample R11 show broad, asymmetric, low-intensity peaks at d(001) values of 10.37 – 12.44 Å, which indicate that both 0W and 1W interlayers are present. Sample R33, a thin mount on a glass slide, equilibrated more fully with the atmosphere inside the aging container and was more hydrated than the corresponding bulk THPEC sample THe/T33; it was dominated by 1W layers, as seen by Ferrage et al., 2005 for samples at similar relative humidity. R75th was similar, and may not have reached complete equilibrium at 75% RH. R75 had mostly 1W interlayers and a few interlayers with 2W spacings (Ferrage et al., 2005).

Figure 11-8 shows an apparent nonlinear relationship between the initial *d*(001) of NaSWy2 and the maximum *d*(001) under CO_2. Sample TDc, with an initial (001) spacing of ~10 Å and mainly 0W interlayers, did not expand. Samples Rov and R11, although their peak centers indicated a spacing <10 Å, had long tails to lower angles and must have contained a considerable number of 1W layers among the dominant 0W layers; they expanded less than 1 Å. Samples with initial (001) spacings of 10-11.5 Å expanded ~1 Å, or ~10%; these samples contained sizable initial quantities of both 0W and 1W interlayers. The three samples with initial (001) spacings ≥ 12.5 Å did not swell. These samples had mainly 1W interlayers.

These observations suggest a model for CO_2 intercalation. Montmorillonites intercalated with aqueous complexes contain complex cations and/or polar species, owing to the negative charge on the silicate layers. Nonpolar molecules do not usually intercalate. Although CO_2 is a rigid, nonpolar linear molecule, CO_2 may react with H_2O groups from clay surfaces and interlayers to form H_2CO_3 and HCO_3^-. These latter groups may interact electrostatically with the adjacent basal oxygen planes and the interlayer cations, and therefore may be the C-bearing complexes in the interlayer. This would explain why at very small H_2O contents, little expansion occurs, because the small quantity of H_2O groups in the interlayer limits the ability of CO_2 to form these complexes. As H_2O content increases, a greater number of these complexes can form. These complexes probably lay flat within the interlayer to maximize the number of bonds with the basal oxygen and siloxane planes of the 2:1 layers and to decrease volume. The thickness of a flat-lying CO_3 complex is approximately equal to that of an O ion or an H_2O molecule, and thus a fully carbonated clay complex is likely to have a (001) spacing equivalent to a 1W interlayer. This model explains why expansion does not proceed beyond an (001) spacing of ~12.5 Å and, therefore, the lack of expansion for the more hydrated RHPEC samples: CO_2 intercalation may occur for samples with all 1W interlayers, although the (001) spacing remains the same. This model may be confirmed using other methods, such as vibrational spectroscopy.

In this study, a series of control experiments involving He were conducted. In the THPEC series, He-exposed samples expanded from 11.02 to 11.24 Å, whereas in the RHPEC the samples expanded from 11.43 to 11.77 Å. Because He probably does not interact with the interlayer, the expansion is most likely related to an increase in the activity of H_2O with an increase in He pressure.

In summary, the Na-exchanged SWy-2 structure expands by approximately 10% with increasing $P(CO_2)$ to ~ 50 bars at 45 ^oC where small amounts of H_2O are present in the interlayer.

11.5.1 Geologic significance

We have shown that CO_2 can significantly affect the structure of Na-exchanged montmorillonite. These results are relevant to any carbon sequestration project involving a caprock or reservoir containing these or other expandable clays. The potential exists for CO_2 to cause swelling of this mineral fraction, which could then cause structural changes to the caprock, possibly swelling pores shut, but also potentially causing formation cracking. Further experimental work is needed to examine the existence and extent of this effect for smectites besides montmorillonite and interlayer cations other than Na.

In particular, it will be important to consider the effect of CO_2 on clays more hydrated than 1W. At the outset of these experiments, the most likely result was thought to be dehydration of montmorillonite by CO_2, but this is clearly not the dominant behavior at low H_2O contents. The R75 data suggest that there may be an H_2O activity and CO_2 pressure range where dehydration is important. Thus, in a single reservoir, CO_2 may cause dehydration of clays in some regions, whereas in other regions it causes swelling.

The range of pressures over which swelling occurs is also an important target for further research. Thus, it is possible that at increasing pressures and variable salt concentrations, the intercalation of CO_2 could be reversed, depending on the activities of H_2O and CO_2. Also, clay-bearing rocks with depositional fabric (*i.e.*, shale) may in some reservoirs be subject to uniaxial pressure, which has the potential to be oriented at an angle to the basal planes of most of the clay particles and thus affect CO_2 intercalation. It is evident that temperature, pressure, and chemical range of the swelling regime are important parameters in any possible contraction regime of montmorillonite under CO_2 pressure. Thus, the rock-mechanical effects of the swelling and the consequences for capillary transport of CO_2 and other fluids through caprocks and reservoirs require much more study before the effects can be incorporated into models to predict reservoir and caprock stability.

The range of pressures (0 – 50 bars) over which CO_2 intercalation was observed is also relevant to planetary atmospheres. Although current Earth and Mars have too little CO_2 in their atmospheres, historic Earth and Mars may have had atmospheres with sufficient CO_2 for smectites to swell from carbonate intercalation. This may have had a variety of consequences on the soils, sediments, and diagenetic processes of the time.

12 X-ray diffraction study of K- and Ca-exchanged montmorillonites in CO_2 atmospheres

12.1 Introduction

Geological carbon sequestration involving the injection of CO_2 into deep saline aquifers has been proposed to reduce global warming. There are many geotechnical and engineering hurdles to overcome to plan and implement a safe and effective CO_2 sequestration project. These include evaluation of the aquifer and its overlying caprock to determine their capacity to stratigraphically trap injected supercritical CO_2 (Brennan et al., 2010; Gaus et al., 2005). Sedimentary caprocks may be comprised of carbonates (Barnes et al., 2009), shales and/or other clay-rich rocks (Comerlati et al., 2006; Lu et al., 2011), or evaporites such as anhydrite or halite (Hangx et al., 2010a).

Clay-rich caprocks are heterogeneous and the migration of fluid through these low-permeability formations generally occurs along fractures or a microporous capillary network (Hildenbrand et al., 2004b). The CO_2 confined in such a system will react with its contents, both as the pure phase and as carbonate dissolved in groundwater, with the rate and progress of the reactions strongly affected by formation heterogeneities (Li et al., 2007). These reactions may increase or decrease the porosity and permeability of the caprock.

Krooss et al., 2003 and Busch et al., 2008 among others, have examined sorption of CO_2 by clay and shale and found sorption to be a volumetrically significant process, although the mechanism of CO_2 interaction with the clay is not clear from these investigations. Many shales and mudrocks contain significant smectite and interstratified illite-smectite (Dudek and Srodon, 2003; Lindgreen et al., 2000; Srodon, 2010), a reactive mineral fraction that could interact with supercritical CO_2. CO_2 could dehydrate these swelling clays, causing shrinkage and microfracturing (Chertkov and Ravina, 2001). On the other hand, Fripiat et al., 1974 found intercalation of CO_2 into smectite clay at cryogenic conditions. Giesting et al., 2012a examined Na-exchanged montmorillonite (a smectite) under pressure using *in situ* X-ray diffraction (XRD) and found that instead of shrinking, the clay swelled by up to ~10% in the [001] direction under CO_2 atmosphere at pressures ≤640 bar and temperatures of 22-45 °C. These results suggest that CO_2, instead of dehydrating the montmorillonite, migrated into its interlayers and caused swelling. Thus, CO_2 and water may have similar effects on aquifers and caprocks with significant amounts of swelling clay. In addition, shales containing smectite can absorb CO_2.

The mechanism of CO_2 intercalation into montmorillonite is difficult to determine from XRD analysis, but the amount of swelling can be predicted by the initial hydration state of the clay prior to the experiment. Using the nomenclature of Ferrage et al., 2005 where a 0W smectite has no interlayer H_2O groups and a 1W smectite interlayer has a single plane of these groups, Giesting et al., 2012a found that only clays with mixed populations of 0W and 1W interlayers showed significant swelling. Thoroughly dehydrated (all 0W

interlayers) or largely water-saturated (all 1W) samples did not respond structurally to CO_2 at the conditions studied.

The focus of the present study was to investigate the reaction of K and Ca-exchanged montmorillonite in different hydration states with CO_2 to determine whether CO_2 causes swelling or dehydration in these clays and whether these responses were reversed upon depressurization. We also investigated the kinetics of the forward and reverse reactions.

12.2 Experimental methods

12.2.1 Equipment

The reflection-mode high-pressure environmental chamber (RHPEC) (Koster van Groos et al., 2003) is mounted on a Siemens D5000 θ-θ powder diffractometer. This chamber can be pressurized to 100 bars and heated to 100 °C. Owing to the long X-ray path length within the RHPEC (nearly 2 cm), the X-ray intensity exiting the chamber drops rapidly with pressure. This attenuation depends on the density of the gas or fluid used to pressurize the chamber; for CO_2, the RHPEC cannot be effectively used at pressures above ~40 bars.

12.2.2 Starting material

A Na-rich montmorillonite (Wyoming smectite SWy-2, Costanzo and Guggenheim, 2001) was used as starting material. Purification, grain size selection, and cation exchange (using 1 M KCl or 0.1 M $CaCl_2$) were described previously (Giesting et al., 2012a).

All experiments used bone dry (<10 ppm H_2O) CO_2 from Airgas, which was regulated from tank pressure before being introduced into the RHPEC.

12.2.3 Sample preparation

Thin, oriented aggregate mounts of KSWy-2 or CaSWy-2 on glass slides were prepared using the method of Moore and Reynolds, 1997 (pp. 214-5). Each sample was then exposed to one of a range of relative humidities. Some samples were dried by heating in a muffle furnace at 70-110 ^{o}C, after which they were placed in a desiccator above Drierite (anhydrite with a cobalt indicator). One KSWy-2 sample was placed directly in the desiccator. Other samples were placed in closed containers in the presence of saturated salt solutions: LiCl (11% RH), $MgCl_2$ (33% RH), $Mg(NO_3)_2$ (55% RH), or NaCl (75% RH). Because the dehydration of CaSWy-2 is sluggish, the 11% RH samples were dried in an oven first and then placed in the LiCl container to age. After aging, the samples were removed from the controlled humidity atmospheres and loaded quickly in the RHPEC. The sample preparation methods are summarized in Table 12-1.

.

Table 12-1. Sample preparation summaries.

Sample	Preparation
KSWy-2-ov	Dried at 70 °C, held in desiccator 7 days
KSWy-2-11	Held at 11% RH > 23 days
KSWy-2-33	Held at 33% RH 14 days
KSWy-2-55	Held at 55% RH 16 days
KSWy-2-75	Held at 75% RH > 45 days
KMR-oven	Dried at 70 °C, held in a desiccator ~14 days
KMR-des	Held in a desiccator 47 days
KMR-11	Held at 11% RH 49 days
KMR-75	Held at 75% RH 52 days
CaSWy-2-ov	Dried at 115 °C 16 days, cooled in desiccator
CaSWy-2-ov11	Dried at 115 °C 8 days, held at 11% RH 8 days
CaSWy-2-33	Held at 33% RH
CaSWy-2-75	Held at 75% RH 7 days
CaMR-ov	Dried at 80 °C, held in desiccator 18 days
CaMR-ov2	Dried at 78 °C, cooled in air
CaMR-des	Held in a desiccator 13 days
CaMR-11	Dried at 80 °C, held at 11% RH 14 days
CaMR-33	Held at 33% RH 20 days
CaMR-75	Held at 75% RH 70 days

12.2.4 Experiment Design

In the short-term experiments (K/CaSWy-2-xxx), samples were treated similarly to the NaSWy-2 RHPEC samples in Giesting et al., 2012a. They were subjected to sequential increases and decreases of CO_2 pressure (these changes took < 1 min), followed by a short equilibration period (~10 min) before analysis. Total time elapsed during the experiments is shown in Table 12-2.

A second group of experiments, referred to as the kinetics experiments (K/CaMR-xxx), were designed to test the tentative conclusion in Giesting et al., 2012a that the montmorillonite-CO_2 reaction reaches equilibrium over timescales of tens of minutes by checking for longer-term structural changes. In these experiments, each pressure change (< 1 min) was followed by a short equilibration period (~10 min) and an initial scan, then one or more additional scans were taken after a period of hours. These times are listed in Table 12-3. Alternation of plain and boldface type is used in Table 12-3 to emphasize where pressure adjustments were performed.

Sample	Center (º)	*d*(001) (Å)	$P(CO_2)$ (bar)	Total time (hr)
KSWy-2-ov	8.60	10.3	0	
	8.57	10.3	1	0.8
	8.56	10.3	2	1.6
	8.46	10.4	5	2.5
	8.04	11.0	10	3.3
	7.75	11.4	16	4.2
	7.55	11.7	21	5.0
	7.51	11.8	31	5.8
	7.41	11.9	41	6.7
	7.47	11.8	16	25.0
	7.44	11.9	11	25.9
	7.51	11.8	6	26.8
	7.58	11.6	3	27.7
	7.72	11.4	2	28.7
	7.85	11.2	1	29.7
KSWy-2-11	7.67	11.5	0	
	7.64	11.6	1	0.8
	7.63	11.6	2	2.1
	7.60	11.6	5	2.9
	7.51	11.8	10	3.8
	7.41	11.9	16	4.6
	7.41	11.9	21	5.4
	7.39	11.9	31	6.5
	7.39	11.9	41	7.4
	7.43	11.9	18	23.8
	7.40	11.9	12	24.9
	7.43	11.9	6	25.8
	7.44	11.9	3	26.7
	7.47	11.8	2	27.7
	7.50	11.8	1	28.8
KSWy-2-33	7.44	11.9	0	
	7.44	11.9	1	0.9
	7.45	11.9	3	1.8
	7.42	11.9	5	2.6
	7.36	12.0	10	3.8
	7.35	12.0	16	4.5
	7.34	12.0	21	5.3
	7.28	12.1	31	6.1
	7.32	12.1	41	7.1
	7.31	12.1	18	23.3
	7.34	12.0	11	24.0
	7.39	11.9	6	24.8
	7.41	11.9	4	25.6
	7.50	11.8	2	26.5
	7.61	11.6	1	27.7
KSWy-2-55	7.37	12.0	0	
	7.33	12.0	1	0.8
	7.34	12.0	2	1.6
	7.31	12.1	5	2.4
	7.28	12.1	10	3.3
	7.29	12.1	16	4.2
	7.24	12.2	21	5.0
	7.27	12.1	31	5.8
	7.28	12.1	41	6.9
	7.26	12.2	17	25.0
	7.30	12.1	11	25.7
	7.32	12.1	6	26.7
	7.36	12.0	3	27.5
	7.37	12.0	2	28.3
	7.44	11.9	1	29.1
KSWy-2-75	7.73	11.4	0	
	7.67	11.5	2	0.8
	7.64	11.6	5	1.6
	7.63	11.6	10	2.4
	7.56	11.7	16	4.0
	7.69	11.5	21	5.1
	7.54	11.7	31	6.0
	7.65	11.5	13	23.9
	7.65	11.5	9	24.7
	7.68	11.5	6	25.4
	7.75	11.4	3	26.2
	7.80	11.3	2	27.2
	7.75	11.4	1	28.0
	7.69	11.5	1	167.5
CaSWy-2-ov	7.53	11.7	0	
	7.46	11.8	1	0.8
	7.34	12.0	2	1.7
	7.42	11.9	3	2.5
	7.28	12.1	7	3.3
	7.14	12.4	10	4.2
	7.07	12.5	15	5.1
	7.03	12.6	21	5.9
	7.06	12.5	17	24.5
	7.12	12.4	11	25.3
	7.11	12.4	7	26.2
	7.14	12.4	4	27.0
	7.16	12.3	3	27.9
	7.15	12.3	2	28.8
	7.13	12.4	1	30.0
CaSWy-2-ov11	7.12	12.4	0	
	7.12	12.4	1	0.8
CaSWy-2-ov11 (cont.)	7.07	12.5	2	1.6
	7.13	12.4	3	2.4
	6.96	12.7	6	3.2
	6.91	12.8	10	4.0
	6.88	12.8	16	5.0
	6.86	12.9	21	5.7
	6.80	13.0	31	6.8
	7.10	12.4	13	24.1
	7.23	12.2	7	25.7
	7.25	12.2	4	27.1
	7.25	12.2	3	27.9
	7.23	12.2	2	30.0
	7.27	12.1	1	30.7
CaSWy-2-33	7.04	12.5	0	
	7.03	12.6	1	0.9
	6.99	12.6	2	1.7
	6.95	12.7	6	2.5
	6.92	12.8	10	3.6
	6.92	12.8	15	4.4
	6.91	12.8	21	5.2
	6.94	12.7	21	23.9
	6.97	12.7	16	24.8
	7.02	12.6	11	25.6
	7.04	12.5	5	47.7
	7.04	12.5	3	48.5
	7.05	12.5	2	49.4
	7.09	12.5	1	51.7
CaSWy-2-75	7.07	12.5	0	
	7.07	12.5	1	1.8
	7.03	12.6	2	2.9
	7.03	12.6	3	3.4
	7.00	12.6	6	4.3
	6.93	12.7	10	5.1
	6.91	12.8	16	5.9
	6.86	12.9	21	6.7
	6.88	12.8	26	7.5
	6.86	12.9	31	8.5
	6.87	12.9	48	9.3
	6.97	12.7	23	23.3
	7.04	12.5	16	24.2
	7.08	12.5	11	25.0
	7.09	12.5	6	25.9
	7.10	12.4	4	26.8
	7.12	12.4	3	27.6
	7.12	12.4	2	28.4
	7.16	12.3	1	30.3

Table 12-3. (001) peak center, CO_2 pressure, and time at pressure at the outset of the scan for all kinetics experiments (see Experiment Design, above, regarding boldface entries and for further discussion)

Sample	Center (º)	*d*(001) (Å)	P(CO_2) (bar)	Time (hr)	Sample	Center (º)	*d*(001) (Å)	P(CO_2) (bar)	Time (hr)	Sample	Center (º)	*d*(001) (Å)	P(CO_2) (bar)	Time (hr)
KMR-ov	7.85	11.2	0	0.0	CaMR-ov	7.85	11.2	0	0.0	CaMR-des (cont.)	5.85	15.1	22	0.0
	7.84	11.3	0	2.0		7.65	11.5	0	2.7		5.89	15.0	8	15.0
	7.69	11.5	2	0.0		7.46	11.8	2	0.0		5.96	14.8	1	0.0
	7.68	11.5	2	2.0		7.40	11.9	2	2.7		5.91	14.9	1	17.5
	7.30	12.1	22	0.0		7.30	12.1	2	5.4	CaMR-11	6.91	12.8	0	0.0
	7.34	12.0	16	4.0		7.28	12.1	2	8.1		6.84	12.9	0	0.7
	7.33	12.0	7	0.0		7.22	12.2	2	10.8		6.72	13.1	6	0.0
	7.32	12.1	3	0.0		7.19	12.3	2	19.6		6.66	13.3	5	0.0
	7.35	12.0	1	96.0		6.88	12.8	23	0.0		6.64	13.3	5	2.7
KMR-des	7.77	11.4	0	0.0		6.58	13.4	20	2.7		6.50	13.6	4	5.4
	7.64	11.6	0	3.0		6.66	13.3	18	5.4		6.56	13.5	3	8.1
	7.58	11.6	2	0.0		6.64	13.3	15	8.1		6.50	13.6	3	10.8
	7.52	11.7	2	3.0		6.64	13.3	12	10.8		6.17	14.3	21	0.0
	7.33	12.0	23	0.0		6.73	13.1	9	19.6		6.14	14.4	19	2.7
	7.25	12.2	12	12.0		6.65	13.3	8	0.0		6.12	14.4	17	5.4
	7.31	12.1	3	0.0		6.68	13.2	4	19.6		6.12	14.4	15	8.1
	7.33	12.0	3	3.0		6.69	13.2	1	0.0		6.12	14.4	12	10.8
	7.37	12.0	1	0.0		6.60	13.4	1	19.6		6.12	14.4	10	13.5
	7.40	11.9	1	12.0	CaMR-ov2	6.27	14.1	0	0.0		6.10	14.5	8	18.0
KMR-11	8.30	10.6	0	0.0		5.97	14.8	21	0.0		6.13	14.4	7	24.6
	8.20	10.8	0	3.0		6.14	14.4	21	1.0		6.12	14.4	4	42.6
	7.97	11.1	2	0.0		6.20	14.2	21	2.0		6.12	14.4	2	0.0
	7.92	11.1	1	12.0		6.25	14.1	21	3.0		6.10	14.5	1	72.2
	7.37	12.0	22	0.0		6.40	13.8	1	0.0	CaMR-33	5.85	15.1	0	0.0
	7.35	12.0	10	18.0		6.33	13.9	1	16.0		5.86	15.1	0	2.0
	7.35	12.0	3	0.0	CaMR-des	7.03	12.6	0	0.0		5.84	15.1	2	0.0
	7.37	12.0	3	3.0		6.84	12.9	1	0.5		5.85	15.1	2	15.0
	7.47	11.8	1	0.0		6.66	13.3	2	0.5		5.77	15.3	23	0.0
	7.42	11.9	1	18.0		6.50	13.6	2	2.3		5.84	15.1	11	45.5
KMR-75	7.21	12.2	0	0.0		6.42	13.8	2	6.0		5.76	15.3	49	0.0
	7.22	12.2	0	3.0		6.36	13.9	2	9.7		5.81	15.2	16	18.0
	7.20	12.3	2	0.0		6.30	14.0	2	13.6	CaMR-75	5.70	15.5	0	0.0
	7.20	12.3	2	3.0		6.24	14.1	2	17.3		5.70	15.5	2	0.0
	7.20	12.3	22	0.0		6.18	14.3	3	0.0		5.71	15.5	2	3.0
	7.22	12.2	6	27.0		6.10	14.5	3	3.7		5.68	15.5	22	0.0
	7.26	12.2	3	0.0		6.08	14.5	3	7.9		5.71	15.5	11	15.0
	7.25	12.2	3	3.0		6.04	14.6	3	11.6		5.74	15.4	3	0.0
	7.27	12.1	1	0.0		6.02	14.7	2	15.3		5.74	15.4	3	3.0
	7.27	12.1	1	18.0		6.02	14.7	2	19.0		5.74	15.4	1	0.0
						5.98	14.8	3	42.0		5.76	15.3	1	18.0

12.2.5 Data collection

Samples were run in the RHPEC at 22-25°C, monitored by a thermocouple in contact with the chamber body; pressure conditions were measured with an external digital Heise gauge accurate to ± 0.1% full scale. The RHPEC was mounted on the Siemens D5000 diffractometer with a Cu X-ray tube, which was operated at 40 kV and 25 mA. Each RHPEC scan used a 0.02 degree step size and a 1.25 or 2 s dwell time, with a resulting analysis time between 45 min and 1 hr. The DataScan program (MDI, v. 4.3.355, 2005) was used for data collection. These data are given without further processing. (001) peak centers at half maximum (*d*(001) values) were determined from these data. We have discussed these measurements and their uncertainty previously (Giesting et al., 2012a).

12.3 Results and Discussion

Diffraction data are given in Figure 12-1 and Figure 12-4. Peak centers, along with experimental parameters, are listed in Table 12-2 and Table 12-3.

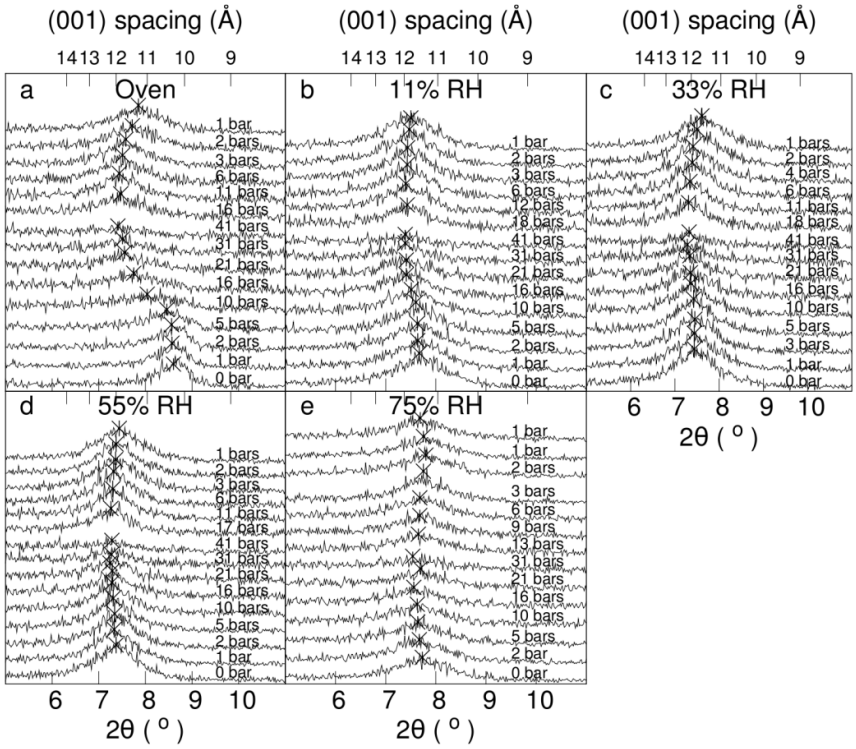


Figure 12-1. KSWy-2 (short-term experiments) diffraction patterns with CO_2 pressure listed for each scan and center at half maximum marked. Scans are in time order with the first data collected at the bottom.

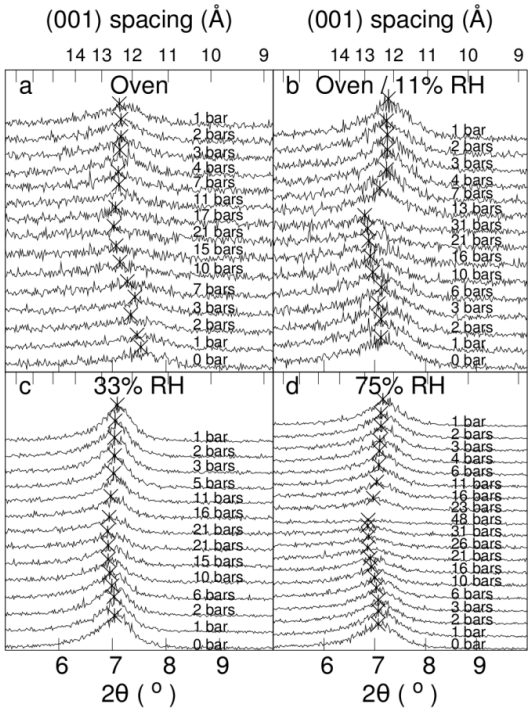


Figure 12-2. CaSWy-2 diffraction patterns presented as in Figure 12-1.

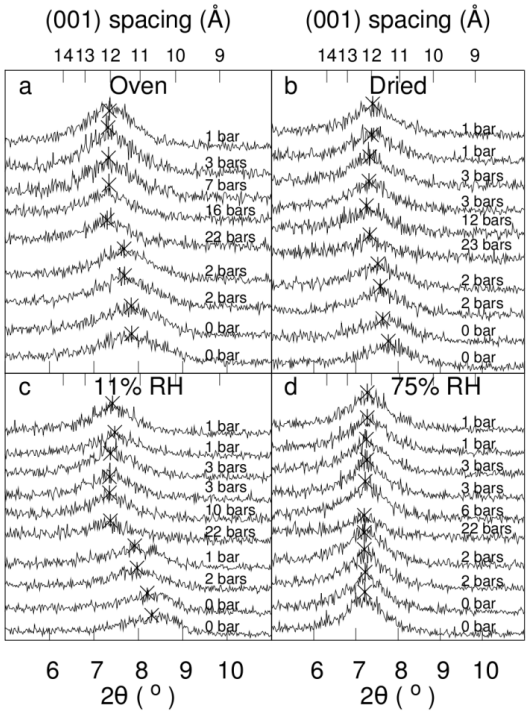


Figure 12-3. KMR diffraction patterns presented as in Figure 12-1.

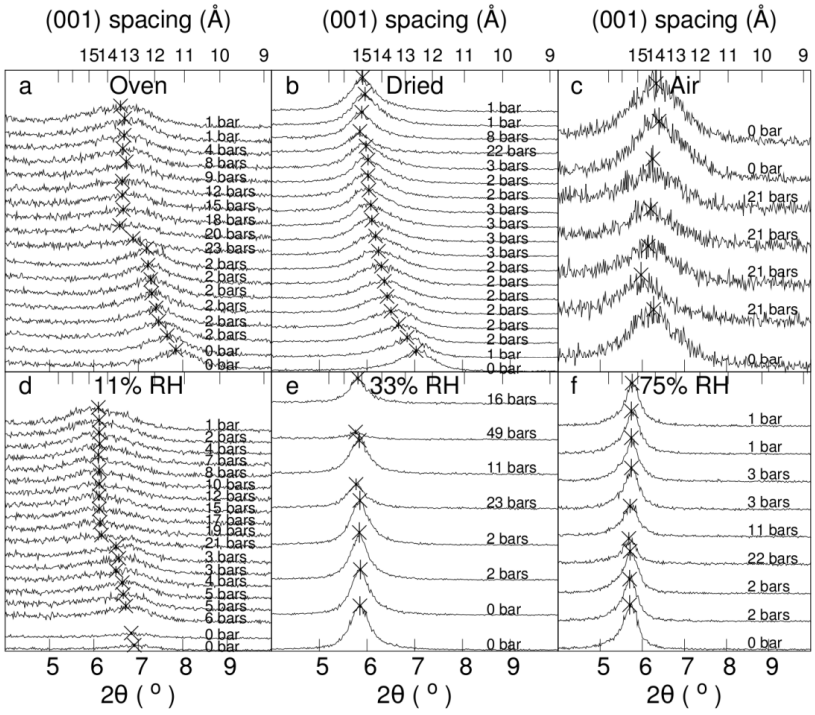


Figure 12-4. CaMR diffraction patterns presented as in Figure 12-1.

12.3.1 Initial material

Montmorillonite-H_2O complexes have been well studied. The hydration of montmorillonite interlayers involves the intercalation of discrete quantities of H_2O groups, and a series of characteristic layer-to-layer spacings results (Ferrage et al., 2005; Giesting et al., 2012a; MacEwan and Wilson, 1984). Our initial

diffraction data (before exposure to CO_2) for each sample fit this hydration model and indicate disordered layer spacings for all samples with intermediate hydration states. In some cases, the observed diffraction patterns for starting material do not match those of (Ferrage et al., 2005) for the same relative humidity. The initial hydration state of these samples is likely not the equilibrium value for their storage conditions owing to brief exposure to the laboratory atmosphere.

12.3.2 Effect of CO_2 exposure: short-term samples

In earlier work, we examined the effect of CO_2 exposure on Na-exchanged montmorillonite (Giesting et al., 2012a) and found that samples dominated by 0W or 1W interlayers had essentially unchanged XRD patterns when exposed to CO_2. In contrast, samples with significant quantities of both 0W and 1W interlayers expanded under CO_2. The short-term experiments with K-exchanged montmorillonite behaved similarly, with the main exception being that the maximum observed spacing for the K samples was lower. The K maximum was 12.1-12.2 Å compared to the Na maximum of ~12.5 Å for samples that did not contain a significant number of 2W interlayers in the initial material. This behavior correlates with the generally lower *d*(001) of hydrated K-exchanged montmorillonite compared to Na-exchanged montmorillonite at the same relative humidity (Ferrage et al., 2005).

Ca-exchanged montmorillonite has a different hydration behavior than Na- and K-exchanged materials: at a given relative humidity, Ca-exchanged montmorillonite has a greater *d*(001) value (Ferrage et al., 2005). This is attributed to the higher charge density Ca^{2+} cations, which more strongly attract the polar H_2O groups. Ca-exchanged montmorillonite expands upon exposure to CO_2 similarly to Na-exchanged and K-exchanged montmorillonite. The short-term experiments using Ca-exchanged samples all had initial *d*(001) ≤ 12.5 Å and these samples expanded to a maximum of 13.0 Å, with no observed barrier to expansion near the 1W value as with Na- and K-exchanged samples.

For short-term experiments, Na- (Giesting et al., 2012a), K-, and Ca-exchanged samples showed significant reversal of CO_2-induced expansion when the CO_2 pressure was released. This is shown in Figure 12-5ab, where the crosses showing reversal represent comparable magnitudes to the circles showing the initial expansion. In most cases the reversal was incomplete, which may be related to intercalation of CO_2 into the interlayers that is not reversed after pressure is reduced to 1 bar, but may also be related to the presence of small amounts of water on experimental components at the outset of the experiment being delivered to the clay and remaining there. In other cases the *d*(001) values decreased below their initial values, showing that some H_2O was removed from the particles during the course of the experimental cycle. For KSWy-2-33 and KSWy-2-55, we attribute this to the sample being at a nearly saturated 1W state at the outset, experienced no CO_2-related swelling, and instead lost a little H_2O during exposure to dry CO_2. For CaSWy-2-ov11 and CaSWy-2-75, these samples appear to be more desiccated by the higher maximum CO_2 pressures to which they were subjected compared to CaSWy-2-ov and CaSWy-2-33.

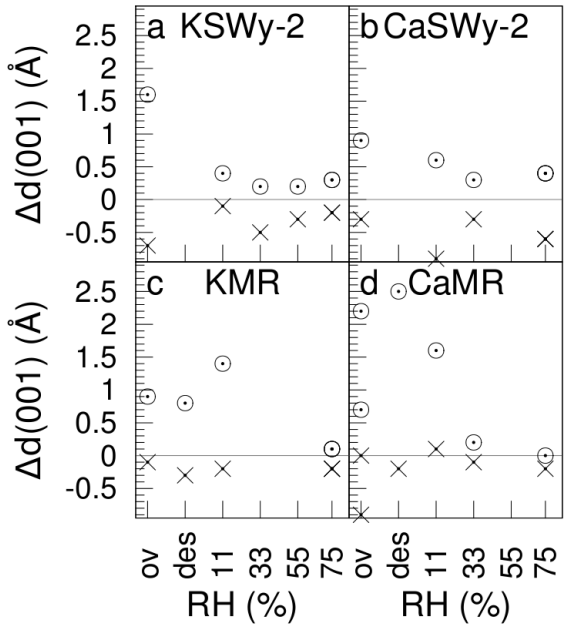


Figure 12-5. Change in d*(001) for each sample studied. Circles: net change in* d*(001) from initial value to value at maximum CO_2 pressure (or the next scan if higher). Crosses: net change in* d*(001) from value at maximum pressure to end of experiment.*

12.3.3 Kinetics experiments

The KMR results (Figure 12-3, Table 12-3) are consistent with the KSWy-2 - CO_2 reaction occurring over relatively short timescales. Maintaining the clay samples at low CO_2 pressures does not produce greater than 0.2 Å expansion over time, and the uncertainty in determining peak positions is similar in magnitude. However, these samples show less change in the *d*(001) value after the CO_2 pressure is released, in contrast to the short-term experiments with KSWy-2 and NaSWy-2 samples. This is shown in Figure 12-5c, where the circles showing initial expansion of samples under CO_2 are further away from the zero line than the crosses showing the magnitude of the reverse reaction. These results suggest that there is a reorganization of the interlayer contents in these clays over time that increases the stability of the clay-CO_2 intercalate.

The CaMR-ov2, CaMR-des, CaMR-33, and CaMR-75 results suggest that the 15-15.5 Å layer spacing, the same spacing as 2W hydrated interlayers, appears to be a limiting value for the CaSWy-2-CO_2 intercalate much like the 12-12.5 Å spacing is a limit for the NaSWy-2[17] and KSWy-2 intercalates.

The CaMR samples show a sluggish forward reaction (Figure 12-4, Table 12-3), in contrast to the KMR samples. Expansion begins at low CO_2 pressures and continues over a period of hours. For the CaMR-ov sample, expansion continued slowly even as pressure was raised to its maximum and then lowered. For the CaMR-des sample, at only 3 bars of CO_2, expansion of 2.5 Å occurred. Over the timescales studied, significant reversal of the reaction was not observed (crosses compared to circles in Figure 12-5d), which is identical to the KMR samples. The exception to this was sample CaMR-ov2, where leaks forced the pressure

to be repeatedly topped off, probably resulting in loss of interlayer H_2O along with leaking CO_2, explaining why the final *d*(001) was lower than the initial value.

Samples KMR-75 and CaMR-75 also had final *d*(001) values lower than their initial values. We attribute this to each sample starting at a saturated 1W or 2W state, experiencing no CO_2-related swelling, then losing a little H_2O during exposure to dry CO_2.

12.3.4 Mechanism of swelling

CO_2 can enter montmorillonite interlayers under the conditions we have studied, depending on the initial H_2O content of the system. The CO_2 may reside in the interlayer as linear molecules or may react with the interlayer walls, cations, or H_2O groups. Although the CO_2 sorption capacity of various clay minerals has been studied before (Busch et al., 2008) there was no direct indication given for the place (faces, edges, interlayer) or the type of reaction (chemical, physical). At cold conditions, linear CO_2 was observed by infrared spectroscopy in montmorillonite (Fripiat et al., 1974). Ongoing sorption and neutron diffraction studies indicate that CO_2 is able to reside in the interlayer spaces as linear molecules (G. Rother, pers. comm.). Because clay interlayers have adjacent polar OH groups, negatively charged sheets, and positively charged cations, it seems reasonable to consider that reactions consuming nonpolar CO_2 in favor of polar carbonate groups may occur as well. Because our Na-exchanged montmorillonite work showed that interlayer H_2O content was an important factor in CO_2 intercalation, we proposed a model where H_2O and CO_2 reacted to form polar H_2CO_3, HCO_3^-, or other carbonate groups in the interlayer (Giesting et al., 2012a). Our observations with K- and Ca-exchanged montmorillonite are compatible with that model. Further experimental studies using, e.g., spectroscopic techniques (Fripiat et al., 1974), as well as molecular modeling (Botan et al., 2010; Cole et al., 2010; Peng et al., 2007; Romanov et al., 2010; Yang and Zhang, 2005), are needed to explore the structural characteristics of smectite-CO_2 intercalates and enhance understanding of their chemical properties (Giesting et al., 2012a).

12.3.5 Significance for geological storage of carbon dioxide

This work shows that the smectite – CO_2 – H_2O reaction observed for NaSWy-2 (Giesting et al., 2012a) also occurs in KSWy-2 and CaSWy-2. Thus, SWy-2 generally swells, not shrinks, upon initial exposure to CO_2. Swelling may have a variety of effects on the ability of formations to retain CO_2. In addition, the absorption of CO_2 by clays with significant interlayer Ca (and possibly other divalent cations) may enhance the mineralization capacity of geological sequestration reservoirs.

Upon CO_2 injection into a reservoir, a plume forms that migrates upwards to the reservoir/seal interface. Bulk CO_2 will enter the caprock through fractures or faults where the capillary entry pressure is exceeded (Chiquet et al., 2007a; Espinoza and Santamarina, 2010; Wollenweber et al., 2010). Supercritical CO_2 will not contact every particle in the clay-dominated shale matrix, but only particles bordering pathways that connect back to the injection point. The transport porosity, i.e., the porosity of these connected pathways

only, is believed to be several orders of magnitude below the total formation porosity (Hildenbrand et al., 2002). Accessibility of the interior of the shale matrix to CO_2 is limited by diffusion (Busch et al., 2008; Busch et al., 2010). CO_2-induced swelling of some clay particles will restrict CO_2 mobility even further by closing some of the pathway connections (Likos and Lu, 2006). On the other hand, loss of CO_2 containment in a reservoir could evolve from the ability of CO_2 to dehydrate clay interlayers, which will produce matrix shrinkage and desiccation cracking. One consequence could be the creation of transport pathways at the caprock/reservoir interface.

Recent work (Schaef et al., 2012) has considered the effect of CO_2 on a similar, but not identical, Ca-exchanged smectite (STx-1). CaSTx-1 in dehydrated (< 1W), moderately hydrated (~ 2W), and more hydrated (> 2W) conditions were reacted with supercritical CO_2. In contrast to our experiments, the dehydrated samples in that study were subjected to vacuum at the end of the experiments, resulting in *d*(001) returning to the original < 1W value. The moderately hydrated samples were found to dehydrate to ≤ 1W conditions after being aged under supercritical CO_2, which is also in sharp contrast to our results. The supercritical CO_2 may have been able to dehydrate these samples, whereas the gaseous (i.e., lower pressure) CO_2 in our experiments was not and instead caused our samples to swell. The more hydrated samples were exposed to wet CO_2, and these clays swelled to a *d*(001) comparable to a 3W hydration state, in contrast to control samples exposed to N_2, where the clay remained near the 2W hydration state. This suggests that in the near-field of a sequestration reservoir, freshly injected, anhydrous, high-partial-pressure CO_2 is likely to cause swelling clays to shrink, resulting in microfracturing of the aquifer and any part of the caprock where the activity of water declines sufficiently owing to displacement by CO_2. In the far-field, where the injected CO_2 is wet, at lower partial pressure, or both, swelling clays appear likely to swell, and this behavior has now been observed for Ca-exchanged clays at a wide range of hydration states from just above 0W to above 2W.

We note that Schaef et al., 2012 state, on the basis of TGA-MS work, that little evidence (a small increase in mass 44 baseline between 400 and 600 °C) for metal carbonation was observed. Because they do not state a temperature range where decarbonation of their clays was observed, their data do not help clarify CO_2-smectite intercalation reaction mechanisms. Complementary methods such as vibrational spectroscopy (Fripiat et al., 1974) are needed to evaluate what configurations (e.g., linear CO_2, hydrogen bonded H_nCO_3, metal carbonate complexes) CO_2 adopts when it is present within clay structures under a broad range of conditions. In addition, we cannot confirm that the montmorillonite-CO_2 reaction has reached equilibrium in these experiments, only that the reaction rate decreased. Longer timescale experiments and, once a kinetics model is developed, chemical simulations are needed to evaluate whether continued clay expansion is expected over the lifetime of geological CO_2 reservoirs.

Our work and other high-pressure studies on CO_2-smectite reactions (Giesting et al., 2012a; Schaef et al., 2012) were conducted under hydrostatic conditions. Clay particles that border on pores and are thus under

hydrostatic stress will be able to expand as described. Particles embedded in the matrix experience non-hydrostatic stress fields. Such stress regimes will interact with the directional expansion of swelling clays, and microfracturing could result from differential swelling of smectite. Non-hydrostatic stress responses were observed in studies on coal interaction with CO_2 (Hol and Spiers, submitted for publication; Majewska and Zietek, 2007). Further innovation in experimental equipment is needed to address these questions.

13 Conclusions and suggestions for future research

13.1 Main Conclusions

(1) CBM and CO_2-ECBM related sorption processes in coal: A review

In the last decade a large amount of data has been published characterizing coals from various coal basins world-wide for their gas sorption capacity. This research was either related to commercial CBM production or to the usage of coal seams as a permanent sink for anthropogenic CO_2 emissions. Presently, producing methane from coal beds is an attractive option and operations are under way or planned in many coal basins around the globe. Gas-in-place determinations using canister desorption tests and CH_4 isotherms are performed routinely and have provided large datasets for correlating gas transport and sorption properties with coal characteristic parameters. In order to address the research performed in the last decades we have reviewed the state of research on sorption of gases (CO_2, CH_4) and water on coal for primary recovery of coalbed methane (CBM), secondary recovery by an enhancement with carbon dioxide injection (CO_2-ECBM), and for permanent storage of CO_2 in coal seams. This chapter discussed and compared the manometric, volumetric and gravimetric methods for recording sorption isotherms and provides an uncertainty analysis. Using published datasets and theoretical considerations, water sorption is found to be an important mechanisms controlling gas sorption on coal, commonly neglected when focusing on dry coal samples only. Most sorption isotherms are still recorded for dry coals, which do not represent in-seam conditions, and water present in the coal has a significant control on CBM gas contents and CO_2 storage potential. When looking at sorption properties as a function of coal rank we find that CO_2 and CH_4 sorption capacities on moisture-equilibrated coals increase with coal rank, while a rather “u-shaped” dependence is observed for dry coals with a minimum around 1.1 to 1.3 % VRr.The ratio of CO_2/CH_4 sorption capacity decreases with coal maturity, making it more effective to store CO2 in low-maturity coals.

(2) Gas saturation and CO_2 enhancement potential of coalbed methane reservoirs as a function of depth

The influence of moisture, temperature, coal rank and differential enthalpy on the methane (CH_4) and carbon dioxide (CO_2) sorption capacity of coals of different rank has been investigated by using high-pressure sorption isotherms at 303, 318, 333K (CH_4) and 318, 333, 348K (CO_2), respectively. The variation of sorption capacity was studied as a function of burial depth of coal seams by using the corresponding Langmuir parameters in combination with a geothermal gradient of 0.03 K/m and a normal hydrostatic pressure gradient. Taking the gas content corresponding to 100% gas saturation at maximum burial depth as a reference value the theoretical CH_4 saturation after uplift of the coal seam was computed as a function of depth. According to these calculations the change in sorption capacity caused by changing p, T conditions during uplift will lead consistently to oversaturation. Therefore the frequently observed

undersaturation of coal seams is most likely related to dismigration (losses into adjacent formations and/or atmosphere). Finally we attempt to identify sweet spots for CO_2-enhanced coal bed methane production. CO_2-ECBM is expected to become less effective with increasing depth because the CO_2/CH_4 sorption capacity ratio decreases with increasing temperature and pressure. Furthermore CO_2-ECBM efficiency will decrease with increasing maturity due to the highest sorption capacity ratio and affinity difference between CO_2 and CH_4 for low mature coals.

(3) A preliminary evaluation of the CO_2 storage potentials in unminable coal seams of the Münster Cretaceous Basin, Germany

The Münster Cretaceous Basin is a synclinal structure containing Upper Cretaceous sediments of local thickness exceeding 1700 m, partially covered by Cenozoic deposits. The underlying basement consists of deep Carboniferous strata with interbedded hard coal seams. The Cretaceous sequence can be subdivided into the Cenomanian-Turonian-Complex, representing a brine aquifer, and the overlying 'Emscher Mergel' (clayey marl), separating the brine from shallow freshwater aquifers. This geological setting potentially offers favourable conditions for geological storage of CO_2 by physical sorption in the coal seams below the 'Emscher Mergel' cap rock formation. This storage option could be combined with the production of coalbed methane (CBM), by means of application of a CO_2-Enhanced Coalbed Methane (ECBM) strategy. A potential storage area of 820 km^2 has been identified by considering local geological, hydrogeological and tectonic settings. This regional study was complemented by the analysis of carbon isotope signatures of CH_4 and CO_2 in shallow aquifers and concentration profiles of methane-in-place. Using the Coal Inventory Calculation Model (KVB-model) of the Geological Survey (GD) of North Rhine-Westphalia, Germany, coal volumes within the study area was estimated to amount to $65x10^9$ metric tons. High-pressure CO_2 sorption isotherms measured on a selected coal sample at different temperatures were used to estimate the sorptive storage capacity of this coal at the pressure and temperature conditions in the seams. Assuming an accessibility of 40% of the total coal as well as a methane-in-place recovery efficiency of 80%, a maximum CO_2 storage potential of 160 million metric tons of CO_2 was estimated for the coal seams down to a depth of 3000 m.

(4) High-pressure methane and carbon dioxide sorption on coal and shale samples from the Paraná Basin, Brazil

The potential for coalbed methane production and carbon dioxide storage in coals, carbonaceous shales and source rocks of the Paraná Basin in Brazil has been evaluated. On coal and carbonaceous shale samples from the Santa Terezinha coalfield and shale samples from two principle petroleum source rocks, high pressure sorption tests, using a manometric method, were applied to determine CH_4 and CO_2 capacities. These were found to range from 0.03 to 0.47 mmol/g for CH_4 and 0.14 to 0.81 mmol/g for CO_2, showing a decrease with decreasing organic matter content. From linear regression it was found that CH_4 sorption

would reach approximately zero, whereas residual CO_2 sorption on mineral matter would be ~0.2 mmol/g. This concludes that the inorganic content of coal/shale is an important factor in CO_2 sorption but rather negligible for CH_4 sorption. Present day gas contents of coals collected from the first CBM well in the Santa Terezinha coalfield represent gas saturations of 0.13–0.38. Carbon dioxide sorption capacities exceeded CH_4 sorption by a factor between 1.9 and 6.9 for these coals. Free sorption capacities and preferential sorption of CO_2 could favour CO_2-enhanced methane recovery and CO_2 storage in coals and shales of the study area. Based upon the calculated coal reserves, gas contents and measured sorption capacities, a total storage potential of 15.3 Gt CO_2 was estimated for an area of 20x40 km in the Santa Terezinha coal field, assuming a combined CO_2 enhanced coalbed methane (ECBM) production and CO_2 storage operation.

(5) Laboratory experiments on environmental friendly means to improve coalbed methane production by carbon dioxide/flue gas injection

We used scaled in situ laboratory core flooding experiments with CO_2, N_2 and flue gas in an environmental cell on to study the efficiency of ECBM. This addresses the question of what the conditions are under which the fluid in the micro pores of the coal is displaced by the CO_2 in the presence of competitive adsorption; and what the role of compositional heterogeneity and fracture anisotropy of coal is for the injection design and the efficiency of CO_2 storage in relation to the swelling and shrinkage characteristics of coal. Another important question is addressed of how the mobile and the immobile water in the coal will affect the exchange process. We attempted to answer these questions by means of downscaled laboratory experiments that are capable of accurately describing the coupled process of multiphase flow, competitive adsorption and geo-mechanics. It is shown that CO_2 has a better sweep efficiency compared to flue gas (mainly composed of N_2 and CO_2) and that dewatering will be an essential step for successful ECBM combined with a CO_2 sequestration process.

(6) Predicting capillarity of mudrocks

Various rock types on 214 samples were investigated, with the main focus on the determination and prediction of the capillary breakthrough and snap-off pressure in mudrocks (e.g. shales, siltstones, mudstones). Knowledge about these two critical pressures is important for both, the prediction of the capillary sealing capacity of natural gas reservoirs or CO_2 storage sites, but also for production estimates from tight gas or shale gas plays. Capillary pressure experiments, when performed on low-permeability core plugs, are difficult and time consuming. Therefore, mercury porosimetry measurements (MIP), known for being quick and easy to conduct, are preferably used in the industry to determine an equivalent value for the capillary breakthrough pressure. When evaluating the database in detail we find that (1) MIP data plot well with the drainage breakthrough pressures determined on sample plugs, while the conversion of the system Hg/air to gas/brine (e.g. CH_4, CO_2) using interfacial and wettability data does not provide a uniform match, potentially caused by non fully water-wet conditions; (2) brine permeability versus capillary

breakthrough pressure determined on sample plugs shows a good match and could provide a first estimate of P_c-values since permeability is easier to determine than capillary breakthrough pressures on shale plugs. For imbibition snap-off pressures a good correlation was found for CH_4 measured on sample plugs only; (3) porosity shows a fairly good correlation with permeability for sandstone only, and with plug-derived capillary breakthrough pressures for sandstones, carbonates and evaporates. No such correlations exist for mudrocks; (4) air and brine-derived permeabilities show an excellent correlation and (5) from the data used we do not infer any direct correlations between specific surface area (SSA), mineralogy or organic carbon content with permeability or capillary pressure however were able to predict permeabilities using a more sophisticated model that relies on several of these parameters. It is further shown that uncertainties in contact angles in the system water/CO_2/rock, deviating from perfectly water-wetting conditions, might be a reason for discrepancies between CO_2-plug and MIP data and this should be the focus for future research.

(7) The Significance of Caprock Sealing Integrity for CO_2 Storage

The safe long-term storage of gas/CO_2 in spatially limited underground volumes requires the combination of a structural trap with intact structural integrity and a suitable low permeability caprock (seal). The occurrence of natural gas reservoirs proves that certain lithotypes do provide efficient seals which can prevent leakage of gas to the atmosphere over long geological time periods (millions of years). In order to assess the risk of CO_2 leakage through caprocks on top of potential storage sites to the surface one has to consider both, the present sealing capacity of the rock and its likelihood to alter in contact with CO_2. We provided an overview of mechanisms affecting sealing integrity of intact (non-fractured/faulted) caprocks. Although certain caprocks can be suitable for hydrocarbons over geological time periods, CO_2 in contact with the seal may pose additional risks. Depending on the lithofacies and the amount of reactive mineral species, CO_2/water/rock interactions might alter the caprock, physical adsorption on organic matter or mineral surfaces will affect sealing integrity and interfacial properties will affect capillary entry and fluid transport behaviour. In summary, leakage by diffusion is not considered of concern and rather can be envisioned to be the rate-determining mechanism for mineral reactions. Capillary leakage can be significant in terms of flow rate after capillary entry pressure is exceeded. This might not be significant for depleted oil and gas reservoirs where reservoir pressurization after CO_2 injection should be below the original reservoir pressure. However for saline aquifers this might become an important factor. CO_2 sorption on clay mineral surfaces and its implication for caprock sealing efficiency has been reported; potential clay mineral swelling, if proven to occur, may either increase or impair the seal capacity. Information on fault leakage has limitations when obtained from lab measurements and should be derived from natural CO_2 analogues. Natural leakage rates range from 10^{1} to 10^{-4} t CO_2/yr/m^2 but many reported values are not representative for a real-case CO_2 storage scenario and fluxes measured at the surface represent only the lower limits of CO_2 amounts escaped from the reservoir.

(8) Experimental investigation of the CO_2 sealing efficiency of caprocks

Using a combination of experimental (petrophysical and mineralogical) methods, the effects of high-pressure CO_2 exposure on fluid transport properties and mineralogical composition of two politic caprocks, a limestone and a clay-rich marl lithotype have been studied. Single and multiphase permeability tests, gas breakthrough and diffusion experiments were conducted under in situ p/T conditions on cylindrical plugs (28.5 mm diameter, 10–20 mm thickness). The capillary CO_2 sealing efficiency of the initially water-saturated sample plugs was found to decrease in repetitive gas breakthrough experiments on the same sample from 0.74 to 0.41 MPa for the limestone and from 0.64 to 0.43 MPa for the marl. Helium breakthrough experiments before and after the CO_2 tests showed a decrease in capillary threshold (snap-off) pressure from 1.81 to 0.62 MPa for the limestone. Repetitive CO_2 diffusion experiments on the marlstone revealed an increase in the effective diffusion coefficient from $7.8x10^{11}$ to $1.2x10^{10}$ m^2 s^{-1}. Single-phase (water) permeability coefficients derived from steady-state permeability tests ranged between 7 and 56 nano-Darcy and showed a consistent increase after each CO_2 test cycle. Effective gas permeabilities were generally one order of magnitude lower than water permeabilities and exhibit the same trend. XRD measurements performed before and after exposure to CO_2 did not reveal any distinct change in the mineral composition for both samples. Similarly, no significant changes were observed in specific surface areas (determined by BET) and pore-size distributions (determined by mercury injection porosimetry). High-pressure CO_2 sorption experiments on powdered samples revealed significant CO_2 sorption capacities of 0.27 and 0.14 mmol/g for the marlstone and the limestone, respectively. The changes in transport parameters in the absence of detectable mineral alterations may be explained by carbonate dissolution and further reprecipitation along a pH profile across the sample plug which would not be subject to quantitative mineral alteration.

(9) Carbon dioxide storage potential of shale

Diffusive transport and gas sorption experiments on one well characterised shale sample (Muderong Shale, Australia) and different clay minerals were performed to obtain information on the sealing integrity and the CO_2 storage potential of these materials. All measurements were performed under reservoir conditions relevant for CO_2 storage (T=45-50°C; p <20 MPa). Repeat diffusion experiments on one shale plug yielded slightly increased effective diffusion coefficients and a decrease in the concentration of the bulk CO_2 volume in the sample. The latter is believed to be dissolved in formation water, sorbed to mineral surfaces or involved with geochemical reactions. For the Muderong Shale, bulk volume CO_2 concentrations are greater within the experimental time frame (222-389 mol/m³), when compared to coal and cemented sandstone (3-4 and 8-10 mol/m^3), respectively. This high CO_2 storage potential could not fully be explained by CO_2 dissolution in water alone. Thus, gas sorption experiments were performed on crushed shale and various clay minerals. High CO_2 sorption capacities (e.g., up to 1 mmol/g for the Muderong Shale) show that

the high CO_2 concentration is related to a combination of CO_2 dissolution in water and gas sorption on clay minerals. Additionally, changes in specific surface areas before and after the sorption experiments and variations in the CO_2 sorption and diffusion behaviour due to repetitive experiments on the identical sample were observed, possibly related to geochemical alteration of the Muderong Shale and the clay minerals. These could not be quantified however and seemed to occur only at high pressures. This concludes that carbon dioxide that migrates from a storage reservoir into the cap rock through the pore network will be immobilised to a certain extent, hence minimising (slow, diffusion-driven) leakage and providing additional CO_2 storage potential.

(10) Interaction of carbon dioxide with Na-exchanged montmorillonite at pressures to 640 bars: Implications for CO_2 sequestration

Na-exchanged montmorillonite forms an intercalate with CO_2 under the conditions $p(CO_2) \leq 640$ bars, T = 24-47°C, as shown by experiments in high-pressure environmental chambers using powder X-ray diffraction techniques. The intercalation of CO_2 depends on the initial H_2O content between the silicate layers of montmorillonite, *i.e.*, expansion occurs where the initial *d*(001) value suggests some H_2O molecules in the interlayer (≥ 10 Å); if the interlayer is occupied by one layer of H_2O (~ 12.5 Å) no expansion is observed. Maximum expansion, to ~12.3 Å, occurred in a sample with an initial *d*(001) of approximately 11.0 Å at $p(CO_2) = 57$ bars. The CO_2 intercalate is identified by an increase in the montmorillonite *d*(001) value and a change in peak shape. The formation of the CO_2 intercalate is complete by ~50 bars; increasing $p(CO_2)$ from 50 to 640 bars does not result in further increases of *d*(001). Thus, Na-exchanged SWy-2 structure expands by approximately 10% with increasing $p(CO_2)$ to ~ 50 bars at 45 ^{o}C where small amounts of H_2O are present in the interlayer. Previous workers suggested that the introduction of CO_2 into sediment would result in volume reduction caused by the dehydration of montmorillonite. This may not be the dominant behavior of montmorillonite at low H_2O contents because of CO_2-induced expansion of swelling clays. Thus, in a smectite-rich cap rock or reservoir formation selected for carbon storage, the capability of the system to hydrodynamically trap CO_2 may be significantly altered by the very presence of CO_2. For example, reductions in pore throat size may impede CO_2 and other fluid flow through the system.

(11) X-ray diffraction study of K- and Ca-exchanged montmorillonites in CO_2 atmospheres

Powder X-ray diffraction shows that K- and Ca-exchanged montmorillonites swell upon interacting with CO_2 at ambient temperatures, depending on their initial hydration state. K-exchanged montmorillonite swells rapidly to a maximum *d*(001) of ~12.2 Å. In contrast, Ca-exchanged montmorillonite swells more slowly, but reaches a maximum *d*(001) of ~15.1 Å. Reaction kinetics differ significantly between the K- and Ca-exchanged montmorillonite complexes. Expansion of K-exchanged montmorillonite samples was rapid, occurring on timescales of tens of minutes or less. The Ca-exchanged montmorillonite samples continued to expand over periods up to 42 hours. Aging of both K- and Ca-exchanged montmorillonite complexes at

elevated CO_2 pressure for 1-2 days resulted in greater stability when CO_2 pressure was released. The observed intercalation reactions have important consequences for carbon sequestration: (1) CO_2 absorption by swelling clays may represent a significant pathway for storage of CO_2. (2) The swelling of smectites under CO_2 pressure may have a significant impact on the permeability of caprock formations.

13.2 Implications for future research

13.2.1 (CO_2-enhanced) coalbed methane production

Tremendous research efforts have been invested into the development of CO_2-ECBM worldwide and several large research and field demonstration projects have been planned and successfully conducted to better understand principles and potentials of this technology. In general CO_2-ECBM did not yet exceed the demonstration stage within Europe, USA, Japan, China and Australia, and is mainly considered as not economic and technically difficult. An exception might be China where several field projects are ongoing, with however a difficult to estimate future outcome.

In the past this technology was considered favourable because of the more beneficial economics due to potentially increased CBM production, lowering the already high costs of this technology. Another argument is that coal-bearing formations are usually close to CO_2 point sources like coal-fired power plants which potentially lower CO_2 transportation costs from the source to the storage site. Technical reasons of not becoming a success story relate to low storage potentials on the one hand, because the already low permeability of the coal formations will decrease even further due to coal swelling following CO_2 sorption. On the other hand CBM operators are not in favour of diluting their coal seam gases with CO_2 and since many coal seams are at relatively shallow depth (e.g. 500 to 1000 m) there are concerns that injected CO_2 might be leaking to the surface. Drilling costs are also considered to be high since well spacing needs to be narrow to account for the low permeabilities. Finally, CBM production, as one of the unconventional gas production technologies, is lacking public acceptance in many parts of the world.

Apart from the limitations for ECBM, primary production of CBM is ongoing and rates are generally increasing, s. Figure 1-9 as an example for the USA. A booming marked has developed in Australia lately and China is picking up quickly. Business enablers are certainly coal seams at relatively shallow depth, maybe around 500 m, with reduced drilling costs and potentially “high” permeabilities (1-10 mD). Especially Permian (“Gondwana”) to be more favourable compared to the Permo-Carboniferous coal seems as illustrated in Figure 13-1, showing the methane Langmuir volume as a function of coal maturity.

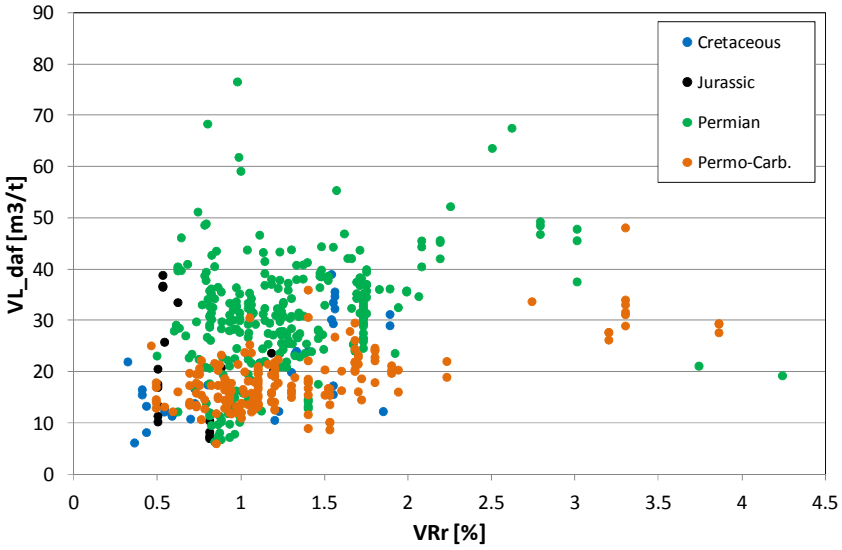


Figure 13-1. Methane Langmuir volume of worldwide coals as a function of coal maturity. Data for different ages of coal deposition is shown where Permian coals originate from continents of the Southern Hemisphere (Australia, Brazil, India) and Permo-Carboniferous coals rather represent coal basins from the Northern Hemisphere (Central Europe, USA). Jurassic and Cretaceous coal seams occur all over the globe (unpublished data, Andreas Busch, 2013).

In general coal-gas interaction is well understood both, from a field development perspective and from laboratory principles. Many European, US and Australian governmental research studies, also with a focus on CO_2-ECBM, have generated a large research output, focusing on sorption capacities and further refining the measurement methodologies, coal swelling following gas sorption on coal, changes in permeability following coal swelling (or shrinkage) and associated poro-elastic effects. Various models have been developed to account for these properties and effort was put into the characterization of the coal pore system, using all kind of different analytical methods. Not many questions remain unsolved and generally a good understanding is created on chances and limitations of CBM and CO_2-ECBM. There are however several aspects that are recommended for future research:

- Sweet-spotting: Several authors have made an attempt to predict preferable temperate and pressure (depth) conditions or coal ranks for either CBM or ECBM production (e.g. Bustin and Bustin, 2008; Gensterblum et al., accepted; Hildenbrand et al., 2006). While these studies clearly show preferable conditions they are based on certain assumptions. The study of one particular coal basin, using present-day gas saturations of the coal seams at varying depth would help further constrain these concepts. Also, sweet-spotting for permeability might be considered. What are controlling factors? What are the most favourable coal types, ages etc.? Can we detect high-permeability areas using geophysical methods or detailed rock mechanics studies and are there parts of the coal basin with the cleat system being rather mineralized by e.g. carbonate or rather open for flow? All these points seem to be valid for shale gas production too.

- Competitive gas adsorption: While many studies have focused on single component CH_4, CO_2, N_2 gas adsorption, only limited studies became available related to gas mixtures. It should be mentioned that these measurements are extremely difficult to perform, relying on sophisticated equipment calibration. While some studies show that CO_2 is always preferentially sorbed under equilibrium conditions compared to CH_4 (e.g. Fitzgerald et al., 2005; Ottiger et al., 2008), other studies indicate that this is not the case, especially under non-equilibrium conditions (Busch et al., 2006). The kinetics and equilibrium conditions of this competitive adsorption should be investigated in more detail.
- Permeability/stress relationships: Permeability is critical in producing a CBM field and besides connectivity of the coal cleat system and mineralization within the cleats itself, the permeability evolution during the time frame of production depends on the stress field. From a laboratory perspective this is a difficult topic since most triaxial setups cannot independently set stresses in the two horizontal and the vertical direction. If a true triaxial setup is available, sample availability can be an issue since mostly block coals of larger diameter are needed.
- Gas sorption under confined stress conditions: One study has demonstrated that with an increase in confining stress the CO_2 sorption capacity of coal decreases significantly (Hol et al., 2010a). It is highly recommended to follow up on this finding, especially with regards to methane. Conclusions of this observation would be a complete misinterpretation of gas saturation in any reservoir where gas adsorption is one of the storage mechanisms (coal, shale). Adsorption measurements on coal sample powders are typically done under hydrostatic pressure conditions and, following the study of Hol et al. (2010), results from these tests would consistently underestimate gas saturations in coal seams. Therefore an in-depth study of this topic is recommended, relying on some sophisticated experimental setup development.
- Water in coal: The influence of water on gas saturation is probably one of the least understood aspects in coal seams. It is found that in water-saturated coals, the gas sorption capacity is more or less limited to the meso-porosity. The reason is that micropores, having the largest surface area and therefore sorption sites, are blocked by water molecules (Prinz and Littke, 2005; Prinz et al., 2004). Therefore a considerable part of the gas in micropores might be blocked and will be difficult to produce, its content depends on coal rank as micro and mesopore surface area depends on coal rank (Prinz and Littke, 2005; Prinz et al., 2004). An open question would be the dynamics of this water content, specifically in the micro/mesopores system. Will it become mobile or not? Will gas production increase when this water becomes mobile or not?

This is just a short list of topics that would require some more focus according to the author, it is no considered to be complete and other researchers will come up with a different list or with different priorities.

13.2.2 Mudrocks as flow barrier for CO_2 storage reservoirs or reservoir for unconventional gas

Shale is probably the least understood reservoir rock for oil and gas production there is, simply because the study of this rock has little history. In the past, focus was more on sandstone and carbonate as conventional reservoirs and shale formations have hardly been cored for standard laboratory testing. For understanding this material in terms of flow and gas sorption capacity, there are similarities for both, CO_2 storage and shale gas. Within the focus area of this thesis, future research efforts should be concentrated to:

- Terminology: Permeability and porosity are usually given without providing further details on the method and the test fluid. It is obvious that different methods will result in different values for these two parameters and research should focus on a better understanding of what method/fluid is determining what value; for instance, mercury porosimetry, He-pycnometry or the Archimedes porosity will determine different porosity values that will all have a different relevance. A systematic comparison of these values is recommended and an evaluation should be done for the respective relevance of these values.
- Two-phase flow in tight rocks: There are limited studies reporting effective permeabilities for tight rocks, like mudrocks or siltstones. These however have not been reported as a function of water saturation. The reason is that it is very difficult to have a good control on water saturation in tight rocks because of its limited mobility under reasonable capillary pressures of <1 MPa and the limitation that currently exist using micro-CT techniques to resolve water saturations the pore space of such materials.
- Capillary entry pressures in mudrocks: Some data has been published on capillary breakthrough and snap-off pressures in mudrocks, as reported in chapter 7 but convincing correlations to other rock physical parameters seem to be missing. A recent study has shown that for almost identical shale plugs large differences have been determined in terms of permeability and capillary pressures (Amann-Hildenbrand et al., 2013). Reasons are unclear and might either be sample heterogeneity or stress unloading/dehydration related formation of microfractures acting as preferred pathways for gas flow. Similarly, Harrington et al., 2012 have shown that gas finds preferred pathways from co-injecting nanoparticles with the test gas and observing its distribution with CT methods. Dilatancy-controlled gas flow might be the reason, rather than capillarity. These findings seem to limit the upscaling of plug derived capillarity data to entire formations however more systematic research is needed to narrow down effects and consequences.
- Dilatancy-controlled gas flow: This transport mechanism is of importance for mudrocks with low tensile strength (like immature shales, Marschall et al., 2005). Clay-rich rock cannot withstand long-term gas pressures with a magnitude greater than the minimum principal stress acting on the rock mass. The process of gas-driven microfracturing leads to an increase of the pore space, which is accompanied by a detectable increase in intrinsic permeability and a change in the capillary pressure-saturation relationship. This phenomenon is important for shale gas operations but also

for the sealing integrity of caprocks above CO_2 reservoirs. While many researchers currently do pick up this topic, the principles and risks (CO_2 storage) or opportunities (shale gas) need to be understood in more detail.

- Sorption on organic matter versus clay minerals: We know that significant amounts of CO_2 is able to adsorb on clay minerals, making them a perfect sink for immobilising it, hence decreasing reservoir pressure in a storage reservoir. It has also been shown that the uptake kinetics is rapid under laboratory conditions and much more rapid than on organic material like coal. Further, it is demonstrated that methane can adsorb on clays, however at much lower quantities compared to carbon dioxide (Liu et al., 2013). The individual contribution of the methane adsorption capacity on the clays compared to organic matter needs to be evaluated in more detail for more sophisticated production estimates. One would expect some rapid production of adsorbed methane from clays, followed by some delayed production from the organic matter. Reasons are that gas is mainly adsorbed in the mesopores between clay platelets that are much better connected than the very small micropores in organic material where most of the gas is adsorbed. This indicates differences in desorption kinetics that need to be understood in more detail.
- CO_2 intercalation in swelling clays: It is known that CO_2 intercalates the interlayer space of swelling clays from the work presented here and that clays in general have a significant CO_2 adsorption capacity. While exact mechanisms remain unexplored, the consequences need to be understood in sufficient more detail. What are the swelling stresses generated and what is the impact on fractures and faults in the subsurface? Is this process rather closing natural transport pathways, hence reducing permeability; or is there a possibility to activate fault plains when sufficient area of the fault plane is affected?
- CO_2 enhanced shale gas production: Some studies have addressed this already and it is a valid enhancement technology to consider, similar to CO_2-ECBM. While the gas exchange mechanisms in coal is insufficiently understood, the understanding is even less for shales and goes back to the previous point on adsorption mechanisms in shales. This is a completely open field for research in the future once considered favourable under any conditions.
- Mechanical stress: Many of the parameters discussed here, like fluid transport and adsorption would be affected by mechanical stress. It is known that permeability depends on effective stress and with increasing stress, the pore space is decreased, leading to reduced permeability. Similarly, and as already noted for coal, it has been documented in the past that a change in effective stress will also impact sorption capacity to an extend we presently do not sufficiently understand.
- Alteration of mudrocks: Little is known about the long-term alteration of clay-rich mudrocks in contact with dry and wet CO_2 or CO_2-saturated brines. Some studies indicated that wettability of some minerals in contact with dry or wet CO_2 change from perfectly water-wet towards mixed-wet conditions with potential consequences for the capillary sealing efficiency of shales. This data is

inferred from laboratory measurements, performed under short time scales of maybe hours or days and no information is available on wettability changes over time periods of months or years, relevant for CO_2 storage. Also, the chemical alteration (dissolution/precipitation) of shale formations is not adequately covered from reported studies. There are some studies that indicate changes in flow properties, however rather within the experimental uncertainty (e.g. Busch et al., 2008; Wollenweber et al., 2010); other studies again, using a larger dataset, do not seem to confirm this behaviour (e.g. Amann-Hildenbrand et al., in press). One study reported an increase in permeability of around one order of magnitude, however is lacking verification and detailed discussion of the results (Armitage et al., 2013). This is an area of further research however also an area that requires sufficient laboratory time accounting for the slow reaction rates between tight rocks such as shales and carbonated brine.

- Drying-out (desiccation) of caprocks: CO_2 is known to take up water in the order of 1-2 vol-%, potentially leading to a dehydration process and dehydration cracking at the reservoir/seal interface or around an leaking annulus in the wellbore. While the mechanism is straightforward, time scales or kinetics of it are not and will certainly depend on size of the pore space, saturation of the CO_2 plume with water and the contact area between the CO_2 plume and the seal. This is critical since dehydration cracks could extend into the seal and potentially altering its ability to act as a suitable barrier for leakage.

These are only few topics that might require improved understanding and it was not the intention to provide a complete list. Also, this is not a priority list since priorities are different for different perspectives at the topic and moreover, priorities do change with an improved understanding of the overall topic.

14 References

Abdou, M.I. and Ahmaed, H.E., 2010. Evaluation of low-solids mud rheological behaviors during shale formation drilling and their effect on pay zone productivity. Petroleum Science and Technology, 28(9): 934-945.

Al-Bazali, T., M., Zhang, J., Chenevert, M., E. and Sharma, M.M., 2009. Estimating the Reservoir Hydrocarbon Capacity Through Measurement of the Minimum Capillary Entry Pressure of Shale Caprocks, SPE Annual Technical Conference and Exhibition. Society of Petroleum Engineers, New Orleans, Louisiana.

Al-Bazali, T.M., Zhang, J. and Sharma, M.M., 2005. Measurement of the sealing capacity of shale caprocks, SPE Anual Technology Conference and Exhibition. October, 9-12, Dallas, Texas.

Alcaniz-Mongue, J., Linares-Solano, A., Rand, B., 2001. Mechanism of Adsorption of Water in Carbon Micropores As Revealed by a Study or Activated Carbon Fibers. J. Phys. Chem., 106(No. 12): 3209 - 3216.

Aldhous, P., 2012. Drilling into the Unknown. New Scientist, 2849: 8-10.

Allardice, D.J., Clemow, L.M., Favas, G., Jackson, W.R., Marshall, M. and Sakurovs, R., 2003. The characterisation of different forms of water in low rank coals and some hydrothermally dried products[small star, filled]. Fuel, 82(6): 661-667.

Allardice, D.J. and Evans, D.G., 1971. The-brown coal/water system: Part 2. Water sorption isotherms on bed-moist Yallourn brown coal. Fuel, 50(3): 236-253.

Alles, S.B., 2008. Experimentelle Untersuchungen zu Fluidtransportprozessen in pelitischen Sedimentgesteinen, RWTH Aachen University, Aachen, Germany, 118 pp.

Amann-Hildenbrand, A., Bertier, P., Busch, A. and Krooss, B.M., accepted. Experimental investigation of the sealing capacity of generic clay-rich caprocks. International Journal of Greenhouse Gas Control.

Amann-Hildenbrand, A., Bertier, P., Busch, A. and Krooss, B.M., in press. Experimental investigation of the sealing capacity of generic clay-rich caprocks. International Journal of Greenhouse Gas Control(0).

Amann-Hildenbrand, A., Bertier, P., Busch, A. and Krooss, B.M., submitted. Transport and retention processes in low-permeable mudstones and shales - an experimental study. International Journal of Greenhouse Gas Control.

Amann-Hildenbrand, A., Busch, A. and Krooss, B., 2013. N2 and CO2 capillary breakthrough experiments on Opalinus Clay, European Geoscience Union General Assembly, Vienna, Austria.

Amann-Hildenbrand, A., Ghanizadeh, A. and Krooss, B.M., 2012. Transport properties of unconventional gas systems. Marine and Petroleum Geology, 31(1): 90-99.

Amann, A., Waschbüsch, M., Bertier, P., Busch, A., Krooss, B.M. and Littke, R., 2011. Sealing rock characteristics under the influence of CO2. Energy Procedia, 4: 5170-5177.

Amarasekera, G., Scarlett, M.J. and Mainwaring, D.E., 1995. Micropore size distributions and specific interactions in coals. Fuel, 74(1): 115-118.

Amorino, C., Bencini, R., Cara, R., Cinti, D., Deriu, G., Fandinò, V., Giannelli, A., Mazzotti, M., Ottiger, S., Pizzino, L., Pini, R., Quattrocchi, F., Sardu, R.G., Storti, G. and Voltattorni, N., 2005. CO2 geological storage by ECBM techniques in the Sulcis area (SW Sardinia Region, Italy), 2nd International Conference on Clean Coal Technology for our Future, Cagliary, Italy.

Angeli, M., Soldal, M., Skurtveit, E. and Aker, E., 2009. Experimental percolation of supercritical CO2 through a caprock. Energy Procedia, 1(1): 3351-3358.

Araújo, C.V., Corrêa da Silva, Z.C. and Rodrigues, R., 1995. Petrographic and geochemical study of coals from Santa Terezinha Coalfield, Rio Grande do Sul, Brazil. Revista Latino-Americana de Geoquimica Otgânica, 1: 28-45.

Armitage, P.J., Faulkner, D.R. and Worden, R.H., 2013. Caprock corrosion. Nature Geosci, 6(2): 79-80.

Armitage, P.J., Faulkner, D.R., Worden, R.H., Aplin, A.C., Butcher, A.R. and Iliffe, J., 2011. Experimental measurement of, and controls on, permeability and permeability anisotropy of caprocks from the CO2 storage project at the Krechba Field, Algeria. J. Geophys. Res., 116(B12): B12208.

Armitage, P.J., Worden, R.H., Faulkner, D.R., Aplin, A.C., Butcher, A.R. and Iliffe, J., 2010. Diagenetic and sedimentary controls on porosity in Lower Carboniferous fine-grained lithologies, Krechba field, Algeria: A petrological study of a caprock to a carbon capture site. Marine and Petroleum Geology, 27(7): 1395-1410.

ASTM, D1412-93. Standard Test Method of eqilibrium moisture of Coal at 96 to 97 percent relative Humidity and 30°C.

Avgul, N.N. and Kiselev, A.V., 1970. Chemistry and Physics of Carbon, 6, New York.

Ayers, W.B., 2002. Coalbed gas systems, resources, and production and a review of contrasting cases from the San Juan and powder river basins. AAPG Bulletin, 86(11): 1853-1890.

Bachu, S., 2000. Sequestration of CO2 in geological media: criteria and approach for site selection in response to climate change. Energy Conversion and Management, 41(9): 953-970.

Bachu, S. and Bennion, B., 2008. Effects of in-situ conditions on relative permeability characteristics of CO2-brine systems. Environmental Geology, 54(8): 1707-1722.

Bachu, S. and Bennion, B., 2009. Interfacial Tension between CO2, Freshwater, and Brine in the Range of Pressure from (2 to 27) MPa, Temperature from (20 to 125) °C, and Water Salinity from (0 to 334 000) mg·L-1. J. Chem. Eng. Data, 54: 765–775.

Bachu, S., Bonijoly, D., Bradshaw, J., Burruss, R., Holloway, S., Christensen, N.P. and Mathiassen, O.M., 2007. CO2 storage capacity estimation: Methodology and gaps. International Journal of Greenhouse Gas Control, 1(4): 430-443.

Bachu, S., Gunter, W.D. and Perkins, E.H., 1994. Aquifer disposal of CO2: Hydrodynamic and mineral trapping. Energy Conversion and Management, 35(4): 269-279.

Bae, J.S. and Bhatia, S.K., 2006. High-Pressure Adsorption of Methane and Carbon Dioxide on Coal. Energy & Fuels, 20(6): 2599-2607.

Baldschuhn, R., Binot, F., Fleig, S. and Kockel, F., 2001. Geotektonischer Atlas von Nordwest-Deutschland und dem Nordsee-Sektor, pp. 153.

Barker, C.E. and Pawlewicz, M.J., 1986. Lecture Notes in Earth Sciences. The correlation of vitrinite reflectance with maximum temperature in humic organic matter., 5. Springer-Verlag, Berlin.

Barker, C.E. and Pawlewicz, M.J., 1994. Calculation of vitrinite reflectance from thermal histories and peak temperatures. A comparison of methods. In: P.K. Mukhopadhyay and W.G. Dow (Editors), ACS Symposium series 570. Vitrinite reflectance as a maturity parameter: applications and limitations, pp. 216–229.

Barnes, D.A., Bacon, D.H. and Kelley, S.R., 2009. Geological sequestration of carbon dioxide in the Cambrian Mount Simon Sandstone: Regional storage capacity, site characterization, and large-scale injection feasibility, Michigan Basin. Environmental Geosciences, 16(3): 163-183.

Baskan, E., 1970. Hydrogeologische Verhältnisse am Südostrand des Münsterschen Kreidebeckens und im Eggegebirge unter besonderer Berücksichtigung der Karsthydrologie. Fortschritte in der Geologie von Rheinland und Westfalen, 17: 537-576.

Battistutta, E., van Hemert, P., Lutynski, M., Bruining, H. and Wolf, K.-H., 2010. Swelling and sorption experiments on methane, nitrogen and carbon dioxide on dry Selar Cornish coal. International Journal of Coal Geology, 84(1): 39-48.

Beamish, B.B. and Crosdale, P.J., 1998. Instantaneous outbursts in underground coal mines: An overview and association with coal type. International Journal of Coal Geology, 35(27-55).

Begossi, R. and Della Fávera, J.C., 2002. Catastrophic floods as possible cause of organic matter accumulation giving rise to coal, Paraná Basin, Brazil. International Journal of Coal Geology, 52: 83-89.

Bennion, B. and Bachu, S., 2006. The Impact of Interfacial Tension and Pore Size Distribution/Capillary Pressure Character on CO2 Relative Permeability at Reservoir Conditions in CO2-Brine Systems Symposium on Improved Oil Recovery SPE/DOE Tulsa, Oklahoma, pp. 10.

Bennion, B. and Bachu, S., 2008. Drainage and Imbibition Relative Permeability Relationships for Supercritical CO2/Brine and H2S/Brine Systems in Intergranular Sandstone, Carbonate, Shale, and Anhydrite Rocks. SPE Reservoir Evaluation & Engineering, 11(3): 487-496.

Berg, R.R., 1975. Capillary pressure in stratigraphic traps. AAPG Bulletin, 59(6): 939-956.

Berg, R.R. and Avery, A.H., 1995. Sealing properties of Tertiary growth faults, Texas Gulf Coast. AAPG Bulletin, 79(3): 375-393.

Bernard, B.B., 1978 Light hydrocarbons in marine sediments, Texas A&M University.

Bertheux, W., 2000. Enhanced CBM production by CO2-injection in water saturated coal: experiments, image analysis and simulations, Delft University of Technology, The Netherlands

Bertier, P., Swennen, R., Laenen, B., Lagrou, D. and Dreesen, R., 2006. Experimental identification of CO2-water-rock interactions caused by sequestration of CO2 in Westphalian and Buntsandstein sandstones of the Campine Basin (NE-Belgium). Journal of Geochemical Exploration, 89(1-3): 10-14.

Bhatia, S.K., 1987. Modelling the pore structure of coal. AICHE Journal, 33(10): 1707-1718.

Bickle, M.J., 2009. Geological carbon storage. Nature Geoscience, 2(12): 815-818.

Bikkina, P.K., 2011. Contact angle measurements of CO2-water-quartz/calcite systems in the perspective of carbon sequestration. International Journal of Greenhouse Gas Control, 5: 1259-1271.

Blunt, M.J. and Scher, H., 1995. Pore-level modeling of wetting. Physical Review E, 52(6): 6387-6403.

Botan, A., Rotenberg, B., Marry, V., Turq, P. and Noetinger, B., 2010. Carbon Dioxide in Montmorillonite Clay Hydrates: Thermodynamics, Structure, and Transport from Molecular Simulation. The Journal of Physical Chemistry C, 114(35): 14962-14969.

Boudou, J.-P., Schimmelmann, A., Ader, M., Mastalerz, M., Sebilo, M. and Gengembre, L., 2008. Organic nitrogen chemistry during low-grade metamorphism. Geochimica et Cosmochimica Acta, 72(4): 1199-1221.

Boulin, P.F., Bretonnier, P., Vassil, V., Samouillet, A., Fleury, M. and Lombard, J.M., 2011. Entry pressure measurements using three unconventional experimental methods, Society of Core Analysts, Austin, Texas, USA, pp. 12.

Boyer, C., Clark, B., Jochen, V., Lewis, R. and Miller, C.K., 2011. Shale Gas: A Global Resource. Oilfield Review 23(3): 28-39.

Bratek, K., Bratek, W., Gerus-Piasecka, I., Jasienko, S. and Wilk, P., 2002. Properties and structure of different rank anthracites. Fuel, 81: 97-108.

Brennan, J.K., Bandosz, T.J., Thomson, K.T. and Gubbins, K.E., 2001. Water in porous carbons. Colloids and Surfaces A: Physicochemical and Engineering Aspects, 187-188: 539-568.

Brennan, S.T., Burruss, R.C., Merrill, M.D., Freeman, P.A. and Ruppert, L.F., 2010. A probabilistic assessment methodology for the evaluation of geologic carbon dioxide storage

Brosse, E., 2005a. Special issue - IFP International Workshop "Gas-Water-Rock Interactions Induced by Reservoir Exploitation, CO2 Sequestration, and other Geological Storage. Oil & Gas Science and Technology - Revue de l'Institut Français du Pétrole, 60(1): 1-206.

Brosse, E., 2005b. Special issue - IFP International Workshop "Gas-Water-Rock Interactions Induced by Reservoir Exploitation, CO2 Sequestration, and other Geological Storage. Oil & Gas Science and Technology - Revue de l'Institut Français du Pétrole, 60(2): 207-433.

Brunauer, S., Emmett, P.H. and Teller, E., 1938. Adsorption of gases in multimolecular layers. Journal of the American Chemical Society 60: 309-319.

Burnham, A.K., 1979a. Reaction kinetics between CO2 and oil-shale residual carbon. 1. Effect of heating rate on reactivity. Fuel, 58(4): 285-292.

Burnham, A.K., 1979b. Reaction kinetics between CO2 and oil-shale residual carbon. 2. Partial-pressure and catalytic-mineral effects. Fuel, 58(10): 713-718.

Burnham, A.K. and Sweeney, J.J., 1989. A chemical kinetic model of vitrinite maturation and reflectance. Geochimica et Cosmochimica Acta, 53(10): 2649-2657.

Busch, A., Alles, S., Gensterblum, Y., Prinz, D., Dewhurst, D.N., Raven, M.D., Stanjek, H. and Krooss, B.M., 2008. Carbon dioxide storage potential of shales. International Journal of Greenhouse Gas Control, 2(3): 297-308.

Busch, A. and Amann-Hildenbrand, A., 2013. Predicting capillarity of mudrocks. Marine and Petroleum Geology, 45(0): 208-223.

Busch, A., Amann-Hildenbrand, A., Bertier, P., Waschbuesch, M. and Krooss, B., M. , 2010. The Significance of Caprock Sealing Integrity for CO2 Storage, SPE International Conference on CO2 Capture, Storage, and Utilization. Society of Petroleum Engineers, New Orleans, Louisiana, USA.

Busch, A. and Gensterblum, Y., 2011. CBM and CO2-ECBM related sorption processes in coal: A review. International Journal of Coal Geology, 87(2): 49-71.

Busch, A., Gensterblum, Y. and Krooss, B.M., 2003a. Methane and CO2 sorption and desorption measurements on dry Argonne Premium Coals: Pure components and mixtures. International Journal of Coal Geology, 55: 205-224.

Busch, A., Gensterblum, Y. and Krooss, B.M., 2007. High-Pressure Sorption of Nitrogen, Carbon Dioxide, and their Mixtures on Argonne Premium Coals. Energy and Fuels, 21: 1640-1645.

Busch, A., Gensterblum, Y., Krooss, B.M. and Littke, R., 2004a. Methane and carbon dioxide adsorption-diffusion experiments on coal: upscaling and modeling. International Journal of Coal Geology, 60(2-4): 151-168.

Busch, A., Gensterblum, Y., Krooss, B.M. and Siemons, N., 2006. Investigation of high-pressure selective adsorption/desorption behaviour of CO2 and CH4 on coals: An experimental study. International Journal of Coal Geology, 66(1-2): 53-68.

Busch, A., Gensterblum, Y., Siemons, N., Krooss, B.M., van Bergen, F., Pagnier, H.J.M. and David, P., 2003b. Investigation of preferential sorption behaviour of CO2 and CH4 on coals by high-pressure adsorption/desorption experiments with gas mixtures, Proceedings of the 2003 Coalbed Methane Symposium, Tuscalosa, pp. 14.

Busch, A., Krooss, B.M. and Gensterblum, Y., 2004b. Carbon dioxide storage in coalbed seams: Adsorption/desorption experiments with carbon dioxide/methane mixtures within the framework of the EU-RECOPOL project, CO2-speicherung in kohleflÃ¶zen: Adsorptions/desorptions-experimente mit CO2/CH4-mischungen im Rahmen des EU-RECOPOL projektes, pp. 473-483.

Busch, A., Krooss, B.M., Gensterblum, Y., van Bergen, F. and Pagnier, H.J.M., 2003c. High-pressure adsorption of methane, carbon dioxide and their mixtures on coals with a special focus on the preferential sorption behaviour. Presented at Geofluids IV, May 12-16, Utrecht., J. Geochem. Expl., 78-79: 671-674.

Busch, A. and Müller, N., 2011. Determining CO2 /brine relative permeability and capillary threshold pressures for reservoir rocks and caprocks: Recommendations for development of standard laboratory protocols. Energy Procedia, 4: 6053-6060.

Bustin, A.M.M. and Bustin, R.M., 2008. Coal reservoir saturation: Impact of temperature and pressure. AAPG Bulletin, 92(1): 77-86.

Bustin, R.M., 2004. Acid Gas Sorption by British Columbia Coals: Implications for Permanent Disposal of Acid Gas in Deep Coal Seams and Possible Co-Production of Methane, University of British Columbia, Vancouver, pp. 126.

Bustin, R.M. and Clarkson, C.R., 1998. Geological Controls on coalbed methane reservoir capacity and gas content. International Journal of Coal Geology, 38: 3-26.

Byrer, C.W.G., H.D., 1999. Appalachian Coals: Potential Reservoirs for sequestering Carbon Dioxide emissions from Power Plants While enhancing CBM Production. Int. CBM Symposium, Univ. of Alabama,Tuscaloosa: 319-327.

Candido, A. and Rostirolla, S., 2007. Análise de fácies e revisão da estratigrafia de seqüências da Formação Ponta Grossa, Bacia do Parná - ênfase nos arenotos de Membro Tibagi. Bulletin Geoci. Petrobras, 15(1): 45-62.

Carles, P., Bachaud, P., Lasseur, E., Berne, P. and Bretonnier, P., 2010. Confining Properties of Carbonated Dogger Caprocks (Parisian Basin) for CO2 Storage Purpose. Oil Gas Sci. Technol. Rev. IFP, 65(3): 461-472.

Carman, P.C., 1956. Flow of gases through porous media. Butterworth, London.

Carroll, R.E. and Pashin, J.C., 2003. Relationship of sorption capacity to coal quality: CO2 sequestration potential of coalbed methane reservoirs in the Black Warrior Basin, International Coalbed Methane Symposium, Tuscaloosa, Al.

Carslaw, H.S. and Jaeger, J.C., 1959. Conduction of heat in solids Oxford University Press, Oxford

Cathles, L.M., Su, Z. and Chen, D., 2010. The physics of gas chimney and pockmark formation, with implications for assessment of seafloor hazards and gas sequestration. Marine and Petroleum Geology, 27(1): 82-91.

Chaback, J.J., Morgan, W.D., Yee, D., 1996. Sorption of nitrogen, methane, carbon dioxide and their mixtures on bituminous coals at in-situ conditions. Fluid Phase Equilibria, 117: 289-296.

Chalbaud, C., Lombard, J.-M., Martin, F., Robin, M., Bertin, H. and Egermann, P., 2007. Two Phase Flow Properties of Brine-CO2 Systems in a Carbonate Core: Influence of Wettability on Pc and kr., Reservoir Characterization and Simulation Conference SPE/EAGE Abu Dhabi, UAE, pp. 10.

Chalbaud, C., Robin, M., Lombard, J.M., Bertin, H. and Egermann, P., 2010. Brine/CO2 Interfacial Properties and Effects on CO2 Storage in Deep Saline Aquifers. Oil Gas Sci. Technol. Rev. IFP, 65(4): 541-555.

Chalbaud, C., Robin, M., Lombard, J.M., Martin, F., Egermann, P. and Bertin, H., 2009. Interfacial tension measurements and wettability evaluation for geological CO2 storage. Advances in Water Resources, 32(1): 98-109.

Chalmers, G.R.L. and Bustin, M.R., 2007. On the effects of petrographic composition on coalbed methane sorption. International Journal of Coal Geology, 69(4): 288-304.

Chapuis, R.P. and Aubertin, M., 2003. On the use of the KozenyÂ–Carman equation to predict the hydraulic conductivity of soils. Canadian Geotechnical Journal, 40(3): 616-628.

Charrière, D. and Behra, P., 2010. Water sorption on coals. Journal of Colloid and Interface Science, 344(2): 460-467.

Charrière, D., Pokryszka, Z. and Behra, P., 2010. Effect of pressure and temperature on diffusion of CO2 and CH4 into coal from the Lorraine basin (France). International Journal of Coal Geology, 81: 373–380.

Chertkov, V.Y. and Ravina, I., 2001. Effect of interaggregate capillary cracks on the hydraulic conductivity of swelling clay soils. Water Resources Research, 37(5): 1245-1256.

Chiquet, P., Broseta, D. and Thibeau, S., 2007a. Wettability alteration of caprock minerals by carbon dioxide. Geofluids, 7: 112–122.

Chiquet, P., Broseta, D., Thibeau, S., 2005. Capillary alteration of shaly caprocks by carbon dioxide, SPE Europec/EAGE Annual Conference, Madrid, Spain, pp. 10.

Chiquet, P., Daridon, J.-L., Broseta, D. and Thibeau, S., 2007b. CO2/water interfacial tensions under pressure and temperature conditions of CO2 geological storage. Energy Conversion and Management, 48(3): 736-744.

Chlou, C.T., Rutherford, D.W., 1993. Sorption of N1 and EGME Vapors on Some Soils, Clays, and Mineral Oxides and Determination of Sample Surface Areas by Use of Sorption Data. Environmental Science and Technology, 27: 1587-1594.

Chun, B.-S. and Wilkinson, G.T., 1995. Interfacial tension in high-pressure carbon dioxide mixtures. Industrial & Engineering Chemistry Research, 34(12): 4371-4377.

Ciembroniewicz, A. and Marecka, A., 1993. Kinetics of CO2 sorption for two Polish hard coals. Fuel, 72(3): 405-408.

Clarkson, C.R. and Bustin, R.M., 1999a. The effect of pore structure and gas pressure upon the transport properties of coal: a laboratory and modeling study. 1. Isotherms and pore volume distributions. Fuel, 78(11): 1333-1344.

Clarkson, C.R. and Bustin, R.M., 1999b. The effect of pore structure and gas pressure upon the transport properties of coal: a laboratory and modeling study. 2. Adsorption rate modeling. Fuel, 78(11): 1345-1362.

Clarkson, C.R. and Bustin, R.M., 2000. Binary gas adsorption/desorption isotherms: effect of moisture and coal composition upon carbon dioxide selectivity over methane. International Journal of Coal Geology, 42: 241-271.

Clayton, J.L., 1998. Geochemistry of coalbed gas – A review. Int J. Coal Geology, 35: 159-173.

CO2Now, 2013. http://co2now.org/ (accessed on June 5th, 2013).

Cole, D.R., Chialvo, A.A., Rother, G., Vlcek, L. and Cummings, P.T., 2010. Supercritical fluid behavior at nanoscale interfaces: Implications for CO2 sequestration in geologic formations. Philosophical Magazine.

Comerlati, A., Ferronato, M., Gambolati, G., Putti, M. and Teatini, P., 2006. Fluid-dynamic and geomechanical effects of CO2 sequestration below the Venice Lagoon. Environ. Eng. Geosci., 12 (3): 211-226.

Coppens, L., 1936. Ann. Mines Belg., 37: 173.

Costanzo, P.A. and Guggenheim, S., 2001. Baseline studies of the Clay Minerals Society Source Clays. Clays and Clay Minerals, 49(5): 371.

Cramer, B., Krooss, B.M. and Littke, R., 1998. Modelling isotope fractionation during primary cracking of natural gas: a reaction kinetic approach. Chemical Geology, 149(3â€“4): 235-250.

Crank, J., 1975. The Mathematics of Diffusion. Oxford University Press, 414 pp.

Crosdale, P.J., 1999. Mixed Methane/carbon Dioxide sorption by coal: New evidence in support of pore-filling models. Int. CBM Symposium, Univ. of Alabama, Tuscaloosa: 359-366.

Crosdale, P.J., Beamish, B.B. and Valix, M., 1998a. Coalbed methane sorption related to coal composition. International Journal of Coal Geology, 35(1-4): 147-158.

Crosdale, P.J., Beamish, B.B. and Valixa, M., 1998b. Coalbed methane sorption related to coal composition. Int J. Coal Geology, 35: 147-158.

Crosdale, P.J., Moore, T.A. and Mares, T.E., 2008. Influence of moisture content and temperature on methane adsorption isotherm analysis for coals from a low-rank, biogenically-sourced gas reservoir. International Journal of Coal Geology, 76(1-2): 166-174.

Cui, X., Bustin, R.M. and Dipple, G., 2004. Selective transport of CO2, CH4, and N2 in coals: insights from modeling of experimental gas adsorption data. Fuel, 83: 293-303.

Damen, K., Faaij, A., van Bergen, F., Gale, J., Lysen, E., 2005. Identification of early opportunities for CO2 sequestration--worldwide screening for CO2-EOR and CO2-ECBM projects. Energy, 30(10): 1931-1952.

Darcey, J.R., Clunie, J.C. and Thomas, D.G., 1958. The adsorption of water by Saran charcoal. Transactions of the Faraday Society, 54: 250-256.

Davies, P.B., 1991. Evaluation of the role of threshold pressure in controlling flow of waste-generated gas into bedded salt at the Waste Isolation Pilot Plant (WIPP), Sandia National Laboratories, Albuquerque, New Mexico

Davies, R.J., Mathias, S.A., Moss, J., Hustoft, S. and Newport, L., Hydraulic fractures: How far can they go? Marine and Petroleum Geology(0).

Davies, R.J., Mathias, S.A., Moss, J., Hustoft, S. and Newport, L., 2012. Hydraulic fractures: How far can they go? Marine and Petroleum Geology, 37(1): 1-6.

Day, S., Duffy, G., Sakurovs, R. and Weir, S., 2008a. Effect of coal properties on CO2 sorption capacity under supercritical conditions. International Journal of Greenhouse Gas Control, 2(3): 342-352.

Day, S., Fry, R. and Sakurovs, R., 2008b. Swelling of Australian coals in supercritical CO2. International Journal of Coal Geology, 74(1): 41-52.

Day, S., Sakurovs, R. and Weir, S., 2008c. Supercritical gas sorption on moist coals. International Journal of Coal Geology, 74(3-4): 203-214.

Day, S.J., Duffy, G.J., Saghafi, A., Sakurovs, R., Rubin, E.S., Keith, D.W., Gilboy, C.F., Wilson, M., Morris, T., Gale, J. and Thambimuthu, K., 2005. Factors controlling CO2 absorption in Australian coals, Greenhouse Gas Control Technologies 7. Elsevier Science Ltd, Oxford: 2221-2224.

de Jong, S.M., Spiers, C.J. and Busch, A., submitted. Development of swelling strain in smectite clays through exposure to CO2. International Journal of Greenhouse Gas Control.

de Jong, S.M., Spiers, C.J., Busch, A. and Wentinck, R., in preparation. Swelling stress development in (smectite) clays through exposure to water and CO2. Environmental Science & Technology.

De Weireld, G., Frere, M. and Jadot, R., 1999. Automated determination of high-temperature and high-pressure gas adsorption isotherms using a magnetic suspension balance. Meas. Sci. Technol., 10: 117–126.

DeGance, A.E., Morgan, W. D., Yee, D., 1993. High Pressure Adsorption of Methane, Nitrogen and Carbon Dioxide on Coal Substrates. Fluid Phase Equilibria, 82: 215-224.

Del Bene, J. and Pople, J.A., 1969. Intermolecular energies of small water polymers. Chemical Physics Letters, 4(7): 426-428.

Deming, D., 1994. Factors necessary to define a pressure seal. AAPG Bulletin, 78(6): 1005-1009.

Dewhurst, D.N. and Hennig, A.L., 2003. Geomechanical properties related to top seal leakage in the Carnarvon Basin, Northwest Shelf, Australia. Petroleum Geoscience, 9(3): 255-263.

Dewhurst, D.N., Jones, R.M. and Raven, M.D., 2002a. Microstructural and petrophysical characterization of Muderong Shale: application to top seal risking. Petroleum Geoscience, 8: 371–383.

Dewhurst, D.N., Raven, M.D., van Ruth, P., Tingate, P.R. and Siggins, A.F., 2002b. Acoustic properties of Muderong Shale. APPEA Journal, 2002: 241-257.

Diamond, W.P. and Schatzel, S.J., 1998a. Measuring the gas content of coal: A review. International Journal of Coal Geology, 35: 311-331.

Diamond, W.P. and Schatzel, S.J., 1998b. Measuring the gas content of coal: A review. International Journal of Coal Geology, 35(1-4): 311-331.

Dölling, M. and Juch, D., 2004. Ein tektonisches Modell des Kreide-Deckgebirges und der Strontianit-Gänge im zentralen Münsterland (zwischen Hamm und Münster). Schriftenr. dt. geol. Ges., 34: 39.

Dooley, J.J., Dahowski, R.T., Davidson, C.L., Wise, M.A., Gupta, N., Kim, S.H. and Malone, E.L., 2006. Carbon Dioxide Capture and Geologic Storage - A core element of a global energy technology strategy to address climate change, PNNL, Richland, WA., PNWD-3602

Dreisbach, F., Staudt, R. & Keller, J.U., 1999. High pressure adsorption data of methane, nitrogen, carbon dioxide and their binary and ternary mixtures on activated carbon. Adsorption, 5: 215-227.

Duan, Z. and Sun, R., 2003. An improved model calculating CO2 solubility in pure water and aqueous NaCl solutions from 273 to 533 K and from 0 to 2000 bar. Chemical Geology, 193: 257-271.

Dubinin, M.M., 1980. Water vapor adsorption and the microporous structures of carbonaceous adsorbents. Carbon, 18(5): 355-364.

Dubinin, M.M. and Serpinsky, V.V., 1981. Isotherm equation for water vapor adsorption by microporous carbonaceous adsorbents. Carbon, 19(5): 402-403.

Dudek, T. and Srodon, J., 2003. Thickness distribution of illite crystals in shales, part II: origin of the distribution and smectite illitization in shales. Clays Clay Miner., 51: 529-542.

Dula, W.F. and Younes, A., 2004. Relations Between Depth, Shale Gouge Ratio, Shale Seal Quality and Probabilistic Fault-Seal Column Heights in the JK Cluster Prospects, Nigeria, Shell restricted report, pp. 25.

Dullien, F.A.L., 1992. *Porous Media: Fluid Transport and Pore Structure*. Academic Press, San Diego.

Dutta, P., Bhowmik, S. and Das, S., 2011. Methane and carbon dioxide sorption on a set of coals from India. International Journal of Coal Geology, 85(3-4): 289-299.

Egermann, P., Lombard, J.-M. and Bretonnier, P., 2006. A fast and accurate method to measure threshold capillary pressure of caprocks under representative conditions, SCA International Symposium, pp. 14.

EIA, 2013. U.S. Coalbed Methane Production. http://www.eia.gov/dnav/ng/hist/rngr52nus_1a.htm (June13., 2013).

Emberley, S., Hutcheon, I., Shevalier, M., Durocher, K., Gunter, W.D., Perkins, E.H., 2004. Geochemical monitoring of fluid-rock interaction and CO2 storage at the Weyburn CO2-injection enhanced oil recovery site, Saskatchewan, Canada. Energy, 29: 1393–1401.

Ennis-King, J. and Paterson, L., 2005. Role of Convective Mixing in the Long-Term Storage of Carbon Dioxide in Deep Saline Formations. SPE Journal of Petroleum Technology, 10(3): 349-356.

Erickson, D. and Jensen, J.R., 2001. CO2 sequestration in an unminable coalbed- San Juan Basin, Colorado, U.S.A. In: D. Williams, B. Durie, P. McMullan, C. Paulson and A. Smith (Editors), Proceedings of the Fifth International Conference on Greenhouse Control Technologies, CSIRO Publishing, Cairns, Australia, pp. 589–592.

Espinoza, D.N. and Santamarina, J.C., 2010. Water-CO2-mineral systems: Interfacial tension, contact angle, and diffusion-Implications to CO2 geological storage. Water Resour. Res., 46(7): W07537.

Faiz, M., Saghafi, A., Sherwood, N. and Wang, I., 2007. The influence of petrological properties and burial history on coal seam methane reservoir characterisation, Sydney Basin, Australia. International Journal of Coal Geology, 70(1-3): 193-208.

Faiz, M.M., 2004. Microbial influences on coal seam gas reservoirs - A review, Australasian Institute of Mining and Metallurgy Publication Series, pp. 133-142.

Faiz, M.M., Saghafi, A., Barclay, S. A., Stalker, L., Sherwood, N. R., Whitford, D. J., 2007. Evaluating geological sequestration of CO2 in bituminous coals: The southern Sydney Basin, Australia as a natural analogue. International Journal of Greenhouse Gas Control, 1(2): 223-235.

Faiz, M.M., Saghafi, A., Barclay, S.A., Stalker, L., Sherwood, N.R., Whitford, D.J., 2006. Distribution of Juvenile CO2 in the Sydney Basin, Australia: A Natural Analogue for CO2 Storage in Bituminous Coals, 8th International Conference on Greenhouse Gas Technology (GHGT8), Trondheim, Norway.

Fei, Y., Marshall, M., Jackson, W.R., Chaffee, A.L. and Allardice, D.J., 2006. A comparison of adsorption isotherms using different techniques for a range of raw, water- and acid-washed lignites. Fuel, 85(10-11): 1559-1565.

Fei, Y., Zhang, C., Marshall, M., Jackson, W.R., Chaffee, A.L. and Allardice, D.J., 2007. The effect of cation content of some raw and ion-exchanged Victorian lignites on their equilibrium moisture content and surface area. Fuel, 86(17-18): 2890-2897.

Ferrage, E., Lanson, B., Sakharov, B.A. and Drits, V.A., 2005. Investigation of smectite hydration properties by modeling experimental X-ray diffraction patterns: Part I. Montmorillonite hydration properties. American Mineralogist, 90: 1358-1374.

Fitzgerald, J.E., Pan, Z., Sudibandriyo, M., Robinson, J.R.L., Gasem, K.A.M. and Reeves, S., 2005. Adsorption of methane, nitrogen, carbon dioxide and their mixtures on wet Tiffany coal. Fuel, 84(18): 2351-2363.

Fitzgerald, J.E., Robinson Jr., R.L. and Gasem, K.A.M., 2006. Modeling high-pressure adsorption of gas mixtures on activated carbon and coal using a simplified local-density model. Languir, 22: 9610-9618.

Folk, R.L., 1980. Petrology of sedimentary rocks. Hemphill Publishing Company, 190 pp.

Frailey, S.M., Rittenhouse, S., Knepp, R., Anderson, A., Leetaru, H., Korse, C., J., R. and Finley, R.J., 2006. Reservoir simulation and GIS modeling as tools for defining geological sequestration capacity: An optimal approach toward more specific assessments, Illinois basin, USA. In: J. Gale, N. Rokke, Z. P. and H. Svenson (Editors), Proceedings of the 8th International Conference on Greenhouse Gas Control Technologies.

Freund, P. and Ormerod, W.G., 1997. Progress toward storage of carbon dioxide. Energy Conversion and Management, 38(Supplement 1): S199-S204.

Fricke, K., 1961. Tiefenwasser, Solquellen und Solewanderung im Bereich des Münsterschen Beckens. Zeitung der deutschen geologischen Gesellschaft, 113: 37-41.

Fripiat, J.J., Cruz, M.L., Bohor, B.F. and Thomas Jr., J., 1974. Interlamellar adsorption of carbon dioxide by smectites. Clays and Clay Minerals, 22: 23-30.

Gale, J. and Freund, P., 2001. Coal-bed methane enhancement with CO2 sequestration worldwide potential. Env. Geosci., 8(3): 210-217.

Gallé, C., 2000. Gas breakthrough pressure in compacted Fo-Ca clay and interfacial gas overpressure in waste disposal context. Applied Clay Science, 17(1-2): 85-97.

Gamson, P., Beamish, B. and Johnson, D., 1996. Coal microstructure and secondary mineralization: their effect on methane recovery. Geological Society, London, Special Publications, 109(1): 165-179.

Gaschnitz, R., 2000. Gasgenese und Gasspeicherung im flözführenden Oberkarbon des Ruhr-Beckens (in German), RWTH-Aachen University, Aachen.

Gaschnitz, R., 2001. Gasgenese und Gasspeicherung im Flözführenden Oberkarbon des Ruhr-Beckens, RWTH Aachen University.

Gasem, K.A.M., Robinson, J., L. and Reeves, S.R., 2002a. Adsorption of pure methane, nitroge and carbon dioxide and their mixtures on San Juan Basin coals. Topical Report.

Gasem, K.A.M., Sudibandriyo, M., Fitzgerald, J.E., Pan, Z. and Robinson Jr., R.L., 2002b. Measurement and modelling of gas adsorption on selected coals. Proceesings of the AICHE Spring National Meeting, New Orleans, Lousiana, March 10-16, 2002.

Gauden, P.A., 2005. Does the Dubinin-Serpinsky theory adequately describe water adsorption on adsorbents with high-energy centers? Journal of Colloid and Interface Science, 282(2): 249-260.

Gaus, I., Audigane, P., AndrÃ©, L., Lions, J., Jacquemet, N., Durst, P., Czernichowski-Lauriol, I. and Azaroual, M., 2008. Geochemical and solute transport modelling for CO2 storage, what to expect from it? International Journal of Greenhouse Gas Control, 2(4): 605-625.

Gaus, I., Azaroual, M. and Czernichowski-Lauriol, I., 2005. Reactive transport modelling of the impact of CO2 injection on the clayey cap rock at Sleipner (North Sea). Chemical Geology, 217(3-4): 319-337.

Gensterblum, Y., Merkel, A., Busch, A. and Krooss, B.M., 2013. High-pressure CH4 and CO2 sorption isotherms as a function of coal maturity and the influence of moisture. International Journal of Coal Geology, 118(0): 45-57.

Gensterblum, Y., Merkel, A., Busch, A. and Krooss, B.M., submitted. High-pressure CH4 and CO2 sorption isotherms as a function of maturity and the influence of moisture. International Journal of Coal Geology.

Gensterblum, Y., Merkel, A., Busch, A., Krooss, B.M. and Littke, R., accepted. Gas saturation and CO2 enhancement potential of coalbed methane reservoirs as a function of depth. AAPG Bulletin.

Gensterblum, Y., van Hemert, P., Billemont, P., Battistutta, E., Busch, A., Krooss, B.M., De Weireld, G. and Wolf, K.H.A.A., 2010. European inter-laboratory comparison of high pressure CO2 sorption isotherms II: Natural coals. International Journal of Coal Geology, 84(2): 115-124.

Gensterblum, Y., van Hemert, P., Billemont, P., Busch, A., Charriére, D., Li, D., Krooss, B.M., de Weireld, G., Prinz, D. and Wolf, K.H.A.A., 2009. European inter-laboratory comparison of high pressure CO2 sorption isotherms. I: Activated carbon. Carbon, 47: 2958-2969.

Gertz, K.H. and Loeschcke, H.H., 1956. Bestimmung des Diffusionskoeffizienten von CO2 in Wasser Zeitschrift für Naturforschung, 11: 61-64.

Gibson, R.G., 1998. Physical character and fluid-flow properties of sandstone-derived fault zones. Geological Society, London, Special Publications, 127(1): 83-97.

Giesting, P., Guggenheim, S., Koster van Groos, A.F. and Busch, A., 2012a. Interaction of carbon dioxide with Na-exchanged montmorillonite at pressures to 640 bars: Implications for CO2 sequestration. International Journal of Greenhouse Gas Control, 8(0): 73-81.

Giesting, P., Guggenheim, S., Koster van Groos, A.F. and Busch, A., 2012b. X-ray Diffraction Study of K- and Ca-Exchanged Montmorillonites in CO2 Atmospheres. Environmental Science & Technology, 46(10): 5623-5630.

Given, P.H., Marzec, A., Barton, W.A., Lynch, L.J., Gerstein, B.C., 1986. The concept of a mobile or molecular phase within the macromolecular network of coals: A debate. Fuel, 65: 155-163.

GLA, 1995. Geologisches Landesamt Nordrhein-Westfalen, Geologie im Münsterland, Krefeld.

Global Carbon Project, 2012. Global Carbon Budget 2012. http://www.globalcarbonproject.org/carbonbudget/ (May 8th 2013).

Global CCS Institute, 2013. Large-scale Integrated CCS Projects. http://www.globalccsinstitute.com/projects/browse (May 8th, 2013).

Goodman, A.L., Busch, A., Bustin, R.M., Chikatamarla, L., Day, S., Duffy, G.J., Fitzgerald, J.E., Gasem, K.A.M., Gensterblum, Y., Hartman, C., Jing, C., Krooss, B.M., Mohammed, S., Pratt, T., Robinson Jr, R.L., Romanov, V., Sakurovs, R., Schroeder, K. and White, C.M., 2007a. Inter-laboratory comparison II: CO2 isotherms measured

on moisture-equilibrated Argonne premium coals at 55Â Â°C and up to 15Â MPa. International Journal of Coal Geology, 72(3-4): 153-164.

Goodman, A.L., Busch, A., Bustin, R.M., Chikatamarla, L., Day, S., Duffy, G.J., Fitzgerald, J.E., Gasem, K.A.M., Gensterblum, Y., Hartman, C., Jing, C., Krooss, B.M., Mohammed, S., Pratt, T., Robinson Jr, R.L., Romanov, V., Sakurovs, R., Schroeder, K. and White, C.M., 2007b. Inter-laboratory comparison II: CO2 isotherms measured on moisture-equilibrated Argonne premium coals at 55C and up to 15 MPa. International Journal of Coal Geology, 72(3-4): 153-164.

Goodman, A.L., Busch, A., Duffy, G., Fitzgerald, J.E., Gasem, K.A.M., Gensterblum, Y., Krooss, B.M., Levy, J., Ozdemir, E., Pan, Z., Robinson, J., R.L., Schroeder, K., Sudibandriyo, M. and White, C., 2004. An Inter-laboratory Comparison of CO2 Isotherms Measured on Argonne Premium Coal Samples. Energy and Fuel, 18: 1175-1182.

Goodman, A.L., Favors, R.N., Hill, M.M. and Larsen, J.W., 2005. Structure Changes in Pittsburgh No. 8 Coal Caused by Sorption of CO2 Gas. Energy & Fuels, 19(4): 1759-1760.

GRI, 1995. A guide to determining coalbed gas contents, GRI Reference No. GRI-94/0396. Gas Research Institute, 204 pp.

Gruszkiewicz, M.S., Naney, M.T., Blencoe, J.G., Cole, D.R., Pashin, J.C. and Carroll, R.E., 2009. Adsorption kinetics of CO2, CH4, and their equimolar mixture on coal from the Black Warrior Basin, West-Central Alabama. International Journal of Coal Geology, 77(1-2): 23-33.

Gumma, S. and Talu, O., 2003. Gibbs Dividing Surface and Helium Adsorption. Adsorption, 9(1): 17-28.

Gunter, W.D., Mavor, M.J. and Robinson, J.R., 2004. CO2 storage and enhanced methane production: Field testing at Fenn-Big Valley, Iberta, Canada, with application, 7th International Conference on Greenhouse Gas Control Technology, Vancouver, Canada.

Gunter, W.D., Perkins, E.H., Hutcheon, I., 2000. Aquifer disposal of acid gases: modelling of water-rock reactions for trapping of acid wastes. Applied Geochemistry, 15(8): 1085-1095.

Gunter, W.D., Wiwehar, B. and Perkins, E.H., 1997. Aquifer disposal of CO2-rich greenhouse gases: Extension of the time scale of experiment for CO2-sequestering reactions by geochemical modelling. Mineralogy and Petrology, 59(1): 121-140.

Gunter, W.D.P., E.H., McCann, T.J., 1993. Aquifer disposal of CO2-rich gases: Reaction design for added capacity. Energy Conversion and Management, 34(9-11): 941-948.

Gutierrez-Rodriguez, J.A., Purcell, R.J. Jr.,Aplan F.F.,, 1984. Estimating the Hydrophobicity of coal. Colloids and Surfaces, 12: 1-25.

Hall, F.E., Zhou, C., Gasem, K.A.M. and Robinson Jr., R.L., 1994. Adsorption of pure methane, nitrogen and carbon dioxide and their binary mixtures on wet Fruitland coals. SPE, 29194: 329-344.

Han, F., Busch, A., Krooss, B.M., Liu, Z., van Wageningen, N. and Yang, J., 2010a. Experimental Study on Fluid Transport Processes in the Cleat and Matrix Systems of Coal. Energy & Fuels, 24(12): 6653-6661.

Han, F., Busch, A., Krooss, B.M., Liu, Z. and Yang, J., 2013. CH4 and CO2 sorption isotherms and kinetics for different size fractions of two coals. Fuel, 108(0): 137-142.

Han, F., Busch, A., van Wageningen, N., Yang, J., Liu, Z. and Krooss, B.M., 2010b. Experimental study of gas and water transport processes in the inter-cleat (matrix) system of coal: Anthracite from Qinshui Basin, China. International Journal of Coal Geology, 81(2): 128-138.

Hangx, S.J.T. and Spiers, C.J., 2009. Reaction of plagioclase feldspars with CO2 under hydrothermal conditions. Chemical Geology, 265(1-2): 88-98.

Hangx, S.J.T., Spiers, C.J. and Peach, C.J., 2010a. The effect of deformation on permeability development in anhydrite and implications for caprock integrity during geological storage of CO2. Geofluids, 10(3): 369-387.

Hangx, S.J.T., Spiers, C.J. and Peach, C.J., 2010b. Mechanical behavior of anhydrite caprock and implications for CO2 sealing capacity. J. Geophys. Res., 115(B7): B07402.

Hanzawa, Y., Kaneko, K., Yoshizawa, N., Pekala, R.W., Dresselhaus, M.S., 1998. The pore structure determination of carbon aerogels. Adsorption, 4: 187-195.

Harpalani, S. and Chen, G., 1997. Influence of gas production induced volumetric strain on permeability of coal. Geotechnical and Geological Engineering, 15: 303-325.

Harpalani, S., Prusty, B.K. and Dutta, P., 2006. Methane/CO2 Sorption Modeling for Coalbed Methane Production and CO2 Sequestration. Energy and Fuels, 20: 1591-1599.

Harper, T.R. and Lundin, E.R., 1997. Fault seal analysis: reducing our dependence on empiricism, Norwegian Petroleum Society Special Publications. Elsevier, Volume 7: 149-164.

Harrington, J.F. and Horseman, S.T., 1999. Gas transport properties of clays and mudrocks. Geological Society, London, Special Publications, 158(1): 107-124.

Harrington, J.F., Milodowski, A.E., Graham, C.C., Rushton, J.C. and Cuss, R.J., 2012. Evidence for gas-induced pathways in clay using a nanoparticle injection technique. Mineralogical Magazine, 76(8): 3327-3336.

Hartman, C. and Pratt, T.J., 2005. A Preliminary Study of the Effect of Moisture on the Carbon Dioxide Storage Capacity in Coal, paper 0533, Proceedings 2005 International Coalbed Methane Symposium, University of Alabama, Tuscaloosa, pp. 9.

Hebach, A., Oberhof, A., Dahmen, N., Kögel, A., Ederer, H. and Dinjus, E., 2002. Interfacial tension at elevated pressure measurements and correlations in the water + carbon dioxide system. J. Chem. Eng. Data, 47: 1540-1546.

Heim, S., Jurisch, S.A., B.M., K., Weniger, P. and Littke, R., 2011. Systematics of pyrolytic N2 and CH4 release from peat and coals of different thermal maturity. International Journal of Coal Geology.

Hemza, P., Sivek, M. and Jirásek, J., 2009. Factors influencing the methane content of coal beds of the Czech part of the Upper Silesian Coal Basin, Czech Republic. International Journal of Coal Geology, 79(1-2): 29-39.

Hendriks, C., Graus, W. and van Bergen, F., 2004. Global Carbon Dioxide Storage Potential and Costs, ECOFYS, Utrecht

Hildenbrand, A., Krooss, B.M., Busch, A. and Gaschnitz, R., 2006. Evolution of methane sorption capacity of coal seams as a function of burial history - A case study from the Campine Basin, NE Belgium. International Journal of Coal Geology, 66(3): 179-203.

Hildenbrand, A., Schloemer, S., Krooss, B. and Littke, R., 2004a. Gas breakthrough experiments on pelitic rocks: comparative study with N_2, CO_2 and CH_4. Geofluids, 4: 61-80.

Hildenbrand, A., Schlömer, S. and Krooss, B.M., 2002. Gas breakthrough experiments on fine-grained sedimentary rocks. Geofluids, 2: 3-23.

Hildenbrand, A., Schlömer, S., Krooss, B.M. and Littke, R., 2004b. Gas breakthrough experiments on pelitic rocks: comparative study with N2, CO2 and CH4. Geofluids, 4: 61-80.

Hills, G.J. and Høiland, H., 1984. Pressure dependence of the surface tension of mercury. Journal of Colloid and Interface Science, 99(2): 463-467.

Hirsch, P.B., 1954. X-Ray Scattering from Coals. Proceedings of the Royal Society of London. Series A. Mathematical and Physical Sciences, 226(1165): 143-169.

Hiss, M., 2006. Lihostartigraphisches Lexikon. Emscher-Formation. Deutsche stratigraphische Kommision. www.bgr.de/app/litholex/gesamt_ausgabe.cfm?id=2008007

Hitchon, B., Gunter, W.D., Gentzis, T. and Bailey, R.T., 1999. Sedimentary basins and greenhouse gases: a serendipitous association. Energy Conversion and Management, 40(8): 825-843.

Hol, S., Peach, C.J. and Spiers, C.J., 2010a. Applied stress reduces the CO2 sorption capacity of coal. International Journal of Coal Geology, 85(1): 128-142.

Hol, S., Peach, C.J. and Spiers, C.J., 2010b. A new experimental method to determine the CO2 sorption capacity of coal, GHGT 10. Energy Procedia, Amsterdam, the Netherlands.

Hol, S., Peach, C.J. and Spiers, C.J., 2011. A new experimental method to determine the CO2 sorption capacity of coal. Energy Procedia, 4: 3125-3130.

Hol, S. and Spiers, C.J., submitted for publication. Competition between adsorption-induced swelling and elastic compression in coal at CO2 pressures up to 100 MPa. Journal of the Mechanics and Physics of Solids.

Holloway, S., 1997. Safety Of The Underground Disposal Of Carbon Dioxide. Energy Conversion and Management, 38: 241-245.

Holz, M., 1998. The Eo-Permian coal seams of the Paraná basin in southernmost Brazil: An analysis of the depositional conditions using sequence stratigraphy concepts. International Journal of Coal Geology, 36: 141-163.

Holz, M. and Kalkreuth, W., 2004. Sequence Stratigraphy and Coal Petrology applied to the Early Permian coal-bearing Rio Bonito Formation, Paraná Basin, Brazil. In: J. Pashin and R. Gastaldo (Editors), Sequence Stratigraphy, Paleoclimate, and Tectonics of Coal-Bearing Strata. AAPG Studies in Geology, 51: 147-167.

Holz, M., Kalkreuth, W. and Alves Rolim, S.B., 2010. Extension of the Parana Basin to offshore Brazil: Implications for coalbed methane evaluation. Marine and Petroleum Geology, 27(5): 1119-1132.

Holz, M., Vieira, P. and Kalkreuth, W., 2000. The Early Permian coal-bearing succession of the Paraná basin in southernmost Brazil: depositional model and sequence stratigraphy. Revista Brasileira de Geosciências, 30: 420-422.

Horikawa, T., Sekida, T., Hayashi, J.i., Katoh, M. and Do, D.D., 2010. A new adsorption-desorption model for water adsorption in porous carbons. Carbon, 49(2): 416-424.

Horseman, S.T., Harrington, J.F. and Sellin, P., 1999. Gas migration in clay barriers. Engineering Geology, 54(1-2): 139-149.

Huang, H., Wang, K., Bodily, D.M. and Hucka, V.J., 1995. Density Measurements of Argonne Premium Coal Samples. Energy & Fuels, 9(1): 20-24.

Humayun, R. and Tomasko, D.L., 2000. High-Resolution Adsorption Isotherms of Supercritical Carbon Dioxide on Activated Carbon. AlCHE Journal, 46(10): 2065-2075.

Hunt, A.M. and Steele, D.J., 1991. Coalbed Methane Development in the Appalachian Basin. Quarterly Review of Methane from Coalseams Technology, 8(4): 10-19.

Ibrahim, M.A., Tek, M.R. and Katz, D.L., 1970. Threshold pressure in gas storage, Pipeline Research Committee, American Gas Association at the University of Michigan, Michigan.

IEA, Geological Storage of CO2.

IEA, 2010. Energy Technology Perspectives.

IEA, 2013. Redrawing the Energy-Climate Map: World Energy Outlook Special Report

IEA (International Energy Agency), 2012. Golden Rules for a Golden Age of Gas, OECD/IEA, Paris

IEAGHG, 2012. Barriers to Implementation of CCS: Capacity Constraints

Iiyama, T., Nishikawa, K., Suszuki, T., Kaneko, K., 1997. Study of the structure of a water molecular assembly in a hydrophobic nanospace at low temperature with in situ X-ray diffraction. Chemical Physics Letters, 274: 152-158.

IPCC, 2005. IPCC Special Report on Carbon Dioxide Capture and Storage. Prepared by Working Group III of the Intergovernmental Panel on Climate Change pp. 442.

IPCC, 2007. Climate Change 2007: The Physical Science Basis, contribution of Working Group I to the Fourth Assessment Report of the IPCC. In: S. Solomon et al. (Editors). Cambridge University Press, Cambridge and New York.

Ito, D., Akaku, K., Okabe, T., Takahashi, T. and Tsujia, T., 2010. Measurement of threshold capillary pressure for seal rocks using the step-by-step approach and the residual pressure approach, GHGT10, Amsterdam, the Netherlands.

IUPAC, 2001. Manual of symbols and terminology for physicochemical quantities and units, pp. 78.

Jerauld, G.R. and Salter, S.J., 1990. The effect of pore-structure on hysteresis in relative permeability and capillary pressure: Pore-level modeling. Transport in Porous Media, 5(2): 103-151.

Joubert, J.I., Clifford, T. and Bienstock, D., 1973. Sorption of Methane in moist coal. Fuel, 52: 181-185.

Joubert, J.I., Grein, T. and Bienstock, D., 1974. Effect of moisture on the methane capacity of American coals. Fuel, 53: 186-191.

Juch, D., 1997. Results of the resources assessment in the West German hardcoal deposits, Proceedings of the XII. International Congress on the Carboniferous and Permian, Warsaw, Poland, pp. 339-344.

Juch, D., Roos, W.-F. and Wolff, M., 1994. Kohleinhaltserfassung in den westdeutschen Steinkohlelagerstätten. Fortschritte in der Geologie von Rheinland und Westfalen, 38: 189-307.

Jung, J.-W. and Wan, J., 2012. Supercritical CO2 and Ionic Strength Effects on Wettability of Silica Surfaces: Equilibrium Contact Angle Measurements. Energy & Fuels, 26(9): 6053-6059.

Jüntgen, H., 1987. Research for future in situ conversion of coal. Fuel, 66(4): 443-453.

Kaffanke, H., 1988. Gasinhalt der Flöze in Explorationsbohrlöchern der Bergbau AG Lippe. Glückauf-Forschungshefte, 49: 38-47.

Kalkreuth, W. and Holz, M., 2000. The coalbed methane potential of the Santa Terezinha coalfield, Rio Grande Do Sul, Brazil. Revista Brasileira de Geociências, 30: 342-345.

Kalkreuth, W., Holz, M., Casagrande, J., Cruz, R., Oliveira, T., Kern, M., Levandowski, J. and Rolim, S., 2008a. O Potencial de Coalbed Methane (CBM) na jazida da Santa Terezinha - modelagem 3D e avaliação do poço de exploração CBM001-ST-RS. Revista Brasileira de Geociências, 38(2): 1-17.

Kalkreuth, W., Holz, M., Kern, M., Burger, H., Schauf, A., Prissang, R., Lemos de Sousa, M. and Rodriguez., C., 2003. The Coalbed Methane Potential of the Paraná Basin, 20 Congresso Brasileiro de P&T em Petróleo & Gás, Rio de Janeiro.

Kalkreuth, W., Holz, M., Kern, M., Machado, G., Mexias, A., Silva, M., Willett, J., R., F. and Burger, H., 2006. Petrology and chemistry of Permian coals from the Paraná Basin: 1. Santa Terezinha, Leão-Butia and Candiota Coalfields, Rio Grande do Sul, Brazil. International Journal of Coal Geology 68: 79-116.

Kalkreuth, W., Levandowsky, J., Holz, M., Busch, A. and Krooss, B.M., 2008b. Preliminary results of high-pressure CH4 and CO2 sorption tests on Permian age coals from the Paraná Basin, Brazil, International Conference on Coal and Organic Petrology, ICCP-TSOP, Oviedo Spain.

Karacan, C.Ö., 2003. Heterogeneous Sorption and Swelling in a Confined and Stressed Coal during CO2 Injection. Energy and Fuel, 17: 1595-1608.

Karacan, C.Ö., 2007. Swelling-induced volumetric strains internal to a stressed coal associated with CO2 sorption. International Journal of Coal Geology, 72(3-4): 209-220

Karge, H., Weitkamp, J. and Ruthven, D., 2008. Fundamentals of Adsorption Equilibrium and Kinetics in Microporous Solids, Adsorption and Diffusion. Molecular Sieves - Science and Technology. Springer Berlin / Heidelberg, 7: 1-43.

Kaszuba, J.P., Janecky, D.R., Snow, M.G., 2003. Carbon dioxide reaction processes in a model brine aquifer at 200°C and 200 bars: implications for geologic sequestration of carbon. Applied Geochemistry, 18: 1065–1080.

Kaszuba, J.P.J., D.R. Snow, M.G., 2005. Experimental evaluation of mixed fluid reactions between supercritical carbon dioxide and NaCl brine: Relevance to the integrity of a geologic carbon repository. Chemical Geology, 217(3-4): 277-293.

Katsube, T.J., 2000. Shale permeability and pore-structure evolution characteristics, Geological Survey of Canada (Current Research 2000-E15), pp. 11.

Katsube, T.J., Mudford, B.S. and Best, M.E., 1991. Petrophysical characteristics of shales from the Scotian shelf. Geophysics, 56(10): 1681-1689.

Katsube, T.J. and Williamson, M.A., 1994. Effects of diagenesis on shale nano-pore structure and implications for sealing capacity. Clay Minerals, 29: 451-461.

Katz, A.J. and Thompson, A.H., 1986. Quantitative prediction of permeability in porous rock. Physical Review B, 34(11): 8179.

Katz, A.J. and Thompson, A.H., 1987. Prediction of Rock Electrical Conductivity From Mercury Injection Measurements. J. Geophys. Res., 92(B1): 599-607.

Kedzior, S., 2009. Accumulation of coal-bed methane in the south-west part of the Upper Silesian Coal Basin (southern Poland). International Journal of Coal Geology, 80(1): 20-34.

Kelch, H.-J., 1963. Beschreibung der Spülproben der Kreide der Bohrung Münsterland 1. Fortschritte in der Geologie von Rheinland und Westfalen, 11: 19-22.

Kelemen, S.R. and Kwiatek, L.M., 2009. Physical properties of selected block Argonne Premium bituminous coal related to CO2, CH4, and N2 adsorption. International Journal of Coal Geology, 77(1-2): 2-9.

Kelemen, S.R., Kwiatek, L.M., Lee, A.G.K., 2006. Swelling and Sorption Response of Selected Argonne Premium Bituminous Coals to CO2, CH4, and N2, International CBM Symposium, Tuscaloosa, Alabama.

Kempka, T., Fernaì ndez-Steeger, T.s., Li, D.-Y., Schulten, M., Schluì^ter, R. and Krooss, B.M., 2011. Carbon Dioxide Sorption Capacities of Coal Gasification Residues. Environmental Science & Technology, 45(4): 1719-1723.

Kharaka, Y.K., Cole, D.R., Hovorka, S.D., Gunter, W.D., Knauss, K.G. and Freifeld, B.M., 2006. Gas-water-rock interactions in Frio Formation following CO2 injection: Implications for the storage of greenhouse gases in sedimentary basins. Geology, 34(7): 577-580.

Kim, Y., Wan, J., Kneafsey, T.J. and Tokunaga, T.K., 2012. Dewetting of Silica Surfaces upon Reactions with Supercritical CO2 and Brine: Pore-Scale Studies in Micromodels. Environmental Science & Technology, 46(7): 4228-4235.

Knauss, K.G., Johnson, J.W. and Steefel, C.I., 2005. Evaluation of the impact of CO2, co-contaminant gas, aqueous fluid and reservoir rock interactions on the geologic sequestration of CO2. Chemical Geology, 217(3-4): 339-350.

Koster van Groos, A.F. and Guggenheim, S., 2009. The stability of methane hydrate intercalates of montmorillonite and nontronite: Implications for carbon storage in ocean-floor environments. American Mineralogist, 94(2-3): 372-379.

Koster van Groos, A.F., Guggenheim, S. and Cornell, C., 2003. Environmental chamber for powder x-ray diffractometers for use at elevated pressures and low temperatures. Review of Scientific Instruments, 74(1): 273-275.

Kotarba, M.J. and Rice, D.D., 2001. Composition and origin of coalbed gases in the Lower Silesian basin, southwest Poland. Applied Geochemistry, 16(7-8): 895-910.

Kovack, G.E., Dewhurst, D.N., Raven, M.D., Kaldi, J.G., 2004. The influence of composition, diagenesis and compaction on seal capacity in the Mudering Shale, Carnarvon Basin. APPEA Journal, 2004: 201-221.

Kronimus, A., Busch, A., Alles, S., Juch, D., Jurisch, A. and Littke, R., 2008. A preliminary evaluation of the CO2 storage potential in unminable coal seams of the Münster Cretaceous Basin, Germany. International Journal of Greenhouse Gas Control, 2(3): 329-341.

Krooss, B. and Schaefer, R.G., 1987a. Experimental measurements of the diffusion parameters of light hydrocarbons in water-saturated sedimentary rocks: I. A new experimental procedure. Organic Geochemistry, 11(2): 193-199.

Krooss, B.M., 1988. Experimental investigation of the molecular migration of C1-C6 hydrocarbons: Kinetics of hydrocarbon release from source rocks. Organic Geochemistry, 13(1-3): 513-523.

Krooss, B.M., Busch, A., Alles, S. and Hildenbrand, A., 2003. Experimental investigation of molecular diffusion of CO2 in coals and shales, International Conference on Gas-Water-Rock Interactions Induced by Reservoir Exploitation, CO2 Sequestration, and other Geological Storage, IFP, Rueil-Malmaison, France.

Krooss, B.M. and Leythaeuser, D., 1988. Experimental measurements of the diffusion parameters of light hydrocarbons in water-saturated sedimentary rocks: II. Results and geochemical significance. Organic Geochemistry, 12(2): 91-108.

Krooss, B.M. and Leythaeuser, D., 1996. Molecular diffusion of light hydrocarbons in sedimentary rocks and its role in migration and dissipation of natural gas. In: D. Schumacher and M.A. Abrams (Editors), Hydrocarbon migration and its near-surface expression. AAPG Hedberg research conference, Vancouver, BC, Canada, 66: 173-183.

Krooss, B.M. and Leythaeuser, D., 1997. Diffusion of Methane and Ethane Through the Reservoir Cap Rock: Implications for the Timing and Duration of Catagenesis: Discussion. AAPG Bulletin, 81(1): 155-161.

Krooss, B.M., Leythaeuser, D. and Schaefer, R.G., 1988a. Light hydrocarbon diffusion in a caprock. Chemical Geology, 71(1-3): 65-76.

Krooss, B.M., Leythaeuser, D. and Schaefer, R.G., 1988b. Light hydrocarbon diffusion in a caprock. Chemical Geology, 71(1â€“3): 65-76.

Krooss, B.M., Leythaeuser, D. and Schaefer, R.G., 1992a. The quantification of diffusive hydrocarbon losses through cap rocks of natural gas reservoirs-A reevaluation. AAPG Bulletin, 76(3): 403-406.

Krooss, B.M., Leythaeuser, D. and Schaefer, R.G., 1992b. The quantification of diffusive hydrocarbon losses through cap rocks of natural gas reservoirs-A reevaluation: Reply. AAPG Bulletin, 76(11): 1842-1846.

Krooss, B.M., Littke, R., MÃ¼ller, B., Frielingsdorf, J., Schwochau, K. and Idiz, E.F., 1995. Generation of nitrogen and methane from sedimentary organic matter: Implications on the dynamics of natural gas accumulations. Chemical Geology, 126(3â€“4): 291-318.

Krooss, B.M. and Schaefer, R.G., 1987b. Experimental measurements of diffusion parameters of light hydrocarbons in water-saturated sedimentary rocks: I. A new experimental procedure. Organic Geochemistry, 11(3): 193-199.

Krooss, B.M., van Bergen, F., Gensterblum, Y., Siemons, N., Pagnier, H.J.M. and David, P., 2002. High-pressure methane and carbon dioxide adsorption on dry and moisture-equilibrated Pennsylvanian coals. International Journal of Coal Geology, 51: 69-92.

Kunz, O.K., R., Wagner, W. and Jaeschke, M., 2007. The GERG-2004 wide-range reference equation of state for natural gases. GERG Technical Monograph 15 Fortschritts-Berichte Verein Deutscher Ingenieue (VDI), 6. VDI-Verlag, Düsseldorf.

Kuuskraa, V.A., Stevens, S., Van Leeuwen, T. and Moodhe, K., 2011. World Shale Gas Resources: An Initial Assessment of 14 Regions Outside the United States, US DOE EIA, Washington, DC

Kvamme, B., Kuznetsova, T., Hebach, A., Oberhof, A. and Lunde, E., 2007. Measurements and modelling of interfacial tension for water+carbon dioxide systems at elevated pressures. Computational Materials Science, 38(3): 506-513.

Lama, R.D., Bodziony, J., 1998. Management of outburst in underground coal mines. Int J. Coal Geology, 35: 83-115.

Lamberson, M.N. and Bustin, R.M., 1993. Coalbed Methane characteristics of Gates formation coals, Northeastern British Columbia: Effect of maceral composition. AAPG Bulletin, 77(12): 2062-2076.

Laubach, S.E., Marrett, R. A., Olson, J. E., Scott, A. R., 1998. Characteristics and origins of coal cleat: A review. Int J. Coal Geology, 35: 175-207.

Laxminarayana, C. and Crosdale, P.J., 1999a. Role of coal type and rank on methane sorption characteristics of Bowen Basin, Australia coals. International Journal of Coal Geology, 40(4): 309-325.

Laxminarayana, C. and Crosdale, P.J., 1999b. Role of coal type and rank on methane sorption charakteristics of Bowen Basin, Australia coals. Int. J. Coal Geology, 40: 309-325.

Laxminarayana, C. and Crosdale, P.J., 2002. Controls on methane sorption capacity of Indian coals. AAPG Bulletin, 86(2): 201-212.

Le Quere, C., Andres, R.J., Boden, T., Conway, T., Houghton, R.A., House, J.I., Marland, G., Peters, G.P., van der Werf, G., Ahlstrom, A., Andrew, R.M., Bopp, L., Canadell, J.G., Ciais, P., Doney, S.C., Enright, C., Friedlingstein, P., Huntingford, C., Jain, A.K., Jourdain, C., Kato, E., Keeling, R.F., Klein Goldewijk, K., Levis, S., Levy, P., Lomas, M., Poulter, B., Raupach, M.R., Schwinger, J., Sitch, S., Stocker, B.D., Viovy, N., Zaehle, S. and Zeng, N., 2012. The global carbon budget 1959-2011. Earth Syst. Sci. Data Discuss., 5(2): 1107-1157.

Lenormand, R. and Zarcone, C., 1984. Role of roughness and edges during imbibition in square capillaries, SPE Annual Technical Conference and Exhibition. 1984 Copyright 1984, American Institute of Mining, Metallurgical, and Petroleum Engineer, Inc., Houston, Texas.

Lenormand, R., Zarcone, C. and Sarr, A., 1983. Mechanisms of the displacement of one fluid by another in a network of capillary ducts. Journal of Fluid Mechanics, 135: 337-353.

Levy, J.H., Day, S.J. and Killingley, J.S., 1997. Methane capacities of Bowen Basin coals related to coal properties. Fuel, 76(9): 813-819.

Leythaeuser, D., Schaefer, R.G. and Yukler, A., 1980. Diffusion of light hydrocarbons through near-surface rocks. Nature, 284(5756): 522-525.

Li, D., Liu, Q., Weniger, P., Gensterblum, Y., Busch, A. and Krooss, B.M., 2010. High-pressure sorption isotherms and sorption kinetics of CH4 and CO2 on coals. Fuel, 89(3): 569-580.

Li, L., Peters, C.A. and Celia, M.A., 2007. Applicability of averaged concentrations in determining geochemical reaction rates in heterogeneous porous media. American Journal of Science, 307(10): 1146-1166.

Li, S., Dong, M., Li, Z., Huang, S., Qing, H. and Nickel, E., 2005. Gas breakthrough pressure for hydrocarbon reservoir seal rocks: implications for the security of long-term CO2 storage in the Weyburn field. Geofluids, 5: 326–334.

Li, X., Boek, E., Maitland, G.C. and Trusler, J.P.M., 2012a. Interfacial Tension of (Brines + CO2): (0.864 NaCl + 0.136 KCl) at Temperatures between (298 and 448) K, Pressures between (2 and 50) MPa, and Total Molalities of (1 to 5) mol·kg-1. Journal of Chemical & Engineering Data, 57(4): 1078-1088.

Li, X., Boek, E.S., Maitland, G.C. and Trusler, J.P.M., 2012b. Interfacial Tension of (Brines + CO2): CaCl2(aq), MgCl2(aq), and Na2SO4(aq) at Temperatures between (343 and 423) K, Pressures between (2 and 50) MPa, and Molalities of (0.5 to 5) mol·kg-1. Journal of Chemical & Engineering Data, 57(5): 1369-1375.

Li, Z., Dong, M., Li, S. and Huang, S., 2006. CO2 sequestration in depleted oil and gas reservoirs--caprock characterization and storage capacity. Energy Conversion and Management, 47(11-12): 1372-1382.

Likos, W.J. and Lu, N., 2006. Pore-scale analysis of bulk volume change from crystalline interlayer swelling in Na+- and Ca2+-smectite. Clays Clay Miner., 54 (4): 515-528.

Lindeberg, E., 1997. Escape of CO2 from aquifers. Energy Conversion and Management, 38(Supplement 1): S235-S240.

Lindgreen, H., Drits, V.A., Sakharov, B.A., Salyn, A.L., Wrang, P. and Dainyak, L.G., 2000. Illite-smectite structural changes during metamorphism in black Cambrian Alum shales from the Baltic area. Am. Mineral., 85: 1223-1238.

Littke, R., Büker, C., Lückge, A., Sachsenhofer, R.F. and Welte, D.H., 1994. A new evaluation of palaeo-heat flows and eroded thicknesses fort he Carboniferous Ruhr basin, western Germany. International Journal of Coal Geology, 26: 155-183.

Littke, R., Krooss, B., Uffmann, A.K., H.M., S. and Horsfield, B., 2011a. Unconventional Gas Resources in the Paleozoic of Central Europe Oil & Gas Science and Technology.

Littke, R., Krooss, B., Uffmann, A.K., Schulz, H.-M. and Horsfield, B., 2011b. Unconventional Gas Resources in the Paleozoic of Central Europe. Oil Gas Sci. Technol. â€“ Rev. IFP Energies nouvelles, 66(6): 953-977.

Liu, D., Yuan, P., Liu, H., Li, T., Tan, D., Yuan, W. and He, H., 2013. High-pressure adsorption of methane on montmorillonite, kaolinite and illite. Applied Clay Science, 85(0): 25-30.

Lotze, F., 1958. Zur Frage der Beziehungen zwischen Chloridgehalt des Grundwassers und Tektonik. Forschungsbericht des Witschafts- und Verkehrsmin. NW, 491: 5-11.

Lu, J., Milliken, K., Reed, R.M. and Hovorka, S., 2011. Diagenesis and sealing capacity of the middle Tuscaloosa mudstone at the Cranfield carbon dioxide injection site, Mississippi, U.S.A. Environmental Geosciences, 18(1): 35-53.

Lu, J., Wilkinson, M., Haszeldine, R.S. and Fallick, A.E., 2009. Long-term performance of a mudrock seal in natural CO2 storage. Geology, 37(1): 35-38.

Lu, L., Sahajwalla, V., Kong, C. and Harris, D., 2001. Quantitative X-ray diffraction analysis and its application to various coals. Carbon, 39: 1821–1833.

Lynch, L.J. and Webster, D.S., 1982. Effect of thermal treatment on the interaction of brown coal and water: a nuclear magnetic resonance study. Fuel, 61(3): 271-275.

Macary, S.M., 1999. Conversion of Air Permeability to Liquid Permeabilities Extracts Huge Source of Information for Reservoir Studies, Middle East Oil Show and Conference, Bahrain.

MacEwan, D.M.C. and Wilson, M.J., 1984. Interlayer and intercalation complexes or clay minerals In: G.W. Brindley and G. Brown (Editors), Crystal Structures of Clay Minerals and Their X-ray Identification. Mineralogical Society, London.

Maddox, M., Ulberg, D. and Gubbins, K.E., 1995. Molecular simulation of simple fluids and water in porous carbons. Fluid Phase Equilibria, 104: 145-158.

Mahajan, O.P., 1991. CO2 surface area of coals: A 25 year paradox. Carbon, 29: 735-742.

Mahajan, O.P., Walker, P.L. Jr., 1970. Water adsorption on coals. Fuel, 50(3): 308-317.

Majewska, Z., Ceglarska-Stefanska, G., Majewski, S. and Zietek, J., 2009. Binary gas sorption/desorption experiments on a bituminous coal: Simultaneous measurements on sorption kinetics, volumetric strain and acoustic emission. International Journal of Coal Geology, 77(1-2): 90-102.

Majewska, Z. and Zietek, J., 2007. Changes of acoustic emission and strain in hard coal during gas sorption-desorption cycles. International Journal of Coal Geology, 70(4): 305-312.

Marecka, A. and Mianowski, A., 1998. Kinetics of CO2 and CH4 sorption on high rank coal at ambient temperatures. Fuel, 77(14): 1691-1696.

Mares, T.E., Moore, T.A. and Moore, C.R., 2009. Uncertainty of gas saturation estimates in a subbituminous coal seam. International Journal of Coal Geology, 77(3-4): 320-327.

Marschall, P., Horseman, S. and Gimmi, T., 2005. Characterisation of Gas Transport Properties of the Opalinus Clay, a Potential Host Rock Formation for Radioactive Waste Disposal Oil & Gas Science and Technology - Rev. IFP, 60(1): 121-139.

Mastalerz, M., Gluskoter, H. and Rupp, J., 2004. Carbon dioxide and methane sorption in high volatile bituminous coals from Indiana, USA. Int J. Coal Geology, 60: 43-55.

Matenaar, I., 2002. Compaction and Microfabric Rearrangement of Fine-Grained Siliciclastic Sediments, University of Newcastle upon Tyne, UK, Newcastle upon Tyne, 131 pp.

Mavor, M.J., Gunter, W.D., Robinson, J.R., 2004. Alberta multiwell micro-pilot testing for CBM properties, enhanced methane recovery and CO2 storage potential, SPE ATCE, Houston, Texas, pp. 15.

Mavor, M.J., Hartman, C. and Pratt, T.J., 2004. Uncertainty in Sorption Isotherm Measurements, 2004 CBM Symposium, Tuscaloosa, Alabama, pp. 14.

Mavor, M.J., Pratt, T.J., Nelson, C.R., 1995. Quantitative Evaluation of Coal Seam Gas Content Estimate Accuracy, SPE Rocky Mountain, Regione/Low-Permeability Reservoir Symposium, Denver, CO.

Mavor, M.J.O., L.B. & Pratt, T.J., 1990. Measurement and evaluation of coal sorption isotherm data. SPE, 20728: 157-170.

Mazumder, S., Siemons, N. and Wolf, K.-H.A.A., 2005. Differential swelling and permeability change of coal in response to CO2 injection for ECBM. SPE, 98475.

Mazumder, S., van Hemert, P., Bruining, J. and Wolf, K.H.A.A., 2003. A preliminary numerical model of CO2 sequestration in coal for improved coalbed methane recovery, CBM Symposium, Tuscaloosa Alabama.

Mazumder, S., van Hemert, P., Busch, A., Wolf, K.H.A.A. and Tejera-Cuesta, P., 2006. Flue gas and pure CO2 sorption properties of coal: A comparative study. International Journal of Coal Geology, 67(4): 267-279.

Mazumder, S., Wolf, K., van Hemert, P. and Busch, A., 2008. Laboratory Experiments on Environmental Friendly Means to Improve Coalbed Methane Production by Carbon Dioxide/Flue Gas Injection. Transport in Porous Media, 75: 63-92.

Mazumder, S. and Wolf, K.H., 2008. Differential swelling and permeability change of coal in response to CO2 injection for ECBM. International Journal of Coal Geology, 74(2): 123-138.

McCarty, R.D. and Arp, V.D., 1990. A new wide range equation of state for helium. Advances in Cryogenic Engineering, 35: 1465-1475.

McCutcheon, A.L., Barton, W.A. and Wilson, M.A., 2001. Kinetics of Water Adsorption/Desorption on Bituminous coals. Energy and Fuel, 15: 1387-1395.

McCutcheon, A.L., Barton, W.A. and Wilson, M.A., 2003. Characterization of Water Adsorbed on Bituminous Coals. Energy & Fuels, 17(1): 107-112.

Medeiros de Araújo, L., Rodrigues, R. and dos Santos Scherer, C., 2004. Interrelação entre a fábrica sedimentar, o conteúdo orgânico e o potencial redox do ambiente deposicional, deduzida das litofácies de rampa disral das seqüências deposicionais da Formação Irati, Permiano da bacia do Paraná. B. Geoci. Petrobras, 12(2): 429-434.

Melnitchenko, A., Thompson, J.G., Volzone, C. and Ortiga, J., 2000. Selective gas adsorption by metal exchanged amorphous kaolinite derivatives. Applied Clay Science, 17: 35–53.

Metcalfe, R.S., Yee, D., Seidle, J.P. and Puri, R., 1991. Review of Research Efforts in Coalbed Methane Recovery, SPE Asia-Pacific Conference. Society of Petroleum Engineers, Perth Australia.

Michel, G., 1963. Untersuchungen über die Tiefenlage der Grenze Süßwasser-Salzwasser im nördlichen Rheinland und anschließenden Teilen Westfalens, zugleich ein Beitrag zur Hydrogeologie und Chemie des tiefen Grundwasserleiters

Michel, G., 1983. Die Sole des Münsterländer Kreide-Beckens. Neues Jahrbuch der Paläontologischen und Geologischen Abhandlungen, 166: 139-159.

Michels, G. and Wouters, H., 1941. Zahlenwerte und Funktionen aus Physik, Chemie, Astromomie Geophysik und Technik, 2. Springer.

Milani, E. and Zalán, P., 1999. An outline of the geology and petroleum systems of the Paleozoic interior basins of South America. Episodes, Journal of International Geoscience, 22(3): 199-205.

Milani, E.J., 1997. Evolucao tectono-estratigrafica da Baca do Parana e seu relacionamento com a geodinamica fanerozoica do Gondwana sul-ocidental, Rio Grande do Sul Federal University, Porto Alegre, 225 pp.

Milani, E.J., Melo, J.H.G., Souza, P.A., Fernandes, L.A. and França, A.B., 2007. Bacia do Paraná. Boletim de Geociências da Petrobrás, Rio de Janeiro, 15(2): 265-287.

Mohammad, S., Fitzgerald, J., Robinson, R.L. and Gasem, K.A.M., 2009. Experimental Uncertainties in Volumetric Methods for Measuring Equilibrium Adsorption. Energy & Fuels, 23(5): 2810-2820.

Montel, F., Caillet, G., Pucheu, A., Caltagirone, J.P., 1993. Diffusion model for predicting reservoir gas losses. Marine and Petroleum Geology, 10: 51-57.

Moore, D. and Reynolds, R.C.J., 1997. X-Ray Diffraction and the Identification and Analysis of Clay Minerals. Second edition. Oxford University Press, New York.

Moore, T.A., 2012. Coalbed Methane: A review. International Journal of Coal Geology(0).

Moore, T.A., submitted. Coalbed Methane: An introductory review. International Journal of Coal Geology.

Moore, T.A. and Crosdale, P.J., 2006. The effect of moisture and temperature on adsorption isotherms of a low-rank coal: Implications for reservoir modeling, International CBM Symposium, Tuscaloosa, Al.

Mu, R. and Malhotra, V.M., 1991. A new approach to elucidate coal-water interactions by an in situ transmission FT-i.r. technique. Fuel, 70(10): 1233-1235.

Muller, E.A., Rull, L.F., Vega, L.F. and Gubbins, K.E., 1996. Adsorption of Water on Activated Carbons: A Molecular Simulation Study. The Journal of Physical Chemistry, 100(4): 1189-1196.

Murata, K., El-Merraoui, M. and Kaneko, K., 2001. A new determination method of absolute adsorption isotherm of supercritical gases under high pressure with a special relevance to density-functional theory study. The Journal of Chemical Physics, 114(9): 4196-4205.

Murray, D., 1996. Coal bed methane in the U.S.A.: analogues for worldwide development. In: R. Gayer and I. Harris (Editors), Coal bed methane and Coal Geology. Geological Society Special Publication No. 109, London: 1-12.

Myers, A.L., 2004. Thermodynamics of Adsorption. In: T.M. Letcher (Editor), Chemical Thermodynamics for Industry, Cambridge, UK.

Nelson, C.R., Steadman, E.N. and Harju, J.A., 2005. Geologic CO2 sequestration potential of the Wyodak-Anderson Coal Zone in the Power River Sytem, Energy & Environmental Research Center: Grand Forks, ND

Nelson, J.S. and Simmons, E.C., 1995. Diffusion of Methane and Ethane Through the Reservoir Cap Rock: Implications For the Timing and Duration of Catagenesis. AAPG Bulletin, 79(7): 1064–1074.

Nelson, J.S., Simmons, E.C., Krooss, B.M., Leythaeuser, D. and Schaefer, R.G., 1992. The quantification of diffusive hydrocarbon losses through cap rocks of natural gas reservoirs; a reevaluation; discussion and reply. AAPG Bulletin, 76(11): 1839-1846.

Nelson, P.H., 1994. Permeability-porosity Relationships In Sedimentary Rocks. The Log Analyst, 35(3).

Neto, E., 1995. Source Rock generative potential of Upper Devonian Shales (Ponta Grossa Formation), Paraná Basin, Brazil. AAPG Bulletin, pp. 85.

Nishino, J., 2001. Adsorption of water vapor and carbon dioxide at carboxylic functional groups on the surface of coal. Fuel, 80: 757-764.

Nodzenski, A., 1998. Sorption and desorption of gases (CH4, CO2) on hard coal and active carbon at elevated pressures. Fuel, 77(11): 1243-1246.

Nuttall, B.C., Drahovzal, J.A., Eble, C.F. and Bustin, R.M., 2009. Regional assessment of suitability of organic-rich shales for carbon sequestration: An example from the Devonian shales of the Illinois and Appalachian Basins, Kentucky. In: M. Grobe, J.C. Pashin and R.L. Dodge (Editors), Carbon dioxide sequestration in geological media-State of science. AAPG Studies in Geology, 59: 173-190.

Nuttall, B.C., Eble, C.F., Drahovzal, J.A. and Bustin, R.M., 2005. Analysis of Devonian black shales in Kentucky for potential carbon dioxide sequestration and enhanced natural gas production. DE-FC26-02NT41442, Kentucky Geological Survey/University of Kentucky, pp. 120.

O'Sullivan, T. and Smith, N.O., 1969. The Solubility and partial molar volume of nitrogen and methane in water and in aqueous sodium chloride from 50 to 125C and 100 to 600Atm. The Journal of Physical Chemistry, 74(7): 1460-1466.

Ohga, K., Fujioka, M., Yamaguchi, S. and Nako, M., 2006. Field tests of CO2 sequestration and ECBM in Japan International CBM Symposium, Tuscaloosa, Alabama, paper # 0635.

Ottiger, S., Pini, R., Storti, G. and Mazzotti, M., 2008. Competitive adsorption equilibria of CO2 and CH4 on a dry coal. Adsorption, 14(4-5): 539-556.

Ottiger, S., Pini, R., Storti, G., Mazzotti, M., Bencini, R., Quattrocchi, F., Sardu, G. and Deriue, G., 2006. Adsorption of Pure Carbon Dioxide and Methane on Dry Coal from the Sulcis Coal Province (SW Sardinia, Italy). Environmental Progress, 25: 355-364.

Ozdemir, E., 2009. Modeling of coal bed methane (CBM) production and CO2 sequestration in coal seams. International Journal of Coal Geology, 77(1-2): 145-152.

Ozdemir, E., Morsi, B.I. and Schroeder, K., 2003. Importance of volume effects to adsorption isotherms of carbon dioxide on coals. Langmuir, 19: 9764-9773.

Ozdemir, E., Morsi, B.I. and Schroeder, K., 2004. CO2 adsorption capacity of Argonne Premium Coals. Fuel, 83: 1085-1094.

Ozdemir, E. and Schroeder, K., 2009. Effect of Moisture on Adsorption Isotherms and Adsorption Capacities of CO2 on Coals. Energy & Fuels, 23(5): 2821–2831.

Padula, V., 1969. Oil shale of Permian Iratí Formation. AAPG Bulletin, 53(3): 591-602.

Palmer, I. and Mansoori, J., 1998. How Permeability Depends on Stress and Pore Pressure in Coalbeds: A New Model. SPE Reservoir Evaluation & Engineering, SPE 52607: 539-544.

Pan, Z. and Connell, L.D., 2007. A theoretical model for gas adsorption-induced coal swelling. International Journal of Coal Geology, 69(4): 243-252.

Pan, Z., Connell, L.D., Camilleri, M. and Connelly, L., 2010. Effects of matrix moisture on gas diffusion and flow in coal. Fuel, 89(11): 3207-3217.

Peng, D.Y. and Robinson, D.B., 1976. A New Two-Constant Equation of State. Ind. Eng. Chem. Fundam., 15(1): 59-64.

Peng, X., Zhao, J. and Cao, D., 2007. Adsorption of carbon dioxide of 1-site and 3-site models in pillared clays: A Gibbs ensemble Monte Carlo simulation. Journal of Colloid and Interface Science, 310(2): 391-401.

Pentland, C.H., 2010. Measurements of Non-wetting Phase Trapping in Porous Media Imperial College London, London, 154 pp.

Peters, G.P., Davis, S.J. and Andrew, R., 2012. A synthesis of carbon in international trade. Biogeosciences, 9(8): 3247-3276.

Pini, R., Ottiger, S., Burlini, L., Storti, G. and Mazzotti, M., 2010. Sorption of carbon dioxide, methane and nitrogen in dry coals at high pressure and moderate temperature. International Journal of Greenhouse Gas Control, 4(1): 90-101.

Pini, R., Ottiger, S., Burlini, L., Storti, G., Mazzotti, M., Bencini, R. and Quattrocchi, F., 2006a. Experimental study of CO2 sequestration by ECBM recovery: the case of Sulcis coal, GHGT8, Trondheim, Norway.

Pini, R., Ottiger, S., Rajendran, A., Storti, G. and Mazzotti, M., 2006b. Reliable measurement of near-critical adsorption by gravimetric method. Adsorption, 12(5): 393-403.

Pone, J.D.N., Halleck, P.M. and Mathews, J.P., 2009. Sorption Capacity and Sorption Kinetic Measurements of CO2 and CH4 in Confined and Unconfined Bituminous Coal. Energy & Fuels, 23(9): 4688-4695.

Prinz, D., 2004. Die Porenstruktur von Kohlen (in German), RWTH Aachen University, Germany, Aachen, 184 pp.

Prinz, D. and Littke, R., 2005. Development of the micro- and ultramicroporous structure of coals with rank as deduced from the accessibility to water. Fuel, 84(12-13): 1655-1662.

Prinz, D., Pyckhout-Hintzen, W., Krooss, B.M. and Littke, R., 2001. Investigations on the Micro- and Mesoporous Structure of Coals of Varying Rank: A Combined Small Angle Neutron Scattering (SANS) and Gas Adsorption Experiments Study. Int. CBM Symposium, Tuscaloosa.

Prinz, D., Pyckhout-Hintzen, W. and Littke, R., 2004. Development of the meso- and macroporous structure of coals with rank as analyzed with small angle neutron scattering and adsorption experiments. Fuel, 83: 547-556.

Pruess, K., 2008. Leakage of CO2 from geologic storage: Role of secondary accumulation at shallow depth. International Journal of Greenhouse Gas Control, 2(1): 37-46.

Pugh, V.J., Thomas, D.C. and Gupta, S.P., 1991. Correlations of Liquid and air permeabilities for use in reservoir engineering studies. The Log Analyst, 32(5).

Purcell, W.R., 1949. Capillary Pressures - Their Measurement Using Mercury and the Calculation of Permeability Therefrom.

Puri, B.R., 1966. Chemisorbed oxygen evolved as carbon dioxide and its influence on surface reactivity of carbons. Carbon, 4(3): 391-400.

Pusch, G., Hoffmann, M., Miehe, R., Schweitzer, P., Siebert, J., 1985. Untersuchungen zur Permeabilität und Porosität von Steinkohlen und Stimulation der Kohlepermeabilität durch Elektroosmose und Extraktion mittels überkritischem CO2 - Stand der Forschung. K2G - Status - Kolloquium, Essen, 3.10.1985: 115-131.

Reeves, S., Gonzalez, R., Gasem, K.A.M., Fitzgerald, J.E., Pan, Z., Sudibandriyo, M. and Robinson Jr., R.L., 2005. Measurement and Prediction of Single- and Multi-Component Methane, Carbon Dioxide and Nitrogen Isotherms for U.S. Coals, ICBM Symposium Tuscaloosa, Tuscaloosa, Alabama.

Reeves, S., Taillefert, A., Pekot, L. and Clarkson, C., 2003. The Allison Unit CO2 - ECBM Pilot: A Reservoir Modeling Study, Topical Report, U.S. Department of Energy (DE-FC26-0NT40924)

Ren, Q.Y., Chen, G.J., Yan, W. and Guo, T.-M., 2000. Interfacial Tension of (CO2 + CH4) + Water from 298 K to 373 K and Pressures up to 30 MPa. J. Chem. Eng. Data 45: 610-612.

Reucroft, P.J., Patel, H., 1986. Gas-induced swelling in coal. Fuel, 65: 816-820.

Reznik, A.A., Singh, P.K. and Foley, W.L., 1984. An analysis of the effect of CO2 injection on the recovery of in-situ methane from bituminous coal: an experimental simulation, Society of Petroleum Engineers (SPE 10822).

Rice, D.D., 1993. Composition and origins of coalbed gas. In: B.E. Law, Rice, D.D (Editor), Hydrocarbons from coal. AAPG studies in Geology, 38: 159-184.

Rice, D.D., Law, B.E. and Clayton, J.L., 1993. Coalbed gas - an undeveloped resource. US Geological Survey Professional Paper, 1570: 389-404.

Romanov, V.N., Cygan, R.T., Howard, B.H., Myshakin, E.M. and Guthrie, G.D., 2010. Mechanisms of CO2 interaction with expansive clay, Proceedings of the 2010 SEA-CSSJ-CMS Trilateral Meeting on Clays, Seville, Spain.

Rose, W. and Bruce, W.A., 1949. Evaluation Of Capillary Character In Petroleum Reservoir Rock. Petroleum Transactions, AIME, 186: 127-142.

Rosenbauer, R.J., Koksalan, T. and Palandri, J.L., 2005. Experimental investigation of CO2-brine-rock interactions at elevated temperature and pressure: Implications for CO2 sequestration in deep-saline aquifers. Fuel Processing Technology, 86(14-15): 1581-1597.

Rother, G., Ilton, E.S., Wallacher, D., Hauss, T., Schaef, H.T., Qafoku, O., Rosso, K.M., Felmy, A.R., Krukowski, E.G., Stack, A.G., Grimm, N. and Bodnar, R.J., in press. CO2 Sorption to Subsingle Hydration Layer Montmorillonite Clay Studied by Excess Sorption and Neutron Diffraction Measurements. Environmental Science & Technology.

Rubes, M., Kysilka, J., Nachtigall, P. and Bludski, O., 2010. DFT/CC investigation of physical adsorption on a graphite (0001) surface. Physical Chemistry Chemical Physics, 12(24): 6438-6444.

Rubes, M., Nachtigall, P., Vondrasek, J. and Bludsky, O., 2009. Structure and Stability of the Water-Graphite Complexes. The Journal of Physical Chemistry C, 113(19): 8412-8419.

Ruckenstein, E., Vaidyanathan, S. and Youngquist, G.R., 1971. Sorption by solids with bidisperse pore structure. Chem. Eng. Science, 26: 1305-1318.

Rudd, N. and Pandey, G.N., 1973. Threshold pressure profiling by continuous injection, SPE Technical Conference and Exhibition, Las Vegas, Nevada.

Ryan, B. and Richardson, D., 2002. The potential for CO2 sequestration in British Columbia coal seams, British Columbia Geological Survey, pp. 20.

Saghafi, A., Faiz, M. and Roberts, D., 2007. CO2 storage and gas diffusivity properties of coals from Sydney Basin, Australia. International Journal of Coal Geology, 70(1-3): 240-254.

Sakurovs, R., Day, S. and Weir, S., 2009. Causes and consequences of errors in determining sorption capacity of coals for carbon dioxide at high pressure. International Journal of Coal Geology, 77(1-2): 16-22.

Sakurovs, R., Day, S., Weir, S. and Duffy, G., 2007. Application of a Modified Dubinin-Radushkevich Equation to Adsorption of Gases by Coals under Supercritical Conditions. Energy and Fuels, 21: 992-997.

Sakurovs, R., Day, S., Weir, S. and Duffy, G., 2008. Temperature dependence of sorption of gases by coals and charcoals. International Journal of Coal Geology, 73(3-4): 250-258.

Salame, I.I. and Bandosz, T.J., 1998. Experimental Study of Water Adsorption on Activated Carbons. Langmuir, 15(2): 587-593.

Salame, I.I. and Bandosz, T.J., 1999. Study of Water Adsorption on Activated Carbons with Different Degrees of Surface Oxidation. Journal of Colloid and Interface Science, 210(2): 367-374.

Salame, I.I. and Bandosz, T.J., 2000. Adsorption of Water and Methanol on Micro- and Mesoporous Wood-Based Activated Carbons. Langmuir, 16(12): 5435-5440.

Schaef, H.T., Ilton, E.S., Qafoku, O., Martin, P.F., Felmy, A.R. and Rosso, K.M., 2012. In situ XRD study of Ca2+ saturated montmorillonite (STX-1) exposed to anhydrous and wet supercritical carbon dioxide. International Journal of Greenhouse Gas Control, 6: 220-229.

Schlömer, S., 1998. Abdichtungseigenschaften pelitischer Gesteine: Experimentelle Charakterisierung und geologische Relevanz, 212 pp.

Schlömer, S. and Krooss, B.M., 1997. Experimental characterisation of the hydrocarbon sealing efficiency of cap rocks. Marine and Petroleum Geology, 14: 565-580.

Schlömer, S. and Krooss, B.M., 2004. Molecular transport of methane, ethane nd nitrogene and the influence of diffusion on the chemical and isotopic composition of natural gas accumulations. Geofluids, 4: 81-108.

Schoenherr, J., Littke, R., Urai, J.L., Kukla, P.A. and Rawahi, Z., 2007. Polyphase thermal evolution in the Infra-Cambrian Ara Group (South Oman Salt Basin) as deduced by maturity of solid reservoir bitumen. Organic Geochemistry, 38(8): 1293-1318.

Schowalter, T.T., 1979a. Mechanics of secondary hydrocarbon migration and entrapment. AAPG Bulletin, 63(5): 723-760.

Schowalter, T.T., 1979b. Mechanics of Secondary Hydrocarbon Migration and Entrapment. AAPG Bulletin, 63(5): 723-760.

Scott, A.R., 2002. Hydrogeologic factors affecting gas content distribution in coal beds. International Journal of Coal Geology, 50(1-4): 363-387.

Scott, S., Anderson, B., Crosdale, P., Dingwall, J. and Leblang, G., 2007. Coal petrology and coal seam gas contents of the Walloon Subgroup - Surat Basin, Queensland, Australia. International Journal of Coal Geology, 70(1-3 SPEC. ISS.): 209-222.

Scottish Carbon Capture and Storage, 2013. CCS - the full chain. http://www.sccs.org.uk/education/downloads/ccs-fullchain.png (May 9th, 2013).

Seewald, H. and Klein, J., 1986. Methansorption an Steinkohle und Kennzeichnung der Porenstruktur. Glückauf-Forschungshefte, 47(3): 149-156.

Senglaub, Y., Brix, M.R., Adriasola, A. and Littke, R., 2005a. New insights into the thermal history of the southwestern lower Saxony basin. Neue Einblicke in die thermische Geschichte des sÃ¼dwestlichen NiedersÃ¤chsischen Beckens, 121(7-8): 296-299.

Senglaub, Y., Brix, M.R., Adriasola, A.C. and Littke, R., 2005b. New information on the thermal history of the southwestern Lower Saxony Basin, northern Germany, based on fission track analysis. International Journal of Earth Sciences, 94(5-6): 876-896.

Senglaub, Y., Littke, R. and Brix, M.R., 2006. Numerical modelling of burial and temperature history as an approach for an alternative interpretation of the Bramsche anomaly, Lower Saxony Basin. International Journal of Earth Sciences, 95(2): 204-224.

Setzmann, U. and Wagner, W., 1991. A new equation of state and tables of thermodynamic properties for methane covering the range from the melting line to 625 K at pressures up to 1000 MPa. Journal of Physical and Chemical Reference Data, 20: 1061-1155.

Shah, V., Broseta, D. and Mouronval, G., 2008. Capillary Alteration of Caprocks by Acid Gases, Symposium on Improved Oil Recovery SPE/DOE Tulsa, Oklahoma, pp. 11.

Shi, J.-Q. and Durucan, S., 2003a. Gas Storage and Flow in Coalbed Reservoirs: Implementation of a Bidisperse Pore Model for Gas Diffusion in Coal Matrix. SPE, 84342: 1-9.

Shi, J.Q. and Durucan, S., 2003b. A bidispere pre diffusion model for methane displacement desorption in coal by CO2 injection. Fuel, 82: 1219-1229.

Shieh, J.-J. and Chunh, T.S., 1999. Gas permeability, diffusivity, and solubility of Poly (4-Vinylpyridine) film. Journal of Polymer Science, 37: 2851-2861.

Shiraki, R. and Dunn, T.L., 2000. Experimental study on water-rock interactions during CO2 flooding in the Tensleep Formation, Wyoming, USA. Applied Geochemistry, 15(3): 265-279.

Siemons, N. and Busch, A., 2007. Measurement and interpretation of supercritical CO2 sorption on various coals. International Journal of Coal Geology, 69(4): 229-242.

Siemons, N., Wolf, K.-H.A.A. and Bruining, J., 2007. Interpretation of carbon dioxide diffusion behavior in coals. International Journal of Coal Geology, 72(3-4): 315-324.

Sircar, S., 1992. Estimation of isosteric heats of adsorption of single gas and multicomponent gas mixtures. Ind. Eng. Chem. Res., 31: 1813-1819.

Sircar, S., 1999. Gibbsian Surface Excess for Gas Adsorptions Revisited. Ind. Eng. Chem. Res., 38: 3670-3682.

Smith, D.M. and Williams, F.L., 1984a. Diffusion models for gas production from coal: Determination of diffusion parameters. Fuel, 63(2): 256-261.

Smith, D.M. and Williams, F.L., 1984b. Diffusion models for gas production from coals-Application to Methane content determination. Fuel, 63: 251-255.

Smith, D.M. and Williams, F.L., 1984c. Diffusional effects in the recovery of methane from coalbeds. SPE, 10821: 529-541.

Soares, J.L., Oberziner, A.L.B., Jose, H.J., Rodrigues, A.E., Moreira, R.F.P.M., 2007. Carbon Dioxide Adsorption in Brazilian Coals. Energy and Fuels, 21: 209-215.

Span, R. and Wagner, W., 1996. A new equation of state for carbon dioxide covering the fluid region from the triple-point temperature to 1100 K at pressures up to 800 MPa. Journal of Physical and Chemical Reference Data, 25(6): 1509-1596.

Sperrevik, S., Gillespie, P.A., Fisher, Q.J., Halvorsen, T., Knipe, R.J., Andreas, G.K. and Robert, H., 2002. Empirical estimation of fault rock properties, Norwegian Petroleum Society Special Publications. Elsevier, Volume 11: 109-125.

Srodon, J., 2010. Quantification of illite and smectite and their layer charges in sandstones and shales from shallow burial depth. Clay Miner., 44: 421-434.

Stach, E., Mackowsky, M.-T., Teichmuller, M., Taylor, G., Chandra, D. and Teichmuller, R., 1982. Stach's Textbook of Coal Petrology, 3rd edition. Gebruder Borntraeger, Berlin.

Steefel, C.I., DePaolo, D.J. and Lichtner, P.C., 2005. Reactive transport modeling: An essential tool and a new research approach for the Earth sciences. Earth and Planetary Science Letters, 240(3â€“4): 539-558.

Stoeckli, H.F., 1990. Microporous carbons and their characterization: The present state of the art. Carbon, 28(1): 1-6.

Streit, J.E. and Watson, M.N., 2004. Estimating Rates of Potential CO2 Loss from Geological Storage Sites for Risk and Uncertainty Analysis, 7th International Conference on Greenhouse Gas Control Technologies, Vancouver, Canada.

Struckmeier, W., 1990. Wasserhaushalt und Hydrologische Systemanalyse des Münsterländer Beckens

Suárez, N., Laredo, E. and Nava, R., 1993. Characterization of four hydrophilic sites in bituminous coal by ionic thermal current measurements. Fuel, 72(1): 13-18.

Sudibandriyo, M., Fitzgerald, J.E., Pan, Z., Robinson, J., R.L. and Gasem, K.A.M., 2002. Measurements and modeling of gas adsorption on selected coals. Langmuir, 19: 5323-5331.

Sudibandriyo, M., Pan, Z., Fitzgerald, J.E., Robinson Jr., R.L. and Gasem, K.A.M., 2003. Adsorption of Methane, Nitrogen, Carbon Dioxide, and Their Binary Mixtures on Dry Activated Carbon at 318.2 K and Pressures up to 13.6 MPa. Langmuir, 19: 5323-5331.

Suess, E. and Whiticar, M.J., 1989. Methane-derived CO2 in pore fluids expelled from the Oregon subduction zone. Palaeogeography, Palaeoclimatology, Palaeoecology, 71(1-2): 119-136.

Suuberg, E.M., Otake, Y, Yun, Y & Deevi, S.C., 1993. Role of moisture in coal structure and the effect of drying upon the accessibility of coal structure. Energy & Fuels, 7: 384-392.

Tang, Y., Jenden, P.D., Nigrini, A. and Teerman, S.C., 1996. Modeling Early Methane Generation in Coal. Energy & Fuels, 10(3): 659-671.

Taraba, B., 2011. Flow calorimetric insight to competitive sorption of carbon dioxide and methane on coal. Thermochimica Acta, 523(1-2): 250-252.

Thomas, L.K., Katz, D.L. and Tek, M.R., 1968. Threshold Pressure Phenomena in Porous Media. 8(2): 174 - 184.

Tonnet, N., Broseta, D., F. and Mouronval, G., 2010. Evaluation of petrophysical properties of a carbonate-rich caprock for CO2 geological storage purposes, SPE EUROPEC/EAGE Annual Conference and Exhibition. Society of Petroleum Engineers, Barcelona, Spain.

Ufer, K., Roth, G., Kleeberg, R., Stanjek, H., Dohrmann, R. and Bergmann, J., 2004. Description of X-ray patterns of turbostratically disordered layer structures with a Rietveld compatible approach. Z. Kristallogr, 219: 519-527.

Ulberg, D.E. and Gubbins, K.E., 1995. Water adsorption in microporous graphitic carbons. Molecular Physics: An International Journal at the Interface Between Chemistry and Physics, 84(6): 1139 - 1153.

United Nations, 1998. Kyoto Protocol To The United Nations Framework

Unsworth, J.F., Fowler, C.S. and Jones, L.F., 1989. Moisture in coal - 2. Maceral effects on pore structure. Fuel, 68: 18-26.

US DOE/EIA, 2011. World Shale Gas Resources: An Initial Assessment of 14 Regions Outside the United States, US DOE/EIA, Washington, DC

van Bergen, F., Krzystolik, P., van Wageningen, N., Pagnier, H., Jura, B., Skiba, J., Winthaegen, P. and Kobiela, Z., 2009a. Production of gas from coal seams in the Upper Silesian Coal Basin in Poland in the post-injection period of an ECBM pilot site. International Journal of Coal Geology, 77: 175-187.

van Bergen, F., Pagnier, H. and Krzystolik, P., 2006. Field experiment of enhanced coalbed methane-CO2 in the Upper Silesian basin of Poland. Environmental Geoscience, 13: 201–224.

van Bergen, F., Pagnier, H.J.M., Krooss, B.M. and van der Meer, L.G.H., 2001. CO2-sequestration in the Netherlands: inventory of the potential for the combination of subsurface carbon dioxide disposal with enhanced coalbed methane production, Proceedings of the 5th International Conference on Greenhouse Gas Control Technologies. CSIRO Publishing, pp. 555-560.

van Bergen, F., Spiers, C., Floor, G. and Bots, P., 2009b. Strain development in unconfined coals exposed to CO2, CH4 and Ar: Effect of moisture. International Journal of Coal Geology, 77(1-2): 43-53.

van Hemert, P., Bruining, H., Rudolph, E.S.J., Wolf, K.-H.A.A. and Maas, J.G., 2009. Improved manometric setup for the accurate determination of supercritical carbon dioxide sorption. Review of Scientific Instruments, 80(3): 035103-11.

van Hemert, P., Rudolph-Floter, S., Wolf, K.-H., A. A. and Bruining, J., 2010. Estimate of Equation of State Uncertainty for Manometric Sorption Experiments: Case Study With Helium and Carbon Dioxide. SPE Journal, 15(1): pp. 146-151.

van Hemert, P., Wolf, K.-H.A.A. and Bruining, J., 2007. The Intrinsic Reliability of Manometric Sorption Apparatus Using Supercritical Carbon Dioxide, SPE Annual Technical Conference and Exhibition, Anaheim, CA, pp. 11.

van Krevelen, D.W., 1993. Coal: Typology-Physics-Chemistry-Constitution. Elsevier, 1002 pp.

Vandamme, M., Brochard, L., Lecampion, B. and Coussy, O., 2010. Adsorption and strain: The CO2-induced swelling of coal. Journal of the Mechanics and Physics of Solids, 58(10): 1489-1505.

Vavra, C.L., Kaldi, J.G. and Sneider, R.M., 1992. Geological application of capillary pressure: A review. AAPG Bulletin, 76(6): 840-850.

Venaruzzo, J.L., Volzone, C., Rueda, M.L. and Ortiga, J., 2002. Modified bentonitic clay minerals as adsorbents of CO, CO2 and SO2 gases. Microporous and Mesoporous Materials, 56: 73-80.

Vivian, J.E. and King, C.J., 1964. Diffusivities of slightly soluble gases in water. AIChE Journal, 10(2): 220-221.

Volzone, C. and Ortiga, J., 2000. O2, CH4 and CO2 gas retentions by acid smectites before and after thermal treatment. Journal of Materials Science, 35: 5291 – 5294.

Volzone, C. and Ortiga, J., 2005. Removal of gases by thermal-acid leached kaolinitic clays: Influence of mineralogical composition. Applied Clay Science.

Volzone, C., Rinaldi, J.O. and Ortiga, J., 2006. Retention of gases by hexadecyltrimethylammonium–montmorillonite clays. Journal of Environmental Management, 79: 247-252.

von Treskow, A., 1985. Die Zusammenhänge zwischen dem Gasinhalt und der Geologie im Ruhrrevier. Glückauf 121: 1747-1755.

Wagner, W. and Pruss, A., 1993. International Equations for the Saturation Properties of Ordinary Water Substance. Revised According to the International Temperature Scale of 1990. Addendum to J. Phys. Chem. Ref. Data, 893 (1987). Journal of Physical and Chemical Reference Data, 22(3): 783-787.

Walker Jr., P.L. and Mahajan, O.P., 1993. Pore structure in coals. Energy and Fuels, 7: 559-560.

Walker Jr., P.L., Verma, S.K., Rivera-Utrilla, J., Davis, A., 1988. Densities, porosities and surface areas of coal macerals as measured by their interaction with gases, vapours and liquids. Fuel, 67: 1615-1623.

Walter, R., 1992. Geologie von Mitteleuropa, 561. E. Schweitzer Bartsche Verlagsbuchhandlung, Stuttgart.

Weast, R.C., 1972. Handbook of Chemistry and Physics (53rd Edn.). Chemical Rubber Co., Cleveland.

Weidmann, M., 2005. Methan führende Grundwässer im nördlichen Gemeindegebiet von Everswinkel (Kreis Warendorf), University of Hannover.

Weishauptová, Z. and Sýkorová, I., 2011. Dependence of carbon dioxide sorption on the petrographic composition of bituminous coals from the Czech part of the Upper Silesian Basin, Czech Republic. Fuel, 90(1): 312-323.

Weniger, P., 2012. Thermal and microbial gas generation, accumulation and dissipation in coal basins : role of sorptive storage capacity evolution, RWTH Aachen University, Aachen, Germany.

Weniger, P., Kalkreuth, W., Busch, A. and Krooss, B.M., 2010. High-pressure methane and carbon dioxide sorption on coal and shale samples from the Paraná Basin, Brazil. International Journal of Coal Geology, 84: 190-205.

White, C.M., Smith, D.H., Jones, K.L., Goodman, A.L., Jikich, S.A., LaCount, R.B., DuBose, S.B., Ozdemir, E., Morsi, B.I. and Schroeder, K.T., 2005. Sequestration of Carbon Dioxide in Coal with Enhanced Coalbed Methane Recoverys: A Review. Energy and Fuel, 19(3): 659-724.

Wiegand, G. and Franck, E.U., 1994. Interfacial tension between water and non-polar fluids up to 473 K and 2800 bar. Ber. Bunsenges. Phys. Chem., 98: 809-817.

Wigand, M., Carey, J.W., Schütt, H., Spangenberg, E. and Erzinger, J., 2008. Geochemical effects of CO2 sequestration in sandstones under simulated in situ conditions of deep saline aquifers. Applied Geochemistry, 23(9): 2735-2745.

Wolf, K.-H.A.A., Barzandji, O.H. and Bruining, J., 1999. Laboratory experiments and simulations on the environmentally friendly improvement of Coalbed Methane production by Carbondioxide injection. Int. CBM Symposium, Univ. of Alabama, Tuscaloosa: 279-290.

Wolf, K.H.A.A., Barzandji, O.H.M., Bertheux, W. and Bruining, J., 2000. CO2-sequestration in The Netherlands. CO2-injection and CH4-production as related to the Dutch situation: Laboratory experiments and field simulation, GHGT-5, Cairns, Australia, pp. 6.

Wollenweber, J., Alles, S., Busch, A., Krooss, B.M., Stanjek, H. and Littke, R., 2010. Experimental investigation of the CO2 sealing efficiency of caprocks. International Journal of Greenhouse Gas Control, 4(2): 231-241.

Wollenweber, J., Alles, S.a., Kronimus, A., Busch, A., Stanjek, H. and Krooss, B.M., 2009. Caprock and overburden processes in geological CO2 storage: An experimental study on sealing efficiency and mineral alterations. Energy Procedia, 1(1): 3469-3476.

Wong, S., Law, D., Deng, X., Robinson, J., Kadatz, B., Gunter, W.D., Jianping, Y., Sanli, F. and Zhiqiang, F., 2007. Enhanced coalbed methane and CO2 storage in anthracitic coals--Micro-pilot test at South Qinshui, Shanxi, China. International Journal of Greenhouse Gas Control, 1(2): 215-222.

Wyllie, M.R.J. and Rose, W., D., 1950. Some Theoretical Considerations Related To The Quantitative Evaluation Of The Physical Characteristics Of Reservoir Rock From Electrical Log Data. Petroleum Transactions, AIME, 189: 105-118.

Yalcin, E. and Durucan, S., 1991. Methane capacities of Zonguldak coals and the factors affecting methane adsorption. Mining Science and Technology, 13: 215-222.

Yamaguchi, S., Ohga, K., Fujioka, M. and Muto, S., 2004. Prospect of CO2 sequestration in the Ishikara coal field, Japan, 7th International Conference on Greenhouse Gas Control Technology, Vancouver, Canada.

Yan, W., Zhao, G.Y., Chen, G.J. and Guo, T.M., 2001. Interfacial Tension of (Methane + Nitrogen) + Water and (Carbon Dioxide + Nitrogen) + Water Systems. J. Chem. Eng. Data, 46(6): 1544-1548.

Yang, D., Gu, Y. and Tontiwachwuthikul, P., 2007. Wettability Determination of the Reservoir Brine - Reservoir Rock System with Dissolution of CO2 at High Pressures and Elevated Temperatures. Energy & Fuels, 22(1): 504-509.

Yang, D., Tontiwachwuthikul, P. and Gu, Y., 2005. Interfacial Interactions between Reservoir Brine and CO2 at High Pressures and Elevated Temperatures. Energy and Fuels, 19: 216-223.

Yang, R.T. and Saunders, J.T., 1985. Adsorption of gases on coals and heattreated coals at elevated temperature and pressure: 1. Adsorption from hydrogen and methane as single gases. Fuel, 64(5): 616-620.

Yang, X. and Zhang, C., 2005. Structure and diffusion behavior of dense carbon dioxide fluid in clay-like slit pores by molecular dynamics simulation. Chemical Physics Letters, 407(4-6): 427-432.

Yang, Y. and Aplin, A.C., 1998. Influence of lithology and compaction on the pore size distribution and modelled permeability of some mudstones from the Norwegian margin. Marine and Petroleum Geology, 15(2): 163-175.

Yang, Y. and Aplin, A.C., 2004. Definition and practical application of mudstone porosity-effective stress relationships. Petroleum Geoscience, 10(2): 153-162.

Yang, Y. and Aplin, A.C., 2007. Permeability and petrophysical properties of 30 natural mudstones. J. Geophys. Res., 112.

Yang, Y. and Aplin, A.C., 2010. A permeability-porosity relationship for mudstones. Marine and Petroleum Geology, 27(8): 1692-1697.

Yee, D., Seidle, J.P. and Hanson, W.B., 1993. Gas Sorption on Coal and Measurements of Gas Content. In: B.E. Law and D.D. Rice (Editors), Hydrocarbons from coal. AAPG Studies in Geology, 38: 203-218.

Yi, J., Akkutlu, I.Y. and Deutsch, C.V., 2008. Gas Transport in Bidisperse Coal Particles: Investigation for an Effective Diffusion Coefficient in Coalbeds. Journal of Canadian Petroleum Technology, 47(10): 20-26.

Yu, H., Guo, W., Cheng, J. and Hu, Q., 2008a. Impact of experimental parameters for manometric equipment on CO2 isotherms measured: Comment on "Inter-laboratory comparison II: CO2 isotherms measured on moisture-equilibrated Argonne premium coals at 55°C and up to 15 MPa" by Goodman et al. (2007). International Journal of Coal Geology, 74(3-4): 250-258.

Yu, H., Yuan, J., Guo, W., Cheng, J. and Hu, Q., 2008b. A preliminary laboratory experiment on coalbed methane displacement with carbon dioxide injection. International Journal of Coal Geology, 73(2): 156-166.

Yu, L. and Wardlaw, N.C., 1986. The influence of wettability and critical pore-throat size ratio on snap-off. Journal of Colloid and Interface Science, 109(2): 461-472.

Zalãn, P.V., Wolff, S., Astolfi, M., Vieira, I., Concelção, J., Appi, V., Neto, E., Cerqueira, J. and Marques, A., 1991. The Paraná Basin, Brazil. In: M. Leighton, D. Kolata, D. Oltz and J. Eidel (Editors), Interior Cratonic Basins. AAPG Memoir, 51: 681-708.

Zalãn, P.V., Wolff, S., Conceição, J.C., Marques, A., Astolfi, M.A., Vieira, I.S., Appi, V.T. and Zanotto, O.A., 1990. Bacia do Paraná. In: G.P. Raja Gabaglia and E.J. Milani (Editors), Origem e Evolução das Bacias Sedimentares: Rio de Janeiro. Petrobras: 135-168.

Zhang, T. and Krooss, B.M., 2001. Experimental investigation on the carbon isotope fractionation of methane during gas migration by diffusion through sedimentary rocks at elevated temperature and pressure. Geochimica et Cosmochimica Acta, 65(16): 2723-2742.

Zhao, D., Feng, Z. and Zhao, Y., Laboratory experiment on coalbed-methane desorption influenced by water injection and temperature. Journal of Canadian Petroleum Technology, 50(7-8): 24-33.

Zhou, W., Stenhouse, M., Sheppard, M. and Walton, F., 2004. Theme 4: Long-Term Risk Assessment of the Storage Site, Petroleum Technology Research Centre, Regina, pp. 211-268.

Zweigel, P., Lindeberg, E., Moen, A. and Wessel-Berg, D., 2004. Towards a methodology for top seal efficacy assessment for Underground CO2 Storage, 7th International Conference on Greenhouse Gas Control Technologies (GHGT-7). Vancouver, Canada.